Coordination Chemistry of Fe–S Clusters Supported by *N*-Heterocyclic Carbenes

by

Alexandra C. Brown

B.S. Chemistry
University of California at Berkeley, 2017

Submitted to the Department of Chemistry
In Partial Fulfillment of the Requirements for the Degree of

Doctor of Philosophy in Chemistry

at the
Massachusetts Institute of Technology

June 2023

Authored by: Alexandra C. Brown
Department of Chemistry
May 12th, 2023

Certified by: Professor Daniel L. M. Suess
Associate Professor of Chemistry
Thesis Supervisor

Accepted by: Professor Adam P. Willard
Associate Professor of Chemistry
Graduate Officer

This thesis has been examined by a committee of the
Department of Chemistry as follows:

Mircea Dincă
W. M. Keck Professor of Energy
Thesis Committee Chair

Daniel. L. M. Suess
Associate Professor of Chemistry
Thesis Supervisor

Christopher C. Cummins
Henry Dreyfus Professor
Thesis Committee Member

Coordination Chemistry of Fe–S Clusters Supported by *N*-Heterocyclic Carbenes

By

Alexandra C. Brown

Submitted to the Department of Chemistry on May 12, 2023 in Partial Fulfilment of the Requirements for the Degree of Doctor of Philosophy in Chemistry

ABSTRACT

Iron–sulfur clusters are ubiquitous in Nature and carry out some of the most challenging multielectron redox reactions in the biosphere while utilizing three primary building blocks: Fe^{2+}, Fe^{3+}, and S^{2-}. Studying synthetic Fe–S clusters aids in understanding the underlying properties of Fe–S clusters that enable this reactivity by providing Fe–S clusters with unusual coordination spheres that are amenable to multiple modes of structural and spectroscopic characterization. Synthetic Fe–S cluster chemistry is hindered by poor control over the coordination sphere of metalloclusters as compared to mononuclear complexes: the large size of metalloclusters means changing the ligand at one metal site often has little effect on the neighboring sites. Here, we introduce a strategy based on the remote steric profiles of ligands on adjacent metal sites (here, monodentate *N*-heterocyclic carbenes), to obtain $[Fe_4S_4]$ clusters for which subsequent reactivity can be localized to a single Fe site. That is, the steric bulk of di-aryl NHC ligands enables isolation of $[Fe_4S_4]$ clusters in which three of the Fe centers are coordinated to NHCs and that further ligand exchange reactivity is localized to the unique Fe site. Following the establishment of this site-differentiation strategy, we demonstrate its application to several outstanding problems in Fe–S cluster chemistry. First, we demonstrate that Fe–S clusters are able to bind and activate π-acidic ligands like CO, resolving the disconnection between the reactivity of Fe–S clusters and the typical reactivity of high-spin, mid-valent Fe centers by showing that Fe–S clusters can access low-valent states which have sufficient π-basicity to activate CO. We expand this chemistry to electronically tunable aryl isocyanide ligands and demonstrate that Fe–S clusters can access multiple electron configurations with varying capacity for π-backbonding, highlighting the importance of Fe–Fe interactions within an Fe–S cluster for tuning the Fe valences and binding π-acidic ligands. We next synthesize an $[Fe_4S_4]$ cluster supported by a bulkier NHC ligand and demonstrate that it can be reduced to reveal a three-coordinate Fe site with no apparent affinity for N_2. Driven by the lack of N_2 affinity in the $[Fe_4S_4]$ cluster—in contrast to $[MoFe_3S_4]$ clusters—we next explore binding of CO at $[MoFe_3S_4]$ clusters to understand the effects of Mo incorporation on intracluster bonding; comparisons between these clusters and analogous $[Fe_4S_4]$–CO clusters reveals that the $[MoFe_3S_4]$–CO clusters exhibit attenuated changes to their structures and spectra over redox events. This suggests that Mo may increase the covalency within the cluster, potentially making access to these low valent states more facile. Lastly, we introduce three studies aimed at modelling biological Fe–S cluster chemistry: revealing reversible homolytic Fe–C bond cleavage at Fe–S clusters to release alkyl radicals and modeling its effects on the selectivity of radical reactions, synthesizing alkene- and alkyne-bound Fe–S clusters, and abstracting Fe^{2+} from $[Fe_4S_4]$ clusters to access the first synthetic $[Fe_3S_4]^+$ clusters.

Thesis supervisor: Daniel L. M. Suess

Title: Associate Professor of Chemistry

Acknowledgements

First and foremost, I want to thank my advisor, Professor Dan Suess, for his mentorship and help in carrying out the work detailed in this thesis. Joining a new research lab as a first-year graduate student was a nerve-wracking decision, but since then I have realized how lucky I was to have had Dan as an advisor. Dan has been a caring and thoughtful mentor over the past six years, and I have learned a tremendous amount from him; his passion and excitement for chemistry has been inspiring and critical to making the Suess lab into the vibrant and exciting place to work that it has been for me. Dan, you have taught me a great deal not only about doing synthetic chemistry, but also about extracting the maximum amount of information from each experiment and about tying a complete research project together. I have learned so much about writing and presenting from you; thank you for putting so much care and attention into helping me improve every document and presentation I have sent you. So much of what I have learned about being a scientist has come from you and I am so fortunate to have had a mentor who has shaped my perspective on chemistry so thoroughly.

Thank you also to my committee, Professor Kit Cummins and Professor Mircea Dincă, for your support and insights over the years; both of you have been a tremendous help in completing this thesis. Thank you Mircea for always keeping me focused on the bigger picture and thank you Kit for your ideas and contributions to my graduate research at several key points. I am very thankful for both of your support of my research as a graduate student and of my professional goals after graduate school.

I have gotten to see the Suess lab grow from the beginning over the past six years, and as a result have had the opportunity to work with many talented and kind colleagues. To the first five students who joined the lab at the same time as me—Dr. Mengshan Ye, Dr. Arun Sridharan, Soop Srisantitham, Ed Badding, and Joe Roddy—thank you all for your bravery and teamwork in getting started as a lab. I am so lucky I got to work with a group of such dedicated and passionate chemists for so many years. Mengshan, thank you for being the best glovebox mate and for keeping perfectly aligned schedules to accommodate both of our highly solvent sensitive work; I am looking forward to seeing everything you do at Berkeley. Arun, you are one of the most precise and artistic people I've gotten to work with, thank you for improving all our figures and for your dedication to making us go out as a lab for dinner together as often as possible. Joe, thank you for bringing some levity to the lab in our early years. Soop, I admire your dedication to both long experiments and to putting our volleyball team on your back. Ed, thank you for being one of my closest friends and for accompanying me for coffee and walks outside constantly despite not even drinking coffee. The summer in this lab before our first year has become one of my favorite memories of graduate school, in part because it was so much fun working with you and learning about chemistry from a completely different perspective than I had heard before—and because we (luckily) ended up becoming fast friends.

In the list of people who joined around the same time as me, I also want to include our first postdocs, Dr. Alex McSkimming and Dr. Niklas Thompson; thank you both for your patience and juggling mentoring six first-year students at the same time. Alex, having the opportunity to learn from your synthetic experience has certainly helped the development of my laboratory skills. Nik, thank you for your patient explanations of different topics in electronic structure and math and for all of your support in the early years of my Ph.D., especially in demonstrating how to establish and communicate on collaborative projects. Your experience in the lab and willingness to help all

of us with computational and Mössbauer experiments was incredibly educational for me and I am glad that we got to work on some of this thesis together.

To the graduate students and postdocs who have joined the lab in the years since—Trever Bostelaar, Gil Namkoong, Brighton Skeel, Jess Kim, Brittany Linn, Hyunsoo Kim, Dr. Young Kim, Dr. Madeleine Ehweiner, and Dr. Mackenzie Field—I have enjoyed working with you all and am excited to see where you take your projects in the future. Thank you all for being outstanding colleagues and for all of the fun we have had together. In particular to everyone who helped our lab weather the pandemic years, thank you for keeping my spirits up and finding chances for us to talk and laugh with each other even when we couldn't be in lab. To the undergrads who have joined our lab, Anna Bair and Josh Lian, thank you for bringing so much enthusiasm and energy to our lab. In particular to Anna, it was wonderful getting to work with you and see you grow as a scientist over the last several years. I am so excited to see everything you accomplish as a graduate student.

To the staff at MIT who have dedicated their time to ensuring the equipment I need to carry out my experiments is running smoothly, thank you for your ceaseless work, creativity, and patience over the years. To Dr. Peter Müller, thank you for keeping the X-ray diffraction facility running and for your excitement and work in solving each unexpected problem I ran into with my data sets. To the staff of the DCIF, Dr. Walt Massefski, Dr. Bruce Adams, and John Grimes, thank you for keeping the DCIF as one of the most well-run shared facilities I have ever encountered. Walt, thank you for listening to all our lab's concerns and needs for NMR and EPR and for figuring out a solution or compromise for any problem we ran into. John, thank you for the same and for introducing our lab to solvent-suppressed NMR, which has been an absolute lifesaver for our research. Bruce, thank you for your excitement at developing new NMR experiments whenever needed; your patience and effort solved many of my NMR problems in ways I never would have known were possible.

My graduate research has been supported by fellowships from the Fannie and John Hertz Foundation as well as the National Science Foundation, and I am appreciative both of the funding support and of the friendships I have made through the Hertz foundation.

I also want to thank my mentors and coworkers from Berkeley who helped me over my very first experiences in research and gave me the confidence to move to MIT for graduate school. Professor John Arnold and his group made an incredibly welcoming place for me as an undergraduate student, and I am so appreciative of the time they spent teaching me as a young student and for their friendship. My mentor as an undergraduate, Professor Alison Altman, was endlessly supportive and patient. Alison, I am so happy that we eventually crossed paths at MIT and that I can now see you start as a professor; your mentorship of me as an undergrad was crucial to everything that has happened since.

There are many people in Boston who have been my friends over my time in graduate school. In particular, I want to thank Katherine Taylor for being my roommate and friend and for always having the most interesting topics to discuss—from politics to reality TV shows. Thank you for all of the time we spent together during the pandemic lockdown ordering sushi and watching strange TV shows. I also want to thank my neighbors, Ed Badding, Tim Kunz, Dio Dieppa-Matos, Jackson Ho, and Mike Payne for all the time spent hanging out and cooking at their house over the years. As I already said, Ed has been one of my closest friends in graduate school and I have had a great time cooking (or ordering Dominos) at his house. Thank you also for our rollerskating trips and for driving me to all sorts of restaurants out of the way, especially to Border Café Sagus after the Harvard location closed. I have been glad to have Tim and Dio join on many

of these cooking adventures and am grateful for the many other memories that have been made at their house. Lastly, I want to thank Victoria Marando for being a constant source of support and happiness in my life. Thank you for the adventures and hikes you have planned for us; I am so excited for everything to come in the future.

Finally, I want to thank my family. To my sister, Elizabeth, thank you for being my friend and little sister; your spirit and kindness to those around you inspire me. To my Aunt Fran, thank you for welcoming me into your home as my only family member on the East Coast, and for enabling me to spend holidays with family (and with the best dog, Arthur). I am happy that I will only live a little farther away from you for the next few years. To my parents, Tom and Catherine Brown, thank you for giving me all of the opportunities you could and for encouraging to follow everything I was interested in, even when it meant moving across the country. I will never be able to express how much I appreciate all of your unconditional support and love.

Table of Contents:

Table of Figures:

Table of Schemes:

Table of Tables:

Respective Contributions

Several chapters in this thesis contain work carried out collaboratively with colleagues at MIT and at Cornell University.

Chapters 3 and 4 : This work was done in collaboration with Dr. Niklas B. Thompson. Nik Thompson and the author of this thesis carried out the density functional theory calculations together.

Chapters 6: This work was done in collaboration with Dr. Alex McSkimming and Dr. Samantha N. MacMillan (Cornell). Alex McSkimming developed the syntheses for $Cp^*MoFe_3S_4(IMes)_2Cl$ and $Cp^*MoFe_3S_4(IMes)_3$ and obtained characterization data. Sam MacMillan collected and analyzed the X-ray absorption spectroscopic data.

Chapter 1. Synthetic Iron-Sulfur Clusters

Reproduced with permission from: Alexandra C. Brown and Daniel L. M. Suess "Synthetic Iron–Sulfur Clusters" In *Comprehensive Coordination Chemistry III*; Constable, E., Parkin, G., Que, L., Eds.; Elsevier, 2021. p. 134-156.

1.1 Introduction

Iron–sulfur (Fe–S) clusters are ubiquitous cofactors found in all kingdoms of life. First identified as mediators in electron-transfer reactions,[1,2] Fe–S proteins are now known to perform an incredibly diverse array of reaction chemistry and cellular functions, including serving in regulatory roles, enabling complex radical chemistry, and catalyzing challenging redox reactions.[3,4] Since the discovery of the Fe–S cluster-containing enzymes in the mid-twentieth century,[1,5–11] biochemists, synthetic chemists, spectroscopists, and theoretical chemists have worked in tandem to understand the complex properties and chemistry of these cofactors.[12] Throughout Fe–S cluster research, synthetic chemistry has both supplied tunable, well-defined models of biological cofactors and provided insight into the functions and electronic structures of Fe–S clusters.

In this chapter, we focus on selected advances in the synthetic chemistry of Fe–S clusters since 2003.[13] We first describe advances in synthetic methodology, which have supported much of the subsequent work discussed in this chapter. We next cover Fe–S clusters with unusual electronic structures with an emphasis on spectroscopic studies and parallels to Fe–S clusters in biological systems. Finally, we discuss the expansive organometallic chemistry of Fe–S clusters.

1.2 Developments in synthetic methodology

Biological Fe–S clusters were discovered in the 1960s[1,5–11] and the first synthetic models were reported shortly thereafter.[14] Since then, hundreds of synthetic Fe–S clusters have been prepared.[15–21] New types of Fe–S clusters continue to be found in nature[22–27] and synthesized in the laboratory, including clusters in high oxidation states, with unusual nuclearities and geometries, and/or with novel modes of site-differentiation. These

developments, examples of which are highlighted below, have expanded the coordination and reaction chemistry of Fe–S clusters and have thereby provided a foundation for ongoing efforts to model biological Fe–S clusters and to utilize these cofactors in catalysis.

1.2.1 Use of sterically encumbering ligands to stabilize oxidized clusters and control cluster nuclearity

Sterically encumbering ligands have propelled developments in inorganic and organometallic chemistry for decades, particularly by providing steric protection and/or exerting steric pressure at mononuclear s-, p-, d-, and f-block complexes. Since metalloclusters in general and Fe–S clusters in particular are typically larger than mononuclear coordination compounds, a different ligand steric profile is required to impact the chemistry of the cluster. As such, the design of sterically imposing ligands for Fe–S clusters remains an active area of research. Here, we highlight the role of sterically encumbering ligands in the isolation of oxidized Fe–S clusters and in providing control over cluster nuclearity.

1.2.2 Isolation of $[Fe_4S_4]^{3+}$ and $[Fe_4S_4]^{4+}$ clusters

Two major families of electron-transfer proteins containing $[Fe_4S_4]$ clusters have been discovered: ferredoxins, which operate on the $[Fe_4S_4]^{2+/1+}$ couple, and HiPIPs (high-potential iron-sulfur proteins), which operate on the $[Fe_4S_4]^{3+/2+}$ couple.[28] Whereas many synthetic $[Fe_4S_4]^{2+/1+}$ clusters have been reported, synthetic $[Fe_4S_4]^{3+}$ clusters are comparatively rare; until 2010, the only isolated example with thiolate ligation was $[Fe_4S_4(STrip)_4]^{-}$ (Trip = 2,4,6-triisopropylphenyl).[29]

As an entry to the synthesis of oxidized $[Fe_4S_4]$ clusters, Tatsumi and coworkers as well as Lee and coworkers reported self-assembly reactions yielding $[Fe_4S_4]$ clusters supported by the bulky bis(trimethylsilyl)amide ligand.[30,31] Such clusters have been isolated in the $[Fe_4S_4]^{4+}$ (**1**), $[Fe_4S_4]^{3+}$ ($[\mathbf{1}]^{-}$), and $[Fe_4S_4]^{2+}$ ($[\mathbf{1}]^{2-}$) core charge states; this series provided the second example of an isolated $[Fe_4S_4]^{3+}$ cluster and the first example of an all-ferric $[Fe_4S_4]^{4+}$ cluster

in a weak ligand field (Scheme 1.1). The high oxidation states in these $[Fe_4S_4]$ clusters are stabilized by the strongly donating amide ligands, which also provide steric protection and

Scheme 1.1 Synthesis of oxidized $[Fe_4S_4]$ clusters with thiolate ligands. (A) Synthesis of thiolate-ligated $[Fe_4S_4]^{3+}$ clusters by protonolysis from bis(trimethylsilyl)amide-ligated clusters and synthesis of a site-differentiated $[Fe_4S_4]^{3+}$ cluster. (B) Self-assembly of an all-ferric $[Fe_4S_4]^{4+}$ cluster from a mononuclear precursor.

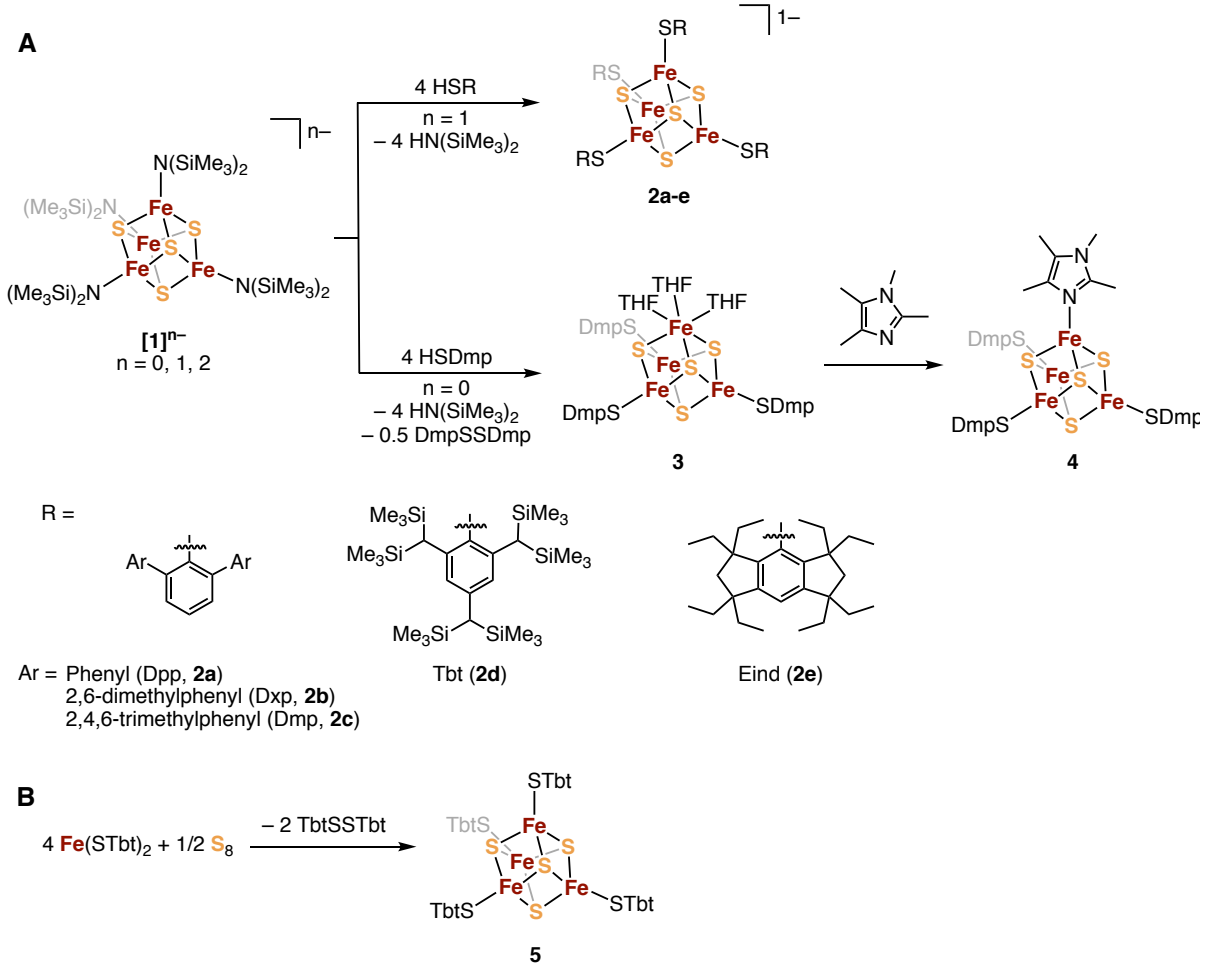

solubility in relatively nonpolar solvents.

Tatsumi and coworkers later reported that $[\mathbf{1}]^-$ could be used as a starting material in protonolysis reactions that generate $[Fe_4S_4]^{3+}$ clusters stabilized by bulky thiolates (**2a-e**, Scheme 1.1A).[32] These clusters, like $[Fe_4S_4(STrip)_4]^-$ and the $[Fe_4S_4]^{3+}$ clusters in HiPIPs, have an $S = 1/2$ ground spin state. The $[Fe_4S_4]^{3+/2+}$ redox couples for **2a-e** shift cathodically with increasing thiolate steric bulk; this was attributed to the bulky thiolate shielding the cluster core from solvent, which destabilizes the more charged $[Fe_4S_4(SR)_4]^{2-}$ (reduced) cluster. Similarly, the $[Fe_4S_4]^{3+}$ clusters in HiPIPs are proposed to be stabilized by a relatively hydrophobic

protein environment.[33,34] For the synthetic clusters, solvent coordination also appears to play a role in cluster decomposition, with the stability of the clusters decreasing with increasing solvent coordinating ability.[29,32]

Although treatment of [**1**]$^-$ with bulky thiols leads to formation of homoleptic $[Fe_4S_4]^{3+}$ clusters, treatment of the all-ferric cluster **1** with the bulky thiol HSDmp (Dmp = 2,6-bis(2,4,6-trimethylphenyl)phenyl) does not yield a homoleptic $[Fe_4S_4]^{4+}$ cluster. Instead, one equiv $SDmp^-$ reduces the cluster, leading to a site-differentiated $[Fe_4S_4]^{3+}$ cluster with three Fe centers coordinated by thiolates and the fourth coordinated by three THF ligands (**3**, Scheme 1.1A).[35] Cluster **3** was the first example of a 3:1 site-differentiated $[Fe_4S_4]^{3+}$ cluster. However, this reaction does not appear to be general; treatment of **1** with HSTbt (Tbt = 2,4,6-tris[bis(trimethylsilyl)methyl]phenyl) results in protonolysis without cluster reduction, providing a homoleptic, all-ferric cluster. Cluster **3** was used to generate the site-differentiated cluster $Fe_4S_4(SDmp)_3(MeIm)$ (**4**, Scheme 1.1A), modeling the $Fe_4S_4(SCys)_3(NHis)$ clusters found in [NiFe] and [FeFe] hydrogenases.[36,37]

An all-ferric, thiolate-ligated $[Fe_4S_4]^{4+}$ cluster (**5**) was synthesized by Tatsumi and coworkers in 2018 by treatment of a mononuclear Fe^{2+} precursor, $Fe(STbt)_2$, with elemental sulfur (Scheme 1.1B).[38] Alternatively, treatment of **1** with HSTbt produces **5** via protonolysis of the bis(trimethylsilyl)amide ligands. Similar to the bulky thiolates in **2a-e**, the thiolate ligands in **5** are proposed to isolate the cluster core from the solvent, stabilizing the highly all-ferric state. Cluster **5** has a diamagnetic ground state, suggesting pairwise antiferromagnetic coupling of the Fe centers, analogous to the coupling patterns proposed for $[Fe_4S_4]^{1+}$, $[Fe_4S_4]^{2+}$, and $[Fe_4S_4]^{3+}$ cluster cores.[39] The $[Fe_4S_4]^{4+}$ oxidation state is not thought to be biologically relevant, but together with the isolation of all-ferrous clusters (*vide infra*, 2.1), it completes the set of possible oxidation states for $[Fe_4S_4]$ clusters composed of Fe^{2+} and Fe^{3+} ions.

1.2.3 P-cluster analogues derived from high-valent clusters

The P-cluster is an [Fe_8S_7] cluster in nitrogenases that mediates electron transfer between the reductase (NifH for the Mo nitrogenase) and the catalytic cofactor (FeMo-co for the Mo nitrogenase).[40–42] The *Azotobacter vinelandii* (*Av*) Mo-nitrogenase P-cluster has been structurally characterized in three redox states—P^N, P^{1+} and P^{OX}—but uncertainty remains about which oxidation states are relevant to N_2 reduction.[41–44] In the P^N (all-ferrous) state, the cluster can be described as two [Fe_4S_4] cubanes fused by a shared μ_6-sulfide vertex. Upon oxidation, Fe–(μ_6-S) bonds are broken and additional bonds to nearby amino acids are formed (Figure 1.1).[45] The synthesis of P-cluster analogues may assist in understanding the P-cluster's redox-linked structural changes, its biosynthesis, and its electronic structure. However, the structural complexity of the P-cluster has made it challenging to synthesize clusters with the

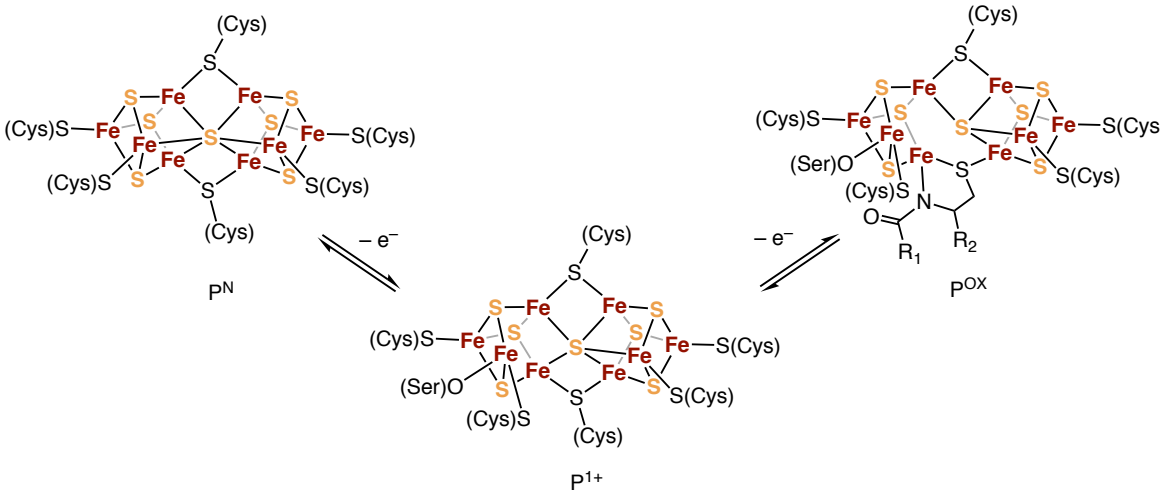

Figure 1.1 Structural interconversions of the P-cluster of *Av* Mo nitrogenase. Upon oxidation, bonds to the μ_6-sulfide are broken and additional bonds to amino acids are formed.

correct geometry and nuclearity.

In 2003, Tatsumi and coworkers reported the synthesis of a structural analogue of the P-cluster in the P^N state, **6a** (Scheme 1.2A).[46] Cluster **6a**, which was prepared using a complex self-assembly system, is an [Fe_8S_7] cluster supported by bis(trimethylsilyl)amide and tetramethylthiourea ligands rather than cysteine thiolates.[46] The terminal ligands can be

substituted by thiolates to yield **6b-i** (Scheme 1.2A).[47] Although **6a-i** are structurally very similar to the P^N cluster, they formally contain two Fe^{3+} centers, making them two electrons more oxidized than the P^N state. The cyclic voltammograms of **6a-i** show two reversible redox events, but the reduced states have not been isolated.[48] Tatsumi and coworkers have additionally reported [Fe_8S_7] clusters containing three bridging thiolate ligands[49,50] and an [Fe_8S_6] cluster containing a μ_4-O in which the oxide adopts an asymmetric coordination environment similar to that of the μ_4-S in P^{OX}.[51] In 2012, Tatsumi and coworkers reported that another P^N structural analogue (**6j**) could be synthesized by reductive fusion of two equivalents of **1** using phosphines as sulfur-atom abstraction reagents (Scheme 1.2B).[52] Although the all-ferric [Fe_4S_4]$^{4+}$ oxidation state of **1** is probably not relevant to the biosynthesis of the P-cluster, this work demonstrates the feasibility of constructing the P-cluster core from two [Fe_4S_4] clusters, as has been proposed for P-cluster biosynthesis.[53,54]

Scheme 1.2 Synthetic analogues of the nitrogenase P-cluster. (A) Synthesis of P-cluster analogues **6a-i** by self-assembly and ligand exchange. (B) Sulfide abstraction from **1** generates a P-cluster analogue, **6j**.

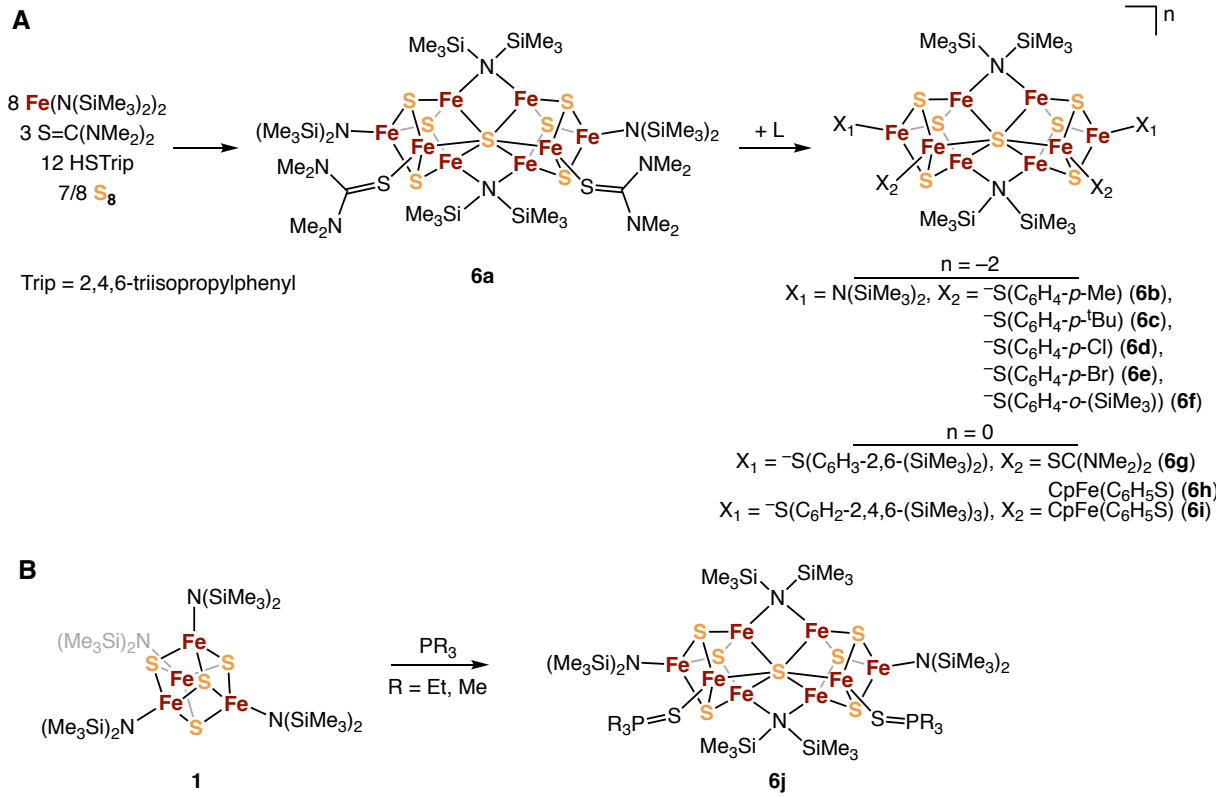

1.2.4 Controlling cluster nuclearity using sterics

Obtaining rational control over the nuclearity of synthetic Fe–S clusters remains an ongoing challenge. The nuclearity of clusters prepared by self-assembly can depend on seemingly minor perturbations; for example, the reaction of $FeCl_2$, S_8, KSPh, and [cation]Cl produces an $[Fe_4S_4Cl_4]^{2-}$cluster (**7**) when [cation] is tetraphenylphosphonium[55] but an $[Fe_6S_6Cl_6]^{3-}$ cluster (**8**) when [cation] is tetraethylammonium (Scheme 1.3A).[56] In other cases, the nuclearity of clusters formed by self-assembly depends on the steric profile of the supporting ligands. For example, treatment of $(PR_3)_2FeCl_2$ with 1.5 equiv $(Me_3Si)_2S$ yields the edge-bridged double cubane $(PR_3)_6Fe_8S_8$ (**9**) when R is isopropyl[57] but yields the basket cluster $(PR_3)_5Fe_7S_6Cl_2$ (**10**) when R is ethyl (Scheme 1.3B).[58] Here, it was proposed that the cone angle of the phosphine ligand controls the cluster nuclearity.[59,60] Systems in which the cluster nuclearity can be predicted and perturbed remain uncommon, in part due to the complexity of Fe–S self-assembly reactions and the wide range of cluster nuclearities that can be obtained. However, progress has been made in probing the steric effects that dictate cluster nuclearity and in perturbing the steric environment to generate new types of Fe–S clusters. Recent examples of tuning sterics to control cluster nuclearity are described below.

Scheme 1.3 Minor perturbations to self-assembly conditions result in isolation of Fe–S clusters with different nuclearities. (A) Self-assembly of Cl-ligated clusters produced different nuclearities depending on the cation. (B) Reaction of $(PR_3)_2FeCl_2$ with $S(SiMe_3)_2$ produces different clusters depending on the steric bulk of the phosphine.

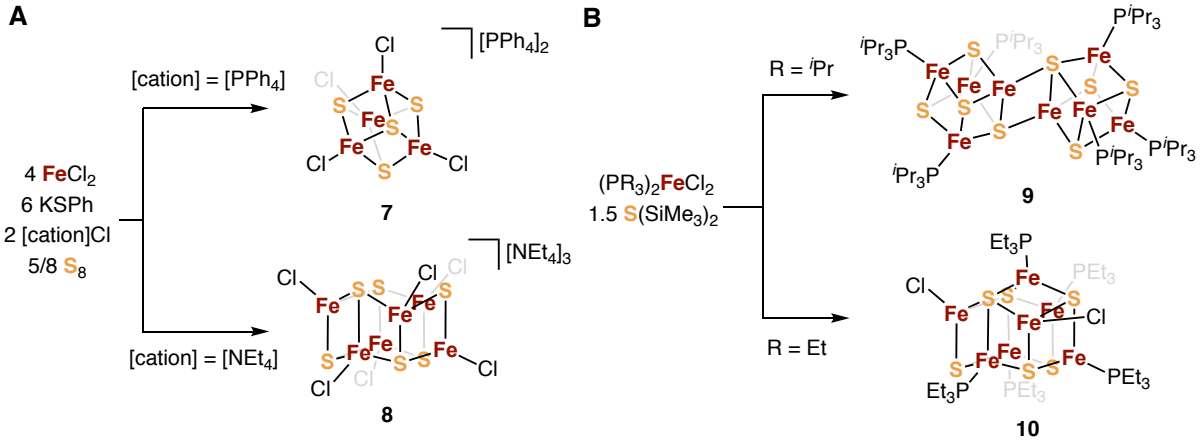

In 2018, McSkimming and Suess reported a method for controlling cluster nuclearity using tridentate imidazolin-2-imine ligands (L(NIm)$_3$).[61] They showed that metalation of these ligands with the preformed cluster [PPh$_4$]$_2$[Fe$_4$S$_4$Cl$_4$] yields different outcomes depending on the steric profile of the nitrogen substituents. The smaller ligand with *N*-methyl substituents reacts with 1.5 equiv [PPh$_4$]$_2$[Fe$_4$S$_4$Cl$_4$] to generate an L(NIm^{Me})$_3$Fe$_6$S$_6$Cl$_3$ cluster (**11**, Scheme 1.4). Rearrangement to form an [Fe$_6$S$_6$] cluster can be suppressed when the metalation is carried

Scheme 1.4 The formation of clusters **11** (Fe$_6$S$_6$) and **12** (Fe$_4$S$_4$) is controlled by the size of N-substituents on the imidazolin-2-imine ligand.

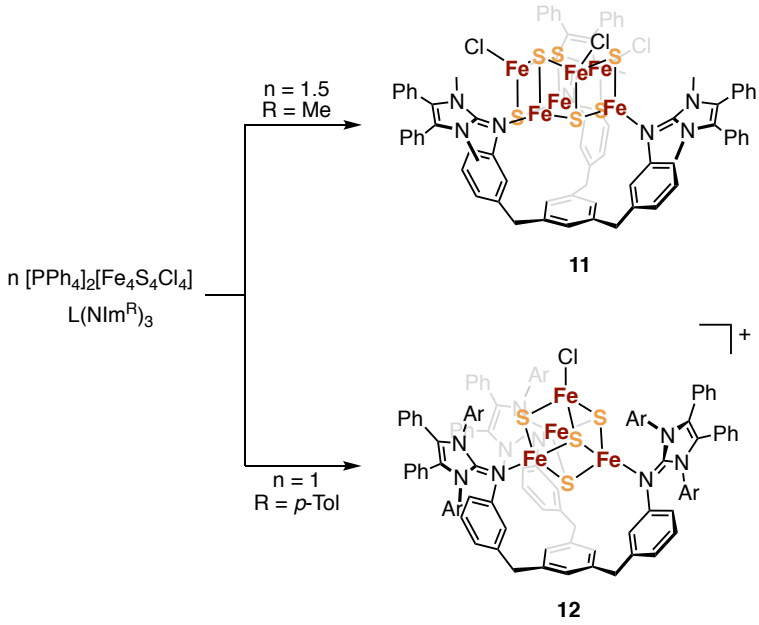

out with a larger ligand featuring *N*-*p*-tolyl substituents, which reacts with 1 equiv [PPh$_4$]$_2$[Fe$_4$S$_4$Cl$_4$] to generate an [L(NIm$^{p\text{Tol}}$)$_3$Fe$_4$S$_4$Cl]$^+$ cluster (**12**, Scheme 1.4). The larger ligand supports a smaller Fe–S cluster because of the changes in ligand geometry required to accommodate a larger cluster. The [Fe$_6$S$_6$]$^{3+}$ cluster of **11** requires all of the imidazole-2-imine ligands to be nearly perpendicular to the molecule's pseudo-C_3 axis, which would result in a steric clash between the *N*-*p*-tolyl substituents on adjacent ligand arms. On the other hand, the *N*-methyl substituents are small enough to accommodate this geometric requirement. This study highlights both the promise of using synthetic chemistry to rationally control the structures of Fe–S clusters and the challenge of designing ligands to support Fe–S clusters with

specific nuclearities; the large size and resultant flexibility of these ligands means they can often accommodate clusters of varying sizes and geometries.

Rigid ligands are in principle more effective templates on which Fe–S clusters can be constructed and can thereby provide more precise control over cluster nuclearity. Murray and coworkers in 2015 reported a planar [Fe_3S_3] cluster synthesized within a triethylbenzene-capped tris(β-diketiminato)cyclophane ligand that had been previously shown to support trinuclear metalloclusters (**13**, Figure 1.2).[62] The three Fe^{3+} ions couple to form an S = 1/2 ground spin state, that same spin state that is observed for open-cuboidal, all-ferric [Fe_3S_4]$^+$ clusters in biological systems.[63] Cluster **13** is a precatalyst for catalytic dinitrogen silylation, though there is evidence that at least some of the sulfides are displaced during catalysis.[64] Nevertheless, the use of a rigid ligand to support an [Fe_3S_3] cluster demonstrates the promise of templating ligands for supporting Fe–S clusters with geometries that are otherwise difficult to access. The controlled synthesis of Fe–S clusters with unusual, sterically imposed geometries may generate clusters with unique electronic structures or reactivities.

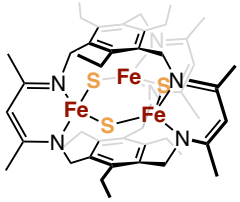

13

Figure 1.2 A rigid cyclophane ligand supports a planar [Fe_3S_3] cluster.

β-Diketiminate-supported Fe–S clusters can also be prepared in the absence of a rigid cyclophane framework. Holland and coworkers used a β-diketiminate ligand with *N,N'*–bis(2,6-diisopropylphenyl substituents to support a diiron complex featuring two three-coordinate Fe^{2+} centers bridged by a μ_2-sulfide (**14**, Scheme 1.5A).[65,66] Carrying out similar reactions using a smaller ligand featuring *N,N'*–bis(2,6-dimethylphenyl) (Xyl) substituents results in complex **15**, with four-coordinate Fe^{2+} centers coordinated by THF.[67] Whereas **14** is

thermally stable, **15** rearranges upon heating to form the higher-nuclearity cluster **16**, an all-ferrous cluster with a unusual face-sharing cubane core (Scheme 1.5B).

Scheme 1.5 Reactions of β-diketiminate-supported [Fe_2S] complexes. (A) Reduction of an [Fe_2S] complex yields an [Fe_2S] complex with Fe^{1+} centers. (B) An [Fe_2S] complex supported by a less bulky β-diketiminate ligand rearranges to form an [$Fe_{10}S_8$] or [Fe_4S_3] cluster upon heating or reduction, respectively.

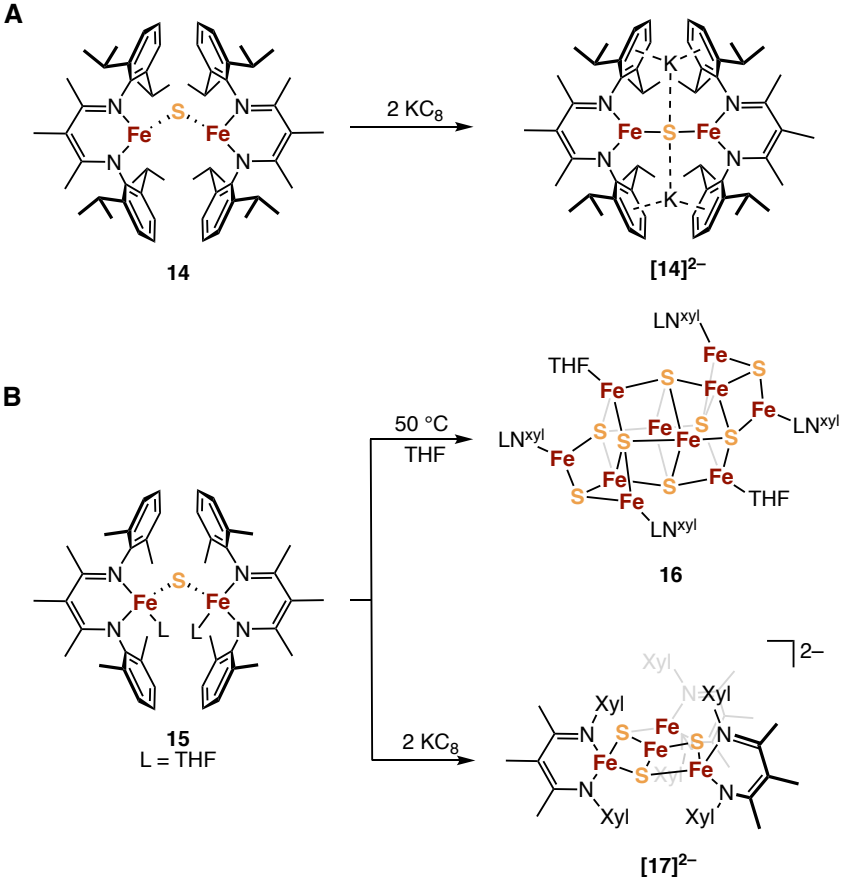

Complex **14** can be reduced by two electrons to form an [Fe_2S] complex with two, three-coordinate Fe^{1+} centers (**[14]**$^{2-}$); **[14]**$^{2-}$ belongs to a small class of Fe–S complexes that contain low-valent Fe.[65,68] On the other hand, reduction of **15** does not lead to an [Fe_2S] cluster and instead induces rearrangement to an [Fe_4S_3] cluster, **[17]**$^{2-}$, in low yields (Scheme 1.5B).[69] Cluster **[17]**$^{2-}$ contains a trigonal-planar Fe center bound to three sulfide ligands and is formally composed of three Fe^{2+} centers and one Fe^{1+} center; oxidation and reduction of **[17]**$^{2-}$ by one electron were also demonstrated. Despite coordination by three weak-field sulfide ligands, the trigonal-planar Fe center is low-spin in all three cluster oxidation states, as established by Mössbauer spectroscopic analysis and *ab initio* calculations. This spin state is attributed to the

very short and highly covalent Fe–S bonds, which result in substantial destabilization of the d(xy) and d(x^2–y^2) orbitals. The differences in the reactivity of **14** and **15** upon reduction highlight the sensitivity of Fe–S cluster chemistry to perturbations in the steric environment, particularly in dictating the structure and nuclearity of clusters formed during structural rearrangements.

1.2.5 New methods for cluster site-differentiation

Site-differentiated [Fe_4S_4] clusters carry out a wide variety of chemical reactions in biology. These include Lewis-acid-type reactions in aconitase,[70] dehydration reactions in (R)-2-hydroxyacyl-CoA dehydratases,[71] electron transfer in several hydrogenases,[36,37] challenging reduction reactions in IspG/H,[72] and primary carbon radical generation in radical SAM enzymes[73] (*vide infra*, 3.1); in each case, catalysis occurs at [Fe_4S_4] clusters coordinated to three cysteine ligands, leaving the fourth Fe center available to bind substrates, other cofactors, or non-cysteine amino acid side chains.

Establishing and maintaining site-differentiation at synthetic [Fe_4S_4] clusters is challenging. Changes to the coordination environment at one Fe center result in only minor perturbations to the environment of the other Fe centers, so it is often difficult to limit reactivity to some but not all Fe sites. This problem is illustrated by simple ligand substitution reactions; addition of fewer than four equivalents of an exogenous ligand to an [Fe_4S_4] cluster typically produces statistical mixtures of clusters reflecting zero, one, two, three, and four substitution events.[74] In 1987, Stack and Holm reported a landmark strategy for limiting this unselective substitution.[75,76] Their approach was to use a tridentate thiolate ligand that could coordinate to three Fe centers of an [Fe_4S_4] cluster, leaving the fourth Fe site available to bind a unique ligand (Figure 1.3A). This platform has had a longstanding influence on the design of chelating ligands for [Fe_4S_4] clusters, including Pohl's[77,78] and Tatsumi's[79] reports of trithiolate ligands with shorter syntheses in 1997 and 2012, respectively, and Suess's related tridentate, neutral-

donor ligands in 2018[61] and 2019[80] (Figure 1.3B). Each ligand is structurally analogous, featuring three donor atoms that are connected to a central benzene ring through five bonds. Other tridentate ligands[81–85] and polypeptide maquettes[86–90] for [Fe_4S_4] clusters have been reported, though they have been less amenable to single-crystal X-ray crystallographic studies. Indeed, other than those that structurally mimic the original Holm framework, the only tridentate ligand that has permitted structural characterization of bound [Fe_4S_4] clusters is the anionic, scorpionate-type ligand reported by Suess and coworkers in 2020 (Figure 1.4).[91]

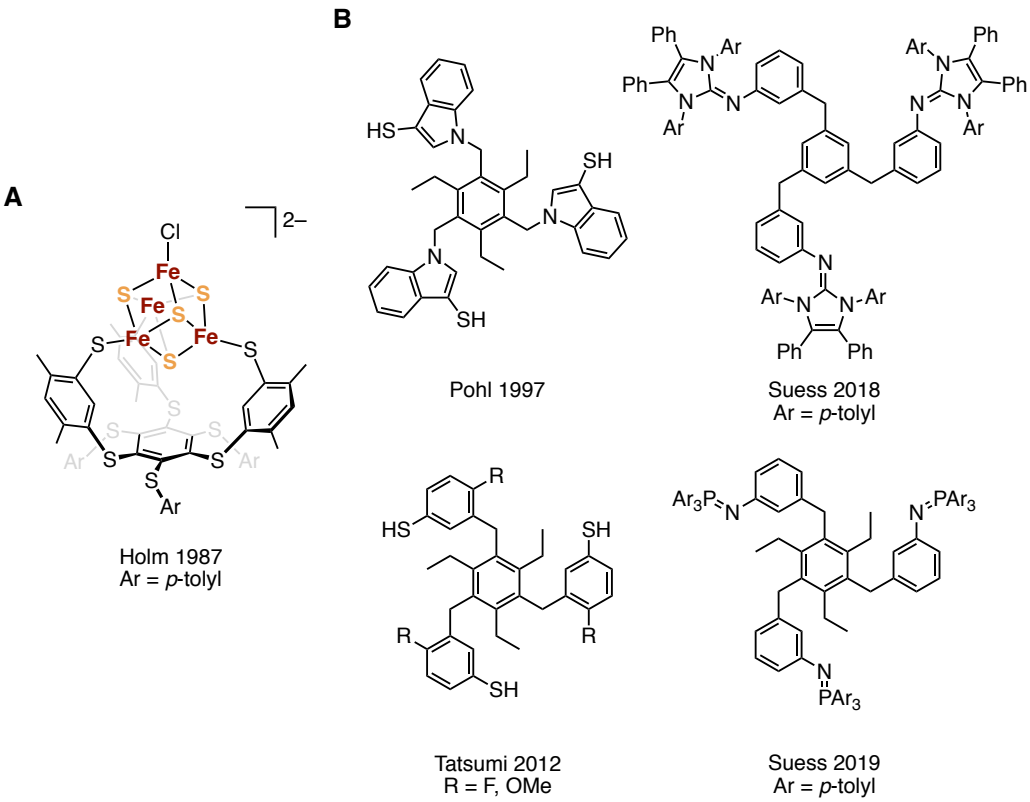

Figure 1.3 Tridentate ligands designed to coordinate [Fe_4S_4] clusters. (A) A tridentate thiolate ligand to support site-differentiated [Fe_4S_4] clusters. (B) Tridentate ligand variations reported by Pohl, Tatsumi, and Suess.

A significant drawback to utilizing these tridentate ligands is that their syntheses are often time-consuming. Indeed, Holm and coworkers described the synthesis of their original trithiolate ligand as "not difficult but [requiring] more than casual effort."[92] As such, there have been continued efforts to develop strategies to access site-differentiated clusters that don't rely on the use of complex, polydentate ligands. These approaches can be split into three major

categories: carrying out salt metathesis in nonpolar solvents, oxidatively cleaving higher-nuclearity clusters, and using sterically protective ligands to preclude formation of homoleptic clusters.

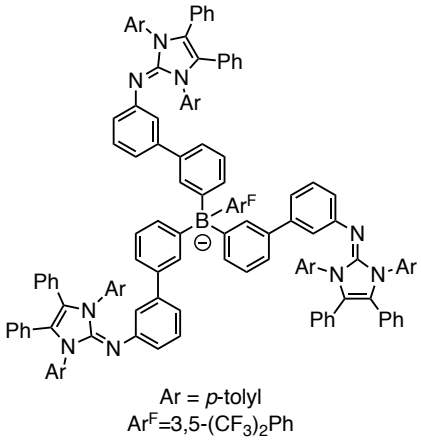

Figure 1.4 A tridentate, expanded scorpionate ligand for 3:1 site-differentiated [Fe_4S_4] clusters.

1.2.6 Salt metathesis in non-polar solvents

One method for site-differentiation that avoids the use of a polydentate ligand entails using salt metathesis to generate neutral Fe–S clusters. Building on work by Coucouvanis and coworkers,[60] Zhou and Holm in 2003 described this strategy in the context of synthesizing 3:1 site-differentiated clusters.[93] Here, addition of the $[PPh_4]^+$ salts of coordinating anions (Cl^-, RS^-) to phosphine-ligated clusters, $[Fe_4S_4(PR_3)_4][BPh_4]$ (**18**, R= Cy, ^{i}Pr), results in precipitation of $[PPh_4][BPh_4]$ and displacement of one phosphine ligand by the added anion (Scheme 1.6). Deng and Holm later expanded the scope of this reaction to access clusters with alkoxide and thiolate ligands from sodium alkoxides and thiolates.[57] Since the resultant $(PR_3)_3Fe_4S_4X$ (**19a-g**) clusters are neutral, they can be separated from charged products by extraction into non-polar solvents. Clusters **19a-g** do not equilibrate to statistical mixtures of clusters with 0–4 of each ligand because redistribution of the anionic ligands would require formation of charged species, a process that is disfavored in nonpolar solvents. However, further phosphine loss to form higher nuclearity $[Fe_8S_8]$ clusters was sometimes observed (**20a-c**, Scheme 1.6), which required manipulation of the $(PR_3)_3Fe_4S_4X$ clusters in the presence of excess phosphine.[57,93] A

related strategy was employed in the synthesis of 2:2 site-differentiated clusters with low-spin Fe^{2+} sites,[94] and Xi and Holm later extended it to the synthesis of site-differentiated $[MoFe_3S_4]^{2+}$ clusters as well.[95] Overall, salt metathesis offers a convenient and relatively general route to generating site-differentiated Fe–S clusters from homoleptic precursors. However, the scope of such reactivity is limited to anions that bind to the Fe site more strongly than phosphines, and it therefore cannot be applied to the generation of site-differentiated Fe–S clusters with weakly-coordinating ligands.

Scheme 1.6 Synthesis of site-differentiated $[Fe_4S_4]$ clusters by salt metathesis and phosphine loss to form $[Fe_8S_8]$ clusters.

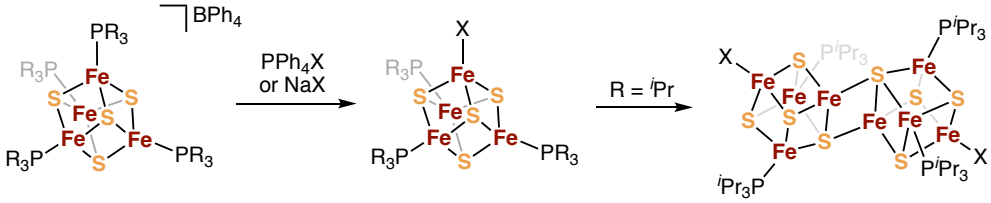

18
R = Cy, ^{i}Pr

X = Cl (**19a**), Br (**19b**) SPh (**19c**), $SSiPh_3$ (**19d**), SSi^iPr_3 (**19e**), $OSiPh_3$ (**19f**), $OSiMe_2{}^tBu$ (**19g**)

X = $SSiPh_3$ (**20a**) SSi^iPr_3 (**20b**) $OSiPh_3$ (**20c**)

1.2.7 Oxidative cleavage of Fe_8S_8 cores

In 2010, Holm and coworkers reported an alternative method for generating $(PR_3)_3Fe_4S_4X$ clusters that entails oxidative cleavage of $[Fe_8S_8]$ (**9**) and $[Fe_{16}S_{16}]$ (**21**) clusters.[57] This strategy was amenable to several oxidant/ligand combinations, including I_2, disulfides (RSSR), and $[Cp_2Fe]^+$ in the presence of alkoxides (**19h-l**, Scheme 1.7), and was applied to $[MoFe_3S_4]^{2+}$ clusters by Xi and Holm.[95] Similar to the salt metathesis method discussed in the previous section, the oxidative cleavage method appears to be limited to the addition of strongly donating, anionic ligands, and the site-differentiated phosphine clusters often lose phosphine ligands to form higher-nuclearity $[Fe_8S_8]$ clusters.

Scheme 1.7 Synthesis of site-differentiated [Fe_4S_4] clusters by oxidative cleavage of [Fe_8S_8] and [$Fe_{16}S_{16}$] clusters.

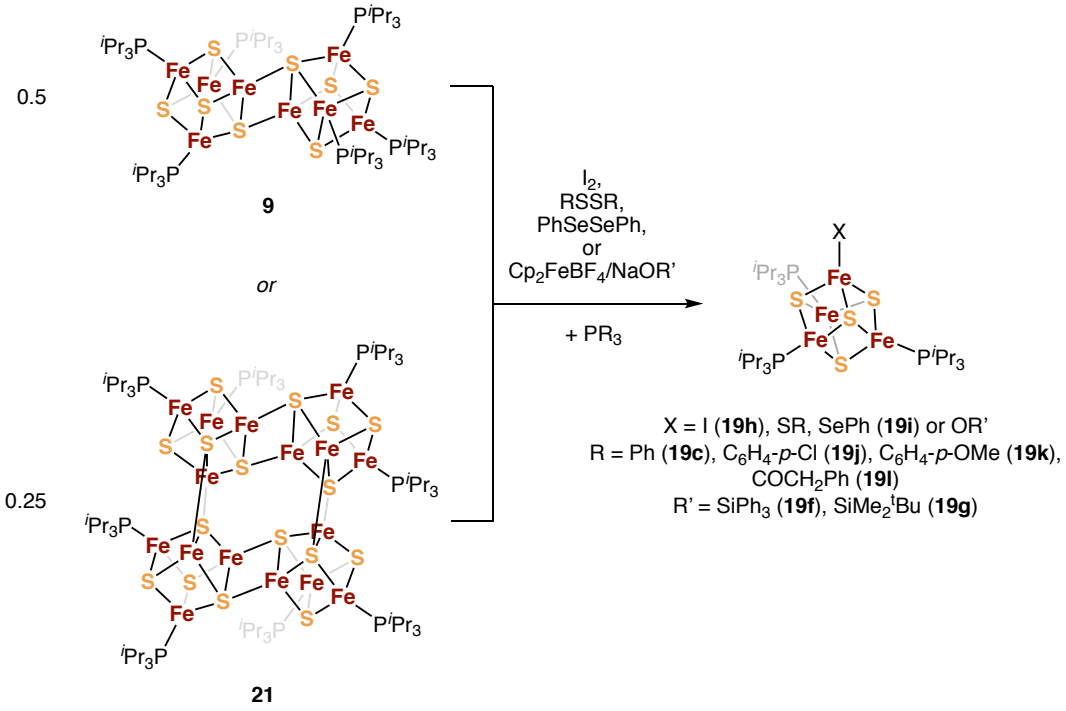

1.2.8 Developments in [Fe_2S_2] cluster chemistry: modeling biological systems with mixed thiolate/nitrogen donor sets

Biological [Fe_2S_2] clusters are found in multiple primary coordination environments, including with four cysteine ligands (ferredoxins), with two histidine and two cysteine ligands (Rieske centers), and with one histidine and three cysteine ligands (mitoNEET clusters and others)[96] (Figure 1.5A). Although many examples of [Fe_2S_2] clusters coordinated by sulfur, oxygen, and nitrogen have been synthesized,[15] synthetic [Fe_2S_2] clusters with mixed primary coordination spheres remain rare.

A synthetic model of Rieske centers featuring mixed N and S donors, **26**, was reported in 2008 by Meyer and coworkers[97] (Figure 1.5B). Cluster **26** was synthesized by sequential addition of a doubly deprotonated diskatylmethane ligand and a dithiolate ligand to an $[Fe_2S_2Cl_4]^{2-}$ precursor. This synthetic approach to site-differentiation—sequential ligand addition to undifferentiated clusters—proved generalizable. In 2014, a new Rieske-type cluster supported by a bis(benzimidazolate) ligand (**27**) was prepared using the same method (Figure

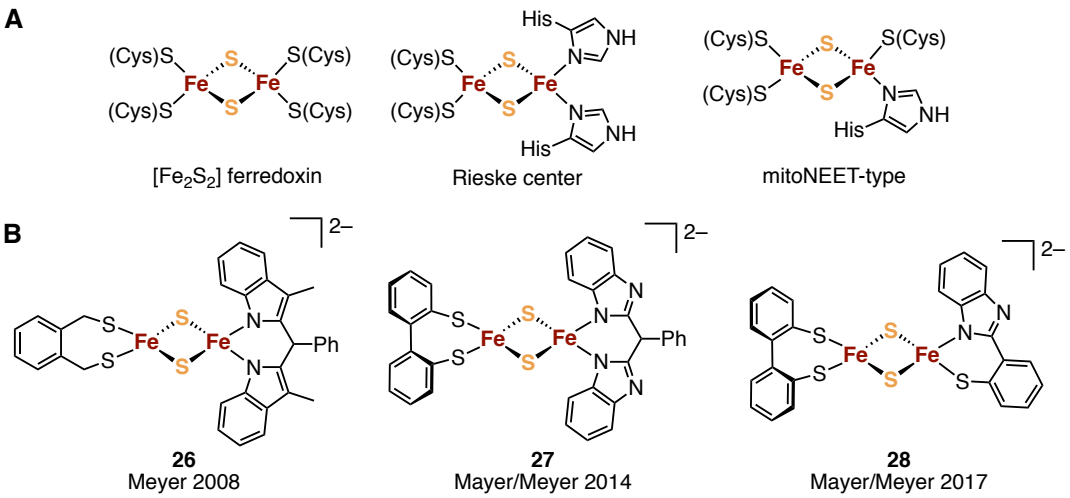

Figure 1.5 Varied coordination environments for biological and synthetic $[Fe_2S_2]$ clusters. (A) Biological $[Fe_2S_2]$ clusters with varying numbers of histidine ligands. (B) Synthetic models for histidine ligated $[Fe_2S_2]$ clusters. The first two are Rieske center models and the last is a model for mitoNEET-type clusters.

1.5B);[98] the imidazolate ligand in **27** more faithfully models the histidine ligands in the Rieske centers than the diskatylmethane ligand in **26**. Both clusters are good spectroscopic models for Rieske clusters, with larger Mössbauer quadrupole splittings for the N-ligated site compared to the S-ligated site, a diamagnetic ground state in the diferric $[Fe_2S_2]^{2+}$ state, and an $S = 1/2$ ground state in the mixed-valent $[Fe_2S_2]^{+}$ state, with the ferrous site localized on the N-ligated site. Following the same sequential addition strategy, a model for mitoNEET clusters that features one nitrogen and three sulfur donors was synthesized in 2017[99] (**28**, Figure 1.5B).

The synthesis of $[Fe_2S_2]$ clusters with mixed N and S donors has enabled investigations of $[Fe_2S_2]$ cluster-mediated proton-coupled electron transfer (PCET) chemistry. In an effort to understand how Fe–S clusters with histidine ligands mediate PCET reactions in biological systems,[100–102] Mayer, Meyer, and coworkers used the Rieske and mitoNEET model clusters with benzimidazolate ligands to study the PCET reactions at synthetic imidazolate-ligated $[Fe_2S_2]$ clusters.[98,99,103,104] Although the N–H bond dissociation free energies for the model compounds were found to be ca. 10–15 kcal/mol lower than those in the biological systems, these studies provided insight into a potential function of heteroleptic His/Cys ligation in modulating the rate of PCET in biological systems: perturbation of the reorganization energy

associated with the PCET reaction. By modifying the degree of localization of the ferrous site in the mixed valent state, heteroleptic ligation of an [Fe_2S_2] cluster tunes the Marcus reorganization energy and therefore the rate of PCET. The direction of this trend depends on the system; while the heteroleptic Rieske model **27** mediates PCET reactions faster than a homoleptic congener (**29,** Figure 1.6),[98] the asymmetric mitoNEET model **28** mediates PCET reactions slower than the homoleptic congener (**30**, Figure 1.6).[99] Together, these studies of PCET reactions at synthetic [Fe_2S_2] clusters—enabled by the development of synthetic protocols for site-differentation of [Fe_2S_2] clusters—yielded insights into how the primary coordination sphere of [Fe_2S_2] clusters can tune the rate of PCET.

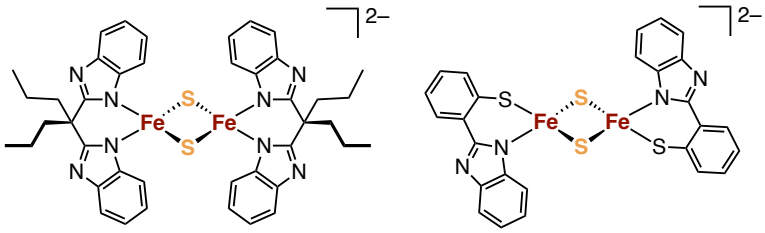

29
Mayer 2012

30
Mayer/Meyer 2017

Figure 1.6 Clusters used in comparative studies of PCET kinetics.

1.2.9 Summary

The developments in synthetic chemistry described in this section underpin much of the progress in synthetic Fe–S chemistry over the last decades. As will be discussed in subsequent sections, these advances have enabled the synthesis of complex clusters with high structural fidelity to their biological counterparts, as well as the discovery of new Fe–S cluster-mediated reactions.

1.3 Fe–S clusters with unexpected electronic structures

The electronic structures of Fe–S clusters have been studied using a battery of spectroscopic and computational techniques, and they continue to attract substantial interest.[105,106] Such studies have benefitted from the synthesis of model clusters that, on one hand, accurately reproduce the structure of biological clusters, and on the other hand, have

highly tunable primary and secondary coordination spheres. Here, we highlight several studies that have employed synthetic Fe–S clusters for understanding biological Fe–S clusters with unusual electronic structures.

1.3.1 All-ferrous [Fe_4S_4] clusters

The [Fe_4S_4] cluster is ubiquitous in biology and exists in nearly all cases in the $[Fe_4S_4]^{3+}$, $[Fe_4S_4]^{2+}$, and/or $[Fe_4S_4]^{+}$ redox states. Notable exceptions are the reduced form of the nitrogenase Fe protein (NifH) of *Azotobacter vinelandii* (*Av*), Fe protein homologs, and the dehydratase activator from *Acidaminococcus fermentans*, whose [Fe_4S_4] clusters can be reduced to the all-ferrous $[Fe_4S_4]^0$ state.[107–110] The discovery by Watt and Reddy in 1994 of an $[Fe_4S_4]^0$ cluster in NifH[107] stimulated interest in synthesizing [Fe_4S_4] clusters in the all-ferrous state, particularly because of the unusual $S = 4$ spin state of the biological $[Fe_4S_4]^0$ clusters.[108] An $S = 4$ ground state was perhaps unexpected since the vast majority of $[Fe_4S_4]^{1+,2+,3+}$ clusters exhibit pairwise spin coupling, and a pairwise coupling pattern in the $[Fe_4S_4]^0$ state would predict an $S = 0$ ground state.[39] Further characterization of the all-ferrous cluster on NifH by Münck and coworkers pointed to an electronic structure in which three Fe centers are antiferromagnetically coupled to the fourth (Figure 1.7).[111] Following these reports, the preparation of synthetic clusters in the $[Fe_4S_4]^0$ state was undertaken to enable comparisons between their electronic structures and those of biological $[Fe_4S_4]^0$ clusters, particularly to determine if the 3:1 spin coupling pattern would be observed in the absence of a protein environment.

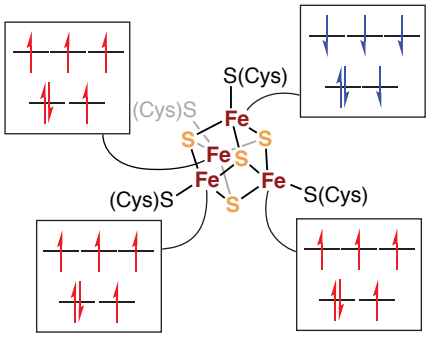

Figure 1.7 Proposed electron coupling diagram for the $S = 4$ $[Fe_4S_4]^0$ cluster of *Av* NifH.

1.3.2 Synthetic methods

Initial attempts to reduce phosphine-supported $[Fe_4S_4]$ clusters resulted in isolation of $[Fe_8S_8]$ and $[Fe_{16}S_{16}]$ clusters owing to the lability of the phosphine ligands, although mass spectrometry provided evidence for initial formation of $[Fe_4S_4]^0$ clusters.[59,93] Reduction of either $[Fe_4S_4(CN)_4]^{3-}$ (**31**) or **18** in the presence of cyanide anions afforded the first isolated $[Fe_4S_4]^0$ cluster, $[NBu_4]_4[Fe_4S_4(CN)_4]$ (**32**) (Scheme 1.8A).[112] Although **32** was structurally

Scheme 1.8 Syntheses of $[Fe_4S_4]^0$ clusters. (A) Synthesis of all-ferrous **32** from $[Fe_4S_4]^+$ clusters with phosphine or cyanide ligands. (B) Synthesis of NHC-ligated clusters **33** and **34** from $[Fe_8S_8]$ phosphine clusters. (C) Self-assembly of **35** from an Fe^0 precursor.

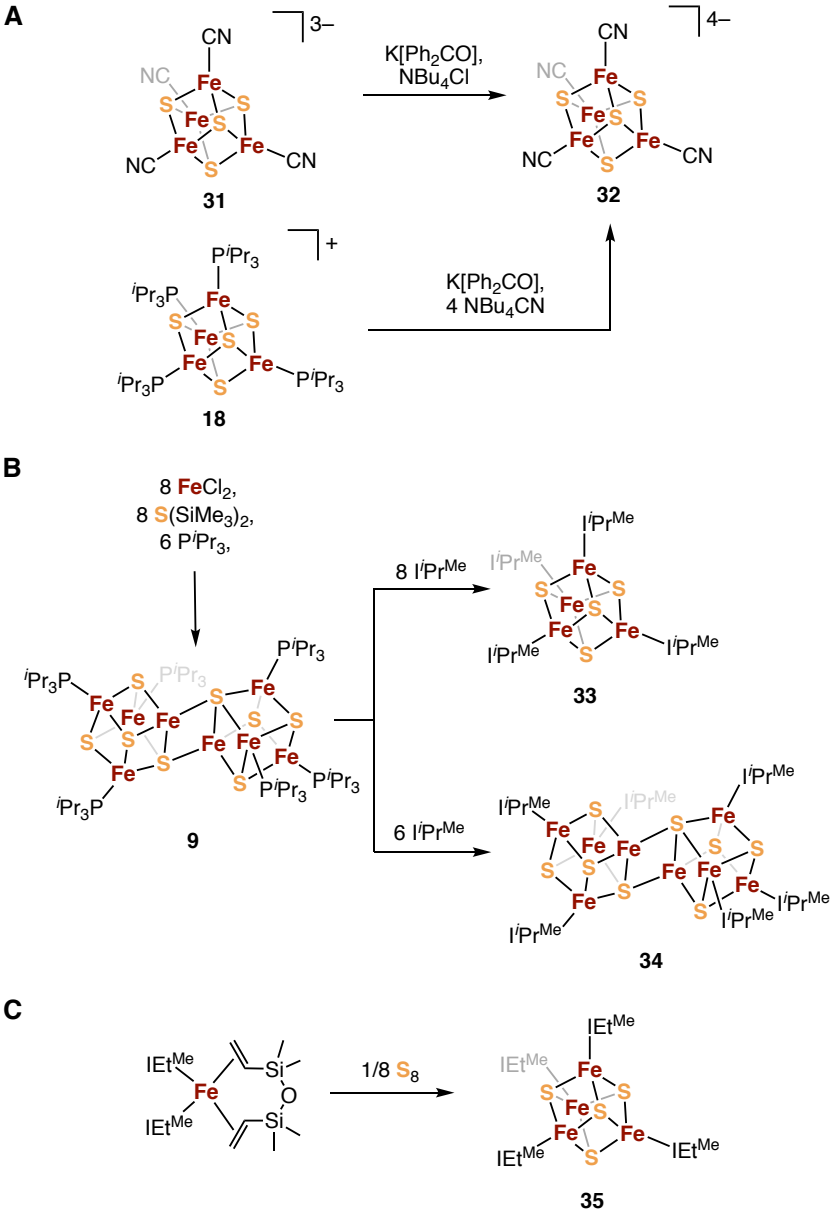

characterized and its Mössbauer isomer shifts (*vide infra*, 1.3.3) supported its assignment as an all-ferrous cluster, the sensitivity of **32** towards oxidation made further study of this species difficult.

Later, a synthetic route to a more stable all-ferrous cluster supported by I^iPr^{Me} was developed by Holm and coworkers (Scheme 1.8B).[58] $(I^iPr^{Me})_4Fe_4S_4$ (**33**) was synthesized by addition of excess I^iPr^{Me} to the phosphine-ligated clusters $(P^iPr_3)_6Fe_8S_8$, (**9**), $(P^iPr_3)_8Fe_{16}S_{16}$ (**21**), or $(PEt_3)_5Fe_7S_6Cl_2$ (**10**). The decreased lability of the NHCs relative to the phosphines prevents aggregation to higher nuclearity Fe–S clusters, although the edge-bridged double cubane $(I^iPr^{Me})_6Fe_8S_8$ (**34**) is accessible via addition of 6 equiv I^iPr^{Me} to **21**. The phosphine-ligated precursors can be prepared by self-assembly starting from $(P^iPr_3)_2FeCl_2$ and $(Me_3Si)_2S$, providing a direct route to all-ferrous Fe–S clusters from mononuclear starting materials. Deng and coworkers prepared a second NHC-ligated $[Fe_4S_4]^0$ cluster (**35**) from mononuclear precursors by treatment of an IEt^{Me}-ligated (IEt^{Me} = 1,3-diethyl-4,5-dimethylimidazol-2-ylidene) Fe^0 precursor with elemental sulfur (Scheme 1.8C).[113]

1.3.3 Geometric and electronic structures

The three synthetic all-ferrous clusters and the all-ferrous cluster of *Av* NifH have similar Fe–Fe distances and Fe–S bond lengths. The $[Fe_4S_4]^0$ cluster of *Av* NifH has an average Fe–S bond length of 2.33(2) Å and an average Fe–Fe distance of 2.65(9) Å;[114] the structural parameters of **32, 33**, and **35** are summarized in Table 1.1.[58,112,113] The structures of **33** and *Av* NifH show a 3:1 structural distortion in which one Fe center has significantly longer Fe–Fe distances, shorter Fe–S distances, and a shorter Fe–C distance than the other three Fe centers, resulting in a cluster core with approximate C_{3v} symmetry (Figure 1.8). Interestingly, other core geometries are observed for **32** and **35**. In cluster **35**, the core has approximate S_4 symmetry and the core of **32** approaches D_{2d} symmetry. Similarly, while the Mössbauer spectra of **33** and all-ferrous NifH reflect approximate 3:1 symmetry, the Mössbauer spectrum of **32** is

best modeled with a 2:2 site fit, consistent with its D_{2d} core symmetry (Table 1.2). The reasons for these structural and spectroscopic variations in synthetic all-ferrous $[Fe_4S_4]$ clusters are unclear, but they may reflect a relatively flat potential energy surface for the core structure, similar to what has been observed in $[Fe_4S_4]^+$ clusters.[57]

Table 1.1 Structural parameters of synthetic and biological $[Fe_4S_4]^0$ clusters.[a]

Cluster	Fe–Fe dist. (Å)	Fe–S dist. (Å)	Approx. symmetry
$[Fe_4S_4(CN)_4]^{4-}$ (**32**)	2.67(2)	2.33(2)	D_{2d}
$(I^iPr^{Me})_4Fe_4S_4$ (**33**)	2.68(1)	2.33(2)	C_{3v}
$(IEt^{Me})_4Fe_4S_4$ (**35**)	2.678(2)	2.335(7)	S_4
Av NifH	2.65(9)	2.33(2)	C_{3v}

[a]: Uncertainties are calculated as the standard deviation of all distances (6 Fe–Fe and 12 Fe–S) in the cluster

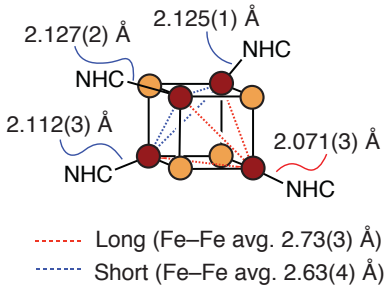

Figure 1.8 Diagram showing the approximate C_{3v} symmetry of **33**. The unique Fe center has long Fe–Fe distances and a short Fe–C(NHC) bond.

Like the $[Fe_4S_4]^0$ cluster of *Av* NifH, cluster **33** has a ground spin state of $S = 4$.[111,115] Magnetic Mössbauer studies on both clusters demonstrated a 3:1 coupling pattern, in which three Fe centers have negative **A(**^{57}**Fe)** tensors and relatively small quadrupole splittings (ΔE_Q) and the fourth has a positive **A** tensor and relatively large ΔE_Q. The presence of one Fe center with a negative **A** tensor and three Fe centers with a positive **A** tensor verified that the $S = 4$ spin state arises from antiferromagnetic coupling of a single Fe center to the other three ferromagnetically coupled Fe centers. Curiously, although in **33** the site with large ΔE_Q has a smaller isomer shift (0.54 mm/s) than the other three Fe sites (0.62 mm/s), in NifH all four Fe centers have the same isomer shift (0.68 mm/s; Table 1.2). Holm, Münck, Bominaar, and coworkers demonstrated computationally[115,116] that the 3:1 electronic and geometric distortions

represent a global energetic minimum for the $S = 4$ state, based on the dependence of the Fe exchange coupling constants on the cluster core geometry. They concluded that this unusual spin state for the $[Fe_4S_4]^0$ redox state is not induced by the protein environment and instead is a spontaneous distortion of the cluster core to C_{3v} geometry in the all-ferrous state. This study predicted an increase in Fe–Fe distance for the Fe center that is antiferromagnetically coupled to the other Fe centers, which allowed for identification of the Fe center with long Fe–Fe distances in the crystal structures of NifH and **33** and for correlation of the spectroscopically unique Fe site with a crystallographic site.

Table 1.2 Mössbauer parameters of $[Fe_4S_4]^0$ clusters.

Cluster	T (K)	δ (mm/s)	ΔE_Q (mm/s)	% of area
$(I^iPr^{Me})_4Fe_4S_4$ (**33**)	77	0.62	1.54	75
		0.54	2.92	25
$[Fe_4S_4(CN)_4]^{4-}$ (**32**)	77	0.65	2.00	50
		0.65	1.45	50
Av NifH	4.2	0.68	1.24	25
		0.68	1.48	25
		0.68	1.72	25
		0.68	3.08	25

Out of the three synthetic $[Fe_4S_4]^0$ clusters, only **33** exhibits the C_{3v} core symmetry that was attributed to the $S = 4$ spin state. The spin states of **32** and **35** were not experimentally determined, and thus it is not clear how their solid-state geometric structures (featuring D_{2d}- and S_4-symmetric cores, respectively) correspond to their electronic structures. Given that the Mössbauer spectrum of **32** also does not reflect the 3:1 intensity distribution associated with the $S = 4$ state, the existence of other ground spin states for $[Fe_4S_4]^0$ clusters should be considered. Interestingly, Watt and coworkers reported an $S = 0$ state for *Av* NifH when reduced with *Av* flavodoxin hydroquinone instead of Ti^{3+} citrate.[117] Together, these observations suggest the potential for multiple core geometries, perhaps associated with different ground spin states, for $[Fe_4S_4]^0$ clusters. These geometric and spin state correlations and the potential biological relevance of these variations remain to be addressed.

Based on the observation of $S = 4$ spin states for all-ferrous $[Fe_4S_4]$ clusters, as well as evidence that $(PR_3)_6Fe_8S_8$ clusters can be described as two fused $S = 4$ cubanes,[118] it has been proposed that the all-ferrous P-cluster in nitrogenase may likewise be comprised of two fused $S = 4$ cubanes that are antiferromagnetically coupled to yield an overall diamagnetic state. While the electronic structure of the diamagnetic P^N cluster is challenging to characterize experimentally, recent computational studies[119,120] support this formulation.

1.3.4 Spectroscopic characterization of the role of heterometals in the nitrogenase catalytic cofactors

The electronic structures of the nitrogenase cofactors FeMo-co, FeV-co, and FeFe-co have been the subject of intense study.[121] The overall charge states of the cofactors, the oxidation states of the constituent metal ions, and the effects of the carbide and heterometals on bonding within the clusters remain under investigation. Heterometal-containing Fe–S cubanes have been studied as model compounds for nitrogenase cofactors, primarily to probe the effects of the heterometal on cluster bonding. We summarize here recent developments in this area, beginning with a brief overview of relevant spectroscopic work on nitrogenases.

The Mo center in the resting state of FeMo-co has been directly probed by several techniques, including early studies that employed Mo X-ray absorption spectroscopy (XAS) or ^{95}Mo electron–nuclear double resonance (ENDOR) spectroscopy. This work was motived in part by efforts to understand the Mo oxidation state and its electronic coupling with the Fe centers. Early Mo XAS studies on FeMo-co by Hodgson and coworkers focused on elucidating the coordination environment of the Mo site, but tentatively proposed an Mo^{4+} or Mo^{3+} oxidation state based on Mo–S distances determined by extended X-ray absorption fine structure (EXAFS) spectroscopy.[122,123] In later studies of FeMo-co using ^{95}Mo ENDOR spectroscopy, Hoffman, Orme-Johnson, and coworkers interpreted the small ^{95}Mo hyperfine coupling as suggesting a diamagnetic Mo^{4+} center rather than Mo^{3+}.[124,125] Additional Mo L-

edge X-ray near-edge spectroscopy (XANES) studies by Hodgson and coworkers compared the XAS spectra of FeMo-co with several synthetic $[MoFe_3S_4]_2$ dicubanes and concluded that the oxidation state of the Mo center in FeMo-co and the cubanes were likely the same.[126] Based on the previous ENDOR experiments, the authors favored a Mo^{4+} assignment, however, Holm and coworkers assigned a Mo^{3+} oxidation state in the $[MoFe_3S_4]^{3+}$ cubanes based on the Mössbauer isomer shifts of the Fe centers.[127] Nevertheless, subsequent valence assignments for the Fe centers of FeMo-co generally assumed a Mo^{4+} oxidation state.[128–130]

In 2014, the assignment of the Mo center in FeMo-co as Mo^{4+} was re-evaluated in a combined Mo high-energy resolution fluorescence-detected XAS (HERFD-XAS) and density functional theory (DFT) computational study.[131] DeBeer, Neese, Einsle, and coworkers compared the Mo K-edge XAS spectra of FeMo-co, $[TpMoFe_3S_4Cl_3]^-$, and $[(TpMoFe_3S_4Cl_2)_2(\mu\text{-}S)]^{2-}$ (Tp = trispyrazolylborate) with dinuclear Mo^{5+}–Fe^{3+} compounds. Mo HERFD-XAS provides increased resolution at the Mo K-edge compared to traditional XAS, increasing the information that can be extracted from the spectra.[132] They found that the energy of the rising edges for all of the MoFe clusters were significantly lower than for the Mo^{5+} compounds, indicating the Mo center in the clusters was more reduced. They also found that the rising edge energy was very similar for the synthetic cubanes and for FeMo-co. Taking into account work from Holm and coworkers that assigned the Mo center in $[MoFe_3S_4]^{3+}$ cubanes as Mo^{3+} (after assigning the Fe centers as $Fe^{2.67+}$ based on Mössbauer isomer shifts),[127] DeBeer, Neese, and Einsle assigned the Mo center in FeMo-co as Mo^{3+} as well. In the cubanes, which are in the $[MoFe_3S_4]^{3+}$ oxidation state, balancing the overall charge with a Mo^{3+} center suggests the Fe centers can be described formally as 2x $Fe^{2.5+}$ and 1x Fe^{3+} center (Figure 1.9).

DFT calculations were used to support the assignment of Mo^{3+} in FeMo-co and suggested that the Mo^{3+} center adopts an electronic configuration with an unusual local $S = 1/2$ spin state (rather than $S = 3/2$ for high-spin, octahedral Mo^{3+}). The assignment of a local $S =$

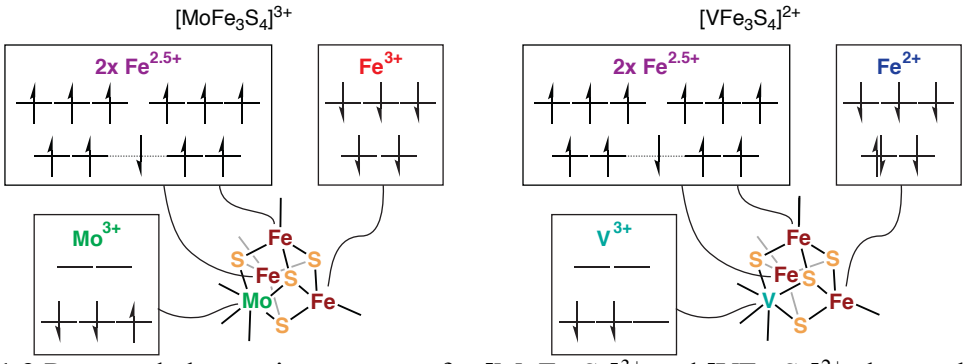

Figure 1.9 Proposed electronic structures for $[MoFe_3S_4]^{3+}$ and $[VFe_3S_4]^{2+}$ clusters based on XAS experiments and DFT calculations. Both Mo and V are in the 3+ oxidation state, with a complement of more reduced Fe centers in the $[VFe_3S_4]^{2+}$ cluster compared to the $[MoFe_3S_4]^{3+}$ cluster.

1/2 spin state aligns well with studies by Cook and Karplus, who calculated the electronic structure of $[MoFe_3S_4(SH)_6]^{3-}$ using broken-symmetry DFT and described the Mo center in this truncated cubane as an $S = 1/2$ Mo^{3+} center.[133,134] The local $S = 1/2$ state at Mo may reflect a non-Hund electronic configuration or non-colinear alignment of cluster spins (spin canting), but it has not been possible to distinguish between these possibilities computationally. In 2019, X-ray magnetic circular dichroism (XMCD) spectroscopy experiments were undertaken to further study the electronic configuration at the Mo^{3+} center.[135] These studies demonstrated that the Mo L_3-edge XMCD spectrum for the cubane $[TpMoFe_3S_4Cl_3]^-$ is not consistent with an isolated $S = 3/2$ Mo^{3+} center. Instead, the XMCD spectrum more closely resembles the calculated response for a distorted, low-spin Mo^{3+} center, supporting the assignment of an $S = 1/2$ Mo^{3+} center in the cubanes.

Later experiments by Einsle, Kovacs, DeBeer, and coworkers on $[VFe_3S_4]$ cubanes and VFe and MoFe proteins compared the effects of Mo and V on the bonding within M–Fe–S clusters. A combination of XAS spectroscopy and DFT calculations were used to support a V^{3+} oxidation state assignment in the $[VFe_3S_4]^{2+}$ cubane, occurring concomitantly with reduction of one Fe^{3+} to Fe^{2+} relative to isoelectronic $[MoFe_3S_4]^{3+}$ cubanes (Figure 1.9).[136] These observations are consistent with previous computational and Mössbauer studies of $[VFe_3S_4]^{2+}$ clusters, in which the Fe centers in the V-containing cubanes were found to be more reduced

on average than the Fe centers in the corresponding Mo-containing cubanes.[127] Additionally, DFT calculations suggest decreased covalency between V and Fe compared to Mo and Fe, consistent with expectations based on the more diffuse 4d orbitals of Mo compared to the 3d orbitals of V.

Both the Mo and V heterometal cubanes differ from $[Fe_4S_4]$ clusters in that BS-DFT localized orbital calculations on $[MoFe_3S_4]^{3+}$ and $[VFe_3S_4]^{2+}$ clusters show simultaneous delocalization of Mo and V electrons over all three adjacent Fe centers. In contrast, localized orbital calculations on $[Fe_4S_4]$ clusters typically show pairwise Fe–Fe interactions, with significant delocalization within—but not between—the pairs.[39] How if at all this difference in bonding is related to the differences in the catalytic efficiencies of FeMo-co, FeV-co, and FeFe-co for nitrogen fixation—FeFe-co is less efficient than FeV-co, which is less efficient than FeMo-co[137–139]—is not understood.

1.3.5 Summary

Despite decades of research, surprising discoveries regarding the electronic structures of Fe–S clusters continue to be made. Synthetic chemistry has provided model compounds that can be thoroughly characterized by a range of structural and spectroscopic techniques. Moreover, it is comparatively simple to systematically alter the donor properties of ligands to synthetic clusters, and this tunability has enabled and will continue to support detailed investigations of Fe–S cluster electronic structure.

1.4 Organometallic chemistry of Fe–S clusters

The last several decades have seen a rapid expansion in the bioorganometallic chemistry of Fe–S clusters. Simultaneously, synthetic chemistry has provided models for organometallic intermediates in biology and has demonstrated that even relatively simply Fe–S clusters can mediate complex organometallic chemistry. Here, we highlight recent examples of synthetic Fe–S clusters modelling the organometallic chemistry of biological cofactors.

1.4.1 Modeling radical generation by radical *S*-adenosyl-L-methionine (SAM) enzymes

Radical SAM enzymes comprise a large superfamily of proteins that perform a wide variety of functions throughout all kingdoms of life.[73] They use an [Fe_4S_4] cluster to reductively cleave SAM and form the primary carbon radical, 5′-dAdo•, which goes on to perform a diverse array of challenging reaction chemistry (most often initiated by H-atom abstraction). Although the 5′-dAdo• was only recently observed,[140,141] its intermediacy has been generally accepted. However, the mechanism of 5′-dAdo• generation and how such a reactive radical is directed toward productive reactivity have been less clear.

In 2016, Broderick, Hoffman, and coworkers used EPR spectroscopy to characterize an organometallic intermediate containing a bond between the 5′-C of the 5′-dAdo group and the unique Fe center of the $[Fe_4S_4]^{3+}$ cluster.[142] This organometallic intermediate was subsequently identified during rapid freeze-quench studies of several radical SAM enzymes with diverse functions, and was therefore proposed to be a common intermediate in generation of the 5′-dAdo• by radical SAM enzymes (Scheme 1.9).[143] A related organometallic species has been characterized in a noncanonical radical SAM enzyme by Ealick, Hoffman, Lin, and coworkers.[144] At the time of these discoveries, there were no well-defined examples of [Fe_4S_4]

Scheme 1.9 Proposed formation of an organometallic intermediate en route to the 5′-dAdo• in radical SAM enzymes. A = adeninyl.

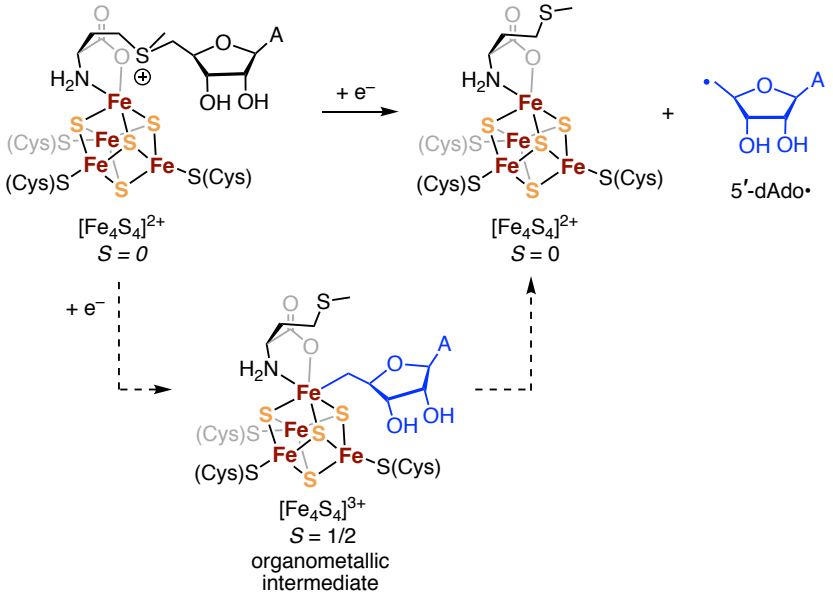

clusters containing alkyl ligands, and thus the interplay between the structure, stability, and reactivity of these rather exotic intermediates was unclear.

In 2019, Suess and coworkers reported the synthesis of an [Fe_4S_4]–alkyl cluster (**36**, Figure 1.10).[80] Cluster **36** features an [Fe_4S_4]$^{2+}$ core charge, one electron more reduced than

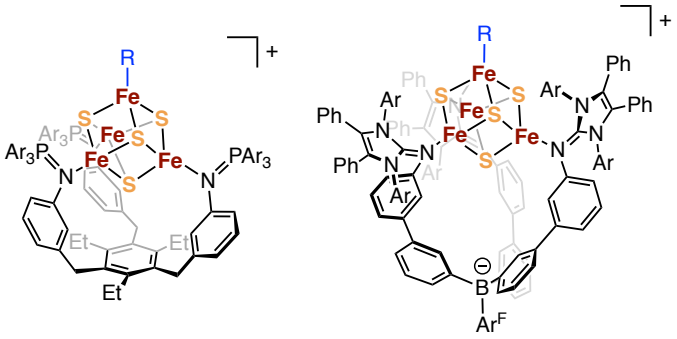

36
R = Et, Ar = *p*-tolyl
[Fe_4S_4]$^{2+}$
S = 0

37
R = Me, Ar = *p*-tolyl
Ar^F=3,5-$(CF_3)_2$Ph
[Fe_4S_4]$^{3+}$
S = 1/2

Figure 1.10 Synthetic [Fe_4S_4]$^{1+}$-alkyl, [Fe_4S_4]$^{2+}$-alkyl, and [Fe_4S_4]$^{3+}$-alkyl clusters.

the [Fe_4S_4]$^{3+}$–R organometallic intermediates observed in enzymatic systems.[72,143–146] In a subsequent study, an [Fe_4S_4]-alkyl cluster in the biologically relevant [Fe_4S_4]$^{3+}$ redox state (**37,** Figure 1.10) was synthesized and characterized; stabilization of this species was achieved using a scorpionate ligand designed for cuboidal metalloclusters (*vide supra*, 1.2).[91] Spectroscopic and computational analysis indicates that **36** and **37** exhibit partial or complete localization of Fe^{3+} at the Fe–alkyl site owing to the strong donicity of the alkyl ligand. In addition, exceptionally low Mössbauer isomer shifts were observed for the alkylated Fe sites (0.30 mm/s for **36** and 0.14 mm/s for **37**); this could prove to be a spectroscopic signature of alkylated intermediates in biology and highlights the strong covalency of the Fe–C bond. Interestingly, the average *g*-value and the *g*-anisotropy of **37** more closely resemble those of typical [Fe_4S_4]$^{3+}$ clusters (i.e., tetrathiolate-ligated clusters) than those of the organometallic intermediates observed in radical SAM enzymes. This difference may be due to the lower coordination number of the alkylated site in **37** (four) compared to the higher coordination number (five or

six) proposed for the alkylated site in radical SAM enzymes. Further synthetic, spectroscopic, and computational work is needed to resolve this and related questions.

1.4.2 Modeling the interstitial carbide in nitrogenase cofactors

In 2002, a high-resolution crystal structure of the nitrogenase MoFe protein revealed an interstitial light atom (C, N, or O) at the center of the Mo nitrogenase cofactor, FeMo-co.[147] It was not until 2011 that the interstitial atom was identified as a carbon;[148,149] subsequently, an interstitial carbide was also identified in the vanadium-nitrogenase cofactor, FeV-co,[150] and the nitrogenase cofactor precursor, the L-cluster.[151] The identification of an interstitial carbide in the nitrogenase cofactors was intriguing because carbide is an unusual ligand for transition metals, particularly for high-spin metals. The rarity of carbide ligands means that very few appropriate synthetic model systems have been developed. Therefore, the carbide's role in catalysis, the mechanism of its biosynthesis, and its effect on the electronic structures of the cofactors are not well understood. The synthesis and reactivity of model Fe–S clusters containing carbide ligands may shed light on these matters.

The early steps of FeMo-co biosynthesis entail fusion of two $[Fe_4S_4]$ clusters coupled with installation of an additional S atom and an interstitial carbide.[152,153] The latter is derived from the methyl group of *S*-adenosylmethionine (SAM) in a complex, radical-mediated process.[154,155] This mechanism for carbide insertion has no synthetic parallel and thus development of model Fe–S clusters containing carbide ligands requires new synthetic strategies.

One approach to installing carbide ligands at Fe–S clusters is to add sulfur ligands to pre-existing Fe–carbide clusters. The Fe–carbide cluster $[Fe_6C(CO)_{16}]^{2-}$ (**40**) was reported in 1971 by Churchill and coworkers[156,157] and contains an interstitial carbide surrounded by an octahedron of low-spin, CO-ligated Fe centers. In 2019, Rauchfuss and coworkers utilized this precursor in the synthesis of a cluster containing Fe, carbide, and sulfide. Treatment of **40** with

Scheme 1.10 Installation of a bridging sulfide at **40** and derivatization of **43** to contain additional sulfur atoms and heterometals.

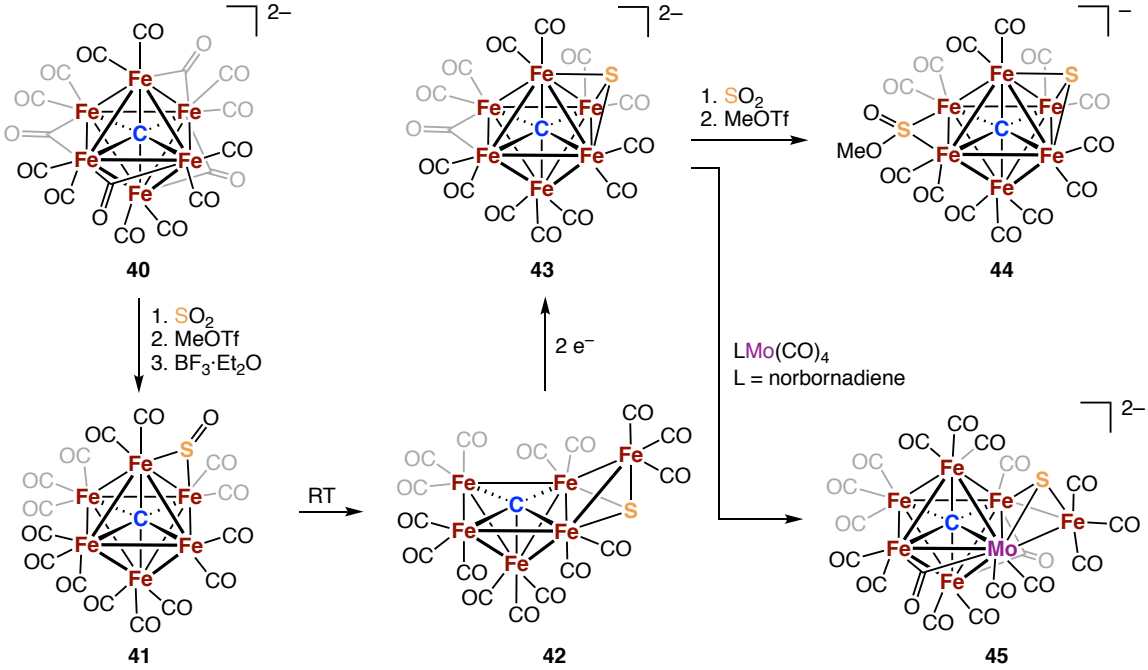

SO_2 formed a cluster containing a bridging SO_2 unit that was subsequently methylated and demethoxylated with MeOTf and $BF_3{\cdot}Et_2O$, respectively, to yield the sulfur monoxide complex $Fe_6C(CO)_{15}(SO)$ (**41**, Scheme 1.10).[158] Cluster **41** spontaneously converts to the sulfide complex, $Fe_6C(CO)_{16}S$ (**42**), by an unknown mechanism. In **42**, the octahedral cluster core is opened and features a five-coordinate carbide; two-electron reduction of **42** results in reformation of an octahedral cluster in which one face is capped by sulfide (**43**). While **43** still has major geometric and electronic differences from FeMoco—including the presence of numerous CO ligands and low-spin Fe sites—this synthetic methodology demonstrates the feasibility of incorporating sulfide into carbide-containing clusters as a route to FeMo-co-like clusters. The authors further demonstrated the installation of additional sulfur ligands (**44**) and heterometals (**45**) into these Fe–C clusters (Scheme 1.10).[159]

Rose and coworkers have also studied the addition of sulfide sources to **40**.[160] Using S_2Cl_2 or elemental sulfur, they synthesized Fe–carbide clusters containing bridging μ_4-sulfide ligands, **47** and **48** (Scheme 1.11). In both cases, clusters containing multiple sulfides and/or

Scheme 1.11 Synthesis of Fe–S–C clusters from electrophilic sulfur sources.

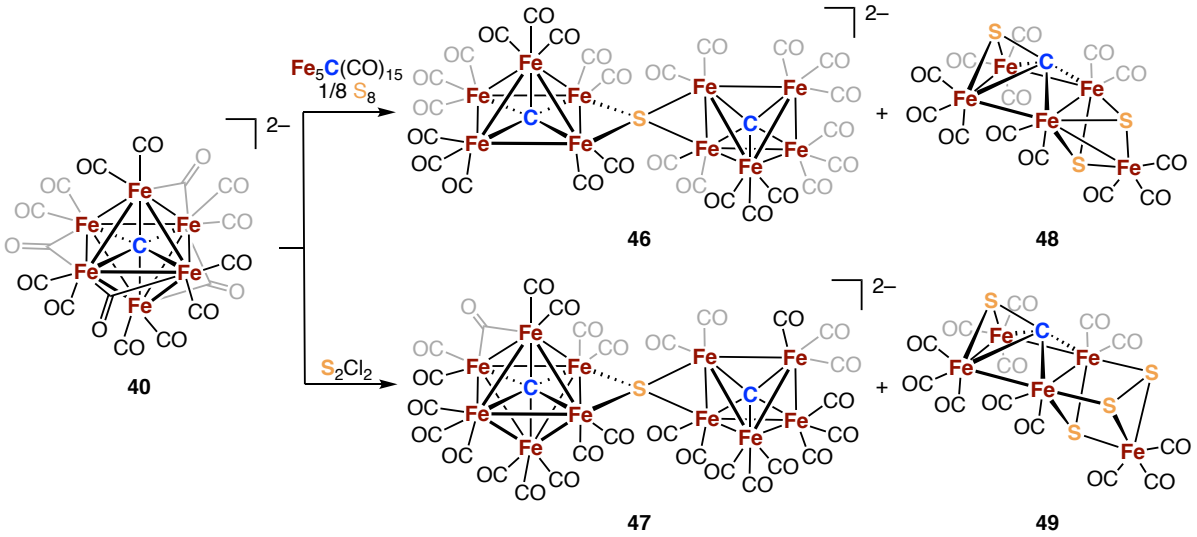

S–C bonds (**48** and **49**) were isolated as side products. The isolation of these byproducts demonstrates that multi-sulfide clusters are accessible from **40** while also highlighting the challenge of delivering sulfur and oxidant equivalents to the low-valent carbonyl cluster **40** in a controlled manner.

Holland, Lancaster, and coworkers have studied [Fe_2S] complexes containing bridging alkylidenes as spectroscopic models for the interstitial carbide in the nitrogenase cofactors (Figure 1.11).[161] The bridging alkylidene is synthesized by addition of a reductant and trimethylsilyldiazomethane to [LFeCl]$_2$ (L = MeC[C(Me)N-(2,6-$Me_2C_6H_3$)]$_2$)[162] followed by treatment of the bridging Fe–C–Fe complex with trimethylphosphine sulfide to yield the cluster **50**, which features an [Fe_2SC] diamond core. An [Fe_2S_2] cluster (**51**) supported by the same ligand was used as a comparison to the alkylidene-bridged species **50**.[163] Using S K-edge XAS, the authors found little perturbation to the covalency of the Fe–S bonds upon replacement of a bridging sulfide with an alkylidene, and using broken symmetry DFT calculations they found that the Fe–C bonds were significantly more covalent than the Fe–S bonds. In addition to serving as a spectroscopic model, **50** may provide a starting point for an alternative, bioinspired approach for synthesizing Fe–S clusters containing a carbide ligand.

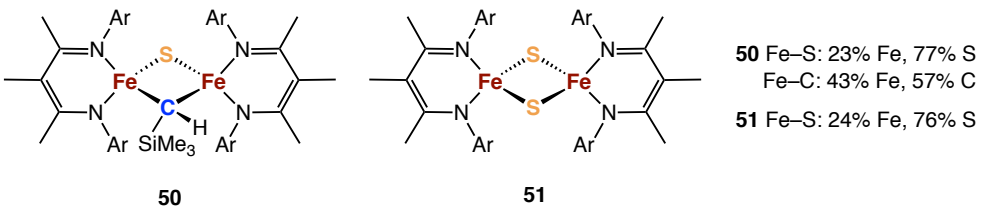

Figure 1.11 Comparative studies of dinuclear Fe–S clusters with and without bridging alkylidene ligands showed little change to the covalency of the Fe–S bond upon replacing S with $CH(SiMe_3)$. Ar = 2,6-dimethylphenyl.

Building on work by Majumdar and Holm,[164] Chen and Holm demonstrated that unique μ_3-ligands can be incorporated into W–Fe–S clusters through ligand metathesis. The initial synthesis of sulfide-deficient W–Fe–S clusters uses Tp*WS_3 (Tp* = tris(3,5-dimethyl-1-pyrazolyl)borate) as a cluster template and source of three cluster sulfides. Addition of FeX_2 (X = Cl^-, Br^-) and a reductant affords [WFe_3S_3] (**52**) and [WFe_2S_3] (**53**) clusters (Scheme 1.12). The sulfur-deficient Clusters **52** and **53** react with sodium salts and/or oxidants to form clusters with bridging imido (**54**), alkoxide (**55**) and nitride (**57**) ligands.[165–167] This ligand metathesis methodology for selective incorporation of unique bridging ligands into Fe–S cluster cores

Scheme 1.12 Incorporation of bridging imido, alkoxide and nitride ligands into W–Fe–S clusters.

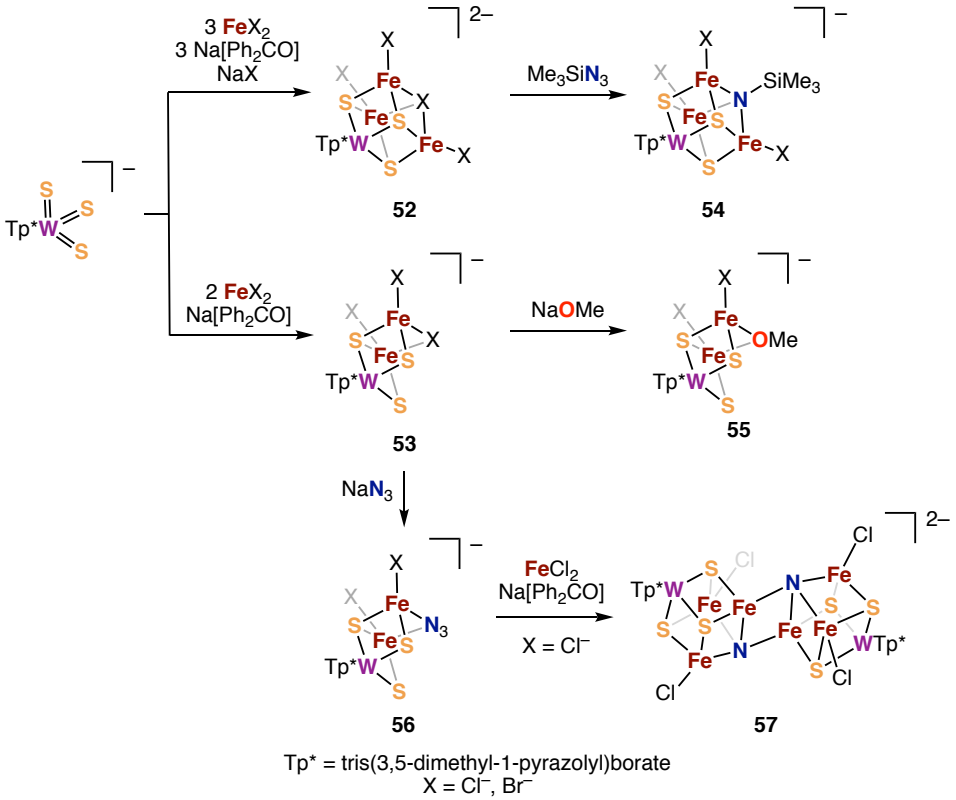

illustrates another approach to the synthesis of Fe–S clusters with carbide ligands. Extension to carbon-based ligands may provide precursors for the synthesis of Fe–S clusters containing carbide ligands.

1.4.3 Fe–S cluster-mediated CO, CO_2 and CN^- reduction

Though inhibition of nitrogenase by CO was recognized early,[168,169] in 2010 and 2011 Lee, Hu, and Ribbe, as well as Seefeldt and coworkers, demonstrated that both FeMo-co and FeV-co within their respective protein frameworks catalytically reduce CO to small-chain hydrocarbons.[170–172] Seefeldt and coworkers later showed that the all-Fe nitrogenase could reduce CO to methane, although no other hydrocarbons were observed.[173] In 2012, Lee, Hu, and Ribbe found that the protein scaffold was not essential for CO reduction—FeMo-co and FeV-co cofactors extracted into N-methylformamide are capable of CO, CO_2, and CN^- coupling to form hydrocarbons, as is the FeMo-co precursor, the L-cluster.[174–176] They also demonstrated that isolated FeMo-co catalyzes coupling of aldehydes with CO to elongate hydrocarbon chains.[177] These CO, CO_2, and CN^- reductions with isolated cofactors require relatively strong reductants such as Eu^{2+} diethylenetriaminepentaacetate (Eu^{2+}-DTPA) or SmI_2.

Table 1.3 Fe–S clusters that reduce CO, CO_2 and CN^-.

Protein-bound	Isolated
FeV-co (VnfDGK, NifDK)	FeV-co
FeMo-co (NifDK, VnfDGK)	FeMo-co
FeFe-co (AnfDGK)	L-cluster
$[Fe_6S_9(SEt)_2]^{4-}$ (NifDK)	$[Fe_6S_9(SEt)_2]^{4-}$
$[Fe_4S_4]$ ($NifH^{Av}$, $NifH^{Ma}$)	$[Cp^*MoFe_5S_9(SH)]^{3-}$ [a]
	$[Fe_4S_4(SCH_2CH_2OH)_4]^{2-}$

a: Cp^* = pentamethylcyclopentadienyl

Continuations of this work by Hu, Ohki, Ribbe, Tatsumi, and coworkers demonstrated that the synthetic clusters $[Fe_6S_9(SEt)_2]^{4-}$ and $[Cp^*MoFe_5S_9(SH)]^{3-}$ (Cp^* = pentamethylcyclopentadienyl) also carry out CO, CO_2 and CN^- coupling under reducing conditions.[178–180] The ability of isolated synthetic clusters to couple C_1 precursors to form

hydrocarbons demonstrates that the unusual structural features of the nitrogenase cofactors—in particular the interstitial carbide—are not essential for this reactivity.

Finally, in 2018, it was shown that hydrocarbon formation is catalyzed by comparatively simple [Fe_4S_4] clusters. Both the [Fe_4S_4] cluster in NifH and the water-soluble cluster [$Fe_4S_4(S(CH_2)_2OH)_4]^{2-}$ reduce CO and CO_2; the latter finding demonstrates that catalysis with [Fe_4S_4] clusters can occur even in the absence of a protein scaffold.[181,182] Table 1.3 summarizes the Fe–S clusters known to carry out these reduction reactions. The catalytic activities depend on solvent, base, and reductant identity, as well as cluster identity; however, only limited direct comparisons can be made with the available data due to differences in reaction conditions. Use of SmI_2 as a reductant and $[LutH]^+$ (Lut = 2,6-dimethylpyridine) or $[Et_3NH]^+$ as acids appears to increase the activity compared to Eu^{2+} reductants and aqueous acids, but also increases the amount of methane produced relative to C–C coupling. Interestingly, in the case of the synthetic [Fe_4S_4] cluster $[Fe_4S_4(S(CH_2)_2OH)_4]^{2-}$, this trend appears to be attenuated: use of $SmI_2/[Et_3NH]^+$ instead of Eu^{2+}/H_2O increases the CO/CO_2 reduction activity with only minor changes to the C_1:$C_{>1}$ product ratio. It is difficult to rationalize these trends at present because the mechanisms of $CO/CO_2/CN^-$ reduction are unclear.

Conceptually related to studies of catalysis by Fe–S clusters outside of a protein scaffold is work by Kanatzidis and coworkers on FeMoS–SnS chalcogels, which are prepared by reaction of halide-ligated Fe–S clusters such as $[Fe_4S_4Cl_4]^{2-}$ and $[Mo_2Fe_6S_8(SPh)_3Cl_6]^{3-}$ with $[Sn_2S_6]^{4-}$ anions; the Fe–S clusters react with the Sn sulfides, forming a cross-linked amorphous gel. In the presence of sodium ascorbate as a reductant and pyridinium chloride as a proton source, these gels were found to be capable of photochemical N_2 fixation to NH_3.[183] Transient UV-vis absorption spectroscopy supports the assignment of a photochemically-excited state as the initial species that reacts with N_2; this exited state decays much more rapidly

in the presence of N_2 than under Ar. Additionally, diffuse reflectance Fourier-transform IR spectroscopic experiments showed N–N stretching frequencies around 1750 cm^{-1} that appear only in the presence of light.[184] One of these bands was found to be sensitive to the presence of H_2O/D_2O, suggesting it may arise from an N_2 reduction intermediate. The presence of Mo in the chalcogels is not required for N_2 fixation, and in fact chalcogels derived from $[Fe_4S_4Cl_4]^{2-}$ reduce N_2 more rapidly than MoFeS chalcogels.[184] Although computational studies support initial binding of N_2 to a photochemically excited state of the Fe–S clusters, the mechanism of N_2 fixation by Fe–S chalcogels remains unknown. Nevertheless, the discovery of photochemical N_2 fixation at Fe–S clusters in chalcogels, in conjuction with findings that synthetic Fe–S clusters promote reductive coupling of C_1 substrates, highlights the promise of utilizing Fe–S clusters outside of a protein environment for challenging catalytic reactions.

1.4.4 Summary

In last two decades, the organometallic chemistry of weak-field Fe–S clusters has been greatly expanded. Developments in synthetic methodology have enabled the synthesis of alkylated Fe–S clusters that are both structural and functional models of enzymatic intermediates. Progress in generating Fe–S–C clusters continues to be made, supporting efforts to understand the properties and reactivity of carbide-containing nitrogenase cofactors. And increasingly, it has been demonstrated that challenging reactions like CO and N_2 reduction are not limited to the complex nitrogenase cofactors, but can be carried out by relatively simple Fe–S clusters. Further synthetic modeling and mechanistic studies are needed to understand the mechanisms of these fascinating reactions.

1.5 Conclusion

The development of Fe–S cluster chemistry continues to benefit from diverse perspectives, including those from biochemistry, synthetic chemistry, spectroscopy, and computational chemistry. The discovery of biological Fe–S clusters with unusual structures

and reactivity continues to motivate the synthesis of structural and functional model complexes, and synthetic chemistry in turn provides insight into the properties of biologically relevant species. Since the last edition of Comprehensive Coordination Chemistry, progress in ligand design and utilization has resulted in new strategies for controlling Fe–S cluster nuclearity, improving the accessibility of site-differentiated clusters, and stabilizing reactive clusters. These methodological advances will continue to propel developments not only in modeling complex biological systems, but also in discovering and studying reactivity that is unique to Fe–S clusters.

1.6 References

(1) Beinert, H.; Sands, R. H. Studies on Succinic and DNPH Dehydrogenase Preparations by Paramagnetic Resonance (EPR) Spectroscopy. *Biochem. Biophys. Res. Commun.* **1960**, *3* (1), 41–46.

(2) Orme-Johnson, W. H. Iron-Sulfur Proteins: Structure And Function. *Annu. Rev. Biochem.* **1973**, *42*, 159–204.

(3) Beinert, H. Recent Developments in the Field of Iron-Sulfur Proteins. *FASEB J.* **1990**, *4* (8), 2483–2491.

(4) Beinert, H. Iron-Sulfur Proteins: Ancient Structures, Still Full of Surprises. *J. Biol. Inorg. Chem.* **2000**, *5* (1), 2–15.

(5) Mortenson, L. E.; Valentine, R. C.; Carnahan, J. E. An Electron Transport Factor from *Clostridium pasterurianum*. *Biochem. Biophys. Res. Commun.* **1962**, *7* (6), 1962.

(6) Fry, K. T.; San Pietro, A. Studies on Photosynthetic Pyridine Nucleotide Reductase. *Biochem. Biophys. Res. Commun.* **1962**, *9* (3), 218–221.

(7) Lovenberg, W.; Buchanan, B. B.; Rabinowitz, J. C. Studies on the Chemical Nature of *Clostridial* Ferredoxin. *J. Biol. Chem.* **1963**, *238* (12), 3899–3913.

(8) Buchanan, B. B.; Lovenberg, W.; Rabinowitz, J. C. A Comparison of *Clostridial* Ferredoxins. *Proc. Natl. Acad. Sci. U. S. A.* **1963**, *49*, 345–353.

(9) Strahs, G.; Kraut, J. Low-Resolution Electron-Density and Anomalous-Scattering-Density Maps of *Chromatium* High-Potential Iron Protein. *J. Mol. Biol.* **1968**, *35* (3), 503–512.

(10) Carter, C. W.; Freer, S. T.; Xuong, N. H.; Alden, R. A.; Kraut, J. Structure of the Iron-Sulfur Cluster in the *Chromatium* Iron Protein at 2.25 Å Resolutions. *Cold Springs Harb. Symp. Quant. Biol.* **1971**, *36*, 381–385.

(11) Carter, C. W.; Kraut, J.; Freer, S. T.; Alden, R. A.; Sieker, L. C.; Adman, E.; Jensen, L. H. A Comparison of Fe_4S_4 Clusters in High-Potential Iron Protein and in Ferredoxin. *Proc. Natl. Acad. Sci. U. S. A.* **1972**, *69* (12), 3526–3529.

(12) Beinert, H.; Holm, R. H.; Münck; Eckard. Iron-Sulfur Clusters : Nature's Modular, Multipurpose Structures. *Science* **1997**, *277* (5326), 653–659.

(13) *Comprehensive Coordination Chemistry II*; Constable, E., McCleverty, J. A., Meyer, T. J., Eds.; Elsevier Science, 2004; Vol. 1–9.

(14) Herskovitz, T.; Averill, B. A.; Holm, R. H.; Ibers, J. A.; Phillips, W. D.; Weiher, J. F. Structure and Properties of a Synthetic Analogue of Bacterial Iron–Sulfur Proteins.

Proc. Natl. Acad. Sci. U. S. A. **1972**, *69* (9), 2437–2441.
(15) Venkateswara Rao, P.; Holm, R. H. Synthetic Analogues of the Active Sites of Iron−Sulfur Proteins. *Chem. Rev.* **2004**, *104* (2), 527–560.
(16) Lee, S. C.; Holm, R. H. The Clusters of Nitrogenase: Synthetic Methodology in the Construction of Weak-Field Clusters. *Chem. Rev.* **2004**, *104* (2), 1135–1157.
(17) Lee, S. C.; Lo, W.; Holm, R. H. Developments in the Biomimetic Chemistry of Cubane-Type and Higher Nuclearity Iron-Sulfur Clusters. *Chem. Rev.* **2014**, *114* (7), 3579–3600.
(18) Holm, R. H.; Lo, W. Structural Conversions of Synthetic and Protein-Bound Iron-Sulfur Clusters. *Chem. Rev.* **2016**, *116* (22), 13685–13713.
(19) Ohta, S.; Ohki, Y. Impact of Ligands and Media on the Structure and Properties of Biological and Biomimetic Iron-Sulfur Clusters. *Coord. Chem. Rev.* **2017**, *338*, 207–225.
(20) Pluth, M. D.; Tonzetich, Z. J. Hydrosulfide Complexes of the Transition Elements: Diverse Roles in Bioinorganic, Cluster, Coordination, and Organometallic Chemistry. *Chem. Soc. Rev.* **2020**, *49* (12), 4070–4134.
(21) Tanifuji, K.; Ohki, Y. Metal-Sulfur Compounds in N_2 Reduction and Nitrogenase-Related Chemistry. *Chem. Rev.* **2020**, *120* (12), 5194–5251.
(22) Lemon, B. J.; Nocek, B.; Peters, J. W. Crystal Structure of a Carbon Monoxide Dehydrogenase Reveals a [Ni-4Fe-5S] Cluster. *Science* **2001**, *293* (5533), 1281–1285.
(23) Aragão, D.; Macedo, S.; Mitchell, E. P.; Romão, C. V.; Liu, M. Y.; Frazão, C.; Saraiva, L. M.; Xavier, A. V.; LeGall, J.; Van Dongen, W. M. A. M.; Hagen, W. R.; Teixeira, M.; Carrondo, M. A.; Lindley, P. Reduced Hybrid Cluster Proteins (HCP) from *Desulfovibrio desulfuricans* ATCC 27774 and *Desulfovibrio vulgaris* (Hildenborough): X-Ray Structures at High Resolution Using Synchrotron Radiation. *J. Biol. Inorg. Chem.* **2003**, *8* (5), 540–548.
(24) Shomura, Y.; Yoon, K. S.; Nishihara, H.; Higuchi, Y. Structural Basis for a [4Fe-3S] Cluster in the Oxygen-Tolerant Membrane-Bound [NiFe]-Hydrogenase. *Nature* **2011**, *479* (7372), 253–256.
(25) Fritsch, J.; Scheerer, P.; Frielingsdorf, S.; Kroschinsky, S.; Friedrich, B.; Lenz, O.; Spahn, C. M. T. The Crystal Structure of an Oxygen-Tolerant Hydrogenase Uncovers a Novel Iron-Sulphur Centre. *Nature* **2011**, *479* (7372), 249–253.
(26) Wagner, T.; Koch, J.; Ermler, U.; Shima, S. Methanogenic Heterodisulfide Reductase (HdrABC-MvhAGD) Uses Two Noncubane [4Fe-4S] Clusters for Reduction. *Science* **2017**, *357* (6352), 699–703.
(27) Jeoung, J. H.; Dobbek, H. ATP-Dependent Substrate Reduction at an $[Fe_8S_9]$ Double-Cubane Cluster. *Proc. Natl. Acad. Sci. U. S. A.* **2018**, *115* (12), 2994–2999.
(28) Hall, D. O.; Rao, K. K.; Cammack, R. The Iron-Sulphur Proteins: Structure, Function and Evolution of a Ubiquitous Group of Proteins. *Sci. Prog.* **1975**, *62* (246), 285–317.
(29) O'Sullivan, T.; Millar, M. M. Synthesis and Study of an Analogue for the $[Fe_4S_4]^{3+}$ Center of Oxidized High-Potential Iron—Sulfur Proteins. *J. Am. Chem. Soc.* **1985**, *107* (13), 4096–4097.
(30) Ohki, Y.; Sunada, Y.; Tatsumi, K. Synthesis of [2Fe-2S] and [4Fe-4S] Clusters Having Terminal Amide Ligands from an Iron(II) Amide Complex. *Chem. Lett.* **2005**, *34* (2), 172–173.
(31) Sharp, C. R.; Duncan, J. S.; Lee, S. C. $[Fe_4S_4]^q$ Cubane Clusters (q = 4+, 3+, 2+) with Terminal Amide Ligands. *Inorg. Chem.* **2010**, *49* (14), 6697–6705.
(32) Tanifuji, K.; Yamada, N.; Tajima, T.; Sasamori, T.; Tokitoh, N.; Matsuo, T.; Tamao, K.; Ohki, Y.; Tatsumi, K. A Convenient Route to Synthetic Analogues of the Oxidized Form of High-Potential Iron-Sulfur Proteins. *Inorg. Chem.* **2014**, *53* (8), 4000–4009.

(33) Carter, C. W.; Kraut, J.; Freer, S. T.; Alden, R. A. Comparison of Oxidation Reduction Site Geometries in Oxidized and Reduced *Chromatium* High Potential Iron Protein and Oxidized *Peptococcus aerogenes* Ferredoxin. *J. Biol. Chem.* **1974**, *249* (19), 6339–6346.
(34) Dey, A.; Jenney Jr., F. E.; Adams, M. W. W.; Babini, E.; Takahashi, Y.; Fukuyama, K.; Hodgson, K. O.; Hedman, B.; Solomon, E. I. Solvent Tuning of Electrochemical Potentials in the Active Sites of HiPIP Versus Ferredoxin. *Science* **2007**, *318* (5855), 1464–1468.
(35) Ohki, Y.; Tanifuji, K.; Yamada, N.; Imada, M.; Tajima, T.; Tatsumi, K. Synthetic Analogues of $[Fe_4S_4(Cys)_3(His)]$ in Hydrogenases and $[Fe_4S_4(Cys)_4]$ in HiPIP Derived from All-Ferric $[Fe_4S_4\{N(SiMe_3)_2\}_4]$. *Proc. Natl. Acad. Sci. U. S. A.* **2011**, *108* (31), 12635–12640.
(36) Volbeda, A.; Charon, M. H.; Piras, C.; Hatchikian, E. C.; Frey, M.; Fontecilla-Camps, J. C. Crystal Structure of the Nickel-Iron Hydrogenase from *Desulfovibrio gigas*. *Nature* **1995**, *373* (6515), 580–587.
(37) Peters, J. W.; Lanzilotta, W. N.; Lemon, B. J.; Seefeldt, L. C. X-Ray Crystal Structure of the Fe-Only Hydrogenase (CpI) from *Clostridium pasteurianum* to 1.8 Angstrom Resolution. *Science* **1998**, *282* (5395), 1853–1858.
(38) Moula, G.; Matsumoto, T.; Miehlich, M. E.; Meyer, K.; Tatsumi, K. Synthesis of an All-Ferric Cuboidal Iron–Sulfur Cluster $[Fe^{III}_4S_4(SAr)_4]$. *Angew. Chem. Int. Ed.* **2018**, *57* (36), 11594–11597.
(39) Noodleman, L.; Peng, C. Y.; Case, D. A.; Mouesca, J. M. Orbital Interactions, Electron Delocalization and Spin Coupling in Iron-Sulfur Clusters. *Coord. Chem. Rev.* **1995**, *144* (C), 199–244.
(40) Danyal, K.; Dean, D. R.; Hoffman, B. M.; Seefeldt, L. C. Electron Transfer within Nitrogenase: Evidence for a Deficit-Spending Mechanism. *Biochemistry* **2011**, *50* (43), 9255–9263.
(41) Seefeldt, L. C.; Hoffman, B. M.; Peters, J. W.; Raugei, S.; Beratan, D. N.; Antony, E.; Dean, D. R. Energy Transduction in Nitrogenase. *Acc. Chem. Res.* **2018**, *51* (9), 2179–2186.
(42) Rutledge, H. L.; Tezcan, F. A. Electron Transfer in Nitrogenase. *Chem. Rev.* **2020**, *120* (12), 5158–5193.
(43) Chan, J. M.; Christiansen, J.; Dean, D. R.; Seefeldt, L. C. Spectroscopic Evidence for Changes in the Redox State of the Nitrogenase P-Cluster during Turnover. *Biochemistry* **1999**, *38* (18), 5779–5785.
(44) Keable, S. M.; Zadvornyy, O. A.; Johnson, L. E.; Ginovska, B.; Rasmussen, A. J.; Danyal, K.; Eilers, B. J.; Prussia, G. A.; LeVan, A. X.; Raugei, S.; Seefeldt, L. C.; Peters, J. W. Structural Characterization of the P1 Intermediate State of the P-Cluster of Nitrogenase. *J. Biol. Chem.* **2018**, *293* (25), 9629–9635.
(45) Peters, J. W.; Stowell, M. H. B.; Soltis, S. M.; Finnegan, M. G.; Johnson, M. K.; Rees, D. C. Redox-Dependent Structural Changes in the Nitrogenase P-Cluster. *Biochemistry* **1997**, *36* (6), 1181–1187.
(46) Ohki, Y.; Sunada, Y.; Honda, M.; Katada, M.; Tatsumi, K. Synthesis of the P-Cluster Inorganic Core of Nitrogenases. *J. Am. Chem. Soc.* **2003**, *1* (14), 4052–4053.
(47) Ohki, Y.; Imada, M.; Murata, A.; Sunada, Y.; Ohta, S.; Honda, M.; Sasamori, T.; Tokitoh, N.; Katada, M.; Tatsumi, K. Synthesis, Structures, and Electronic Properties of [8Fe-7S] Cluster Complexes Modeling the Nitrogenase P-Cluster. *J. Am. Chem. Soc.* **2009**, *131* (36), 13168–13178.
(48) Ohki, Y.; Murata, A.; Imada, M.; Tatsumi, K. C-H Bond Activation of Decamethylcobaltocene Mediated by a Nitrogenase Fe8S7 P-Cluster Model. *Inorg.*

Chem. **2009**, *48* (10), 4271–4273.
(49) Ohki, Y.; Ikagawa, Y.; Tatsumi, K. Synthesis of New [8Fe-7S] Clusters: A Topological Link between the Core Structures of P-Cluster, FeMo-Co, and FeFe-Co of Nitrogenases. *J. Am. Chem. Soc.* **2007**, *129* (34), 10457–10465.
(50) Hashimoto, T.; Ohki, Y.; Tatsumi, K. Synthesis of Coordinatively Unsaturated Mesityliron Thiolate Complexes and Their Reactions with Elemental Sulfur. *Inorg. Chem.* **2010**, *49* (13), 6102–6109.
(51) Ohta, S.; Ohki, Y.; Hashimoto, T.; Cramer, R. E.; Tatsumi, K. A Nitrogenase Cluster Model [Fe_8S_6O] with an Oxygen Unsymmetrically Bridging Two Proto-Fe_4S_3 Cubes: Relevancy to the Substrate Binding Mode of the Femo Cofactor. *Inorg. Chem.* **2012**, *51* (21), 11217–11219.
(52) Ohki, Y.; Tanifuji, K.; Yamada, N.; Cramer, R. E.; Tatsumi, K. Formation of a Nitrogenase P-Cluster [Fe_8S_7] Core via Reductive Fusion of Two All-Ferric [Fe_4S_4] Clusters. *Chem. Asian J.* **2012**, *7* (10), 2222–2224.
(53) Hu, Y.; Ribbe, M. W. Biosynthesis of the Metalloclusters of Molybdenum Nitrogenase. *Microbiol. Mol. Biol. Rev.* **2011**, *75* (4), 664–677.
(54) Burén, S.; Jiménez-Vicente, E.; Echavarri-Erasun, C.; Rubio, L. M. Biosynthesis of Nitrogenase Cofactors. *Chem. Rev.* **2020**, *120* (12), 4921–4968.
(55) Appelt, R.; Vahrenkamp, H.; Darensbourg, D. J.; Phelps, A. L.; Adams, M. J.; Daresbourg, D. J.; Phelps, A. L. Cyanometal-Substituted Derivatives of the Fe_4S_4 Cluster Core. *Inorg. Synth.* **2004**, *34*, 161–166.
(56) Kanatzidis, M. G.; Dunham, W. R.; Hagen, W. R.; Coucouvanis, D. A New Iron-Sulphide Cluster Containing the 'Prismane' $[Fe_6(\mu\text{-}S)_6]^{3+}$ Core. Synthesis, Structure, and Properties of $[Et_4N]_3[Fe_6S_6Cl_6]$. *J. Chem. Soc. - Ser. Chem. Commun.* **1984**, No. 6, 356–358.
(57) Deng, L.; Majumdar, A.; Lo, W.; Holm, R. H. Stabilization of 3:1 Site-Differentiated Cubane-Type Clusters in the $[Fe_4S_4]^{1+}$ Core Oxidation State by Tertiary Phosphine Ligation: Synthesis, Core Structural Diversity, and $S = 1/2$ Ground States. *Inorg. Chem.* **2010**, *49* (23), 11118–11126.
(58) Deng, L.; Holm, R. H. Stabilization of Fully Reduced Iron-Sulfur Clusters by Carbene Ligation: The $[Fe_nS_n]^0$ Oxidation Levels (n = 4, 8). *J. Am. Chem. Soc.* **2008**, *130* (30), 9878–9886.
(59) Goh, C.; Segal, B. M.; Huang, J.; Long, J. R.; Holm, R. H. Polycubane Clusters: Synthesis of $[Fe_4S_4(PR_3)_4]^{1+,0}$ (R = Bu(t), Cy, Pr(i)) and $[Fe_4S_4]^0$ Core Aggregation upon Loss of Phosphine. *J. Am. Chem. Soc.* **1996**, *118* (47), 11844–11853.
(60) Tyson, M. A.; Demadis, K. D.; Coucouvanis, D. Uncharged Mixed-Ligand Clusters with the $[Fe_4S_4]^+$ and $[Fe_4S_4]^{2+}$ Cores. Synthesis, Structural Characterization, and Properties of the $Fe_4S_4X(^TBu_3P)_3$ (X = Cl, Br, I) and $Fe_4S_4(SPh)_2(^TBu_3P)_2$ Cubanes. *Inorg. Chem.* **1995**, *34* (18), 4519–4520.
(61) McSkimming, A.; Suess, D. L. M. Selective Synthesis of Site-Differentiated Fe_4S_4 and Fe_6S_6 Clusters. *Inorg. Chem.* **2018**, *57* (23), 14904–14912.
(62) Lee, Y.; Jeon, I. R.; Abboud, K. A.; García-Serres, R.; Shearer, J.; Murray, L. J. A [3Fe-3S]$^{3+}$ Cluster with Exclusively μ-Sulfide Donors. *Chem. Commun.* **2016**, *52* (6), 1174–1177.
(63) Kent, T. A.; Huynh, B. H.; Eckard, M. Iron-Sulfur Proteins: Spin-Coupling Model for Three-Iron Clusters. *Proc. Natl. Acad. Sci. U. S. A.* **1980**, *77* (11), 6574–6576.
(64) Ferreira, R. B.; Cook, B. J.; Knight, B. J.; Catalano, V. J.; García-Serres, R.; Murray, L. J. Catalytic Silylation of Dinitrogen by a Family of Triiron Complexes. *ACS Catal.* **2018**, *8* (8), 7208–7212.
(65) Rodriguez, M. M.; Stubbert, B. D.; Scarborough, C. C.; Brennessel, W. W.; Bill, E.;

Holland, P. L. Isolation and Characterization of Stable Iron(I) Sulfide Complexes. *Angew. Chem. Int. Ed.* **2012**, *51* (33), 8247–8250.
(66) Vela, J.; Stoian, S.; Flaschenriem, C. J.; Münck, E.; Holland, P. L. A Sulfido-Bridged Diiron(II) Compound and Its Reactions with Nitrogenase-Relevant Substrates. *J. Am. Chem. Soc.* **2004**, *126* (14), 4522–4523.
(67) DeRosha, D. E.; Arnet, N. A.; Mercado, B. Q.; Holland, P. L. A [2Fe−1S] Complex That Affords Access to Bimetallic and Higher-Nuclearity Iron−sulfur Clusters. *Inorg. Chem.* **2019**, *58* (13), 8829–8834.
(68) Anderson, J. S.; Peters, J. C. Low-Spin Pseudotetrahedral Iron(I) Sites in $Fe_2(\mu\text{-}S)$ Complexes. *Angew. Chem. Int. Ed.* **2014**, *53* (23), 5978–5981.
(69) DeRosha, D. E.; Chilkuri, V. G.; Van Stappen, C.; Bill, E.; Mercado, B. Q.; DeBeer, S.; Neese, F.; Holland, P. L. Planar Three-Coordinate Iron Sulfide in a Synthetic [4Fe-3S] Cluster with Biomimetic Reactivity. *Nat. Chem.* **2019**, *11* (11), 1019–1025.
(70) Beinert, H.; Kennedy, M. C.; Stout, C. D. Aconitase as Iron−Sulfur Protein, Enzyme, and Iron-Regulatory Protein. *Chem. Rev.* **1996**, *96* (7), 2335–2374.
(71) Knauer, S. H.; Buckel, W.; Dobbek, H. Structural Basis for Reductive Radical Formation and Electron Recycling in (R)-2-Hydroxyisocaproyl-CoA Dehydratase. *J. Am. Chem. Soc.* **2011**, *133* (12), 4342–4347.
(72) Wang, W.; Oldfield, E. Bioorganometallic Chemistry with IspG and IspH: Structure, Function, and Inhibition of the $[Fe_4S_4]$ Proteins Involved in Isoprenoid Biosynthesis. *Angew. Chem. Int. Ed.* **2014**, *53* (17), 4294–4310.
(73) Broderick, J. B.; Duffus, B. R.; Duschene, K. S.; Shepard, E. M. Radical S-Adenosylmethionine Enzymes. *Chem. Rev.* **2014**, *114* (8), 4229–4317.
(74) Holm, R. H.; Ciurli, S.; Weigel, J. A.; Lippard, S. J. Subsite-Specific Structures and Reactions in Native and Synthetic [4Fe-4S] Cubane-Type Clusters. In *Progress in Inorganic Chemistry*; Lippard, S. J., Ed.; John Wiley & Sons, Inc., 1990; pp 1–74.
(75) Stack, T. D. P.; Holm, R. H. Subsite-Specific Functionalization of the $[4Fe\text{-}4S]^{2+}$ Analogue of Iron-Sulfur Protein Clusters. *J . Am. Chem. Soc.* **1987**, *109* (8), 2546–2547.
(76) Stack, T. D. P.; Holm, R. H. Subsite-Differentiated Analogues of Biological $[4Fe\text{-}4S]^{2+}$ Clusters: Synthesis, Solution and Solid-State Structures, and Subsite-Specific Reactions. *J. Am. Chem. Soc.* **1988**, *110* (8), 2484–2494.
(77) Walsdorff, C.; Saak, W. A Preorganised Doubly Tripodal Hexathiol: Syntheses and Crystal Structures of Complexes with Two 3:1 Subsite-Differentiated Fe_4S_4 clusters. *Chem. Commun.* **1997**, No. 19, 1931–1932.
(78) Walsdorff, C.; Saak, W.; Pohl, S. A New Preorganized Tridentate Ligand Bearing Three Indolethiolate Groups. Preparation of 3:1 Subsite-Differentiated Fe_4S_4 Clusters. *J. Chem. Soc. Dalton Trans.* **1997**, No. 11, 1857–1861.
(79) Terada, T.; Wakimoto, T.; Nakamura, T.; Hirabayashi, K.; Tanaka, K.; Li, J.; Matsumoto, T.; Tatsumi, K. Tridentate Thiolate Ligands: Application to the Synthesis of the Site-Differentiated [4Fe-4S] Cluster Having a Hydrosulfide Ligand at the Unique Iron Center. *Chem. Asian J.* **2012**, *7*, 920–929.
(80) Ye, M.; Thompson, N. B.; Brown, A. C.; Suess, D. L. M. A Synthetic Model of Enzymatic $[Fe_4S_4]$-Alkyl Intermediates. *J. Am. Chem. Soc.* **2019**, *141* (34), 13330–13335.
(81) Whitener, M. A.; Peng, G.; Holm, R. H. Subsite-Differentiated Analogues of Biological [4Fe-4S] Clusters Effected by Binding of a Macrocyclic Polyether Trithiol. *Inorg. Chem.* **1991**, *30* (10), 2411–2417.
(82) van Strijdonck, P. F.; E H van Haare, J. A.; M van der Linden, J. G.; Steggerda, J. J.; M Nolte, R. J. Novel Subsite-Differentiated [4Fe-4S] Clusters Based on

Cyclotriveratrylene. *Inorg. Chem* **1994**, *33* (6), 999–1000.
(83) van Strijdonck, G. P. F.; Van Haare, J. A. E. H.; Hönen, P. J. M.; Van Den Schoor, R. C. M.; Feiters, M. C.; Van Der Linden, J. G. M.; Steggerda, J. J.; Nolte, R. J. M. Cyclotriveratrylene Models for [4Fe–4S] Proteins: 3:1 Subsite Differentiation and Modulation of the Redox Potential. *J. Chem. Soc. Dalton Trans.* **1997**, No. 1, 449–461.
(84) Barclay, J. E.; Evans, D. J.; Garcia, G.; Santana, M. D.; Torralba, M. C.; Yago, J. M. Binding of the $\{MoFe_3S_4\}^{3+}$ Core by a Tridentate Thiolate and Chemical Analogues of the Molybdenum Co-Ordination Environment in the Iron-Molybdenum Cofactor of Nitrogenase. *J. Chem. Soc. Dalt. Trans.* **1995**, No. 12, 1965–1971.
(85) Martens, C. F.; Bongers, M. M. G.; Kenis, P. J. A.; Czajka, R.; Feiters, M. C.; Van Der Linden, J. G. M.; Nolle, R. J. M. Characterization of a [4Fe-4S]-Ferredoxin Model Based on a Concave Tetradentate Thiol Ligand System. *Chem. Ber.* **1997**, *130* (1), 23–33.
(86) Gibney, B. R.; Mulholland, S. E.; Rabanal, F.; Dutton, L. P. Ferredoxin and Ferredoxin – Heme Maquettes. *Proc. Natl. Acad. Sci. U. S. A.* **1996**, *93*, 15041–15046.
(87) Mulholland, S. E.; Gibney, B. R.; Rabanal, F.; Leslie Dutton, P. Characterization of the Fundamental Protein Ligand Requirements of $[4Fe\text{-}4S]^{(2+/+)}$ Clusters with Sixteen Amino Acid Maquettes. *J. Am. Chem. Soc.* **1998**, *120* (40), 10296–10302.
(88) Mulholland, S. E.; Gibney, B. R.; Rabanal, F.; Dutton, P. L. Determination of Nonligand Amino Acids Critical to $[4Fe\text{-}4S]^{(2+/+)}$ Assembly in Ferredoxin Maquettes. *Biochemistry* **1999**, *38* (32), 10442–10448.
(89) Antonkine, M. L.; Koay, M. S.; Epel, B.; Breitenstein, C.; Gopta, O.; Gärtner, W.; Bill, E.; Lubitz, W. Synthesis and Characterization of de Novo Designed Peptides Modelling the Binding Sites of [4Fe-4S] Clusters in Photosystem I. *Biochim. Biophys. Acta - Bioenerg.* **2009**, *1787* (8), 995–1008.
(90) Hoppe, A.; Pandelia, M. E.; Gärtner, W.; Lubitz, W. $[Fe_4S_4]$- and $[Fe_3S_4]$-Cluster Formation in Synthetic Peptides. *Biochim. Biophys. Acta - Bioenerg.* **2011**, *1807* (11), 1414–1422.
(91) McSkimming, A.; Sridharan, A.; Thompson, N. B.; Müller, P.; Suess, D. L. M. An $[Fe_4S_4]^{3+}$-Alkyl Cluster Stabilized by an Expanded Scorpionate Ligand. *J. Am. Chem. Soc.* **2020**, *142* (33), 14314–14323.
(92) Zhou, J.; Hu, Z.; Münck, E.; Holm, R. H. The Cuboidal Fe_3S_4 Cluster: Synthesis, Stability, and Geometric and Electronic Structures in a Non-Protein Environment. *J. Am. Chem. Soc.* **1996**, *118* (8), 1966–1980.
(93) Zhou, H.-C.; Holm, R. H. Synthesis and Reactions of Cubane-Type Iron−Sulfur−Phosphine Clusters, Including Soluble Clusters of Nuclearities 8 and 16. *Inorg. Chem.* **2003**, *42* (1), 11–21.
(94) Goh, C.; Weigel, J. A.; Holm, R. H. The [2:2] Site-Differentiated Clusters $[Fe_4S_4L_2(RNC)_6]$ Containing Two Low-Spin Iron(II) Sites. *Inorg. Chem.* **1994**, *33* (22), 4861–4868.
(95) Xi, B.; Holm, R. H. The $[MoFe_3S_4]^{2+}$ Oxidation State: Synthesis, Substitution Reactions, and Structures of Phosphine-Ligated Cubane-Type Clusters with the $S = 2$ Ground State. *Inorg. Chem.* **2011**, *50* (13), 6280–6288.
(96) Bak, D. W.; Elliott, S. J. Alternative FeS Cluster Ligands: Tuning Redox Potentials and Chemistry. *Curr. Opin. Chem. Biol.* **2014**, *19* (1), 50–58.
(97) Ballmann, J.; Albers, A.; Demeshko, S.; Dechert, S.; Bill, E.; Bothe, E.; Ryde, U.; Meyer, F. A Synthetic Analogue of Rieske-Type [2Fe-2S] Clusters. *Angew. Chem. Int. Ed.* **2008**, *47* (49), 9537–9541.
(98) Albers, A.; Demeshko, S.; Dechert, S.; Saouma, C. T.; Mayer, J. M.; Meyer, F. Fast

Proton-Coupled Electron Transfer Observed for a High-Fidelity Structural and Functional [2Fe-2S] Rieske Model. *J. Am. Chem. Soc.* **2014**, *136* (10), 3946–3954.
(99) Bergner, M.; Dechert, S.; Demeshko, S.; Kupper, C.; Mayer, J. M.; Meyer, F. Model of the MitoNEET [2Fe-2S] Cluster Shows Proton Coupled Electron Transfer. *J. Am. Chem. Soc.* **2017**, *139* (2), 701–707.
(100) Zu, Y.; Fee, J. A.; Hirst, J. Complete Thermodynamic Characterization of Reduction and Protonation of the Bc1-Type Rieske [2Fe-2S] Center of *Thermus thermophilus* [6]. *J. Am. Chem. Soc.* **2001**, *123* (40), 9906–9907.
(101) Zu, Y.; Couture, M. M. J.; Kolling, D. R. J.; Crofts, A. R.; Eltis, L. D.; Fee, J. A.; Hirst, J. Reduction Potentials of Rieske Clusters: Importance of the Coupling between Oxidation State and Histidine Protonation State. *Biochemistry* **2003**, *42* (42), 12400–12408.
(102) Bak, D. W.; Zuris, J. A.; Paddock, M. L.; Jennings, P. A.; Elliott, S. J. Redox Characterization of the FeS Protein MitoNEET and Impact of Thiazolidinedione Drug Binding. *Biochemistry* **2009**, *48* (43), 10193–10195.
(103) Saouma, C. T.; Kaminsky, W.; Mayer, J. M. Protonation and Concerted Proton-Electron Transfer Reactivity of a Bis-Benzimidazolate Ligated [2Fe-2S] Model for Rieske Clusters. *J. Am. Chem. Soc.* **2012**, *134* (17), 7293–7296.
(104) Saouma, C. T.; Pinney, M. M.; Mayer, J. M. Electron Transfer and Proton-Coupled Electron Transfer Reactivity and Self-Exchange of Synthetic [2Fe-2S] Complexes: Models for Rieske and MitoNEET Clusters. *Inorg. Chem.* **2014**, *53* (6), 3153–3161.
(105) Sharma, S.; Sivalingam, K.; Neese, F.; Chan, G. K. L. Low-Energy Spectrum of Iron-Sulfur Clusters Directly from Many-Particle Quantum Mechanics. *Nat. Chem.* **2014**, *6* (10), 927–933.
(106) Chilkuri, V. G.; Debeer, S.; Neese, F. Ligand Field Theory and Angular Overlap Model Based Analysis of the Electronic Structure of Homovalent Iron-Sulfur Dimers. *Inorg. Chem.* **2020**, *59* (2), 984–995.
(107) Watt, G. D.; Reddy, K. R. N. Formation of an All Ferrous Fe_4S_4 Cluster in the Iron Protein Component of *Azotobacter vinelandii* Nitrogenase. *J. Inorg. Biochem.* **1994**, *53* (4), 281–294.
(108) Angove, H. C.; Yoo, S. J.; Burgess, B. K.; Münck, E. Mössbauer and EPR Evidence for an All-Ferrous Fe_4S_4 Cluster with $S = 4$ in the Fe Protein of Nitrogenase. *J. Am. Chem. Soc.* **1997**, *119* (37), 8730–8731.
(109) Hans, M.; Buckel, W.; Bill, E. Spectroscopic Evidence for an All-Ferrous $[4Fe\text{-}4S]^0$ Cluster in the Superreduced Activator of 2-Hydroxyglutaryl-CoA Dehydratase from *Acidaminococcus fermentans*. *J. Biol. Inorg. Chem.* **2008**, *13* (4), 563–574.
(110) Hiller, C. J.; Stiebritz, M. T.; Lee, C. C.; Liedtke, J.; Hu, Y. Tuning Electron Flux through Nitrogenase with Methanogen Iron Protein Homologues. *Chem. Eur. J.* **2017**, *23* (64), 16152–16156.
(111) Yoo, S. J.; Angove, H. C.; Burgess, B. K.; Hendrich, M. P.; Münck, E. Mossbauer and Integer-Spin EPR Studies and Spin-Coupling Analysis of the $[4Fe\text{-}4S]^0$ Cluster of the Fe Protein from *Azotobacter vinelandii* Nitrogenase. *J. Am. Chem. Soc.* **1999**, *121* (11), 2534–2545.
(112) Scott, T. A.; Berlinguette, C. P.; Holm, R. H.; Zhou, H. C. Initial Synthesis and Structure of an All-Ferrous Analogue of the Fully Reduced $[Fe_4S_4]^0$ Cluster of the Nitrogenase Iron Protein. *Proc. Natl. Acad. Sci. U. S. A.* **2005**, *102* (28), 9741–9744.
(113) Zhang, H.; Ouyang, Z.; Liu, Y.; Zhang, Q.; Wang, L.; Deng, L. (Aminocarbene)(Divinyltetramethyldisiloxane)Iron(0) Compounds: A Class of Low-Coordinate Iron(0) Reagents. *Angew. Chem. Int. Ed.* **2014**, *53* (32), 8432–8436.
(114) Strop, P.; Takahara, P. M.; Chiu, H. J.; Angove, H. C.; Burgess, B. K.; Rees, D. C.

Crystal Structure of the All-Ferrous [4Fe-4S]^0 Form of the Nitrogenase Iron Protein from *Azotobacter vinelandii*. *Biochemistry* **2001**, *40* (3), 651–656.
(115) Chakrabarti, M.; Deng, L.; Holm, R. H.; Münck, E.; Bominaar, E. L. Mössbauer, Electron Paramagnetic Resonance, and Theoretical Studies of a Carbene-Based All-Ferrous Fe_4S_4 Cluster: Electronic Origin and Structural Identification of the Unique Spectroscopic Site. *Inorg. Chem.* **2009**, *48* (7), 2735–2747.
(116) Chakrabarti, M.; Münck, E.; Bominaar, E. L. Density Functional Theory Study of an All Ferrous 4Fe-4S Cluster. *Inorg. Chem.* **2011**, *50* (10), 4322–4326.
(117) Lowery, T. J.; Wilson, P. E.; Zhang, B.; Bunker, J.; Harrison, R. G.; Nyborg, A. C.; Thiriot, D.; Watt, G. D. Flavodoxin Hydroquinone Reduces *Azotobacter vinelandii* Fe Protein to the All-Ferrous Redox State with a $S = 0$ Spin State. *Proc. Natl. Acad. Sci. U. S. A.* **2006**, *103* (46), 17131–17136.
(118) Chakrabarti, M.; Deng, L.; Holm, R. H.; Münck, E.; Bominaar, E. L. The Modular Nature of All-Ferrous Edge-Bridged Double Cubanes. *Inorg. Chem.* **2010**, *49* (4), 1647–1650.
(119) Li, Z.; Guo, S.; Sun, Q.; Chan, G. K. L. Electronic Landscape of the P-Cluster of Nitrogenase as Revealed through Many-Electron Quantum Wavefunction Simulations. *Nat. Chem.* **2019**, *11* (11), 1026–1033.
(120) Cao, L.; Börner, M. C.; Bergmann, J.; Caldararu, O.; Ryde, U. Geometry and Electronic Structure of the P-Cluster in Nitrogenase Studied by Combined Quantum Mechanical and Molecular Mechanical Calculations and Quantum Refinement. *Inorg. Chem.* **2019**, *58* (15), 9672–9690.
(121) Van Stappen, C.; Decamps, L.; Cutsail, G. E.; Bjornsson, R.; Henthorn, J. T.; Birrell, J. A.; Debeer, S. The Spectroscopy of Nitrogenases. *Chem. Rev.* **2020**, *120* (12), 5005–5081.
(122) Cramer, S. P.; Hodgson, K. O.; Gillum, W. O.; Mortenson, L. E. The Molybdenum Site of Nitrogenase. Preliminary Structural Evidence from X-Ray Absorption Spectroscopy. *J. Am. Chem. Soc.* **1978**, *100* (11), 3398–3407.
(123) Cramer, S. P.; Gillum, W. O.; Hodgson, K. O.; Mortenson, L. E.; Stiefel, E. I.; Chisnell, J. R.; Brill, W. J.; Shah, V. K. The Molybdenum Site of Nitrogenase. 2. A Comparative Study of Mo-Fe Proteins and the Iron-Molybdenum Cofactor by X-Ray Absorption Spectroscopy. *J. Am. Chem. Soc.* **1978**, *100* (12), 3814–3819.
(124) Hoffman, B. M.; Roberts, J. E.; Orme-Johnson, W. H. ^{95}Mo and ^{1}H ENDOR Spectroscopy of the Nitrogenase MoFe Protein. *J. Am. Chem. Soc.* **1982**, *104* (3), 860–862.
(125) Venters, R. A.; Nelson, M. J.; McLean, P. A.; True, A. E.; Levy, M. A.; Hoffman, B. M.; Orme-Johnson, W. H. ENDOR of the Resting State of Nitrogenase Molybdenum-Iron Proteins from *Azotobacter vinelandii*, *Klebsiella pneumoniae*, and *Clostridium pasteurianum*: ^{1}H, ^{57}Fe, ^{95}Mo, and ^{33}S Studies. *J. Am. Chem. Soc.* **1986**, *108* (12), 3487–3498.
(126) Hedman, B.; Frank, P.; Roe, A. L.; Gheller, S. F.; Newton, W. E.; Hodgson, K. O. New Structural Insights into the Iron-Molybdenum Cofactor from *Azotobacter vinelandii* Nitrogenase through Sulfur K and Molybdenum L X-Ray Absorption Edge Studies. *J. Am. Chem. Soc.* **1988**, *110* (12), 3798–3805.
(127) Carney, M. J.; Kovacs, J. A.; Zhang, Y. P.; Papaefthymiou, G. C.; Spartalian, K.; Frankel, R. B.; Holm, R. H. Comparative Electronic Properties of Vanadium-Iron-Sulfur and Molybdenum-Iron-Sulfur Clusters Containing Isoelectronic Cubane-Type $[VFe_3S_4]^{2+}$ and $[MoFe_3S_4]^{3+}$ Cores. *Inorg. Chem.* **1987**, *26* (5), 719–724.
(128) Lee, H. I.; Hales, B. J.; Hoffman, B. M. Metal-Ion Valencies of the FeMo Cofactor in CO-Inhibited and Resting State Nitrogenase by ^{57}Fe Q-Band ENDOR. *J. Am. Chem.*

Soc. **1997**, *119* (47), 11395–11400.
(129) Yoo, S. J.; Angove, H. C.; Papaefthymiou, V.; Burgess, B. K.; Münck, E. Mossbauer Study of the MoFe Protein of Nitrogenase from *Azotobacter vinelandii* Using Selective ^{57}Fe Enrichment of the M-Centers. *J. Am. Chem. Soc.* **2000**, *122* (20), 4926–4936.
(130) Harris, T. V.; Szilagyi, R. K. Comparative Assessment of the Composition and Charge State of Nitrogenase FeMo-Cofactor. *Inorg. Chem.* **2011**, *50* (11), 4811–4824.
(131) Bjornsson, R.; Lima, F. A.; Spatzal, T.; Weyhermüller, T.; Glatzel, P.; Bill, E.; Einsle, O.; Neese, F.; Debeer, S. Identification of a Spin-Coupled Mo(III) in the Nitrogenase Iron-Molybdenum Cofactor. *Chem. Sci.* **2014**, *5* (8), 3096–3103.
(132) Lima, F. A.; Bjornsson, R.; Weyhermüller, T.; Chandrasekaran, P.; Glatzel, P.; Neese, F.; DeBeer, S. High-Resolution Molybdenum K-Edge X-Ray Absorption Spectroscopy Analyzed with Time-Dependent Density Functional Theory. *Phys. Chem. Chem. Phys.* **2013**, *15* (48), 20911–20920.
(133) Cook, M.; Karplus, M. Electronic Structure of the $MoFe_3S_4(SH)_6^{3-}$ Ion. *J. Am. Chem. Soc.* **1985**, *107* (1), 257–259.
(134) Cook, M.; Karplus, M. Electronic Structure of the $MoFe_3S_4(SH)_6^{3-}$ Ion: A Broken-Symmetry Metal-Sulfur Cluster. *J. Chem. Phys.* **1985**, *83*, 6344–6366.
(135) Kowalska, J. K.; Henthorn, J. T.; Van Stappen, C.; Trncik, C.; Einsle, O.; Keavney, D.; DeBeer, S. X-Ray Magnetic Circular Dichroism Spectroscopy Applied to Nitrogenase and Related Models: Experimental Evidence for a Spin-Coupled Molybdenum(III) Center. *Angew. Chem. Int. Ed.* **2019**, *58* (28), 9373–9377.
(136) Rees, J. A.; Bjornsson, R.; Kowalska, J. K.; Lima, F. A.; Schlesier, J.; Sippel, D.; Weyhermüller, T.; Einsle, O.; Kovacs, J. A.; DeBeer, S. Comparative Electronic Structures of Nitrogenase FeMoco and FeVco. *Dalton Trans.* **2017**, *46* (8), 2445–2455.
(137) Harris, D. F.; Lukoyanov, D. A.; Kallas, H.; Trncik, C.; Yang, Z. Y.; Compton, P.; Kelleher, N.; Einsle, O.; Dean, D. R.; Hoffman, B. M.; Seefeldt, L. C. Mo-, V-, and Fe-Nitrogenases Use a Universal Eight-Electron Reductive-Elimination Mechanism to Achieve N_2 Reduction. *Biochemistry* **2019**, *58* (30), 3293–3301.
(138) Eady, R. R. Structure-Function Relationships of Alternative Nitrogenases. *Chem. Rev.* **1996**, *96* (7), 3013–3030.
(139) Schneider, K.; Müller, A. Iron-Only Nitrogenase: Exceptional Catalytic, Structural and Spectroscopic Features. In *Catalysts for Nitrogen Fixation. Nitrogen Fixation: Origins, Applications, and Research Progress*; Smith, B. E., Richards, R. L., Newton, W. E., Eds.; 2004; Vol. 1.
(140) Yang, H.; McDaniel, E. C.; Impano, S.; Byer, A. S.; Jodts, R. J.; Yokoyama, K.; Broderick, W. E.; Broderick, J. B.; Hoffman, B. M. The Elusive 5′-Deoxyadenosyl Radical: Captured and Characterized by Electron Paramagnetic Resonance and Electron Nuclear Double Resonance Spectroscopies. *J. Am. Chem. Soc.* **2019**, *141* (30), 12139–12146.
(141) Sayler, R. I.; Stich, T. A.; Joshi, S.; Cooper, N.; Shaw, J. T.; Begley, T. P.; Tantillo, D. J.; Britt, R. D. Trapping and Electron Paramagnetic Resonance Characterization of the 5′dAdo• Radical in a Radical S-Adenosyl Methionine Enzyme Reaction with a Non-Native Substrate. *ACS Cent. Sci.* **2019**, *5* (11), 1777–1785.
(142) Horitani, M.; Shisler, K.; Broderick, W. E.; Hutcheson, R. U.; Duschene, K. S.; Marts, A. R.; Hoffman, B. M.; Broderick, J. B. Radical SAM Catalysis via an Organometallic Intermediate with an Fe-[5'-C]-Deoxyadenosyl Bond. *Science* **2016**, *352* (6287), 822–825.
(143) Byer, A. S.; Yang, H.; Mcdaniel, E. C.; Kathiresan, V.; Impano, S.; Pagnier, A.; Watts, H.; Denler, C.; Vagstad, A. L.; Rn Piel, J.; Duschene, K. S.; Shepard, E. M.; Shields,

T. P.; Scott, L. G.; Lilla, E. A.; Yokoyama, K.; Broderick, W. E.; Hoffman, B. M.; Broderick, J. B. Paradigm Shift for Radical S-Adenosyl-L-Methionine Reactions: The Organometallic Intermediate Ω Is Central to Catalysis. *J. Am. Chem. Soc.* **2018**, *140* (28), 8634–8638.
(144) Dong, M.; Kathiresan, V.; Fenwick, M. K.; Torelli, A. T.; Zhang, Y.; Caranto, J. D.; Dzikovski, B.; Sharma, A.; Lancaster, K. M.; Freed, J. H.; Ealick, S. E.; Hoffman, B. M.; Lin, H. Organometallic and Radical Intermediates Reveal Mechanism of Diphthamide Biosynthesis. *Science* **2018**, *359* (6381), 1247–1250.
(145) Xu, W.; Lees, N. S.; Adedeji, D.; Wiesner, J.; Jomaa, H.; Hoffman, B. M.; Duin, E. C. Paramagnetic Intermediates of (E)-4-Hydroxy-3-Methylbut-2-Enyl Diphosphate Synthase (GcpE/IspG) under Steady-State and Pre-Steady-State Conditions. *J. Am. Chem. Soc.* **2010**, *132* (41), 14509–14520.
(146) Xu, W.; Lees, N. S.; Hall, D.; Welideniya, D.; Hoffman, B. M.; Duin, E. C. A Closer Look at the Spectroscopic Properties of Possible Reaction Intermediates in Wild-Type and Mutant (E)-4-Hydroxy-3-Methylbut-2-Enyl Diphosphate Reductase. *Biochemistry* **2012**, *51* (24), 4835–4849.
(147) Einsle, O.; Tezcan, F. A.; Andrade, S. L. A.; Schmid, B.; Yoshida, M.; Howard, J. B.; Rees, D. C. Nitrogenase MoFe-Protein at 1.16 Å Resolution: A Central Ligand in the FeMo-Cofactor. *Science* **2002**, *297* (5587), 1696–1700.
(148) Spatzal, T.; Aksoyoglu, M.; Zhang, L.; Andrade, S. L. A.; Schleicher, E.; Weber, S.; Rees, D. C.; Einsle, O. Evidence for Interstitial Carbon in Nitrogenase FeMo Cofactor. *Science* **2011**, *334* (6058), 940.
(149) Lancaster, K. M.; Roemelt, M.; Ettenhuber, P.; Hu, Y.; Ribbe, M. W.; Neese, F.; Bergmann, U.; DeBeer, S. X-Ray Emission Spectroscopy Evidences a Central Carbon in the Nitrogenase Iron-Molybdenum Cofactor. *Science* **2011**, *334* (6058), 974–977.
(150) Rees, J. A.; Bjornsson, R.; Schlesier, J.; Sippel, D.; Einsle, O.; DeBeer, S. The Fe-V Cofactor of Vanadium Nitrogenase Contains an Interstitial Carbon Atom. *Angew. Chem. Int. Ed.* **2015**, *54* (45), 13249–13252.
(151) Lancaster, K. M.; Hu, Y.; Bergmann, U.; Ribbe, M. W.; Debeer, S. X-Ray Spectroscopic Observation of an Interstitial Carbide in NifEN-Bound FeMoco Precursor. *J. Am. Chem. Soc.* **2013**, *135* (2), 610–612.
(152) Rubio, L. M.; Ludden, P. W. Biosynthesis of the Iron-Molybdenum Cofactor of Nitrogenase. *Annu. Rev. Microbiol.* **2008**, *62*, 93–111.
(153) Ribbe, M. W.; Hu, Y.; Hodgson, K. O.; Hedman, B. Biosynthesis of Nitrogenase Metalloclusters. *Chem. Rev.* **2014**, *114* (8), 4063–4080.
(154) Wiig, J. A.; Hu, Y.; Lee, C. C.; Ribbe, M. W. Radical SAM-Dependent Carbon Insertion into the Nitrogenase M-Cluster. *Science* **2012**, *337* (6102), 1672–1675.
(155) Wiig, J. A.; Hu, Y.; Ribbe, M. W. Refining the Pathway of Carbide Insertion into the Nitrogenase M-Cluster. *Nat. Commun.* **2015**, *6*, 8–13.
(156) Churchill, M. R.; Wormald, J.; Knight, J.; Mays, M. J. Synthesis and Crystallographic Characterization of $[Me_4N^+]_2[Fe_6(CO)_{16}C^{2-}]$, a Hexanuclear Carbidocarbonyl Derivative of Iron. *J. Am. Chem. Soc.* **1971**, *93* (12), 3073–3074.
(157) Churchill, M. R.; Wormald, J. Crystal and Molecular Structure of Tetramethylammonium Carbidohexadecacarbonylhexaferrate(2-), $[Me_4N]_2[Fe_6(CO)_{16}C]$, a Hexanuclear Iron Cluster Complex with an Encapsulated Six-Co-Ordinate Carbon Atom. *J. Chem. Soc. Dalt. Trans.* **1974**, No. 22, 2410–2415.
(158) Liu, L.; Rauchfuss, T. B.; Woods, T. J. Iron Carbide-Sulfide Carbonyl Clusters. *Inorg. Chem.* **2019**, *58* (13), 8271–8274.
(159) Liu, L.; Woods, T. J.; Rauchfuss, T. B. Reactions of $[Fe_6C(CO)_{14}(S)]^{2-}$: Cluster Growth, Redox, Sulfiding. *Eur. J. Inorg. Chem.* **2020**, 3460–3465.

(160) Joseph, C.; Cobb, C. R.; Rose, M. Single-Step Insertion of Sulfides and Thiolate into Iron Carbide-Carbonyl Clusters: Unlocking the Synthetic Door to FeMoco Analogues. *Angew. Chem. Int. Ed.* **2020**. https://doi.org/10.1002/anie.202011517.
(161) Nagelski, A. L.; Fataftah, M. S.; Bollmeyer, M. M.; McWilliams, S. F.; MacMillan, S. N.; Mercado, B. Q.; Lancaster, K. M.; Holland, P. L. The Influences of Carbon Donor Ligands on Biomimetic Multi-Iron Complexes for N_2 Reduction. *Chem. Sci.* **2020**, 11, 12710-12720.
(162) Reesbeck, M. E.; Grubel, K.; Kim, D.; Brennessel, W. W.; Mercado, B. Q.; Holland, P. L. Diazoalkanes in Low-Coordinate Iron Chemistry: Bimetallic Diazoalkyl and Alkylidene Complexes of Iron(II). *Inorg. Chem.* **2017**, *56* (3), 1019–1022.
(163) Reesbeck, M. E.; Rodriguez, M. M.; Brennessel, W. W.; Mercado, B. Q.; Vinyard, D.; Holland, P. L. Oxidized and Reduced [2Fe-2S] Clusters from an Iron(I) Synthon. *J. Biol. Inorg. Chem.* **2015**, *20* (5), 875–883.
(164) Majumdar, A.; Holm, R. H. Specific Incorporation of Chalcogenide Bridge Atoms in Molybdenum/Tungsten- Iron-Sulfur Single Cubane Clusters. *Inorg. Chem.* **2011**, *50* (21), 11242–11251.
(165) Zheng, B.; Chen, X. D.; Zheng, S. L.; Holm, R. H. Selenium as a Structural Surrogate of Sulfur: Template-Assisted Assembly of Five Types of Tungsten-Iron-Sulfur/Selenium Clusters and the Structural Fate of Chalcogenide Reactants. *J. Am. Chem. Soc.* **2012**, *134* (14), 6479–6490.
(166) Xu, G.; Wang, Z.; Ling, R.; Zhou, J.; Chen, X. D.; Holm, R. H. Ligand Metathesis as Rational Strategy for the Synthesis of Cubane-Type Heteroleptic Iron–Sulfur Clusters Relevant to the FeMo Cofactor. *Proc. Natl. Acad. Sci. U. S. A.* **2018**, *115* (20), 5089–5092.
(167) Xu, G.; Zhou, J.; Wang, Z.; Holm, R. H.; Chen, X. D. Controlled Incorporation of Nitrides into W-Fe-S Clusters. *Angew. Chem. Int. Ed.* **2019**, *58* (46), 16469–16473.
(168) Hwang, J. C.; Chen, C. H.; Burris, R. H. Inhibition of Nitrogenase-Catalyzed Reductions. *Biochim. Biophys. Acta* **1973**, No. 292, 256–270.
(169) Rivera Ortiz, J. M.; Burris, R. H. Interactions Among Substrates and Inhibitors of Nitrogenase. *J. Bacteriol.* **1975**, *123* (2), 537–545.
(170) Lee, C. C.; Hu, Y.; Ribbe, M. W. Vanadium Nitrogenase Reduces CO. *Science* **2010**, *329* (5992), 642.
(171) Hu, Y.; Lee, C. C.; Ribbe, M. W. Extending the Carbon Chain: Hydrocarbon Formation Catalyzed by Vanadium/Molybdenum Nitrogenases. *Science* **2011**, *333* (6043), 753–755.
(172) Yang, Z. Y.; Dean, D. R.; Seefeldt, L. C. Molybdenum Nitrogenase Catalyzes the Reduction and Coupling of CO to Form Hydrocarbons. *J. Biol. Chem.* **2011**, *286* (22), 19417–19421.
(173) Harris, D. F.; Jimenez-Vicente, E.; Yang, Z. Y.; Hoffman, B. M.; Dean, D. R.; Seefeldt, L. C. CO as a Substrate and Inhibitor of H^+ Reduction for the Mo-, V-, and Fe-Nitrogenase Isozymes. *J. Inorg. Biochem.* **2020**, *213*, 111278.
(174) Lee, C. C.; Hu, Y.; Ribbe, M. W. ATP-Independent Formation of Hydrocarbons Catalyzed by Isolated Nitrogenase Cofactors. *Angew. Chem. Int. Ed.* **2012**, *51* (8), 1947–1949.
(175) Lee, C. C.; Hu, Y.; Ribbe, M. W. Insights into Hydrocarbon Formation by Nitrogenase Cofactor Homologs. *MBio* **2015**, *6* (2), 1–6.
(176) Lee, C. C.; Hu, Y.; Ribbe, M. W. Catalytic Reduction of CN-, CO, and CO_2 by Nitrogenase Cofactors in Lanthanide-Driven Reactions. *Angew. Chem. Int. Ed.* **2015**, *54* (4), 1219–1222.
(177) Lee, C. C.; Hu, Y.; Ribbe, M. W. Reduction and Condensation of Aldehydes by the

Isolated Cofactor of Nitrogenase. *ACS Cent. Sci.* **2018**, *4* (10), 1430–1435.
(178) Tanifuji, K.; Lee, C. C.; Ohki, Y.; Tatsumi, K.; Hu, Y.; Ribbe, M. W. Combining a Nitrogenase Scaffold and a Synthetic Compound into an Artificial Enzyme. *Angew. Chem. Int. Ed.* **2015**, *54* (47), 14022–14025.
(179) Sickerman, N. S.; Tanifuji, K.; Lee, C. C.; Ohki, Y.; Tatsumi, K.; Ribbe, M. W.; Hu, Y. Reduction of C_1, Substrates to Hydrocarbons by the Homometallic Precursor and Synthetic Mimic of the Nitrogenase Cofactor. *J. Am. Chem. Soc.* **2017**, *139* (2), 603–606.
(180) Tanifuji, K.; Sickerman, N.; Lee, C. C.; Nagasawa, T.; Miyazaki, K.; Ohki, Y.; Tatsumi, K.; Hu, Y.; Ribbe, M. W. Structure and Reactivity of an Asymmetric Synthetic Mimic of Nitrogenase Cofactor. *Angew. Chem. Int. Ed.* **2016**, *55* (50), 15633–15636.
(181) Stiebritz, M. T.; Hiller, C. J.; Sickerman, N. S.; Lee, C. C.; Tanifuji, K.; Ohki, Y.; Hu, Y. Ambient Conversion of CO_2 to Hydrocarbons by Biogenic and Synthetic [Fe_4S_4] Clusters. *Nat. Catal.* **2018**, *1* (6), 444–451.
(182) Rebelein, J. G.; Stiebritz, M. T.; Lee, C. C.; Hu, Y. Activation and Reduction of Carbon Dioxide by Nitrogenase Iron Proteins. *Nat. Chem. Biol.* **2017**, *13* (2), 147–149.
(183) Banerjee, A.; Yuhas, B. D.; Margulies, E. A.; Zhang, Y.; Shim, Y.; Wasielewski, M. R.; Kanatzidis, M. G. Photochemical Nitrogen Conversion to Ammonia in Ambient Conditions with FeMos-Chalcogels. *J. Am. Chem. Soc.* **2015**, *137* (5), 2030–2034.
(184) Liu, J.; Kelley, M. S.; Wu, W.; Banerjee, A.; Douvalis, A. P.; Wu, J.; Zhang, Y.; Schatz, G. C.; Kanatzidis, M. G. Nitrogenase-Mimic Iron-Containing Chalcogels for Photochemical Reduction of Dinitrogen to Ammonia. *Proc. Natl. Acad. Sci. U. S. A.* **2016**, *113* (20), 5530–5535.

Chapter 2. Controlling Substrate Binding to Fe_4S_4 Clusters through Remote Steric Effects

Introduction

Fe–S cluster enzymes catalyze a diverse array of reactions central to metabolism, human health, and the biogeochemical cycles of the elements.[1–4] In addition to their widespread utility in electron transfer, many Fe–S enzymes including radical *S*-adenosylmethionine enzymes,[4] enzymes involved in isoprenoid biosynthesis (IspG and IspH),[5] aconitase,[6] nitrogenase,[7] and [NiFe]-CO dehydrogenase[8] react directly with substrates. In these cases, the environment of the cluster is carefully tuned by the surrounding amino acid residues to enable reactivity that would otherwise be thermodynamically and kinetically unfavorable. Realizing this exquisite control over binding and reactivity in synthetic Fe–S clusters remains an important challenge both to model the chemistry of biological Fe–S clusters and to generate synthetic Fe–S cluster catalysts.[9] To localize cluster reactivity to one Fe site, 3:1 site-differentiated [Fe_4S_4] clusters have been reported that feature chelating thiolate ligands[10–19] or monodentate phosphine[20–22] and thiolate[23] ligands (Chart 2.1). However, in all cases, these ligands offer limited opportunities to modify the environment at the apical Fe site because their steric bulk is positioned away from its coordination sphere. This is illustrated in each case by the stability of the corresponding homoleptic or pseudo-homoleptic complexes (Chart 2.1); even the most encumbering ligands are unable to prevent binding of an additional bulky ligand to the apical Fe site.[10,20–23] The challenge of controlling substrate binding at the apical Fe in these clusters contrasts decades of advances in mononuclear transition-metal chemistry in which steric parameterization[24,25] and modification have enabled the isolation of reactive and coordinatively unsaturated species.

As part of our efforts to develop reactive Fe–S clusters in protein-like environments, we herein describe the design and preparation of 3:1 site-differentiated $[Fe_4S_4]^+$ clusters bound

Table 2.1. Representative site-differentiated [Fe_4S_4] clusters and their (pseudo-)homoleptic counterparts

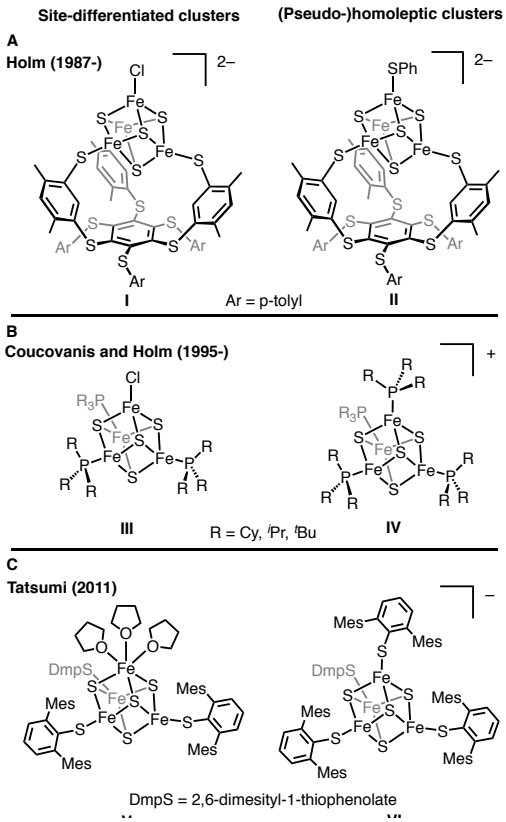

by *N*-heterocyclic carbene (NHC) ligands that are sufficiently encumbering to prevent homoleptic complex formation. We chose to study NHC ligands because of their strong σ-donor properties, which have resulted in their widespread use in chemical synthesis and catalysis. Previous studies have shown that NHCs can stabilize highly reduced Fe–S clusters: whereas $(PR_3)_4Fe_4S_4$ (R = Cy, ^{t}Bu, ^{i}Pr) clusters disproportionate to higher nuclearity clusters with concomitant loss of phosphine,[26] the analogous $(NHC)_4Fe_4S_4$ (NHC = 1,3-diisopropyl-4,5-dimethylimidazol-2-ylidene [I^{i}Pr^{Me}] or 1,3-diethyl-4,5-dimethylimidazol-2-ylidene [IEt^{Me}]) clusters are thermally stable and can be isolated in pure form.[27,28] In comparison to other ligands for Fe–S clusters such as phosphines or thiolates, NHCs offer unique opportunities to modify the steric environment at the apical Fe site because their steric bulk is oriented toward the cluster core.[25,29] We demonstrate that in $(NHC)_4Fe_4S_4X$ clusters, increasing the length of the NHC through *N*,*N*'-diaryl substitution is key to forming and maintaining a

substitutionally labile site at the apical Fe and that the thermodynamics for substrate binding can be dramatically altered through these remote steric effects.

Results and Discussion

Although no examples of $(NHC)_3Fe_4S_4X$ clusters have been reported,[36] we envisioned that substitution of the PCy_3 ligands in $(PCy_3)_3Fe_4S_4Cl$ with isolable NHCs could furnish the desired 3:1 site-differentiated $(NHC)_3Fe_4S_4Cl$ clusters. Indeed, reaction of $(PCy_3)_3Fe_4S_4Cl$ with three equivalents of I^iPr^{Me} or IMes (IMes = 1,3-dimesitylimidazol-2-ylidene) gives the site-differentiated Fe–S clusters $(I^iPr^{Me})_3Fe_4S_4Cl$ (**1**) and $(IMes)_3Fe_4S_4Cl$ (**2**), respectively (Scheme 2.1).

Scheme 2.1. Preparation of NHC-ligated, 3:1 site-differentiated $[Fe_4S_4]^+$ clusters

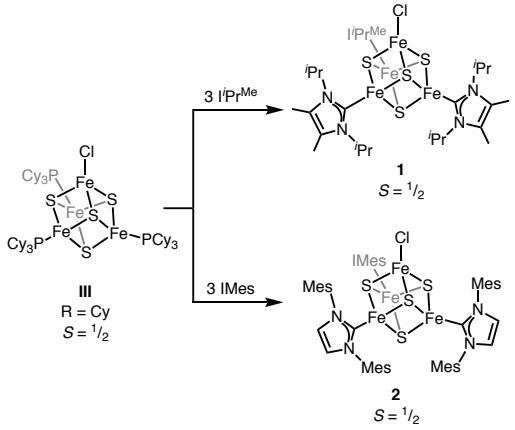

The ^1H NMR spectra (Fig. S2.1 and S2.3) show that both **1** and **2** have C_{3v} symmetry in solution and that the Fe–C bonds rotate freely at room temperature (RT). The structure of **1** was determined by X-ray diffraction (XRD) and shows the three NHCs oriented approximately coplanar to one another, leaving the coordination sphere of the apical Fe largely open (Fig. 2.1). In contrast, the IMes ligands in **2** are rotated vertically such that one set of mesityl groups is oriented toward the apical chloride (Fig. 2.1). The added length of IMes as compared to I^iPr^{Me} forces the NHCs to be more aligned with the molecule's pseudo-C_3 axis and engenders greater steric protection of the apical Fe site. The Fe–S distances within the clusters are highly variable (from 2.2567(8) to 2.321(1) Å for **1** and from 2.253(1) to 2.312(1) Å for **2**); such variability of Fe–S bond lengths in $[Fe_4S_4]^+$ clusters has been previously observed and

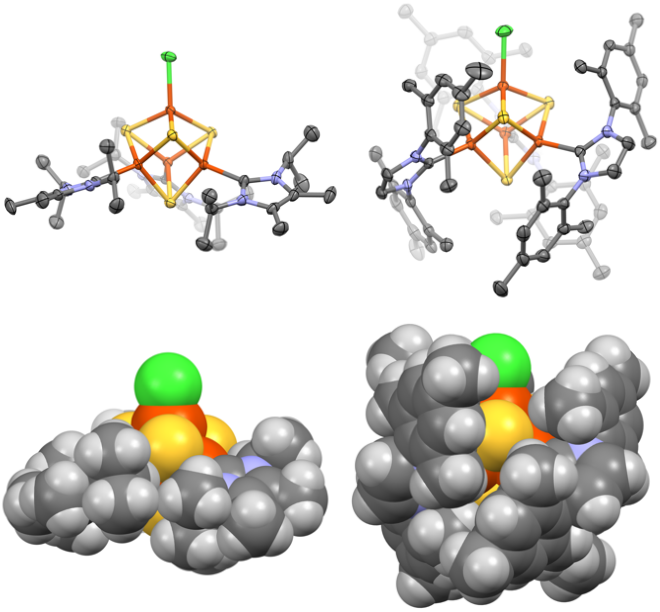

Figure 2.1. Thermal ellipsoid (50%; top) and space-filling (bottom) plots of **1** (left) and **2** (right) showing the increased steric protection of the apical Fe in **2** compared to **1**. Hydrogen atoms (top) and solvent molecules (top and bottom) are omitted for clarity. Color scheme: Fe (orange), S (yellow), Cl (green), N (blue), C (dark-grey), and H (light-grey).

attributed to a shallow potential energy surface for core deformations.[21] This compressibility is exemplified by the structure of **2**, for which one molecule in the asymmetric unit displays the common elongated tetragonal distortion (two Fe_2S_2 rhombs with elongated bonds between them), while the other molecule displays less symmetric distortions. The clusters **1** and **2** display similar EPR spectra with $g_{iso} \sim 2$ (Fig. 2.2A and 2.2B) and similar UV/Vis spectra (Fig. S2.18 and S2.19). These findings are consistent with the similar Tolman electronic parameters for I^{i}Pr^{Me} and IMes (2047.8 and 2049.6, respectively[37]) and demonstrate that differences in the donor properties of I^{i}Pr^{Me} and IMes minimally affect the electronic structures of the clusters. The EPR spectra of **1** and **2** are indicative of a ground $S = ½$ spin state; this spin state has been observed for all $[Fe_4S_4]^+$ clusters with phosphine ligands and most synthetic and biological $[Fe_4S_4]^+$ clusters with thiolate ligands.[20,22,26,38–44]

Abstraction of the chloride ligand of **1** with sodium tetrakis[(3,5-trifluoromethyl)phenyl]borate ($NaBAr^{F}_{4}$) in tetrahydrofuran (THF) at –78 °C leads to formation of a dark-brown solution and an insoluble black precipitate (Scheme 2.2). The ^{1}H NMR spectrum of the soluble material shows bound $I^{i}Pr^{Me}$ and $[BAr^{F}_{4}]^{-}$ resonances in a 4:1 ratio. We therefore posited that the isolable product of this reaction was the homoleptic cluster $[(I^{i}Pr^{Me})_{4}Fe_{4}S_{4}][BAr^{F}_{4}]$ (**3**), which was previously proposed to be generated upon electrochemical oxidation of $(I^{i}Pr^{Me})_{4}Fe_{4}S_{4}$.[27] This assignment was confirmed by independent synthesis of **3** (treatment of **1** with $NaBAr^{F}_{4}$ in the presence of one equivalent of $I^{i}Pr^{Me}$) and characterization by XRD (Fig. S2.26). The structure of **3** shows shorter Fe–C (2.060(7) Å) and Fe–S (2.29(3) Å) bond lengths compared to those of the previously reported reduced $(I^{i}Pr^{Me})_{4}Fe_{4}S_{4}$ complex (2.11(2) and 2.33(2) Å, respectively).[27] A decrease of Fe–C and Fe–S

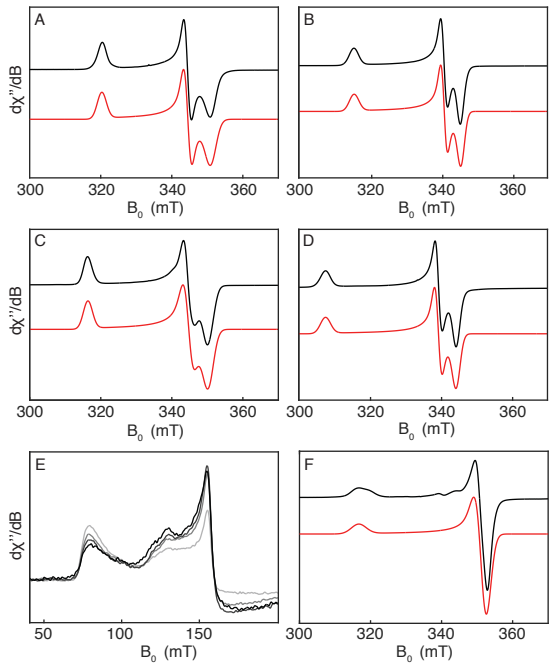

Figure 2.2. X-band EPR spectra (black) and simulations (red) of **1** (A, 15 K, 15 μW, g = [2.090 1.943 1.908]), **2** (B, 15 K, 126 μW, g = [2.122 1.964 1.937]), **4** (C, 15 K, 63 μW, g = [2.116 1.942 1.911]), **5** (D, 15 K, 63 μW, g = [2.177 1.973 1.944]), and the mixture formed upon reacting **1** with $NaBAr^{F}_{4}$ in the presence of excess ^{t}BuNC at low-field (E, showing the EPR spectra of **6** at 5 K (light gray), 8 K (medium gray), 10 K (dark gray), 15 K (black), 250 μW) and mid-field (F, showing the EPR spectrum of **3** at 15 K, 250 μW, g = [2.114 1.903 1.903], with minor impurities).

bond lengths upon oxidation is also observed for the $[Fe_4S_4]^0$ and $[Fe_4S_4]^{1+}$ clusters, $[Fe_4S_4(CN)_4]^{4-}$ and $[Fe_4S_4(CN)_4]^{3-}$.[45]

In contrast, treatment of **2** with $NaBAr^F{}_4$ in THF at –78 °C leads to the formation of one major product in approximately 90% purity (Scheme 2.2). The ^{1}H NMR spectrum of the product in C_6D_6 displays a ratio of 3:1 between the bound IMes and $[BAr^F{}_4]^-$ resonances and

Scheme 2.2. Studies of chloride abstraction from **1** and **2**

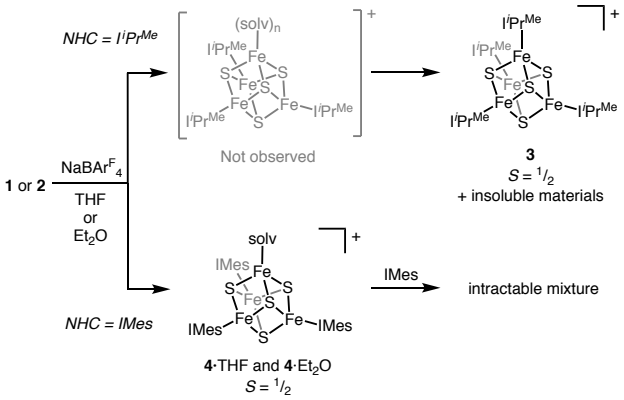

broadened resonances corresponding to excess THF at 3.6 and 1.7 ppm, suggesting the formation of a THF adduct (**4**•THF). Lyophilizing samples from benzene to remove excess THF resulted in the appearance of two resonances at 17.73 and 7.86 ppm that each integrate for four protons relative to the IMes resonances and are assigned to a bound THF ligand (Fig. S2.9). The EPR spectrum of **4**•THF is rhombic with *g*-values that are similar to those of **2** (Fig. 2.2C). Single crystals grown in Et_2O layered with pentane were studied by XRD and confirmed

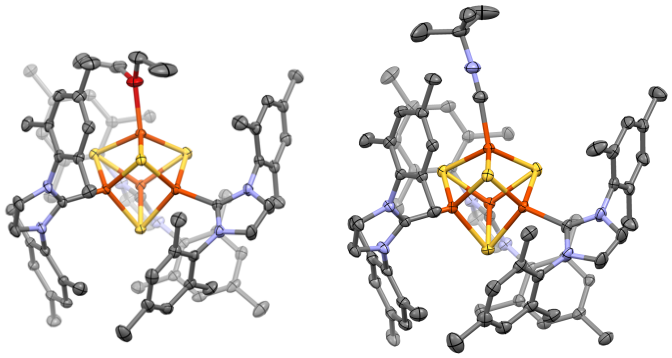

Figure 2.3. Thermal ellipsoid plots (50%) of **4**•Et_2O (left) and **5** (right). Hydrogen atoms, solvent molecules, and anions have been omitted for clarity. Color scheme: Fe (orange), S (yellow), O (red), N (blue), and C (dark gray).

the structure of **4**•Et_2O (Fig. 2.3) in which Et_2O is ligated to the apical Fe site. The pseudo-C_3

arrangement of the mesityl groups is similar to that in **2,** in which the mesityl groups form a well-defined cavity around the apical Fe site.

Although **1** readily undergoes ligand redistribution following halide abstraction, the analogous redistribution of ligands from **4** to generate $[(IMes)_4Fe_4S_4][BAr^F{}_4]$ is disfavored; formation of the homoleptic cluster is not observed upon treatment of **2** with $NaBAr^F{}_4$, and attempted generation of $[(IMes)_4Fe_4S_4][BAr^F{}_4]$ by reaction of **4** with IMes leads to an intractable mixture. The steric bulk of IMes—particularly its length, owing to the *N*,*N*'-dimesityl substituents—stabilizes **4** with respect to rearrangement reactions and allows for the generation of a complex with a labile coordination site.

We next sought to determine if the IMes ligands in **4** exert sufficient steric pressure at the apical Fe site to prevent formation of a coordinatively saturated, octahedral geometry upon substitution of the ether ligand with one or more strong-field ligands. We elected to study isocyanide binding because isocyanides are isoelectronic to N_2 and CO (substrates for synthetic

Scheme 2.3. Studies of isocyanide binding to (A) $[(LS_3)Fe_4S_4Cl]^{2-}$ and (B) **1** and **2**

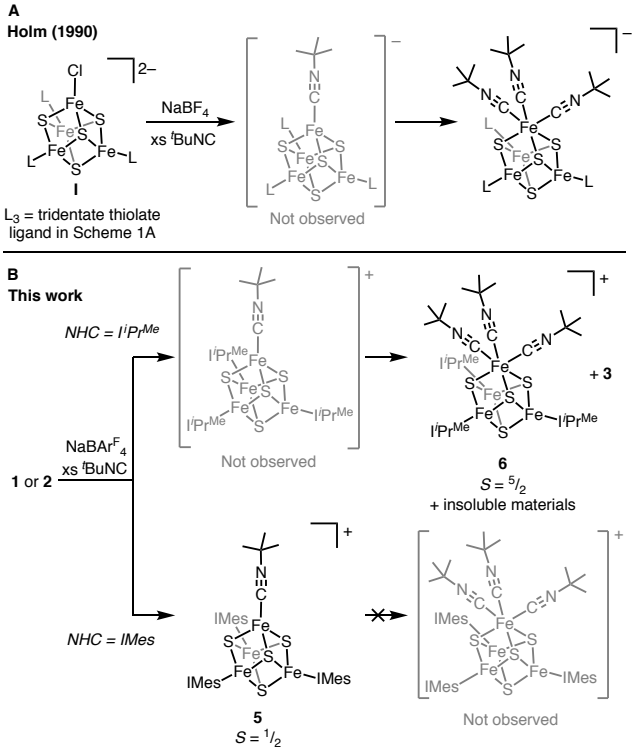

and biogenic Fe–S clusters) and because of the strong driving force for binding three equivalents of isocyanide to generate a valence-localized, low-spin Fe^{2+} site: all reported examples of isocyanide binding to $[Fe_4S_4]$ clusters demonstrate that binding three isocyanides is more favorable than binding one or two (e.g. Scheme 2.3A).[46–51] We therefore expected that if sterically feasible, the apical Fe in **4** would also bind three equivalents of isocyanide. On the other hand, if the IMes ligands impart sufficient steric pressure at the unique Fe site, only one isocyanide would bind, maintaining the apical Fe in a local high-spin configuration. Thus, we used isocyanide binding to test the hypothesis that the thermodynamics of ligand binding could be controlled through remote steric effects.

Addition of $NaBAr^F_4$ to **2** in the presence of excess ^{t}BuNC at –78 °C or addition of excess ^{t}BuNC to **4**•THF leads to the formation of a single product with an $S = {}^1/_2$ ground state (Scheme 2.3B, Fig. 2.2D). In addition to the IMes-derived resonances, the ^{1}H NMR spectrum of the product displays a singlet integrating for 9 protons at 1.36 ppm that we assign to a bound ^{t}BuNC ligand (Fig. S2.10). Together, these observations suggest that only one equivalent of ^{t}BuNC is bound, such that the apical Fe remains tetrahedral and high-spin (Fig. S2.25). An XRD experiment confirmed the assignment of this product as $[(IMes)_3Fe_4S_4(CN^tBu)][BAr^F_4]$ (**5**; Fig. 2.3). Consistent with the tetrahedral Fe geometry and high-spin state, the Fe–C bond is long (1.972(2) Å) compared to those of other Fe–S cluster isocyanide complexes (Fe–C (avg.): 1.84(3) Å), all of which adopt a local low-spin configuration.[46–50] Outside of its unprecedented nature in the Fe–S cluster literature, **5** is an uncommon example of a structurally characterized, terminal Fe isocyanide complex with a high-spin ground state.[52–56]

To determine if the binding of a single equivalent of ^{t}BuNC in **5** is indeed dictated by the steric pressure imposed by the IMes ligands, we carried out halide abstraction from **1** with $NaBAr^F_4$ in the presence of excess ^{t}BuNC (Scheme 2.3B). Although significant amounts of both insoluble materials and **3** were generated, an additional product was observed that is

marked by its highly shifted ^{1}H NMR signals at 17.43 and 9.03 ppm (derived from the backbone C*H*$_3$ and isopropyl C*H*$_3$ groups of the I^{i}Pr^{Me} ligands) as well as a new signal at 0.52 ppm (derived from ^{t}BuNC ligands). These resonances integrate in a 2:4:3 ratio, which suggests a cluster with three I^{i}Pr^{Me} ligands (18 and 36 H) and three ^{t}BuNC ligands (27 H; see Fig. S2.11). This new product decomposed to unidentified species after several hours at RT as evidenced by the concurrent disappearance of all three ^{1}H NMR resonances, and as such we were unable to characterize it by XRD. However, we further analyzed the initially formed mixture by IR (Fig. S2.17) and EPR spectroscopies (Fig. 2.2E and 2.2F). The reaction mixture shows absorbances in the IR spectrum assigned to bound isocyanide N–C stretches at 2132 and 2074 cm^{-1} (Fig. S2.17). EPR spectroscopy revealed one species with an $S = {}^5/_2$ spin state in addition to the $S = {}^1/_2$ signal for **3**. The ^{1}H NMR, IR, and EPR spectroscopic data are consistent with the formulation [(I^{i}Pr^{Me})$_3$Fe$_4$S$_4$(CN^{t}Bu)$_3$][BAr$^F{}_4$] (**6**); the $S = {}^5/_2$ spin state derives from valence isolation of a low-spin, apical Fe^{2+} site bound to an $S = {}^5/_2$ [Fe$_3$S$_4$]$^-$ cluster that has been previously identified in protein-bound [ZnFe$_3$S$_4$]$^+$ clusters (Fig. S2.25).[57,58] Variable temperature EPR spectroscopy (Fig. 2.2E) confirmed that the signals between $g_{eff} \sim 9$ and $g_{eff} \sim 4$ arise from a single species, and plotting the relative intensities as a function of temperature yields $D = 2.7(2)$ cm^{-1} (where D is the zero-field splitting; see ESI). This value is similar in magnitude but opposite in sign to those of the protein-bound [ZnFe$_3$S$_4$]$^+$ clusters in *D. gigas* ferredoxin II ($D = –2.7(5)$ cm^{-1}) and *P. furiousis* ferredoxin ($D = –2.7(5)$ cm^{-1}).[57,58]

That **6** is formed upon halide abstraction from **1** in the presence of ^{t}BuNC was expected based on previous studies of isocyanide binding to Fe–S clusters and is in contrast to the IMes-ligated clusters, for which **5** is generated with no evidence for the tri-isocyanide adduct [(IMes)$_3$Fe$_4$S$_4$(CN^{t}Bu)$_3$][BAr$^F{}_4$]. The IMes ligands in **5** prevent binding of additional equivalents of ^{t}BuNC despite the strong electronic driving force for binding three equivalents; binding three ^{t}BuNC ligands to the apical Fe would necessitate that the NHC ligands lie

approximately coplanar to one another and perpendicular to the pseudo-C_3 axis of the molecule to allow the isocyanides to project over the imidazolylidene rings. Although this coplanarity is accessible for I^{i}Pr^{Me}-ligated clusters, it is not possible for IMes-ligated clusters (Fig. 2.3).

Conclusions

We have demonstrated that the thermodynamic landscape for substrate binding to the apical Fe in a synthetic [Fe_4S_4] cluster can be dramatically altered through remote steric effects. Whereas 3:1 site-differentiated [Fe_4S_4]$^+$ clusters supported by the sterically unencumbering I^{i}Pr^{Me} ligand display typical reactivity towards ^{t}BuNC (binding three ^{t}BuNC ligands per labile Fe site), clusters supported by IMes bind only one ^{t}BuNC ligand to form **5**. Because of the steric pressure afforded by the IMes ligands, the apical Fe in **5** remains high-spin even in the presence of an excess of a strongly π-accepting ligand. Moreover, upon halide abstraction from **1**, the small I^{i}Pr^{Me} ligands do not prevent ligand redistribution and the undesired homoleptic cluster **3** is formed. In contrast, the steric bulk afforded by the *N*,*N*'-diaryl substituents of IMes in **2** allows for generation of a substitutionally labile, ether-ligated [Fe_4S_4]$^+$ cluster. The difference in reactivity between **1** and **2** is attributed to sterically imposed site-differentiation in **2**: the length of the NHC renders it unfavorable to form a homoleptic [$(NHC)_4Fe_4S_4$]$^+$ cluster upon abstraction of the apical chloride ligand. This strategy of imposing site-differentiation through remote steric effects complements established strategies of employing chelating ligands to generate site-differentiated Fe–S clusters and allows for control over the coordination environment of the apical Fe. We anticipate that the principles delineated in this work will allow for the isolation of Fe–S clusters in protein-like environments that exhibit new bonding and reactivity.

References

(1) Flint, D. H.; Allen, R. M. Iron-Sulfur Proteins with Nonredox Functions. *Chem. Rev.* **1996**, *96* (7), 2315–2334.

(2) Beinert, H.; Holm, R. H.; Munck, E. Iron-Sulfur Clusters: Nature's Modular, Multipurpose Structures. *Science* **1997**, *277* (5326), 653–659.

(3) Johnson, D. C.; Dean, D. R.; Smith, A. D.; Johnson, M. K. Structure, Function and Formation of Biological Iron-Sulfur Clusters. *Annu. Rev. Biochem.* **2005**, *74*, 247–281.

(4) Broderick, J. B.; Duffus, B. R.; Duschene, K. S.; Shepard, E. M. Radical S-Adenosylmethionine Enzymes. *Chem. Rev.* **2014**, *114* (8), 4229–4317.

(5) Wang, W.; Oldfield, E. Bioorganometallic Chemistry with IspG and IspH: Structure, Function, and Inhibition of the [Fe_4S_4] Proteins Involved in Isoprenoid Biosynthesis. *Angew. Chemie - Int. Ed.* **2014**, *53* (17), 4294–4310.

(6) Beinert, H.; Kennedy, M. C.; Stout, C. D. Aconitase as Iron−Sulfur Protein, Enzyme, and Iron-Regulatory Protein. *Chem. Rev.* **1996**, *96* (7), 2335–2374.

(7) Burgess, B. K.; Lowe, D. J. Mechanism of Molybdenum Nitrogenase. *Chem. Rev.* **1996**, *96* (7), 2983–3012.

(8) Can, M.; Armstrong, F. A.; Ragsdale, S. W. Structure, Function, and Mechanism of the Nickel Metalloenzymes, CO Dehydrogenase, and Acetyl-CoA Synthase. *Chem. Rev.* **2014**, *114* (8), 4149–4174.

(9) Ohta, S.; Ohki, Y. Impact of Ligands and Media on the Structure and Properties of Biological and Biomimetic Iron-Sulfur Clusters. *Coord. Chem. Rev.* **2017**, *338*, 207–225.

(10) Stack, T. D. P.; Holm, R. H. Subsite-Differentiated Analogues of Biological [4Fe-4S]$^{2+}$ Clusters: Synthesis, Solution and Solid-State Structures, and Subsite-Specific Reactions. *J. Am. Chem. Soc.* **1988**, *110* (8), 2484–2494.

(11) Stack, T. D. P.; Holm, R. H. Subsite-Specific Functionalization of the [4Fe-4S]$^{2+}$ Analogue of Iron-Sulfur Protein Clusters. *J . Am. Chem. Soc.* **1987**, *109* (8), 2546–2547.

(12) Stack, T. D. P.; Weigel, J. A.; Holm, R. H. The Cavitand Concept in the Synthesis of Subsite-Differentiated Analogues of Biological [4Fe-4S/Se]$^{2+}$ Clusters: Cluster Capture Reactions, Ligand Conformational Analysis, and the Structure of a Trigonal [4Fe-4Se]$^{2+}$ Analogue. *Inorg. Chem.* **1990**, *29* (19), 3745–3760.

(13) Walsdorff, C.; Saak, W. A Preorganised Doubly Tripodal Hexathiol: Syntheses and Crystal Structures of Complexes with Two 3:1 Subsite-Differentiated Fe_4S_4 Clusters. *Chem. Commun.* **1997**, 1931–1932..

(14) Walsdorff, C.; Saak, W.; Pohl, S. A New Preorganized Tridentate Ligand Bearing Three Indolethiolate Groups. Preparation of 3 : 1 Subsite-Differentiated Fe_4S_4 Clusters. *J. Chem. Soc. Dalton Trans.* **1997**, 1857–1861.

(15) Barclay, J. E.; Evans, D. J.; Garcia, G.; Santana, M. D.; Torralba, M. C.; Yago, J. M. Binding of the {$MoFe_3S_4$}$^{3+}$ Core by a Tridentate Thiolate and Chemical Analogues of the Molybdenum Co-Ordination Environment in the Iron-Molybdenum Cofactor of Nitrogenase. *J. Chem. Soc. Dalton Trans.* **1995**, 1965–1971.

(16) Terada, T.; Wakimoto, T.; Nakamura, T.; Hirabayashi, K.; Tanaka, K.; Li, J.; Matsumoto, T.; Tatsumi, K. Tridentate Thiolate Ligands: Application to the Synthesis of the Site-Differentiated [4Fe-4S] Cluster Having a Hydrosulfide Ligand at the Unique Iron Center. *Chem. Asian J.* **2012**, *7*, 920–929.

(17) Zhou, C.; Raebiger, J. W.; Segal, B. M.; Holm, R. H. The Influence of Net Charge on the Redox Potentials of Fe_4S_4 Cubane-Type Clusters in Aprotic Solvents. *Inorganica Chim. Acta* **2000**, *300–302*, 892–902.

(18) Weigel, J. A.; Holm, R. H. Intrinsic Binding Properties of a Differentiated Iron Subsite in Analogues of Native $[Fe_4S_4]^{2+}$ Clusters. *J. Am. Chem. Soc.* **1991**, *113* (11), 4184–4191.
(19) Ciurli, S.; Carrié, M.; Weigel, J. A.; Carney, M. J.; Stack, T. D. P.; Papaefthymiou, G. C.; Holm, R. H. Subsite-Differentiated Analogues of Native $[4Fe\text{-}4S]^{2+}$ Clusters: Preparation of Clusters with Five- and Six-Coordinate Subsites and Modulation of Redox Potentials and Charge Distributions. *J. Am. Chem. Soc.* **1990**, *112* (7), 2654–2664.
(20) Zhou, H.-C.; Holm, R. H. Synthesis and Reactions of Cubane-Type Iron−Sulfur−Phosphine Clusters, Including Soluble Clusters of Nuclearities 8 and 16. *Inorg. Chem.* **2003**, *42* (1), 11–21.
(21) Deng, L.; Majumdar, A.; Lo, W.; Holm, R. H. Stabilization of 3:1 Site-Differentiated Cubane-Type Clusters in the $[Fe_4S_4]^{1+}$ Core Oxidation State by Tertiary Phosphine Ligation: Synthesis, Core Structural Diversity, and $S = 1/2$ Ground States. *Inorg. Chem.* **2010**, *49* (23), 11118–11126.
(22) Tyson, M. A.; Demadis, K. D.; Coucouvanis, D. Uncharged Mixed-Ligand Clusters with the $[Fe_4S_4]^{+}$ and $[Fe_4S_4]^{2+}$ Cores. Synthesis, Structural Characterization, and Properties of the $Fe_4S_4X(^TBu_3P)_3$ (X = Cl, Br, I) and $Fe_4S_4(SPh)_2(^TBu_3P)_2$ Cubanes. *Inorg. Chem.* **1995**, *34* (18), 4519–4520.
(23) Ohki, Y.; Tanifuji, K.; Yamada, N.; Imada, M.; Tajima, T.; Tatsumi, K. Synthetic Analogues of $[Fe_4S_4(Cys)_3(His)]$ in Hydrogenases and $[Fe_4S_4(Cys)_4]$ in HiPIP Derived from All-Ferric $[Fe_4S_4\{N(SiMe_3)_2\}_4]$. *PNAS* **2011**, *108* (31), 12635–12640.
(24) Tolman, C. A. Phosphorus Ligand Exchange Equilibriums on Zerovalent Nickel. Dominant Role for Steric Effects. *J. Am. Chem. Soc.* **1970**, *92* (10), 2956–2965.
(25) Gómez-Suárez, A.; Nelson, D. J.; Nolan, S. P. Quantifying and Understanding the Steric Properties of N-Heterocyclic Carbenes. *Chem. Commun.* **2017**, *53*, 2650–2660.
(26) Goh, C.; Segal, B. M.; Huang, J.; Long, J. R.; Holm, R. H. Polycubane Clusters: Synthesis of $[Fe_4S_4(PR_3)_4]^{1+,0}$ (R = Bu(t), Cy, Pr(i)) and $[Fe_4S_4]^0$ Core Aggregation upon Loss of Phosphine. *J. Am. Chem. Soc.* **1996**, *118* (47), 11844–11853.
(27) Deng, L.; Holm, R. H. Stabilization of Fully Reduced Iron-Sulfur Clusters by Carbene Ligation: The $[Fe_nS_n]^0$ Oxidation Levels (n = 4, 8). *J. Am. Chem. Soc.* **2008**, *130* (30), 9878–9886.
(28) Zhang, H.; Ouyang, Z.; Liu, Y.; Zhang, Q.; Wang, L.; Deng, L. (Aminocarbene)(Divinyltetramethyldisiloxane)Iron(0) Compounds: A Class of Low-Coordinate Iron(0) Reagents. *Angew. Chemie - Int. Ed.* **2014**, *53* (32), 8432–8436.
(29) Huang, J.; Schanz, H.-J.; Stevens, E. D.; Nolan, S. P. Stereoelectronic Effects Characterizing Nucleophilic Carbene Ligands Bound to the Cp*RuCl (Cp* = η^5-C_5Me_5) Moiety: A Structural and Thermochemical Investigation. *Organometallics* **1999**, *18* (12), 2370–2375.
(30) Yakelis, N. A.; Bergman, R. G. Safe Preparation and Purification of Sodium Tetrakis[(3,5-Trifluoromethyl) Phenyl]Borate ($NaBArF_{24}$): Reliable and Sensitive Analysis of Water in Solutions of Fluorinated Tetraarylborates. *Organometallics* **2005**, *24* (14), 3579–3581.
(31) Bantreil, X.; Nolan, S. P. Synthesis of *N*-Heterocyclic Carbene Ligands and Derived Ruthenium Olefin Metathesis Catalysts. *Nat. Protoc.* **2011**, *6* (1), 69–77.
(32) Hintermann, L. Expedient Syntheses of the *N*-Heterocyclic Carbene Precursor Imidazolium Salts IPr·HCl, IMes·HCl and IXy·HCl. *Beilstein J. Org. Chem.* **2007**, *3* (22).
(33) Kuhn, N.; Kratz, T. Synthesis of Imidazol-2-Ylidenes by Reduction of Imidazole-2(3H)-Thiones. *Synthesis* **1993**, *1993* (6), 561–562.

(34) Stoll, S.; Schweiger, A. EasySpin, a Comprehensive Software Package for Spectral Simulation and Analysis in EPR. *J. Magn. Reson.* **2006**, *178* (1), 42–55.
(35) Hübschle, C. B.; Sheldrick, G. M.; Dittrich, B. ShelXle: A Qt Graphical User Interface for SHELXL. *J. Appl. Crystallogr.* **2011**, *44* (6), 1281–1284.
(36) The Fe_4S_4 cluster [CAAC–H][(CAAC)$Fe_4S_4Br_3$] (CAAC = cyclic (alkyl)(amino)carbene) has been reported: Zhang, Y. Y.; Mei, T.; Yang, D.; Zhang, Y. Y.; Wang, B.; Qu, J. Synthesis and Reactivity of Thiolate-Bridged Multi-Iron Complexes Supported by Cyclic (Alkyl)(Amino)Carbene. *Dalton Trans.* **2017**, *46*, 15888–15896.
(37) Nelson, D. J.; Nolan, S. P. Quantifying and Understanding the Electronic Properties of N-Heterocyclic Carbenes. *Chem. Soc. Rev.* **2013**, *42* (16), 6723.
(38) Lane, R. W.; Wedd, A. G.; Gillum, W. O.; Laskowski, E. J.; Holm, R. H.; Frankel, R. B.; Papaefthymiou, G. C. Synthesis and Electronic Properties of the Tetranuclear Trianions $[Fe_4S_4(SR)_4]^{3-}$, Analogues of the 4-Fe Active Sites of Reduced Ferredoxins. *J. Am. Chem. Soc.* 1977, *99* (7), 2350–2352.
(39) Laskowski, E. J.; Frankel, R. B.; Gillum, W. O.; Papaefthymiou, G. C.; Renaud, J.; Ibers, J. A.; Holm, R. H. Synthetic Analogs of the 4-Fe Active Sites of Reduced Ferredoxins. Electronic Properties of the Tetranuclear Trianions $[Fe_4S_4(SR)_4]^{3-}$ and the Structure of $[(C_2H_5)_3(CH_3)N]_3[Fe_4S_4(SC_6H_5)_4]$. *J. Am. Chem. Soc.* **1978**, *100* (17), 5322–5337.
(40) Stephan, D. W.; Papaefthymiou, G. C.; Frankel, R. B.; Holm, R. H. Analogues of the $[4Fe\text{-}4S]^{+}$ Sites of Reduced Ferredoxins: Structural and Spectroscopic Properties of $[(C_2H_5)_4N]_3[Fe_4S_4(S\text{-}p\text{-}C_6H_4Br)_4]$ in Crystalline and Solution Phases. *Inorg. Chem* **1983**, *22*, 1550–1557.
(41) Carney, M. J.; Papaefthymiou, G. C.; Spartalian, K.; Frankel, R. B.; Holm, R. H. Ground Spin State Variability in $[Fe_4S_4(SR)_4]^{3-}$. Synthetic Analogs of the Reduced Clusters in Ferredoxins and Other Iron-Sulfur Proteins: Cases of Extreme Sensitivity of Electronic State and Structure to Extrinsic Factors. *J. Am. Chem. Soc.* **1988**, *110* (18), 6084–6095.
(42) Carney, M. J.; Papaefthymiou, G. C.; Frankel, R. B.; Holm, R. H. Contribution from the Alternative Spin States in Synthetic Analogues of Biological [4Fe-4S]+ Clusters: Further Cases of Variable Ground States and the Structure of $(Et_4N)_3[Fe_4S_4(S\text{-}o\text{-}C_6H_4StBu)_4]$, Containing a Reduced Cluster with a Compressed Tetragonal Distortion; **1989**; *28*, 1497-1503.
(43) Carney, M. J.; Holm, R. H.; Papaefthymiou, G. C.; Frankel, R. B. Demonstration of Alternative Spin States in Clusters Containing the Biologically Relevant $[Fe_4S_4]^{1+}$ Core. *J. Am. Chem. Soc.* **1986**, *108* (12), 3519–3521.
(44) Venkateswara Rao, P.; Holm, R. H. Synthetic Analogues of the Active Sites of Iron−Sulfur Proteins. *Chem. Rev.* **2004**, *104* (2), 527–560.
(45) Scott, T. A.; Berlinguette, C. P.; Holm, R. H.; Zhou, H.-C. Initial Synthesis and Structure of an All-Ferrous Analogue of the Fully Reduced $[Fe_4S_4]^0$ Cluster of the Nitrogenase Iron Protein. *Proc. Natl. Acad. Sci* **2005**, *102* (28), 9741–9744.
(46) Harmjanz, M.; Saak, W.; Haase, D.; Pohl, S. Aryl Isonitrile Binding to $[Fe_4S_4]$ Clusters: Formation of $[Fe_4S_4]^{+}$ and $[\{Fe_4S_4\}_2]^{2+}$ cores. *Chem. Commun.* **1997**, 951–952.
(47) Weigel, J. A.; Holm, R. H.; Srivastava, K. K. P.; Day, E. P.; Münck, E. Isonitrile Binding to a Site-Differentiated Synthetic Analogue of Biological [4Fe-4S] Clusters: Equilibria, Magnetic Interactions and the Spin-Isolated [3Fe-4S] Cluster Fragment, and the Structure of a Low-Spin Iron(II) Subsite. *J. Am. Chem. Soc.* **1990**, *112* (22), 8015–8023

(48) Goh, C.; Weigel, J. A.; Holm, R. H. The [2:2] Site-Differentiated Clusters $[Fe_4S_4L_2(RNC)_6]$ Containing Two Low-Spin Iron(II) Sites. *Inorg. Chem.* **1994**, *33* (22), 4861–4868.
(49) Goh, C.; Nivorozhkin, A.; Yoo, S. J.; Bominaar, E. L.; Mu, E.; Holm, R. H. The Mixed-Valence Double-Cubanoid Cluster $[Fe_8S_{12}(Bu^tNC)_{12}]$: Synthesis , Structure , and Exchange Coupling of a New Structural Array of Four Fe (III) Sites. *Inorg. Chem* **1998**, *37* (12), 2926–2932.
(50) Cai, L.; Segal, B. M.; Long, J. R.; Scott, M. J.; Holm, R. H. Octanuclear Iron–Sulfur Clusters with Symmetrically Coupled Fe_4S_4 and Fe_4S_5 Cores. *J. Am. Chem. Soc.* **1995**, *117* (34), 8863–8864.
(51) Weigel, J. A.; Holm, R. H.; Surerus, K. K.; Munck, E. Spin-Isolation of the [3Fe-4S] Fragment of a [4Fe-4S] Cluster: Electronic Properties of the $[3Fe\text{-}4S]^0$ Cluster. *J. Am. Chem. Soc.* **1989**, *111* (26), 9246–9247.
(52) Bellows, S. M.; Brennessel, W. W.; Holland, P. L. Effects of Ligand Halogenation on the Electron Localization, Geometry and Spin State of Low-Coordinate (β-Diketiminato)Iron Complexes. *Eur. J. Inorg. Chem.* **2016**, *2016* (20), 3344–3355.
(53) Bellow, J. A.; Yousif, M.; Cabelof, A. C.; Lord, R. L.; Groysman, S. Reactivity Modes of an Iron Bis(Alkoxide) Complex with Aryl Azides: Catalytic Nitrene Coupling vs Formation of Iron(III) Imido Dimers. *Organometallics* **2015**, *34* (12), 2917–2923.
(54) Chiang, K. P.; Barrett, P. M.; Ding, F.; Smith, J. M.; Kingsley, S.; Brennessel, W. W.; Clark, M. M.; Lachicotte, R. J.; Holland, P. L. Ligand Dependence of Binding to Three-Coordinate Fe(II) Complexes. *Inorg. Chem.* **2009**, *48* (12), 5106–5116.
(55) Esposito, V.; Solari, E.; Floriani, C.; Re, N.; Rizzoli, C.; Chiesi-Villa, A. Binding and Redox Properties of Iron(II) Bonded to an Oxo Surface Modeled by Calix[4]Arene. *Inorg. Chem.* **2000**, *39* (12), 2604–2613.
(56) Collins, T. J.; Fox, B. G.; Hu, Z. G.; Kostka, K. L.; Rickard, C. E. F.; Wright, L. J. High Valent Transition Metal Chemistry. Synthesis and Characterization of an Intermediate-Spin Iron(IV) Complex of a Strong π-Acid Ligand. *J. Am. Chem. Soc.* **1992**, *114* (22), 8724–8725.
(57) Surerus, K. K.; Münck, E.; Moura, I.; Moura, J. J. G.; LeGall, J. Evidence for the Formation of a $ZnFe_3S_4$ Cluster in Desulfovibrio Gigas Ferredoxin II. *J. Am. Chem. Soc.* **1987**, *109* (12), 3805–3807.
(58) Srivastava, K. K. P.; Surerus, K. K.; Conover, R. C. Moessbauer Study of Zinc-Iron-Sulfur $ZnFe_3S_4$ and Nickel-Iron-Sulfur $NiFe_3S_4$ Clusters in Pyrococcus Furiosus Ferredoxin. *Inorg. Chem.* **1993**, 32, 927–936.

Supporting Information

Experimental methods:

General Considerations: Unless otherwise noted, all reactions were performed using standard Schlenk techniques or in an LC Technologies inert atmosphere glove box under an atmosphere of nitrogen (< 1 ppm O_2/H_2O). Glassware was dried in an oven at 160 °C prior to use. Molecular sieves (3 Å) and Celite® were activated by heating to 300 °C overnight under vacuum prior to storage under an atmosphere of nitrogen. Diethyl ether (Et_2O), benzene, pentane, and acetonitrile were degassed by sparging with argon, dried by passing through a column of activated alumina, and stored under an atmosphere of nitrogen over 3 Å molecular sieves. Tetrahydrofuran (THF) was distilled from sodium/benzophenone and stored under an atmosphere of nitrogen over 3 Å molecular sieves. C_6D_6 was degassed by three freeze–pump–thaw cycles and stored under an atmosphere of nitrogen over 3 Å activated molecular sieves. $(PCy_3)_3Fe_4S_4Cl$,[20] $NaBAr^F{}_4$,[30] IMes,[31,32], I^iPr^{Me}[33] and $[(PCy_3)_4Fe_4S_4][BPh_4]$[26] were prepared according to literature procedures. *t*-butylisocyanide (^{t}BuNC) was degassed by three freeze-pump thaw cycles and stored under an atmosphere of nitrogen. PPh_4Cl was dried at 150 °C under vacuum for 16 h before use. All other reagents were purchased and used as received. NMR spectra were recorded on Bruker and Varian spectrometers. ^1H and $^{13}C\{^1H\}$ chemical shifts are given relative to residual solvent peaks. FT-IR samples were taken as thin films using a Bruker Alpha Platinum ATR spectrometer with OPUS software in a glovebox under an N_2 atmosphere. Diagnostic IR stretches are reported in the experimental details. EPR spectra were recorded on a Bruker EMX spectrometer at 9.37 GHz as frozen glasses. Simulations were performed using EasySpin[34] (5.2.21) in Matlab (R2017b). UV-vis spectra were taken on a Cary 50 spectrometer. Elemental analyses were performed at Robertson Microlit laboratories or Midwest Microlab. X-ray structural determinations were performed at the MIT diffraction facility using a Bruker X8 diffractometer with an APEX II CCD detector or a Bruker D8

Venture diffractometer with a Photon2 CPAD detector. Diffraction data was collected, integrated, and corrected for absorption using Bruker APEX3 software and its associated modules (SAINT, SADABS, TWINABS). Structural solutions and refinements (on F^2) were carried out using SHELXT and SHELXL-2018 in ShelXle.[35] Ellipsoid plots and figures were made using Mercury.

(I^iPr^{Me})$_3$Fe$_4$S$_4$Cl (1): (PCy_3)$_3$Fe$_4$S$_4$Cl (204 mg, 0.166 mmol) was suspended in Et_2O (5 mL). A solution of I^iPr^{Me} (134 mg, 0.743 mmol) in Et_2O (2 mL) was added and the dark-brown suspension was stirred for 4 h. The black solid was collected on a frit and washed with Et_2O (3 x 10 mL). This procedure gave material of > 90% purity as determined by ^{1}H NMR spectroscopy (Fig. S2.1) and was used for further reaction studies. Yield: 123 mg (80 %). To remove trace PCy_3-containing products, the crude material could be recrystallized by mixing Et_2O (3 mL) into a benzene solution of **1** (50 mg in 1 mL) followed by storage at −35 °C overnight. The crystals could be washed quickly with benzene (5 × 1 mL) to obtain product of higher purity as judged by ^{1}H NMR spectroscopy (Fig. S2.2). Yield 4 mg (8%). ^{1}H NMR (400 MHz, C_6D_6, 293 K) δ 2.81 (36H, ^{i}Pr-CH_3), 4.81 (18H, backbone CH_3), 9.14 (6H, br, ^{i}Pr-CH). UV−vis (THF): λ_{max} (nm): 345 nm (ε = 12000 L/mol·cm). EPR: g_1 = 2.090, g_2 = 1.943, g_3 = 1.908 (toluene, 15 K, 9.37 GHz). Elemental analysis data were not obtained owing to the presence of trace impurities. X-ray quality crystals were grown by diffusion of Et_2O into fluorobenzene at ambient temperature.

(IMes)$_3$Fe$_4$S$_4$Cl (2): (PCy_3)$_3$Fe$_4$S$_4$Cl (1.00 g, 0.814 mmol) was dissolved in benzene (10 mL). A solution of IMes (810 mg, 2.66 mmol) in benzene (10 mL) was added dropwise and the dark-brown solution was stirred for 16 h. The mixture was then filtered through Celite, concentrated to 10 mL, and layered with pentane (40 mL). The mixture was allowed to stand for 2 h, then the black crystals were collected on a frit and washed with pentane (3 × 1 mL). Yield: 820 mg (77%) of pure compound as assessed by ^{1}H NMR (Fig. S2.3) and EPR (Fig. 2.2B)

spectroscopies. ^{1}H NMR (500 MHz, C_6D_6, 293 K) δ 2.09 (36H, Mes *o*-C*H*$_3$), 2.26 (18H, Mes *p*-C*H*$_3$), 5.86 (6H, backbone CH), 6.91 (12H, Mes CH). UV−vis (THF): λ_{max} (nm): 324 nm (ε = 18000 L/mol·cm). EPR: g_1 = 2.122, g_2 = 1.964, g_3 = 1.937 (toluene, 15 K, 9.37 GHz). Evans method (C_6D_6, 293 K): 3.2 μ_B. Found: C, 57.99; H, 5.56; N, 6.42. Calc. for $C_{63}H_{72}N_6Fe_4S_4Cl$: C, 58.19; H, 5.58; N, 6.46. X-ray quality crystals were grown by diffusion of pentane into Et_2O at –35 °C.

Compound **2** can also be prepared without isolation of $(PCy_3)_3Fe_4S_4Cl$. $[(PCy_3)_4Fe_4S_4][BPh_4]$ (500 mg, 0.280 mmol) was dissolved in CH_2Cl_2 (5 mL). A solution of PPh_4Cl (140 mg, 0.373 mmol) in CH_2Cl_2 (2 mL) was added and the brown solution was stirred for 10 min. The mixture was then filtered through Celite and the solvent was removed *in vacuo*. The black solids were triturated with benzene to remove residual CH_2Cl_2 and a solution of IMes (280 mg, 0.822 mmol) in benzene (10 mL) was added. The brown solution was stirred for 16 h. The mixture was then filtered through Celite, concentrated to 5 mL, and layered with pentane (40 mL). The mixture was allowed to stand for 2 h, then the black crystals were collected on a frit and washed with pentane (3 × 1 mL). Yield: 303 mg (83 %). The spectroscopic data were identical to that described above.

$[(I^iPr^{Me})_4Fe_4S_4][BAr^F_4]$/$[(I^iPr^{Me})_4Fe_4S_4][BPh_4]$ (3) *Method 1*: To a solution of $NaBPh_4$ (18.6 mg, 0.054 mmol) and I^iPr^{Me} (9.9 mg, 0.055 mmol) in THF (2 mL) was added $(I^iPr^{Me})_3Fe_4S_4Cl$ (50 mg, 0.054 mmol) in benzene (2 mL). The solution was stirred for 1 h and filtered through Celite. The solvent was removed *in vacuo* to yield $[(I^iPr^{Me})_4Fe_4S_4][BPh_4]$ in >90% purity as determined by ^{1}H NMR and EPR spectroscopies (Fig. S2.4 and S2.22). Yield: 63 mg (84%). ^{1}H NMR (400 MHz, H_8-THF, 293 K) δ 3.17 (48 H, ^{i}Pr-CH_3), 6.63 (24H, backbone CH_3), 6.83 (4H, $[BPh_4]^-$), 6.99 (8H, $[BPh_4]^-$), 7.50 (8H, $[BPh_4]^-$). ^{i}Pr–CH resonances were not observed. UV−vis (THF): λ_{max} (nm): 355 nm (ε = 12000 L/mol·cm). EPR: $g_\parallel$ = 2.114, $g_\perp$ = 1.903 (toluene/THF 10:1, 15 K, 9.37 GHz). Elemental analysis data were not obtained owing to the

presence of trace impurities. X-ray quality crystals were grown by vapor diffusion of pentane into a fluorobenzene solution at ambient temperature.

The $[BPh_4]^-$ salt could be converted to the $[BAr^F{}_4]^-$ salt by dissolution in minimal THF (0.5 mL) followed by addition of $NaBAr^F{}_4$ (1 equiv) in Et_2O (4 mL). The solution was stirred for 5 min, then pumped down and extracted into C_6D_6 (0.5 mL). The ^1H NMR spectrum was identical to that of material generated by halide abstraction with $NaBAr^F{}_4$. ^1H NMR (400 MHz, C_6D_6, 293 K) δ 2.99 (48H, ^{i}Pr-CH_3), 6.15 (24H, backbone CH_3), 6.17 (6H, br, ^{i}Pr-CH), 7.68 (4H, $[BAr^F{}_4]^-$), 8.37 (8H, $[BAr^F{}_4]^-$).

Method 2: To a solution of $[(PCy_3)_4Fe_4S_4][BAr^F{}_4]$ in C_6D_6 (0.5 mL) (generated *in situ* by anion exchange of $[(PCy_3)_4Fe_4S_4][BPh_4]$ (20 mg, 0.011 mmol) in CH_2Cl_2 (1 mL) with $NaBAr^F{}_4$ (9.9 mg, 0.011 mmol) in Et_2O (1 mL), followed by extraction with Et_2O (1 mL) and filtration through Celite to remove $NaBPh_4$) was added a solution of I^iPr^{Me} (8.1 mg, 0.045 mmol) in C_6D_6 (0.5 mL). A ^1H NMR spectrum recorded after 30 minutes of stirring was identical to that of material from method 1 (Fig. S2.6).

Method 3: Solutions of $(I^iPr^{Me})_3Fe_4S_4Cl$ (50.5 mg, 0.0388 mmol) in THF (4 mL) and $NaBAr^F{}_4$ (34.1 mg, 0.0385 mmol) in THF (4 mL) were cooled to –78 °C. The $NaBAr^F{}_4$ solution was added dropwise to the $(I^iPr^{Me})_3Fe_4S_4Cl$ solution and the resulting mixture was stirred for 2 h at –78 °C. The solution was then warmed to room temperature and the solvent removed *in vacuo*. The solids were extracted with 3:1 C_6D_6/THF (1 mL), removing a black precipitate. The ^1H NMR spectrum was identical to that of material from method 1 (Fig. S2.7).

$[(IMes)_3Fe_4S_4(THF)][BAr^F{}_4]$ (4): Solutions of $(IMes)_3Fe_4S_4Cl$ (50.5 mg, 0.0388 mmol) in THF (4 mL) and $NaBAr^F{}_4$ (34.1 mg, 0.0385 mmol) in THF (4 mL) were cooled to –78 °C. The $NaBAr^F{}_4$ solution was added dropwise to the $(IMes)_3Fe_4S_4Cl$ solution and the resulting mixture was stirred for 2 h at –78 °C. The solution was then warmed to room temperature and the solvent removed *in vacuo*. The dark-brown, sticky solids were redissolved in benzene (1 mL)

and filtered through Celite to remove NaCl. This material was used as generated in > 90 % purity as determined by ^{1}H NMR (Fig. S2.8 and S2.9) and EPR (Fig. 2.2C) spectroscopies. ^{1}H NMR (400 MHz, C_6D_6, 293 K) δ 1.97 (36H, Mes *o*-C*H*$_3$), 2.24 (18H, Mes *p*-C*H*$_3$), 5.97 (6H, backbone CH), 6.80 (12H, Mes CH), 7.70 (4H, $[BAr^F_4]^-$), 7.75 (4H, br, THF), 8.44 (8H, $[BAr^F_4]^-$), 17.75 (4H, br, THF). EPR: $g_1 = 2.116$, $g_2 = 1.942$, $g_3 = 1.911$ (toluene/THF 10:1, 15 K, 9.37 GHz). Elemental analysis data were not obtained owing to the presence of trace impurities. X-ray quality crystals of **4**·Et_2O were grown by layering of pentane onto an Et_2O solution and storage at –35 °C overnight.

[(IMes)$_3$Fe$_4$S$_4$(CN^{t}Bu)][BAr$^F_4$] (5): A solution of (IMes)$_3$Fe$_4$S$_4$Cl (50 mg, 0.039 mmol) in THF (4 mL) and a solution of NaBAr$^F_4$ (34.1 mg, 0.0385 mmol) with ^{t}BuNC (10.5 mg, 0.126 mmol) in THF (4 mL) were cooled to –78 °C. The NaBAr$^F_4$/^{t}BuNC solution was added dropwise to the solution of **1** and the resulting mixture was stirred for 3 h at –78 °C. The solution was then warmed to room temperature and filtered through Celite. The solvent was removed *in vacuo* and the dark-brown solids were recrystallized by layering Et_2O (0.5 mL) with pentane (2 mL) to yield black crystals that were washed with pentane (3 x 1 mL). Yield: 68.3 mg (80 %) of pure compound as established by ^{1}H NMR (Fig. S2.10) and EPR (Fig. 2.2D) spectroscopies. ^{1}H NMR (400 MHz, C_6D_6, 293 K) δ 1.37 (9H, ^{t}BuNC) 2.07 (36H, Mes *o*-C*H*$_3$), 2.32 (18H, Mes *p*-C*H*$_3$), 6.22 (6H, backbone CH), 6.94 (12H, Mes CH), 7.71 (4H, $[BAr^F_4]^-$), 8.46 (8H, $[BAr^F_4]^-$). FT-IR (thin film, cm^{-1}): 2121 (m, N-C stretch). UV–vis (THF): λ_{max} (nm): 360 nm (ε = 11000 L/mol·cm). EPR: $g_1 = 2.177$, $g_2 = 1.972$, $g_3 = 1.944$ (toluene/THF 10:1, 15 K, 9.37 GHz). Evans method (C_6D_6, 293 K): 3.2 μ_B. Found: C, 53.76; H, 4.49; N, 4.23. Calc. for $C_{100}H_{93}N_7Fe_4S_4BF_{24}$: C, 54.32; H, 4.24; N, 4.43. X-ray quality crystals were grown by layering pentane onto an Et_2O solution and storing at –35 °C overnight.

[(I^{i}Pr^{Me})$_4$Fe$_4$S$_4$(CN^{t}Bu)$_3$][BAr$^F_4$] (6) and [(I^{i}Pr^{Me})$_4$Fe$_4$S$_4$][BAr$^F_4$] (3): A solution of (I^{i}Pr^{Me})$_3$Fe$_4$S$_4$Cl (7.2 mg, 0.0078 mmol) in benzene (1 mL) was added dropwise to a solution

of $NaBAr^F_4$ (6.8 mg, 0.0077 mmol) and ^{t}BuNC (5.6 mg, 0.067 mmol) in Et_2O (1 mL). The solution was stirred for 1 h and filtered through Celite to remove dark solids. The solvent was removed *in vacuo*. A ^{1}H NMR spectrum of the crude material showed a mixture of **6** and **3** (Fig. S2.11). The resulting sticky oil was dissolved in toluene or Et_2O and studied immediately; **6** decomposes upon standing in Et_2O at RT. Yield (in situ, *vs.* a ferrocene internal standard): **6**: 0.0014 mmol (18 %); **3**: 0.0011 mmol (14 %). ^{1}H NMR (400 MHz, C_6D_6, 293 K) δ 0.52 (27H, ^{t}BuNC of **6**), 2.99 (48H, ^{i}Pr-CH_3 of **3**), 6.20 (24H, backbone CH_3 of **3**), 7.66 (4H, $[BAr^F_4]^-$), 8.30 (8H, $[BAr^F_4]^-$), 9.03 (36H, ^{i}Pr-CH_3 of **6**), 17.43 (18H, backbone CH_3 of **6**). FT-IR (thin film, cm^{-1}): 2132 (m, N–C stretch), 2074 (m, N–C stretch). EPR: **6**: g_{eff} = 8.583, 5.214, 4.242, (toluene/THF 10:1, 5 K, 9.37 GHz); **3**: $g_{\|}$ = 2.114, $g_{\perp}$ = 1.903 (toluene/THF 10:1, 15 K, 9.37 GHz). Elemental analysis data were not obtained owing to the instability of **6.**

A. NMR Spectra:

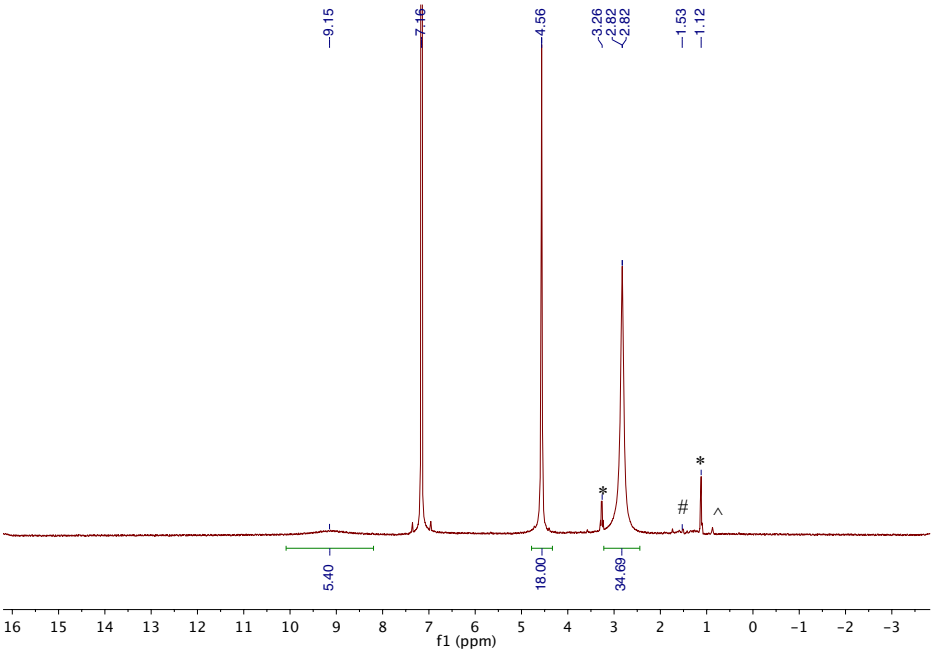

Figure S2.1: ^{1}H NMR spectrum (400 MHz) of **1** in C_6D_6 at 293 K, as generated. (*Et_2O, ^ pentane, # PCy_3-containing impurities (~5%))

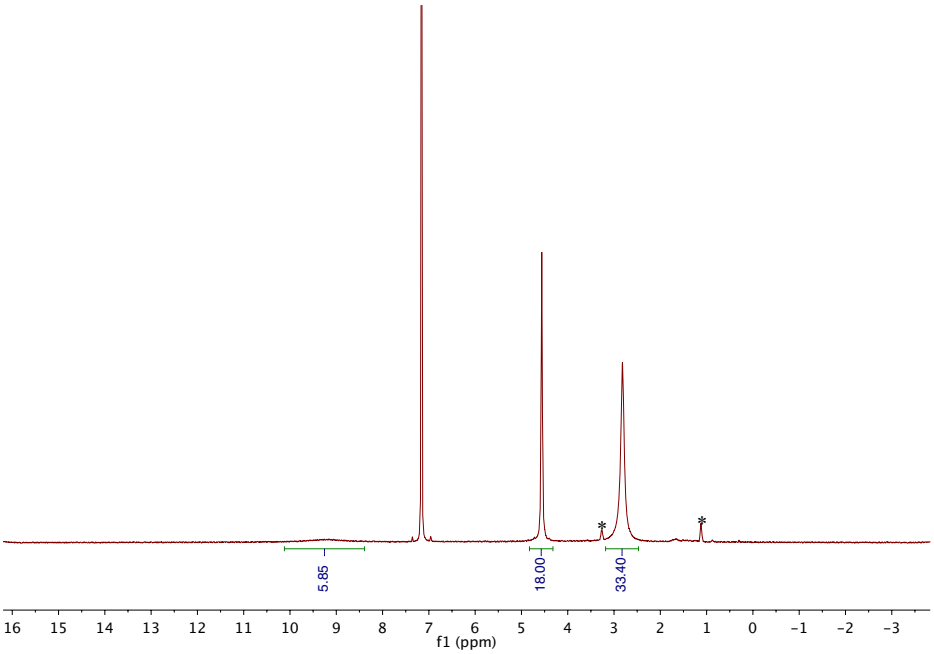

Figure S2.2: ^{1}H NMR spectrum (400 MHz) of **1** in C_6D_6 at 293 K following a recrystallization and washing procedure. (* Et_2O)

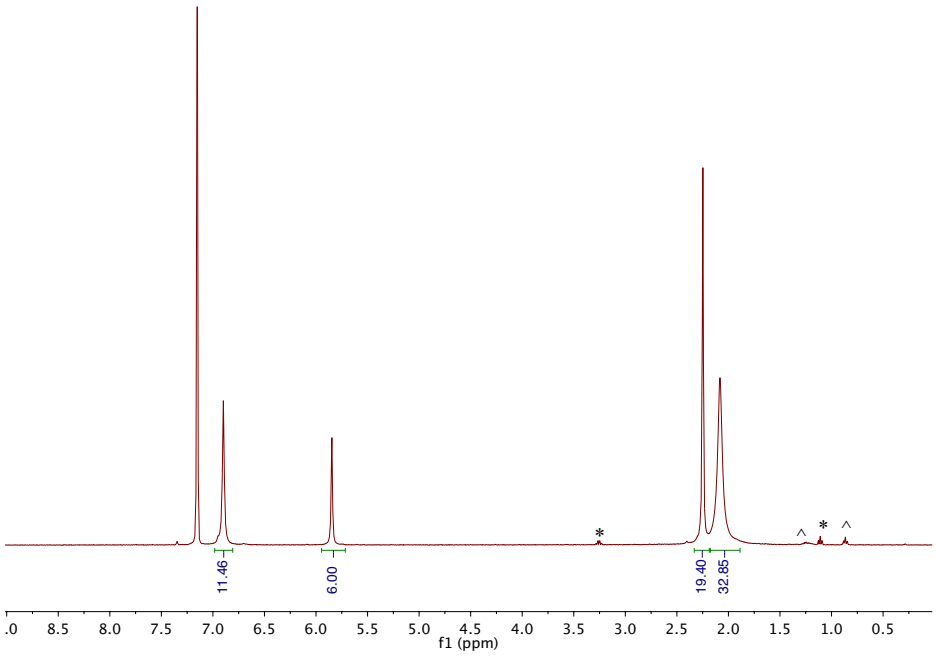

Figure S2.3: ^{1}H NMR spectrum (500 MHz) of **2** in C_6D_6 at 293 K (* Et_2O, ^ pentane)

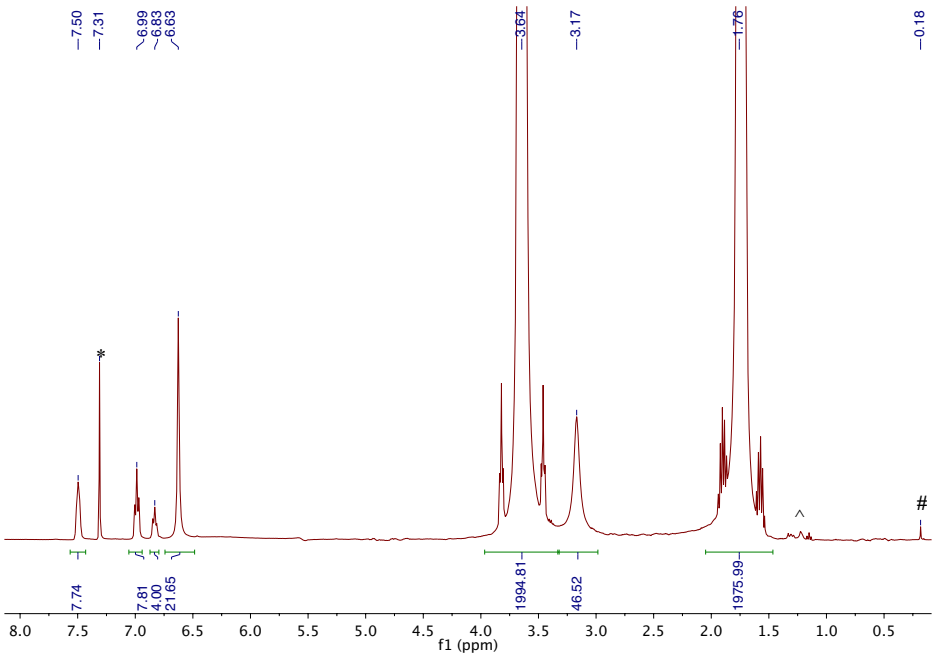

Figure S2.4: ^{1}H NMR spectrum (400 MHz) of **3**[BPh_4] in THF with C_6D_6 at 293 K. (* C_6D_5H, ^ pentane, # grease)

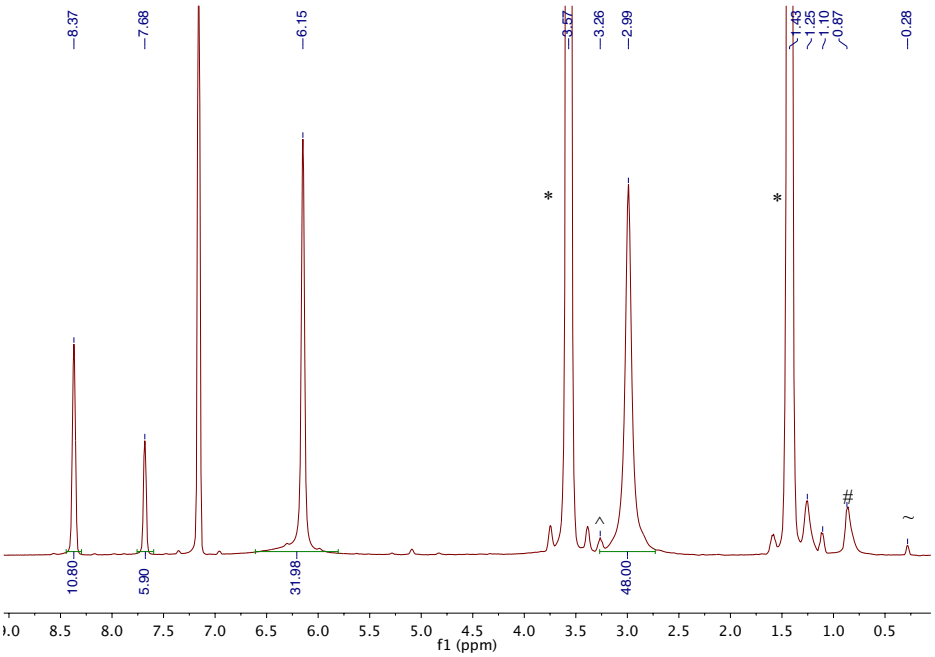

Figure S2.5: ^{1}H NMR spectrum (400 MHz) of **3**[BAr^{F}_{4}] in C_6D_6 with THF (co-solvent) at 293 K as generated by method 1. (* THF, ^ Et_2O, # pentane, ~ grease)

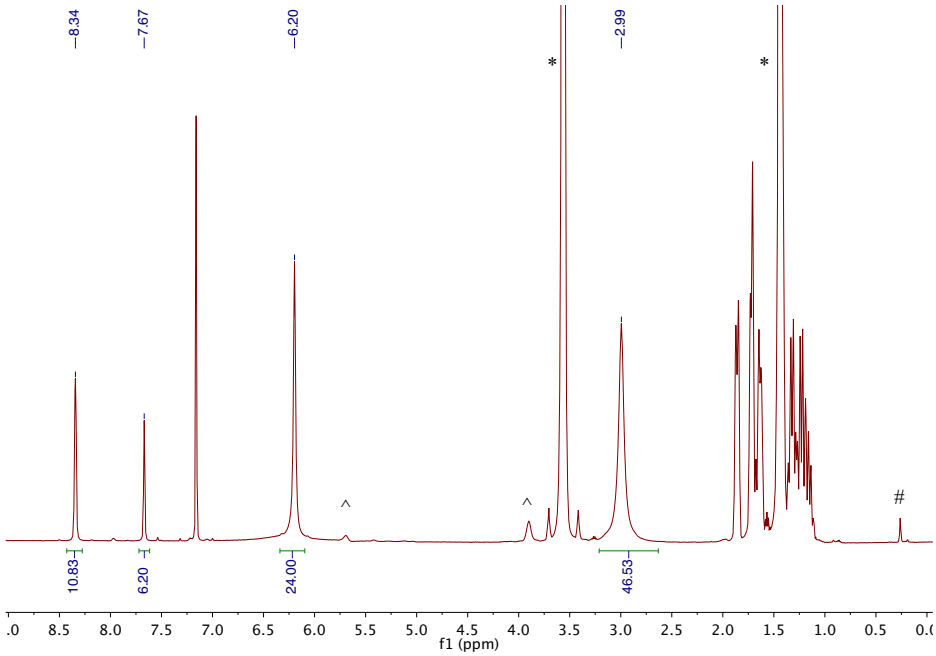

Figure S2.6: Crude ^{1}H NMR spectrum (500 MHz) of **3**[BAr^{F}_{4}] in C_6D_6 and THF (co-solvent) at 293 K as generated from phosphine displacement from [$(PCy_3)_4Fe_4S_4$][BAr^{F}_{4}] (method 2). Sharp peaks between 1 and 2 ppm are free PCy_3. (* THF, # grease, ^ unknown)

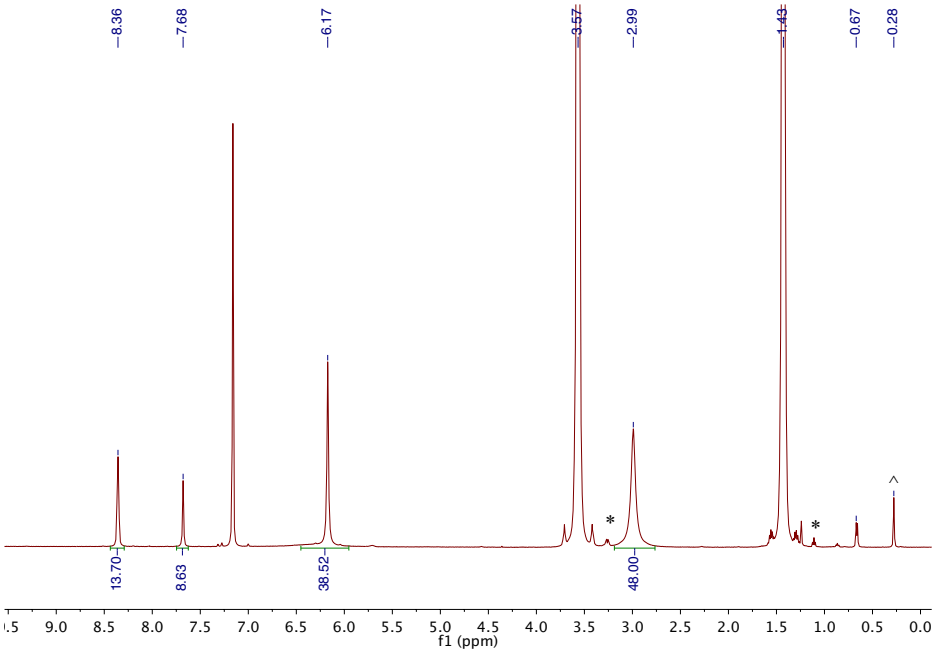

Figure S2.7: Crude ^{1}H NMR spectrum (500 MHz) of **3**[BAr$^{F}_{4}$] in C_6D_6 and THF (co-solvent) at 293 K as generated from method 3. (* Et_2O, ^ grease, # free I^{i}Pr^{Me})

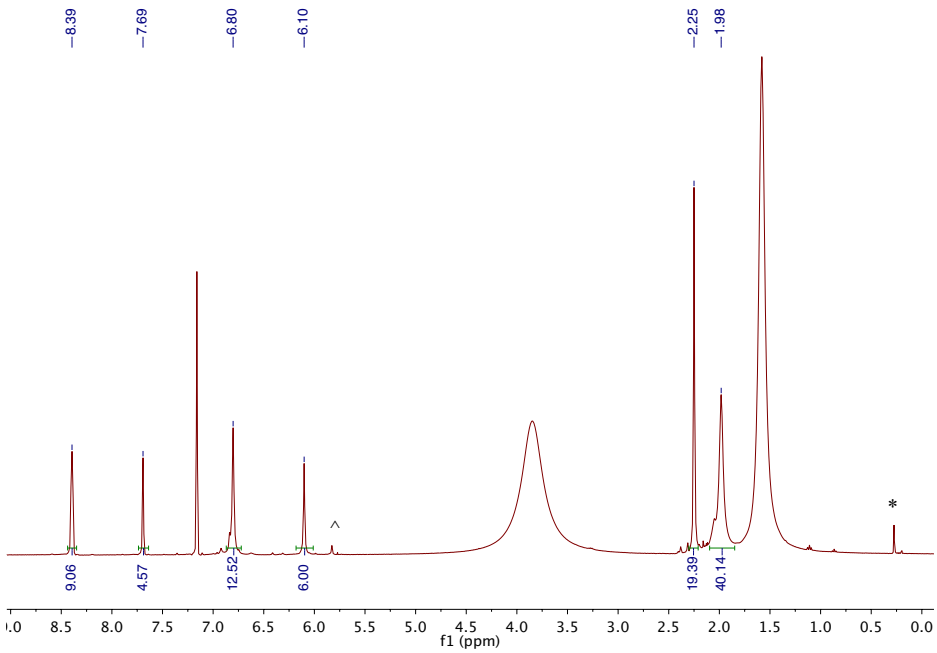

Figure S2.8: Representative crude ^{1}H NMR spectrum (400 MHz) of **4** in C_6D_6 with THF (co-solvent) at 293 K. Broad resonances at 3.7 and 1.5 ppm are attributed to rapidly exchanging bound and free THF. (^ unknown, # pentane, * grease)

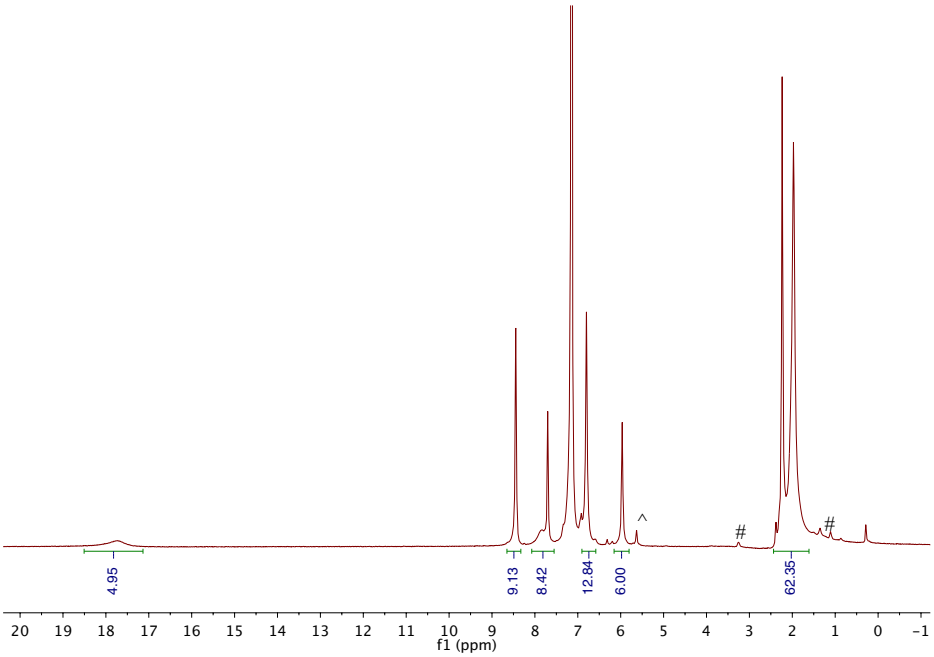

Figure S2.9: Representative ^{1}H NMR spectrum (400 MHz) of **4** in C_6D_6 at 293 K following lyophilization from benzene. The THF resonances have decreased in intensity to 1 equiv per cluster and shifted to 17.75 and 7.85 ppm. (^ unknown, * grease, # Et_2O)

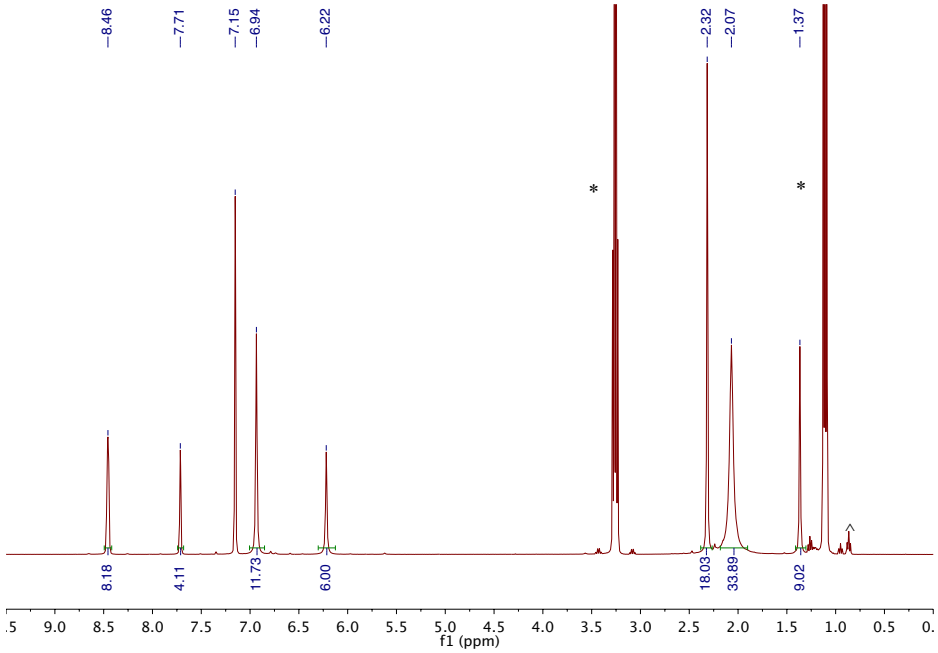

Figure S2.10: ^{1}H NMR spectrum (400 MHz) of **5** in C_6D_6 with Et_2O (co-solvent) at 293 K. (* Et_2O, ^ pentane)

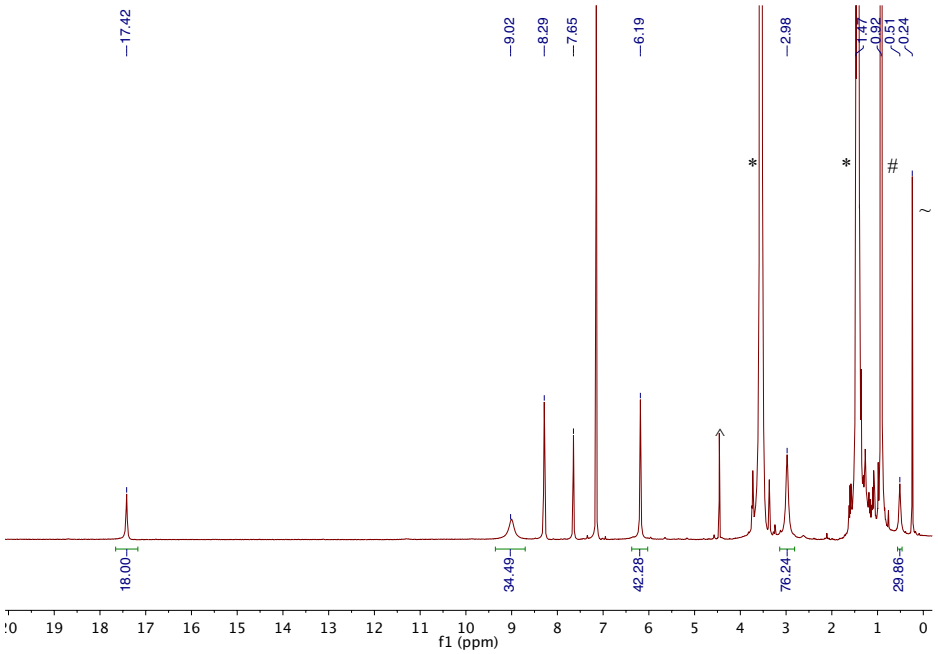

Figure S2.11: ^{1}H NMR spectrum of crude reaction mixture from halide abstraction from **1** in the presence of ^{t}BuNC in C_6D_6 with THF (co-solvent) at 293K. Peaks at 17.43 and 9.03 and 0.52 arise from **6**, peaks at 6.02 and 2.99 arise from **3.** (* THF, # free ^{t}BuNC, ~ grease, ^ unknown impurity present in ^{t}BuNC)

B. Infrared Spectra

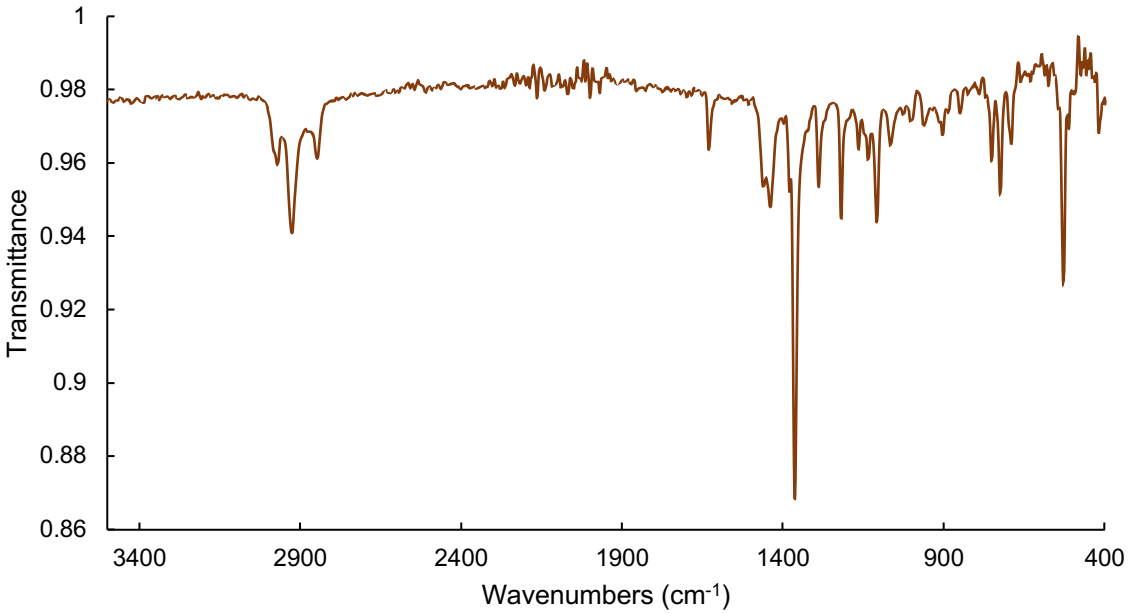

Figure S2.12: IR spectrum of **1**

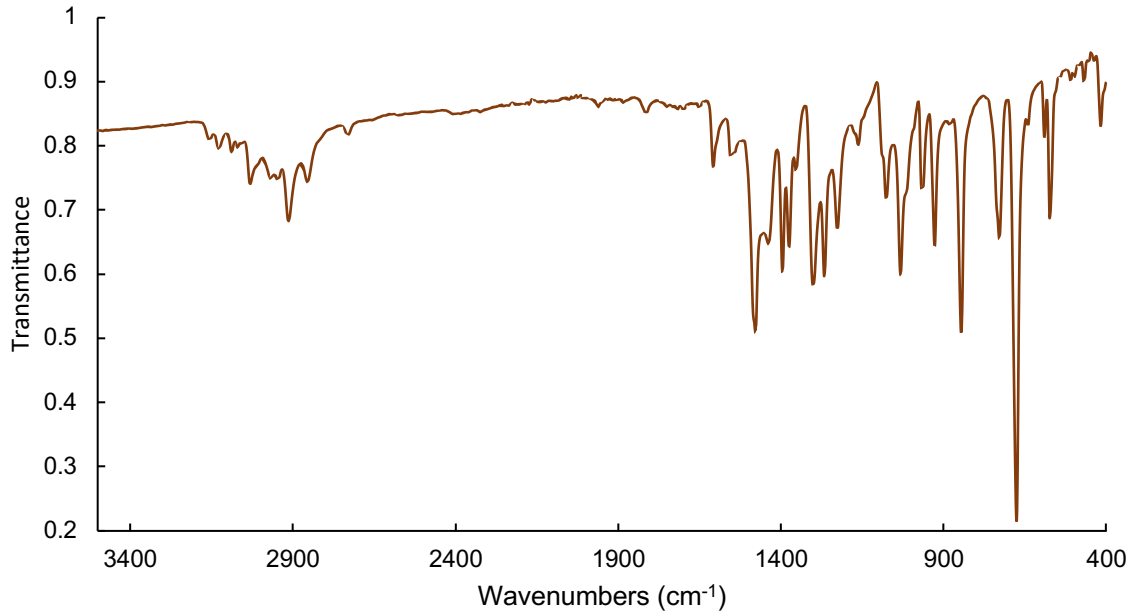

Figure S2.13: IR spectrum of **2**

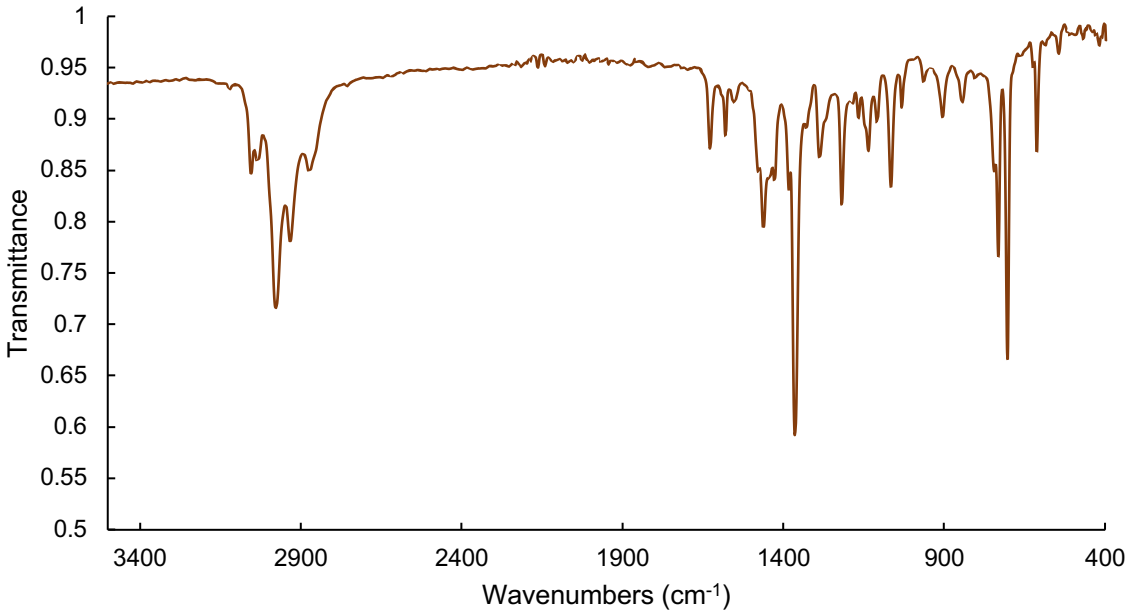

Figure S2.14: IR spectrum of **3**[BPh_4]

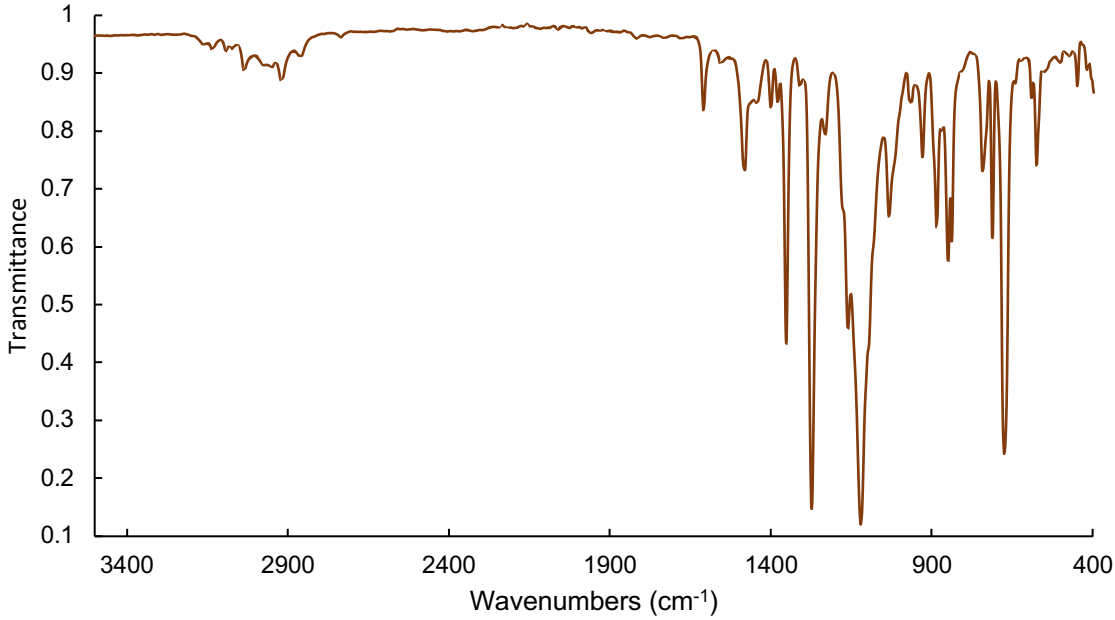

Figure S2.15: IR spectrum of **4**·THF

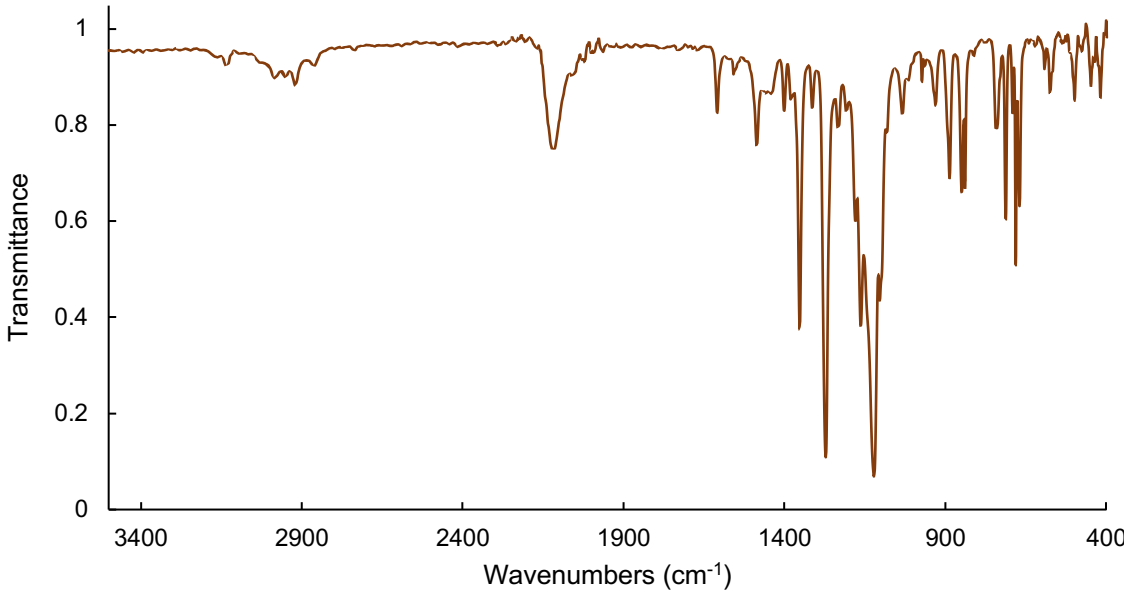

Figure S2.16: IR spectrum of **5**

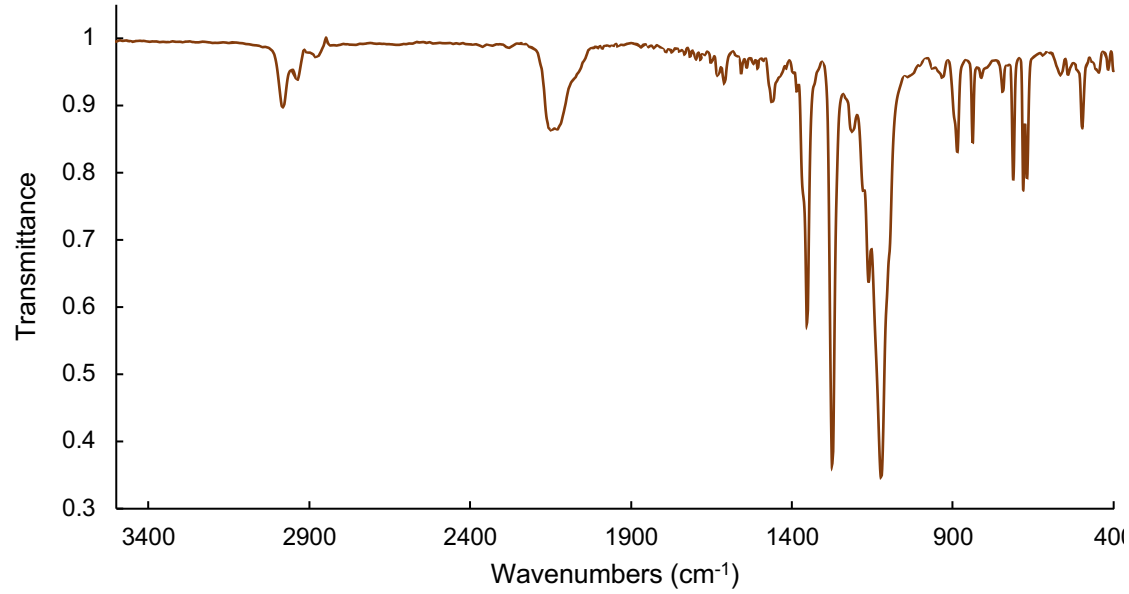

Figure S2.17: IR spectrum of a mixture of **3**[BAr^{F}_{4}] and **6**

C. UV-Vis spectra

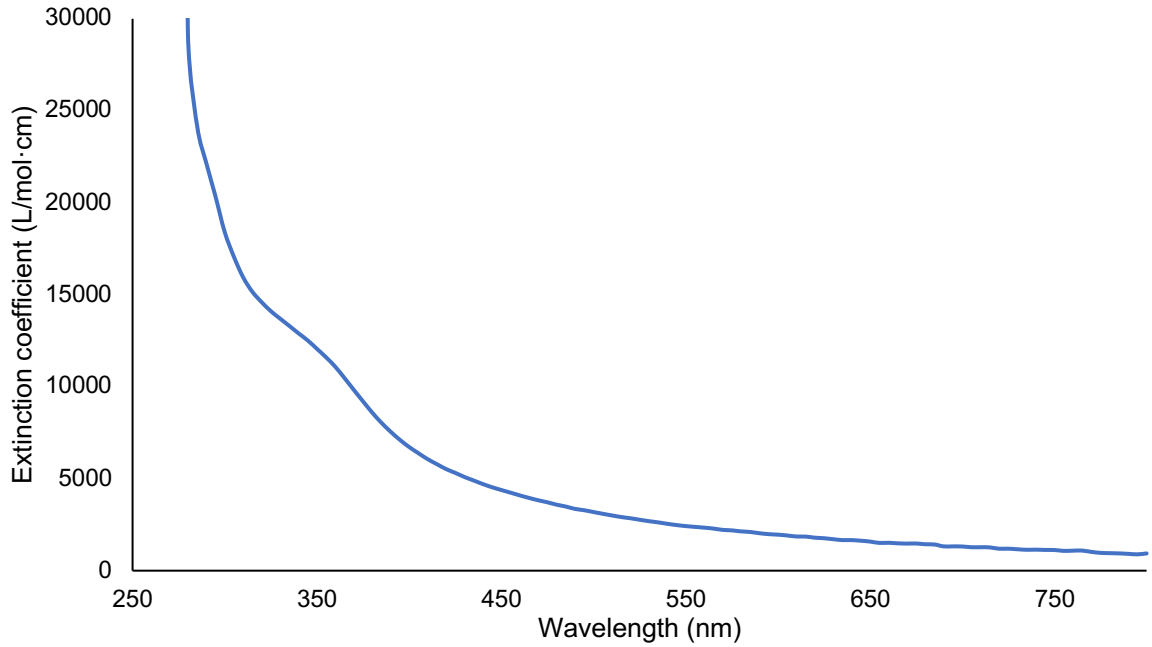

Figure S2.18: UV-Vis spectrum of **1** in THF

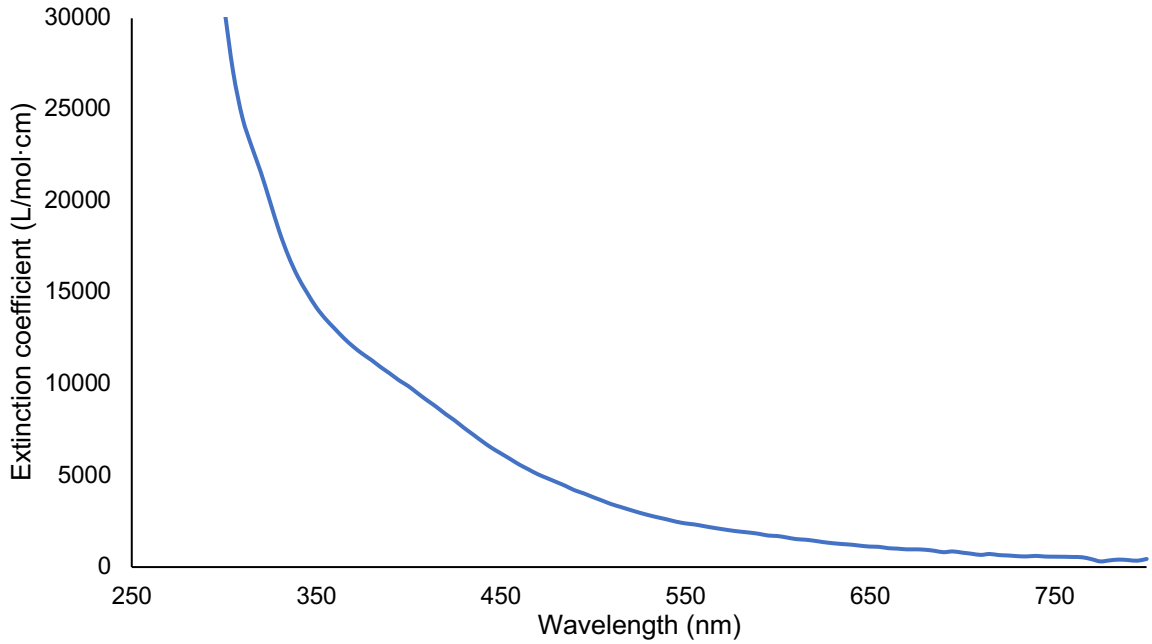

Figure S2.19: UV-Vis spectrum of **2** in THF

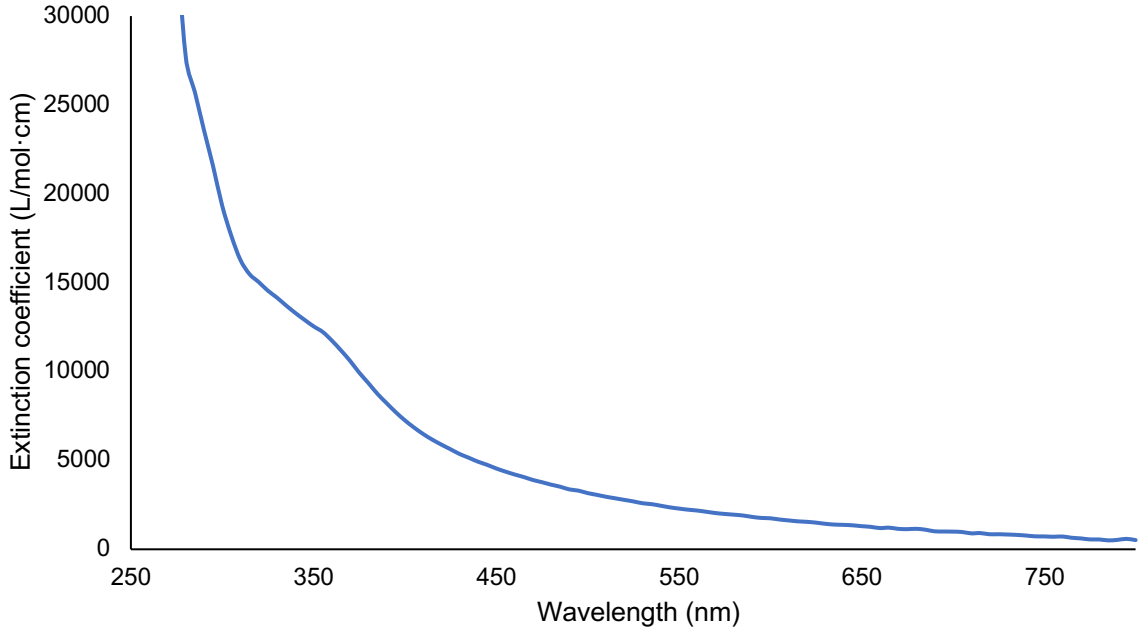

Figure S2.20: UV-Vis spectrum of **3**[BPh_4] in THF

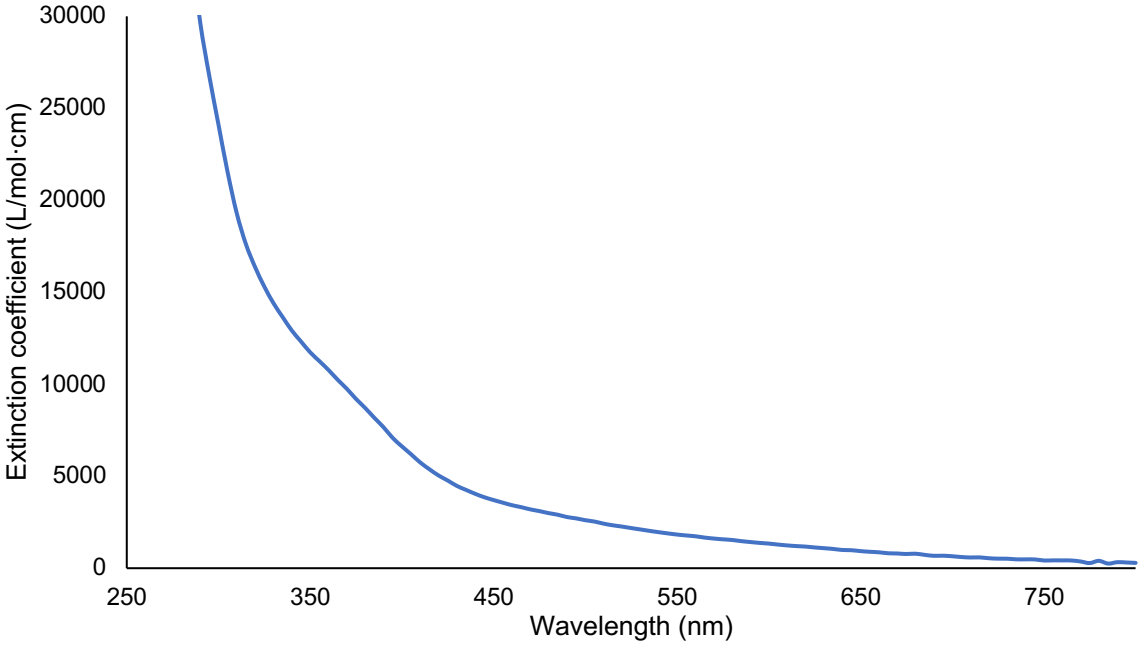

Figure S2.21: UV-Vis spectrum of **5** in THF

D. EPR Simulation Parameters and Determination of *D*

All EPR spectra listed in the table below were collected as frozen solutions in either toluene or 10:1 toluene/THF. The linewidths of the spectra were simulated as *g* strain with the parameters given below

Table S2.1: Simulation Parameters for EPR spectra of compounds **1** through **5**

Compound	*g* values	g_{avg}	*g*-strain
1	2.090 1.943 1.908	1.98	0.018 0.01 0.0184
2	2.122 1.964 1.937	2.01	0.02 0.0085 0.012
3	2.114 1.903 1.903	1.97	0.032 0.019 0.019
4	2.116 1.942 1.911	1.99	0.019 0.0154 0.0183
5	2.177 1.973 1.944	2.03	0.021 0.0072 0.0121

The EPR spectrum of **3** contained an ~ 10% impurity, which could be simulated as shown in Fig. S2.22

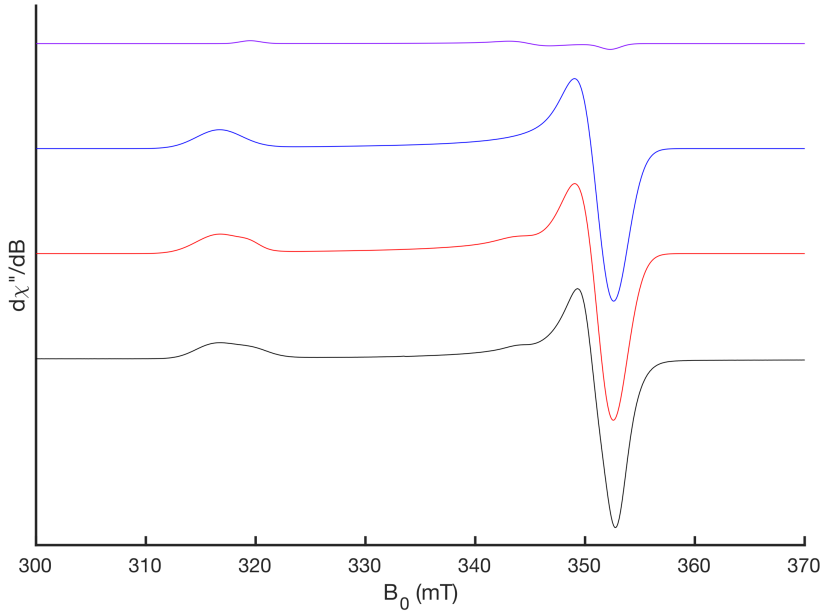

Figure S2.22: X-Band CW EPR spectrum of **3** (1 mM) in toluene/THF 10:1 at 15 K (black) and total simulation (red). Simulation of **3** (blue) and a 10% impurity (purple). Microwave power: 250 μW. Simulation parameters: **3**: *g* = [2.114 1.903 1.903] *g*-strain = [0.032 0.019 0.019]; impurity: *g* = [2.095 1.941 1.90] *g*-strain = [0.013 0.018 0.01]

To determine the value of the zero-field splitting parameter, D, in **6**, variable temperature EPR spectra of the mixture of **6** and **3** were collected at low field (Fig. S2.23).

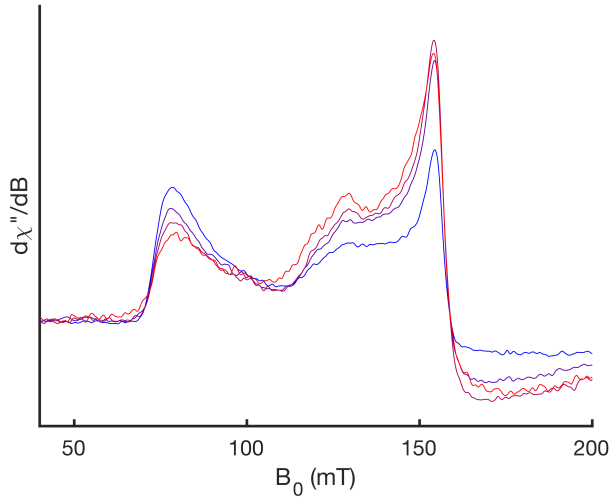

Figure S2.23: EPR spectrum of **6** and **3** (1 mM) in toluene/THF 10:1 at low field, highlighting the signal arising from **6**. Microwave power: 250 µW. Temperature: 5 K (blue), 8 K (purple), 10 K (red-purple), 15 K (red).

Based on the rhombogram for an $S = {}^5/_2$ system,[1] the signal at $g_{eff} = 8.58$ (ca. 80 mT) is assigned to transitions within the $m_s = \pm{}^1/_2$ doublet (the tailing to lower g_{eff}-values presumably arises from strain in D and/or E) and the signal at $g_{eff} = 4.24$ (ca. 150 mT) is assigned to transitions within the $m_s = \pm{}^3/_2$ doublet. With increasing temperature, the $m_s = \pm{}^1/_2$ doublet decreases in intensity and the $m_s = \pm{}^3/_2$ doublet increases in intensity, indicating that $D > 0$.

To determine the magnitude of D, the intensities of the $m_s = \pm{}^1/_2$ and $\pm{}^3/_2$ doublets (I_2 and I_1, respectively) were calculated as an average of 40 points between a field strength of 77.9 and 81.9 mT and 145.9 and 149.9 mT, respectively.

The difference in energy of the $m_s = \pm{}^3/_2$ and $\pm{}^1/_2$ is given by the Boltzmann distribution:

$$C\frac{I_1}{I_2} = e^{-\Delta E/kT}$$

where C is a constant that accounts for the difference in transition probabilities for the $m_s = \pm{}^1/_2$ and $\pm{}^3/_2$ doublets, k is the Boltzmann constant, and

$$\Delta E = 2D$$

for an $S = {}^5/_2$ spin system with $D > 0$.

Plotting

$$\ln\left(\frac{I_1}{I_2}\right) = -\frac{\Delta E}{kT} - \ln(C)$$

yields a slope of $2D/k$ = 7.9(5) K (Fig. S2.24) corresponding to D = 2.7(2) cm^{-1}.
This is similar in magnitude but opposite in sign to the values of D reported for $[ZnFe_3S_4]^+$ clusters.[2,3]

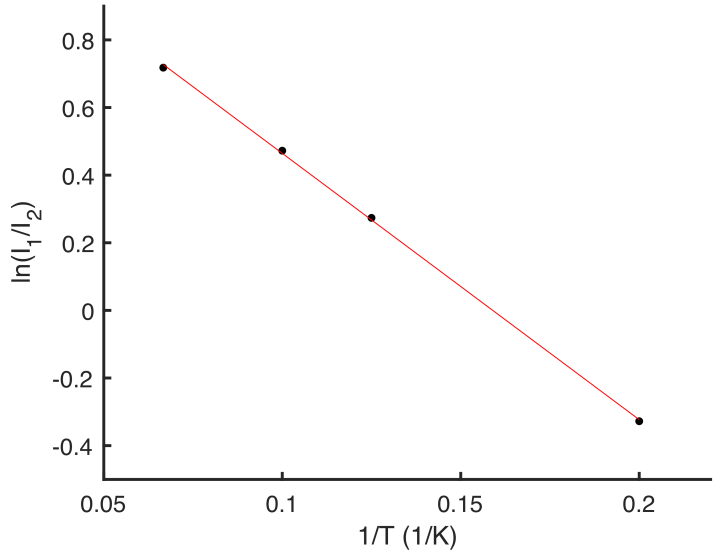

Figure S2.24: Plot of $\ln(I_1/I_2)$ vs 1/T. I_1 arises from the $m_s = \pm 3/2$ doublet and I_2 arises from the $m_s = \pm 1/2$ doublet.

E. Spin coupling scheme for **5** and **6**

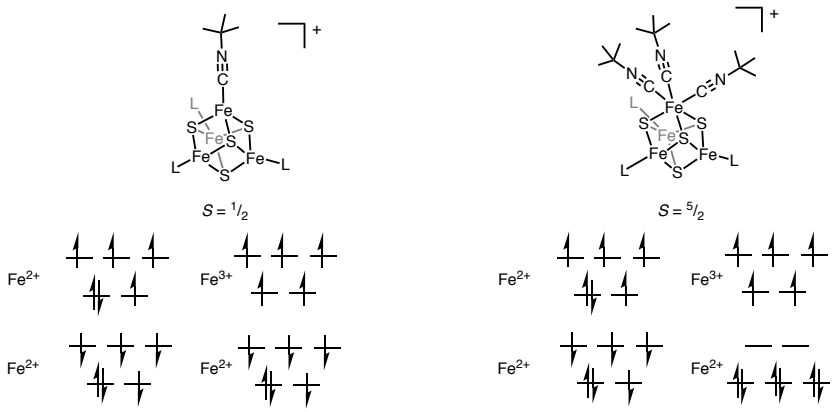

Figure S2.25: Spin coupling scheme for $[Fe_4S_4]^+$ clusters with one (left) or three (right) isocyanide ligands. Binding one isocyanide yields an electronic structure that is typical of $S = {}^1/_2$ $[Fe_4S_4]^+$ clusters with four locally high-spin Fe sites. Binding three isocyanides induces a low-spin, valence-trapped Fe^{2+} configuration at the apical Fe site. The spin-coupling scheme for the remaining Fe centers includes a co-aligned, $S = {}^9/_2$ mixed-valent pair antiferromagnetically coupled to an $S = 2$ Fe^{2+} site to yield an overall spin state of $S = {}^5/_2$.

F. Crystallographic details

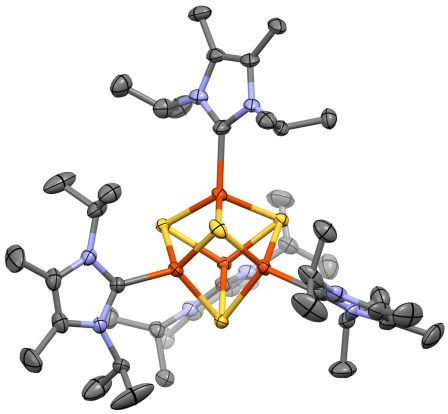

Figure S2.26: Thermal ellipsoid (50%) plot of **5**[BPh_4]. Hydrogen atoms and anion omitted for clarity.

1: Crystallized as a non-merohedral twin. A second domain was found using cell_now, twinning was taken into account during data integration, scaling was done with TWINABS, and the data was refined against the HKLF5 file

2: Crystallized as a non-merohedral twin. A second domain was found using cell_now, twinning was taken into account during data integration, scaling was done with TWINABS, and the data was refined against the HKLF5 file.

3: One carbene ligand is disordered over two positions in about a 76:24 ratio. One half of the carbene positions of the minority component were resolved and the disordered atoms were refined with appropriate distance and angle restraints and rigid bond restraints. A B-level alert is present in the CheckCIF report due to two H-atoms of the disordered carbenes in close contact.

4: The bound Et_2O and several $–CF_3$ groups in the $[BAr^F{}_4]^-$ anion were modelled as disordered over two positions and the disordered atoms were refined with appropriate distance and angle restraints and rigid bond restraints. A B-level alert is present in the CheckCIF report due to the elongated ellipsoids of the CF_3 group.

5: Several $–CF_3$ groups in the $[BAr^F{}_4]^-$ anion were modelled as disordered over two positions and the disordered atoms were refined with appropriate distance and angle restraints and rigid bond restraints. A B-level alert is present in the CheckCIF report the presence of a close-contact between H-atoms of the disordered pentane and the tBuNC ligand; this is due to inaccurate H-atoms positions on the disordered pentane molecule.

G. References

(1) Hagen, W. R. EPR spectroscopy as a probe of metal centres in biological systems. *Dalton Trans*. 4415 (2006).

(2) Surerus, K. K., Münck, E., Moura, I., Moura, J. J. G. & LeGall, J. Evidence for the Formation of a $ZnFe_3S_4$ Cluster in Desulfovibrio gigas Ferredoxin II. *J. Am. Chem. Soc*. **109,** 3805–3807 (1987).

(3) Srivastava, K. K. P., Surerus, K. K. & Conover, R. C. Moessbauer study of zinc-iron-sulfur $ZnFe_3S_4$ and nickel-iron-sulfur $NiFe_3S_4$ clusters in Pyrococcus furiosus ferredoxin. *Inorg. Chem*. **32,** 927–936 (1993).

Chapter 3. Evidence for Low-valent Electronic Configurations in Iron–Sulfur Clusters

Introduction

First characterized over sixty years ago as electron-transfer mediators,[1,2] Fe–S cluster proteins are now known to perform a wide range of functions.[3,4] Their diverse reactivity includes carrying out some of the most kinetically challenging multi-electron redox reactions in the biosphere,[4–6] and such reactivity is enabled by the unique chemical properties of their Fe–S cofactors. Despite their prominence in redox biochemistry and the redox versatility of Fe more generally,[7–10] biological Fe–S clusters are thought to feature only Fe^{2+} and Fe^{3+} ions (and mixed-valent pairs with average oxidation states of $Fe^{2.5+}$).[4,5,11] And although the $[2Fe]_H$ subcluster in the [FeFe]-hydrogenase features low-valent Fe in several intermediates,[12] no biological Fe–S cluster has been reduced beyond the all-Fe^{2+} state (Figure 3.1A). In the realm of synthetic chemistry, $[Fe_4S_4(NO)_4]$ clusters[13] were initially assumed to feature Fe^{1+} centers;[14,15] however, the $\{Fe–NO\}^7$ centers[16] in these and related clusters were later shown[17] to be better described as Fe^{3+} centers bound to $^3[NO]^-$ ligands (these findings are recapitulated in broken-symmetry density functional theory (BS-DFT) calculations reported in the SI, page S32). Additionally, a few super-reduced synthetic Fe–S clusters/complexes have been reported, including an $(Fe^{1+})_2(\mu\text{-S})$ complex,[18] an $Fe_2(\mu\text{-S})$ complex in two charge states featuring low-valent Fe ($Fe^{1+}Fe^{2+}$ and $2Fe^{1+}$),[19] and a planar $[Fe_4S_3]$ cluster in two charge states featuring Fe^{1+}.[20] In each example, the state with low-valent Fe was generated by reduction past the all-ferrous state. However, such redox couples (*e.g.*, $[Fe_4S_4]^{0/1-}$) are not thought to be accessible for biological Fe–S clusters.

That biological Fe–S clusters do not access Fe^{1+} valences limits the d-electron count of their individual sites to six or fewer, which in turn imposes significant limitations on their coordination chemistry. This is illustrated by considering binding and activation of the

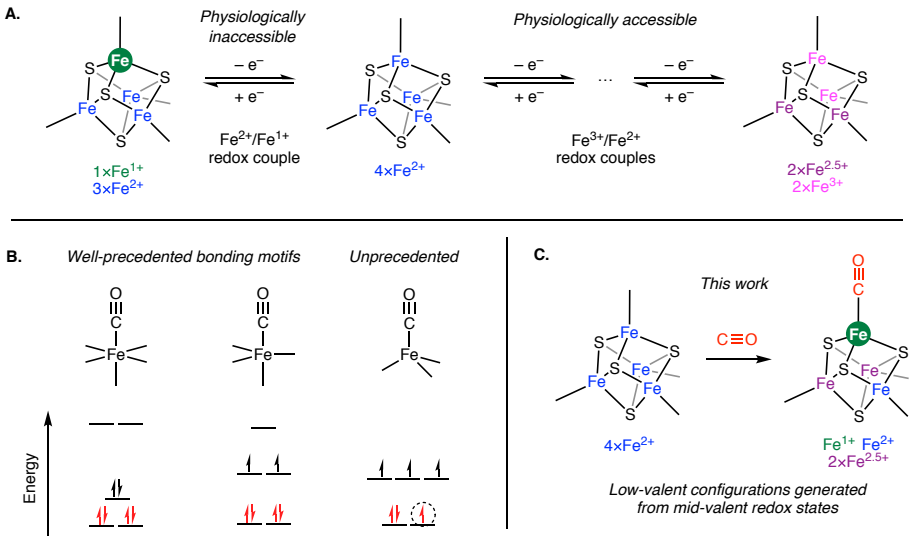

Figure 3.1. Inability of biological Fe–S clusters to access low-valent states and its consequences for small molecule activation. (A) $[Fe_4S_4]$ clusters as a case study: redox chemistry at Fe–S clusters occurs on $Fe^{3+/2+}$ redox couples with $Fe^{2+/1+}$ couples being physiologically inaccessible. (B) Basis for weak CO binding and activation at high-spin Fe^{2+} centers: incomplete occupation of π-backbonding orbitals (circled). Red electrons indicate electrons involved in π-backbonding interactions. (C) This work demonstrates that Fe–S clusters formally comprised of Fe^{2+} and/or Fe^{3+} centers can access low-valent Fe through redox disproportionation, thereby attaining electronic configurations that allow for strong bond activation while avoiding $Fe^{2+/1+}$ redox couples.

archetypal π-acidic ligand, CO, at Fe^{2+} ions in varying coordination geometries (Figure 3.1B). Low-spin, octahedral Fe^{2+}–CO complexes are common and famous for their stability, and trigonal bipyramidal, intermediate-spin Fe^{2+}–CO complexes have also been reported.[21–26] In contrast, CO adducts of high-spin, octahedral Fe^{2+} are much rarer,[27] and CO binding only occurs at low temperature with no C–O bond activation. These differences in CO activation and binding strength can be rationalized by the occupation of the two Fe–CO π-backbonding orbitals; both low-spin octahedral and intermediate-spin trigonal bipyramidal geometries allow full occupation of the π-backbonding orbitals, whereas a high-spin configuration results in incomplete occupation of these orbitals, leading to diminished CO binding affinity and activation. Consistent with this logic, no tetrahedral CO adduct of Fe^{2+} has been isolated; such a complex would be high-spin with partially unoccupied π-backbonding orbitals, and would therefore have an extremely low affinity for CO.

Given these observations from mononuclear Fe chemistry, it is perhaps surprising that Fe–S clusters featuring high-spin, mid-valent Fe centers (Fe^{2+} and Fe^{3+}) have emerged as promising catalysts for reducing CO and other π-acidic ligands. For example, nitrogenases reductively couple CO to hydrocarbons,[28–31] and this Fischer-Tropsch-type chemistry has been further demonstrated for a wide range of Fe–S clusters both bound to and isolated from protein hosts.[32–38] The unusual ability of Fe–S clusters to activate CO stands in contrast to the predicted inability of analogous high-spin, mid-valent mononuclear Fe complexes to bind CO, let alone to engender strong C–O bond activation. This fundamental disconnection prompted us to examine the geometric and electronic structures of CO-bound Fe–S clusters. Below, we detail unexpected links between Fe–S clusters and low-valent Fe chemistry, and we demonstrate that, in fact, Fe–S clusters can access low-valent configurations that give rise to exceptional C–O bond activation (Figure 3.1C).

Results

To study CO binding and activation at an Fe–S cluster, we utilized synthetic [Fe_4S_4] clusters in which three Fe centers are each supported by the sterically protective *N*-heterocyclic carbene (NHC) ligand, IMes (1,3-dimesitylimidazol-2-ylidene); this arrangement leaves the remaining Fe site available for substrate binding.[39] Our approach to preparing CO-bound clusters was to abstract Cl• or Cl^- from $(IMes)_3Fe_4S_4Cl$ (**1-Cl**) in the presence of CO. We expected to observe the formation of polycarbonylated clusters featuring low-spin Fe sites[40,41] and/or bridging CO structures,[42–44] and we predicted that the simplest structures—those featuring a single CO bound to the unique, tetrahedral Fe site—would be thermodynamically unfavorable for the reason articulated above: $[Fe_4S_4]^{+/0}$ clusters composed of tetrahedral Fe^{2+} and Fe^{3+} sites should have very weak affinity for CO.

To our surprise, the terminal, monocarbonylated adducts are in fact the products of these reactions. Specifically, reduction of **1-Cl** via Cl• abstraction using $Ti(N[^tBu]Ar)_3$ (Ar = 3,5-dimethylphenyl)[45] in the presence of CO generates the $(IMes)_3Fe_4S_4CO$ (**1-CO**) in 78% yield with loss of $ClTi(N[^tBu]Ar)_3$ (Fig. 3.2A). Cluster **1-CO** has an $S = 2$ ground state as established by EPR spectroscopy[46] and SQUID magnetometry (Fig. S3.7 and S3.22). The cyclic voltammogram of **1-CO** shows a reversible oxidation event at –1.54 V vs. Fc/Fc^+ corresponding to the $[Fe_4S_4]^{0/1+}$ couple and an irreversible oxidation at ca. –0.5 V corresponding to oxidation of $[(IMes)_3Fe_4S_4CO]^+$ ($[\mathbf{1\text{-}CO}]^+$) (Fig. S3.23 and S3.24). The $[Fe_4S_4]^{0/1+}$ couple is ca. 400 mV more positive than other reported $[Fe_4S_4]^{0/+}$ redox couples[47–49] owing to the cluster's strongly π-accepting CO ligand. The one-electron oxidized cluster, [**1-CO**]$^+$, was prepared by reacting CO with $[(IMes)_3[Fe_4S_4(OEt_2)][BArF_4]$ (generated by Cl^- abstraction from **1-Cl**; $[BArF_4]^-$ = tetrakis[3,5-bis(trifluoromethyl)phenyl]borate).[39] The EPR spectrum of [**1-CO**]$^+$ features a rhombic signal (**g** = [2.116, 1.944, 1.912]) and establishes an $S = 1/2$ ground spin state for the cluster (Fig. S3.8). Both CO complexes were fully characterized

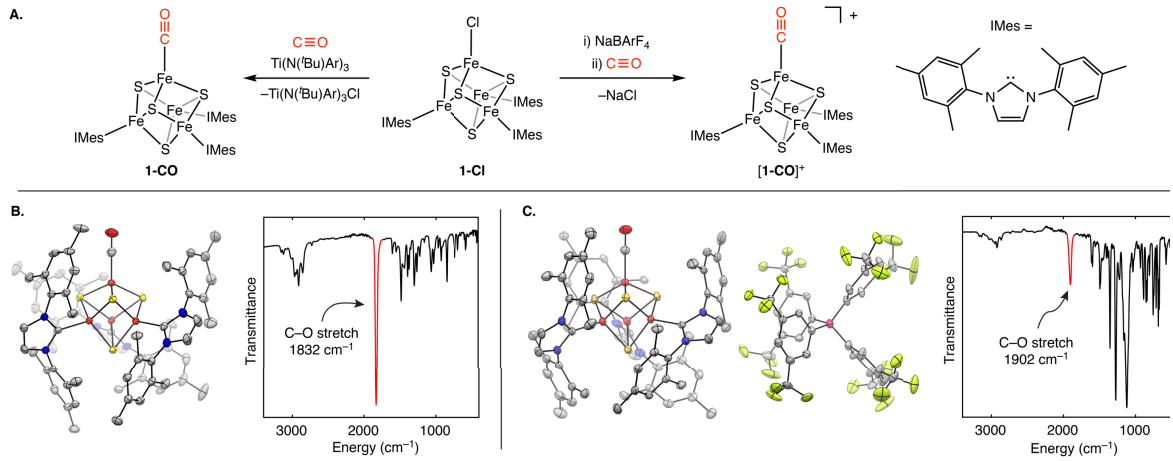

Figure 3.2. Synthesis and characterization of CO-bound $[Fe_4S_4]$ clusters. (A) Synthesis of **1-CO** and **[1-CO]**$^+$. Ar = 3,5-dimethylphenyl; Ar^F = 3,5-bis(trifluoromethyl)phenyl. Structural and infrared spectroscopic characterization of (B) **1-CO** and (C) **[1-CO]**$^+$. Thermal ellipsoid plots shown at 50% probability with carbon (gray), iron (orange), sulfur (yellow), nitrogen (blue), oxygen (red), boron (pink) and fluorine (green). Solvent molecules and H-atoms are omitted for clarity. The C–O stretches in the IR spectra are highlighted in red.

and their structures were confirmed by single-crystal X-ray diffraction (Fig. 3.2B and 3.2C); we discuss their structural and spectroscopic properties in greater detail below.

A striking property of **1-CO** and **[1-CO]**$^+$ is the extent to which their CO ligands are activated. Indeed, their C–O stretching frequencies of 1832 cm^{-1} and 1902 cm^{-1}, respectively, are comparable to those of mononuclear Fe^{1+}–CO complexes, (ν(C–O) = 1850–1907 cm^{-1})[24,25,50] and intermediate spin Fe^{2+}–CO complexes (ν(C–O) = 1899–1966 cm^{-1}).[21–26] Such remarkable degrees of C–O activation for **1-CO** and **[1-CO]**$^+$ are inconsistent with what would be expected for a high-spin Fe^{2+}–CO center, for which ν(C–O) would likely be > 2100 cm^{-1}.[27]

The high degree of C–O activation in **1-CO** and **[1-CO]**$^+$ necessitates reevaluation of our initial assumptions about their electronic structures, namely that the tetrahedral Fe centers in these clusters are each high-spin, d^6 Fe^{2+} or d^5 Fe^{3+}. There are two scenarios that would enable full occupation of the Fe–CO π-backbonding orbitals, and thereby account for the observed strong C–O activation: either the Fe–CO site could maintain an Fe^{2+} valence and adopt a low- or intermediate-spin electronic configuration, or it could adopt a low-valent configuration. Although computational analysis can provide insights into the local spin state of

the Fe–CO site (*vide infra*), this information is difficult to extract experimentally. Nevertheless, we disfavor the first hypothesis in part because the Fe–CO sites in **1-CO** and [**1-CO**]$^+$ display nearly perfect tetrahedral geometries (τ_4 = 0.92 in both **1-CO** and [**1-CO**]$^+$, where τ_4 is a parameterization of four-coordinate geometries that takes on a value of 1 for a perfect tetrahedron)[51] imposed by the cuboidal structure of the cluster. In contrast, four-coordinate intermediate-spin Fe^{2+} complexes exhibit a significant distortion from tetrahedral symmetry due to the Jahn-Teller effect.[52–54] We therefore designed experiments to test the alternative hypothesis that the Fe–CO sites adopt low-valent configurations.

Mössbauer spectroscopy is widely used to determine the valences of Fe sites in Fe–S clusters.[55,56] In particular, the isomer shift reflects both the formal Fe valence and the covalency of Fe–ligand bonding, where a higher isomer shift corresponds to a lower valence and decreased Fe–ligand covalency. These trends move in concert for typical Fe–S clusters (*i.e.*, those ligated by π-donor ligands such as thiolates), but they counteract one another for Fe sites featuring strong π-acceptors such as CO.[57] For the latter, a lower valence would engender stronger Fe–CO covalency via π-backbonding, and these two effects would impact the isomer shift in opposing directions. For this reason, the valences of the Fe–CO sites in **1-CO** and [**1-CO**]$^+$ cannot be directly inferred from their isomer shifts. We therefore analyzed the valences of the three NHC-ligated sites in **1-CO** and [**1-CO**]$^+$, and used this information to deduce the valences of the CO-ligated Fe sites.

Determination of the valences of the NHC-ligated sites in **1-CO** and [**1-CO**]$^+$ requires suitable reference molecules for which the valences are uncontroversial. For these purposes, we examined the Mössbauer spectroscopic properties of the homoleptic, NHC-ligated clusters, $[I^iPr^{Me}{}_4Fe_4S_4]^{0/+}$ (**2** and [**2**]$^+$; I^iPr^{Me} = 1,3-diisopropyl-4,5-dimethylimidazol-2-ylidene),[39,49] which have the same $[Fe_4S_4]$ core electron count as **1-CO** and [**1-CO**]$^+$, respectively. The Mössbauer spectrum of **2** in Fig. 3.3A is consistent with previous reports[49,58] and features a 3:1

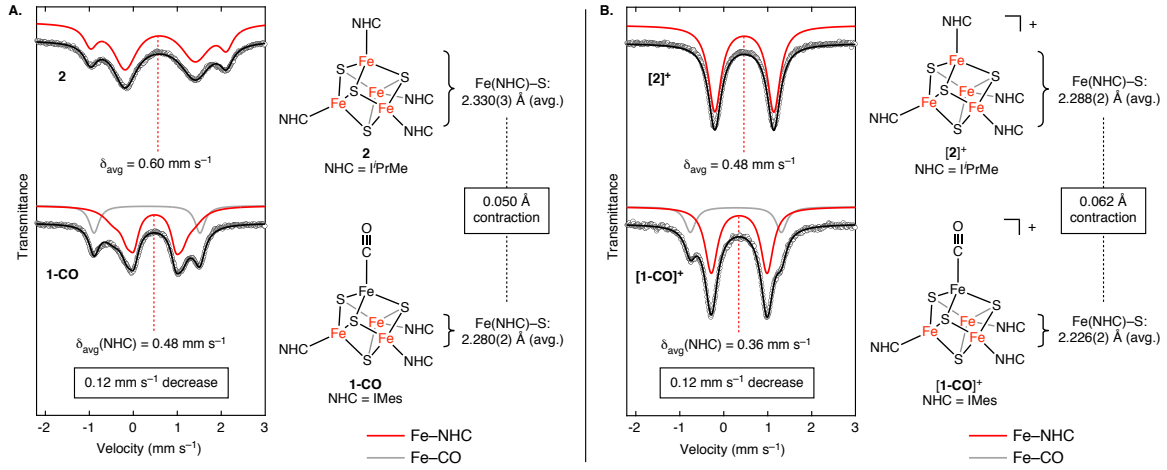

Figure 3.3. Spectroscopic and structural evidence for low-valent Fe configurations in $[Fe_4S_4]$–CO complexes. (A) 80 K Mössbauer spectra of **2** (top left) and **1-CO** (bottom left) and contraction of (NHC)Fe–S distances upon CO binding (right). (B) 80 K Mössbauer spectra of $[\mathbf{2}]^+$ (top left) and $[\mathbf{1\text{-}CO}]^+$ (bottom left) and contraction of (NHC)Fe–S distances upon CO binding (right). Red and gray lines show simulated parameters for the NHC- and CO-ligated Fe centers, respectively. The total simulations are shown in black. See Table 3.1 for tabulated parameters.

pattern of peaks representing the three coaligned Fe^{2+} centers and the one antiferromagnetically coupled Fe^{2+} center, respectively. The Mössbauer spectrum of $[\mathbf{2}]^+$ has not been previously described; it displays a single quadrupole doublet (δ = 0.48 mm s^{-1} and $|\Delta E_Q|$ = 1.34 mm s^{-1}; Fig. 3.3 and Table 3.1) indicating complete valence averaging for $[\mathbf{2}]^+$ on the Mössbauer timescale. The average isomer shifts (δ_{avg}) of the Fe centers in **2** and $[\mathbf{2}]^+$ are 0.60 and 0.48 mm s^{-1}, respectively (80 K, Fig. 3.3), and the magnitude of the decrease in δ_{avg} upon oxidation (0.12

Table 3.1. Mössbauer and structural parameters for **1-CO**, **2**, $[\mathbf{1\text{-}CO}]^+$, and $[\mathbf{2}]^+$.[a]

	Mössbauer parameters				Structural parameters			
	NHC-bound Fe (avg.)		CO-bound Fe		NHC-bound Fe (avg.)		CO-bound Fe (avg.)	
	δ (mm s^{-1})	$\lvert\Delta E_Q\rvert$ (mm s^{-1})	Δ (mm s^{-1})	$\lvert\Delta E_Q\rvert$ (mm s^{-1})	Fe–S (Å)	Fe–C (Å)	Fe–S (Å)	Fe–C (Å)
1-CO	0.48	1.34	0.32	2.408	2.280(2)	2.053(2)	2.259(1)	1.772(2)
2	0.60	1.97	—	—	2.330(3)	2.109(5)	–	–
$[\mathbf{1\text{-}CO}]^+$	0.36	1.27	0.28	2.069	2.226(2)	2.029(2)	2.199(1)	1.789(2)
$[\mathbf{2}]^+$	0.48	1.34	—	—	2.288(2)	2.060(5)	–	–

[a]: The uncertainty in the average of Fe–S and Fe–C bond lengths is given as the root sum of the squares of the individual estimated standard deviations.

mm s^{-1} for a 0.25 electron oxidation per Fe site) is similar to what has been observed in other Fe–S clusters.[55] The δ_{avg} for [**2**]$^+$ is similar to that of previously reported $[Fe_4S_4]^+$ clusters supported by IMes ligands (~0.5 mm s^{-1}; Fig. S3.19-S3.22 and Table S3.3), indicating that δ_{avg} for NHC-ligated $[Fe_4S_4]^+$ typically fall within a narrow range regardless of the identity of the NHC or the pattern of site-differentiation. Note that we and others[55] prefer to extrapolate valences using δ_{avg} because (i) δ_{avg} does not depend on the model used to fit spectra comprised of multiple overlapping quadrupole doublets, and (ii) it cancels out differences in δ for individual sites that have the same valence but are magnetically and/or structurally inequivalent (*e.g.*, for the two classes of Fe sites in **2**)[58].

In the Mössbauer spectra of **1-CO** and [**1-CO**]$^+$ (Fig. 3.3 and Table 3.1), the quadrupole doublets corresponding to the Fe–CO sites can be identified by their large quadrupole splittings (2.408 mm s^{-1} and 2.069 mm s^{-1}, respectively) and, for **1-CO**, by the modest temperature dependence of the simulated parameters for the Fe–CO site (in contrast to those of the Fe–NHC sites, which begin to converge at high temperatures; see SI page S10). The low isomer shifts for the Fe–CO sites (0.32 mm s^{-1} in **1-CO** and 0.28 mm s^{-1} in [**1-CO**]$^+$) are similar to those observed for low-valent Fe–CO complexes[24,25] and reflect high Fe–CO covalency as a result of π-backbonding with CO. The large quadrupole splitting is likewise consistent with significant Fe–CO π-backbonding, which increases the anisotropy of the local electric field gradient. The remaining Mössbauer signals arise from the NHC-ligated sites and can be modeled as three quadrupole doublets for **1-CO** (see SI section F) and a single quadrupole doublet for [**1-CO**]$^+$; similarly to [**2**]$^+$, the latter exhibits full valence delocalization amongst its NHC-ligated sites on the timescale of the Mössbauer experiment. For both **1-CO** and [**1-CO**]$^+$, the δ_{avg} values for the NHC-ligated sites—0.48 mm s^{-1} and 0.36 mm s^{-1}, respectively—are 0.12 mm s^{-1} lower than those in their homoleptic congeners, which suggests that the NHC sites in **1-CO** and [**1-CO**]$^+$ are significantly more oxidized than the NHC sites in **2** and [**2**]$^+$. As

Table 3.2. Charge states of the Fe centers in **1-CO**, **2**, [**1-CO**]$^+$, and [**2**]$^+$ as deduced from Mössbauer spectroscopic analysis.

	Cluster charge	NHC-bound Fe	CO-bound Fe
1-CO	$[Fe_4S_4]^0$	3 x $Fe^{2.25+}$	1 x $Fe^{1.25+}$
2		4 x Fe^{2+}	—
[**1-CO**]$^+$	$[Fe_4S_4]^{1+}$	3 x $Fe^{2.5+}$	1 x $Fe^{1.5+}$
[**2**]$^+$		4 x $Fe^{2.25+}$	—

deduced from the Mössbauer spectra of **2** and [**2**]$^+$ (*vide supra)*, the magnitude of this change in the average isomer shift—0.12 mm s^{-1}—corresponds to an oxidation of 0.25 electrons per Fe center, and the average valence of the NHC-ligated Fe sites in **1-CO** and [**1-CO**]$^+$ are therefore estimated to be $Fe^{2.25+}$ and $Fe^{2.5+}$, respectively (compared with Fe^{2+} and $Fe^{2.25+}$ for **2** and [**2**]$^+$, respectively, Table 3.2). In aggregate, the three NHC-ligated sites in **1-CO** and [**1-CO**]$^+$ are 0.75 electrons more oxidized than the analogous Fe–NHC sites in **2** and [**2**]$^+$, respectively, leaving the Fe–CO site in each cluster 0.75 electrons more reduced. Thus, based on this analysis, the experimentally deduced Fe–CO valences in **1-CO** and [**1-CO**]$^+$ are $Fe^{1.25+}$ and $Fe^{1.5+}$, respectively (Table 3.2).

The structural parameters of **1-CO** and [**1-CO**]$^+$ are also consistent with intramolecular charge transfer from the Fe–NHC sites to the Fe–CO sites (Fig. 3.3 and Table 3.1). The NHC-bound Fe sites in **1-CO** and [**1-CO**]$^+$ display shorter average Fe–S distances (by ~0.05 Å) and Fe–C(NHC) distances (by 0.06 Å for the neutral clusters and 0.031 Å for the cationic clusters) relative to those in **2** and [**2**]$^+$. Both trends are reflect enhanced donation from the sulfide and NHC ligands to the NHC-bound Fe sites in **1-CO** and [**1-CO**]$^+$, and are thereby consistent with the conclusions from the Mössbauer spectroscopic analysis: the NHC-bound Fe sites are more oxidized in the CO complexes than in the homoleptic, NHC-bound clusters. Note that shortened Fe–S bonds were also observed in a recent computational model of a CO-bound nitrogenase intermediate featuring a four-coordinate Fe–CO site.[59]

The experimental picture described above—massive C–O bond activation and charge depletion at the NHC-bound sites—is consistent with substantial charge redistribution among the Fe–NHC and Fe–CO sites, resulting in electronic configurations featuring low-valent, CO-bound Fe centers. We further evaluated the electronic structures of these clusters using BS-DFT (TPSS and TPSSh functionals and def2-TZVP basis sets), analyzed the BS-DFT solutions in terms of localized molecular orbitals, and demonstrated that the experimental Mössbauer parameters are reproduced *in silico* (see SI). As expected, the computed localized orbitals of **2** and [**2**]$^{+}$ are consistent with the canonical electronic structures of $[Fe_4S_4]^0$ and $[Fe_4S_4]^+$ clusters (featuring $4\times Fe^{2+}$ centers for **2** and $2\times Fe^{2+}$ and $2\times Fe^{2.5+}$ centers for [**2**]$^{+}$). In contrast, the localized orbital calculations and Löwdin population analyses of **1-CO** indicate that it adopts an unprecedented electronic structure for $[Fe_4S_4]^0$ clusters; rather than featuring $4\times Fe^{2+}$ ions, the Fe valences in **1-CO** consist of $1\times Fe^{1+}$–CO, $1\times Fe^{2+}$, and $2\times Fe^{2.5+}$ (Fig. 3.4A). The occupied valence orbitals on the CO-bound Fe include five β-spin and two α-spin orbitals with primarily Fe 3d character, four of which have symmetry that allows for π-backbonding with CO. Importantly, the oxidized counterpart to the one-electron-reduced Fe–CO site was identified as a mixed-valent pair of $2\times Fe^{2.5+}$ ions in which the hole is delocalized over two Fe centers via the double-exchange mechanism (Fig. 3.4A).[60] In addition, the Fe^{2+} site adopts a local $S = 1$ configuration; such non-Hund configurations have been observed in BS-DFT calculations of other Fe–S clusters.[61,62]

The BS-DFT calculations on [**1–CO**]$^{+}$ are complicated by a dependence of the calculated electronic structure on the functional (SI). Calculations using the TPSS functional arrive at an electronic structure in which the two π-backbonding orbitals on the Fe–CO site are fully occupied and localized on the Fe–CO site, and one of the unpaired electrons on this site is delocalized onto a spin-aligned NHC-ligated Fe center (Fig. 3.4B). Calculations using the

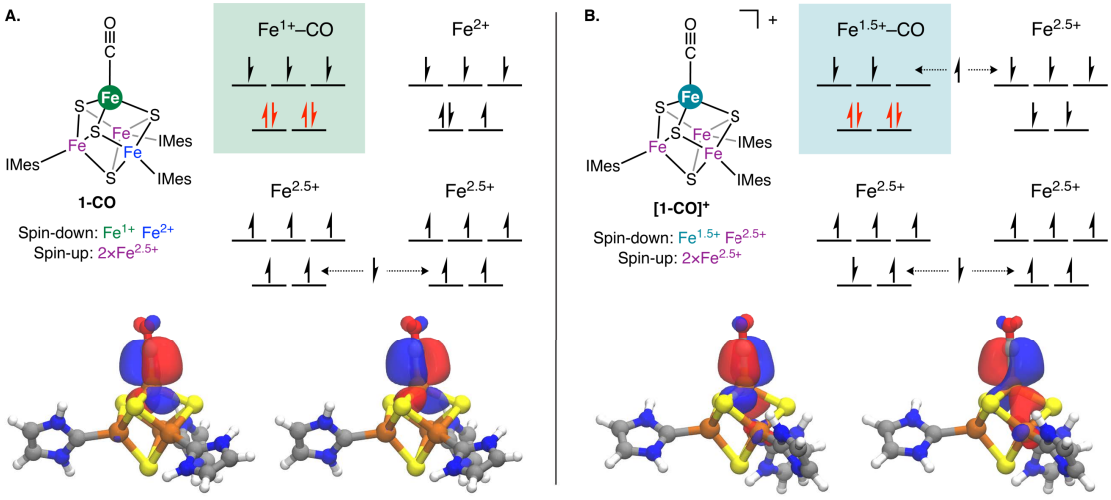

Figure 3.4. Qualitative calculated molecular orbital diagrams for **1-CO** (A) and [**1-CO**]$^+$ (B) showing the fully populated Fe–CO π-backbonding orbitals (highlighted in red). The isosurface plots (bottom, 0.04 au) show the localized π-backbonding orbitals in the α-spin manifold. See SI for computational details.

TPSSh functional converge to an electronic structure more similar to that of **1-CO**, except one of the α-spin electrons involved in Fe–CO π-backbonding is further delocalized between the Fe–CO and the spin-aligned Fe–NHC center (Fig. S3.27). We favor the electronic structure obtained using the TPSS functional because the $[Fe_4S_4]^+$ core of an optimized structure displays pseudo-C_{3v} symmetry akin to that observed in the X-ray crystal structure of [**1-CO**]$^+$ (SI page S27). Regardless of the functional chosen, a Löwdin population analysis of the Fe-centered orbitals in [**1-CO**]$^+$ leads to approximate valence assignments as follows: $Fe^{1.5+}$ for the Fe–CO, $Fe^{2.5+}$ for the spin-aligned Fe–NHC site, and $2\times Fe^{2.5+}$ for the remaining NHC ligated sites (SI page S25). The computed valence for the Fe–CO site in [**1-CO**]$^+$ is higher than that in **1-CO**, which is consistent with its weaker extent of C–O bond activation ($\Delta\nu$(C–O) = 70 cm^{-1}) as well as its shorter Fe–S and longer Fe–CO bond lengths (Table 3.1).

Discussion

The experimental and computational analysis presented above demonstrates that Fe–S clusters can achieve low-valent electronic configurations at individual Fe sites, allowing for substantial activation of π-accepting substrates such as CO. Such configurations are generated by an intracluster electron transfer process that is conceptually related to valence rearrangements observed in other metalloclusters[12,26,63–66] in which the existing metal ion valences are shuffled between cluster sites. However, the processes observed for **1-CO** and [**1-CO**]$^{+}$ are distinct in that CO binding induces generation of valences that were not initially present in the cluster. To illustrate, consider the valence distributions possible for $[Fe_4S_4]^0$ clusters (the core charge state in **1-CO**): in the canonical, all-ferrous electronic structure, no valence rearrangement can occur because each Fe has the same valence (Fe^{2+}). Instead, the results presented herein show that CO binding induces valence disproportionation, which entails electron transfer from an NHC-ligated Fe center to the Fe–CO center, splitting two Fe^{2+} valences to generate Fe^{1+}–CO and an Fe^{3+} center (the latter is additionally stabilized by generation of a mixed-valent 2×$Fe^{2.5+}$–NHC pair). Low-valent configurations are likewise accessed in [**1-CO**]$^{+}$ by partial disproportionation of 2×Fe^{2+} centers to give a configuration with substantial Fe^{1+}/Fe^{3+} character. In both cases, the formal oxidation of NHC-bound Fe sites is accompanied by substantial Fe–S bond contraction, indicating a role for the entire cluster in promoting C–O bond weaking.[67,68]

The ability to undergo valence disproportionation allows for the generation of low-valent configurations without necessitating super-reduction of an Fe^{2+} site in an all-ferrous cluster to Fe^{1+}. For $[Fe_4S_4]$ clusters in particular, such super-reduced states (*i.e.*, $[Fe_4S_4]^{1-}$) have not been characterized and would presumably only be generated at extremely low potentials. However, two related questions remain regarding the biological relevance of the low-valent states characterized in this work: (1) Do the synthetic clusters reported herein have access to

low-valent configurations only because they are supported by NHC ligands (as opposed to more biorelevant donors such as thiolates); and (2) Would the redox states at which we observe low-valent configurations be accessible at physiologically relevant potentials?

To address the first question, we compare the redox properties of **2** ($[Fe_4S_4]^0$) and $[\mathbf{2}]^+$ ($[Fe_4S_4]^+$) with those of synthetic, thiolate-ligated $[Fe_4S_4]$ clusters. The $[Fe_4S_4]^+$ state in $[Fe_4S_4(SPh)_4]^{3-}$ is stable between –2.13 and –1.40 V (vs. Fc/Fc^+, in MeCN),[47] whereas the analogous state in $[\mathbf{2}]^+$ is stable in a positively shifted window: between –1.91 V and –0.75 V (vs. Fc/Fc^+, in *o*-DFB). This illustrates that NHC-ligated clusters are less reducing than their thiolate-ligated analogues,[49] and we therefore conclude that the intramolecular electron transfer process that generates low-valent Fe in **1–CO** and $[\mathbf{1–CO}]^+$ is not a result of the NHC ligands rendering the cluster especially reducing. For this reason, we expect that if **1–CO** and $[\mathbf{1–CO}]^+$ were supported by three thiolate ligands instead of three IMes ligands, we would similarly observe low-valent electronic configurations for the CO-bound site; computational analysis of the hypothetical cluster $[(SCH_3)_3Fe_4S_4(CO)]^{3-}$ supports this conclusion (SI page S30).

To address the second question, we first note that the redox state of $[\mathbf{1–CO}]^+$ ($[Fe_4S_4]^+$) is commonly observed in biology,[4,6] and, although rarer, that of **1–CO** ($[Fe_4S_4]^0$) has also been characterized in Fe–S proteins.[69–72] However, direct comparisons between the potentials at which these states are generated in biological systems and synthetic systems cannot be made because of the different conditions in which the potentials were measured; for example, for thiolate-ligated clusters it is well-established[73,74] that the redox potentials of biological $[Fe_4S_4]$ clusters are positively shifted relative to those of synthetic $[Fe_4S_4]$ clusters. Nevertheless, we can address the question at hand by considering how CO binding would affect the redox couples of Fe–S clusters. Because of the strong π-acidity of CO, we would expect a positive shift upon substituting an NHC or thiolate for CO. This is observed experimentally for the molecules described herein; for $[\mathbf{1\text{-}CO}]^+$, the $[Fe_4S_4]^{1+}$ state is stable between –1.54 and –0.50

V, compared with –1.91 to –0.75 V for [**2**]$^{+}$ (both vs. Fc/Fc^{+} under identical conditions; see SI). Likewise, CO binding to a thiolate-ligated, biological [Fe_4S_4] cluster would shift the cluster's redox couples positively, and therefore the redox states at which we observe low-valent Fe ([Fe_4S_4]^{0} and [Fe_4S_4]$^{+}$) would remain accessible using biological reductants. On this basis, we surmise that low-valent Fe centers can be generated in Fe–S clusters at physiologically accessible redox potentials.

Conclusion

In conclusion, we have shown that Fe–S clusters, even when comprised of exclusively Fe^{2+} and Fe^{3+} ions, can undergo intramolecular valence disproportionation to access low-valent electronic configurations. This expands the range of characterized electronic configurations for formally mid-valent Fe–S clusters and connects the chemistry of Fe–S clusters to that of low-valent Fe. Moreover, these low-valent configurations enable substantial substrate bond activation without having to proceed through highly negative redox couples; this design principle can be further exploited in catalysis and may account for Nature's utilization of Fe–S clusters for activating some of the strongest bonds in the biosphere.

References

(1) Beinert, H.; Sands, R. H. Studies on succinic and DNPH dehydrogenase preparations by Paramagnetic Resonance (EPR) Spectroscopy. *Biochem. Biophys. Res. Commun.* **1960**, *3* (1), 41–46.

(2) Orme-Johnson, W. H. Iron-sulfur proteins: Structure and function. *Annu. Rev. Biochem.* **1973**, *42*, 159–204.

(3) Flint, D. H.; Allen, R. M. Iron-sulfur proteins with nonredox functions. *Chem. Rev.* **1996**, *96* (7), 2315–2334.

(4) Beinert, H.; Holm, R. H.; Münck; Eckard. Iron-sulfur clusters: Nature's modular, multipurpose structures. *Science* **1997**, *277* (5326), 653–659.

(5) Hagen, W. R. EPR spectroscopy of iron–sulfur proteins. *Adv. Inorg. Chem.* **1992**, *38*, 165–222.

(6) Beinert, H. Iron-sulfur proteins: Ancient structures, still full of surprises. *J. Biol. Inorg. Chem.* **2000**, *5* (1), 2–15.

(7) Beck, B. W. Highly-reduced metal carbonyls. **1991**, *30* (2), 168–169.

(8) Sharma, V. K. Ferrate(VI) and Ferrate(V) oxidation of organic compounds: Kinetics and mechanism. *Coord. Chem. Rev.* **2013**, *257* (2), 495–510.

(9) Berry, J. F.; Bill, E.; Bothe, E.; DeBeer George, S.; Meinert, B.; Neese, F.; Wieghardt, K. An octahedral coordination complex of iron(VI). *Science* **2006**, *312* (5782), 1937–

1941.
(10) Martinez, J. L.; Lutz, S. A.; Yang, H.; Xie, J.; Telser, J.; Hoffman, B. M.; Carta, V.; Pink, M.; Losovyj, Y.; Smith, J. M. Structural and spectroscopic characterization of an Fe(VI) bis(imido) complex. *Science* **2020**, 370, 356–359.
(11) Hagen, W. R. EPR spectroscopy of complex biological iron–sulfur systems. *J. Biol. Inorg. Chem.* **2018**, *23* (4), 623–634.
(12) Land, H.; Senger, M.; Berggren, G.; Stripp, S. T. Current State of [FeFe]-Hydrogenase Research: Biodiversity and Spectroscopic Investigations. *ACS Catal.* **2020**, *10* (13), 7069–7086.
(13) Gall, R. S., Chu, C. T. W. and Dahl, L. F. Preparation, structure, and bonding of two cubane-like iron-nitrosyl complexes, $Fe_4(NO)_4(\mu_3\text{-}S)_4$ and $Fe_4(NO)_4(\mu_3\text{-}S_2)(\mu_3\text{-}NC(CH_3)_3)_2$: Stereochemical consequences of bridging ligand substitution on a completely bonding tetrametal cluster unit and of different terminal ligands on the cubane-like Fe_4S_4 core. *J. Am. Chem. Soc.* **1974**, *96* (12), 4019–4023.
(14) Chu, C. T. W. Yip-Kwai Lo, F. and Dahl, L. F. Synthesis and stereochemical analysis of the $[Fe_4(NO)_4(\mu_3\text{-}S)_4]^n$ Series (n = 0,−1) which possesses a cubanelike Fe_4S_4 core: direct evidence for the antibonding tetrametal character of the unpaired electron upon a one-electron reduction of a completely bonding tetrahedral metal cluster. *J. Am. Chem. Soc.* **1982**, *104* (12), 3409–3422.
(15) Goh, C. and Holm, R. H. Synthesis and structures of the cuboidal iron-sulfur-nitrosyl-phosphine clusters $[Fe_4S_3(NO)_4(PR_3)_3]^{0,1+}$ (R = Et, Pr^i, C_6H_{11}). *Inorg. Chim. Acta* **1998**, *270* (4), 46–54.
(16) Enemark, J. H.; Feltham, R. D. Principles of Structure, Bonding, and Reactivity for Metal Nitrosyl Complexes. *Coord. Chem. Rev.* **1974**, *13* (4), 339–406.
(17) Hopmann, K. H., Ghosh, A. & Noodleman, L. Density functional theory calculations on Mössbauer parameters of nonheme iron nitrosyls. *Inorg. Chem.* **2009**, *48* (19), 9155–9165.
(18) Rodriguez, M. M.; Stubbert, B. D.; Scarborough, C. C.; Brennessel, W. W.; Bill, E.; Holland, P. L. Isolation and characterization of stable iron(I) sulfide complexes. *Angew. Chem. Int. Ed.* **2012**, *51* (33), 8247–8250.
(19) Anderson, J. S. and Peters, J. C. Low-spin pseudotetrahedral iron(I) sites in $Fe_2(\mu\text{-}S)$ complexes. *Angew. Chem. Int. Ed.* **2014**, *53* (23), 5978–5981.
(20) DeRosha, D. E.; Chilkuri, V. G.; Van Stappen, C.; Bill, E.; Mercado, B. Q.; DeBeer, S.; Neese, F.; Holland, P. L. Planar three-coordinate iron sulfide in a synthetic [4Fe-3S] cluster with biomimetic reactivity.*Nat. Chem.* **2019**, *11* (11), 1019–1025.
(21) Ray, M.; Golombek, A. P.; Hendrich, M. P.; Young, V. G.; Borovik, A. S. Synthesis and structure of a trigonal monopyramidal Fe(II) complex and its paramagnetic carbon monoxide derivative. *J. Am. Chem. Soc.* **1996**, *118* (25), 6084–6085.
(22) Nguyen, D. H.; Hsu, H. F.; Millar, M.; Koch, S. A.; Achim, C.; Bominaar, E. L.; Münck, E. Nickel(II) thiolate complex with carbon monoxide and its Fe(II) analog: Synthetic models for CO adducts of nickel-iron-containing enzymes.*J. Am. Chem. Soc.* **1996**, *118* (37), 8963–8964.
(23) Davies, S. C.; Durrant, M. C.; Hughes, D. L.; Richards, R. L.; Roger Sanders, J. Iron, cobalt and vanadium complexes of the $N(CH_2CH_2S)_3^{3-}$ ligand with chloride, azide, cyanide and carbonyl co-ligands. *J. Chem. Soc. Dalt. Trans.* **2000**, 24, 4694–4701.
(24) Lee, Y.; Peters, J. C. Silylation of iron-bound carbon monoxide affords a terminal Fe carbyne. *J. Am. Chem. Soc.* **2011**, *133* (12), 4438–4446.
(25) Rittle, J.; Peters, J. C. Fe-N_2/CO complexes that model a possible role for the interstitial C atom of FeMo-cofactor (FeMoco). *Proc. Natl. Acad. Sci. U.S.A.* **2013**, *110* (40), 15898–15903.

(26) Arnett, C. H.; Chalkley, M. J.; Agapie, T. A Thermodynamic model for redox-dependent binding of carbon monoxide at site-differentiated, high spin iron clusters. *J. Am. Chem. Soc.* **2018**, *140* (16), 5569–5578.
(27) Bloch, E. D.; Hudson, M. R.; Mason, J. A.; Chavan, S.; Crocellà, V.; Howe, J. D.; Lee, K.; Dzubak, A. L.; Queen, W. L.; Zadrozny, J. M.; Geier, S. J.; Lin, L. C.; Gagliardi, L.; Smit, B.; Neaton, J. B.; Bordiga, S.; Brown, C. M.; Long, J. R. Reversible CO binding enables tunable CO/H_2 and CO/N_2 separations in metal-organic frameworks with exposed divalent metal cations. *J. Am. Chem. Soc.* **2014**, *136* (30), 10752–10761.
(28) Lee, C. C.; Hu, Y.; Ribbe, M. W. Vanadium nitrogenase reduces CO. *Science* **2010**, *329* (5992), 642.
(29) Hu, Y.; Lee, C. C.; Ribbe, M. W. Extending the carbon chain: Hydrocarbon formation catalyzed by vanadium/molybdenum nitrogenases. *Science* **2011**, *333* (6043), 753–755.
(30) Yang, Z. Y.; Dean, D. R.; Seefeldt, L. C. Molybdenum nitrogenase catalyzes the reduction and coupling of CO to form hydrocarbons. *J. Biol. Chem.* **2011**, *286* (22), 19417–19421.
(31) Seefeldt, L. C.; Yang, Z. Y.; Lukoyanov, D. A.; Harris, D. F.; Dean, D. R.; Raugei, S.; Hoffman, B. M. Reduction of substrates by nitrogenases. *Chem. Rev.* **2020**, *120* (12), 5082–5106.
(32) Lee, C. C.; Hu, Y.; Ribbe, M. W. ATP-independent formation of hydrocarbons catalyzed by isolated nitrogenase cofactors. *Angew. Chem. Int. Ed.* **2012**, *51* (8), 1947–1949.
(33) Lee, C. C.; Hu, Y.; Ribbe, M. W. Catalytic reduction of CN^-, CO, and CO_2 by nitrogenase cofactors in lanthanide-driven reactions. *Angew. Chem. Int. Ed.* **2015**, *54* (4), 1219–1222.
(34) Lee, C. C.; Hu, Y.; Ribbe, M. W. Insights into hydrocarbon formation by nitrogenase cofactor homologs. *MBio* **2015**, *6* (2), 1–6.
(35) Tanifuji, K.; Lee, C. C.; Ohki, Y.; Tatsumi, K.; Hu, Y.; Ribbe, M. W. Combining a nitrogenase scaffold and a synthetic compound into an artificial enzyme. *Angew. Chem. Int. Ed.* **2015**, *54* (47), 14022–14025.
(36) Sickerman, N. S.; Tanifuji, K.; Lee, C. C.; Ohki, Y.; Tatsumi, K.; Ribbe, M. W.; Hu, Y. Reduction of C1 substrates to hydrocarbons by the homometallic precursor and synthetic mimic of the nitrogenase cofactor. *J. Am. Chem. Soc.* **2017**, *139* (2), 603–606.
(37) Stiebritz, M. T.; Hiller, C. J.; Sickerman, N. S.; Lee, C. C.; Tanifuji, K.; Ohki, Y.; Hu, Y. Ambient conversion of CO_2 to hydrocarbons by biogenic and synthetic $[Fe_4S_4]$ clusters. *Nat. Catal.* **2018**, *1* (6), 444–451.
(38) Lee, C. C.; Tanifuji, K.; Newcomb, M.; Liedtke, J.; Hu, Y.; Ribbe, M. W. A A comparative analysis of the CO-reducing activities of MoFe Proteins containing Mo- and V-Nitrogenase cofactors. *ChemBioChem* **2018**, *19* (7), 649–653.
(39) Brown, A. C.; Suess, D. L. M. Controlling Substrate Binding to Fe_4S_4 Clusters through Remote Steric Effects. *Inorg. Chem.* **2019**, *58* (8), 5273–5280.
(40) Han, J.; Coucouvanis, D. A A new function of the (μ_3-S) ligand in an Fe_4S_4 cluster: synthesis and structure of the high-nuclearity Mo/Fe/S Cluster, $Fe(DMF)Cl(Cl_4\text{-cat})_2\text{-}Mo_2Fe_2S_4(PEt_3)_2ClFe_4S_4(PEt_3)_3(CO)_6Cl$. *J. Am. Chem. Soc.* **2002**, *123* (45), 11304–11305.
(41) Ogino, H.; Inomata, S.; Tobita, H. Abiological iron−sulfur clusters. *Chem Rev.* **1998**, *98*, 2093–2121.
(42) Spatzal, T.; Perez, K. A.; Einsle, O.; Howard, J. B.; Rees, D. C. Ligand binding to the FeMo-cofactor: Structures of CO-bound and reactivated nitrogenase. *Science* **2014**,

345 (6204), 1620–1623.
(43) Rohde, M.; Grunau, K.; Einsle, O. CO binding to the FeV cofactor of CO-reducing vanadium nitrogenase at atomic resolution. *Angew. Chem. Int. Ed.* **2020**, *59* (52), 23626–23630.
(44) Buscagan, T. M.; Perez, K. A.; Maggiolo, A. O.; Rees, D. C.; Spatzal, T. Structural characterization of two CO molecules bound to the nitrogenase active site. *Angew. Chem. Int. Ed.* **2021**, *60* (11), 5704–5707
(45) Peters, J. C.; Johnson, A. R.; Odom, A. L.; Wanandi, P. W.; Davis, W. M.; Cummins, C. C. Assembly of molybdenum/titanium μ-oxo complexes via radical alkoxide C-O cleavage. *J. Am. Chem. Soc.* **1996**, *118* (42), 10175–10188.
(46) Hendrich, M. P.; Debrunner, P. G. Integer-Spin Electron Paramagnetic Resonance of Iron Proteins. *Biophys. J.* **1989**, *56* (3), 489–506.
(47) Zhou, C.; Raebiger, J. W.; Segal, B. M.; Holm, R. H. The influence of net charge on the redox potentials of Fe_4S_4 cubane-type clusters in aprotic solvents. *Inorganica Chim. Acta* **2000**, *300–302*, 892–902.
(48) Scott, T. A.; Berlinguette, C. P.; Holm, R. H.; Zhou, H.-C. Initial synthesis and structure of an all-ferrous analogue of the fully reduced $[Fe_4S_4]^0$ cluster of the nitrogenase iron protein. *Proc. Natl. Acad. Sci. U.S.A.* **2005**, *102* (28), 9741–9744.
(49) Deng, L.; Holm, R. H. Stabilization of fully reduced iron-sulfur clusters by carbene ligation: The $[Fe_nS_n]^0$ oxidation levels (n = 4, 8). *J. Am. Chem. Soc.* **2008**, *130* (30), 9878–9886.
(50) Kisko, J. L.; Hascall, T.; Parkin, G. The synthesis, structure, and reactivity of phenyl tris(3-tert- butylpyrazolyl)borato iron methyl, [PhTp(Bu^t)]FeMe: Isolation of a four-coordinate monovalent iron carbonyl complex, [PhTp(Bu^t)]FeCO. *J. Am. Chem. Soc.* **1998**, *120* (40), 10561–10562.
(51) Yang, L.; Powell, D. R.; Houser, R. P. Structural variation in copper(I) complexes with pyridylmethylamide ligands: Structural analysis with a new four-coordinate geometry index, τ4. *J. Chem. Soc. Dalt. Trans.* **2007**, 9, 955–964.
(52) Hawrelak, E. J.; Bernskoetter, W. H.; Lobkovsky, E.; Yee, G. T.; Bill, E.; Chirik, P. J. Square planar vs tetrahedral geometry in four coordinate iron(II) complexes. *Inorg. Chem.* **2005**, *44* (9), 3103–3111.
(53) Milocco, F.; De Vries, F.; Siebe, H. S.; Engbers, S.; Demeshko, S.; Meyer, F.; Otten, E. Widening the window of spin-crossover temperatures in bis(formazanate)iron(II) complexes via steric and noncovalent interactions. *Inorg. Chem.* **2021**, *60* (3), 2045–2055.
(54) Liu, Y.; Luo, L.; Xiao, J.; Wang, L.; Song, Y.; Qu, J.; Luo, Y.; Deng, L. Four-coordinate iron(II) diaryl compounds with monodentate N-Heterocyclic carbene ligation: Synthesis, characterization, and their tetrahedral-square planar isomerization in solution. *Inorg. Chem.* **2015**, *54* (10), 4752–4760.
(55) Venkateswara Rao, P.; Holm, R. H. Synthetic analogues of the active sites of iron−sulfur proteins. *Chem. Rev.* **2004**, *104* (2), 527–560.
(56) Pandelia, M. E.; Lanz, N. D.; Booker, S. J.; Krebs, C. Mössbauer spectroscopy of Fe/S proteins. *Biochim. Biophys. Acta - Mol. Cell Res.* **2015**, *1853* (6), 1395–1405.
(57) Ye, S.; Bill, E.; Neese, F. Electronic structures of the $[Fe(N_2)(SiP^iPr_3)]^{+1/0/-1}$ electron transfer series: A counterintuitive correlation between isomer shifts and oxidation states. *Inorg. Chem.* **2016**, *55* (7), 3468–3474.
(58) Chakrabarti, M.; Deng, L.; Holm, R. H.; Münck, E.; Bominaar, E. L. Mössbauer, electron paramagnetic resonance, and theoretical studies of a carbene-based all-ferrous Fe_4S_4 cluster: Electronic origin and structural identification of the unique spectroscopic site. *Inorg. Chem.* **2009**, *48* (7), 2735–2747.

(59) Spiller, N.; Bjornsson, R.; Debeer, S.; Neese, F. Carbon monoxide binding to the iron-molybdenum cofactor of nitrogenase: A detailed quantum mechanics/molecular mechanics investigation. *Inorg. Chem.* **2021**, *60* (23), 18031–18047.
(60) Noodleman, L.; Peng, C. Y.; Case, D. A.; Mouesca, J. M. Orbital interactions, electron delocalization and spin coupling in iron-sulfur clusters. *Coord. Chem. Rev.* **1995**, *144* (C), 199–244.
(61) Monesca, J. M.; Chen, J. L.; Noodleman, L.; Bashford, D.; Case, D. A. Density Functional/Poisson-Boltzmann calculations of redox potentials for iron-sulfur clusters. *J. Am. Chem. Soc.* **1994**, *116* (26), 11898–11914.
(62) Bjornsson, R.; Lima, F. A.; Spatzal, T.; Weyhermüller, T.; Glatzel, P.; Bill, E.; Einsle, O.; Neese, F.; DeBeer, S.; Hoffman, B. M. Identification of a spin-coupled Mo(III) in the nitrogenase iron–molybdenum cofactor. *Chem. Sci.* **2014**, *5* (8), 3096–3103.
(63) Pantazis, D. A.; Ames, W.; Cox, N.; Lubitz, W.; Neese, F. Two interconvertible structures that explain the spectroscopic properties of the oxygen-evolving complex of photosystem II in the S2 state. *Angew. Chem. Int. Ed.* **2012**, *51* (39), 9935–9940.
(64) Kuppuswamy, S.; Powers, T. M.; Johnson, B. M.; Brozek, C. K.; Krogman, J. P.; Bezpalko, M. W.; Berben, L. A.; Keith, J. M.; Foxman, B. M.; Thomas, C. M. One-electron oxidation chemistry and subsequent reactivity of diiron imido complexes. *Inorg. Chem.* **2014**, *53* (11), 5429–5437.
(65) Eames, E. V.; Betley, T. A. Site-isolated redox reactivity in a trinuclear iron complex. *Inorg. Chem.* **2012**, *51* (19), 10274–10278.
(66) Anderton, K. J.; Knight, B. J.; Rheingold, A. L.; Abboud, K. A.; García-Serres, R.; Murray, L. J. Reactivity of hydride bridges in a high-spin $[Fe_3(\mu\text{-}H)_3]^{3+}$ cluster: Reversible H_2/CO exchange and Fe-H/B-F bond metathesis. *Chem. Sci.* **2017**, *8* (5), 4123–4129.
(67) Powers, T. M.; Betley, T. A. Testing the polynuclear hypothesis: Multielectron reduction of small molecules by triiron reaction sites. *J. Am. Chem. Soc.* **2013**, *135* (33), 12289–12296.
(68) McSkimming, A.; Suess, D. L. M. Dinitrogen binding and activation at a molybdenum–iron–sulfur cluster. *Nat. Chem.* **2021**, *13* (7), 666–670..
(69) Angove, H. C.; Yoo, S. J.; Burgess, B. K.; Münck, E. Mössbauer and EPR evidence for an all-ferrous Fe_4S_4 cluster with S = 4 in the Fe protein of nitrogenase. *J. Am. Chem. Soc.* **1997**, *119* (37), 8730–8731.
(70) Yoo, S. J.; Angove, H. C.; Burgess, B. K.; Hendrich, M. P.; Münck, E. Mossbauer and integer-spin EPR studies and spin-coupling analysis of the $[4Fe\text{-}4S]^0$ cluster of the Fe protein from *Azotobacter vinelandii* nitrogenase. *J. Am. Chem. Soc.* **1999**, *121* (11), 2534–2545.
(71) Hans, M.; Buckel, W.; Bill, E. Spectroscopic evidence for an all-ferrous $[4Fe\text{-}4S]^0$ cluster in the superreduced activator of 2-hydroxyglutaryl-CoA dehydratase from *Acidaminococcus fermentans*. *J. Biol. Inorg. Chem.* **2008**, *13* (4), 563–574.
(72) Lowery, T. J.; Wilson, P. E.; Zhang, B.; Bunker, J.; Harrison, R. G.; Nyborg, A. C.; Thiriot, D.; Watt, G. D. Flavodoxin hydroquinone reduces *Azotobacter vinelandii* Fe protein to the all-ferrous redox state with a S = 0 spin state. *Proc. Natl. Acad. Sci. U.S.A.* **2006**, *103* (46), 17131–17136.
(73) Hill, C. L.; Renaud, J.; Holm, R. H.; Mortenson, L. E. Synthetic analogues of the active sites of iron-sulfur proteins. 15. Comparative polarographic potentials of the $[Fe_4S_4(SR)_4]^{2-,3-}$ and *Clostridium pasteurianum* ferredoxin redox couples. *J. Am. Chem. Soc.* **1977**, *99* (8), 2549–2557.
(74) Watt, G. D.; Reddy, K. R. N. Formation of an all ferrous $[Fe_4S_4]$ cluster in the iron protein component of *Azotobacter vinelandii* nitrogenase. *J. Inorg. Biochem.* **1994**, *53*

(4), 281–294.

Supporting Information.

Experimental Methods

General Considerations

All reactions were performed using standard Schlenk techniques or in an LC Technologies inert atmosphere glove box under an atmosphere of nitrogen. Glassware was dried in an oven at 160 °C prior to use. Molecular sieves (3 Å), and Celite® were activated by heating to 300 °C overnight under vacuum prior to storage under an atmosphere of nitrogen. Tetrahydrofuran (THF) was distilled from sodium/benzophenone, *o*-difluorobenzene (DFB) and fluorobenzene (PhF) were distilled from CaH_2, C_6D_6 was degassed by three freeze–pump–thaw cycles, and other solvents were degassed by sparging with argon and dried by passing through a column of activated alumina. All solvents were stored under an atmosphere of nitrogen over 3 Å molecular sieves.

Synthetic procedures

$(IMes)_3Fe_4S_4Cl$,[1] $[(IMes)_3Fe_4S_4(OEt_2)][BAr^F{}_4]$,[2] $(I^iPr^{Me})_4Fe_4S_4$,[3] $[(I^iPr^{Me})_4Fe_4S_4][BPh_4]$,[1] $Ti(N^tBuAr)_3$,[4] and $Na[BAr^F{}_4]$[5] were prepared according to literature procedures. The purity of all compounds was assessed by a variety of spectroscopic and analytical methods as detailed below. Compound **1-CO** is air sensitive but can be isolated as a crystalline solid in high purity as determined by NMR, IR, and Mössbauer spectroscopic analysis despite the modestly low carbon content obtained by elemental analysis. Compound $[\mathbf{1\text{-}CO}]^+$ is unstable to vacuum, preventing collection of elemental analysis data, but can be generated in high purity in solution as determined by NMR, IR, EPR, and Mössbauer spectroscopic analysis.

Spectroscopy

NMR spectra were recorded on Bruker 400 and 500 MHz spectrometers. ^1H chemical shifts are given relative to residual solvent peaks. Solvent suppression for NMR in protonated

solvents was carried out using WET solvent suppression.[6] FT-IR samples were taken as thin films using a Bruker Alpha Platinum ATR spectrometer with OPUS software in a glovebox under an N_2 atmosphere. EPR spectra were recorded on a Bruker EMX spectrometer at 9.37 GHz (perpendicular mode) or 9.39 GHz (parallel mode) as frozen glasses. Simulations were performed using EasySpin[7] (5.2.21) in Matlab (R2017b). UV-vis spectra were recorded on a Cary 50 spectrometer. Zero-field 80 K ^{57}Fe Mössbauer spectra were measured with a SEE co. MS3 W301 constant-acceleration spectrometer. Variable temperature (5–200 K) zero-field ^{57}Fe Mössbauer spectra were measured with a SEE co. W302 constant-acceleration spectrometer. Isomer shifts are quoted relative to α-Fe foil at room temperature; Mössbauer spectra were simulated with WMOSS v.4.[8] SQUID data was collected on a Quantum Design MPMS3 SQUID magnetometer in the range of 2–300 K with a 1.0 T applied field. X-ray structural determinations were performed at the MIT diffraction facility using a Bruker X8 diffractometer with an APEX II CCD detector or a Bruker D8 Venture diffractometer with a Photon2 CPAD detector. Diffraction data was collected, integrated, and corrected for absorption using Bruker APEX3 software and its associated modules (SAINT, SADABS, TWINABS). Structural solutions and refinements (on F^2) were carried out using SHELXT and SHELXL-2018 in ShelXle.[9] Ellipsoid plots and figures were made using Mercury.

$(IMes)_3Fe_4S_4CO$ (**1-CO**)

$(IMes)_3Fe_4S_4Cl$ (480 mg, 0.369 mmol) was dissolved in THF (10 mL) and frozen in liquid N_2 in a Schlenk flask. A solution of $Ti(N(^tBu)Ar)_3$ (323 mg, 0.560 mmol) in THF (10 mL) was layered on top and frozen. The flask was capped with a septum and removed from the glovebox. The flask was evacuated and CO (14 mL) was added via syringe. The reaction was warmed to room temperature and stirred vigorously for 5 minutes. The solvent was removed in vacuo and the solid residue was washed with pentane (3×5 mL) to remove $ClTi(NRAr)_3$. The remaining

dark solids were extracted into THF (5 mL), layered with pentane (15 mL), and stored at room temperature for 16 h. Dark-brown crystals of **1-CO** were collected and washed with pentane (3×5 mL). Yield: 374 mg (78%). Crystals for x-ray diffraction were grown by vapor diffusion of pentane into a solution of **1-CO** in THF at room temperature. ^{1}H NMR (400 MHz, C_6D_6, 293 K) δ 9.03 (s, 6H, backbone C*H*), 7.80 (s, 12H, Mes *m*-C*H*), 2.91 (s, 18H, Mes *p*-CH_3), 2.71 (s, 36H, Mes *o*-CH_3). EPR: g_{eff} = 8.59 (toluene, 5 K, 9.39 GHz). FT-IR (thin film, cm^{-1}): 1832 (C–O stretch); 1789 (^{13}C–O stretch, calc. 1791). Anal. Found: C, 59.65; H, 6.34; N, 5.92. Calcd for $C_{64}H_{72}N_6Fe_4S_4CO\cdot(C_5H_{12})$: C, 60.71; H, 6.20; N, 6.16.

[(IMes)$_3$Fe$_4$S$_4$CO][BAr$^F{}_4$] ([**1-CO**]$^+$)

[(IMes)$_3$Fe$_4$S$_4$(OEt$_2$)][BAr$^F{}_4$] (35.5 mg, 16.1 μmol) was dissolved in fluorobenzene (0.5 mL) and frozen in liquid N_2 in a septum capped NMR tube. CO (1.0 mL) was added via syringe. The solution was warmed to room temperature with vigorous agitation. Cluster [**1-CO**]$^+$ was used as-generated because significant decomposition occurs when it is placed under dynamic vacuum. Yield (*in-situ*, measured *vs.* hexamethyldisiloxane internal standard): 15.3 μmol (95 %). Crystals for x-ray diffraction were grown by layering pentane onto a solution of [**1-CO**]$^+$ in PhF, followed by storage at –35 °C for two weeks. ^{1}H NMR (400 MHz, PhF, 293 K, internally referenced to Et_2O (1.11 and 3.31 ppm)) δ 8.32 (s, 8H, [BAr$^F{}_4$]$^-$), 7.62 (s, 4H, [BAr$^F{}_4$]$^-$), 5.97 (s, 6H, backbone C*H*), 2.51 (s, 18H, Mes *p*-CH_3), 2.14 (s, 36H, Mes *o*-CH_3). The Mes *m*-C*H* resonance was obscured by the solvent. EPR: g_1 = 2.116, g_2 = 1.944, g_3 = 1.912 (toluene, 15 K, 9.37 GHz). FT-IR (thin film, cm^{-1}): 1902 (C–O stretch), 1862 (^{13}C–O stretch, calc. 1860).

B. NMR spectra

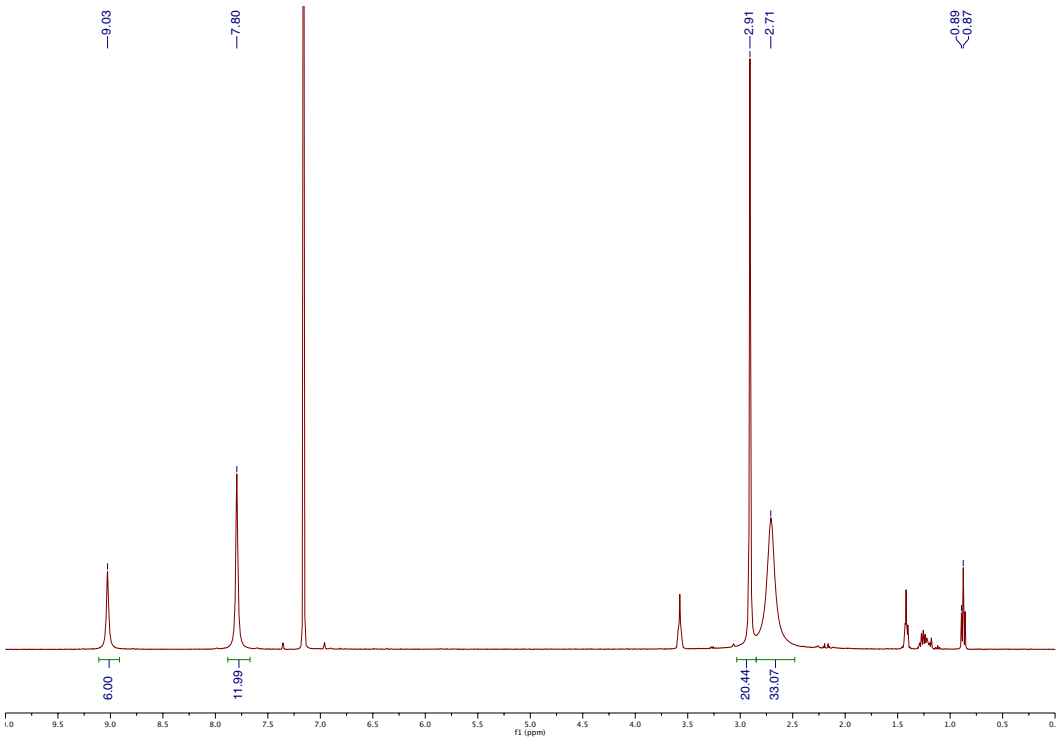

Figure S3.1. ^{1}H NMR spectrum of **1-CO** in C_6D_6 at 293 K.

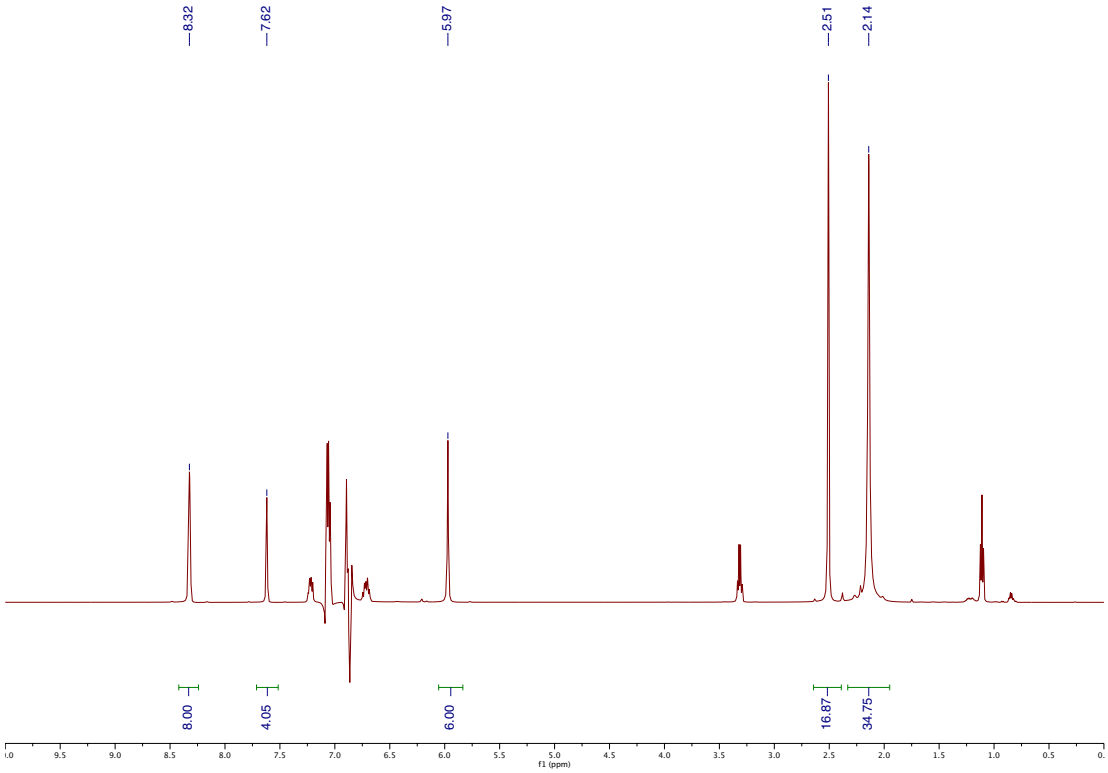

Figure S3.2. ^{1}H NMR spectrum of [**1-CO**]$^{+}$ in C_6H_5F at 293 K. The region between 6.6 and 7.3 ppm contains one IMes resonance that is obscured by suppressed PhF resonances.

C. IR spectra

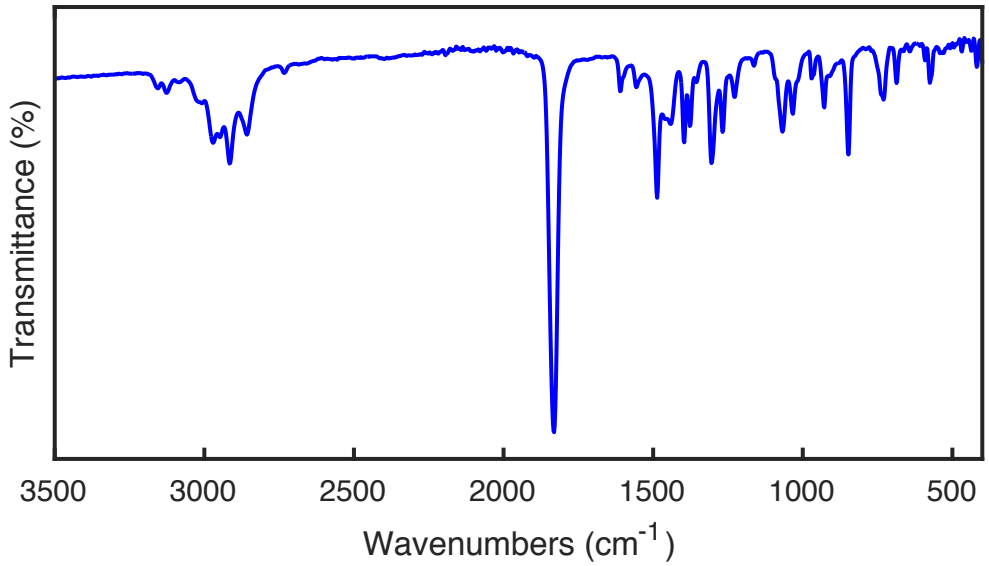

Figure S3.3. IR spectrum of **1-CO**. C–O stretch: 1832 cm^{-1}.

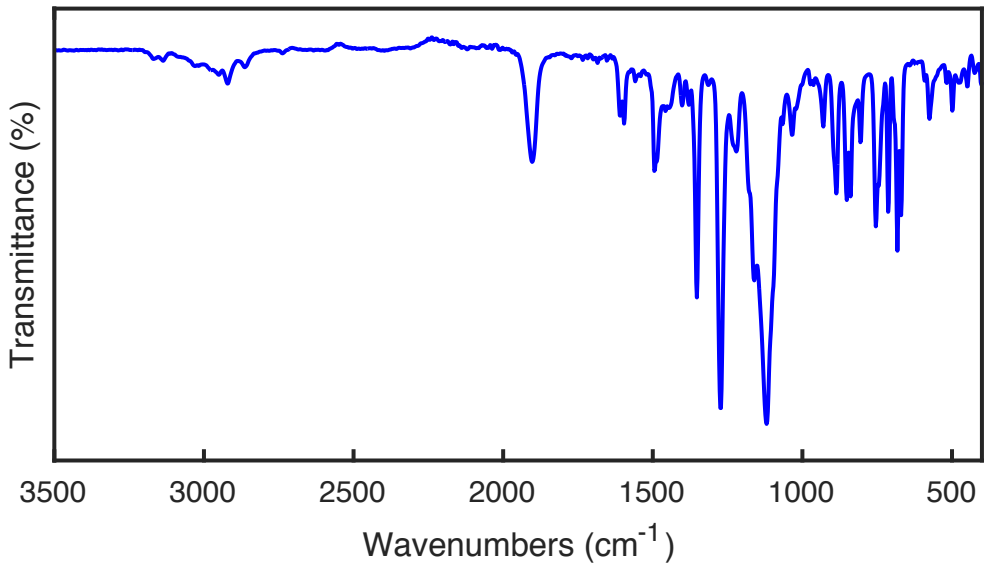

Figure S3.4: IR spectrum of [**1-CO**]$^{+}$. C–O stretch: 1902 cm^{-1}.

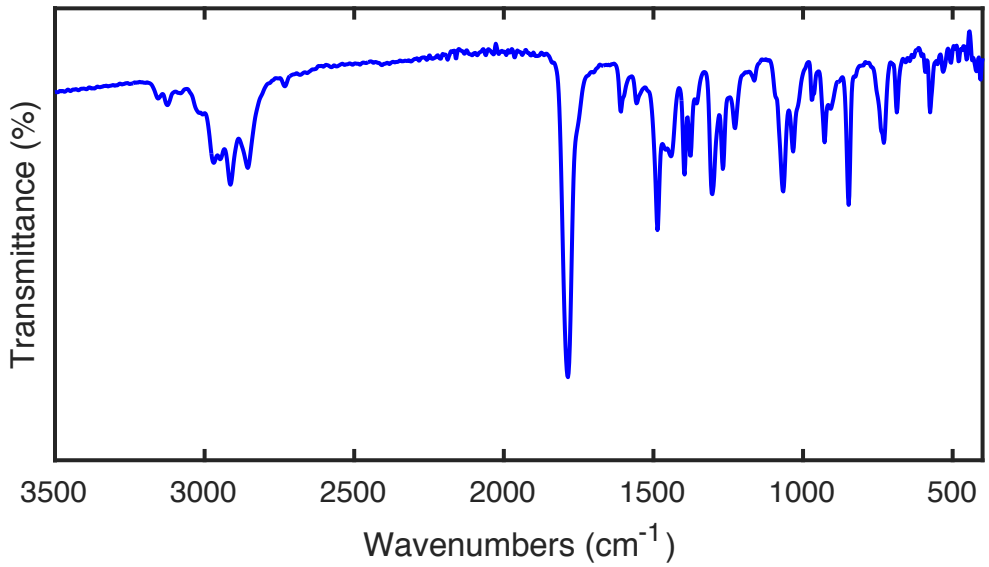

Figure S3.5: IR spectrum of 1-^{13}CO. C–O stretch: 1787 cm^{-1}.

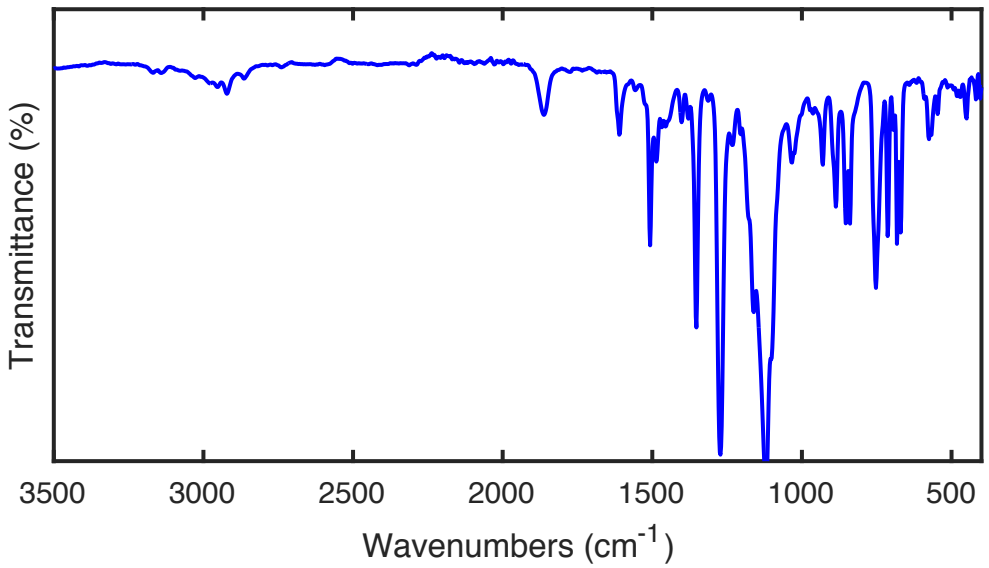

Figure S3.6: IR spectrum of [**1-^{13}CO**]$^{+}$. C–O stretch: 1862 cm^{-1}.

D. EPR Spectra

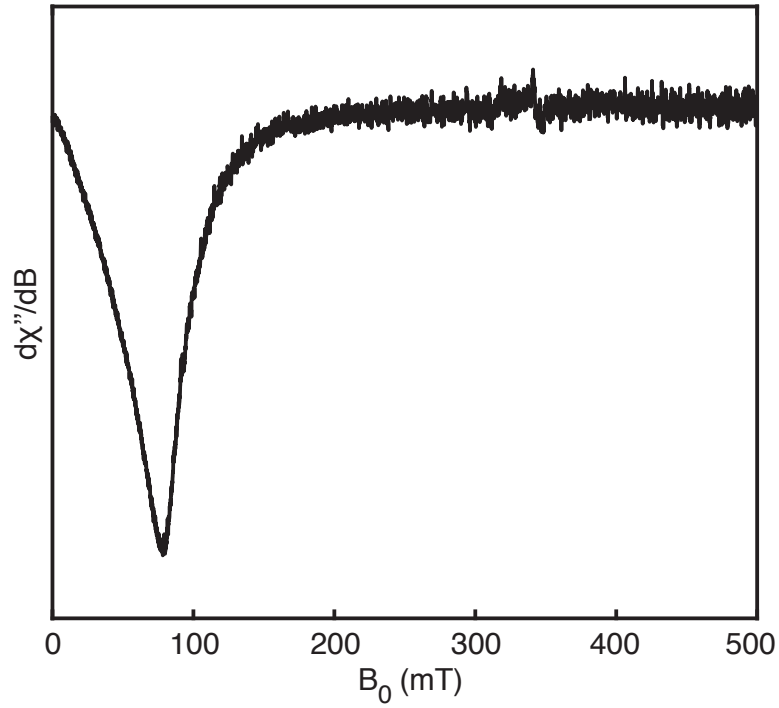

Figure S3.7: X-Band CW EPR spectrum of **1-CO** (5 mM) in toluene at 5 K (parallel mode). Microwave power: 1 mW; microwave frequency: 9.393 GHz.

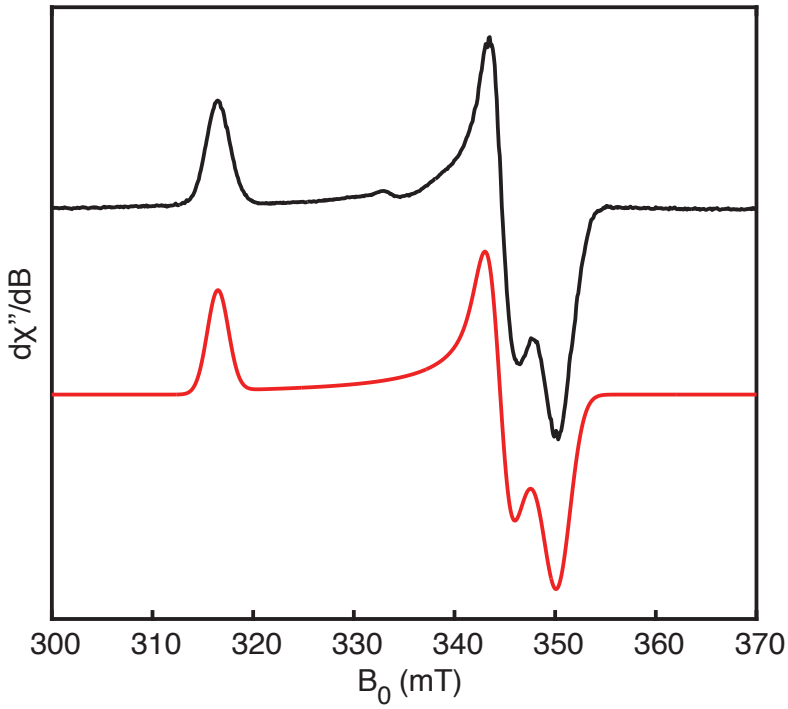

Figure S3.8: X-Band CW EPR spectrum of [**1-CO**]$^+$ (1 mM) in fluorobenzene at 15 K (perpendicular mode, black) and simulation (red). Microwave power: 63 μW; microwave frequency: 9.373 GHz; simulation parameters: g = [2.116 1.944 1.912], g-strain = [0.015 0.014 0.016].

E. UV-vis spectra

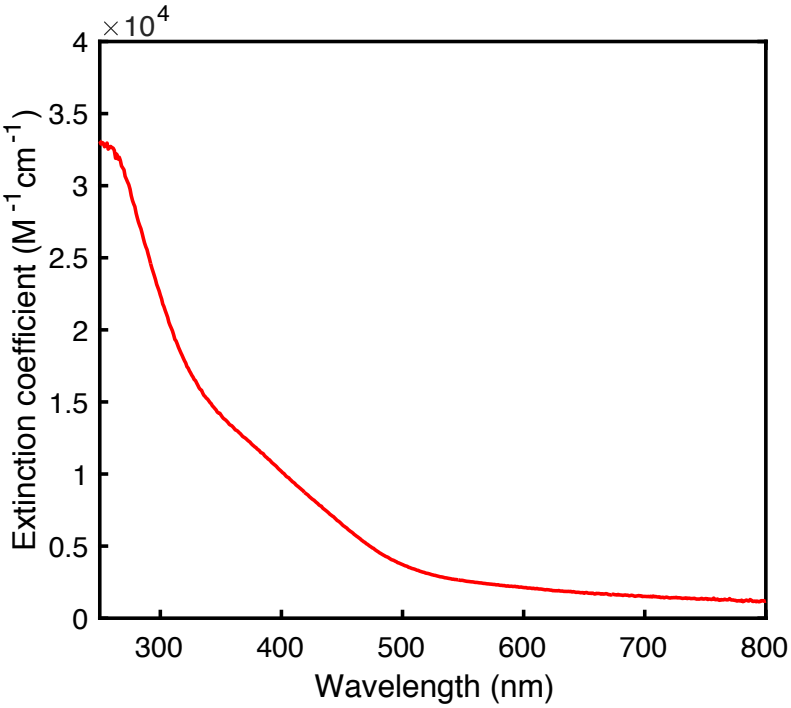

Figure S3.9: UV-vis spectrum of **1-CO** in THF.

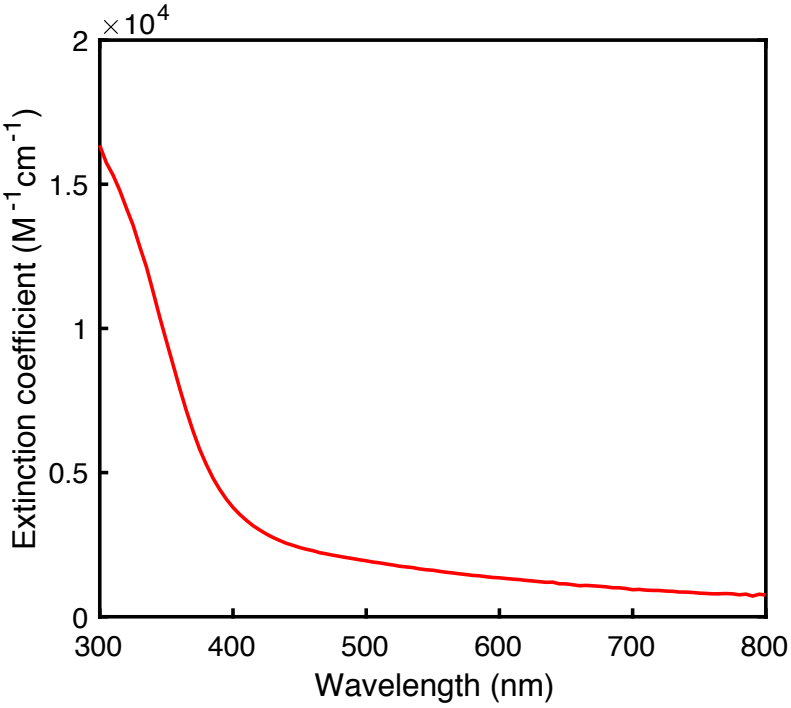

Figure S3.10: UV-vis spectrum of [**1-CO**]$^+$ in *o*–DFB.

F. VT Mössbauer spectra of 1-CO

The zero-field Mössbauer spectrum of **1-CO** was recorded at seven temperatures from 5 K to 200 K. At 5 K, all four sites have approximately the same linewidth and so 24 different fits to the data are possible. These simulations can be groups into major classes A–C based on the quadrupole splittings of the doublets. Class A simulations have two wide ($|\Delta E_Q| \sim 2.5$ mm s^{-1}) and two narrow ($|\Delta E_Q| \sim 1$ mm s^{-1}) quadrupole doublets. Class B simulations have one wide, one narrow, and two intermediate ($|\Delta E_Q| \sim 1.7$ mm s^{-1}) quadrupole doublets. Class C simulations have four intermediate quadrupole doublets. A representative simulation from each

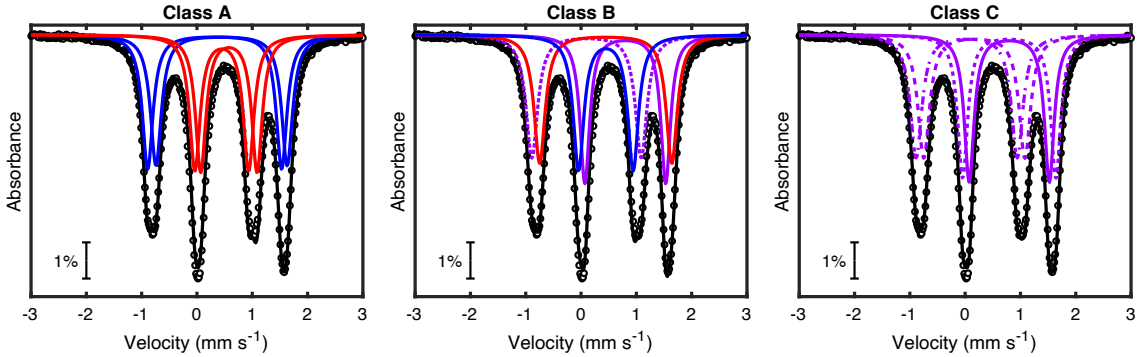

Figure S3.11: Mössbauer spectrum of **1-CO** at 5 K with simulations from class A (left), B (middle) and C (right). Narrow quadrupole doublets are red, wide quadrupole doublets are blue, and intermediate quadrupole doublets are purple. Intermediate quadrupole doublets have either unreasonably high or low isomer shifts for Fe–NHC sites.

class is shown in Figure S3.11 and representative parameters are summarized in Table S3.1. Simulations in class B and class C require the isomer shift of at least one Fe–NHC site to be either unreasonably small (~ 0.1 mm s^{-1}) or unreasonably large (~ 0.8 mm s^{-1}) given that the typical range for isomer shifts corresponding to tetrahedral sites in $[Fe_4S_4]$ clusters is ~0.30–0.65 mm s^{-1}.[3,10] For this reason, we prefer simulations from class A, in which there are four possible fits (one with both pairs of doublets nested, one with both pairs staggered, and two with one pair nested and one pair staggered) and all isomer shifts are between 0.3 and 0.6 mm s^{-1}. We chose the specific simulation in Figure S3.11 (left) based on agreement with calculations (section H) and a variable temperature Mössbauer study (*vide infra*), which found

that the two quadrupole doublets with wide quadrupole splittings have very different temperature-dependent behavior.

Table S3.1: Representative simulations for the Mössbauer spectrum of **1-CO** at 5 K.

Simulation		δ (mm·s^{-1})	$\lvert\Delta E_Q\rvert$ (mm·s^{-1})
A1	Site 1	0.320	2.422
	Site 2	0.445	2.373
	Site 3	0.525	1.125
	Site 4	0.502	0.867
B1	Site 1	0.099	1.978
	Site 2	0.800	1.462
	Site 3	0.446	2.389
	Site 4	0.449	0.988
C1	Site 1	0.166	1.828
	Site 2	0.798	1.449
	Site 3	0.028	1.828
	Site 4	0.798	1.685

In the variable-temperature Mössbauer data, it was observed that one (gray) of the two doublets with large quadrupole splitting ($|\Delta E_Q| \sim 2$ mm s^{-1}, gray and purple) has relatively invariant isomer shift, quadrupole splitting, and linewidth over the studied temperature range. On this basis (discussed further below) and based on the computed Mössbauer parameters (section H), we assign this gray doublet to the Fe–CO site; the parameters for the purple doublet are more variable and are thus easily simulated with the wide doublet staggered at 5 K. This constraint eliminates two of the four potential 'class A' simulations for the data. The doublets with smaller quadrupole splittings ($|\Delta E_Q| \sim 1$ mm s^{-1}, blue and red), can be fit with either similar isomer shifts (nested) or similar quadrupole splittings (staggered). Simulations at each

temperature with both nested and staggered fits are presented in Figures S3.12–S3.18. Parameters for all fits are presented in Tables S3.1–S3.3 and in Figure S3.19.

The VT-Mössbauer spectra of **1-CO** reveal that, regardless of the chosen fit, the quadrupole splitting for one Fe–NHC site (purple) has a more pronounced temperature dependence than the other sites (Tables S3.2 and S3.3; Figure S3.19). In addition, the isomer shift of this Fe site has an unusual temperature dependence, increasing slightly between 20 K and 150 K with increasing temperature (as opposed to the more typical decrease in isomer shift with increasing temperature due to the second-order Doppler effect). Such an inverse temperature dependence of the isomer shift of one Fe site is indicative of an exchange process that interconverts two or more Fe sites. At low temperatures (*e.g.*, 5 K), the exchange process is much slower than the Mössbauer timescale, and thus the three Fe–NHC doublets have similar, sharp linewidths. As the temperature is raised, the exchange process becomes more competitive with the Mössbauer timescale, and as such the three Fe–NHC doublets begin to converge to a single doublet. In particular, the doublet with the most distinct parameters (purple) broadens the most and shifts the most quickly, as expected. Note that even up to 200 K, the three Fe–NHC sites are spectroscopically distinct on this timescale (in contrast to, for example, the three Fe–NHC sites in [**1-CO**]$^+$, which are spectroscopically equivalent even at 80 K). The parameters for the doublet assigned to the Fe–CO site do not change with temperature beyond a slight decrease in the isomer shift due to the second-order Doppler effect because this site is chemically distinct from the Fe–NHC sites and is therefore not involved in this exchange process. We prefer the nested fit for the Mössbauer spectrum of **1-CO** at all temperatures because the similarity of the isomer shifts for two of the Fe–NHC sites better aligns with the crystallographic symmetry, in which two Fe sites have very similar Fe–S and Fe–C distances, and with the computed Mössbauer parameters (See SI section H).

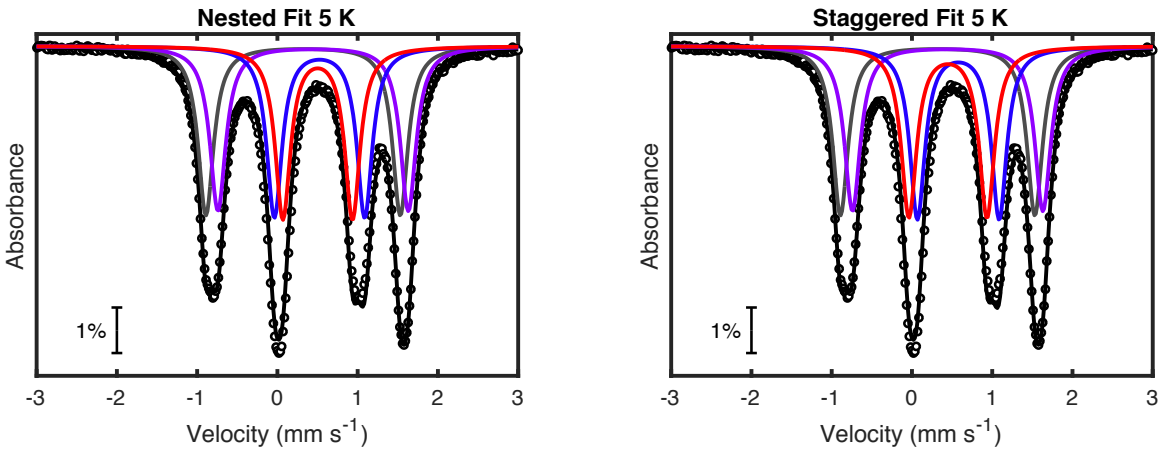

Figure S3.12: Mössbauer spectrum of **1-CO** at 5 K with nested (left) and staggered (right) fits for the central quadrupole doublets.

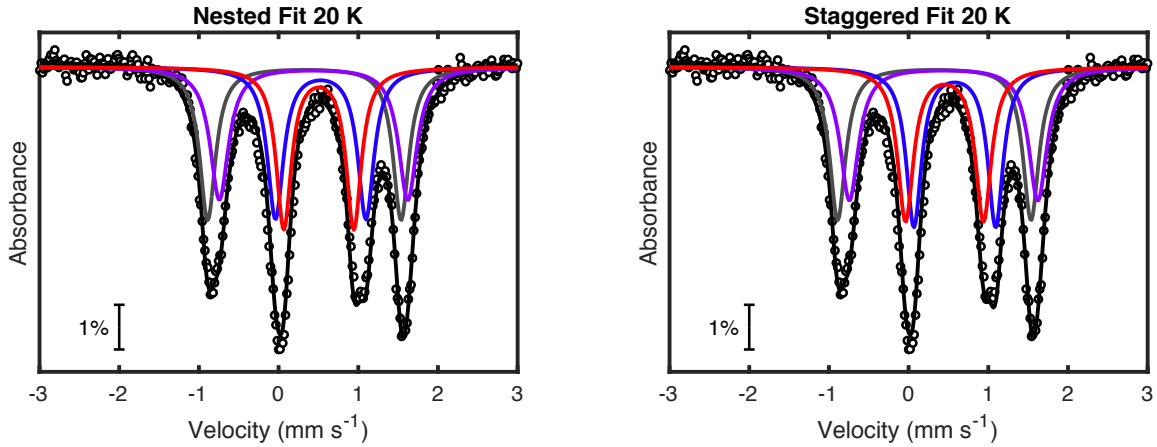

Figure S3.13: Mössbauer spectrum of **1-CO** at 20 K with nested (left) and staggered (right) fits for the central quadrupole doublets.

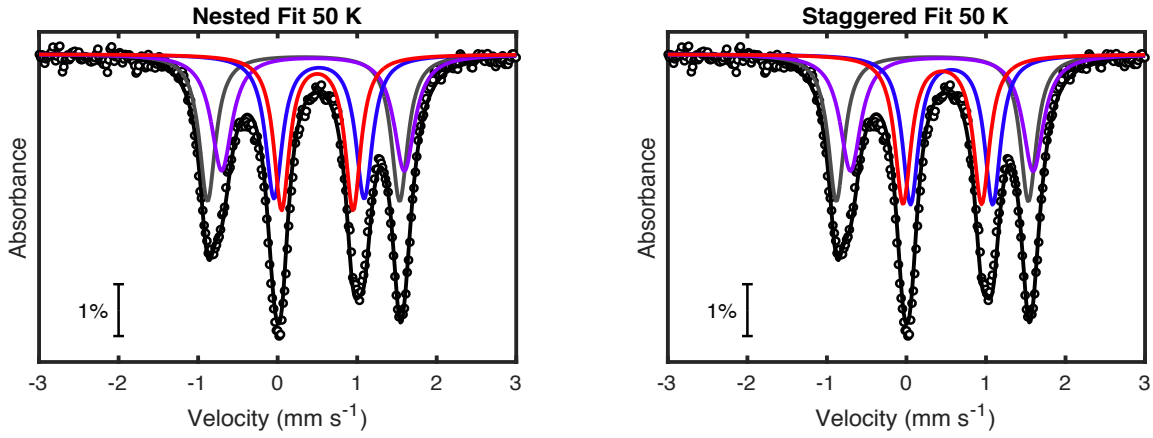

Figure S3.14: Mössbauer spectrum of **1-CO** at 50 K with nested (left) and staggered (right) fits for the central quadrupole doublets.

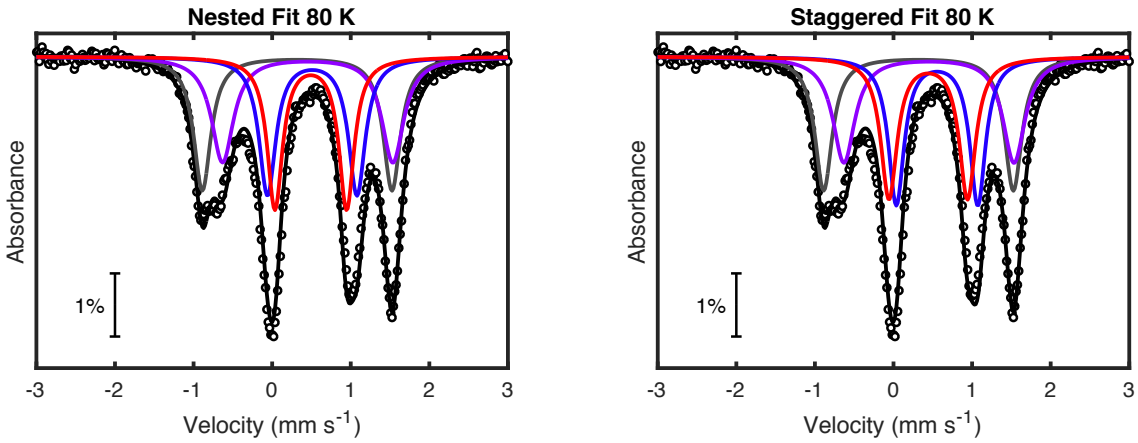

Figure S3.15: Mössbauer spectrum of **1-CO** at 80 K with nested (left) and staggered (right) fits for the central quadrupole doublets.

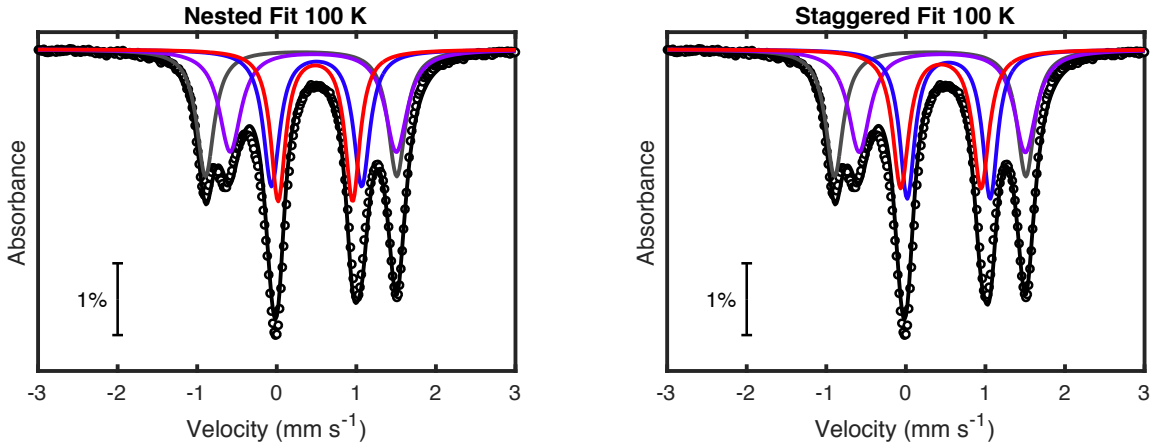

Figure S3.16: Mössbauer spectrum of **1-CO** at 100 K with nested (left) and staggered right) fits for the central quadrupole doublets.

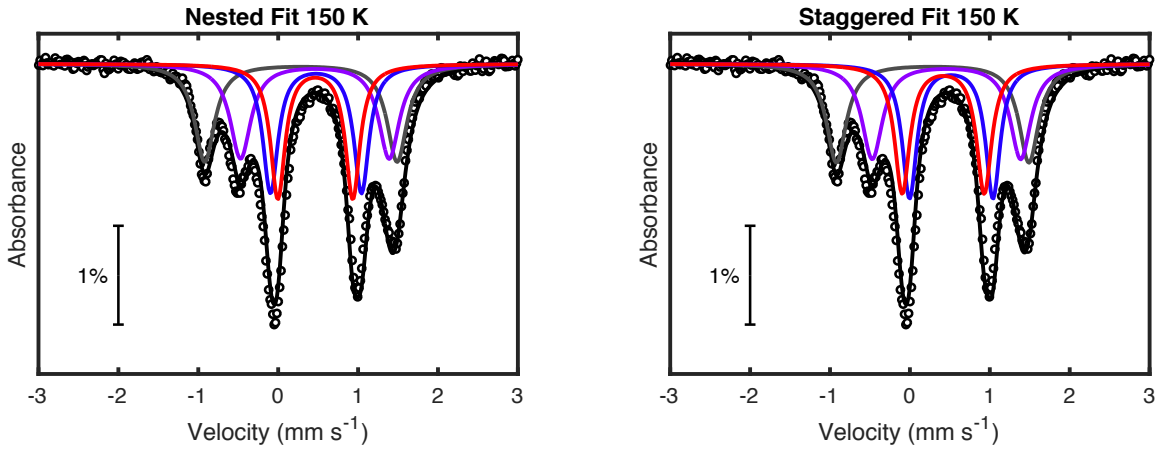

Figure S3.17: Mössbauer spectrum of **1-CO** at 150 K with nested (left) and staggered (right) fits for the central quadrupole doublets.

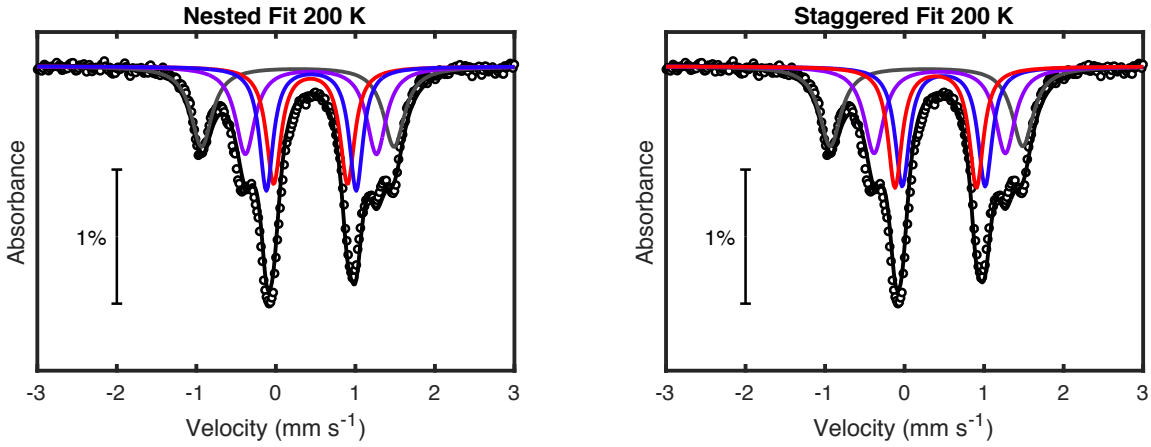

Figure S3.18: Mössbauer spectrum of **1-CO** at 200 K with nested (left) and staggered (right) fits for the central quadrupole doublets.

Table S3.2: Fit parameters for VT-Mössbauer data of **1-CO** with a nested fit for the central quadrupole doublets.

Fe site		**5 K**	**20 K**	**50 K**	**80 K**	**100 K**	**150 K**	**200 K**
1 (gray) Fe–CO	δ (mm·s^{-1})	0.320	0.323	0.325	0.317	0.306	0.284	0.276
	$\lvert\Delta E_Q\rvert$ (mm·s^{-1})	2.422	2.427	2.415	2.413	2.405	2.408	2.420
2 (purple) Fe–NHC	δ (mm·s^{-1})	0.445	0.439	0.444	0.452	0.458	0.459	0.440
	$\lvert\Delta E_Q\rvert$ (mm·s^{-1})	2.373	2.365	2.297	2.167	2.088	1.860	1.649
3 (blue) Fe–NHC	δ (mm·s^{-1})	0.525	0.528	0.521	0.509	0.501	0.473	0.446
	$\lvert\Delta E_Q\rvert$ (mm·s^{-1})	1.125	1.136	1.134	1.139	1.133	1.139	1.130
4 (red) Fe–NHC	δ (mm·s^{-1})	0.502	0.504	0.499	0.491	0.485	0.464	0.437
	$\lvert\Delta E_Q\rvert$ (mm·s^{-1})	0.867	0.879	0.899	0.913	0.936	0.938	0.929

Table S3.3: Fit parameters for VT-Mössbauer data of **1-CO** with a staggered fit for the central quadrupole doublets.

Fe site		**5 K**	**20 K**	**50 K**	**80 K**	**100 K**	**150 K**	**200 K**
1 (gray) Fe–CO	δ (mm·s^{-1})	0.320	0.323	0.325	0.318	0.305	0.284	0.276
	$\lvert\Delta E_Q\rvert$ (mm·s^{-1})	2.422	2.427	2.415	2.414	2.404	2.409	2.420
2 (purple) Fe–NHC	δ (mm·s^{-1})	0.445	0.439	0.445	0.451	0.457	0.458	0.441
	$\lvert\Delta E_Q\rvert$ (mm·s^{-1})	2.373	2.365	2.296	2.164	2.088	1.857	1.650
3 (blue) Fe–NHC	δ (mm·s^{-1})	0.577	0.579	0.568	0.554	0.539	0.527	0.492
	$\lvert\Delta E_Q\rvert$ (mm·s^{-1})	1.019	1.026	1.033	1.037	1.042	1.044	1.043
4 (red) Fe–NHC	δ (mm·s^{-1})	0.448	0.451	0.451	0.442	0.441	0.417	0.391
	$\lvert\Delta E_Q\rvert$ (mm·s^{-1})	0.973	0.978	0.988	1.000	1.010	1.026	1.025

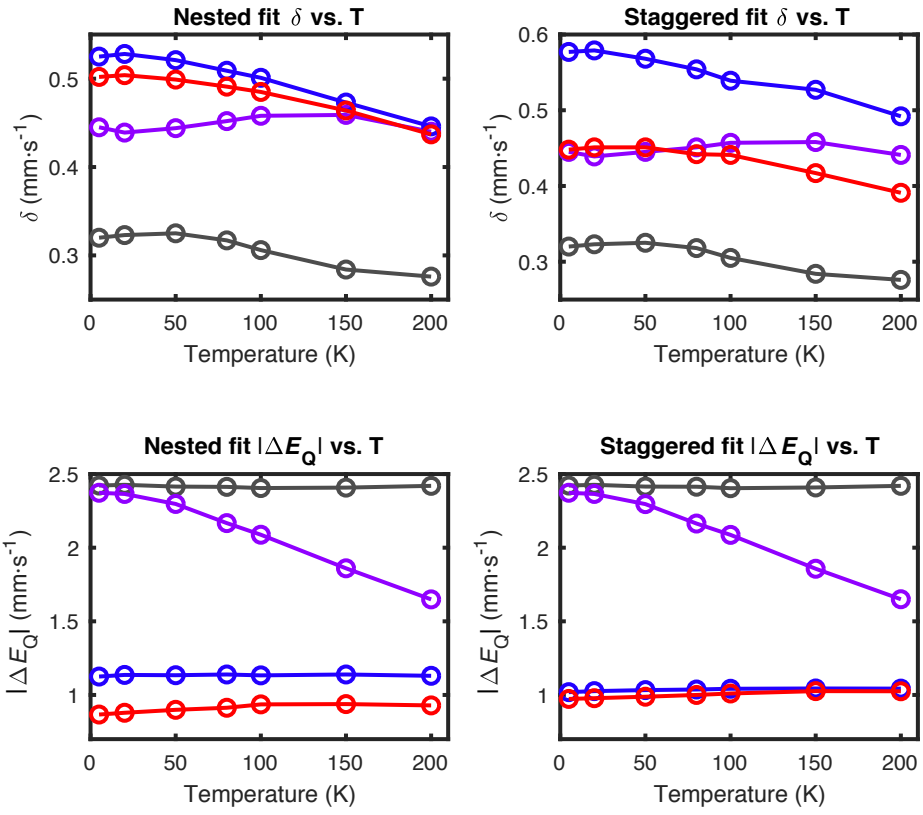

Figure S3.19: Plots of Mössbauer parameters vs. T for nested and staggered fits of VT-Mössbauer data for **1-CO**.

G. Additional Mössbauer spectra

The compounds **1-Cl**, $[(IMes)_3Fe_4S_4(OEt_2)][BAr^F{}_4]$ and $[(IMes)_3Fe_4S_4(CN^tBu)][BAr^F{}_4]$ have been previously reported;[1,2] their 80 K Mössbauer spectra are reported here (Figures S3.20-S3.22). In all cases, the Fe site ligated by the unique ligand cannot be readily identified in the Mössbauer spectrum. The spectra are simulated using four nested quadrupole doublets with arbitrary parameters. As such, we discuss only the average isomer shift of each cluster because it does not depend on the simulation. The average isomer shifts for the four Fe sites are 0.52, 0.52 and 0.48 $mm \cdot s^{-1}$, respectively. All are similar to or higher than the isomer shift of the Fe sites in $[\mathbf{2}]^+$, confirming that $[\mathbf{2}]^+$ is a good comparison for typical NHC-ligated $[Fe_4S_4]^+$ clusters and that the unusually low isomer shifts of the NHC-ligated sites in $[\mathbf{1\text{-}CO}]^{0/+}$ are do not arise from other effects (*e.g.*, decreased symmetry of the site-differentiated clusters).

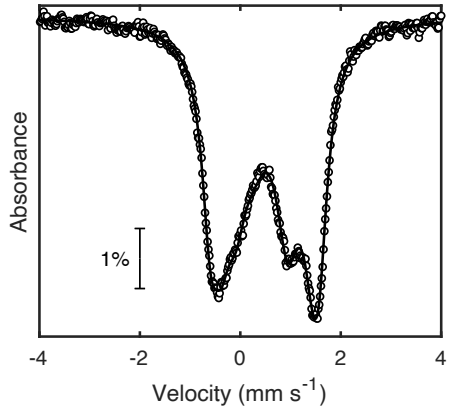

Figure S3.20: Mössbauer spectrum of **1-Cl** at 80 K (dots) and total simulation (black line) using parameters in Table S3.4.

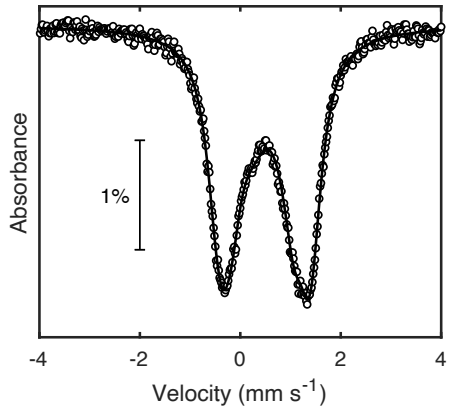

Figure S3.21: Mössbauer spectrum of $[(IMes)_3Fe_4S_4(OEt_2)]^+$ at 80 K (dots) and total simulation (black line) using parameters in Table S3.4.

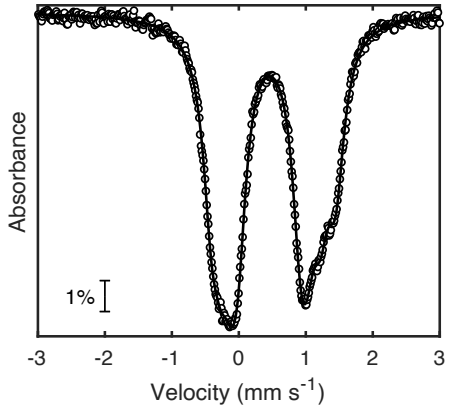

Figure S3.22: Mössbauer spectrum of $[(IMes)_3Fe_4S_4(CN^tBu)]^+$ at 80 K (dots) and total simulation (black line) using parameters in Table S3.4.

Table S3.4: Fit parameters for supplementary 80 K Mössbauer spectra.[a]

Compound		δ (mm·s^{-1})	$\lvert\Delta E_Q\rvert$ (mm·s^{-1})	Γ (mm·s^{-1})
$[(IMes)_3Fe_4S_4(OEt_2)]^+$	Site 1	0.479	1.930	0.509
	Site 2	0.461	1.240	0.510
	Site 3	0.615	0.707	0.800
	Site 4	0.507	1.694	0.471
	Avg δ	**0.516**	–	–
1-Cl	Site 1	0.485	2.169	0.409
	Site 2	0.416	1.020	0.547
	Site 3	0.648	0.767	0.800
	Site 4	0.523	1.813	0.475
	Avg δ	**0.518**		
$[(IMes)_3Fe_4S_4(CN^tBu)]^+$	Site 1	0.518	1.857	0.312
	Site 2	0.477	1.485	0.330
	Site 3	0.452	1.128	0.329
	Site 4	0.454	0.921	0.305
	Avg δ	**0.475**	–	–

[a]: Note that the parameters for the individual quadrupole doublets are not physically meaningful because the spectra cannot be fit by a unique, reliable simulation.

H. SQUID magnetometry of 1-CO

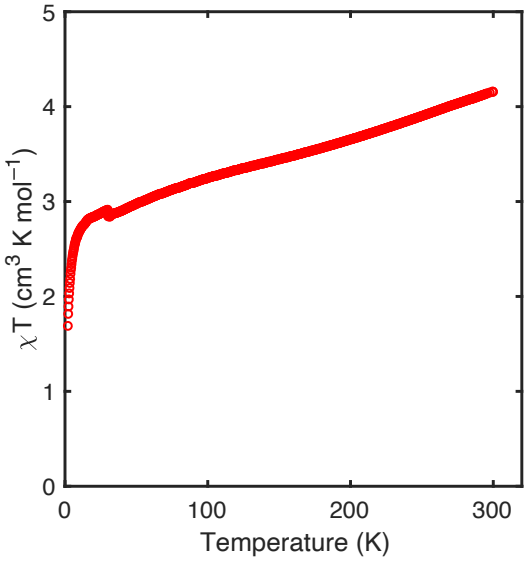

Figure S3.23: SQUID magnetometry data (χT vs. T) for **1-CO** collected at a field of 1 T. Data are corrected for diamagnetic contributions using Pascal's constants. The values of χT at low temperature (ca. 2.8 cm^3 K mol^{-1}) are close to the expectation value for an $S = 2$ system (3.0 cm^3 K mol^{-1}). The increase in χT with increasing temperature may be attributed to temperature independent paramagnetism (TIP) or population of higher spin excited states.

I. Cyclic voltammetry

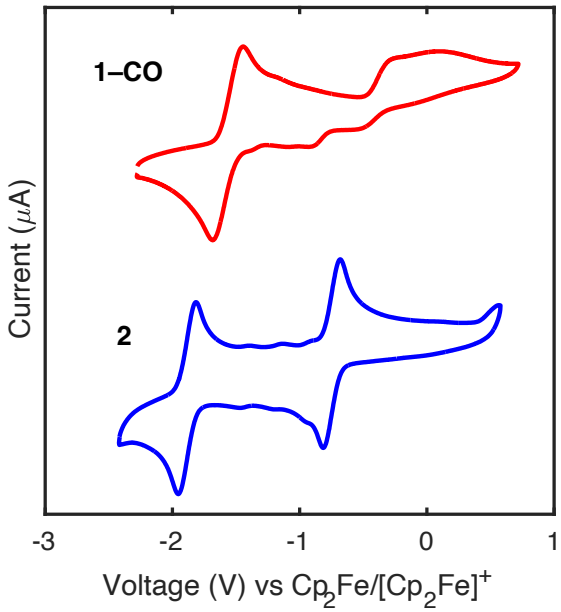

Figure S3.24: Cyclic voltammagrams of **1-CO** and **2** (2 mM) in *o*-DFB (0.2 M $[NPr_4][BAr^F{}_4]$).

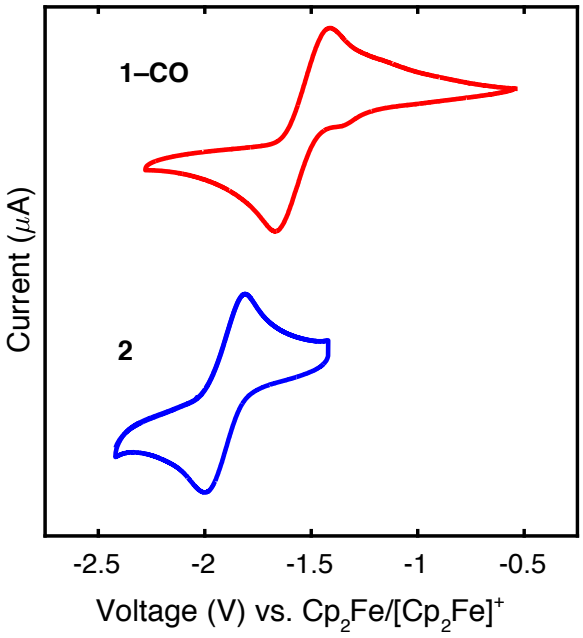

Figure S3.25: Cyclic voltammagrams of **1-CO** and **2** (2 mM) in *o*-DFB (0.2 M $[NPr_4][BAr^F{}_4]$) showing only the reversible 0/1+ redox couples. The **1-CO**/[**1-CO**]$^+$ redox couple is at –1.54 V and the **2**/[**2**]$^+$ redox couple is at –1.91 V vs. $Cp_2Fe/[Cp_2Fe]^+$.

J. Computational details

General Considerations

All calculations were carried out using version 4.1.2 of the ORCA program package[11] using the broken-symmetry (BS) approach to approximate the multireference electronic states of Fe–S clusters. BS solutions were constructed using the FlipSpin feature of ORCA.

Coordinates for non-H atoms in **1-CO**, [**1-CO**]$^+$, **2**, [**2**]$^+$, $[Fe_4S_4(NO)_4]$, and $[Fe_4S_4(NO)_4]^-$ were taken from X-ray crystallographic coordinates. To improve the efficiency of the calculations, the mesityl substituents on the IMes ligands were simplified to H. The positions of all H atoms were optimized.

Single point calculations for were performed using both the TPSS and TPSSh (10% Hartree-Fock) functionals.[12,13] For non-Fe atoms, the DKH-def2-TZVP basis set was used;[14] for Fe atoms, the CP(PPP) basis set was used[15] and the radial integration accuracy was increased (IntAcc 7). For all calculations, the DKH2 relativistic correction[16] and the general-purpose Coulomb fitting basis set SARC/J were used;[17] all basis sets were fully decontracted. Solid-state effects were approximated using the CPCM solvation model with an infinite dielectric.[18] Wavefunctions were optimized along a low-spin BS surface generated from an initial high-spin calculation by flipping the spins on two Fe sites. Calculations using the TPSSh functional were accelerated through the use of the RIJCOSX approximation with a fine auxiliary integration grid (GridX7).[19]

Gas-phase geometry optimizations of [**1-CO**]$^+$ were performed using the TPSSh and TPSS functionals. To reduce numerical instability during optimizations, we employed the larger def2-TZVPP basis, recontracted for use with the ZORA scalar-relativistic Hamiltonian, along with the SARC/J auxiliary basis on all atoms.[14,17,20] Grimme's atom-pairwise correction with Becke-Johnson damping (D3BJ) was included to account for the effects of dispersion.[21,22] All optimizations were conducted along $M_S = 1/2$ broken-symmetry surfaces,

generated from an initial high-spin reference by flipping the spins on the Fe–CO site along with an Fe–NHC site (the choice of the NHC-bound site is arbitrary). Alternative solutions in which the Fe–CO site is assigned majority-spin were found to be substantially higher in energy. Frequency calculations at the stationary points confirm that the structures obtained are true minima.

Mössbauer parameters were calculated from the crystallographically determined coordinates with relaxed hydrogen atoms. The Mössbauer parameters were computed using the "eprnmr" module of ORCA. To convert the calculated Fe core electron densities (in a.u.) to δ (in mm s^{-1}), the following equation was employed, $\delta(\text{mm s}^{-1}) = \alpha[\rho_0(\text{a.u.}) - C] + \beta$ using the calibration constants determined by Bjornsson and co-workers[23] ($\alpha = -0.176832008$; $\beta = 0.359641078$; $C = 23600$) for the TPSSh functional.

To analyze localized orbitals, we employed the intrinsic bond orbital (IBO) method developed by Knizia,[24] which applies Pipek-Mezey localization[25] in a basis of so-called intrinsic atomic orbitals (IAOs) and analyzed the resultant orbitals using a Löwdin population analysis. We tested this method using alternative localization methods (Foster-Boys[26] and Pipek-Mezey[25]) and population schemes (Löwdin, Mulliken, Hirshfeld in Multiwfn[27]) for **1-CO** and found that all methods afforded qualitatively the same electronic structures and valences (see Table S3.9).

1. Electronic structures of **2** and [**2**]$^{+}$

To establish a computational methodology for assigning the valences of the Fe centers in **1-CO** and [**1-CO**]$^{+}$, we initially performed single-point calculations using the crystallographic coordinates of **2** and [**2**]$^{+}$ (CSD deposition numbers 703093 and 1886878, respectively). For [**2**]$^{+}$, broken-symmetry solutions were calculated by flipping the spins on a pair of Fe centers to converge an $S = 1/2$ solution; for **2** the spins on a single Fe center were flipped to obtain an $S = 4$ solution. The calculated electronic structures showed little dependence on the functional chosen and showed good agreement with the canonical electronic structures of $[Fe_4S_4]^{+}$ clusters[28] (for [**2**]$^{+}$) and those of $S = 4$ $[Fe_4S_4]^{0}$ clusters[29] (for **2**). The qualitative electronic structures are depicted in Figure S3.26 and the valence assignments according to a Löwdin population analysis are summarized in Table S3.5. The valences on **2** and [**2**]$^{+}$ were calculated by assigning any Fe 3d orbital that was predominantly (>70 %) localized on a single Fe center entirely to that center and partitioning the remaining Fe 3d electrons between Fe centers according to a Löwdin population analysis; similar methods have previously been applied to assigning valences in Fe–S clusters.[23,30,31] The valences calculated in this manner align well with the canonical valence assignments (four Fe^{2+} centers in **2** and two Fe^{2+} and two $Fe^{2.5+}$ centers in [**2**]$^{+}$).

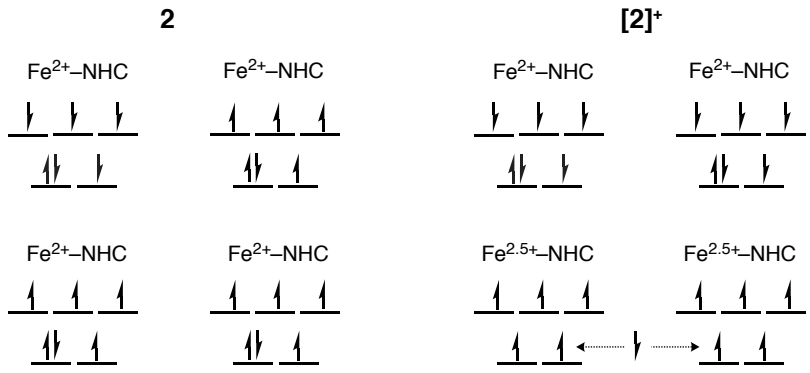

Figure S3.26: Qualitative molecular orbital diagrams for the electronic structure of **2** and [**2**]$^{+}$ calculated with both the TPSSh and TPSS functionals.

Table S3.5: Valence assignments of the Fe centers in **2** and [**2**]$^{+}$.

2	Fe1	Fe2	Fe3	Fe4
TPSSh	2.14+	2.00+	2.10+	2.08+
TPSS	2.14+	2.00+	2.09+	2.09+
[2]$^{+}$	Fe1	Fe2	Fe3	Fe4
TPSSh	2.54+	2.00+	2.00+	2.54+
TPSS	2.55+	2.04+	2.19+	2.53+

Note: Valence assignments are computed as follows: Orbitals >70% localized to a single Fe center were assigned entirely to that Fe center. Electrons delocalized between two Fe centers were partitioned between the metal centers according to a Löwdin population analysis.

2. Electronic structure of **1-CO**

Single-point calculations were performed on the structure obtained from the crystallographic coordinates of **1-CO** following the optimization of hydrogen atom positions using both the TPSS and TPSSh functionals. Broken symmetry solutions were constructed by flipping the spins on the Fe–CO site and an Fe–NHC site to converge an $S = 2$ solution; all 6 possible combinations of flipping the spins on two Fe were considered (TPSS functional) and the lowest energy determinant (BS01) was used for further calculations (Table S3.6). Very similar electronic structures were obtained using both functionals. A qualitative molecular

Table S3.6: Relative energies of BS-DFT determinants (flipping pairs of Fe spins, TPSS functional). Naming convention is BSij, where i,j are the indices of the Fe centers on which the spins were flipped. Fe0 is coordinated to CO; Fe1, Fe2, and Fe3 are coordinated to NHCs.

BS	Spin on Fe–CO	Rel. energy (kcal/mol)
BS01	minority	0
BS02	minority	+3.6
BS03	minority	+4.3
BS12	majority	+6.0
BS13[a]	minority	–
BS23	majority	+6.0

[a]: BS13 converged to the same electronic structure calculated for BS01

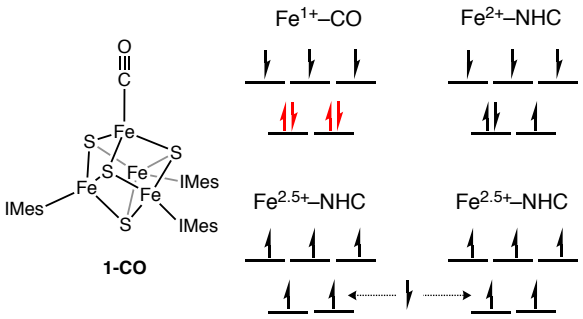

Figure S3.27: Qualitative molecular orbital diagrams for the electronic structure of **1-CO** calculated with both the TPSSh and TPSS functionals.

orbital diagram for the electronic structure of **1-CO** is shown in Figure S3.27 and the Löwdin population analyses of the localized molecular orbitals involved in Fe–CO π-backbonding are shown in Table S3.7. That all backbonding orbitals are primarily (>70%) composed of Fe 3d orbitals supports the assignment of the Fe–CO as Fe^{1+}–CO. The overall valence assignments of the four Fe centers are summarized Table S3.8, according to the same methodology used to assign the valences in **2** and $[\mathbf{2}]^+$ (*vide supra*). We used the computed electronic structure of **1-CO** to test multiple orbital localization methods and ensure that the electronic structure and valence assignments were not dependent on the method; all tested localization schemes and population analyses showed similar valence assignments (Table S3.9); we prefer IAO-IBO localization and Löwdin population analyses for consistency with previous work.[32–34]

Table S3.7: Orbital compositions for Fe–CO π-backbonding orbitals in **1-CO** calculated using the TPSS and TPSSh functionals.

1-CO	α		α		β		β	
Functional	Fe%	CO%	Fe%	CO%	Fe%	CO%	Fe%	CO%
TPSS	74.4	21.0	73.9	22.0	79.7	13.2	80.6	14.5
TPSSh	73.0	22.9	74.8	21.2	83.2	11.4	83.0	11.8

Table S3.8: Valence assignments of the four Fe centers in **1-CO**.

Functional	Fe–CO	Fe–NHC (1)	Fe–NHC (2)	Fe–NHC (3)
TPSSh	1.00+	2.00+	2.56+	2.53+
TPSS	1.42+	1.78+	2.55+	2.54+

Note: Valence assignments are computed as follows: Orbitals >70% localized to a single Fe center were assigned entirely to that Fe center. Electrons shared between Fe and CO (see Table S3.7) were assigned to the metal center. Electrons delocalized between two Fe centers were partitioned between the metal centers according to a Löwdin population analysis.

Table S3.9: Valence assignments of the four Fe centers in **1-CO** under different localization methods
(TPSS functional).

Loc. method	Pop. Analysis method	Fe–CO	Fe–NHC (1)	Fe–NHC (2)	Fe–NHC (3)
IAO-IBO	**Löwdin**	**1.42+**	**1.78+**	**2.55+**	**2.54+**
	Mulliken	1.40+	1.76+	2.54+	2.52+
	Hirshfeld	1.46+	1.79+	2.57+	2.56+
Pipek-Mezey	Löwdin	1.44+	1.72+	2.55+	2.54+
	Mulliken	1.41+	1.69+	2.52+	2.51+
	Hirshfeld	1.48+	1.74+	2.57+	2.57+
Foster-Boys	Löwdin	1.48+	1.74+	2.56+	2.55+
	Mulliken	1.43+	1.69+	2.51+	2.53+
	Hirshfeld	1.51+	1.75+	2.58+	2.57+

Note: Valence assignments are computed as follows: Orbitals >70% localized to a single Fe center were assigned entirely to that Fe center. Electrons shared between Fe and CO (see Table S3.7) were assigned to the metal center. Electrons delocalized between two Fe centers were partitioned between the metal centers according to the population analysis scheme. Bolded methodology is used for later calculations.

3. Electronic structure of [**1-CO**]$^+$

Broken symmetry solutions were constructed by flipping the spins on the Fe–CO site and an Fe–NHC site to converge an $S = 1/2$ solution; all 6 possible combinations of flipping the spins on two Fe centers were considered (TPSS functional) and the lowest energy determinant (BS01) was used for further calculations (Table S3.10). Unlike for **1-CO**,

Table S3.10: Relative energies of BS-DFT determinants (flipping pairs of Fe spins, TPSS functional). Naming convention is BSij, where i,j are the the indices of the Fe centers on which the spins were flipped. Fe0 is coordinated to CO; Fe1, Fe2, and Fe3 are coordinated to NHCs.

BS	Spin on Fe–CO	Rel. energy (kcal/mol)
BS01	minority	0
BS02	minority	+1.3
BS03	minority	+0.97
BS12	majority	+3.0
BS13	majority	+2.9
BS23	majority	+2.5

different electronic structures were obtained from calculations on [**1-CO**]$^+$ using the TPSS and TPSSh functionals. As described in the main text, the electronic structure obtained using the TPSSh functional is quite similar to that obtained for **1-CO**, except that one of the Fe-CO π-backbonding electrons is delocalized onto the spin-aligned Fe site (Figure S3.28, left). On the other hand, the electronic structure obtained using the TPSS functional has all four Fe–CO π-backbonding electrons localized on the Fe–CO site with one of the remaining electrons instead delocalized onto an adjacent Fe center (Figure S3.28, right). The Löwdin population analyses of the seven orbitals with a significant contribution from the Fe–CO are summarized in table S3.11 and the overall valence assignments are shown in table S3.12. We note that despite the difference in electronic structure, the valence assignments of the individual Fe centers in [**1-CO**]$^+$ are relatively insensitive to the functional chosen, suggesting that the

different electronic structures do not represent significantly different distributions of charge between the Fe centers and instead represent different ways to achieve low-valent character at the Fe–CO unit.

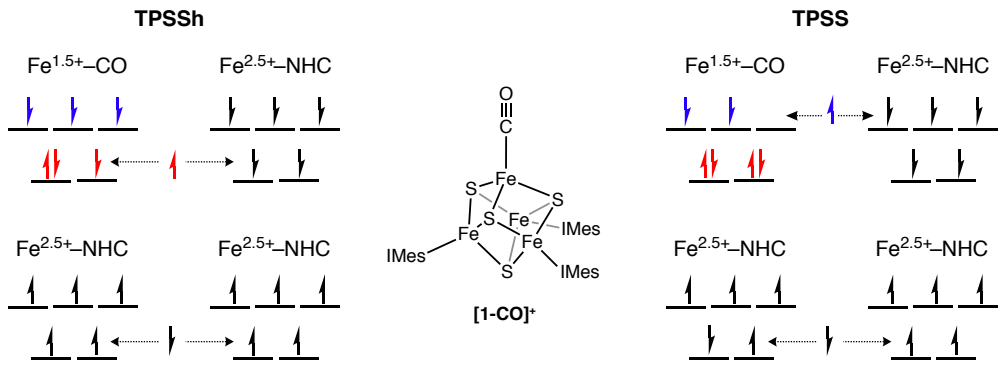

Figure S3.28: Qualitative molecular orbital diagrams for the electronic structure of [**1-CO**]$^+$ calculated using the TPSSh and TPSS functionals.

Table S3.11: Orbitals compositions for Fe–CO π-backbonding orbitals in [**1-CO**]$^+$ calculated using the TPSS and TPSSh functionals.

[**1-CO**]$^+$	α		α		β		β	
Functional	Fe%	CO%	Fe%	CO%	Fe%	CO%	Fe%	CO%
TPSS	48.0	10.1	72.8	20.0	86.0	8.1	82.1	12.5
TPSSh	75.0	16.9	71.1	15.8	79.5	14.2	77.0	13.1

Table S3.12: Valence assignments of the four Fe centers in [**1-CO**]$^+$.

Functional	Fe–CO	Fe–NHC (1)	Fe–NHC (2)	Fe–NHC (3)
TPSSh	1.42+	2.59+	2.53+	2.53+
TPSS	1.54+	2.61+	2.45+	2.65+

Note: Valence assignments are computed as follows: Orbitals >70% localized to a single Fe center were assigned entirely to that Fe center. Electrons shared between Fe and CO (see Table S3.11) were assigned to the metal center. Electrons delocalized between two Fe centers were partitioned between the metal centers according to a Löwdin population analysis.

4. Optimized geometries of [**1-CO**]$^+$

Given the functional dependence of the electronic structure as described above, we conducted gas-phase geometry optimizations on [**1-CO**]$^+$ using the TPSS and TPSSh functionals to further investigate its electronic structure.

The geometry of the [Fe_4S_4] core in [**1-CO**]$^+$ is unusual among [Fe_4S_4]$^+$ clusters. The cores of [Fe_4S_4]$^+$ clusters most commonly exhibit a tetragonal distortion away from idealized T_d symmetry, resulting in an approximately D_{2d} core symmetry arising from a compression along an S_4 axis passing through two parallel Fe_2S_2 faces of the cube (a pattern of 4 short and 8 long Fe–S bonds).[10] The solid-state structure of [**1-CO**]$^+$ does not exhibit such a distortion; rather, it features an approximate C_{3v} core symmetry with the C_3 axis passing through the Fe–CO vector. The three shortest Fe–S bonds (2.198(6) Å) connect the CO-bound site to the remaining Fe ions, while the remaining nine, long Fe–S bonds lie within the narrow range of 2.216 to 2.236 Å.

Geometry optimizations using the TPSSh functional invariably gave a core structure with long Fe–S bonds compared to the crystallographic structure of [**1-CO**]$^+$ and a tetragonally-compressed, approximately D_{2d} symmetric core (Table S3.10). The Fe–CO distance in this structure is 0.1 Å longer than observed crystallographically with a correspondingly high C–O stretching frequency of 2018.6 cm^{-1} (scaled by 0.9686, found by

Table S3.13: Comparison of crystallographic and optimized geometries of [**1-CO**]$^+$.

Parameter (Å)	XRD	TPSS	TPSSh
Fe–CO	1.789	1.777	1.891
Fe–C (avg., NHC sites)	2.030	1.929	2.043
Fe–S (avg, CO site)	2.198	2.147	2.281
Fe–S (avg. NHC sites)	2.225	2.156	2.283
Fe–Fe (avg.)	2.639	2.477	2.617
Mean absolute deviation	–	0.08	0.06

interpolating between the fundamental scaling factors for TPSS//def2-TZVPP and TPSS0//def2-TZVPP.[35])

Using the TPSS functional, a structure with a relatively compressed inorganic core was obtained (Table S3.13). This structure does not exhibit a discernable core distortion, with each Fe–S distance lying in the narrow range of 2.134 to 2.185 Å; these short Fe–S bond distances are more similar to the crystallographically determined Fe–S bond distances than those calculated using the TPSSh functional. For the TPSS optimized structure, a C–O stretching frequency of 1950.2 cm^{-1} was calculated (here, a scaling factor of 0.9810 was taken from ref. 35), which more closely aligns with the experimental value (1902 cm^{-1}) than that calculated from the TPSSh solution. On the basis that the TPSS-optimized geometry better captures the experimental geometry of [**1-CO**]$^+$ (in terms of short Fe–S bond lengths and non-D_{2d} core symmetry) and the extent of C–O activation in [**1-CO**]$^+$, we tentatively favor the electronic structure calculated above using the TPSS functional, in which one of the non-Fe–CO backbonding electrons is delocalized to achieve approximately an $Fe^{1.5+}$ valence.

5. Mössbauer parameters

Using the method reported by Bjornsson and coworkers,[23] we calculated the Mössbauer parameters for **1-CO,** [**1-CO**]$^+$, **2** and [**2**]$^+$ using the TPSSh functional and crystallographic coordinates (Table S3.14). The calculated Mössbauer parameters show good agreement with the experimentally observed parameters and replicate both the large quadrupole splitting and low isomer shift of the Fe site bound to CO.

Table S3.14: Calculated Mössbauer parameters for **1-CO**, [**1-CO**]$^+$, **2**, and [**2**]$^+$.

	Fe site	Exp.		Calc.	
		δ (mm s^{-1})	$\lvert\Delta E_Q\rvert$ (mm s^{-1})	δ (mm s^{-1})	$\lvert\Delta E_Q\rvert$ (mm s^{-1})
1-CO	Fe–CO	0.32	2.408	0.33	2.664
	Fe–NHC	0.49	1.253	0.47	1.205
	Fe–NHC	0.49	0.951	0.46	1.106
	Fe–NHC	0.47	1.814	0.44	1.038
[**1-CO**]$^+$	Fe–CO	0.28	2.069	0.28	2.603
	Fe–NHC	0.36	1.268	0.31	1.155
	Fe–NHC	0.36	1.268	0.32	1.387
	Fe–NHC	0.36	1.268	0.32	1.403
2	Fe1	0.62	1.596	0.58	1.685
	Fe2	0.58	3.091	0.52	3.153
	Fe3	0.62	1.596	0.58	1.379
	Fe4	0.62	1.596	0.60	1.627
[**2**]$^+$	Fe1	0.48	1.342	0.41	1.685
	Fe2	0.48	1.342	0.49	3.237
	Fe3	0.48	1.342	0.48	2.584
	Fe4	0.48	1.342	0.41	1.030

Note: in the spectra of [**1-CO**]$^+$ and [**2**]$^+$, the Fe–NHC sites are observed as a single quadrupole doublet representing the average of the three and four sites, respectively.

6. Calculated electronic structures of $[(MeS)_3Fe_4S_4CO]^{3-}$

To support the proposal that thiolate-ligated $[Fe_4S_4]$ clusters bound to CO would contain low valent Fe centers, we calculated localized molecular orbitals for an $[Fe_4S_4]^0$ cluster supported by three methyl thiolate ligands and one carbon monoxide ligand. We limited this study to the $[Fe_4S_4]^0$ state instead of the $[Fe_4S_4]^+$ state because of the complicated dependence of the electronic structure of $[\mathbf{1\text{-}CO}]^+$ on the functional used (*vide supra*). Geometry optimizations were performed using the TPSS functional on three spin surfaces, with the Fe–CO in either the majority or minority spin. These three spin states were chosen because they are plausible for all-ferrous $[Fe_4S_4]^0$ clusters: The $S = 2$ spin state is observed for **1-CO**, the $S = 4$ spin state is observed for **2**, and the $S = 0$ spin state has been proposed to be present in the $[Fe_4S_4]^0$ cluster in the Fe protein of nitrogenase.[36] The results are summarized in Table S3.15. The localized orbitals for the lower energy electronic configuration in each spin state were then calculated using the TPSSh functional to ensure the results were not functional dependent. Although the precise electronic structures of each spin state differed, in all optimized geometries the Fe–CO was found to adopt a low-valent electronic configuration in which the CO π-backbonding orbitals were fully occupied (4 electrons) and with similar calculated charges on the Fe–CO site as those found for **1-CO** (Table S3.8). The electronic structure of the $S = 2$, Fe–CO minority spin state (same as the calculated electronic structure of **1-CO**) is depicted pictorially in Figure S3.29. This supports the proposal that if Fe–S clusters bound to CO and thiolate ligands were synthesized, they would contain low-valent Fe sites.

Table S3.15: Valence assignments of the four Fe centers in $[(MeS)_3Fe_4S_4CO]^{3-}$ according to spin state. Fe1 is bound to CO, Fe2–Fe4 are bound to thiolates.

Spin state	Fun.	Fe–CO spin	Rel. energy (kcal/mol)	Fe1	Fe2	Fe3	Fe4
S = 2	TPSS	majority	0	1.31+	2.53+	2.52+	1.95+
		minority	+0.69	1.44+	2.60+	2.13+	2.16+
	TPSSh	majority	–	1.00+	2.86+	1.85+	2.41+
		minority[a]	–	1.32+	2.00+	2.40+	2.45+
S = 4	TPSS	majority	+14.6	1.00+	2.00+	2.53+	2.52+
		minority	+0.30	1.34+	2.15+	2.30+	2.50+
	TPSSh	minority	–	1.00+	2.28+	2.20+	2.73+
S = 0	TPSS	majority	+6.21	0.77+	2.43+	2.46+	2.49+
		minority	+6.26	0.77+	2.43+	2.46+	2.49+
	TPSSh	majority	–	1.00+	3.00+	2.00+	2.00+

Note: Valence assignments are computed as follows: Orbitals >70% localized to a single Fe center were assigned entirely to that Fe center. Electrons shared between Fe and CO were assigned to the metal center. Electrons delocalized between two Fe centers were partitioned between the metal centers according to a Löwdin population analysis. [a] Corresponds to the electronic structure calculated for **1-CO**.

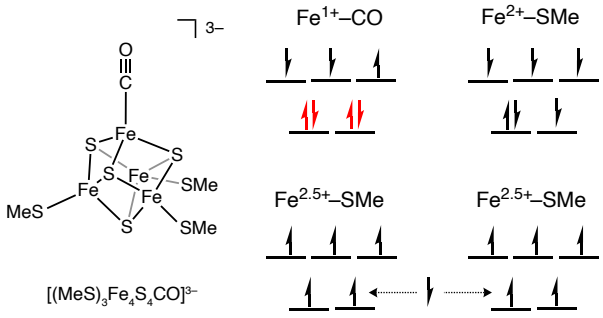

Figure S3.29: Qualitative molecular orbital diagrams for the electronic structure of $[(MeS)_3Fe_4S_4CO]^{3-}$ calculated with the TPSSh functional for an $S = 2$ spin state with the Fe–CO in the minority spin.

7. Assignment of Fe(III)–[^{3}NO]$^-$ in $[Fe_4S_4(NO)_4]^{0/-}$

Atomic coordinates for $[Fe_4S_4(NO)_4]$ and $[Fe_4S_4(NO)_4]^-$ were obtained from the CSD (deposition codes 1705878 and 110095, respectively). Cluster $[Fe_4S_4(NO)_4]$ can be considered as formally composed of four $\{Fe–NO\}^7$ units and $[Fe_4S_4(NO)_4]^-$ as composed of two $\{Fe–NO\}^7$ units and two $\{Fe–NO\}^{7.5}$ units. We calculated the electronic structure of the clusters using both the TPSS and TPSSh functionals.

Calculations using the TPSSh functional revealed five localized orbitals on each Fe center with primarily Fe 3d character. Two additional orbitals localized on NO but with significant Fe character could also be found. A Löwdin population analysis of the four orbitals with Fe–NO character on each Fe center shows two orbitals with ~80% Fe and ~15% NO character and two orbitals with ~30% Fe and ~65% NO character. Precise orbitals compositions are provided in Table S3.16. That two of the Fe–NO bonding orbitals are primarily localized on NO supports assignment of the $\{Fe–NO\}^7$ units as Fe(III)–[^{3}NO]$^-$ instead of Fe(I)–[NO]$^+$. Partitioning the Fe–NO orbitals according to their parentage and

Table S3.16: Orbitals compositions for Fe–NO orbitals in $[Fe_4S_4(NO)_4]$ calculated using the TPSSh functional.

$[Fe_4S_4(NO)_4]$ TPSSh	α		α		β		β		Ox. state[1]
Fe center	Fe %	NO %	Fe %	NO %	Fe %	NO %	Fe %	NO %	
Fe 1 ($\{Fe–NO\}^7$)	35.7	61.8	37.7	60.3	83.1	13.4	82.7	14.2	2.60+
Fe 2 ($\{Fe–NO\}^7$)	37.5	59.4	39.6	58.4	83.3	13.1	82.5	14.2	2.57+
Fe 3 ($\{Fe–NO\}^7$)	83.3	13.4	82.6	14.3	37.5	59.5	39.3	58.7	2.57+
Fe 4 ($\{Fe–NO\}^7$)	83.4	13.2	82.7	14.1	36.8	60.6	38.5	59.4	2.59+

[1]Oxidation states were computed by partitioning the orbitals in the table according to their parentage and assigning the remaining Fe 3d orbitals entirely to the Fe center they were localized on.

assigning the remaining Fe 3d orbitals as entirely localized on Fe gives a formal charge of $Fe^{2.58+}$ for all four Fe centers.

Calculations using the TPSS functional result in a different distribution of the π-backbonding electrons across the four π-symmetric orbitals, but very similar oxidation state assignments for the Fe centers ($Fe^{2.56+}$, Table S3.17).

Table S3.17: Orbitals compositions for Fe–NO orbitals in $[Fe_4S_4(NO)_4]$ calculated using the TPSS functional.

$[Fe_4S_4(NO)_4]$ TPSS	α		α		β		β		Ox. state[1]
Fe center	Fe %	NO %	Fe %	NO %	Fe %	NO %	Fe %	NO %	
Fe 1 ({Fe–NO}^{7})	50.4	47.1	49.3	47.1	69.1	27	70.9	25.2	2.60 +
Fe 2 ({Fe–NO}^{7})	50.5	46.9	51.9	45.5	71.4	24.2	72.3	23.6	2.54 +
Fe 3 ({Fe–NO}^{7})	71.4	24.7	70.1	26.1	51.5	44.9	51.8	45.9	2.55 +
Fe 4 ({Fe–NO}^{7})	71.0	24.7	71.8	24.1	49.7	48	51.2	44.6	2.56 +

[1]Oxidation states were computed by partitioning the orbitals in the table according to their parentage and assigning the remaining Fe 3d orbitals entirely to the Fe center they were localized on.

$[Fe_4S_4(NO)_4]^-$ has one additional electron, such that it is formally composed of two {Fe–NO}^{7} and two {Fe–NO}$^{7.5}$ centers. Calculations on this cluster with both the TPSS and TPSSh functionals revealed very similar formal oxidation states for the {Fe–NO}^{7} centers (*i.e.*, approximately $Fe^{2.6+}$). The additional electron is delocalized between two spin-aligned Fe centers; the oxidation states of the two more reduced Fe centers are approximately $Fe^{2.25+}$.

Taken together, the calculations presented here and those previously reported for Roussin's black salt[14] support the description of {Fe–NO}^{7} centers as Fe(III)–$[^3NO]^-$ rather than Fe(I)–$[NO]^+$. Therefore, $[Fe_4S_4(NO)_4]$ clusters should not be considered to contain low valent Fe centers.

K. Crystallographic details

1-CO: The structure contained solvent accessible voids in which the solvent could not be satisfactorily modeled. SQUEEZE[37] was used to account for the contributions of the disordered solvent to the diffraction data. Two reflections were omitted due to interference from the beamstop.

[1-CO]$^+$: Disorder was present in PhF and pentane residues in the lattice and in the -CF_3 groups of the [BAr^F_4] anion. The disorder was modeled using similarity restraints on 1-2 and 1-3 distances and displacement parameters and rigid bond restraints. Two B-level alerts in the CheckCIF report arise due to the lattice solvent and -CF_3 disorder.

References

(1) Brown, A. C.; Suess, D. L. M. Controlling Substrate Binding to Fe_4S_4 Clusters through Remote Steric Effects. *Inorg. Chem.* **2019**, *58* (8), 5273–5280.

(2) Brown, A. C.; Suess, D. L. M. Reversible Formation of Alkyl Radicals at [Fe_4S_4] Clusters and Its Implications for Selectivity in Radical SAM Enzymes. *J. Am. Chem. Soc.* **2020**, *142* (33), 14240–14248.

(3) Deng, L.; Holm, R. H. Stabilization of Fully Reduced Iron-Sulfur Clusters by Carbene Ligation: The $[Fe_nS_n]^0$ Oxidation Levels (n = 4, 8). *J. Am. Chem. Soc.* **2008**, *130* (30), 9878–9886.

(4) Peters, J. C.; Johnson, A. R.; Odom, A. L.; Wanandi, P. W.; Davis, W. M.; Cummins, C. C. Assembly of Molybdenum/Titanium μ-Oxo Complexes via Radical Alkoxide C-O Cleavage. *J. Am. Chem. Soc.* **1996**, *118* (42), 10175–10188.

(5) Yakelis, N. A.; Bergman, R. G. Safe Preparation and Purification of Sodium Tetrakis[(3,5-Trifluoromethyl) Phenyl]Borate ($NaBArF_{24}$): Reliable and Sensitive Analysis of Water in Solutions of Fluorinated Tetraarylborates. *Organometallics* **2005**, *24* (14), 3579–3581.

(6) Smallcombe, S. H.; Patt, S. L.; Keifer, P. A. WET Solvent Suppression and Its Applications to LC NMR and High-Resolution NMR Spectroscopy. *J. Magn. Reson. Ser. A* **1995**, *117* (2), 295–303.

(7) Stoll, S.; Schweiger, A. EasySpin, a Comprehensive Software Package for Spectral Simulation and Analysis in EPR. *J. Magn. Reson.* **2006**, *178* (1), 42–55.

(8) Prisecaru, I. WMOSS4 Mössbauer Spectral Analysis Software, www.wmoss.org.

(9) Hübschle, C. B.; Sheldrick, G. M.; Dittrich, B. ShelXle: A Qt Graphical User Interface for SHELXL. *J. Appl. Crystallogr.* **2011**, *44* (6), 1281–1284.

(10) Venkateswara Rao, P.; Holm, R. H. Synthetic Analogues of the Active Sites of Iron−Sulfur Proteins. *Chem. Rev.* **2004**, *104* (2), 527–560.

(11) Neese, F. The ORCA Program System. *Wiley Interdiscip. Rev. Comput. Mol. Sci.* **2012**, *2* (1), 73–78.

(12) Tao, J.; Perdew, J. P.; Staroverov, V. N.; Scuseria, G. E. Climbing the Density Functional Ladder: Nonempirical Meta–Generalized Gradient Approximation Designed for Molecules and Solids. *Phys. Rev. Lett.* **2003**, *91* (14), 3–6.

(13) Staroverov, V. N.; Scuseria, G. E.; Tao, J.; Perdew, J. P. Comparative Assessment of a New Nonempirical Density Functional: Molecules and Hydrogen-Bonded Complexes. *J. Chem. Phys.* **2003**, *119* (23), 12129–12137.

(14) Pantazis, D. A.; Chen, X. Y.; Landis, C. R.; Neese, F. All-Electron Scalar Relativistic Basis Sets for Third-Row Transition Metal Atoms. *J. Chem. Theory Comput.* **2008**, *4* (6), 908–919.

(15) Neese, F. Prediction and Interpretation of the ^{57}Fe Isomer Shift in Mössbauer Spectra by Density Functional Theory. *Inorganica Chim. Acta* **2002**, *337* (1), 181–192.

(16) Reiher, M. Relativistic Douglas-Kroll-Hess Theory. *Wiley Interdiscip. Rev. Comput. Mol. Sci.* **2012**, *2* (1), 139–149.

(17) Weigend, F. Accurate Coulomb-Fitting Basis Sets for H to Rn. *Phys. Chem. Chem. Phys.* **2006**, *8* (9), 1057–1065.

(18) Barone, V.; Cossi, M. Conductor Solvent Model. *J. Phys. Chem. A* **1998**, *102* (97), 1995–2001.

(19) Neese, F.; Wennmohs, F.; Hansen, A.; Becker, U. Efficient, Approximate and Parallel Hartree-Fock and Hybrid DFT Calculations. A “Chain-of-Spheres” Algorithm for the Hartree-Fock Exchange. *Chem. Phys.* **2009**, *356* (1–3), 98–109.

(20) Van Wüllen, C. Molecular Density Functional Calculations in the Regular Relativistic

Approximation: Method, Application to Coinage Metal Diatomics, Hydrides, Fluorides and Chlorides, and Comparison with First-Order Relativistic Calculations. *J. Chem. Phys.* **1998**, *109* (2), 392–399.
(21) Grimme, S.; Antony, J.; Ehrlich, S.; Krieg, H. A Consistent and Accurate Ab Initio Parametrization of Density Functional Dispersion Correction (DFT-D) for the 94 Elements H-Pu. *J. Chem. Phys.* **2010**, *132* (15).
(22) Grimme, S.; Ehrlich, S.; Goerigk, L. Effect of the Damping Function in Dispersion Corrected Density Functional Theory. *J. Comput. Chem.* **2011**, *32*, 1456–1465.
(23) Bjornsson, R.; Neese, F.; DeBeer, S. Revisiting the Mössbauer Isomer Shifts of the FeMoco Cluster of Nitrogenase and the Cofactor Charge. *Inorg. Chem.* **2017**, *56* (3), 1470–1477.
(24) Knizia, G. Intrinsic Atomic Orbitals: An Unbiased Bridge between Quantum Theory and Chemical Concepts. *J. Chem. Theory Comput.* **2013**, *9* (11), 4834–4843.
(25) Pipek, J.; Mezey, P. G. A Fast Intrinsic Localization Procedure Applicable for Ab Initio and Semiempirical Linear Combination of Atomic Orbital Wave Functions. *J. Chem. Phys.* **1989**, *90* (9), 4916–4926.
(26) Foster, J. M.; Boys, S. F. Canonical Configurational Interaction Procedure. *Rev. Mod. Phys.* **1960**, *32* (2), 300–302.
(27) Lu, T.; Chen, F. Multiwfn: A Multifunctional Wavefunction Analyzer. *J. Comput. Chem.* **2012**, *33* (5), 580–592.
(28) Noodleman, L.; Peng, C. Y.; Case, D. A.; Mouesca, J. M. Orbital Interactions, Electron Delocalization and Spin Coupling in Iron-Sulfur Clusters. *Coord. Chem. Rev.* **1995**, *144* (C), 199–244.
(29) Chakrabarti, M.; Deng, L.; Holm, R. H.; Münck, E.; Bominaar, E. L. Mössbauer, Electron Paramagnetic Resonance, and Theoretical Studies of a Carbene-Based All-Ferrous Fe_4S_4 Cluster: Electronic Origin and Structural Identification of the Unique Spectroscopic Site. *Inorg. Chem.* **2009**, *48* (7), 2735–2747.
(30) Bjornsson, R.; Lima, F. A.; Spatzal, T.; Weyhermüller, T.; Glatzel, P.; Bill, E.; Einsle, O.; Neese, F.; Debeer, S. Identification of a Spin-Coupled Mo(III) in the Nitrogenase Iron-Molybdenum Cofactor. *Chem. Sci.* **2014**, *5* (8), 3096–3103.
(31) Rees, J. A.; Bjornsson, R.; Kowalska, J. K.; Lima, F. A.; Schlesier, J.; Sippel, D.; Weyhermüller, T.; Einsle, O.; Kovacs, J. A.; DeBeer, S. Comparative Electronic Structures of Nitrogenase FeMoco and FeVco. *Dalton Trans.* **2017**, *46* (8), 2445–2455.
(32) Ye, M.; Thompson, N. B.; Brown, A. C.; Suess, D. L. M. A Synthetic Model of Enzymatic $[Fe_4S_4]$-Alkyl Intermediates. *J. Am. Chem. Soc.* **2019**, *141* (34), 13330–13335.
(33) McSkimming, A.; Sridharan, A.; Thompson, N. B.; Müller, P.; Suess, D. L. M. An $[Fe_4S_4]^{3+}$-Alkyl Cluster Stabilized by an Expanded Scorpionate Ligand. *J. Am. Chem. Soc.* **2020**, *142* (33), 14314–14323.
(34) Sridharan, A.; Brown, A. C.; Suess, D. L. M. A Terminal Imido Complex of an Iron–Sulfur Cluster. *Angew. Chem. Int. Ed.* **2021**, *60* (23), 12802–12806.
(35) Kesharwani, M. K.; Brauer, B.; Martin, J. M. L. Frequency and Zero-Point Vibrational Energy Scale Factors for Double-Hybrid Density Functionals (and Other Selected Methods): Can Anharmonic Force Fields Be Avoided? *J. Phys. Chem. A* **2015**, *119* (9), 1701–1714.
(36) Lowery, T. J.; Wilson, P. E.; Zhang, B.; Bunker, J.; Harrison, R. G.; Nyborg, A. C.; Thiriot, D.; Watt, G. D. Flavodoxin Hydroquinone Reduces *Azotobacter Vinelandii* Fe Protein to the All-Ferrous Redox State with a $S = 0$ Spin State. *Proc. Natl. Acad. Sci. U.S.A.* **2006**, *103* (46), 17131–17136.

(37) Spek, A. L. PLATON SQUEEZE: A Tool for the Calculation of the Disordered Solvent Contribution to the Calculated Structure Factors. *Acta Crystallogr. Sect. C Struct. Chem.* **2015**, *71*, 9–18.

Chapter 4. A Role for Spin Isomerism in Small Molecule Activation at Iron-Sulfur Clusters

Introduction

Although Earth's atmosphere contains vast amounts of nitrogen, most is in its chemically inert form, N_2, which cannot be directly incorporated into biomass. Nature's solution to this problem is to fix N_2 to NH_3; the only known biological catalysts for this reaction are nitrogenases, all of which feature Fe–S clusters in their active sites.[1–4] Additionally, it has been shown that both biogenic and synthetic Fe–S clusters reduce the isoelectronic diatomic, CO, to hydrocarbons.[5–17] The ability of Fe–S clusters to bind and activate these π-acidic ligands is perhaps surprising because the local valences and spin states of the individual Fe centers—typically high-spin, between Fe^{2+} and Fe^{3+}—don't allow for strong Fe–L π-backbonding;[18–20] compared with low-valent Fe (*i.e.*, Fe^{1+} or more reduced), the Fe 3d orbitals in Fe^{2+}/Fe^{3+} are relatively contracted, and high-spin configurations prohibit full occupation of the two backbonding orbitals, resulting in Fe centers with limited π-basicity (Figure 4.1A). As such, the electronic basis for activation of π-acidic ligands at Fe–S clusters and related metalloclusters is not fully understood.

We recently showed that one way that an Fe–S cluster can engage in strong π-backbonding is by adopting electronic configurations in which the substrate-bound Fe site is locally low-valent.[21] Specifically, spectroscopic and computational analysis showed that the formally all-ferrous, $[Fe_4S_4]^0$ cluster, $(IMes)_3Fe_4S_4$-CO (**1-CO**), is in fact better described as one in which the Fe_{CO} site has low-valent, Fe^{1+} character, with the other three sites being comprised of $1xFe^{2+}$ and $2xFe^{2.5+}$ ions. Thus, the $Fe^{1+}{}_{CO}$ site is generated by an intramolecular valence disproportionation whereby two $Fe^{2+}{}_{IMes}$ sites become two $Fe^{2.5+}{}_{IMes}$ sites. Such a configuration at the $Fe^{1+}{}_{CO}$ site gives it the appropriate number of valence electrons (d^7) for strong backbonding with the CO ligand, and thereby accounts for the high degree of C–O bond weakening, as indicated by the low ν(C–O)

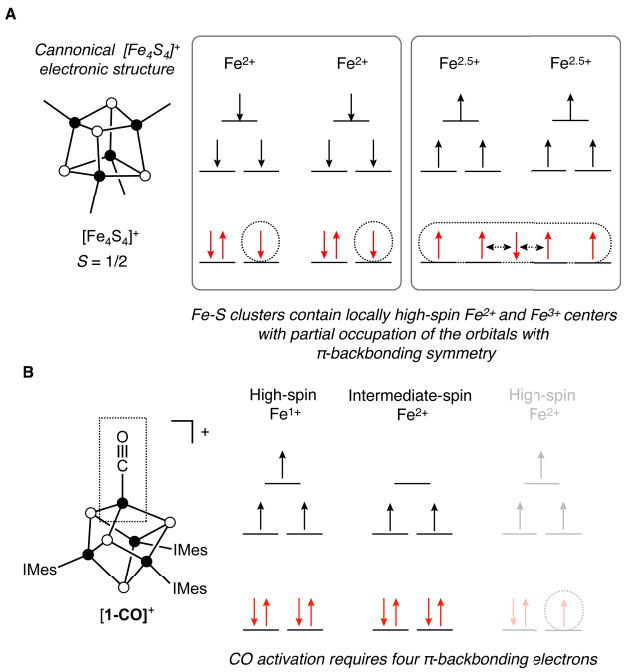

Figure 4.1. A) Cannonical electronic structure $[Fe_4S_4]^+$ clusters consisting of two Fe^{2+} centers antiferromagnetically coupled to a mixed-valent, double-exchange coupled, $Fe^{2.5+}/Fe^{2.5+}$ pair. The Fe sites in the cluster have incompletely occupied π-backbonding orbitals. B) Binding and activation of CO requires a π-basic Fe site with four electrons in π-backbonding orbitals.

energy (1832 cm^{-1}). The oxidized congener, $[\mathbf{1\text{-}CO}]^+$, likewise displayed a low ν(C–O) (1902 cm^{-1}, similar to that of the mononuclear high-spin Fe^{1+} complexes) with Fe_{IMes} sites that appear to be oxidized as demonstrated by their low Mössbauer isomer shifts. BS-DFT calculations on both charge states likewise supported ground state electronic structures containing a π-basic Fe site with four electrons in orbitals involved in π-backbonding.

In the present work, we demonstrate a mechanism through which Fe–S cluster states that can activate π-acidic ligands may be accessed: spin isomerism,[22] which here refers to the reconfiguration of spin within a cluster without changing the individual site valences or total spin quantum number, *S*. Specifically, we show through combined experimental and computational analysis that two spin isomers are accessible for $S = 1/2$ $[Fe_4S_4]^+$ clusters: one characterized by the typical electronic structure of $[Fe_4S_4]^+$ clusters (Fig 4.1A), and the other by an atypical electronic

structure that allows for maximal π-bonding with a π-acidic ligand. The consequences of these findings are discussed in the context of small molecule activation at Fe–S clusters.

The design of the current study arose from our efforts to understand the properties of [**1-CO**]$^{+}$ and how they differ from those of typical [Fe_4S_4]$^{1+}$ clusters, such as the isoelectronic cluster [**1-CN^{t}Bu**]$^{+}$.[23] Notably, the geometric structure of [Fe_4S_4] core of [**1-CN^{t}Bu**]$^{+}$ is similar to that of other members of the [**1-L**]$^{+}$ family[23,24] (and synthetic [Fe_4S_4]$^{+}$ clusters more generally[25]), possessing a tetragonally compressed core with eight long distances averaging 2.28(2) Å and four short distances averaging 2.237(8) Å. This structure is markedly different from that of [**1-CO**]$^{+}$, which shows very short Fe–S distances (2.219(3) Å avg.) and no compression axis. The electronic origin of the unusual structure of [**1-CO**]$^{+}$ was not resolved in our prior study (*e.g.*, whether it was a consequence of configurations featuring a low-valent Fe^{1+}_{CO} site, or if it had some other origin). To investigate this matter, we sought a ligand that could be rationally modified to access clusters that would span both structure types. We surmised that clusters bound by electronically tunable arylisocyanide (CNAr) ligands ([**1-CNAr**]$^{+}$)[26–30] could serve this purpose, and, moreover, that studies of this series would identify the origin of the unusual (and unresolved) electronic structure of [**1-CO**]$^{+}$.[21] We herein report this study and its implications for understanding the activation of π-acids at Fe–S clusters.

Results

1. Synthesis and IR Spectroscopic Characterization

Starting from the previously reported cluster [**1-OEt$_2$**]$^+$,[23,24] ten members of the [**1-CNAr**]$^+$ series were synthesized via displacement of Et_2O at the unique Fe site by an electronically diverse group of CNAr ligands (Scheme 4.1). The Ar groups range from the electron-donating 4-NMe_2 group to electron-withdrawing 3,5-$(CF_3)_2$ groups. All clusters were isolated as dark-brown, crystalline solids and have a well-isolated doublet ground spin state as indicated by their EPR spectra (see SI). The EPR spectra of all members of the series are rhombic and very similar to one another; g_{avg} has a very small range and generally increases with as the CNAr group becomes more electron withdrawing (g_{avg} = 2.033 for [**1-CNAr$^{4\text{-NMe2}}$**]$^+$ to g_{avg} = 2.051 [**1-CNAr$^{3,5\text{-(CF3)2}}$**]$^+$, Fig. S4.25 through S4.34).

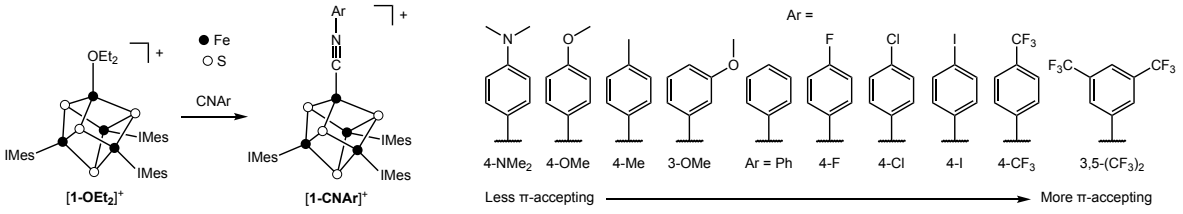

Scheme 4.1. Synthesis of the [**1-CNAr**]$^+$ series. IMes = 3,5-dimesitylimidazol-2-ylidine; Ar^F = 3,5-bis(trifluoromethyl)phenyl.

We initially obtained crystallographic characterization of [**1-CNAr$^{4\text{-NMe2}}$**]$^+$ and [**1-CNAr$^{3,5\text{-(CF3)2}}$**]$^+$ to compare the structures to the crystal structures of [**1-CN^{t}Bu**]$^+$[23] and [**1-CO**]$^+$[21] and ensure that the electronic range spanned by the aryl isocyanide ligands was sufficient to capture the structural differences between these two endpoints (Figure 4.2A and 4.2B), particulary since aryl isocyanides are stronger σ-donors and weaker π-acids than CO.[27,31–33] Indeed, close inspection of the crystal structures reveals that the $[Fe_4S_4]^+$ cores of the two extremes of the [**1-CNAr**]$^+$ series

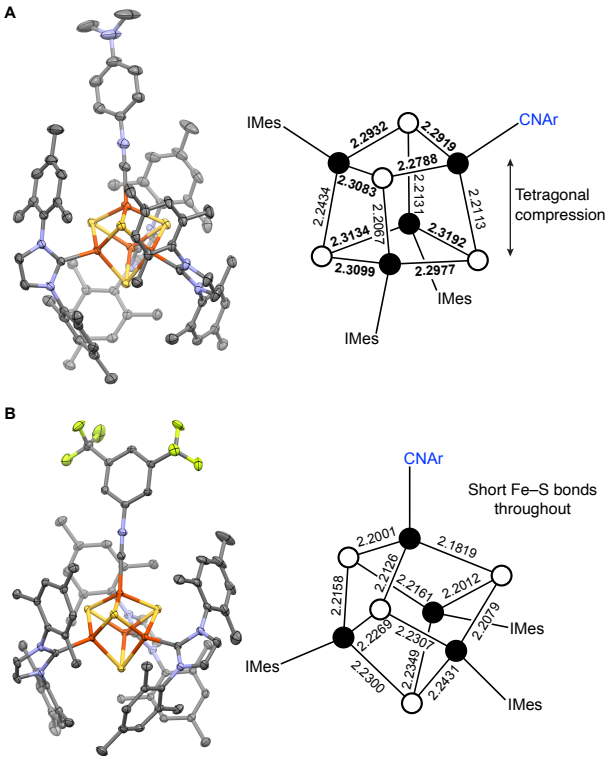

Figure 4.2. Crystallographic structures of [**1-CNAr$^{4\text{-NMe2}}$**]$^+$ (A, left) and [**1-CNAr$^{3,5\text{-(CF3)2}}$**]$^+$ (B, left) and cartoons depicting core Fe–S bond distances (right). The long Fe–S bonds in [**1-CNAr$^{4\text{-NMe2}}$**]$^+$ are bolded. Color scheme: carbon (gray), nitrogen (blue), iron (orange), sulfur (yellow), fluorine (green). Ellipsoids at the 50% probability level.

match closely with the crystallographic structures of [**1-CN^{t}Bu**]$^+$ and [**1-CO**]$^+$, respectively. The [Fe_4S_4]$^+$ core of [**1-CNAr$^{3,5\text{-(CF3)2}}$**]$^+$ is contracted relative to that of [**1-CNAr$^{4\text{-NMe2}}$**]$^+$ as indicated by the volumes of the tetrahedra defined by their four S atoms (S_4 volume), which are 5.498 and 5.072 Å^3, respectively, compared to 5.471 and 5.116 Å^3 for [**1-CN^{t}Bu**]$^+$ and [**1-CO**]$^+$, respectively. The core of [**1-CNAr$^{4\text{-NMe2}}$**]$^+$ exhibits a pattern of eight long and four parallel, short, Fe–S bonds, which is similar to the tetragonally compressed core of [**1-CN^{t}Bu**]$^+$ and common among [Fe_4S_4]$^+$ clusters.[25] Meanwhile, the core of [**1-CNAr$^{3,5\text{-(CF3)2}}$**]$^+$ is very similar to the [Fe_4S_4]$^+$ core of [**1-CO**]$^+$, displaying uniformly short Fe–S bonds and pseudo-C_{3v} symmetry. Thus, the [**1-CNAr**]$^+$ series serves its intended purpose by spanning the two previously observed structure types.

With confidence that the [**1-CNAr**]$^{+}$ series spans the electronic regime separating the structures of [**1-CO**]$^{+}$ and [**1-CN^{t}Bu**]$^{+}$, we turned to spectroscopic characterization of the ten-member [**1-CNAr**]$^{+}$ series. IR spectra were recorded as solutions in 1,2-difluorobenzene (DFB). For each cluster, a well-resolved feature corresponding to the C–N stretch was observed (full spectra are shown in Fig. S4.14 through S4.23, and representative spectra in the region of interest are shown in Fig. 4.3A). For each cluster, the energy of the C–N stretching frequency, ν(C–N), was taken as

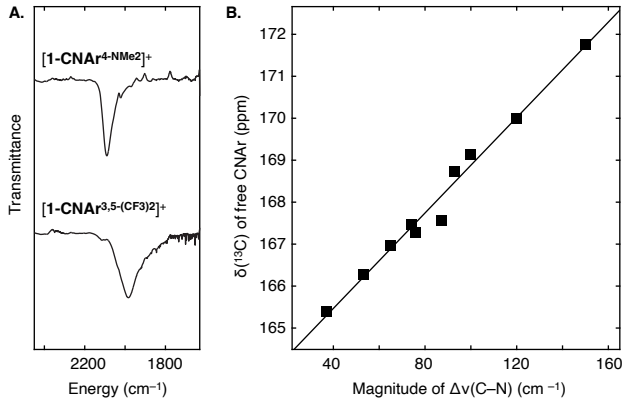

Figure 4.3. Electronic effects on C–N bond weakening in the [**1-CNAr**]$^{+}$ series. A) Representative IR spectra of [**1-CNAr$^{4\text{-NMe2}}$**]$^{+}$ and [**1-CNAr$^{3,5\text{-(CF3)2}}$**]$^{+}$. B) Correlation between the ^{13}C NMR chemical shift of the free CNAr ligand and the degree of C–N bond weakening (the magnitude of Δν(C–N)) and least-squares line.

the weighted average of all wavelengths in the peak (see SI for details). Across the series, ν(C–N) varies from 2085 cm^{-1} to 1979 cm^{-1} (for [**1-CNAr$^{4\text{-NMe2}}$**]$^{+}$ and [**1-CNAr$^{3,5\text{-(CF3)2}}$**]$^{+}$, respectively); these ν(C–N) values are lower than those typically observed for high-spin[34–37] Fe^{2+} complexes (ca. 2150 cm^{-1}) and higher than those of low-spin Fe^{+} complexes (ca. 1970 cm^{-1}).[38] The IR spectra of the free isocyanides were recorded under identical conditions, and for each member of the [**1-CNAr**]$^{+}$ series we calculated Δν(C–N): the change in the isocyanide ν(C–N) upon coordination to the Fe–S cluster. As expected, the largest decrease is observed for the most electron-deficient CNAr group, CNAr$^{3,5\text{-(CF3)2}}$, which has the lowest-energy acceptor orbitals, resulting in the best energetic matching with the filled Fe d orbitals, the strongest Fe–CNAr backbonding, and the

greatest C–N bond weakening. Similar reasoning explains why the cluster with the least-accepting CNAr ligand, $CNAr^{4\text{-}NMe2}$, displays the smallest Δν(C–N). There is a strong, positive correlation between Δν(C–N) and the ^{13}C NMR chemical shift of isocyanide carbon of the free CNAr ligands ($\delta(^{13}C)$, which has been previously shown to be a reliable indicator of the electronic properties of aryl isocyanides[39]; Fig. 4.3B); a similar correlation is observed between Δν(C–N) and the Hammett parameter, σ (Fig. S4.42).[40,41] Given the excellent correlation between these electronic parameters and Δν(C–N) for the [**1-CNAr**]$^+$ series, Δν(C–N) will be used in the analysis below as both a measure of the degree of C–N bond weakening and as a proxy for the electronic properties of the isocyanide.

2. Mössbauer Spectroscopic Characterization

The zero-field Mössbauer spectrum of each cluster was recorded at 80 K as a frozen solution in 1,2-difluorobenzene. All spectra are shown in the SI (Figures S4.46 through S4.55) and representative spectra for [**1-CNAr$^{4\text{-}NMe2}$**]$^+$ and [**1-CNAr$^{3,5\text{-}(CF3)2}$**]$^+$ are shown in Fig. 4.4A. The spectra generally display partly resolved quadrupole doublets at the low-energy and/or high-energy edges of the signal (ca. –1 and +1.5 mm s^{-1}, respectively), which we assign to a quadrupole doublet corresponding to one site (25% of the total area) with a relatively high $|\Delta E_Q|$; alternative models in which these minor features arise from different quadrupole doublets do not give reasonable simulated parameters (Figure S4.56). Additionally, we favor the assignment of these features to a single quadrupole doublet because of the close resemblance of the spectrum of [**1-CNAr$^{3,5\text{-}(CF3)2}$**]$^+$ with that of [**1-CO**]$^+$,[21] which showed better resolution of the high-$|\Delta E_Q|$ quadrupole doublet. In [**1-CO**]$^+$, this doublet was assigned to the Fe_{CO} site owing to the larger electric field gradient imparted by the strongly π-accepting CO ligand, and we likewise assign the corresponding quadrupole doublet in [**1-CNAr$^{3,5\text{-}(CF3)2}$**]$^+$ to the Fe_{CNAr} site. The remaining intensity in the [**1-**

CNAr$^{3,5\text{-}(CF3)2}$]$^+$ spectrum corresponds to the three Fe_{IMes} sites whose individual parameters cannot be reliably simulated due to poor resolution and/or magnetic equivalence on the Mössbauer time scale at 80 K. Therefore, although we simulated the contributions from the three Fe_{IMes} sites using three quadrupole doublets, we discuss only their average parameters.

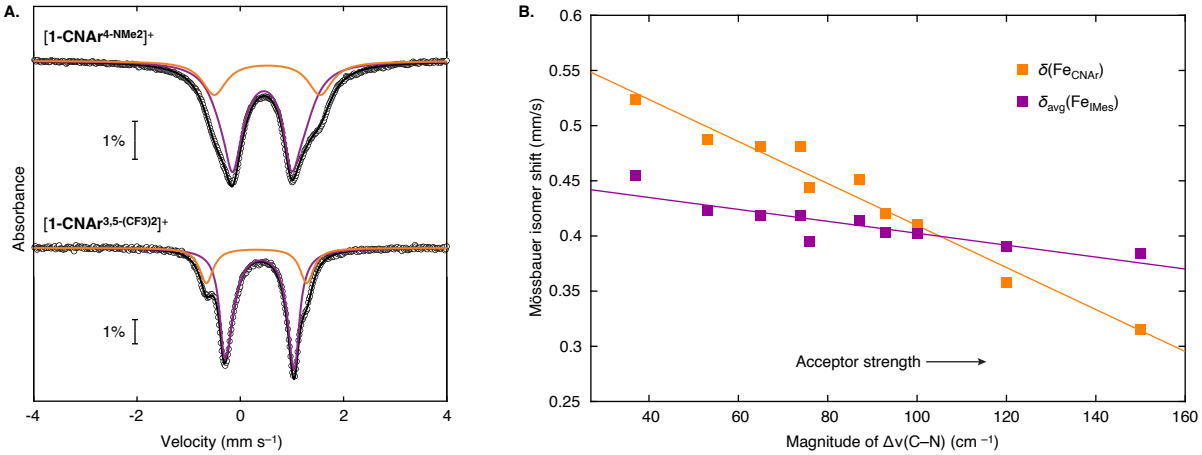

Figure 4.4. Mössbauer characterization of the [**1-CNAr**]$^+$ series. A) Representative Mössbauer spectra recorded at 80 K. Data (circles), total simulation (black trace), simulation of the Fe_{CNAr} site (orange trace), and combined simulation of the three Fe_{IMes} sites. See SI for more details. B) Correlation between the magnitude of Δν(C–N) and the Mössbauer isomer shifts of the two classes of sites ($\delta(Fe_{CNAr})$ and $\delta_{avg}(Fe_{IMes})$) showing how lowering the acceptor orbitals on the isocyanide (higher Δν(C–N)) results in a depletion of charge throughout the cluster and especially at Fe_{CNAr}. Given the uncertainties in the Mössbauer simulations (described in the text), we do not include error estimations in this plot or interpret the trends quantitatively.

With reasonable simulation parameters for [**1-CNAr$^{3,5\text{-}(CF3)2}$**]$^+$ in hand, we simulated the spectrum of the cluster with the next-most electronically similar isocyanide, [**1-CNAr$^{4\text{-}CF3}$**]$^+$, using the parameters of [**1-CNAr$^{3,5\text{-}(CF3)2}$**]$^+$ as the initial conditions. In this manner, we sequentially simulated the spectra of the rest of the series. Thus, although we were not able to obtain a unique simulation for any member of the series for the reasons described above, we could obtain globally consistent simulations, each of which is itself reasonable.

Several important observations arise from analysis of the simulated Mössbauer data. First, for every member of the series, $\delta(Fe_{CNAr})$ is higher than $\delta(Fe_{CO})$ in [**1-CO**]$^+$ (0.28 mm s^{-1}), consistent

with none of the CNAr ligands being as proficient at π-backbonding as CO. Second, the isomer shifts for the Fe_{CNAr} sites ($\delta(Fe_{CNAr})$) decrease in an approximately linear fashion with increasing acceptor strength of the CNAr ligand (plotted in Fig. 4.3B and tabulated in Table S4.3), as expected because a stronger acceptor will form more π-backbonding interactions with the Fe_{CNAr} site, which will lower $\delta(Fe_{CNAr})$.[42] Third, $\delta_{avg}(Fe_{IMes})$ also decreases with increasing acceptor strength of the CNAr ligand, albeit less dramatically than observed for the Fe_{CNAr} sites. Nevertheless, the observation of a change in $\delta_{avg}(Fe_{IMes})$ with changes in the electronic properties of CNAr demonstrates a role for the entire cluster in cooperatively activating the CNAr ligand: even the Fe_{IMes} sites feel the effects of increased back-donation to the CNAr ligand. In contrast to δ, $|\Delta E_Q|$ varies little (ca. 0.3 mm s^{-1} for $|\Delta E_Q|(Fe_{CNAr})$ and 0.16 mm s^{-1} for $|\Delta E_Q|_{avg}(Fe_{IMes})$) and does not appear to be correlated with Δν(C–N) (Figure S4.57).

Notably, $\delta(Fe_{CNAr}) > \delta_{avg}(Fe_{IMes})$ for the clusters with the least activated CNAr ligands, whereas this is reversed for clusters with the most activated CNAr ligands. The relative ordering of $\delta(Fe_{CNAr})$ and $\delta_{avg}(Fe_{IMes})$ reflects the competing effects of the Fe d electron population (*i.e.*, the valence) and the Fe–L covalency. All things being equal, a higher d electron count will lead to higher δ,[43] while greater Fe–L covalency will lower δ.[42] For each member of the series, the stronger acceptor character of the CNAr ligand compared with IMes favors higher d counts at the Fe_{CNAr} site (*i.e.*, localization of Fe^{2+} (or lower) instead of $Fe^{2.5+}$).[24,44,45] But for the clusters with the most-accepting CNAr ligands (*e.g.*, [**1-CNAr$^{3,5\text{-}(CF3)2}$**]$^+$) the effects on δ of the stronger Fe–CNAr covalency (compared with Fe–IMes) apparently outweigh the effects of the higher d-electron count, resulting in $\delta_{avg}(Fe_{IMes}) > \delta(Fe_{CNAr})$.

3. Structural Evidence for Distinct Electronic Structures

Up to this point, the data presented on the [**1-CNAr**]$^+$ series indicate that the degree of C–N bond weakening as well as changes in charge density and covalency throughout the cluster are continuously tuned by the electronic properties of the CNAr ligands. The following structural and computational analyses (Sections 3-5) complicate this picture, pointing to *discrete* magnetostructural changes across the series; we attribute these to spin isomerism.

High-resolution structures of the remaining members of the [**1-CNAr**]$^+$ series were obtained; structures are shown in the SI (Figures S4.59 through S4.66). Each cluster crystallized with one molecule in the asymmetric unit with the exception of [**1-CNAr$^{4\text{-F}}$**]$^+$, for which we report average values from the two crystallographically independent molecules. At first glance, the structures are very similar to one another and to other members of the $(IMes)_3Fe_4S_4$ family, exhibiting pseudo-C_3 symmetry with the three IMes ligands arranged in a propeller-like fashion aroud the cluster core.

Based on the observations that several properties of the cluster ($\Delta\nu$(C–N), $\delta(Fe_{CNAr})$, and $\delta_{avg}(Fe_{IMes})$) vary approximately linearly with simple electronic descriptors for the isocyanide ligand (σ and $\delta(^{13}C)$), it might be expected that the structural changes across the series should also track linearly with these electronic parameters. In fact, this is not the case. Instead, the clusters roughly fall into one of two categories, adopting either a 'typical' structure type similar to that of [**1-CN^{t}Bu**]$^+$ and [**1-CNAr$^{4\text{-NMe2}}$**]$^+$, or an atypical, 'contracted' structure type similar to that of [**1-CO**]$^+$ and [**1-CNAr$^{3,5\text{-(CF3)2}}$**]$^+$. For a given cluster, the strucure type is dictated by the acceptor strength of the CNAr ligand: the six members with the least C–N bond weakening ([**1-CNAr$^{4\text{-NMe2}}$**]$^+$ through [**1-CNPh$^{4\text{-F}}$**]$^+$) have a typical structure, while the remaining four members ([**1-CNAr$^{4\text{-Cl}}$**]$^+$ through [**1-CNAr$^{3,5\text{-(CF3)2}}$**]$^+$) have a contracted structure. This is demonstrated in the plot of S_4 volume vs. $\Delta\nu$(C–N) (Fig. 4.5A) in which the six clusters with typical structures are

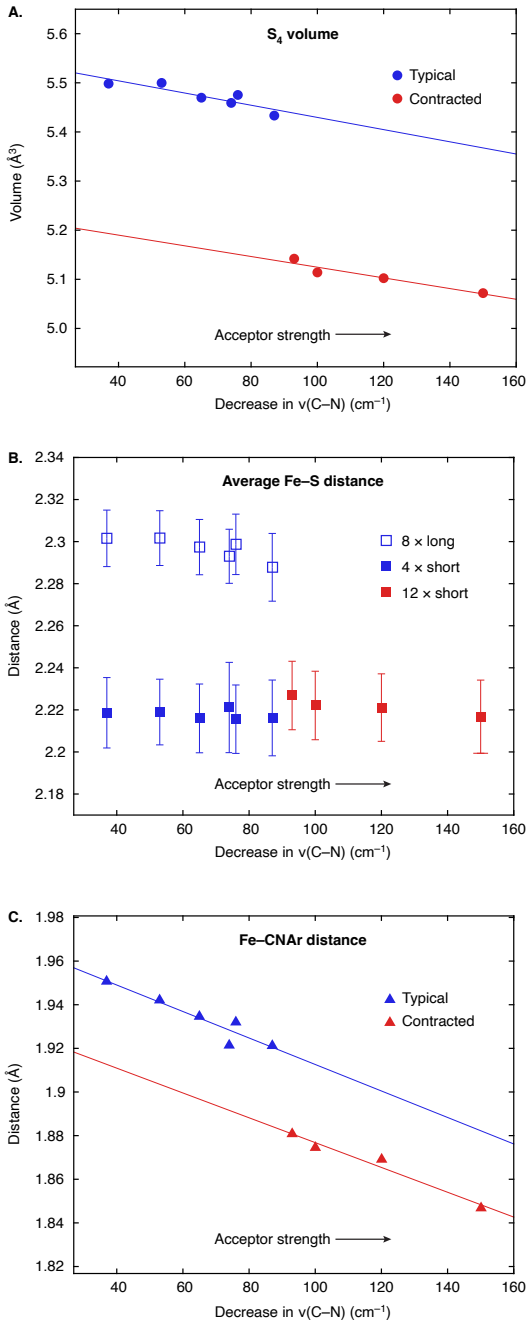

Figure 4.5. Plots of the structural parameters of [**1-CNAr**]$^{+}$ complexes. All plots show the separation of core parameters into a typical region (blue) with weakly accepting ligands and a contracted region (red) with strongly accepting ligands. A) Plot of S_4 volume vs. π-acceptor strength with least-squares fit lines for the typical and contracted regions B) Plot of average Fe–S distance vs. π-acceptor strength with error bars representing the standard deviation of the average value for each point. C) Plot of Fe-C(Nar) distance vs. π-acceptor strength with least-squares fit lines for the typical and contracted regions.

clustered around 5.5 Å^3, whereas the remaining four contracted members have S_4 volumes of approximately 5.1 Å^3. The 'cliff' between structure types occurs in the narrow electronic space between [**1-CNAr$^{4\text{-F}}$**]$^+$ and [**1-CNAr$^{4\text{-Cl}}$**]$^+$. Similar trends are observed for the average Fe–S distances, d_{avg}(Fe–S) (Table S4.9). More tellingly, Fig. 4.5B shows that, whereas the Fe–S distances for the clusters [**1-CNAr$^{4\text{-NMe2}}$**]$^+$ through [**1-CNPh$^{4\text{-F}}$**]$^+$ are separated into eight long and four short bonds (typical of a tetragonally distorted structure), those of the remaining clusters ([**1-CNAr$^{4\text{-Cl}}$**]$^+$ through [**1-CNAr$^{3,5\text{-(CF3)2}}$**]$^+$) are all short, and indeed of similar length as the short bonds in the typical structures. Overall, the foregoing analysis reveals the unusual finding that the ten clusters fall into two categories: six with a typical structure, and four with an atypical, contracted structure.

The plot of *d*(Fe–CNAr) vs. Δν(C–N) (Fig. 4.5C) shows the remarkable range of Fe–CNAr distances observed across the series—approximately 0.1 Å, from 1.951(2) Å in [**1-CNAr$^{4\text{-NMe2}}$**]$^+$ to 1.847(1) in [**1-CNAr$^{3,5\text{-(CF3)2}}$**]$^+$, consistent with the broad range of Δν(C–N) across the series (*vide supra*). Similarly to the plots of the other cluster metrics (Fig. 4.5A and 4.5B), a discontinuity is observed between [**1-CNAr$^{4\text{-F}}$**]$^+$ and [**1-CNAr$^{4\text{-Cl}}$**]$^+$, and there is an approximately linear relationship between Δν(C–N) and *d*(Fe–CNAr) on either side of the discontinuity.

Interestingly, for all three metrics (S_4 volume, d_{avg}(Fe–S), and *d*(Fe–CNAr)), the slopes *versus* Δ(ν(C–N) for both the typical and compressed structure classes are approximately the same. That is, within each structure class, the structural parameters change by a similar magnitude for a given degree of increasing acceptor properties of the CNAr ligand. A difference in the slopes between structure classes might have indicated that one structure class enabled more tunable π-backbonding than the other, perhaps due to the adoption of low-valent configurations in only one of the two

classes. However, no change in the slopes is observed and instead what is unusual is the existence of the two structure classes separated by a relatively abrupt transition.

Before further interpreting these results, it is important to note that the observed structural differences are not due to crystal packing effects. Although several clusters with typical structures ([**1-CNAr$^{4\text{-NMe2}}$**]$^+$, [**1-CNAr$^{4\text{-OMe}}$**]$^+$, [**1-CNAr$^{4\text{-Me}}$**]$^+$, and [**1-CNAr$^{3\text{-OMe}}$**]$^+$) crystallized with essentially the same unit cell, and several clusters with contracted structures ([**1-CNAr$^{4\text{-Cl}}$**]$^+$, [**1-CNAr$^{4\text{-I}}$**]$^+$, and [**1-CNAr$^{4\text{-CF3}}$**]$^+$) likewise crystallized with similar unit cells (distinct from those of the typical structures), there appears to be no preference for one unit cell over another based on the steric profile of the isocyanide. For example, the CNAr ligands with 4-CH_3 and 4-Cl substituents are of similar size, yet [**1-CNAr$^{4\text{-Me}}$**]$^+$ and [**1-CNAr$^{4\text{-Cl}}$**]$^+$ do not crystallize in the same unit cell. On the other hand, the CNAr ligands with 4-NMe_2 and 3-OMe substituents have quite different shapes and yet [**1-CNAr$^{4\text{-NMe2}}$**]$^+$ and [**1-CNAr$^{3\text{-OMe}}$**]$^+$ crystallize in the same unit cell. Moreover, three clusters ([**1-CNPh**]$^+$, [**1-CNAr$^{4\text{-F}}$**]$^+$, and [**1-CNAr$^{3,5\text{-(CF3)2}}$**]$^+$) each crystallized in unique unit cells, but their $[Fe_4S_4]^+$ cores still fall into one of the two classes. Thus, to the extent that there is a connection between the unit cell and the $[Fe_4S_4]^+$ core structure type, it seems that the $[Fe_4S_4]^+$ core structure is more likely to determine the unit cell, and not the other way around.

4. Computational Evidence for Distinct Electronic Structures

The foregoing results demonstrate that although the degree of C–N bond weakening can be finely tuned across the [**1-CNAr**]$^+$ series, the clusters fall into one of two classes of geometric structures. We next investigated whether, for a single isocyanide ligand (CNMe), the two structure classes could be observed computationally, reasoning that such an observation would both provide support for the existence of two distinct structure types and allow us to probe the electronic structures of each.

We began by conducting two geometry optimizations of the model cluster $[(NHC^H)_3Fe_4S_4(CNMe)]^+$ (NHC^H = imidazole-2-ylidene; TPSS/def2-TZVP; see SI for computational details):[46,47] (A) one with an initial structure resembling the typical structure, with coordinates taken from [**1-CNAr$^{4\text{-NMe2}}$**]$^+$ (for all atoms common to the truncated model), and (B) one with an initial structure resembling the contracted structure, with coordinates taken from [**1-CNAr$^{3,5\text{-(CF3)2}}$**]$^+$. The optimized cluster in (A) retained its typical structure, with eight long and four short Fe–S distances, while that in (B) retained its contracted structure, with twelve short Fe–S distances (Fig. 4.6A). For both structures, the absolute Fe–S and Fe–C(NHC) bond lengths are contracted relative to the bond lengths observed crystallographically (compared to [**1-CNAr$^{4\text{-NMe2}}$**]$^+$ for (A) and to [**1-CNAr$^{3,5\text{-(CF3)2}}$**]$^+$ for (B)), consistent with the systematic contraction of the cluster core for calculations with the TPSS functional observed previously for **1-CO** and [**1-CO**]$^+$, [21]; nevertheless, the computed structures reproduce the experimental differences between the two structure types.

We next constructed a potential energy surface for both minima by varying the Fe–C(NMe) distance and reoptimizing the cluster geometry at each point (see Figure 4.6B and SI for details). The two minima from the optimization studies above were found to exist on distinct potential energy surfaces with distinct structures and energies at each Fe–C(NMe) distance. That is, even at the point where the calculated structures have the same energy (*i.e.* an Fe–C(NMe) bond length of 1.96 Å), the optimized structures are drastically different—the one derived from (A) retains the hallmarks of the typical structure (*e.g.*, a relatively large S_4 volume (5.615 Å^3) and a pattern of eight long and four short Fe–S bonds) and the one derived from (B) retains the hallmarks of the contracted structure (*e.g.*, a relatively small S_4 volume of 4.874 Å^3 and twelve short Fe–S bonds).

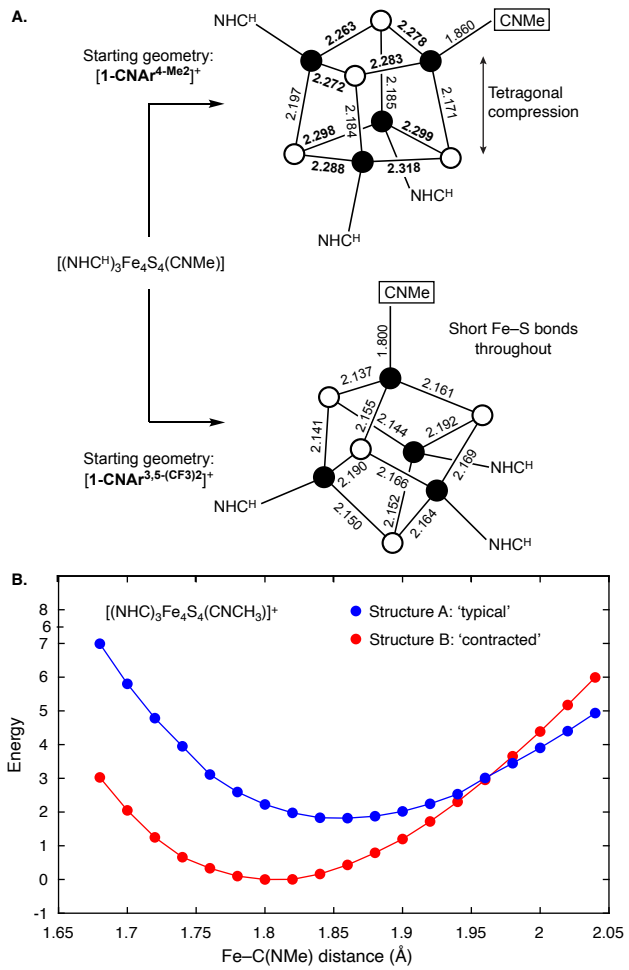

Figure 4.6. Calculations on $[(NHC^{H})_3Fe_4S_4(CNMe)]^+$. A) The obtained geometry for $[(NHC^{H})_3Fe_4S_4(CNMe)]^+$ is dependent on the initial conditions. If the geometry optimization is initialized with coordinates adapted from the crystallographic structure of [**1-CNAr$^{4\text{-NMe2}}$**]$^+$, the calculation converges to a typical structure with eight long and four short Fe–S bonds. If the geometry optimization is initialized with coordinates adapted from the crystallographic structure of [**1-CNAr$^{3,5\text{-(CF3)2}}$**]$^+$, the calculation converges to a contracted structure with short Fe–S bonds. B) These two minima exist on separate potential energy surfaces and do not cross between surfaces when the Fe–C(NMe) bond distance is scanned.

To learn if the relative energies of these two minima are impacted by the acceptor strength of the isocyanide, we conducted an analogous series of optimizations with the model cluster $[(NHC^{H})_3Fe_4S_4(CNCH_2CF_3)]^+$, expecting that the electron-withdrawing CF_3 group should favor the contracted structure, as observed experimentally in the [**1-CNAr**]$^+$ series, where the stronger acceptors adopt contracted structures. We again found two local minima, with the contracted

structure being favored by 2.48 kcal mol^{-1} over the typical structure, a greater difference than that observed for [(NHC^{H})$_3$Fe$_4$S$_4$(CNMe)]$^+$ (1.82 kcal mol^{-1}). Note that although the relative energy of the two structures is useful in delineating such trends, we do not quantitatively interpret these energies because (i) the optimizations were performed on a truncated model, and thus cannot be directly compared to the [**1-CNAr**]$^+$ series, and (ii) such small energy differences are likely to be heavily influenced by the computational methodology. Nevertheless, these *in silico* studies support the existence of two nearly isoenergetic, structurally distinct states for complexes of the form [**1-CNR**]$^+$, with the contracted structure being more favorable for more strongly accepting isocyanides.

5. Computational Evidence for Spin Isomers

We next evaluated the electronic structures of the two minima (the typical structure and the contracted structure) found for [(NHC^{H})$_3$Fe$_4$S$_4$(CNMe)]$^+$ by analyzing the BS-DFT energetic minima in terms of localized molecular orbitals (IAOIBO localization).[48,49]

In the typical structure, the localized molecular orbitals are similar to those canonically observed for [Fe$_4$S$_4$]$^+$ clusters:[50] An S = 9/2 pair of Fe$^{2.5+}_{NHC}$ centers coupled via the double exchange mechanism and two spin aligned Fe^{2+} (Fe$_{NHC}$ and Fe$_{CNMe}$) centers with S = 4 antiferromagnetically coupled to the Fe$^{2.5+}_{NHC}$ pair (Figure 4.7A, left). Unlike the canonical orbital description for [Fe$_4$S$_4$]$^+$ clusters, however, the spin up electron on the Fe$^{2+}_{NHC}$ in the minority spin (aligned with Fe$_{CNMe}$) is delocalized onto the Fe$_{CNMe}$ site into an orbital with Fe–CNMe backbonding character. The localized orbitals at the Fe$_{CNMe}$ center are shown in Figure 4.7C with the electron that is delocalized between the Fe$_{CNMe}$ and Fe$_{NHC}$ centers on the bottom left. This delocalization (Figure 4.7A, right) results in a resonance structure best described as a high-spin Fe$^{1+}_{CNMe}$ center spin-aligned with a high-spin Fe$^{3+}_{NHC}$ center. Contributions from the Fe^{1+}/Fe^{3+}

resonance structure provide low valent character to the ground state of the typical structure type, enabling activation of π-acidic ligands.

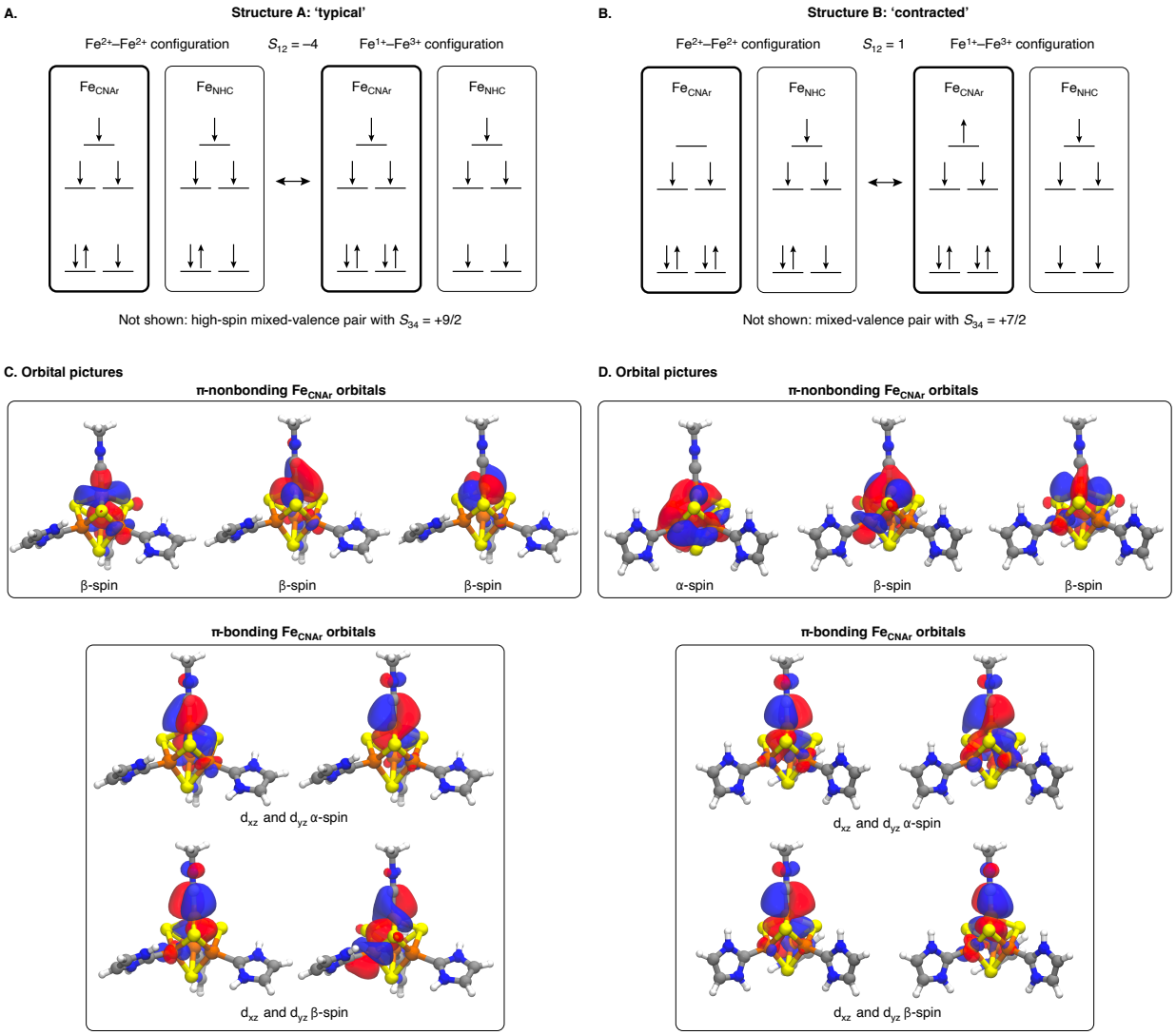

Figure 4.7. Localized molecular orbitals diagrams for $[(NHC^{H})_3Fe_4S_4CNMe]^+$. A) Delocalization of a π-backbonding electron between the Fe_{CNMe} and Fe_{NHC} sites in the typical structure. B) Delocalization of a π-nonbonding electron between the Fe_{CNMe} and Fe_{NHC} sites in the contracted structure. C) Localized molecular orbitals centered on Fe_{CNMe} showing the seven electrons partially on Fe in the typical structure D) Localized molecular orbitals centered on Fe_{CNMe} showing the seven electrons partially on Fe in the contracted structure.

For the contracted structure, the localized molecular orbitals are very different from those described above (Figure 4.7B), especially at the Fe_{CNMe} site. In the contracted structure, there are four electrons in orbitals involved in Fe–CNMe backbonding, all of which which are localized to

the Fe–CNMe site—none of these electrons are delocalized onto an adjacent spin-aligned Fe_{NHC} site as they are in the typical structure (Figure 4.7D, bottom). Instead, the remaining three π-nonbackbonding electrons are involved in delocalization to adjacent Fe_{NHC} centers (Figure 4.7D, top). All three (one α-spin and two β-spin) π-nonbonding orbitals are partically delocalized onto adjacent Fe_{NHC} centers, making the pairwise delocalization diagrams like those used in Figure 4.7B a substantial simplification of the complete localized orbital picture. However, the pairwise scheme provides a useful basis for understanding the more complete delocalized orbital diagram (Figure 4.7B). Described in this pairwise delocalization paradigm, one resonance depiction of the contracted structure is that the Fe_{CNMe} site has become intermediate spin Fe^{2+} and its spins are aligned parallel to an adjacent Fe^{2+} site. In the other resonance contributor, one α-spin electron on the Fe_{NHC} center is delocalized back to the Fe_{CNMe} site, again leading to a configuration described an Fe^{1+}/Fe^{3+} pair. These two resonance structures are composed of the same valences that describe the typical electronic structure but use different mechanisms to achieve them: delocalization of π-backbonding electrons in the typical structure and of π-nonbonding electrons in the contracted structure. The primary difference between the two structure types is thus *which* electrons are involved in delocalization, with the contracted structure featuring more complete localization of the π-backbonding orbitals to the Fe_{CNMe} site.

In addition to consideration of the localized molecular orbital depictions presented above, we note that calculations on the contracted structure generally show more d-electron delocalization between Fe centers overall. For example, all six π-nonbonding orbitals (in both the α and β spin manifolds) on the Fe_{CNMe} center have contributions from one or more of the Fe_{NHC} centers. Additionally, several electrons in the contracted structure are delocalized between the Fe_{NHC} centers, while in the typical structure, only one electron is delocalized between Fe_{NHC} sites. The

increased electron delocalization seen in the contracted structures compared to the typical structures likely reflects increased metal-metal covalency resulting from the shorter Fe–S and Fe–Fe distances (Table S4.11 and S4.12). This covalency is also reflected in the symmetry of the contacted structure type (the three Fe_{NHC} sites are nearly equivalent), as well as the Mössbauer spectra of [**1-CNAr$^{3,5\text{-}(CF3)2}$**]$^+$ and [**1-CO**]$^+$ (which show essentially one signal for the Fe_{NHC} sites). This symmetry would not be predicted from the exchange-coupled pairwise orbital description presented above: we would expect that the structural and Mössbauer parameters of two of the three Fe_{IMes} sites (the two sites not involved in electron delocalization to the Fe_{CNAr} site) to be essentially invariant to the electronic nature of the isocyanides. This is not observed experimentally: for the clusters featuring the most withdrawing isocyanides, the isomer shifts of all three Fe_{IMes} sites are in fact equivalent. The high symmetry of the contracted structure type and the increased delocalization noted from the computational results, support a covalent depiction of the intra-cluster bonding in which all three Fe_{IMes} sites contribute similarly to activation of the π-acidic ligand.

Although the localized pictures presented above are useful in understanding the valences of the clusters and relating the π-acid bound clusters to those with typical ligands for Fe–S clusters, one must also consider electronic structures with significant contributions from metal-metal covalency[51,52] instead of, or in addition to, models based on only exchange coupling, with the metal-metal bonds contributing electron density to the apical Fe site to enable cooperative activation of the π-acid using electron density from all the metal centers.

Discussion

The foregoing results demonstrate that $[Fe_4S_4]^+$ clusters bound by π-acidic ligands can adopt one of two $S = 1/2$ ground states that differ in their geometric and electronic structures. Both spin isomers can have contributions from resonance structures with a canonical valence distribution ($2xFe^{2+}$ and $2xFe^{2.5+}$) as well as resonance structures in which the π-acid-bound Fe has an Fe^{1+} valence ($1xFe^{1+}$, $1xFe^{3+}$, and $2xFe^{2.5+}$). For the typical spin isomer, the π-acid-bound Fe has only partial occupancy of its backbonding orbitals in the canonical resonance structure; full occupation of the backbonding orbitals occurs only to the extent that the low-valent configuration contributes to the ground state. In contrast, for the contracted spin isomer, both resonance contributors feature a fully occupied set of backbonding orbitals for the π-acid-bound Fe. Thus, the contracted spin isomer allows for strong backbonding even if the low-valent configuration is not dominant. That is, even if the auxiliary Fe sites are not sufficiently reducing to generate an Fe^{1+} center at the π-acid-bound Fe, by adopting the 'contracted' spin isomer, the cluster provides the π-acid-bound Fe the critical electronic feature for strong backbonding: full occupation of the orbitals of proper symmetry.

Having established that the two structure types observed crystallographically are spin isomers of one another, we considered how and on what timescale the two isomers might interconvert. First, in a crystal lattice, the packing forces are sufficient to ensure that the cluster core is locked into one structural configuration on the timescale of X-ray diffraction experiment (> 1 h), enabling visualization of both spin isomers separately by X-ray crystallography. On the other hand, the Mössbauer parameters of the [**1-CNAr**]$^+$ series, for spectra collected on samples in frozen solution, vary linearly across the series without the abrupt 'cliff' observed in the structural parameters. Two possible explanations for the discrepancy between the solution and crystallographic measurements

are apparent. First, the Mössbauer parameters could be very similar for both spin isomers, such that no discontinuity is observable across the [**1-CNAr**]$^{+}$ series. Alternatively, the two spin isomers could interconvert in frozen solution on the Mössbauer timescale (ca. 10^{-7} s), such that we observe an average of the Mössbauer parameters for each spin isomer. We are at present unable to differentiate between these two possibilities.

We next describe how the π-acidity of the CNAr ligand induces the transition between the two spin isomers in the [**1-CNAr**]$^{+}$ series. The primary effect of lowering the energy of the acceptor orbitals on the CNAr ligand is the lowering of the backbonding orbitals of the Fe_{CNAr} site (Fig. 4.8A); the other Fe_{CNAr} orbitals not directly engaged in backbonding will also decrease in energy (albeit to a lesser extent), as will the orbitals of the entire cluster (consistent with the experimentally observed decrease in $\delta_{avg}(Fe_{IMes})$ across the series). In the regime in which the typical spin isomer is favored, one of the π-backbonding orbitals on the Fe_{CNAr} site mixes with a

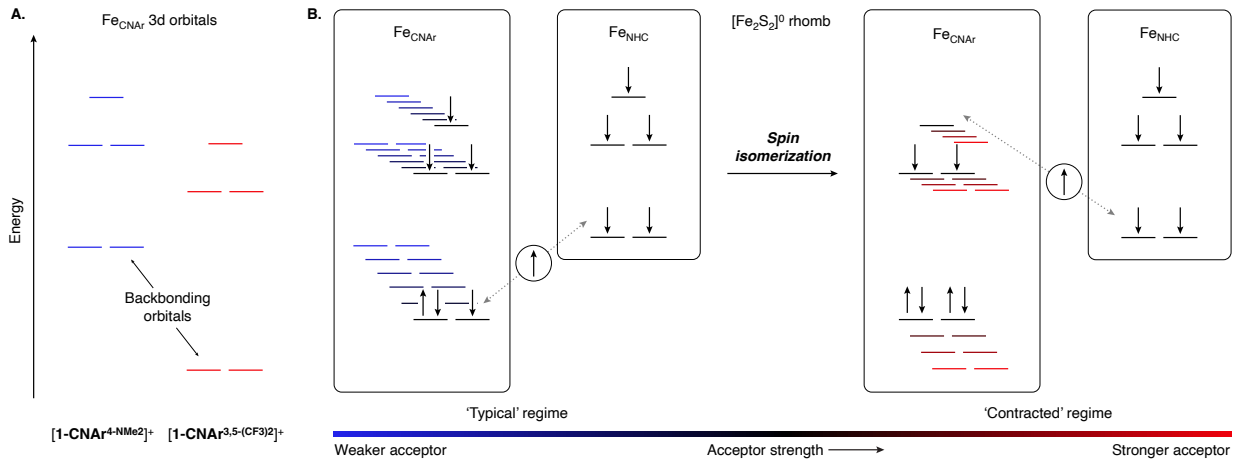

Figure 4.8. Cartoon depicting the orbital origin of the transition between the typical and contracted electronic structures. A) Increasing the π-acidity of the isocyanide leads to a decrease in d-orbital energy, particularly for the orbitals involved in π-backbonding. B) As the isocyanide becomes a stronger π-acceptor, the energy of the π-backbonding orbitals drops, disfavoring delocalization of the π-backbonding electrons. For ligands that are sufficiently strong π-acids, this leads to localization of the π-backbonding orbitals at the Fe–CNAr site and delocalization of a π-nonbonding electron instead.

3d orbital on the other Fe^{2+}_{NHC} site; this is the mechanism by which low-valent configurations are accessed in the typical spin isomer. As the disparity in the energies of these two orbitals grows, the Fe^{2+}_{NHC} site increasingly shares this electron with the Fe^{2+}_{CNAr} site, eventually resulting in full electron transfer from the Fe_{NHC} site to the Fe_{CNAr} π-backbonding orbital (Figure 4.8B). Concomitantly, the charge separation induced in this state is stabilized by additional electron delocalization of a π-nonbonding electron from Fe_{CNAr} back to Fe_{NHC}. This explanation accounts for both the observation that stronger acceptors favor the contracted spin isomer and the abrupt transition between the two spin isomers within the series. Additionally, the contracted spin isomer structure displays shorter Fe–S and Fe–Fe distances compared to the typical spin isomer, which enables increased covalency within the contracted cluster compared to typical Fe–S clusters. This high degree of covalency enables all three Fe_{NHC} sites to contribute electron density to the Fe_{CNAr} site and towards activation of the π-acidic ligand. In other words, at the crossover point between the two spin isomers, the π-backbonding demand of the isocyanide ligand is so great that it cannot be filled by redistribution of the electron density on only the pair of spin-aligned Fe centers. Instead, by transitioning to the contracted spin isomer, all three Fe_{NHC} sites are able to participate in sharing electron density with the Fe_{CNAr} sites in order to achieve sufficient π-backbonding electron density for the stronger π-accepting ligands.

Conclusion

With the series of aryl isocyanide-coordinated Fe–S clusters presented herein, we have explored the continuum between the typical electronic structure of Fe–S clusters and the low-valent electronic structure induced by coordinating sufficiently π-acidic ligand. The typical electronic structure and contracted structure induced by binding a strongly π-acidic ligand can be differentiated by their structural parameters and do not exist on a smooth continuum. Rather, they are related by an abrupt geometric change and adoption of a new electronic configuration for sufficiently strongly π-accepting ligands. This demonstrates the tremendous sensitivity of Fe–S cluster electronic structure to the nature of the coordinating ligands—a series of electronically variable aryl isocyanide ligands are sufficient to induce large structural and electronic changes in the cluster. However, it additionally demonstrates the tremendous flexibility of Fe–S clusters: the cluster can readily access and tune several different electronic structures depending on the electronic nature of the coordination sphere. The multitude of accessible electronic structure for Fe–S clusters is key to enabling the wide range of coordination chemistry these clusters carry out in Nature: Fe–S clusters can access states comprised of high-spin Fe^{2+}/Fe^{3+} ions to mediate radical and Lewis-acid type chemistry but also are able to access π-basic configurations that are able to activate π-acidic substrates.

References

(1) *Catalysts for Nitrogen Fixation: Nitrogenases, Relevant Chemical Models, and Commercial Processes*, 1st ed.; Smith, B. E., Richards, R. L., Newton, W. E., Eds.; Springer Dordrecht, 2004.

(2) Harris, D. F.; Lukoyanov, D. A.; Kallas, H.; Trncik, C.; Yang, Z. Y.; Compton, P.; Kelleher, N.; Einsle, O.; Dean, D. R.; Hoffman, B. M.; Seefeldt, L. C. Mo-, V-, and Fe-Nitrogenases Use a Universal Eight-Electron Reductive-Elimination Mechanism to Achieve N_2 Reduction. *Biochemistry* **2019**, *58* (30), 3293–3301.

(3) Hoffman, B. M. .; Lukoyanov, D.; Dean, D. R.; Seefeldt, L. C. Nitrogenase: A Draft Mechanism. *Acc. Chem. Res.* **2013**, *46* (2), 587–595.

(4) Schneider, K.; Müller, A. Iron-Only Nitrogenase: Exceptional Catalytic, Structural and Spectroscopic Features. In *Catalysts for Nitrogen Fixation. Nitrogen Fixation: Origins, Applications, and Research Progress*; Smith, B. E., Richards, R. L., Newton, W. E., Eds.; 2004; Vol. 1.

(5) Lee, C. C.; Hu, Y.; Ribbe, M. W. Vanadium Nitrogenase Reduces CO. *Science* **2010**, *329* (5992), 642.

(6) Hu, Y.; Lee, C. C.; Ribbe, M. W. Extending the Carbon Chain: Hydrocarbon Formation Catalyzed by Vanadium/Molybdenum Nitrogenases. *Science* **2011**, *333* (6043), 753–755.

(7) Tanifuji, K.; Sickerman, N.; Lee, C. C.; Nagasawa, T.; Miyazaki, K.; Ohki, Y.; Tatsumi, K.; Hu, Y.; Ribbe, M. W. Structure and Reactivity of an Asymmetric Synthetic Mimic of Nitrogenase Cofactor. *Angew. Chem. Int. Ed.* **2016**, *55* (50), 15633–15636.

(8) Stiebritz, M. T.; Hiller, C. J.; Sickerman, N. S.; Lee, C. C.; Tanifuji, K.; Ohki, Y.; Hu, Y. Ambient Conversion of CO2 to Hydrocarbons by Biogenic and Synthetic [Fe_4S_4] Clusters. *Nat. Catal.* **2018**, *1* (6), 444–451.

(9) Rebelein, J. G.; Stiebritz, M. T.; Lee, C. C.; Hu, Y. Activation and Reduction of Carbon Dioxide by Nitrogenase Iron Proteins. *Nat. Chem. Biol.* **2017**, *13* (2), 147–149.

(10) Yang, Z. Y.; Dean, D. R.; Seefeldt, L. C. Molybdenum Nitrogenase Catalyzes the Reduction and Coupling of CO to Form Hydrocarbons. *J. Biol. Chem.* **2011**, *286* (22), 19417–19421.

(11) Harris, D. F.; Jimenez-Vicente, E.; Yang, Z. Y.; Hoffman, B. M.; Dean, D. R.; Seefeldt, L. C. CO as a Substrate and Inhibitor of H^+ Reduction for the Mo-, V-, and Fe-Nitrogenase Isozymes. *J. Inorg. Biochem.* **2020**, *213* (September), 111278.

(12) Lee, C. C.; Hu, Y.; Ribbe, M. W. ATP-Independent Formation of Hydrocarbons Catalyzed by Isolated Nitrogenase Cofactors. *Angew. Chem. Int. Ed.* **2012**, *51* (8), 1947–1949.

(13) Lee, C. C.; Hu, Y.; Ribbe, M. W. Insights into Hydrocarbon Formation by Nitrogenase Cofactor Homologs. *MBio* **2015**, *6* (2), 1–6.

(14) Lee, C. C.; Hu, Y.; Ribbe, M. W. Catalytic Reduction of CN-, CO, and CO_2 by Nitrogenase Cofactors in Lanthanide-Driven Reactions. *Angew. Chem. Int. Ed.* **2015**, *54* (4), 1219–1222.

(15) Lee, C. C.; Hu, Y.; Ribbe, M. W. Reduction and Condensation of Aldehydes by the Isolated Cofactor of Nitrogenase. *ACS Cent. Sci.* **2018**, *4* (10), 1430–1435.

(16) Tanifuji, K.; Lee, C. C.; Ohki, Y.; Tatsumi, K.; Hu, Y.; Ribbe, M. W. Combining a Nitrogenase Scaffold and a Synthetic Compound into an Artificial Enzyme. *Angew. Chem. Int. Ed.* **2015**, *54* (47), 14022–14025.

(17) Sickerman, N. S.; Tanifuji, K.; Lee, C. C.; Ohki, Y.; Tatsumi, K.; Ribbe, M. W.; Hu, Y. Reduction of C1, Substrates to Hydrocarbons by the Homometallic Precursor and Synthetic Mimic of the Nitrogenase Cofactor. *J. Am. Chem. Soc.* **2017**, *139* (2), 603–606.

(18) Beinert, H.; Holm, R. H.; Münck; Eckard. Iron-Sulfur Clusters : Nature's Modular,

Multipurpose Structures. *Science* **1997**, *277* (5326), 653–659.
(19) Hagen, W. R. EPR Spectroscopy of Iron—Sulfur Proteins. *Adv. Inorg. Chem.* **1992**, *38*, 165–222.
(20) Hagen, W. R. EPR Spectroscopy of Complex Biological Iron–Sulfur Systems. *J. Biol. Inorg. Chem.* **2018**, *23* (4), 623–634.
(21) Brown, A. C.; Thompson, N. B.; Suess, D. L. M. Evidence for Low-Valent Electronic Configurations in Iron−Sulfur Clusters. *J. Am. Chem. Soc.* **2022**, *144* (20), 9066–9073.
(22) Al-Afyouni, M. H.; Suturina, E.; Pathak, S.; Atanasov, M.; Bill, E.; Derosha, D. E.; Brennessel, W. W.; Neese, F.; Holland, P. L. Spin Isomers and Ligand Isomerization in a Three-Coordinate Cobalt(I) Carbonyl Complex. *J. Am. Chem. Soc.* **2015**, *137* (33), 10689–10699.
(23) Brown, A. C.; Suess, D. L. M. Controlling Substrate Binding to Fe_4S_4 Clusters through Remote Steric Effects. *Inorg. Chem.* **2019**, *58* (8), 5273–5280.
(24) Brown, A. C.; Suess, D. L. M. Valence Localization in Alkyne and Alkene Adducts of Synthetic $[Fe_4S_4]$+ Clusters. *Inorg. Chem.* **2023**, *62* (5), 1911–1918.
(25) Venkateswara Rao, P.; Holm, R. H. Synthetic Analogues of the Active Sites of Iron−Sulfur Proteins. *Chem. Rev.* **2004**, *104* (2), 527–560.
(26) Škoch, K.; Císařová, I.; Štěpnička, P. Selective Gold-Catalysed Synthesis of Cyanamides and 1-Substituted 1H-Tetrazol-5-Amines from Isocyanides. *Chem. Eur. J.* **2018**, *24* (52), 13788–13791.
(27) Carpenter, A. E.; Mokhtarzadeh, C. C.; Ripatti, D. S.; Havrylyuk, I.; Kamezawa, R.; Moore, C. E.; Rheingold, A. L.; Figueroa, J. S. Comparative Measure of the Electronic Influence of Highly Substituted Aryl Isocyanides. *Inorg. Chem.* **2015**, *54* (6), 2936–2944.
(28) Essenmacher, G. J.; Treichel, P. M. Electrochemistry of a Series of Hexakis(Aryl Isocyanide)Chromium(0) Complexes. *Inorg. Chem.* **1977**, *16* (4), 800–806.
(29) Treichel, P. M.; Mueh, H. J. Electrochemical Studies on $[Mn(CNR)_6]^+$ Complexes. *Inorg. Chem* **1977**, *16* (5), 1167–1169.
(30) Barybin, M. V.; Brennessel, W. W.; Kucera, B. E.; Minyaev, M. E.; Sussman, V. J.; Young, V. G.; Ellis, J. E. Homoleptic Isocyanidemetalates of 4d- and 5d-Transition Metals: $[Nb(CNXyl)_6]^-$, $[Ta(CNXyl)_6]^-$, and Derivatives Thereof. *J. Am. Chem. Soc.* **2007**, *129* (5), 1141–1150.
(31) Sarapu, A. C.; Fenske, R. F. The Transition Metal-Isocyanide Bond. An Approximate Molecular Orbital Study. *Inorg. Chem.* **1975**, *14* (2), 247–253.
(32) Yamamoto, Y. Zerovalent Transition Metal Complexes of Organic Isocyanides. *Coord. Chem. Rev.* **1980**, *32*, 193–233.
(33) King, R. B.; Saran, M. S. Isocyanide-Metal Complexes. II. Carbonyl and Cyanide Stretching Modes in Tertbutyl Isocyanide Derivatives of the Octahedral Metal Carbonyls. *Inorg. Chem.* **1974**, *13* (1), 74–78.
(34) Bellows, S. M.; Brennessel, W. W.; Holland, P. L. Effects of Ligand Halogenation on the Electron Localization, Geometry and Spin State of Low-Coordinate (β-Diketiminato)Iron Complexes. *Eur. J. Inorg. Chem.* **2016**, *2016* (20), 3344–3355.
(35) Bellow, J. A.; Yousif, M.; Cabelof, A. C.; Lord, R. L.; Groysman, S. Reactivity Modes of an Iron Bis(Alkoxide) Complex with Aryl Azides: Catalytic Nitrene Coupling vs Formation of Iron(III) Imido Dimers. *Organometallics* **2015**, *34* (12), 2917–2923.
(36) Chiang, K. P.; Barrett, P. M.; Ding, F.; Smith, J. M.; Kingsley, S.; Brennessel, W. W.; Clark, M. M.; Lachicotte, R. J.; Holland, P. L. Ligand Dependence of Binding to Three-Coordinate

Fe(II) Complexes. *Inorg. Chem.* **2009**, *48* (12), 5106–5116.
(37) Esposito, V.; Solari, E.; Floriani, C.; Re, N.; Rizzoli, C.; Chiesi-Villa, A. Binding and Redox Properties of Iron(II) Bonded to an Oxo Surface Modeled by Calix[4]Arene. *Inorg. Chem.* **2000**, *39* (12), 2604–2613.
(38) Turculet, L.; Feldman, J. D.; Tilley, T. D. Coordinatively and Electronically Unsaturated Zwitterionic Iron Silyl Complexes Featuring the Tripodal Phosphine Ligand $[PhB(CH_2P^iPr_2)_3]^-$. *Organometallics* **2003**, *22* (23), 4627–4629.
(39) Kim, M.; Euler, W. B.; Rosen, W. LFER Correlation of 13C Chemical Shift in Para-Substituted Phenyl Isocyanide: Implications for Formation of a Unique Polymer. *J. Org. Chem.* **1997**, *62* (11), 3766–3769.
(40) Hansch, C.; Leo, A.; Taft, R. W. A Survey of Hammett Substituent Constants and Resonance and Field Parameters. *Chem. Rev.* **1991**, *91* (2), 165–195.
(41) Hammett, L. P. The Effect of Structure upon the Reactions of Organic Compounds. Temperature and Solvent Influences. *J. Chem. Phys.* **1936**, *4* (9), 613–617.
(42) Ye, S.; Bill, E.; Neese, F. Electronic Structures of the $[Fe(N_2)(SiP^iPr_3)]^{+1/0/-1}$ Electron Transfer Series: A Counterintuitive Correlation between Isomer Shifts and Oxidation States. *Inorg. Chem.* **2016**, *55* (7), 3468–3474.
(43) *Physical Methods in Bioinorganic Chemistry: Spectroscopy and Magnetism*; Que, L., Ed.; University Science Books: Sausalito.
(44) Ye, M.; Thompson, N. B.; Brown, A. C.; Suess, D. L. M. A Synthetic Model of Enzymatic $[Fe_4S_4]$-Alkyl Intermediates. *J. Am. Chem. Soc.* **2019**, *141* (34), 13330–13335.
(45) McSkimming, A.; Sridharan, A.; Thompson, N. B.; Müller, P.; Suess, D. L. M. An [Fe4S4]3+-Alkyl Cluster Stabilized by an Expanded Scorpionate Ligand. *J. Am. Chem. Soc.* **2020**, *142* (33), 14314–14323. https://doi.org/10.1021/jacs.0c06334.
(46) Tao, J.; Perdew, J. P.; Staroverov, V. N.; Scuseria, G. E. Climbing the Density Functional Ladder: Nonempirical Meta–Generalized Gradient Approximation Designed for Molecules and Solids. *Phys. Rev. Lett.* **2003**, *91* (14), 3–6.
(47) Pantazis, D. A.; Chen, X. Y.; Landis, C. R.; Neese, F. All-Electron Scalar Relativistic Basis Sets for Third-Row Transition Metal Atoms. *J. Chem. Theory Comput.* **2008**, *4* (6), 908–919.
(48) Pipek, J.; Mezey, P. G. A Fast Intrinsic Localization Procedure Applicable for Ab Initio and Semiempirical Linear Combination of Atomic Orbital Wave Functions. *J. Chem. Phys.* **1989**, *90* (9), 4916–4926.
(49) Knizia, G. Intrinsic Atomic Orbitals: An Unbiased Bridge between Quantum Theory and Chemical Concepts. *J. Chem. Theory Comput.* **2013**, *9* (11), 4834–4843.
(50) Noodleman, L.; Peng, C. Y.; Case, D. A.; Mouesca, J. M. Orbital Interactions, Electron Delocalization and Spin Coupling in Iron-Sulfur Clusters. *Coord. Chem. Rev.* **1995**, *144* (C), 199–244.
(51) Powers, T. M.; Betley, T. A. Testing the Polynuclear Hypothesis: Multielectron Reduction of Small Molecules by Triiron Reaction Sites. *J. Am. Chem. Soc.* **2013**, *135* (33), 12289–12296.
(52) Zhao, Q.; Betley, T. A. Synthesis and Redox Properties of Triiron Complexes Featuring Strong Fe-Fe Interactions. *Angew. Chem. Int. Ed.* **2011**, *50* (3), 709–712.

Supporting Information

A. Experimental Methods

General Considerations

All reactions were performed using standard Schlenk techniques or in an LC Technologies inert atmosphere glove box under an atmosphere of nitrogen. Glassware was dried in an oven at 160 °C prior to use. Molecular sieves (3 Å), and Celite® were activated by heating to 300 °C overnight under vacuum prior to storage under an atmosphere of nitrogen. Tetrahydrofuran (THF) was distilled from sodium/benzophenone, *o*-difluorobenzene (DFB) and fluorobenzene (PhF) were distilled from CaH_2, C_6D_6 was degassed by three freeze–pump–thaw cycles, and other solvents were degassed by sparging with argon and dried by passing through a column of activated alumina. All solvents were stored under an atmosphere of nitrogen over 3 Å molecular sieves.

NMR spectra were recorded on Bruker 400 and 500 MHz spectrometers. ^{1}H chemical shifts are given relative to residual solvent peaks. Solvent suppression for NMR in protonated solvents was carried out using WET solvent suppression.[1] EPR spectra were recorded on a Bruker EMX spectrometer at 9.37 GHz as frozen glasses. Simulations were performed using EasySpin[2] (5.2.21) in Matlab (R2017b). UV-vis spectra were recorded on a Cary 50 spectrometer. Zero-field ^{57}Fe Mössbauer spectra were measured with a constant-acceleration spectrometer at 80K. Isomer shifts are quoted relative to α-Fe foil at room temperature; Mössbauer spectra were simulated with WMOSS v.4.[3] X-ray structural determinations were performed at the MIT diffraction facility using a Bruker X8 diffractometer with an APEX II CCD detector or a Bruker D8 Venture diffractometer with a Photon2 CPAD detector. Diffraction data was collected, integrated, and corrected for absorption using Bruker APEX3 software and its associated modules (SAINT,

SADABS, TWINABS). Structural solutions and refinements (on F^2) were carried out using SHELXT and SHELXL-2018 in ShelXle.[4] Ellipsoid plots and figures were made using Mercury.

$(IMes)_3Fe_4S_4Cl$[5], $NaBAr^F_4$[6] and $[(IMes)_3Fe_4S_4(OEt_2)][BAr^F_4]$[7] were prepared according to literature procedures.

Statement on Compound Purity

The purity of all compounds was assessed by a variety of spectroscopic and analytical methods as detailed below. All isocyanide complexes [**1-CNAr**]$^+$ are air-sensitive but can be isolated as crystalline solids in high purity as determined by NMR, EPR, and Mössbauer spectroscopic analysis as well as H and N content from elemental analysis. Low C content was obtained by elemental analysis as has been observed for other members of this class of molecules[7–10] and in other contexts.[11] Elemental analysis results are as follows:

[**1-CNAr$^{4\text{-NMe2}}$**][BAr^F_4]: Anal. Found: C, 52.08; H, 4.04; N, 4.89. Calcd. for $C_{104}H_{94}N_8Fe_4S_4BF_{24}$: C, 54.92; H, 4.17; N, 4.93.

[**1-CNAr$^{4\text{-OMe}}$**][BAr^F_4]: Anal. Found: C, 50.02; H, 3.93; N, 4.01. Calcd. for $C_{103}H_{91}N_7Fe_4S_4BF_{24}O$: C, 54.71; H, 4.06; N, 4.34.

[**1-CNAr$^{4\text{-Me}}$**][BAr^F_4]: Anal. Found: C, 51.58; H, 3.86; N, 4.27. Calcd. for $C_{103}H_{91}N_7Fe_4S_4BF_{24}$: C, 55.10; H, 4.09; N, 4.37.

[**1-CNAr$^{3\text{-OMe}}$**][BAr^F_4]: Anal. Found: C, 52.63; H, 4.17; N, 4.18. Calcd. for $C_{103}H_{91}N_7Fe_4S_4BF_{24}O$: C, 54.71; H, 4.06; N, 4.34.

[**1-CNPh**][BAr^F_4]: Anal. Found: C, 52.24; H, 3.85; N, 4.29. Calcd. for $C_{102}H_{89}N_7Fe_4S_4BF_{24}$: C, 54.91; H, 4.02; N, 4.39.

[**1-CNAr$^{4\text{-F}}$**][BAr$^{F}_4$]: Anal. Found: C, 52.37; H, 3.98; N, 4.23. Calcd. for $C_{102}H_{88}N_7Fe_4S_4BF_{25}$: C, 54.47; H, 3.94; N, 4.36.

[**1-CNAr$^{4\text{-Cl}}$**][BAr$^{F}_4$]: Anal. Found: C, 49.60; H, 3.77; N, 4.12. Calcd. for $C_{102}H_{88}N_7Fe_4S_4BF_{24}Cl$: C, 54.07; H, 3.92; N, 4.33.

[**1-CNAr$^{4\text{-I}}$**][BAr$^{F}_4$]: Anal. Found: C, 46.34; H, 3.72; N, 3.73. Calcd. for $C_{102}H_{88}N_7Fe_4S_4BF_{24}I$: C, 51.97; H, 3.76; N, 4.16.

[**1-CNAr$^{4\text{-CF3}}$**][BAr$^{F}_4$]: Anal. Found: C, 49.89; H, 3.67; N, 4.10. Calcd. for $C_{103}H_{88}N_7Fe_4S_4BF_{27}$: C, 53.81; H, 3.86; N, 4.26.

[**1-CNAr$^{3,5\text{-(CF3)2}}$**][BAr$^{F}_4$]: Anal. Found: C, 44.79; H, 3.43; N, 3.41. Calcd. for $C_{103}H_{88}N_7Fe_4S_4BF_{27}\cdot(C_6H_4F_2)_2$: C, 53.68; H, 3.69; N, 3.78.

General procedure for isocyanide synthesis:

4-dimethyaminophenylisocyanide, 4-methoxyphenylisocyanide, 4-methylphenylisocyanide, 3-methoxyphenylisocyanide, phenylisocyanide, 4-fluorophenylisocyanide, 4-chlorophenylisocyanide, 4-iodophenylisocyanide, and 4-trifluoromethylphenylisocyanide were prepared according to a modification of literature procedure.[12] The respective aniline (5 g) was dissolved in toluene (10 mL) and formic acid (1.2 equiv.) was added dropwise. The resulting solution was heated to 60 °C and stirred overnight. Saturated aqueous $NaHCO_3$ was added followed by dichloromethane and the organic layer was separated. The organic layer was dried over Na_2SO_4 and rotovapped to dryness to provide the intermediate formamide. The formamide was used in the next step without further purification.

The formamide was dissolved in dichloromethane (50 mL) and triethylamine (3.2 equiv.) was added. The mixture was cooled to 0 °C and phosphorous oxychloride (1.1 equiv.) was added

dropwise. The solution was stirred at 0 °C for 15 minutes, warmed to room temperature, and stirred for an additional three hours. The mixture was cooled to 0 °C and quenched by slow addition of saturated aqueous $NaHCO_3$. After initial gas evolution, dichloromethane was added and the organic layer was separated and dried over Na_2SO_4. The dichloromethane was concentrated to a total volume of 10 mL and purified by passing it through a plug of silica gel (4 cm) with dichloromethane. The isocyanide was isolated by evaporation. Spectroscopic properties were consistent with previous reports.[12–14]

3,5-bis(trifluoromethyl)phenylisocyanide was synthesized as above with the following minor modifications: diisopropylamine was used as a base in place of triethylamine and the reaction was allowed to proceed at room temperature for 24 h.[15] Spectroscopic properties were consistent with previous reports.[15]

General procedure for synthesis of $[Fe_4S_4]$ isocyanide adducts:

Method A: $[(IMes)_3Fe_4S_4(OEt_2)][BAr^F{}_4]$ (50 mg, 0.023 mmol) was dissolved in 1 mL of Et_2O. A solution of isocyanide in Et_2O (0.024 mmol from a 10 mg/mL stock solution, 1.05 equiv) was added dropwise. The solution was concentrated to 0.5 mL and *n*-pentane (7 mL) was added to precipitate the product as black microcrystals. Yields were typically around 90%.

Method B: $(IMes)_3Fe_4S_4Cl$ (50 mg, 0.038 mmol) was dissolved in 1 mL of Et_2O and cooled to –78 °C. A solution $NaBArF_4$ in Et_2O (0.68 mL of a 50 mg/mL stock solution, 0.038 mmol, 1 equiv.) was added dropwise followed immediately by a solution of isocyanide in Et_2O (0.038 mmol from a 10 mg/mL stock solution, 1 equiv.). The mixture was stirred at –78 °C for 5 minutes then allowed to warm to room temperature. The solution was filtered through Celite, concentrated to a total

volume of 0.5 mL, and *n*-pentane (7 mL) was added to precipitate the product as black microcrystals. Yields were typically between around 75%.

The two methods were applied to the preparation of all ten isocyanide adducts; both methods gave material of comparable purity for all isocyanides except $CNAr^{3,5\text{-}(CF3)2}$, for which method B was preferred. For the remainder, method A was more facile and higher yielding. NMR spectra were recorded in Et_2O and chemical shifts are reported referenced to residual silicone grease at 0.11 ppm.

[**1-CNAr$^{4\text{-}NMe2}$**][$BAr^F{}_4$]: Method A. Yield: 49.6 mg (96 %). Crystals for X-ray diffraction were grown by layering *n*-pentane onto a solution of [**1-CNAr$^{4\text{-}NMe2}$**]$^+$ in DFB, followed by storage at –35 °C overnight. ^{1}H NMR (400 MHz, Et_2O, 293 K) δ 8.14 (d, J = 8.9 Hz, 2H, CNAr *o*-H), 7.73 (s, 8H, [$BAr^F{}_4$]$^-$), 7.50 (s, 4H, [$BAr^F{}_4$]$^-$), 7.38 (s, 6H, backbone CH), 7.00 (d, J = 8.9 Hz, 2H, CNAr *m*-H), 6.97 (s, 12H, Mes *m*-H), 2.67 (s, 6H, CNAr N(CH_3)$_2$), 2.39 (s, 18H, Mes *p*-CH_3), 2.33 (s, 36H, Mes *o*-C*H*$_3$). EPR: g_1 = 2.176, g_2 = 1.976, g_3 = 1.948 (10:1 toluene:Et_2O, 20 K, 9.37 GHz). FT-IR (DFB solution, cm^{-1}): 2085.

[**1-CNAr$^{4\text{-}OMe}$**][$BAr^F{}_4$]**:** Method A. Yield: 47.8 mg (93%). Crystals for X-ray diffraction were grown by layering *n*-pentane onto a solution of [**1-CNAr$^{4\text{-}OMe}$**]$^+$ in DFB, followed by storage at –35 °C overnight. ^{1}H NMR (400 MHz, Et_2O, 293 K) δ 8.05 (br s, 2H, CNAr *o*-H), 7.72 (s, 8H, [$BAr^F{}_4$]$^-$), 7.49 (s, 4H, [$BAr^F{}_4$]$^-$), 7.34 (s, 6H, backbone CH), 7.14 (d, J = 8.6 Hz, 2H, CNAr *m*-H), 6.96 (s, 12H, Mes *m*-H), 3.84 (s, 3H, CNAr OCH_3), 2.89 (s, 18H, Mes *p*-CH_3), 2.30 (s, 36H, Mes *o*-C*H*$_3$). EPR: g_1 = 2.181, g_2 = 1.981, g_3 = 1.952 (10:1 toluene:Et_2O, 20 K, 9.37 GHz). FT-IR (DFB solution, cm^{-1}): 2072.

[**1-CNAr$^{4\text{-Me}}$**][BAr$^{F}{}_4$]**:** Method B. Yield: 61.2 mg (85%). Crystals for X-ray diffraction were grown by layering *n*-pentane onto a solution of [**1-CNAr$^{4\text{-Me}}$**]$^+$ in DFB, followed by storage at –35 °C overnight. ^{1}H NMR (400 MHz, Et_2O, 293 K) δ 7.76 (d, J = 8.0 Hz, 2H, CNAr *o*-H), 7.73 (s, 8H, [BAr$^{F}{}_4$]$^-$), 7.49 (s, 4H, [BAr$^{F}{}_4$]$^-$), 7.49 (d, J = 8.0 Hz, 2H, CNAr *m*-H), 7.32 (s, 6H, backbone CH), 6.96 (s, 12H, Mes *m*-H), 2.37 (s, 18H, Mes *p*-CH_3), 2.34 (s, 3H, CNAr *p*-CH_3), 2.29 (s, 36H, Mes *o*-C*H*$_3$). EPR: g_1 = 2.181, g_2 = 1.982, g_3 = 1.952 (10:1 toluene:Et_2O, 20 K, 9.37 GHz). FT-IR (DFB solution, cm^{-1}): 2061.

[**1-CNAr$^{3\text{-OMe}}$**][BAr$^{F}{}_4$]**:** Method A. Yield: 42.1 mg (82%). Crystals for X-ray diffraction were grown by layering *n*-pentane onto a solution of [**1-CNAr$^{3\text{-OMe}}$**]$^+$ in DFB, followed by storage at –35 °C overnight. ^{1}H NMR (400 MHz, Et_2O, 293 K) δ 7.72 (s, 8H, [BAr$^{F}{}_4$]$^-$), 7.49 (s, 4H, [BAr$^{F}{}_4$]$^-$), 7.46 (br s, 1H, CNAr Ar-H), 7.32 (br s, 1H, CNAr Ar-H), 7.29 (s, 6H, backbone CH), 7.14 (br s, 1H, CNAr Ar-H), 7.08 (d, J = 7.4 Hz, 1H, CNAr Ar-H), 6.96 (s, 12H, Mes *m*-H), 3.96 (s, 3H, CNAr OCH_3), 2.38 (s, 18H, Mes *p*-CH_3), 2.28 (s, 36H, Mes *o*-C*H*$_3$). EPR: g_1 = 2.187, g_2 = 1.989, g_3 = 1.961 (10:1 toluene:Et_2O, 20 K, 9.37 GHz). FT-IR (DFB solution, cm^{-1}): 2052.

[**1-CNPh**][BAr$^{F}{}_4$]**:** Method A. Yield: 48.7 mg (86%). Crystals for X-ray diffraction were grown by layering *n*-pentane onto a solution of [**1-CNPh**]$^+$ in Et_2O, followed by storage at –35 °C overnight. ^{1}H NMR (500 MHz, Et_2O, 293 K) δ 7.78 (br s, 2H, CNAr *o*-H), 7.73 (s, 8H, [BAr$^{F}{}_4$]$^-$), 7.58 (t, J = 7.0 Hz, 2H, CNAr *m*-H), 7.52 (br s, 1H, CNAr *p*-H) 7.50 (s, 4H, [BAr$^{F}{}_4$]$^-$), 7.30 (s, 6H, backbone CH), 6.97 (s, 12H, Mes *m*-H), 2.38 (s, 18H, Mes *p*-CH_3), 2.28 (s, 36H, Mes *o*-

C*H*$_3$). EPR: g_1 = 2.181, g_2 = 1.984, g_3 = 1.956 (10:1 toluene:Et_2O, 20 K, 9.37 GHz). FT-IR (DFB solution, cm^{-1}): 2054.

[**1-CNAr$^{4\text{-F}}$**][BAr^F_4]**:** Method B. Yield: 64.6 mg (75%). Crystals for X-ray diffraction were grown by layering *n*-pentane onto a solution of [**1-CNAr$^{4\text{-F}}$**]$^+$ in Et_2O, followed by storage at –35 °C overnight. ^{1}H NMR (500 MHz, Et_2O, 293 K) δ 7.88 (br s, 2H, CNAr *o*-H), 7.72 (s, 8H, [BAr^F_4]$^-$), 7.49 (s, 4H, [BAr^F_4]$^-$), 7.38 (t, J = 7.0 Hz, 2H, CNAr *m*-H), 7.27 (s, 6H, backbone CH), 6.96 (s, 12H, Mes *m*-H), 2.37 (s, 18H, Mes *p*-CH_3), 2.26 (s, 36H, Mes *o*-C*H*$_3$). ^{19}F NMR (470 MHz, Et_2O, 293 K) δ –62.8 ([BAr^F_4]$^-$), –110 (CNAr *p*-F). EPR: g_1 = 2.182, g_2 = 1.984, g_3 = 1.955 (10:1 toluene:Et_2O, 20 K, 9.37 GHz). FT-IR (DFB solution, cm^{-1}): 2041.

[**1-CNAr$^{4\text{-Cl}}$**][BAr^F_4]**:** Method A. Yield: 51.6 mg (99%). Crystals for X-ray diffraction were grown by layering *n*-pentane onto a solution of [**1-CNAr$^{4\text{-Cl}}$**]$^+$ in Et_2O, followed by storage at –35 °C overnight. ^{1}H NMR (400 MHz, Et_2O, 293 K) δ 7.72 (s, 8H, [BAr^F_4]$^-$), 7.62 (s, 4H, CNAr *o*-H and *m*-H), 7.49 (s, 4H, [BAr^F_4]$^-$), 7.23 (s, 6H, backbone CH), 6.96 (s, 12H, Mes *m*-H), 2.38 (s, 18H, Mes *p*-CH_3), 2.25 (s, 36H, Mes *o*-C*H*$_3$). EPR: g_1 = 2.188, g_2 = 1.990, g_3 = 1.963 (10:1 toluene:Et_2O, 20 K, 9.37 GHz). FT-IR (DFB solution, cm^{-1}): 2034.

[**1-CNAr$^{4\text{-I}}$**][BAr^F_4]**:** Method A. Yield: 48.1 mg (89%). Crystals for X-ray diffraction were grown by layering *n*-pentane onto a solution of [**1-CNAr$^{4\text{-I}}$**]$^+$ in Et_2O, followed by storage at –35 °C overnight. ^{1}H NMR (400 MHz, Et_2O, 293 K) δ 7.95 (d, J = 8.5 Hz, 2H, CNAr *o*-H), 7.72 (s, 8H, [BAr^F_4]$^-$), 7.49 (s, 4H, [BAr^F_4]$^-$), 7.34 (d, J = 8.5 Hz, 2H, CNAr *m*-H), 7.22 (s, 6H, backbone CH),

6.96 (s, 12H, Mes *m*-H), 2.39 (s, 18H, Mes *p*-CH_3), 2.24 (s, 36H, Mes *o*-C*H*$_3$). EPR: $g_1 = 2.186$, $g_2 = 1.990$, $g_3 = 1.963$ (10:1 toluene:Et_2O, 20 K, 9.37 GHz). FT-IR (DFB solution, cm^{-1}): 2027.

[**1-CNAr$^{4\text{-}CF3}$**][BAr^F_4]**:** Method A. Yield: 41.1 mg (78%). Crystals for X-ray diffraction were grown by layering *n*-pentane onto a solution of [**1-CNAr$^{4\text{-}CF3}$**]$^+$ in Et_2O, followed by storage at –35 °C overnight. ^{1}H NMR (400 MHz, Et_2O, 293 K) δ 7.87 (d, J = 8.0 Hz, 2H, CNAr *o*-H), 7.73 (s, 8H, [BAr^F_4]$^-$), 7.49 (s, 4H, [BAr^F_4]$^-$), 7.40 (d, J = 8.0 Hz, 2H, CNAr *m*-H), 7.13 (s, 6H, backbone CH), 6.97 (s, 12H, Mes *m*-H), 2.38 (s, 18H, Mes *p*-CH_3), 2.22 (s, 36H, Mes *o*-C*H*$_3$). ^{19}F NMR (470 MHz, Et_2O, 293 K) δ –61.4 (CNAr *p*-CF_3), –62.8 ([BAr^F_4]$^-$). EPR: $g_1 = 2.183$, $g_2 = 1.990$, $g_3 = 1.962$ (10:1 toluene:Et_2O, 20 K, 9.37 GHz). FT-IR (DFB solution, cm^{-1}): 2006.

[**1-CNAr$^{3,5\text{-}(CF3)2}$**][BAr^F_4]**:** Method B. Yield: 75 mg (83%). Crystals for X-ray diffraction were grown by layering *n*-pentane onto a solution of [**1-CNAr$^{3,5\text{-}(CF3)2}$**]$^+$ in DFB, followed by storage at –35 °C overnight. ^{1}H NMR (400 MHz, Et_2O, 293 K) δ 7.72 (s, 8H, [BAr^F_4]$^-$), 7.49 (s, 4H, [BAr^F_4]$^-$), 7.42 (s, 2H, CNAr *o*-H), 7.23 (s, 1H, CNAr *p*-H), 7.02 (s, 12H, Mes *m*-H), 6.94 (s, 6H, backbone CH), 2.41 (s, 18H, Mes *p*-CH_3), 2.19 (s, 36H, Mes *o*-C*H*$_3$). ^{19}F NMR (470 MHz, Et_2O, 293 K) δ –62.6 ([BAr^F_4]$^-$), –63.2 (CNAr *m,m*-CF_3). EPR: $g_1 = 2.193$, $g_2 = 1.996$, $g_3 = 1.965$ (10:1 toluene:Et_2O, 20 K, 9.37 GHz). FT-IR (DFB solution, cm^{-1}): 1979.

NMR spectra

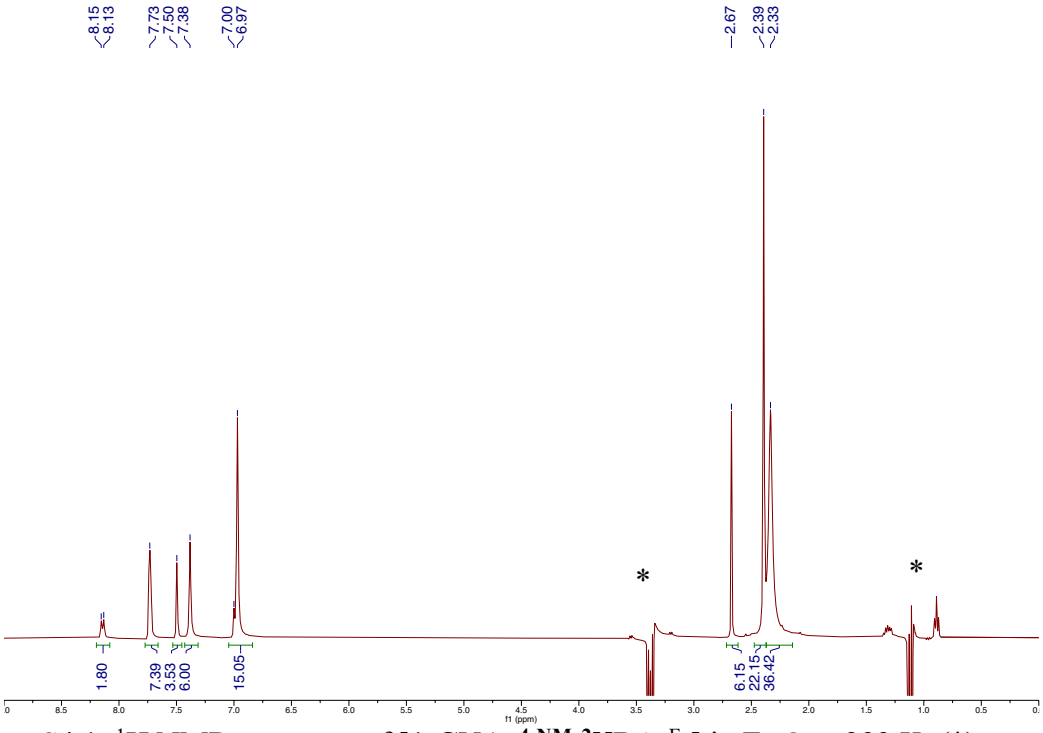

Figure S4.1: ^{1}H NMR spectrum of [**1-CNAr$^{4\text{-NMe2}}$**][BAr$^{F}_{4}$] in Et_2O at 293 K. (*) Suppressed Et_2O resonances.

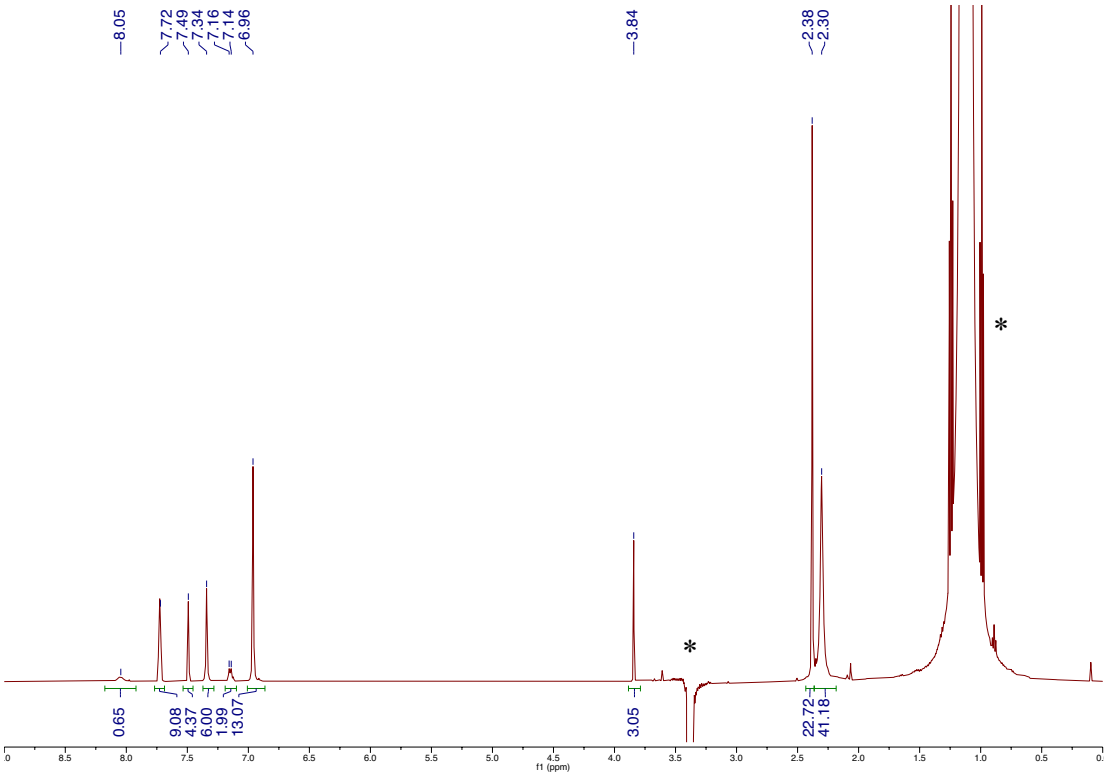

Figure S4.2: ^{1}H NMR spectrum of [**1-CNAr$^{4\text{-OMe}}$**][BAr$^{F}_{4}$] in Et_2O at 293 K. (*) Suppressed Et_2O resonances.

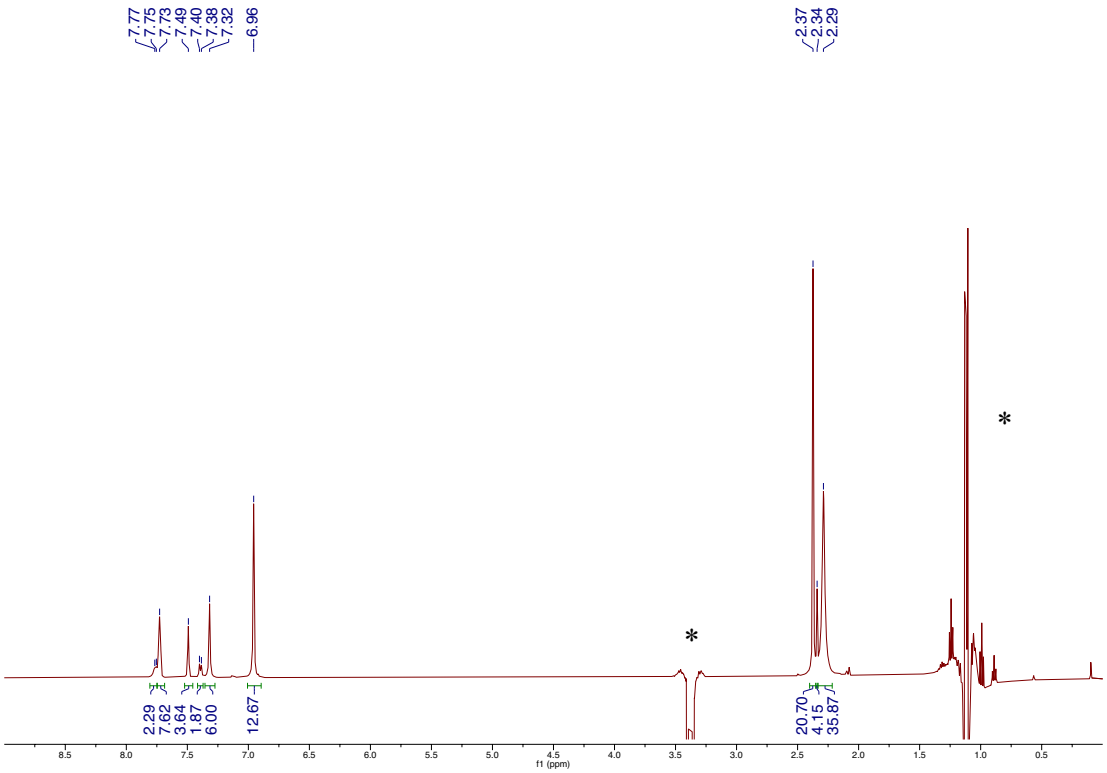

Figure S4.3: ^{1}H NMR spectrum of [**1-CNAr$^{4\text{-Me}}$**][BAr$^{F}_{4}$] in Et_2O at 293 K. (*) Suppressed Et_2O resonances.

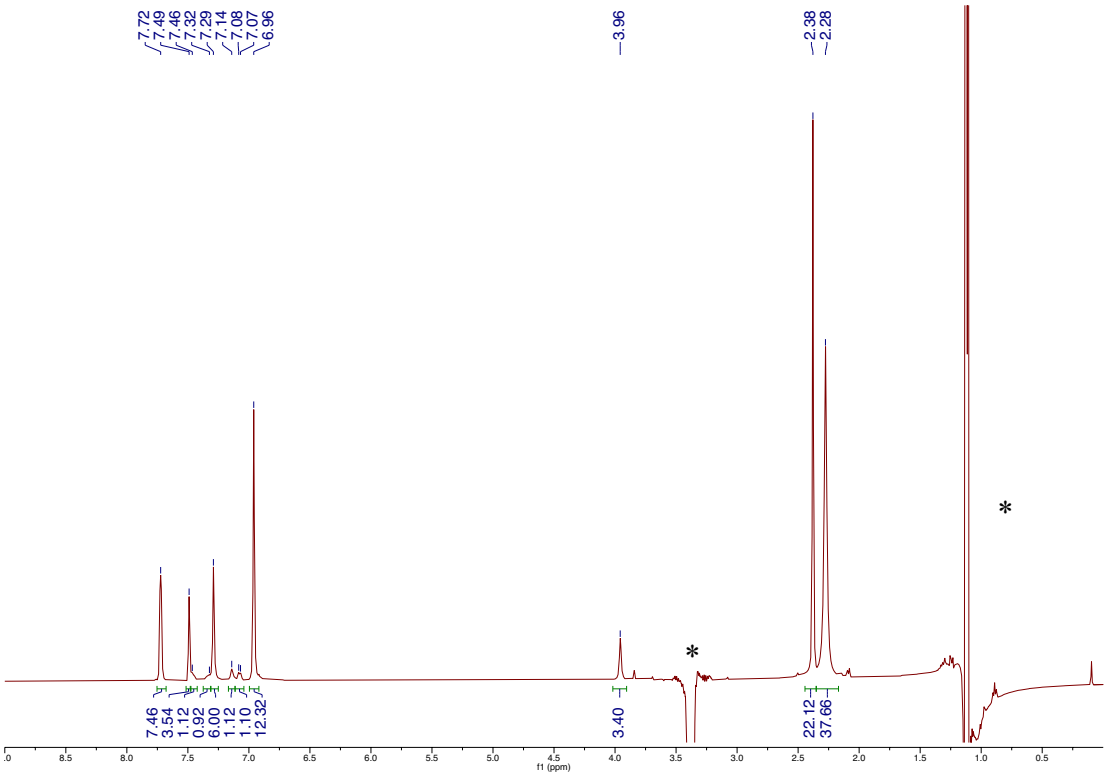

Figure S4.4: ^{1}H NMR spectrum of [**1-CNAr$^{3\text{-OMe}}$**][BAr$^{F}_{4}$] in Et_2O at 293 K. (*) Suppressed Et_2O resonances.

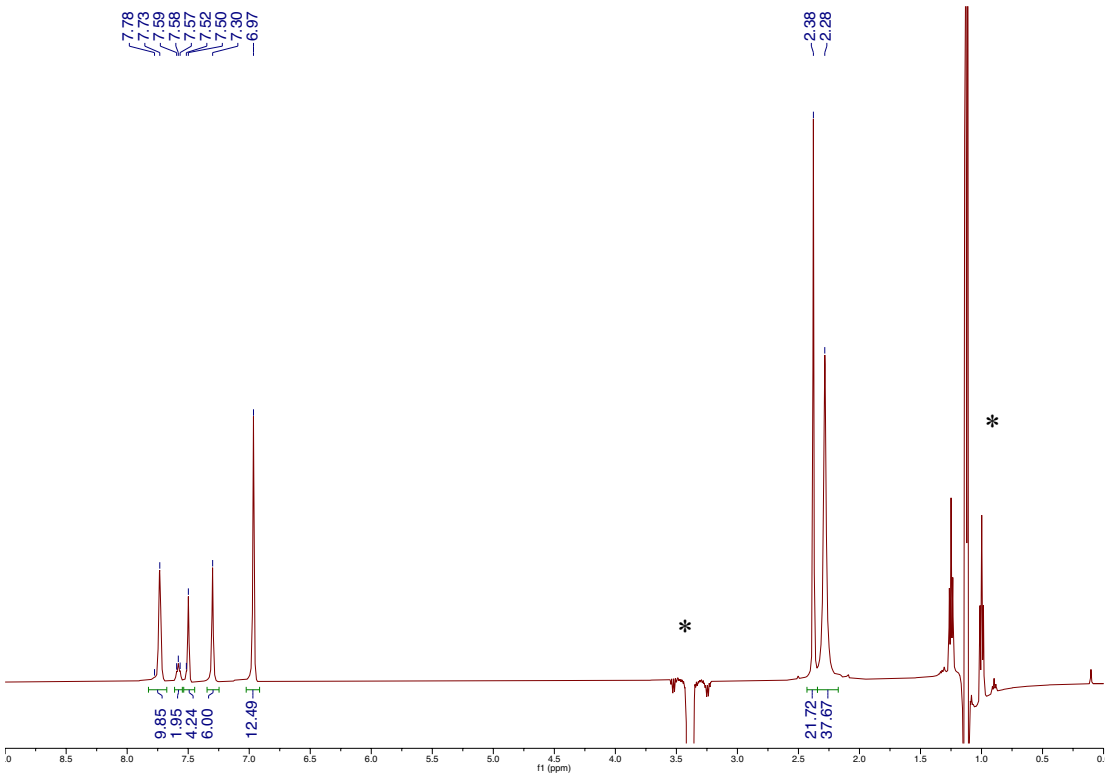

Figure S4.5: ^{1}H NMR spectrum of [**1-CNPh**][BAr$^{F}_{4}$] in Et_2O at 293 K. (*) Suppressed Et_2O resonances.

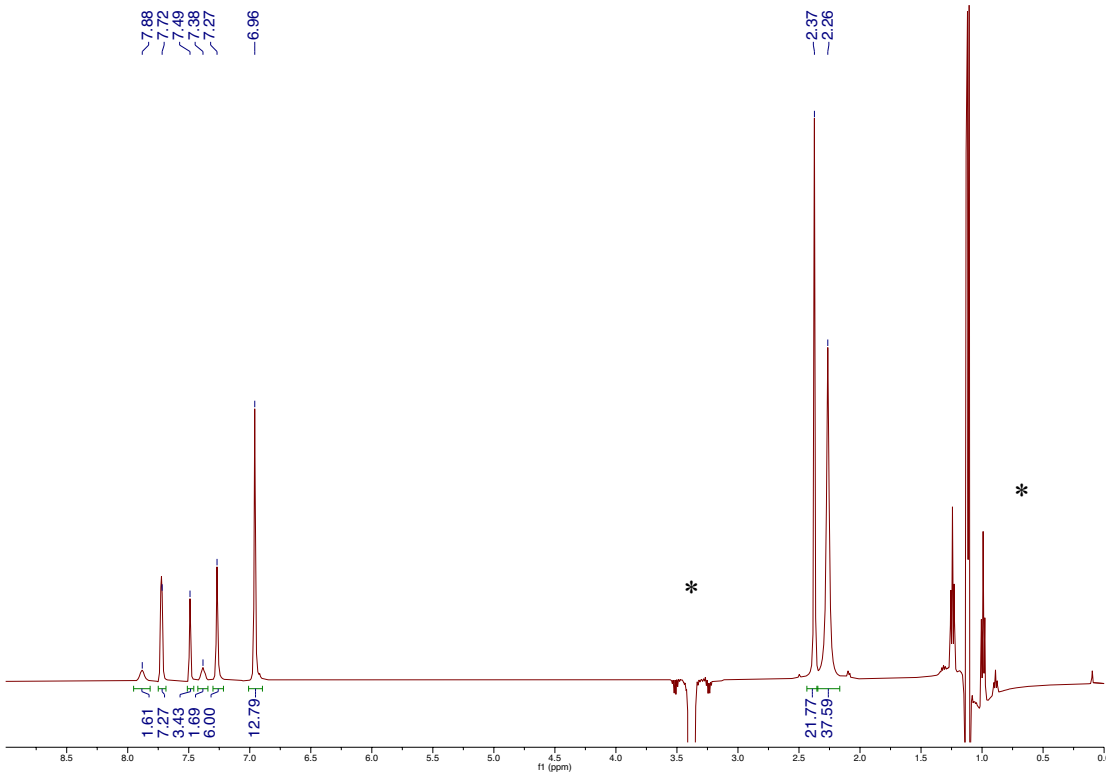

Figure S4.6: ^{1}H NMR spectrum of [**1-CNAr$^{4\text{-F}}$**][BAr$^{F}_{4}$]in Et_2O at 293 K. (*) Suppressed Et_2O resonances.

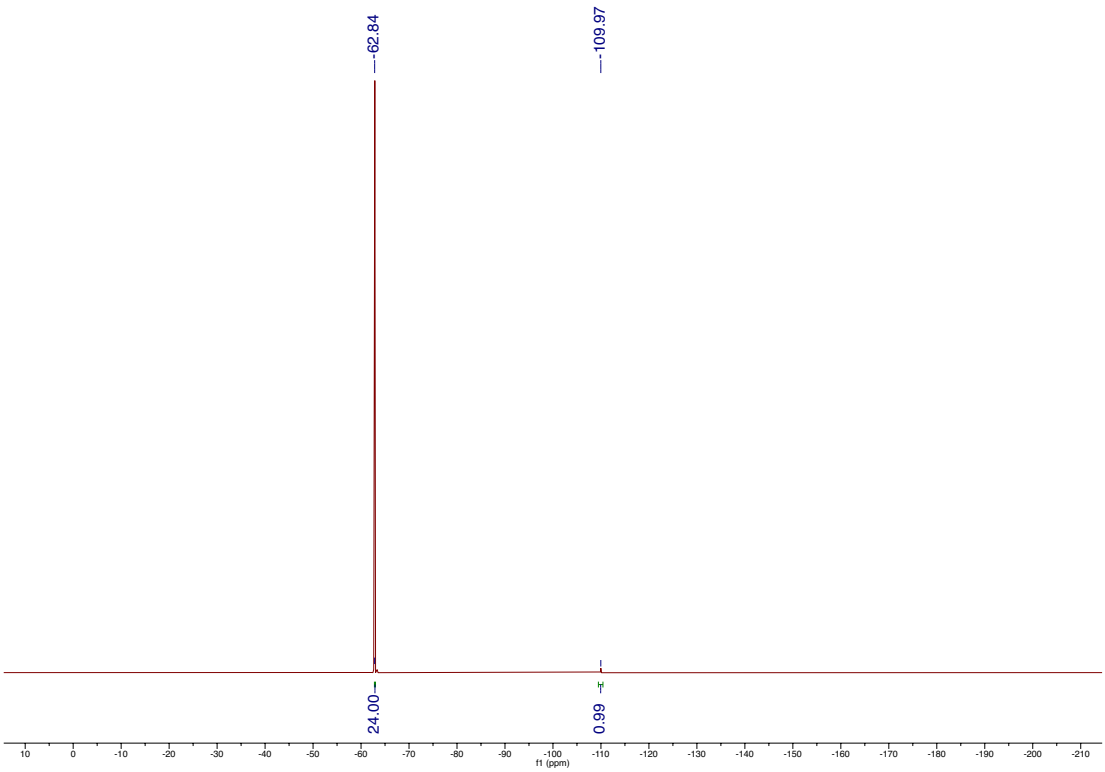

Figure S4.7: ^{19}F NMR spectrum of [**1-CNAr$^{4\text{-F}}$**][BAr$^{F}_{4}$]in Et_2O at 293 K.

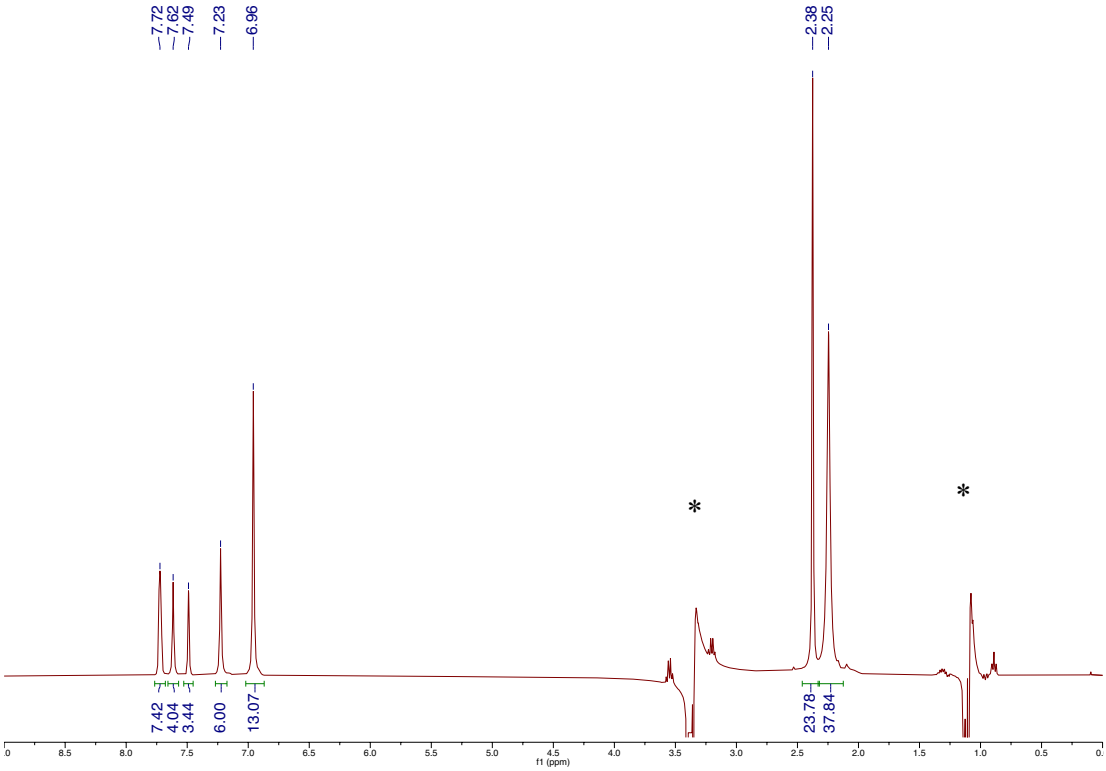

Figure S4.8: ^{1}H NMR spectrum of [**1-CNAr$^{4\text{-Cl}}$**][BAr$^{F}_{4}$] in Et_2O at 293 K. (*) Suppressed Et_2O resonances.

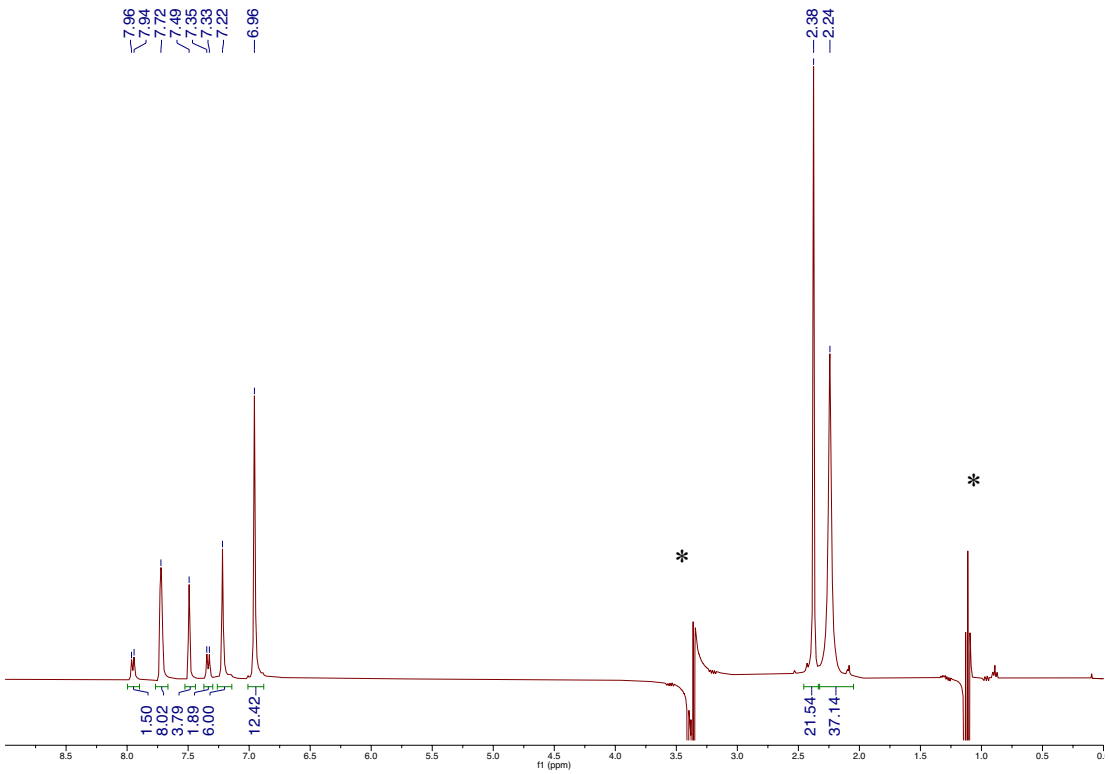

Figure S4.9: ^{1}H NMR spectrum of [**1-CNAr$^{4\text{-I}}$**][BAr$^{F}_{4}$] in Et_2O at 293 K. (*) Suppressed Et_2O resonances.

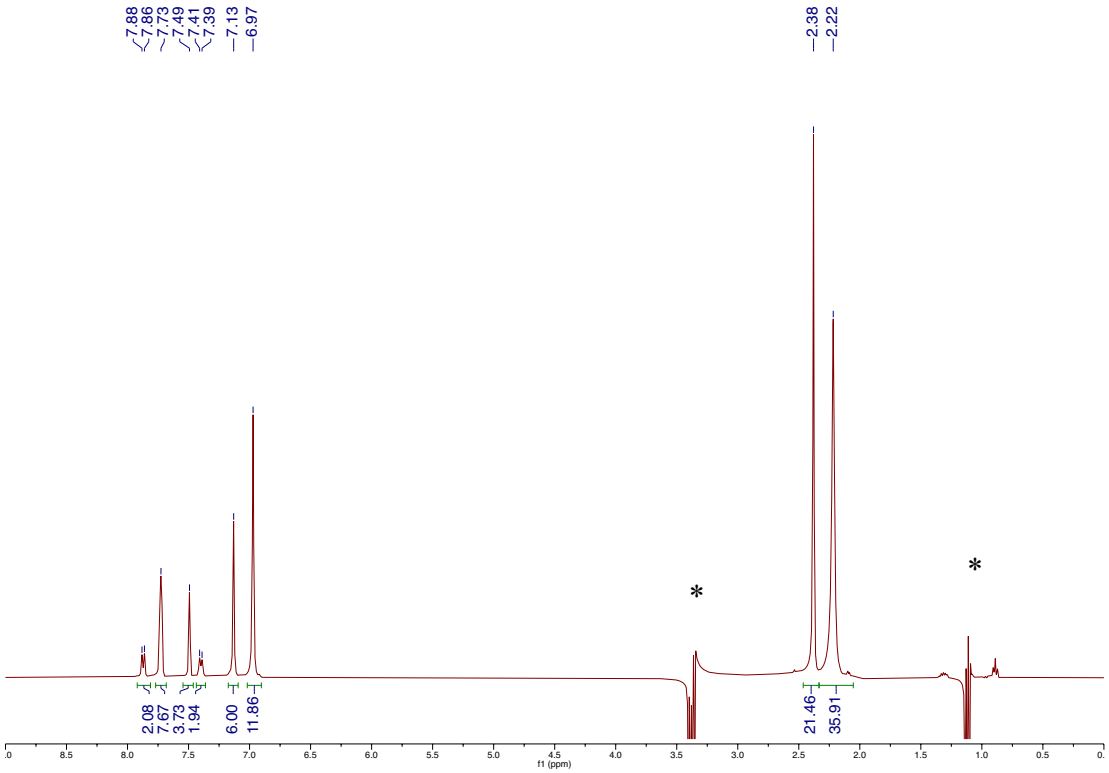

Figure S4.10: ^{1}H NMR spectrum of [**1-CNAr$^{4\text{-CF3}}$**][BAr$^{F}_{4}$] in Et_2O at 293 K. (*) Suppressed Et_2O resonances.

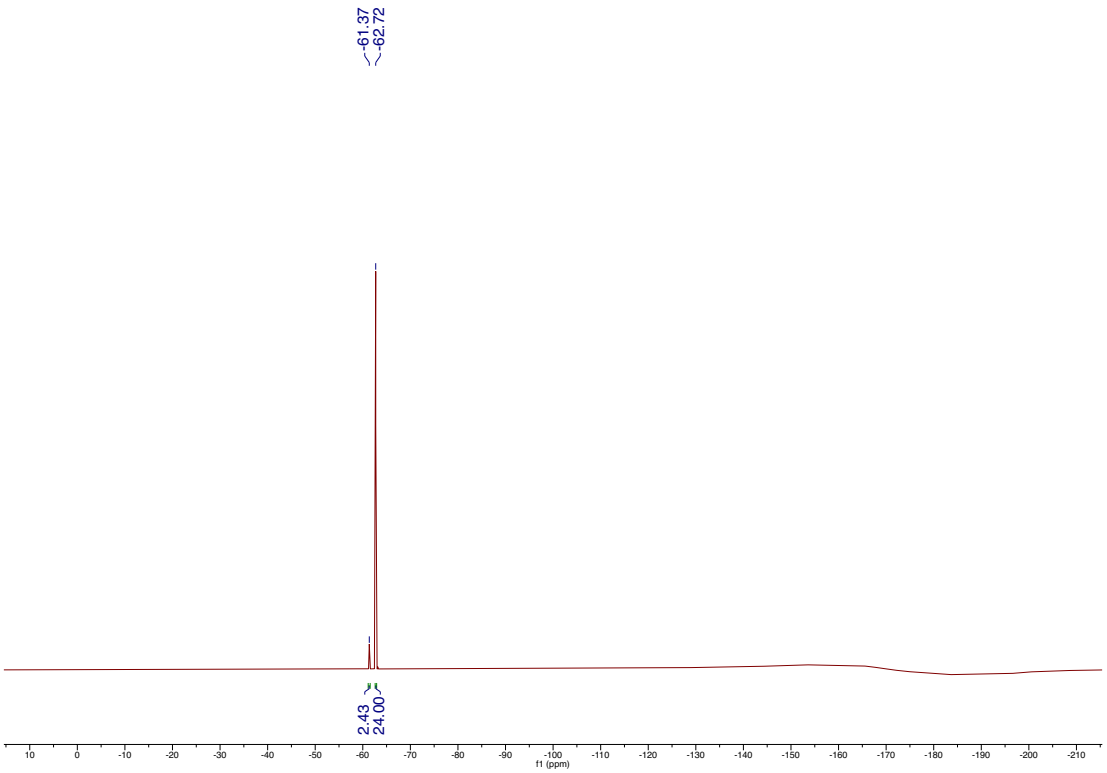

Figure S4.11: ^{19}F NMR spectrum of [**1-CNAr$^{4\text{-}CF3}$**][BAr$^{F}_{4}$] in Et_2O at 293 K.

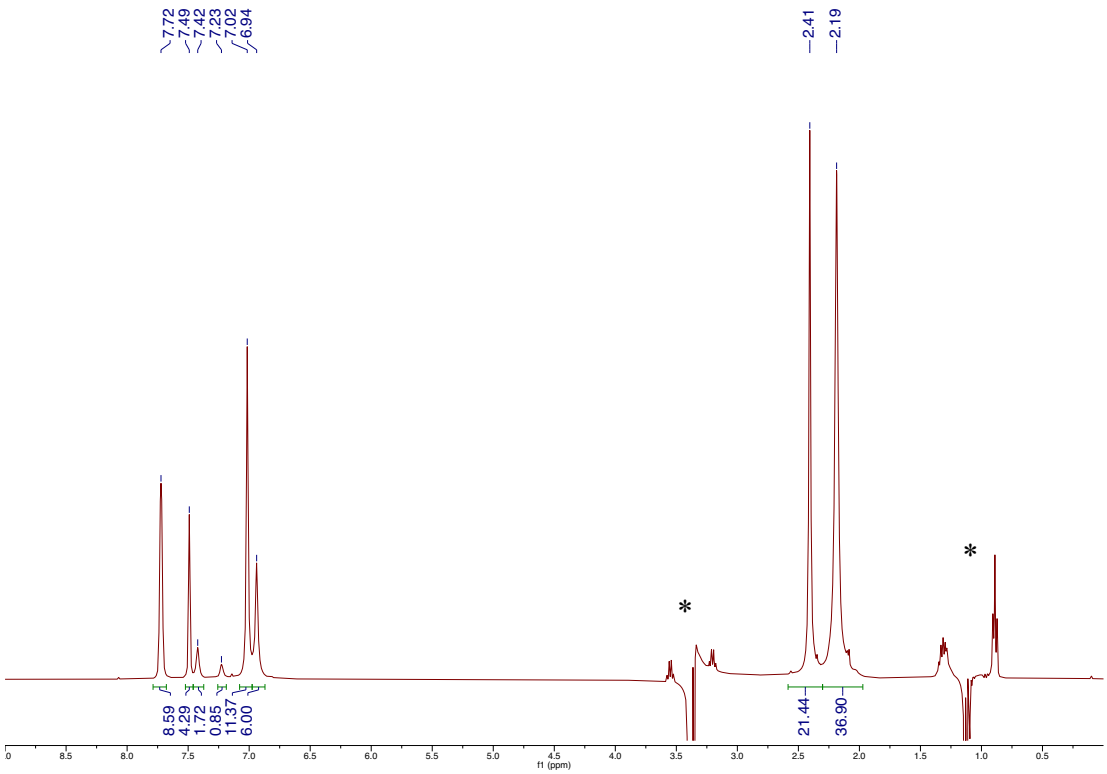

Figure S4.12: ^{1}H NMR spectrum of [**1-CNAr$^{3,5\text{-}(CF3)2}$**][BAr$^{F}_{4}$] in Et_2O at 293 K. (*) Suppressed Et_2O resonances.

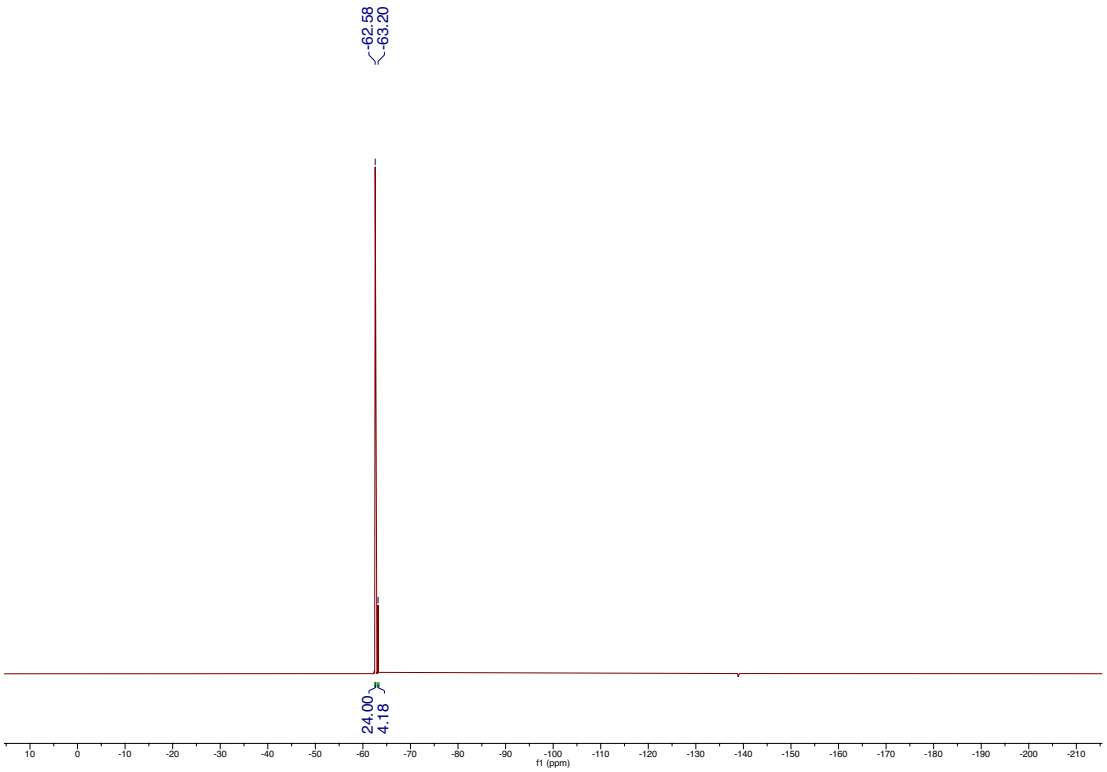

Figure S4.13: ^{19}F NMR spectrum of [**1-CNAr$^{3,5\text{-}(CF3)2}$**][BAr$^{F}_{4}$] in Et_2O at 293 K.

B. IR Spectra

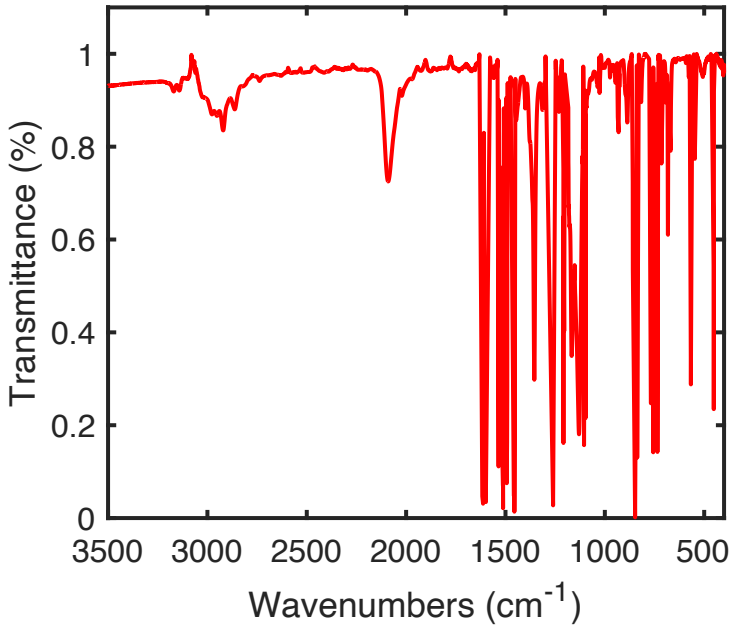

Figure S4.14: Solution IR spectrum of [**1-CNAr$^{4\text{-NMe2}}$**][BAr$^{F}_{4}$] in DFB. Corrected for solvent absorbance by subtraction of a blank spectrum of DFB and removal of peaks with transmittance outside the range [0,1].

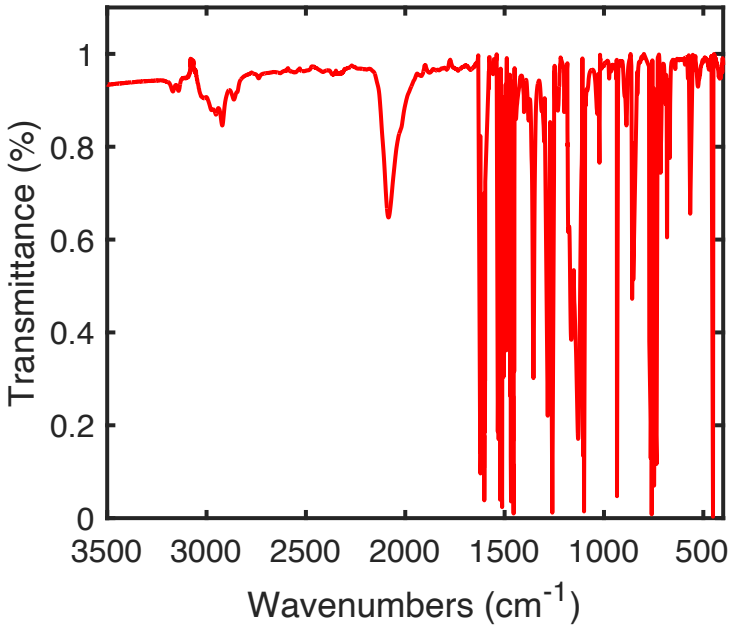

Figure S4.15: Solution IR spectrum of [**1-CNAr$^{4\text{-OMe}}$**][BAr$^{F}_{4}$] in DFB. Corrected for solvent absorbance by subtraction of a blank spectrum of DFB and removal of peaks with transmittance outside the range [0,1].

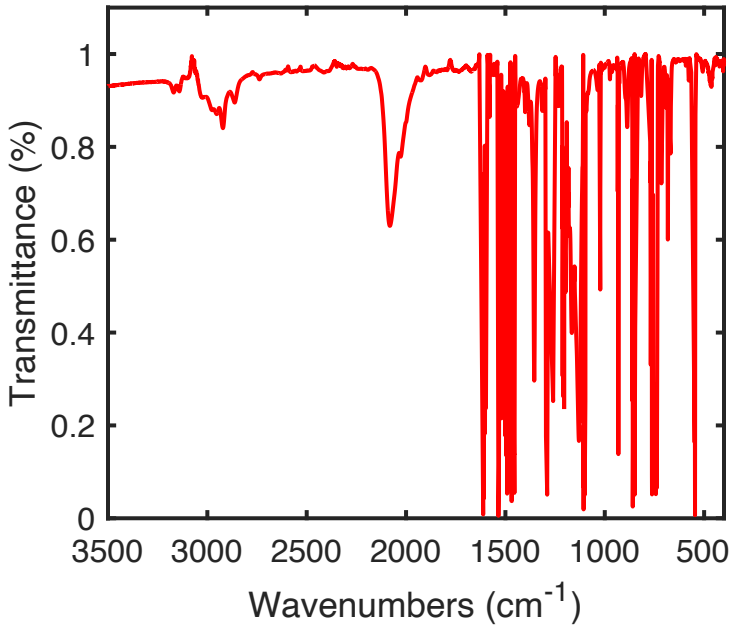

Figure S4.16: Solution IR spectrum of [**1-CNAr$^{4\text{-Me}}$**][BAr$^{F}_{4}$] in DFB. Corrected for solvent absorbance by subtraction of a blank spectrum of DFB and removal of peaks with transmittance outside the range [0,1].

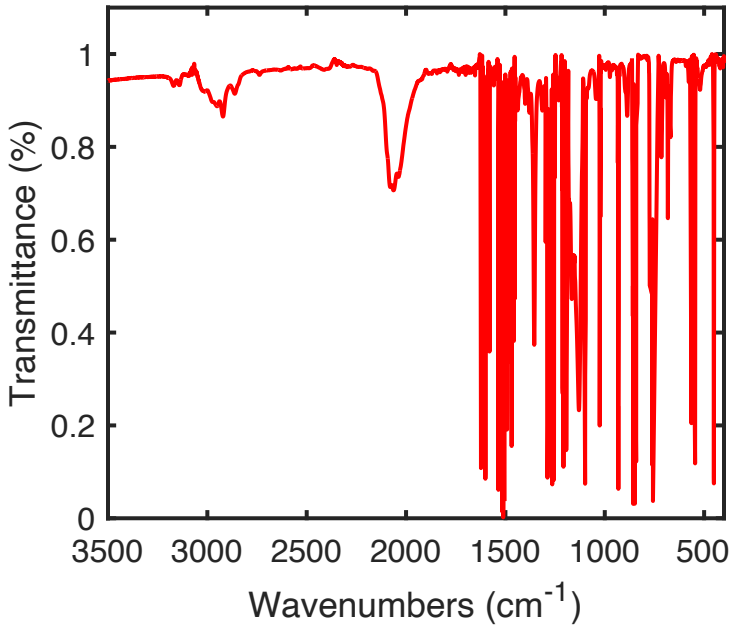

Figure S4.17: Solution IR spectrum of [**1-CNAr$^{3\text{-OMe}}$**][BAr$^{F}_{4}$] in DFB. Corrected for solvent absorbance by subtraction of a blank spectrum of DFB and removal of peaks with transmittance outside the range [0,1].

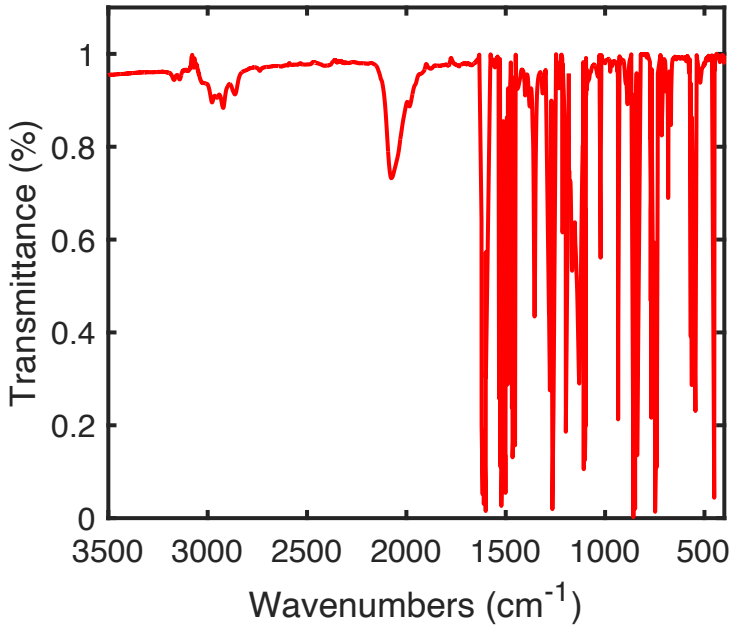

Figure S4.18: Solution IR spectrum of [**1-CNPh**][BAr^F_4] in DFB. Corrected for solvent absorbance by subtraction of a blank spectrum of DFB and removal of peaks with transmittance outside the range [0,1].

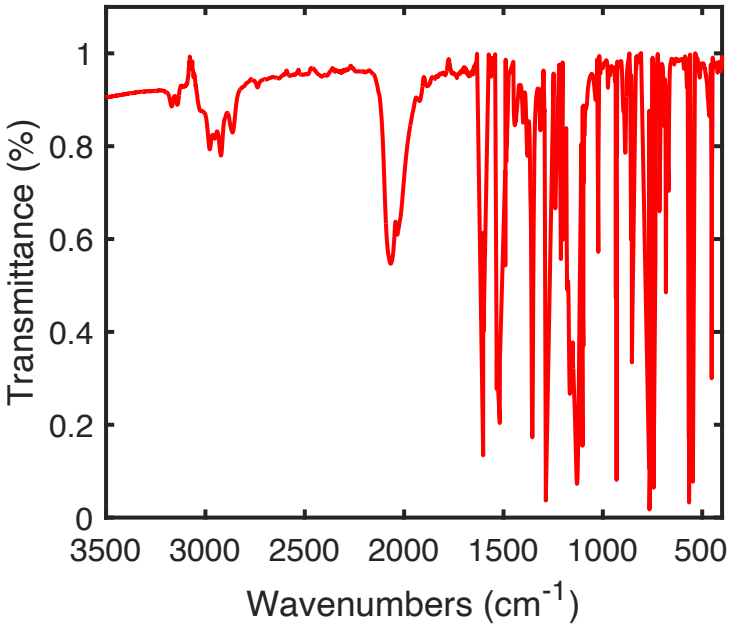

Figure S4.19: Solution IR spectrum of [**1-CNAr$^{4\text{-F}}$**][BAr^F_4] in DFB. Corrected for solvent absorbance by subtraction of a blank spectrum of DFB and removal of peaks with transmittance outside the range [0,1].

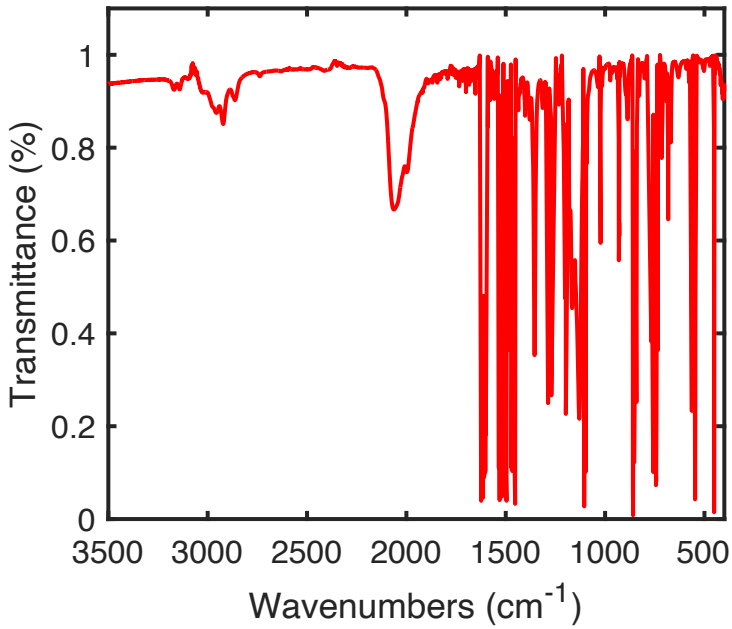

Figure S4.20: Solution IR spectrum of [**1-CNAr$^{4\text{-Cl}}$**][BAr$^{F}_{4}$] in DFB. Corrected for solvent absorbance by subtraction of a blank spectrum of DFB and removal of peaks with transmittance outside the range [0,1].

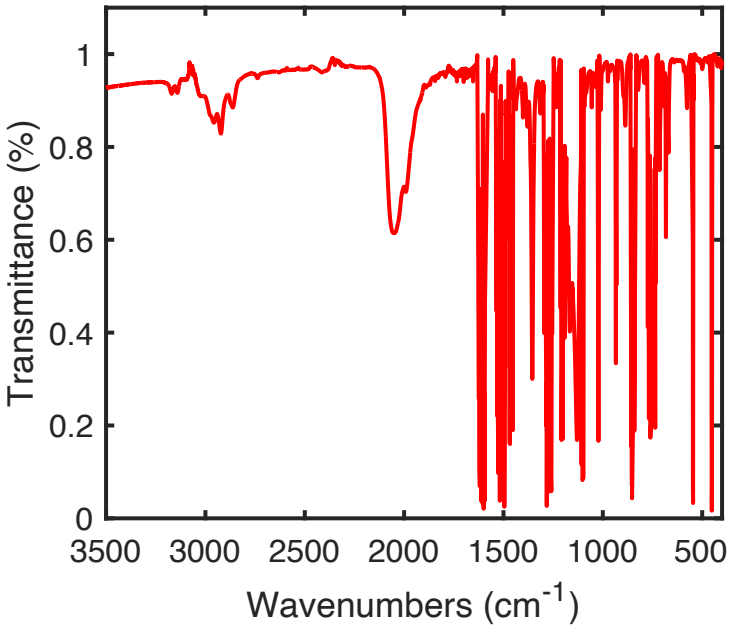

Figure S4.21: Solution IR spectrum of [**1-CNAr$^{4\text{-I}}$**][BAr$^{F}_{4}$] in DFB. Corrected for solvent absorbance by subtraction of a blank spectrum of DFB and removal of peaks with transmittance outside the range [0,1].

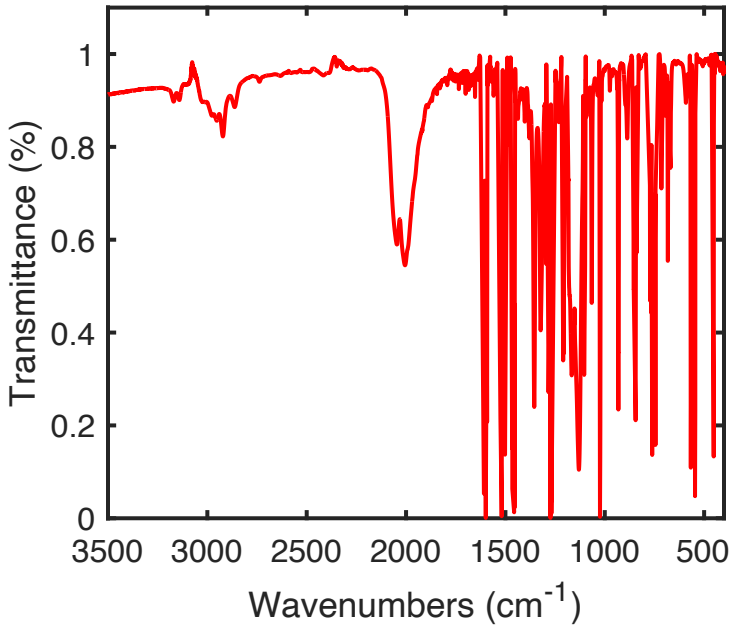

Figure S4.22: Solution IR spectrum of [**1-CNAr$^{4\text{-CF3}}$**][BAr$^{F}_{4}$] in DFB. Corrected for solvent absorbance by subtraction of a blank spectrum of DFB and removal of peaks with transmittance outside the range [0,1].

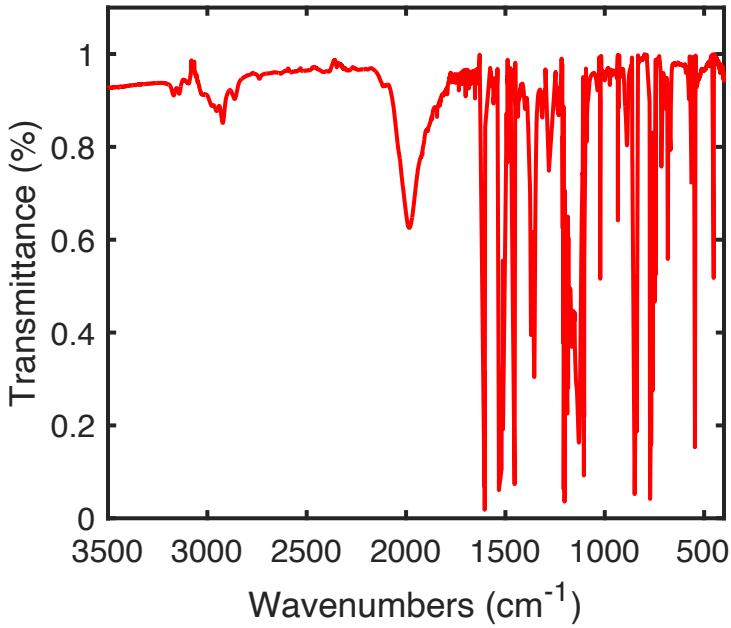

Figure S4.23: Solution IR spectrum of [**1-CNAr$^{3,5\text{-(CF3)2}}$**][BAr$^{F}_{4}$] in DFB. Corrected for solvent absorbance by subtraction of a blank spectrum of DFB and removal of peaks with transmittance outside the range [0,1].

The lineshapes of the [**1-CNAr**]$^+$ series are complex and so solution IR spectra isocyanide stretching peaks were fit as follows: For the range of the IR spectrum between 2200 cm^{-1} and 1780 cm^{-1}, points arising from the isocyanide C–N stretch were assigned as any point with a transmittance below 90%. Examination of the peaks defined by this routine demonstrated that this captured all of the peak intensity for all isocyanides without capturing the baseline of the solution IR experiment. The points assigned to the peak were weighted by intensity and the weighted average value was used to assigned ν(C–N). Free isocyanides in solution displayed much sharper and more symmetrical peaks and thus the peaks were assigned as the point of minimum transmittance. Values are tabulated in table S4.1.

Table S4.1: IR stretching frequencies for [**1-CNAr**]$^+$ and free isocyanides.

	ν(C–N)		
Ar	[**1-CNAr**]$^+$	Free	$\Delta\nu$(C–N)
4-NMe2	2085	2122	37
4-OMe	2072	2125	53
4-Me	2061	2126	65
3-OMe	2052	2128	76
Ph	2054	2128	74
4-F	2041	2128	87
4-Cl	2034	2127	93
4-I	2027	2127	100
4-CF_3	2006	2126	120
3,5-$(CF_3)_2$	1979	2129	150

In addition to plotting Δν(C–N) vs. δ(^{13}C) (see main text figure 4.2), we can plot Δν(C–N) vs. the Hammett parameter, σ, which is a well-established measure of aryl substituent electronic properties[16,17] (SI Fig. S4.24).

The Δν(C–N) shows a similar positive correlation with the Hammett parameter and δ^{13}C, but the correlation of Δν(C–N) with the Hammett parameter is modestly weaker. This is attributed to the different responsiveness of an isocyanide group and a benzoic acid (for which the equilibrium position of the hydrolysis reaction defines the Hammett parameter) to the changing electronics of the aryl substituents. Since δ^{13}C is defined specifically for isocyanides, it displays a stronger correlation with Δν(C–N).

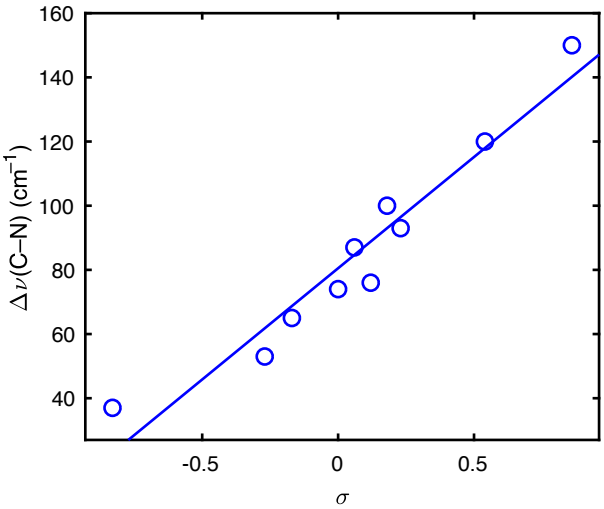

Figure S4.24: Plot of the Hammett parameter, σ, vs. Δν(C–N) for the [**1-CNAr**]$^{+}$ series

C. EPR Spectra

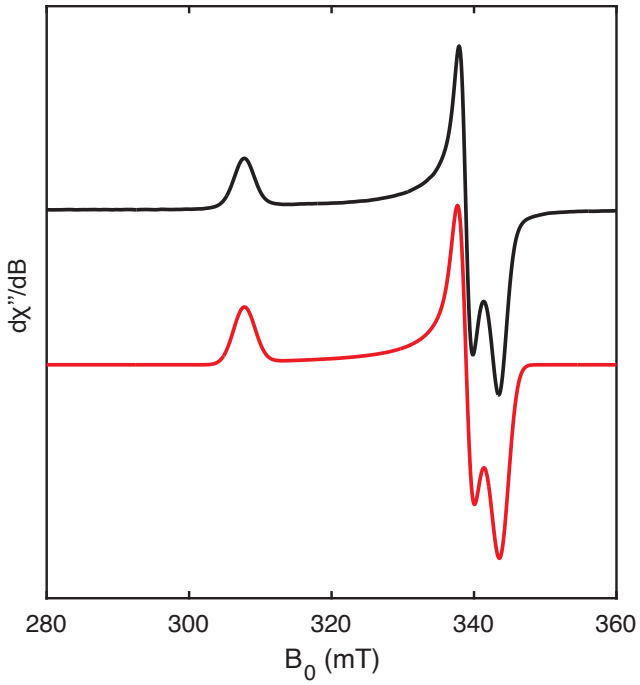

Figure S4.25: EPR spectrum of [**1-CNAr$^{4\text{-NMe2}}$**][BAr$^{F}_{4}$] in Et_2O/Tol (10:1) at 20 K (perpendicular mode, black) and simulation (red). Microwave power: 63 μW; microwave frequency: 9.3715 GHz; simulation parameters: *g* = [2.176 1.976 1.948], *g*-strain = [0.024 0.011 0.015].

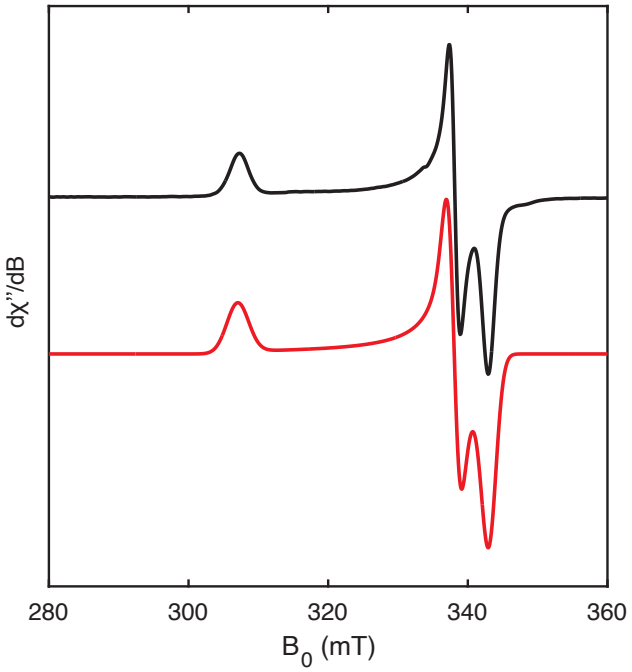

Figure S4.26: EPR spectrum of [**1-CNAr$^{4\text{-OMe}}$**][BAr$^{F}_{4}$] in Et_2O/Tol (10:1) at 20 K (perpendicular mode, black) and simulation (red). Microwave power: 63 μW; microwave frequency: 9.3717 GHz; simulation parameters: *g* = [2.181 1.981 1.952], *g*-strain = [0.025 0.01 0.013].

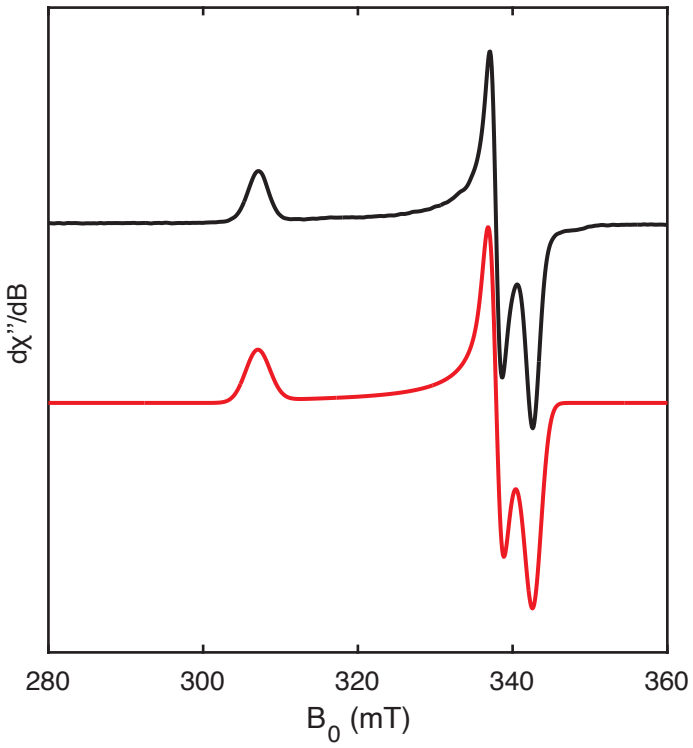

Figure S4.27: EPR spectrum of [**1-CNAr$^{4\text{-Me}}$**][BAr$^{F}_{4}$] in Et_2O/Tol (10:1) at 20 K (perpendicular mode, black) and simulation (red). Microwave power: 16 μW; microwave frequency: 9.3719 GHz; simulation parameters: *g* = [2.181 1.982 1.954], *g*-strain = [0.025 0.009 0.013].

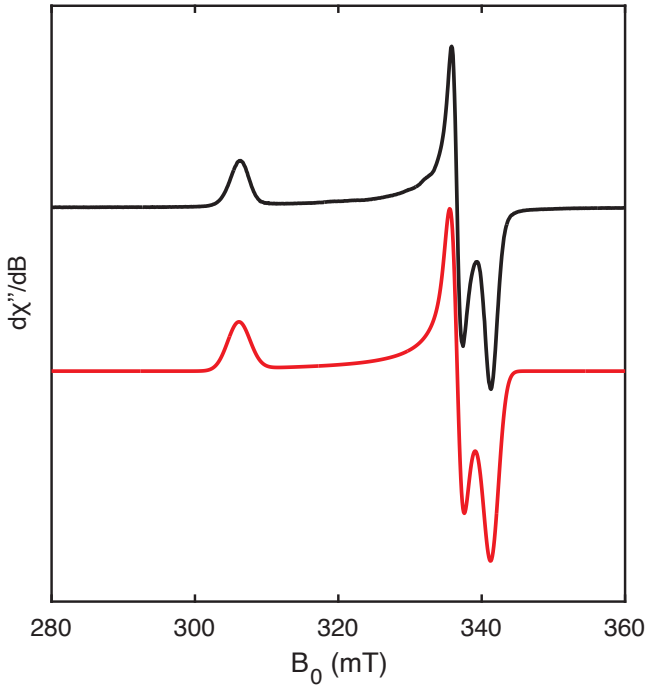

Figure S4.28: EPR spectrum of [**1-CNAr$^{3\text{-OMe}}$**][BAr$^{F}_{4}$] in Et_2O/Tol (10:1) at 20 K (perpendicular mode, black) and simulation (red). Microwave power: 63 μW; microwave frequency: 9.3690 GHz; simulation parameters: *g* = [2.187 1.989 1.961], *g*-strain = [0.025 0.009 0.013].

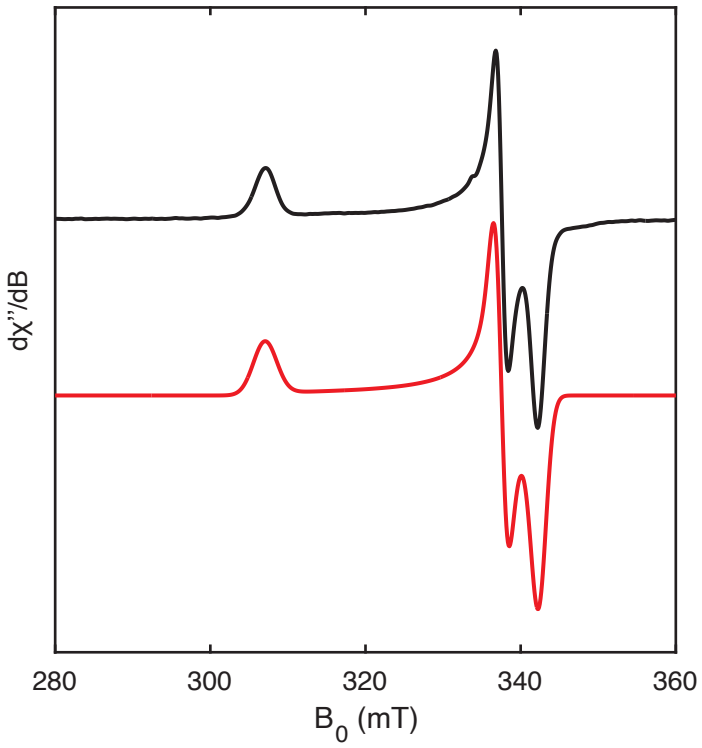

Figure S4.29: EPR spectrum of [**1-CNPh**][BAr^F_4] in Et_2O/Tol (10:1) at 20 K (perpendicular mode, black) and simulation (red). Microwave power: 16 μW; microwave frequency: 9.3718 GHz; simulation parameters: *g* = [2.181 1.984 1.956], *g*-strain = [0.024 0.009 0.012].

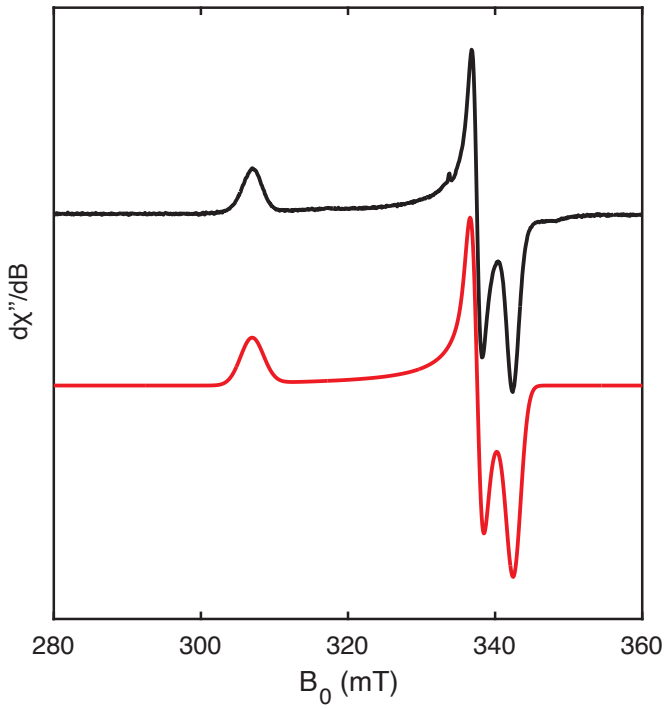

Figure S4.30: EPR spectrum of [**1-CNAr$^{4\text{-F}}$**][BAr^F_4] in Et_2O/Tol (10:1) at 20 K (perpendicular mode, black) and simulation (red). Microwave power: 16 μW; microwave frequency: 9.3728 GHz; simulation parameters: *g* = [2.182 1.984 1.955], *g*-strain = [0.025 0.008 0.012].

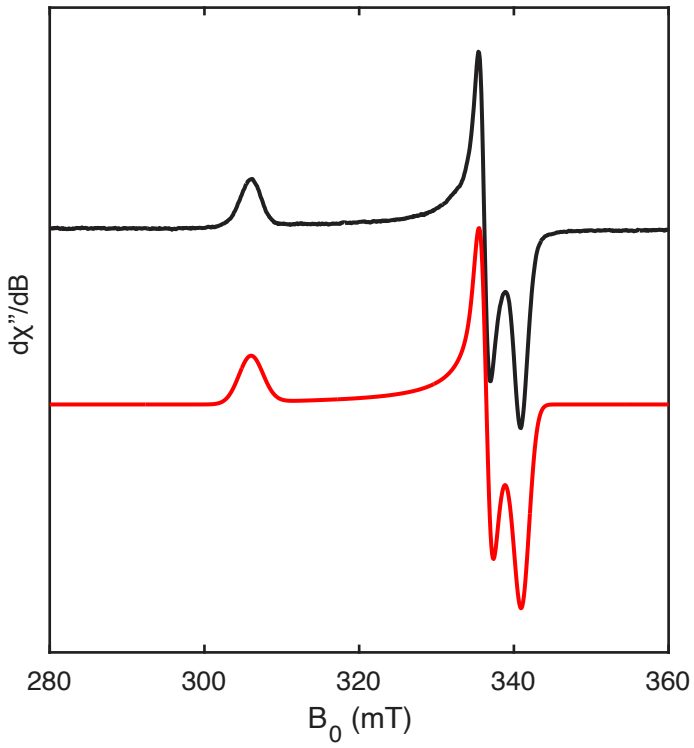

Figure S4.31: EPR spectrum of [**1-CNAr$^{4\text{-Cl}}$**][BAr$^{F}_4$] in Et_2O/Tol (10:1) at 20 K (perpendicular mode, black) and simulation (red). Microwave power: 16 μW; microwave frequency: 9.3698 GHz; simulation parameters: *g* = [2.188 1.99 1.963], *g*-strain = [0.025 0.008 0.012].

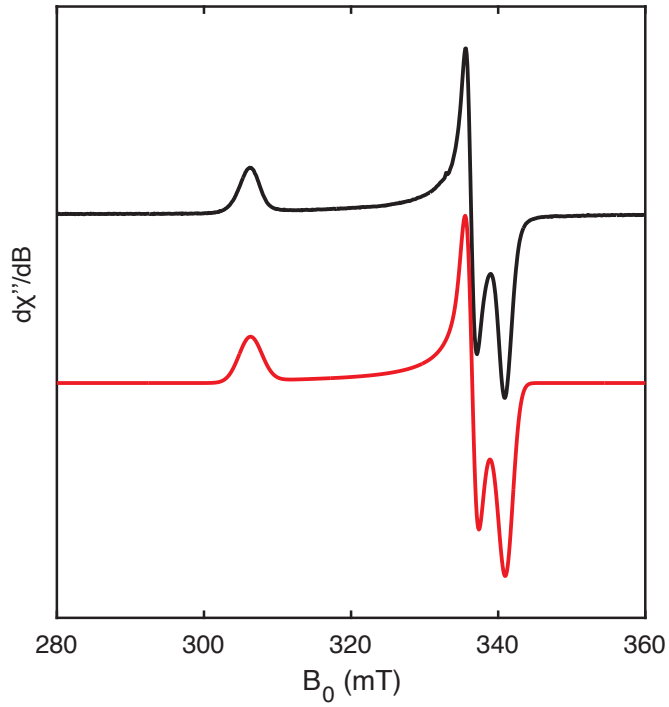

Figure S4.32: EPR spectrum of [**1-CNAr$^{4\text{-I}}$**][BAr$^{F}_4$] in Et_2O/Tol (10:1) at 20 K (perpendicular mode, black) and simulation (red). Microwave power: 63 μW; microwave frequency: 9.3704 GHz; simulation parameters: *g* = [2.186 1.990 1.963], *g*-strain = [0.025 0.008 0.012].

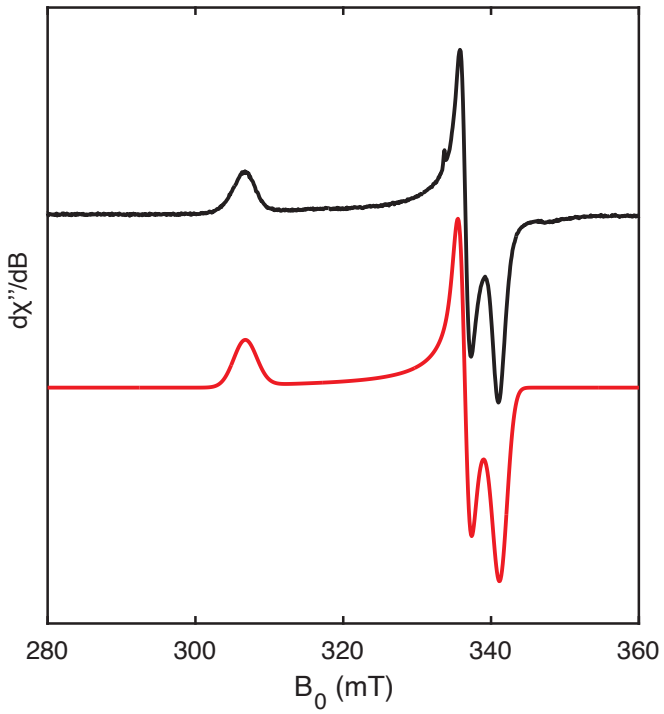

Figure S4.33: EPR spectrum of [**1-CNAr$^{4\text{-CF3}}$**][BAr$^{F}_{4}$] in Et_2O/Tol (10:1) at 20 K (perpendicular mode, black) and simulation (red). Microwave power: 16 μW; microwave frequency: 9.3704 GHz; simulation parameters: g = [2.183 1.990 1.962], g-strain = [0.025 0.008 0.012].

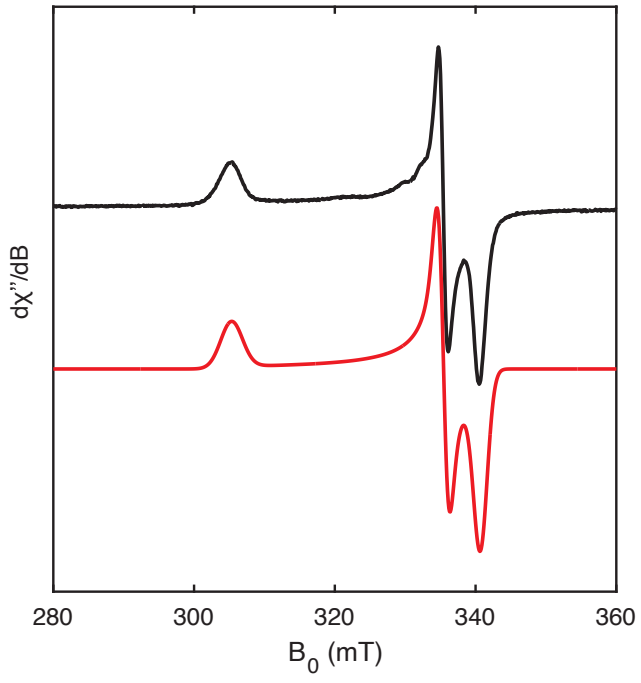

Figure S4.34: EPR spectrum of [**1-CNAr$^{3,5\text{-(CF3)2}}$**][BAr$^{F}_{4}$] in Et_2O/Tol (10:1) at 20 K (perpendicular mode, black) and simulation (red). Microwave power: 252 μW; microwave frequency: 9.3697 GHz; simulation parameters: g = [2.193 1.996 1.965], g-strain = [0.025 0.008 0.012].

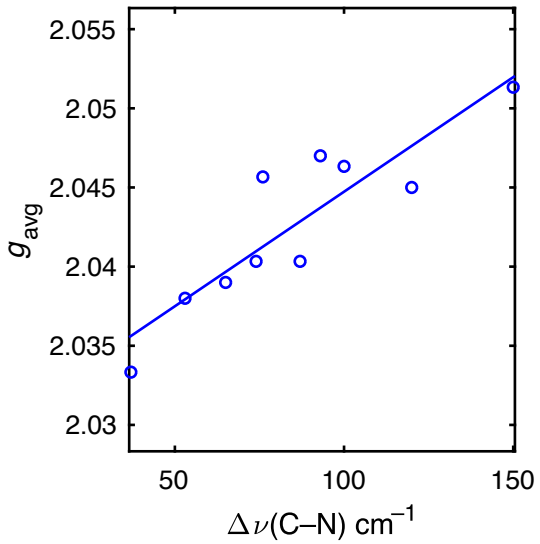

Figure S4.35: Plot of g_{avg} vs. Δν(C–N); g_{avg} varies little over the series but shows a weak positive correlation with Δν(C–N).

D. UV-vis spectra

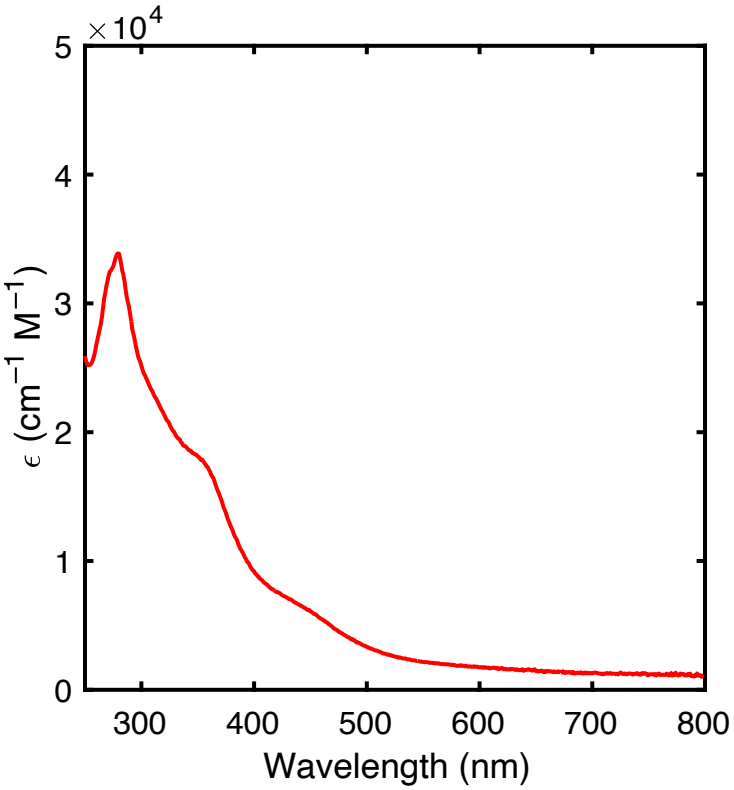

Figure S4.36: UV-vis spectrum of [**1-CNAr4-^{NMe2}**][BAr^F_4] in Et_2O

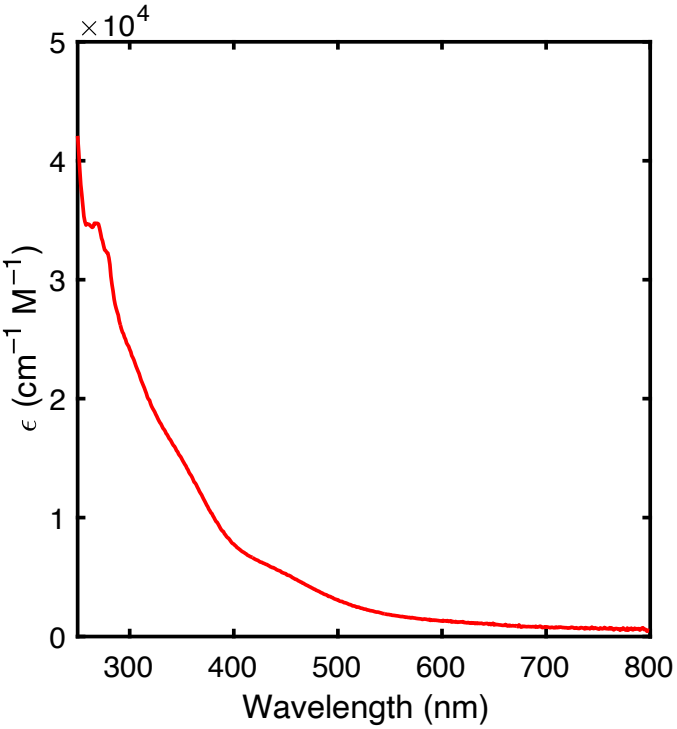

Figure S4.37: UV-vis spectrum of [**1-CNAr$^{4\text{-}OMe}$**][BAr^F_4] in Et_2O

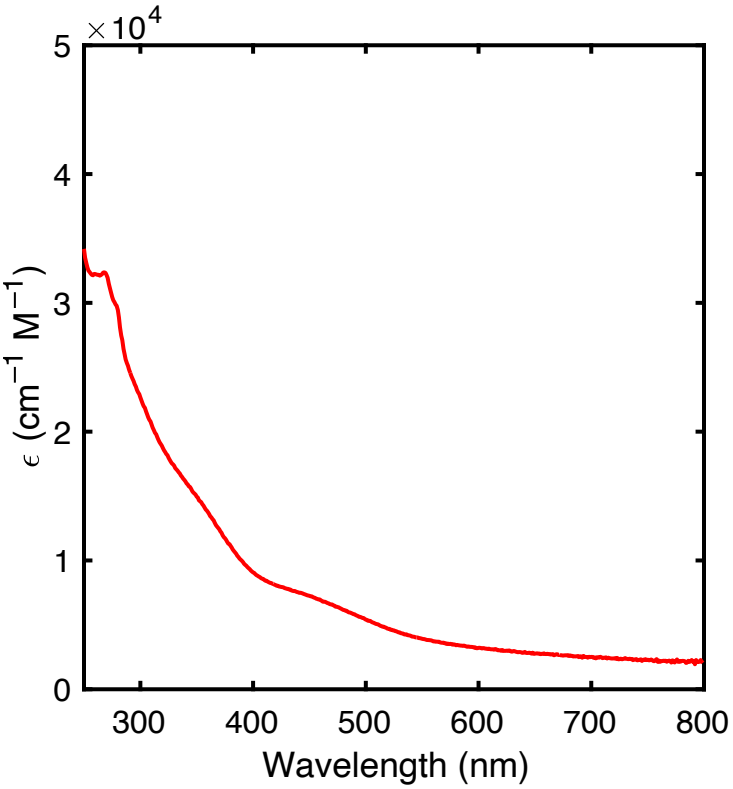

Figure S4.38: UV-vis spectrum of [**1-CNAr$^{4\text{-Me}}$**][BAr$^{F}_{4}$] in Et_2O

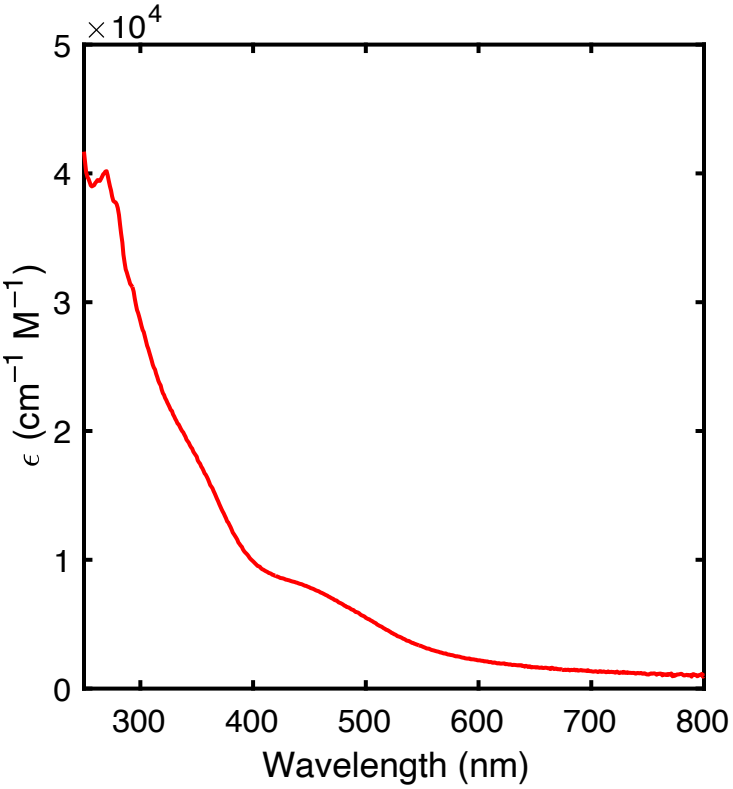

Figure S4.39: UV-vis spectrum of [**1-CNAr$^{3\text{-OMe}}$**][BAr$^{F}_{4}$] in Et_2O

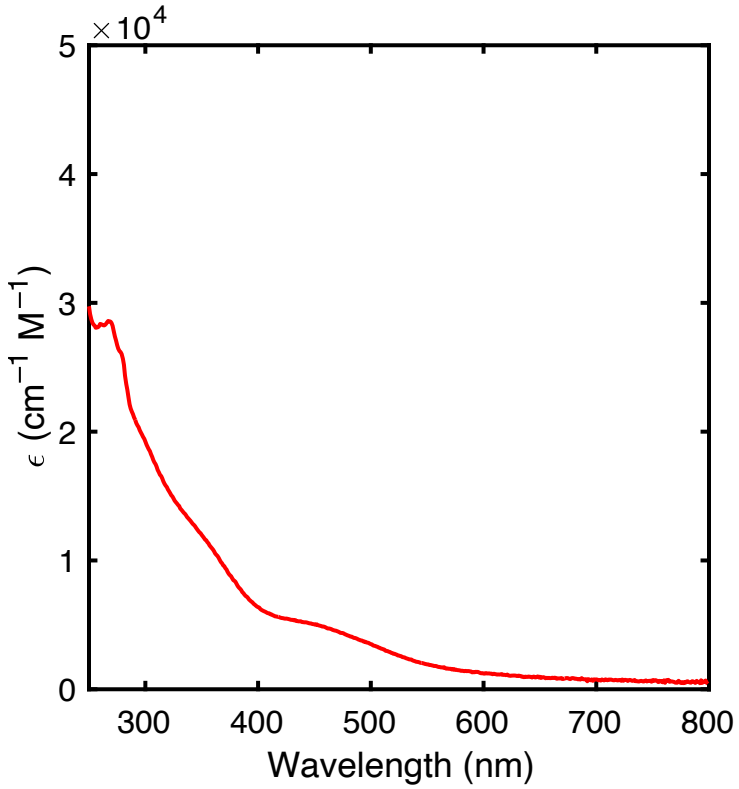

Figure S4.40: UV-vis spectrum of [**1-CNPh**][BAr^F_4] in Et_2O

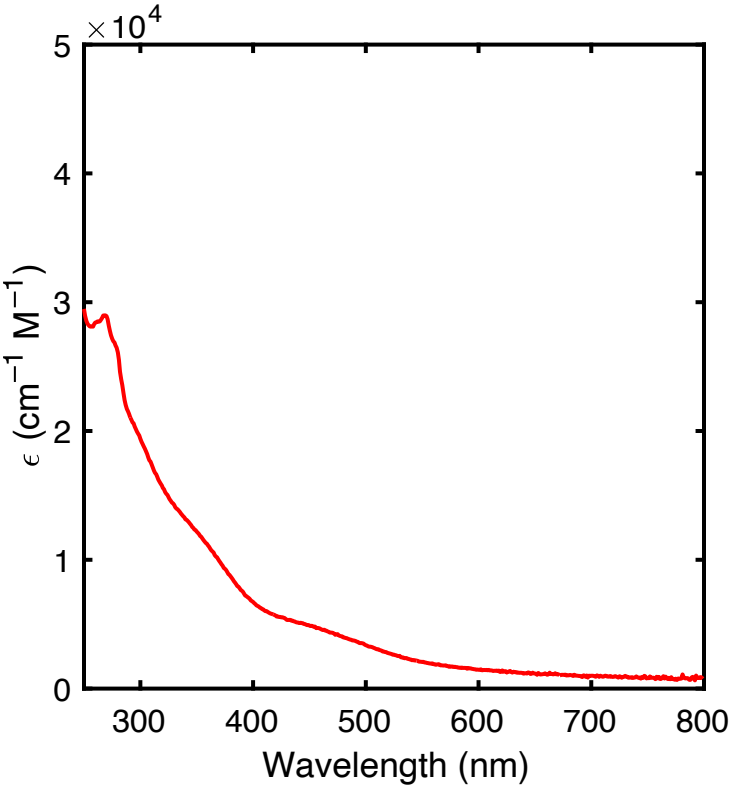

Figure S4.41: UV-vis spectrum of [**1-CNAr$^{4\text{-F}}$**][BAr^F_4] in Et_2O

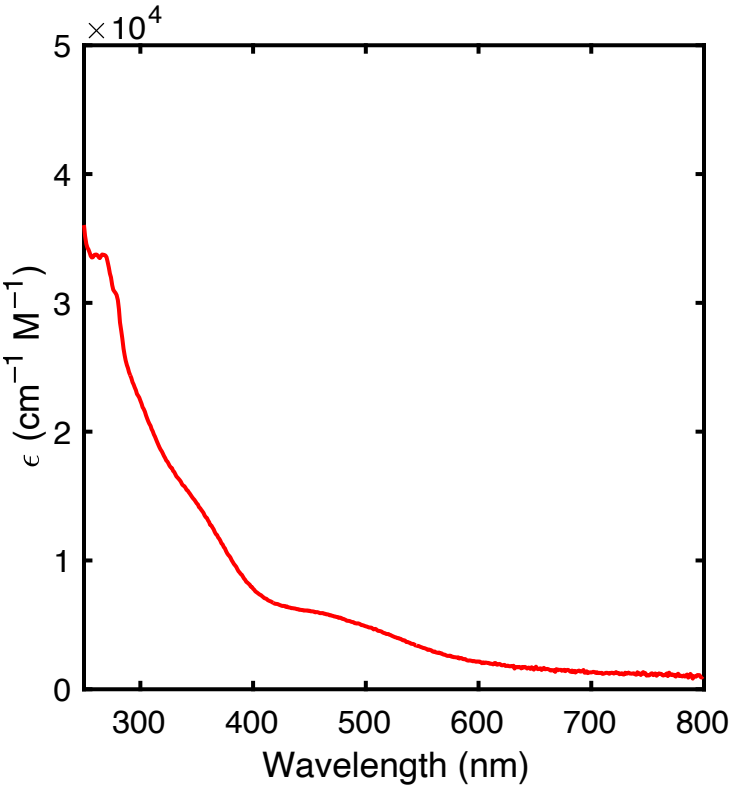

Figure S4.42: UV-vis spectrum of [**1-CNAr$^{4\text{-Cl}}$**][BAr$^{F}_4$] in Et_2O

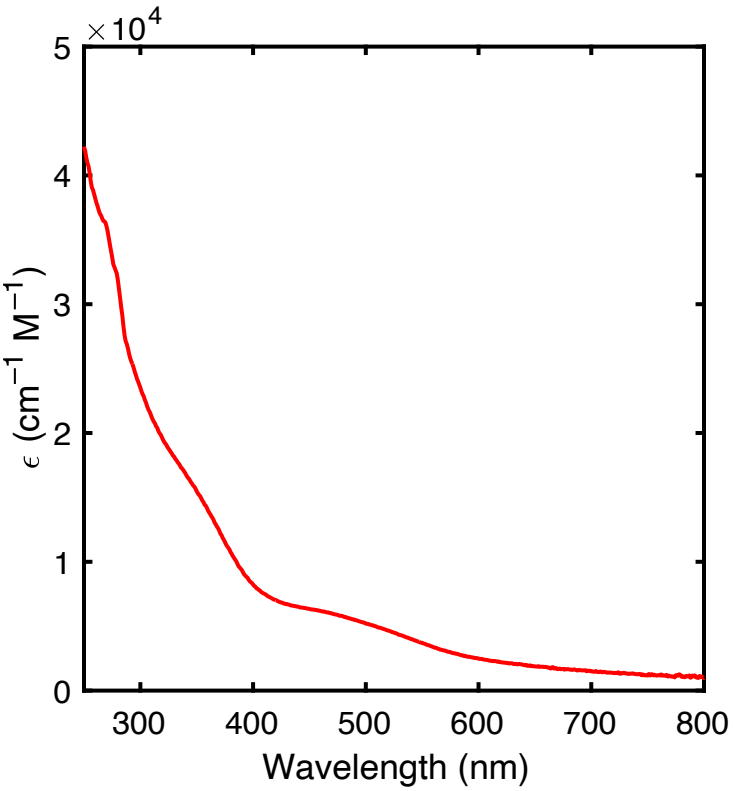

Figure S4.43: UV-vis spectrum of [**1-CNAr$^{4\text{-I}}$**][BAr$^{F}_4$] in Et_2O

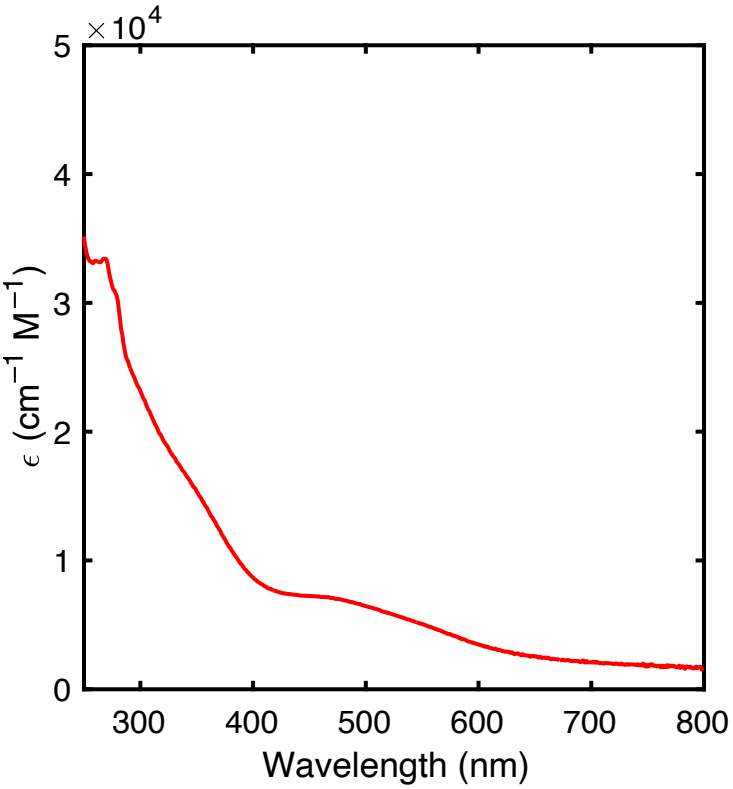

Figure S4.44: UV-vis spectrum of [**1-CNAr$^{4\text{-CF3}}$**][BAr$^{F}_{4}$] in Et_2O

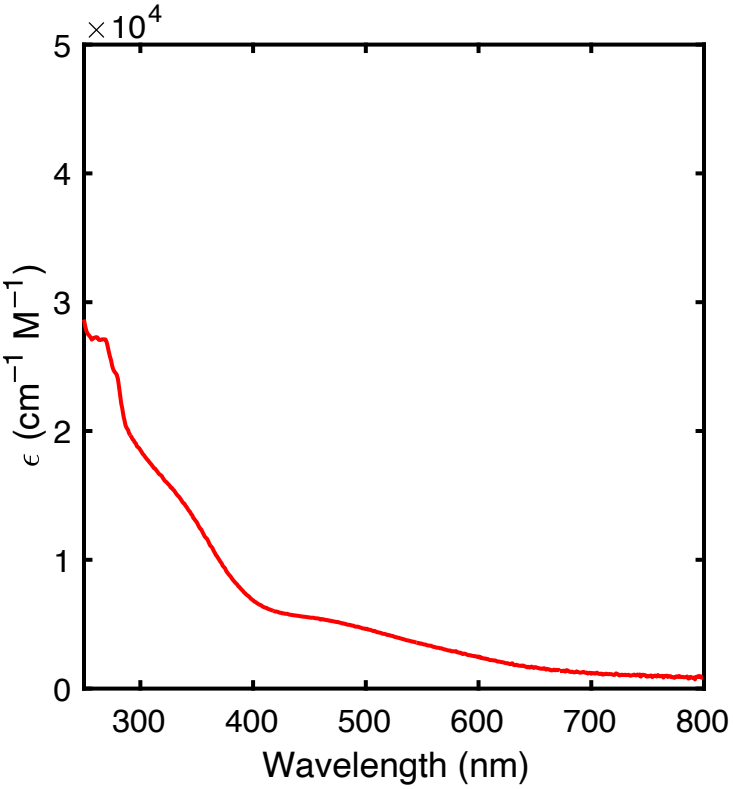

Figure S4.45: UV-vis spectrum of [**1-CNAr$^{3,5\text{-(CF3)2}}$**][BAr$^{F}_{4}$] in Et_2O.

E. Mossbauer spectra

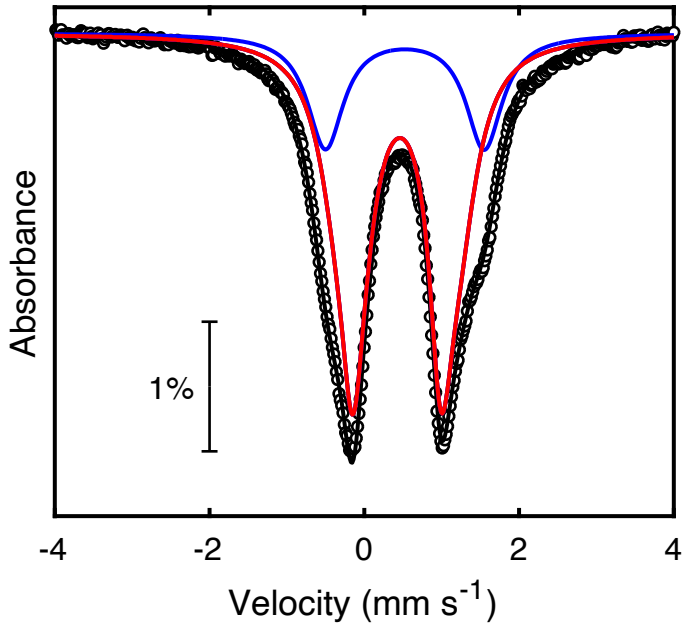

Figure S4.46: Mössbauer spectrum of [**1-CNAr$^{4\text{-NMe2}}$**][BAr$^{F}_{4}$] at 80 K as a frozen solution in DFB (dots: data, black: total simulation, red: Fe_{IMes} sites, blue: Fe_{CNAr} site).

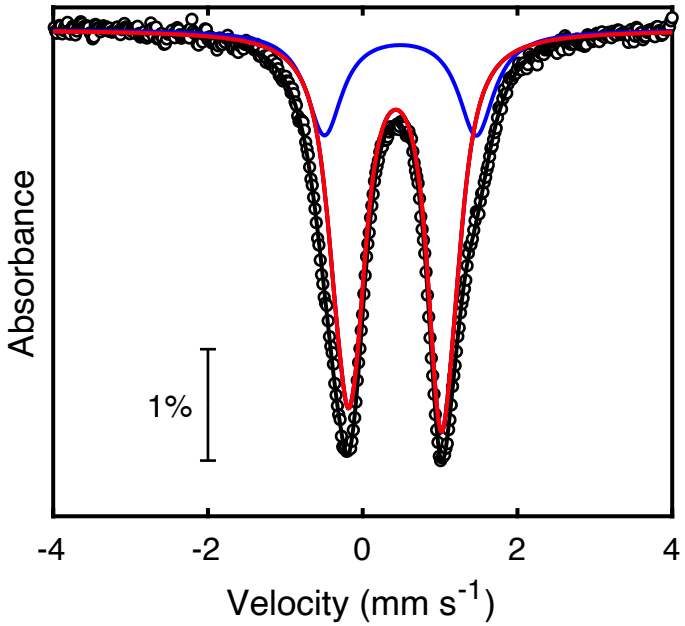

Figure S4.47: Mössbauer spectrum of [**1-CNAr$^{4\text{-OMe}}$**][BAr$^{F}_{4}$] at 80 K as a frozen solution in DFB. (dots: data, black: total simulation, red: Fe_{IMes} sites, blue: Fe_{CNAr} site).

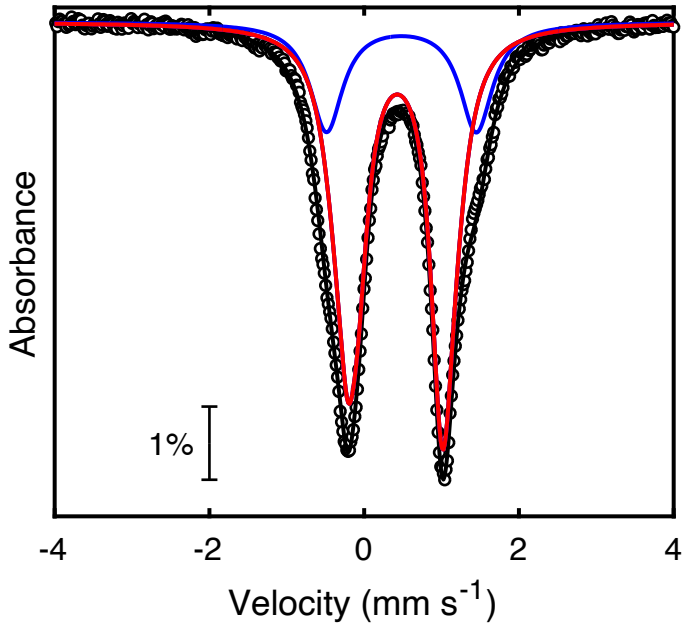

Figure S4.48: Mössbauer spectrum of [**1-CNAr$^{4\text{-Me}}$**][BAr$^{F}_{4}$] at 80 K as a frozen solution in DFB (dots: data, black: total simulation, red: Fe$_{IMes}$ sites, blue: Fe$_{CNAr}$ site).

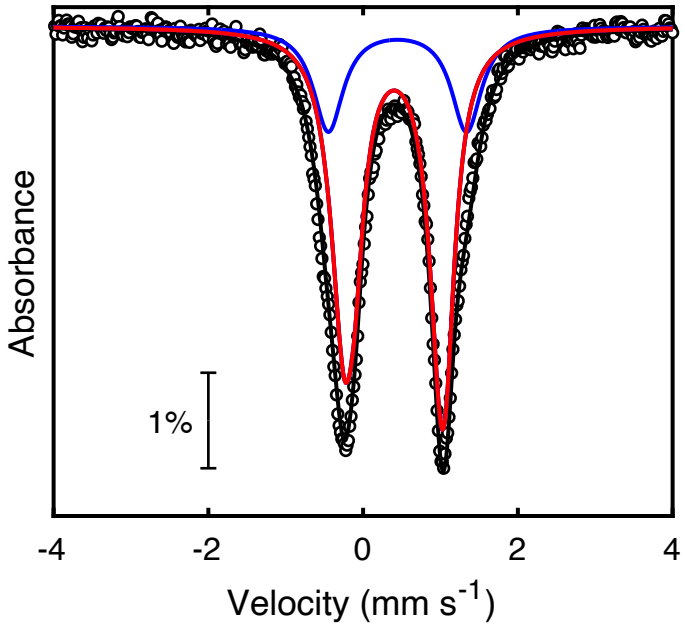

Figure S4.49: Mössbauer spectrum of [**1-CNAr$^{3\text{-OMe}}$**][BAr$^{F}_{4}$] at 80 K as a frozen solution in DFB (dots: data, black: total simulation, red: Fe$_{IMes}$ sites, blue: Fe$_{CNAr}$ site).

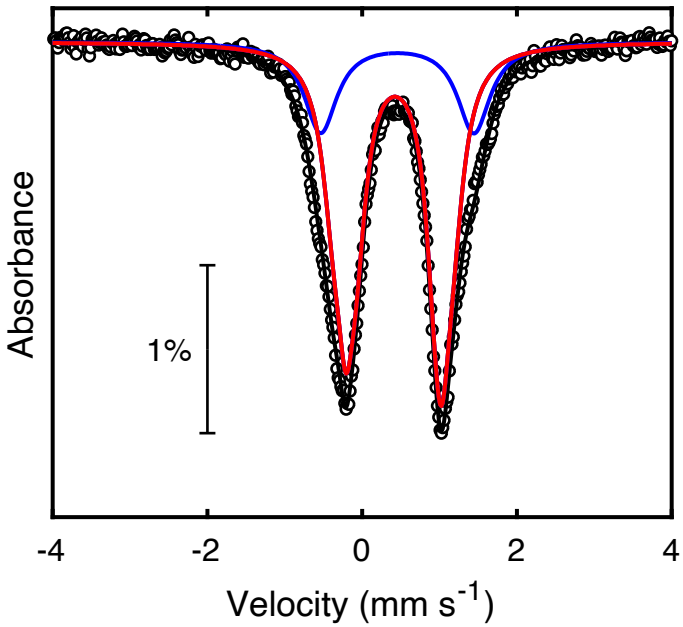

Figure S4.50: Mössbauer spectrum of [**1-CNPh**][BAr^F_4] at 80 K as a frozen solution in DFB (dots: data, black: total simulation, red: Fe_{IMes} sites, blue: Fe_{CNAr} site).

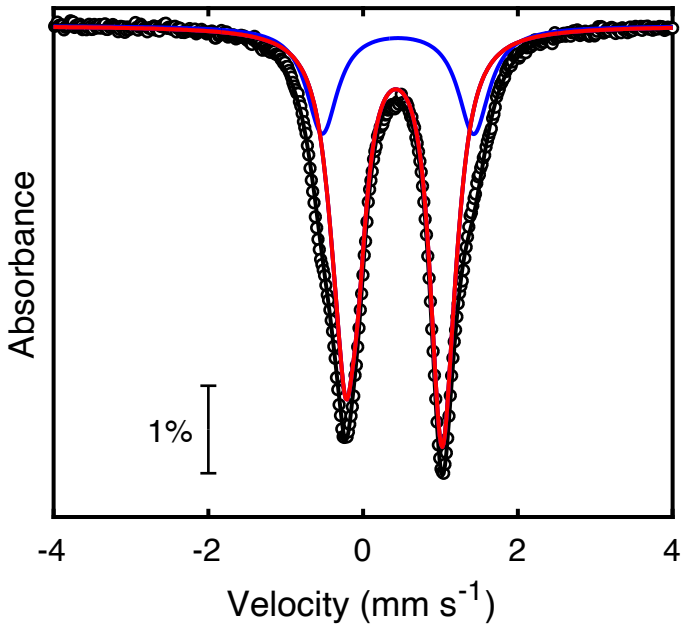

Figure S4.51: Mössbauer spectrum of [**1-CNAr$^{4\text{-F}}$**][BAr^F_4] at 80 K as a frozen solution in DFB (dots: data, black: total simulation, red: Fe_{IMes} sites, blue: Fe_{CNAr} site).

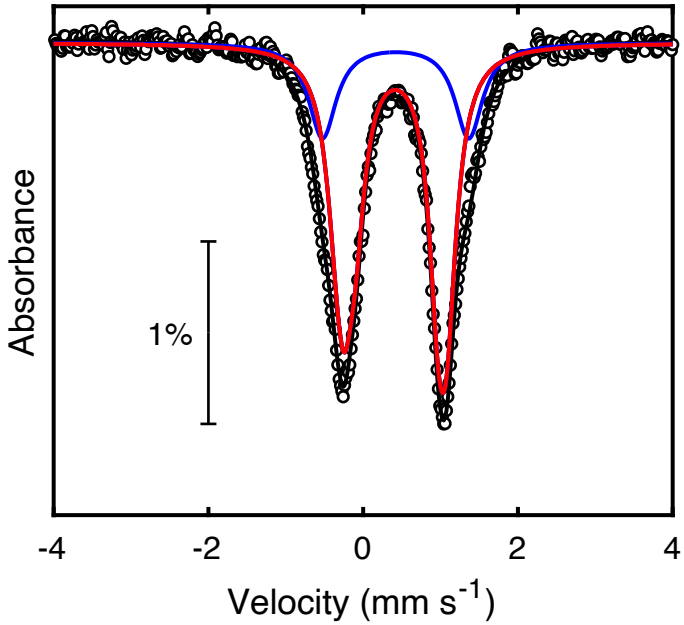

Figure S4.52: Mössbauer spectrum of [**1-CNAr$^{4\text{-Cl}}$**][BAr$^{F}{}_{4}$] at 80 K as a frozen solution in DFB (dots: data, black: total simulation, red: Fe_{IMes} sites, blue: Fe_{CNAr} site).

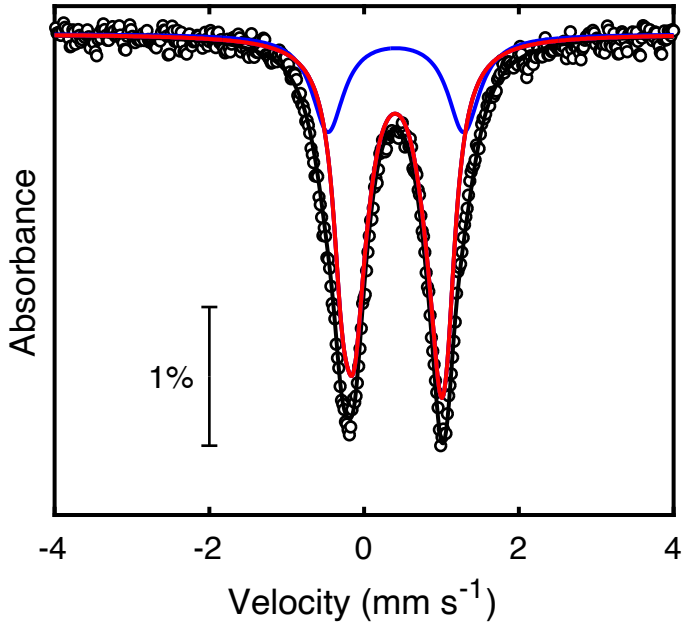

Figure S4.53: Mössbauer spectrum of [**1-CNAr$^{4\text{-I}}$**][BAr$^{F}{}_{4}$] at 80 K as a frozen solution in DFB (dots: data, black: total simulation, red: Fe_{IMes} sites, blue: Fe_{CNAr} site).

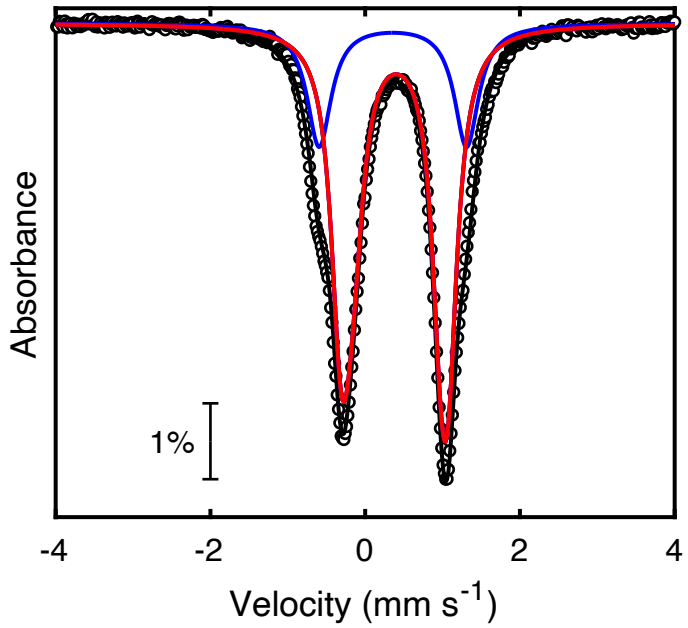

Figure S4.54: Mössbauer spectrum of [**1-CNAr$^{4\text{-CF3}}$**][BAr$^{F}_{4}$] at 80 K as a frozen solution in DFB (dots: data, black: total simulation, red: Fe_{IMes} sites, blue: Fe_{CNAr} site).

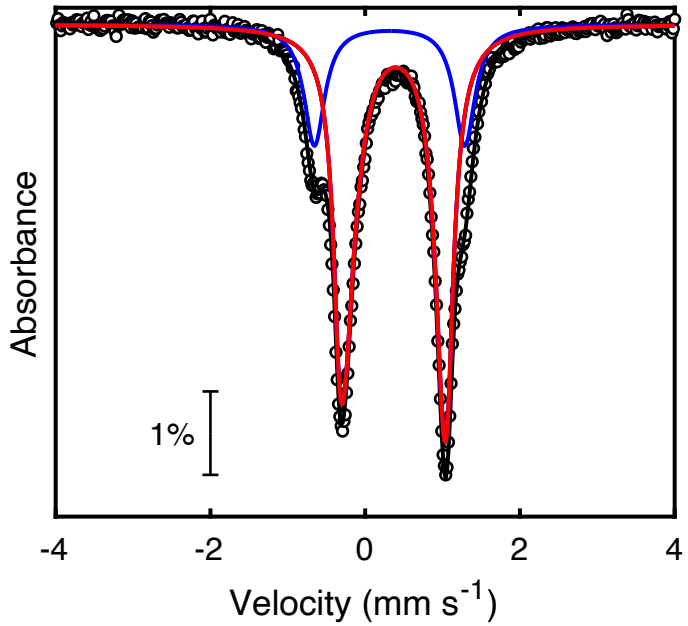

Figure S4.55: Mössbauer spectrum of [**1-CNAr$^{3,5\text{-(CF3)2}}$**][BAr$^{F}_{4}$] at 80 K as a frozen solution in DFB (dots: data, black: total simulation, red: Fe_{IMes} sites, blue: Fe_{CNAr} site).

Mossbauer simulation details: As described in the main text, the Mössbauer spectra of [**1-CNAr**]$^+$ show partially resolved quadrupole doublets at the low and high energy edges of the signal, which are assigned to the unique isocyanide site (expected to have large quadrupole splittings due to high covalency at that site). Alternative models in which these sites are assigned to different quadrupole doublets show unreasonable isomer shift parameters for at least one site (Fig S4.56 and Table S4.2 show examples for the two extremes of the series, [**1-CNAr^{NMe2}**]$^+$ and [**1-CNAr$^{3,5\text{-}(CF3)2}$**]$^+$).

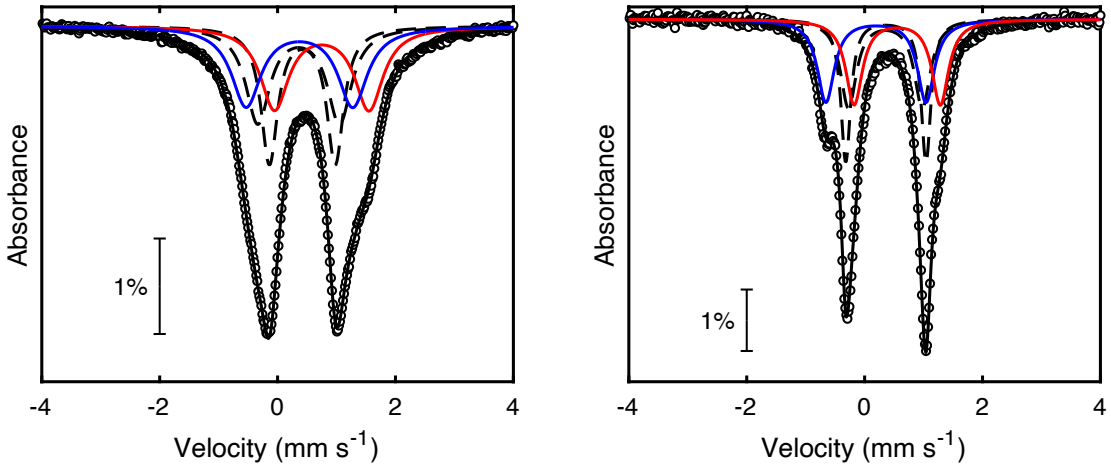

Figure S4.56: Mössbauer spectra of [**1-CNAr^{NMe2}**]$^+$ (left) and [**1-CNAr$^{3,5\text{-}(CF3)2}$**]$^+$ (right) showing alternative fits where the high and low energy shoulders on the signal are fit to different quadrupole doublets (red and blue), total simulation (black) and quadrupole doublets for the other two sites (black dashed). The parameters for the red and blue sites have unreasonable high or low isomer shifts (Table S4.2).

Table S4.2: Mössbauer parameters for alternative fits of [**1-CNAr**]$^+$ complex spectra. Unreasonable values are shown in red.

Compound		Red	Blue	Black 1	Black 2
4-NMe_2	δ (mm s^{-1})	0.749	0.371	0.357	0.420
	$\lvert\Delta E_Q\rvert$ (mm s^{-1})	1.603	1.809	1.386	1.117
	Γ (mm s^{-1})	0.579	0.600	0.495	0.343
3,5-$(CF_3)_2$	δ (mm s^{-1})	0.192	0.553	0.361	0.353
	$\lvert\Delta E_Q\rvert$ (mm s^{-1})	1.699	1.462	1.362	1.253
	Γ (mm s^{-1})	0.350	0.340	0.200	0.358

To simulate the Mössbauer spectra of the [**1-CNAr**]$^{+}$ series, we fit each spectrum to four quadrupole doublets, first assigning the doublet with the widest quadrupole splitting to the isocyanide-bound site for reasons discussed above. This site, which results in low and high energy shoulders on the sides of the signals, can be simulated with a unique set of parameters which do not depend on the values used to simulate the rest of the spectrum. The remaining intensity, attributed to three IMes ligated sites, cannot be simulated with one unique simulation. Hence, we choose to discuss only the average parameters for these sites because the averages do not depend on which simulation is chosen. We chose to use a self-consistent set of simulations, constructed by first simulating the spectrum of [**1-CNAr$^{3,5\text{-}(CF3)2}$**]$^{+}$ by least-squares fitting with the [**1-CO**]$^{+}$ parameters as starting values. We then worked upwards through the [**1-CNAr**]$^{+}$ series, simulating the spectrum of [**1-CNAr$^{4\text{-}CF3}$**]$^{+}$ with the parameters for [**1-CNAr$^{3,5\text{-}(CF3)2}$**]$^{+}$ as starting values and so on. The simulated Mössbauer parameters for all isocyanides are shown in table S4.3.

Table S4.3: Mössbauer parameters for [**1-CNAr**]$^{+}$ complexes

Compound		Fe_{CNAr}	$Fe_{IMes}1$	$Fe_{IMes}2$	$Fe_{IMes}3$	Fe_{IMes} avg.
4-NMe_2	δ (mm s^{-1})	0.524	0.502	0.449	0.414	0.455
	$\lvert\Delta E_Q\rvert$ (mm s^{-1})	2.050	1.105	1.600	1.134	1.280
	Γ (mm s^{-1})	0.565	0.555	0.600	0.335	–
4-OMe	δ (mm s^{-1})	0.487	0.437	0.414	0.417	0.423
	$\lvert\Delta E_Q\rvert$ (mm s^{-1})	1.962	1.007	1.510	1.219	1.245
	Γ (mm s^{-1})	0.556	0.379	0.418	0.327	–
4-Me	δ (mm s^{-1})	0.481	0.409	0.445	0.401	0.418
	$\lvert\Delta E_Q\rvert$ (mm s^{-1})	1.936	1.236	1.043	1.489	1.256
	Γ (mm s^{-1})	0.509	0.297	0.347	0.462	–
3-OMe	δ (mm s^{-1})	0.444	0.444	0.413	0.328	0.395
	$\lvert\Delta E_Q\rvert$ (mm s^{-1})	1.786	1.114	1.315	1.296	1.242
	Γ (mm s^{-1})	0.472	0.320	0.306	0.462	–
Ph	δ (mm s^{-1})	0.454	0.409	0.434	0.401	0.418
	$\lvert\Delta E_Q\rvert$ (mm s^{-1})	1.980	1.238	1.017	1.536	1.256
	Γ (mm s^{-1})	0.513	0.265	0.333	0.369	–
4-F	δ (mm s^{-1})	0.451	0.406	0.439	0.397	0.414
	$\lvert\Delta E_Q\rvert$ (mm s^{-1})	1.957	1.255	1.028	1.488	1.257
	Γ (mm s^{-1})	0.487	0.274	0.326	0.409	–
4-Cl	δ (mm s^{-1})	0.420	0.357	0.484	0.367	0.403
	$\lvert\Delta E_Q\rvert$ (mm s^{-1})	1.890	1.204	1.174	1.411	1.263
	Γ (mm s^{-1})	0.434	0.285	0.318	0.349	–
4-I	δ (mm s^{-1})	0.410	0.393	0.467	0.347	0.402
	$\lvert\Delta E_Q\rvert$ (mm s^{-1})	1.754	0.897	1.208	1.263	1.123
	Γ (mm s^{-1})	0.497	0.473	0.300	0.296	–

Table S4.3(cont.): Mössbauer parameters for [**1-CNAr**]$^+$ complexes

Compound		Fe_{CNAr}	$Fe_{IMes}1$	$Fe_{IMes}2$	$Fe_{IMes}3$	Fe_{IMes} avg.
4-CF_3	δ (mm s^{-1})	0.358	0.351	0.456	0.365	0.391
	$\lvert\Delta E_Q\rvert$ (mm s^{-1})	1.905	1.238	1.206	1.410	1.285
	Γ (mm s^{-1})	0.379	0.295	0.335	0.301	–
3,5-$(CF_3)_2$	δ (mm s^{-1})	0.315	0.374	0.414	0.364	0.384
	$\lvert\Delta E_Q\rvert$ (mm s^{-1})	1.943	1.252	1.137	1.390	1.260
	Γ (mm s^{-1})	0.324	0.247	0.437	0.201	–

A plot showing the correlation of the isomer shifts for Fe_{CNAr} and for Fe_{IMes} with Δν(C–N) is shown in the main text (Figure 4.3B), demonstrating that δ decreases systematically for less electron rich isocyanides. On the other hand, $|\Delta E_Q|$ varies little over the series and is apparently not very responsive to changes in Δν(C–N) (Figure S4.57).

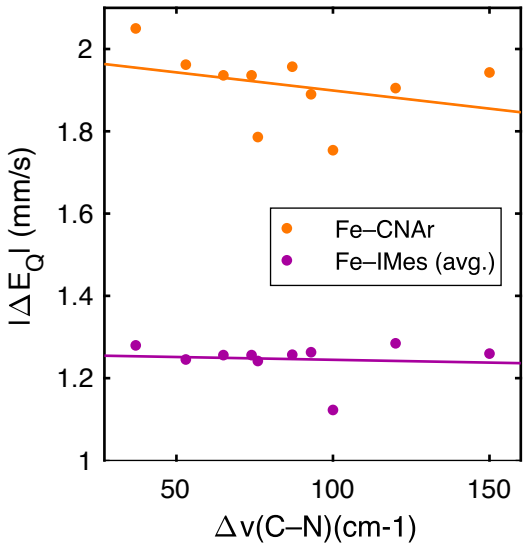

Figure S4.57. Plot of $|\Delta E_Q|(Fe_{CNAr})$ (orange) and $|\Delta E_Q|(Fe_{IMes})$ vs Δν(C–N). $|\Delta E_Q|(Fe_{CNAr})$ shows a weak negative correlation with Δν(C–N), while $|\Delta E_Q|(Fe_{IMes})$ is essentially invariant across the series.

F. Computational Details

General Considerations

All calculations were carried out using version 4.1.2 of the ORCA program package[18] using the broken-symmetry (BS) approach to approximate the multireference electronic states of Fe–S clusters. BS solutions were constructed using the FlipSpin feature of ORCA.

Coordinates for non-H atoms were taken from X-ray crystallographic coordinates for [**1-CNAr$^{4\text{-NMe2}}$**]$^+$ and [**1-CNAr$^{3,5\text{-(CF3)2}}$**]$^+$. To improve the efficiency of the calculations, the mesityl substituents on the IMes ligands were simplified to H and, for model system calculations, the isocyanide was simplified to CNMe or $CNCH_2CF_3$. The positions of all H atoms were optimized.

Geometry optimizations of $[(NHC^H)_3Fe_4S_4CNMe]^+$ and $[(NHC^H)_3Fe_4S_4CNCH_2CF_3]^+$ were performed using the TPSS or TPSSh functionals[19,20] and single point calculations on [**1-CNAr$^{4\text{-NMe2}}$**]$^+$ and [**1-CNAr$^{3,5\text{-(CF3)2}}$**]$^+$ were performed using the TPSS functional. Calculations using the TPSSh functional were accelerated through the use of the RIJCOSX approximation with a fine auxiliary integration grid (GridX7).[21] The DKH-def2-TZVP basis set was used for all atoms.[22] For all calculations, the DKH2 relativistic correction[23] and the general-purpose Coulomb fitting basis set SARC/J were used;[24] all basis sets were fully decontracted. Solid-state effects were approximated using the CPCM solvation model with an infinite dielectric.[25] All optimizations were conducted along $M_S = 1/2$ broken-symmetry surfaces, generated from an initial high-spin reference by flipping the spins on the Fe–CNMe site along with an Fe–NHC site (for geometry optimizations, the choice of the NHC-bound site is arbitrary; for calculations on crystallographic coordinates all six possible spin flip combinations were calculated). Numerical frequency calculations at the stationary points confirm that the optimized structures are true minima. To analyze localized orbitals, we employed the intrinsic bond orbital (IBO) method developed by

Knizia,[26] which applies Pipek-Mezey localization[27] in a basis of so-called intrinsic atomic orbitals (IAOs) and analyzed the resultant orbitals using a Löwdin population analysis. This methodology has been previously applied to Fe–S clusters.[8,10,28–30]

Computational Results

1. Geometry optimization of $[(NHC^{H})_3Fe_4S_4CNMe]^+$

Geometry optimizations were performed by starting with the crystallographic coordinates of [**1-CNAr$^{4\text{-NMe2}}$**]$^+$ and [**1-CNAr$^{3,5\text{-(CF3)2}}$**]$^+$, truncating the aryl group to CH_3, and optimizing the geometry. Two different minima were found, with parameters as in table S4.4. A frequency calculation confirmed that both structures were true minima.

Table S4.4: Structural parameters for two calculated energetic minima for $[(NHC^{H})_3Fe_4S_4CNMe]^+$

Structure	Fe–CNMe Å	Fe–NHC (avg.) Å	Fe–S (avg.) Å	S_4 volume Å^3
Contracted	1.800	1.910	2.160	4.878
Typical	1.860	1.987	2.253	5.599

2. Relaxed coordinate scans of Fe–C(NMe) bond length

A relaxed coordinate scan of the Fe–C(NMe) bond length was conducted between 1.68 and 2.04 Å. At all coordinates, the contracted and typical structures were found to exist on separate potential energy surfaces; that is, the calculated structure at all Fe–C(NMe) bond lengths resembled the geometry the calculated was initialized with, and no intermediates were found that transitioned one structure type into the other. Even at the Fe–C(NMe) bond length where the two structures were approximately isoenergetic (1.96 Å, $|\Delta E|$ = 0.06 kcal/mol), the two optimized geometries were very different (Table S4.5).

Table S4.5: Structural parameters for two calculated energetic minima for $[(NHC^{H})_3Fe_4S_4CNMe]^+$

Structure	Fe–CNMe Å	Fe–NHC (avg.) Å	Fe–S (avg.) Å	S_4 volume $Å^3$
Contracted	1.960	1.908	2.159	4.874
Typical	1.960	1.988	2.254	5.615

3. Geometry optimization of $[(NHC^{H})_3Fe_4S_4CNCH_2CF_3]^+$

Geometry optimizations were performed in the same manner as those for $[(NHC^{H})_3Fe_4S_4CNMe]^+$, but the aryl group was truncated to CH_2CF_3 to make a more electron withdrawing isocyanide. Again, two minima were found (structural parameters summarized in table S4.6) and they were confirmed to be true minima through a frequency calculation. The Fe–C(NCH_2CF_3) distances were shorter than in Fe–C(NMe) for both minima, consistent with $CNCH_2CF_3$ being a stronger π-acceptor than CNMe

Table S4.6: Structural parameters for two calculated energetic minima for $[(NHC^{H})_3Fe_4S_4CNCH_2CF_3]^+$

Structure	Fe–CNMe Å	Fe–NHC (avg.) Å	Fe–S (avg.) Å	S_4 volume $Å^3$
Contracted	1.776	1.913	2.163	4.901
Typical	1.821	1.987	2.248	5.566

4. Orbital localizations for both energetic minima for $[(NHC^{H})_3Fe_4S_4CNMe]^+$

Orbital localizations were performed on both minima using IAOIBO localization and a Löwdin population analysis. Orbitals localized > 70 % on a single Fe site were assigned to that Fe site; delocalized orbitals were partitioned according to the Löwdin population analysis. The calculated valences were normalized so the total Fe valence would sum to 9+ to account for contributions of

S and C(NHC) centers to the d-orbitals. The calculated Fe valences are summarized in Table S4.7 and qualitative orbital diagrams are shown in Figure S4.58. The orbitals in the typical structure are

Table S4.7: Calculated Fe valences for $[(NHC^{H})_3Fe_4S_4CNMe]^+$. Fe0 is bound to CNMe; Fe1 is its spin-aligned pair

Structure	Fe0	Fe1	Fe2	Fe3
Contracted	1.65+	2.67+	2.71+	1.97+
Typical	1.55+	2.47+	2.49+	2.49+

well-localized, with only two orbitals that are more than 10% delocalized between 2 Fe centers and none with significant contributions from more than two Fe centers. As a result, the qualitative orbital diagram in Figure S4.58 is a good representation of the localized orbital picture. On the other hand, the localized orbital picture from the contracted picture is much more complicated, with seven orbitals having contributions >30 % from more than one Fe center and three of those orbitals having contributions > 10 % from three or more Fe centers. This reflects the greater covalency of the contracted structure compared to the compressed structure and means that the pairwise orbital description shown in Figure S4.58 is a significant simplification. Therefore, the entire Löwdin population analysis for the contracted structure is shown in Table S4.8 with exact orbital compositions for all orbitals with > 30% contributions from more than one Fe. The orbitals

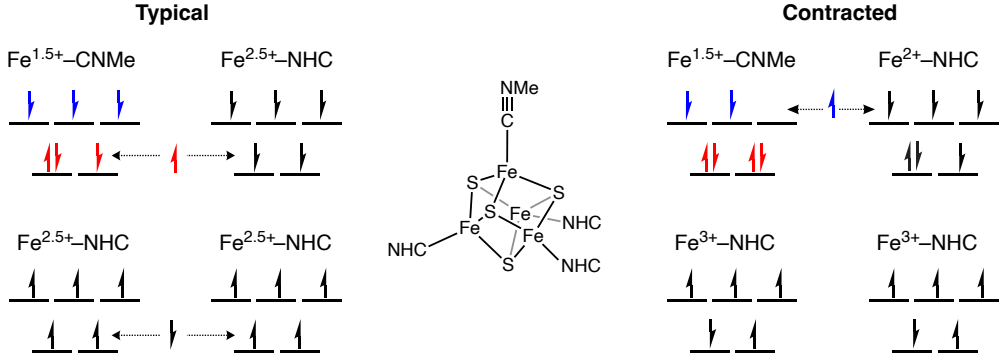

Figure S4.58. Qualitative orbital diagrams for the localized orbitals of the typical and contracted structures with CNMe

with π-backbonding symmetry are highlighted in red and those with Fe–CNMe π-nonbonding are highlighted in blue.

Table S4.8: Löwdin population analysis for $[(NHC^{H})_3Fe_4S_4CNMe]^+$. Fe0 is bound to CNMe; Fe1 is its spin-aligned pair. Orbital contributions below 10% are removed for clarity.

	Fe0	Fe1	Fe2	Fe3
74a			1	
75a			1	
91a			1	
81a				1
80a				1
93a				1
83a	1			
141a	1			
148a		1		
89a	0.16	0.66		
144a	0.16	0.17	0.29	0.30
142a	0.21		0.36	0.26
70b		1		
96b		1		
90b		1		
81b		1		
88b	1			
80b	1			
98b			0.25	0.60
97b			0.49	0.41
95b	0.59			0.27
89b	0.59		0.30	
146b	0.25	0.44	0.13	0.11

5. Orbital localizations for both energetic minima for $[(NHC^{H})_3Fe_4S_4CNCH_2CF_3]^+$

Orbital localizations on $[(NHC^{H})_3Fe_4S_4CNCH_2CF_3]^+$ were performed analogously to those on $[(NHC^{H})_3Fe_4S_4CNMe]^+$. The calculated valences are summarized in table S4.9.

Table S4.9: Calculated Fe valences for $[(NHC^{H})_3Fe_4S_4CNCH_2CF_3]^+$. Fe0 is bound to CNMe; Fe1 is its spin-aligned pair

Structure	Fe0	Fe1	Fe2	Fe3
Contracted	1.71+	2.23+	2.46+	2.53+
Typical	1.53+	2.57+	2.54+	2.54+

G. Crystallographic Details

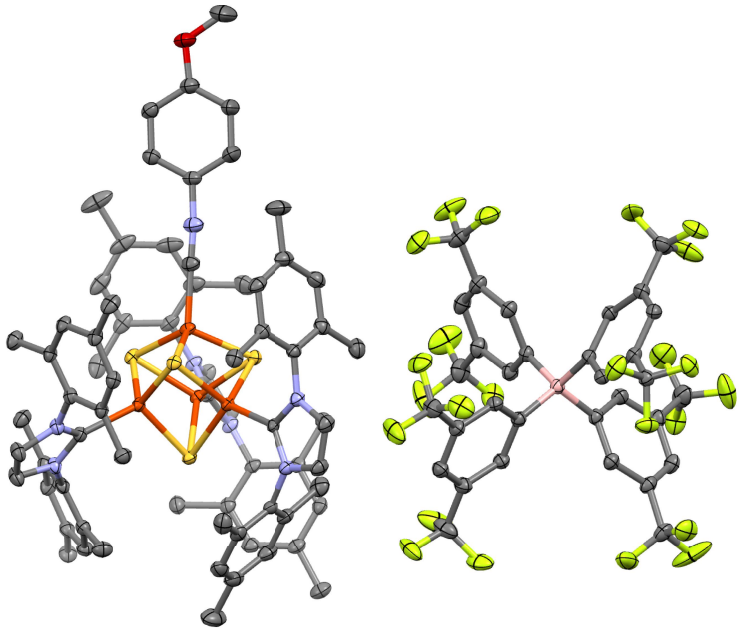

Figure S4.59: X-ray crystallographic structure of [**1-CNAr$^{4\text{-OMe}}$**]$^{+}$; carbon (gray), nitrogen (blue), iron (orange), and sulfur (yellow), oxygen (red), fluorine (green), boron (pink) with ellipsoids at the 50% probability level.

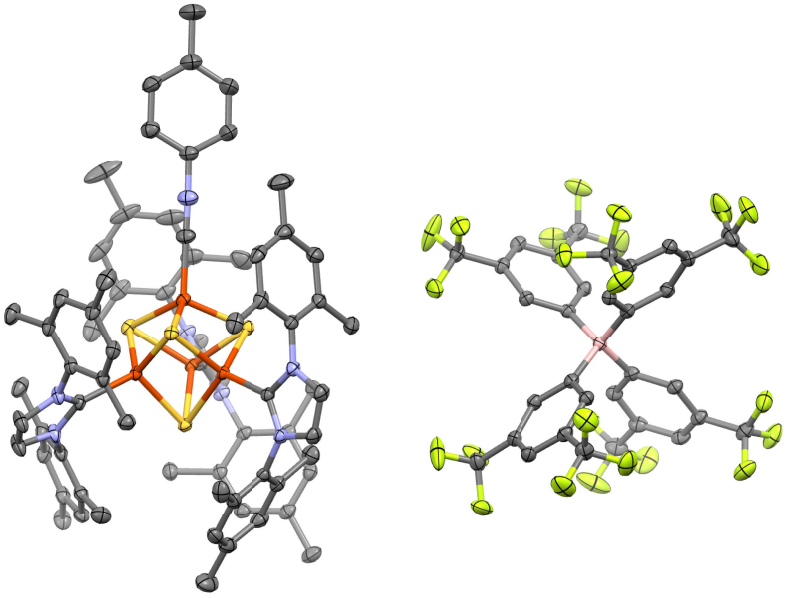

Figure S4.60: X-ray crystallographic structure of [**1-CNAr$^{4\text{-Me}}$**]$^{+}$; carbon (gray), nitrogen (blue), iron (orange), and sulfur (yellow), fluorine (green), boron (pink) with ellipsoids at the 50% probability level.

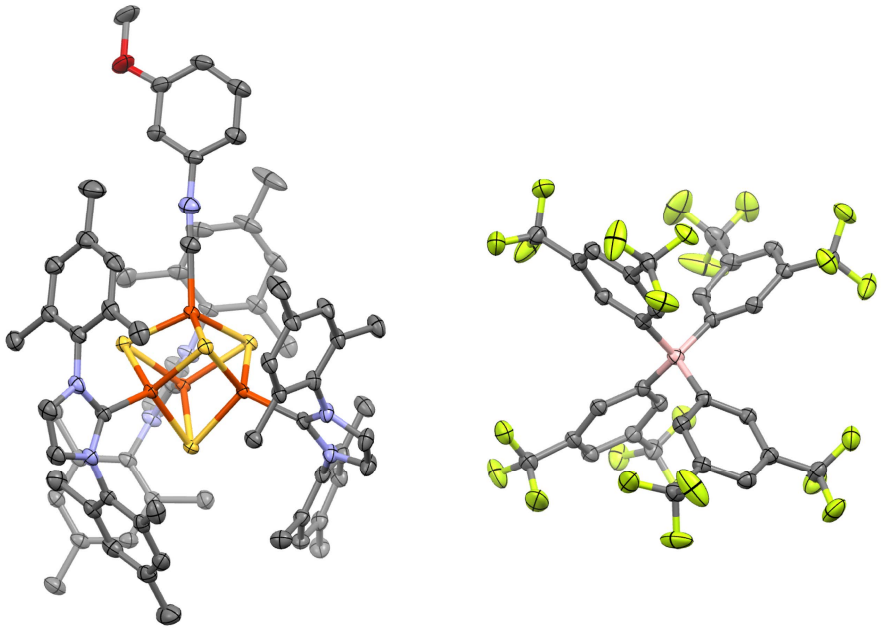

Figure S4.61: X-ray crystallographic structure of [**1-CNAr**$^{\mathbf{3\text{-}OMe}}$]$^{+}$; carbon (gray), nitrogen (blue), iron (orange), and sulfur (yellow), oxygen (red), fluorine (green), boron (pink) with ellipsoids at the 50% probability level.

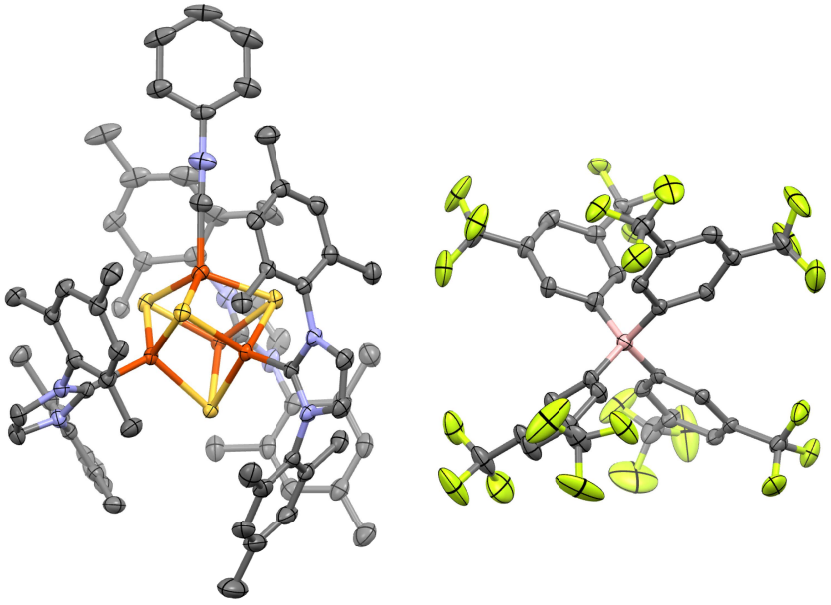

Figure S4.62: X-ray crystallographic structure of [**1-CNPh**]$^{+}$; carbon (gray), nitrogen (blue), iron (orange), and sulfur (yellow), fluorine (green), boron (pink) with ellipsoids at the 50% probability level.

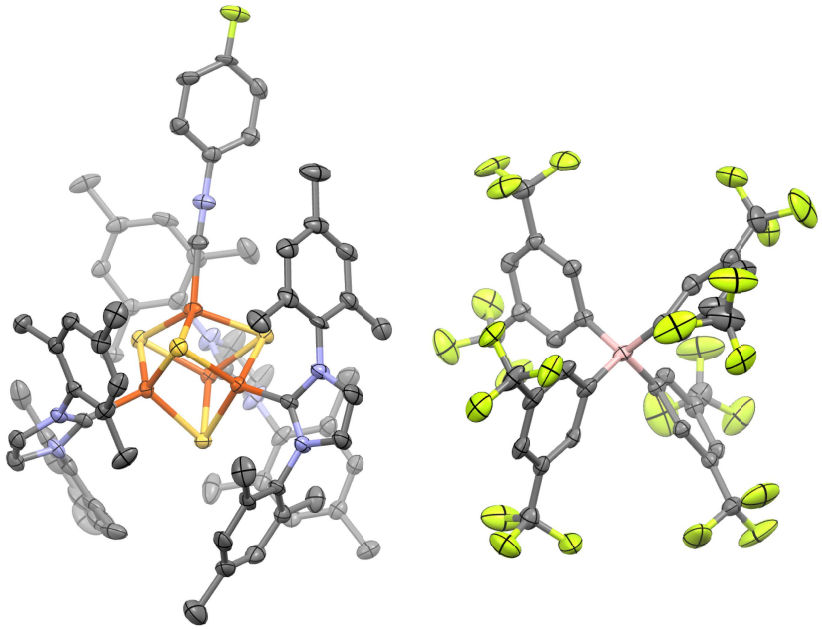

Figure S4.63: X-ray crystallographic structure of [**1-CNAr$^{4\text{-F}}$**]$^{+}$; carbon (gray), nitrogen (blue), iron (orange), and sulfur (yellow), fluorine (green), boron (pink) with ellipsoids at the 50% probability level.

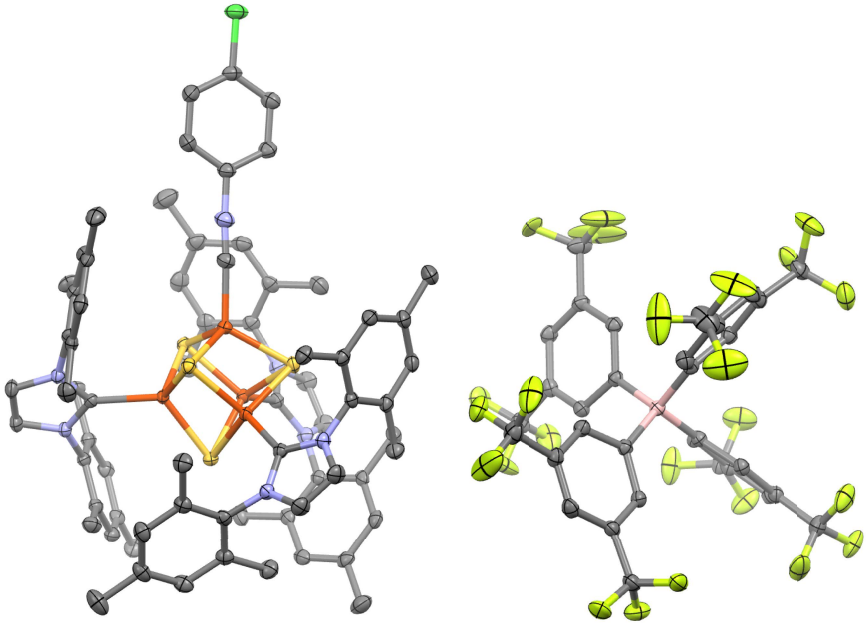

Figure S4.64: X-ray crystallographic structure of [**1-CNAr$^{4\text{-Cl}}$**]$^{+}$; carbon (gray), nitrogen (blue), iron (orange), and sulfur (yellow), chlorine (dark green), fluorine (green), boron (pink) with ellipsoids at the 50% probability level.

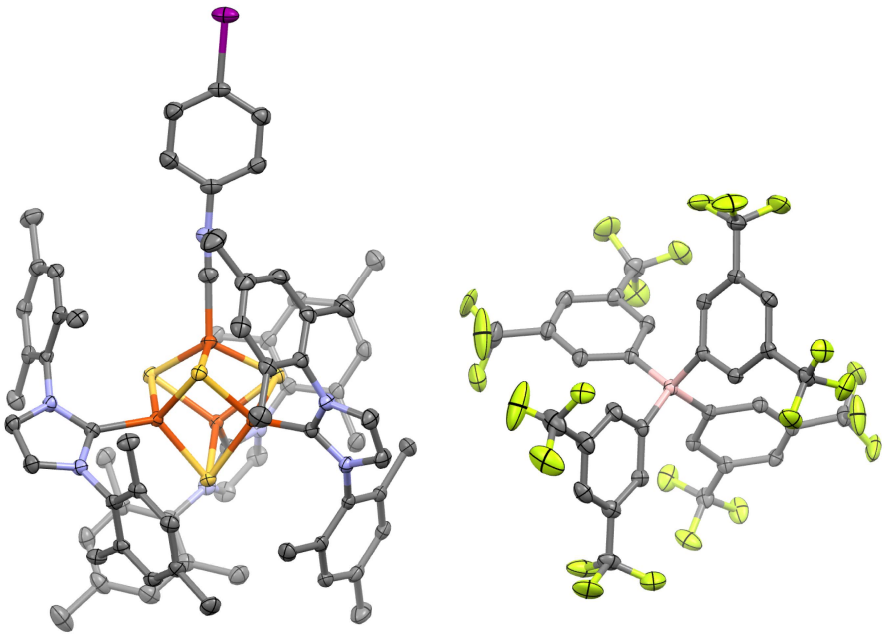

Figure S4.65: X-ray crystallographic structure of [**1-CNAr$^{4\text{-I}}$**]$^{+}$; carbon (gray), nitrogen (blue), iron (orange), and sulfur (yellow), iodine (purple), fluorine (green), boron (pink) with ellipsoids at the 50% probability level.

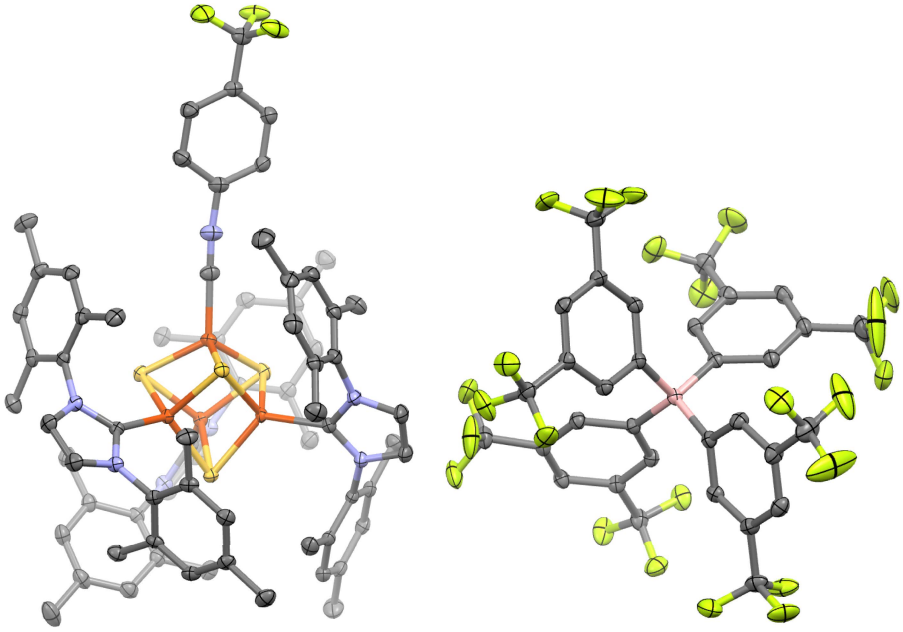

Figure S4.66: X-ray crystallographic structure of [**1-CNAr$^{4\text{-CF3}}$**]$^{+}$; carbon (gray), nitrogen (blue), iron (orange), and sulfur (yellow), fluorine (green), boron (pink) with ellipsoids at the 50% probability level.

Tabulated bond parameters:

Table S4.10: Fe–C(NAr) distances for [**1-CNAr**]$^+$ complexes

Aryl substituent	Fe–C distance (Å)
4-NMe_2	1.951(2)
4-OMe	1.942(2)
4-Me	1.935(1)
3-OMe[a]	1.95(1)
Ph	1.921(2)
4-F	1.92(1)
4-Cl	1.881(2)
4-I	1.875(3)
4-CF_3	1.869(2)
3,5-$(CF_3)_2$	1.847(2)

[a]: depending on the refinement of the whole molecule disorder, this bond length can vary ±0.01 Å, so we provide an estimated error instead of the ESD.

Table S4.11: Average Fe–S distances for [**1-CNAr**]$^+$ complexes[a]

Aryl substituent	Fe–S distance (avg, Å)	Short Fe–S (avg, Å)	Long Fe–S (avg. Å)
4-NMe_2	2.274(2)	2.218(1)	2.302(2)
4-OMe	2.274(1)	2.2190(8)	2.302(1)
4-Me	2.270(1)	2.2160(7)	2.2974(9)
3-OMe	2.247(3)	2.218(2)	2.299(2)
Ph	2.242(1)	2.2211(8)	2.293(1)
4-F	2.264(6)	2.216(4)	2.288(5)
4-Cl	2.227(2)	–	–
4-I	2.222(2)	–	–
4-CF_3	2.221(1)	–	–
3,5-$(CF_3)_2$	2.217(1)	–	–

[a]: Errors are calculated as the RMS sum of the ESDs for individual bonds

Table S4.12: Average Fe–Fe distances for [**1-CNAr**]$^+$ complexes[a]

Aryl substituent	Fe–Fe distance (avg, Å)
4-NMe_2	2.6963(9)
4-OMe	2.6947(7)
4-Me	2.6913(5)
3-OMe	2.698(1)
Ph	2.6914(7)
4-F	2.681(2)
4-Cl	2.6596(7)
4-I	2.6506(9)
4-CF_3	2.6512(7)
3,5-$(CF_3)_2$	2.6462(5)

[a]: Errors are calculated as the RMS sum of the ESDs for individual bonds

Table S4.13: Average Fe–C(NHC) distances for [**1-CNAr**]$^+$ complexes[a]

Aryl substituent	Fe–C distance (avg, Å)
4-NMe_2	2.066(3)
4-OMe	2.067(2)
4-Me	2.064(2)
3-OMe	2.068(3)
Ph	2.069(3)
4-F	2.06(1)
4-Cl	2.031(3)
4-I	2.023(3)
4-CF_3	2.024(2)
3,5-$(CF_3)_2$	2.025(2)

[a]: Errors are calculated as the RMS sum of the ESDs for individual bonds

Table S4.14: Average S_4 volume for [**1-CNAr**]$^+$ complexes

Aryl substituent	Fe–C distance (avg, Å)
4-NMe_2	5.498
4-OMe	5.500
4-Me	5.470
3-OMe	5.475
Ph	5.459
4-F	5.433
4-Cl	5.142
4-I	5.114
4-CF_3	5.102
3,5-$(CF_3)_2$	5.072

Refinement Details:

[**1-CNAr$^{4\text{-NMe2}}$**][BAr$^{F}_{4}$]: Crystallized from DFB/pentane in P–1 with a mixture of lattice DFB and pentane. Several –CF_3 groups on the [BAr$^{F}_{4}$] anion and the lattice solvent were disordered. The disorder was modeled using similarity restraints on 1-2 and 1-3 distances and displacement parameters and rigid bond restraints.

[**1-CNAr$^{4\text{-OMe}}$**][BAr$^{F}_{4}$]: Crystallized from DFB/pentane in P–1 with pentane in the crystallographic lattice. Several –CF_3 groups on the [BAr$^{F}_{4}$] anion, the aryl isocyanide substituent, and the lattice solvent were disordered. The disorder was modeled using similarity restraints on 1-2 and 1-3 distances and displacement parameters and rigid bond restraints.

[**1-CNAr$^{4\text{-Me}}$**][BAr$^{F}_{4}$]: Crystallized from DFB/pentane in P–1 with pentane in the crystallographic lattice. Several –CF_3 groups on the [BAr$^{F}_{4}$] anion and the lattice solvent were disordered. The disorder was modeled using similarity restraints on 1-2 and 1-3 distances and displacement parameters and rigid bond restraints.

[**1-CNAr$^{3\text{-OMe}}$**][BAr$^{F}_{4}$]: Crystallized from DFB/pentane in P–1 with pentane in the crystallographic lattice. Several –CF_3 groups on the [BAr$^{F}_{4}$] anion, one mesityl substituent, and the aryl group on the isocyanide were disordered. This disorder was modeled using similarity restraints on 1-2 and 1-3 distances and displacement parameters and rigid bond restraints. Additionally, the cluster core displayed a small amount of whole-molecule disorder, with positions for the minor component Fe and S atoms identified. The Fe and S atoms of this minor component (ca. 7%) were refined isotopically.

[**1-CNPh**][BAr^F_4]: Crystallized from Et_2O/pentane in P–1 with pentane and Et_2O in the crystallographic lattice. The lattice solvent, one mesityl substituent, the entire [BAr^F_4] anion, and the phenyl substituent of the isocyanide were disordered over two positions. The disorder was modeled using similarity restraints on 1-2 and 1-3 distances and displacement parameters and rigid bond restraints.

[**1-CNAr$^{4\text{-F}}$**][BAr^F_4]: Crystallized from DFB/pentane in $P2_1$ as an inversion twin that was refined with the inversion twin law and a BASF parameter and with pentane in the crystallographic lattice. Several $–CF_3$ groups on the [BAr^F_4] anion and the lattice solvent were disordered. The disorder was modeled using similarity restraints on 1-2 and 1-3 distances and displacement parameters and rigid bond restraints. Some of the solvent atoms were refined isotropically due to multicomponent disorder.

[**1-CNAr$^{4\text{-Cl}}$**][BAr^F_4]: Crystallized from Et_2O/pentane in P–1 with Et_2O in the crystallographic lattice. Several $–CF_3$ groups on the [BAr^F_4] anion and one molecule of lattice solvent were disordered. The disorder was modeled using similarity restraints on 1-2 and 1-3 distances and displacement parameters and rigid bond restraints.

[**1-CNAr$^{4\text{-I}}$**][BAr^F_4]: Crystallized from Et_2O/pentane in P–1 with Et_2O in the crystallographic lattice. Several $–CF_3$ groups on the [BAr^F_4] anion and one molecule of lattice solvent were disordered. The disorder was modeled using similarity restraints on 1-2 and 1-3 distances and displacement parameters and rigid bond restraints.

[**1-CNAr$^{4\text{-}CF3}$**][BAr$^{F}_{4}$]: Crystallized from Et_2O/pentane in P–1 with Et_2O in the crystallographic lattice. Several –CF_3 groups on the [BAr$^{F}_{4}$] anion and one molecule of lattice solvent were disordered. The disorder was modeled using similarity restraints on 1-2 and 1-3 distances and displacement parameters and rigid bond restraints. Some of the [BAr$^{F}_{4}$] disordered F atoms were refined isotropically because they were very minor occupancy.

[**1-CNAr$^{3,5\text{-}(CF3)2}$**][BAr$^{F}_{4}$]: Crystallized from DFB/pentane in P–1. Several –CF_3 groups on the [BAr$^{F}_{4}$] anion were disordered. The disorder was modeled using similarity restraints on 1-2 and 1-3 distances and displacement parameters and rigid bond restraints.

H. References

(1) Smallcombe, S. H.; Patt, S. L.; Keifer, P. A. WET Solvent Suppression and Its Applications to LC NMR and High-Resolution NMR Spectroscopy. *J. Magn. Reson. Ser. A* **1995**, *117* (2), 295–303.

(2) Stoll, S.; Schweiger, A. EasySpin, a Comprehensive Software Package for Spectral Simulation and Analysis in EPR. *J. Magn. Reson.* **2006**, *178* (1), 42–55.

(3) Prisecaru, I. WMOSS4 Mössbauer Spectral Analysis Software, www.wmoss.org.

(4) Hübschle, C. B.; Sheldrick, G. M.; Dittrich, B. ShelXle: A Qt Graphical User Interface for SHELXL. *J. Appl. Crystallogr.* **2011**, *44* (6), 1281–1284.

(5) Brown, A. C.; Suess, D. L. M. Controlling Substrate Binding to Fe 4 S 4 Clusters through Remote Steric Effects. *Inorg. Chem.* **2019**, *58* (8), 5273–5280.

(6) Yakelis, N. A.; Bergman, R. G. Safe Preparation and Purification of Sodium Tetrakis[(3,5-Trifluoromethyl) Phenyl]Borate (NaBArF 24): Reliable and Sensitive Analysis of Water in Solutions of Fluorinated Tetraarylborates. *Organometallics* **2005**, *24* (14), 3579–3581.

(7) Brown, A. C.; Suess, D. L. M. Valence Localization in Alkyne and Alkene Adducts of Synthetic [Fe4S4]+ Clusters. *Inorg. Chem.* **2022**.

(8) Sridharan, A.; Brown, A. C.; Suess, D. L. M. A Terminal Imido Complex of an Iron–Sulfur Cluster. *Angew. Chem. Int. Ed.* **2021**, *60* (23), 12802–12806.

(9) McSkimming, A.; Suess, D. L. M. Dinitrogen Binding and Activation at a Molybdenum–Iron–Sulfur Cluster. *Nat. Chem.* **2021**, *13* (7), 666–670.

(10) Kim, Y.; Sridharan, A.; Suess, D. L. M. The Elusive Mononitrosylated [Fe4S4] Cluster in Three Redox States. *Angew. Chem. Int. Ed.* **2022**.

(11) Kuveke, R. E. H.; Barwise, L.; Ingen, Y. Van; Vashisth, K.; Roberts, N.; Chitnis, S. S.; Dutton, J. L.; Martin, C. D.; Melen, R. L. An International Study Evaluating Elemental Analysis. *ChemRxiv* **2022**, 10.26434/chemrxiv-2022-k5xvx.

(12) Škoch, K.; Císařová, I.; Štěpnička, P. Selective Gold-Catalysed Synthesis of Cyanamides and 1-Substituted 1H-Tetrazol-5-Amines from Isocyanides. *Chem. Eur. J.* **2018**, *24* (52), 13788–13791.

(13) Tran, C. C.; Kawaguchi, S. I.; Kobiki, Y.; Matsubara, H.; Tran, D. P.; Kodama, S.; Nomoto, A.; Ogawa, A. Palladium-Catalyzed Diarylation of Isocyanides with Tetraarylleads for the Selective Synthesis of Imines and α-Diimines. *J. Org. Chem.* **2019**, *84* (18), 11741–11751.

(14) Porcheddu, A.; Giacomelli, G.; Chimica, D. Microwave-Assisted Synthesis of Isonitriles : A General Simple Methodology Multicomponent Reactions Have Become an Important Component of the Combinatorial Chemist ' s Library , as a Great Number of Compounds Can Be Produced in a Rapid These Reactions , A. *J. Org. Chem.* **2005**, *70* (17), 2361–2363.

(15) Carpenter, A. E.; Mokhtarzadeh, C. C.; Ripatti, D. S.; Havrylyuk, I.; Kamezawa, R.; Moore, C. E.; Rheingold, A. L.; Figueroa, J. S. Comparative Measure of the Electronic Influence of Highly Substituted Aryl Isocyanides. *Inorg. Chem.* **2015**, *54* (6), 2936–2944.

(16) Hammett, L. P. The Effect of Structure upon the Reactions of Organic Compounds. Temperature and Solvent Influences. *J. Chem. Phys.* **1936**, *4* (9), 613–617.

(17) Hansch, C.; Leo, A.; Taft, R. W. A Survey of Hammett Substituent Constants and Resonance and Field Parameters. *Chem. Rev.* **1991**, *91* (2), 165–195.

(18) Neese, F. The ORCA Program System. *Wiley Interdiscip. Rev. Comput. Mol. Sci.* **2012**, *2* (1), 73–78.
(19) Tao, J.; Perdew, J. P.; Staroverov, V. N.; Scuseria, G. E. Climbing the Density Functional Ladder: Nonempirical Meta–Generalized Gradient Approximation Designed for Molecules and Solids. *Phys. Rev. Lett.* **2003**, *91* (14), 3–6.
(20) Staroverov, V. N.; Scuseria, G. E.; Tao, J.; Perdew, J. P. Comparative Assessment of a New Nonempirical Density Functional: Molecules and Hydrogen-Bonded Complexes. *J. Chem. Phys.* **2003**, *119* (23), 12129–12137.
(21) Neese, F.; Wennmohs, F.; Hansen, A.; Becker, U. Efficient, Approximate and Parallel Hartree-Fock and Hybrid DFT Calculations. A "chain-of-Spheres" Algorithm for the Hartree-Fock Exchange. *Chem. Phys.* **2009**, *356* (1–3), 98–109.
(22) Pantazis, D. A.; Chen, X. Y.; Landis, C. R.; Neese, F. All-Electron Scalar Relativistic Basis Sets for Third-Row Transition Metal Atoms. *J. Chem. Theory Comput.* **2008**, *4* (6), 908–919.
(23) Reiher, M. Relativistic Douglas-Kroll-Hess Theory. *Wiley Interdiscip. Rev. Comput. Mol. Sci.* **2012**, *2* (1), 139–149.
(24) Weigend, F. Accurate Coulomb-Fitting Basis Sets for H to Rn. *Phys. Chem. Chem. Phys.* **2006**, *8* (9), 1057–1065.
(25) Barone, V.; Cossi, M. Conductor Solvent Model. *J. Phys. Chem. A* **1998**, *102* (97), 1995–2001.
(26) Knizia, G. Intrinsic Atomic Orbitals: An Unbiased Bridge between Quantum Theory and Chemical Concepts. *J. Chem. Theory Comput.* **2013**, *9* (11), 4834–4843.
(27) Pipek, J.; Mezey, P. G. A Fast Intrinsic Localization Procedure Applicable for Ab Initio and Semiempirical Linear Combination of Atomic Orbital Wave Functions. *J. Chem. Phys.* **1989**, *90* (9), 4916–4926.
(28) Ye, M.; Thompson, N. B.; Brown, A. C.; Suess, D. L. M. A Synthetic Model of Enzymatic [Fe4S4]-Alkyl Intermediates. *J. Am. Chem. Soc.* **2019**, *141* (34), 13330–13335.
(29) McSkimming, A.; Sridharan, A.; Thompson, N. B.; Müller, P.; Suess, D. L. M. An [Fe4S4]3+-Alkyl Cluster Stabilized by an Expanded Scorpionate Ligand. *J. Am. Chem. Soc.* **2020**, *142* (33), 14314–14323.
(30) Brown, A. C.; Thompson, N. B.; Suess, D. L. M. Evidence for Low-Valent Electronic Configurations in Iron–Sulfur Clusters. *J. Am. Chem. Soc.* **2022**, *144* (20), 9066–9073.

Chapter 5. An Iron-Sulfur Cluster with a Highly Pyramidalized Three-Coordinate Iron Center That Has an Imperceptibly Low Affinity for Dinitrogen

Introduction

The three nitrogenase isozymes (Mo, V, and all-Fe) each employ Fe-S clusters for converting N_2 to NH_3.[1–6] For all nitrogenases, N_2 binding is thought to occur at one or more Fe sites of its catalytic cofactor, FeMo-co, after addition of several protons and electrons.[3,4,7–11] This activation process—involving protonation and expulsion of a 'belt' sulfide from FeMo-co,[12–19] hydride formation followed by H_2 reductive elimination,[4,20,21] and/or other processes[22,23] that disrupt FeMo-co's resting state structure—is presumably required to generate Fe sites that are sufficiently electron-releasing and/or low-coordinate for binding N_2. In particular, the reductive explusion of a hydrosulfide ligand from FeMo-co is analogous to a common way to synthesize N_2 coordination complexes: reduction of an M–X unit (X = anionic ligand), which triggers loss of X^- and opens a coordination site for N_2 binding at the reduced metal center (Figure 5.1A). However, for Fe–S clusters, such reductions often lead to cluster oligomerization reactions that outcompete N_2

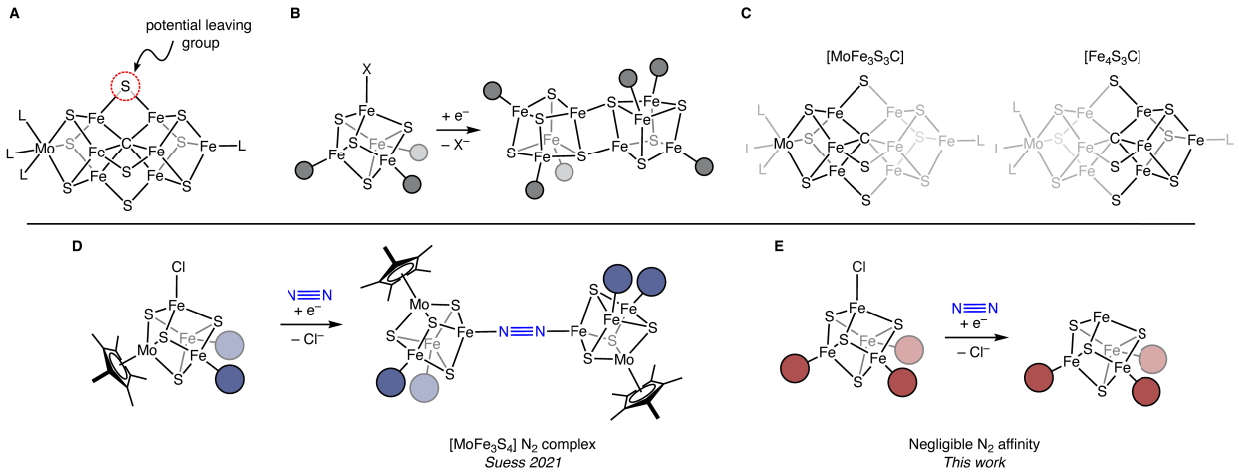

Figure 5.1. Dinitrogen chemistry of Fe–S clusters. A) Explusion of a hydrosulfide bridging ligand from FeMo-co may generate an open coordination site for N2 B) Synthetic Fe–S clusters are prone to oligomerization via formation of intercluster Fe-S bonds upon reduction. C) FeMo-co can be envisioned as fused $[MoFe_3S_3C]$ and $[Fe_4S_3C]$ clusters. D) Synthetic $[MoFe_3S_4]$–N_2 clusters have been prepared. E) Here, we report that reduction of an $[Fe_4S_4]$ cluster leads to a species with a three coordinate Fe site that has negligible N_2 affinity.

binding. For example, in many cases reduction of [$MoFe_3S_4$] and [Fe_4S_4] clusters to the all-ferrous state results in formation of edge-bridged double cubanes (EBDCs; Figure 5.1B) rather than N_2 binding.[24–27] Indeed, only recently were the first N_2 complexes of Fe–S clusters disclosed: those based on [$MoFe_3S_4$] clusters reported by our group[28] and those based on [Mo_3FeS_4] clusters reported by Ohki *et al*., all of which have cuboidal M–S cores containing Mo centers and in which oligomerization was prevented by sterically encumbering ligands on adjacent metal sites (Figure 5.1D).[29]

The aforementioned synthetic work utilized Mo-Fe-S clusters because FeMo-co contains both Fe and Mo, however we have been attempting to prepare N_2 complexes of Fe-S clusters containing only Fe, and specifically [Fe_4S_4] clusters, for two reasons. First, because FeMo-co can be viewed both structurally and magnetically as two fused cubanes: one [$MoFe_3S_3C$] and one [Fe_4S_3C] that share a vertex at the central carbide and are further connected via three 'belt' sulfides (Figure 5.1C). Thus, insofar as studying the N_2 chemistry of an [$MoFe_3S_4$] cluster can inform on the principles behind N_2 reduction by FeMo-co, so too can studying the N_2 chemistry of an [Fe_4S_4] cluster, which resembles the other cubane substructure of FeMo-co. Second, not all nitrogenase cofactors contain Mo: the all-Fe nitrogenase contains only Fe in its catalytic cofactor.[2,30–32] Therefore, understanding the differences between how [$MoFe_3S_4$] and [Fe_4S_4] clusters bind and activate N_2 may inform on the basis for the divergent catalytic properties of the Mo and all-Fe nitrogenases.

By analogy to our preparation of N_2 complexes of [$MoFe_3S_4$] clusters, we surmised that N_2 binding at an [Fe_4S_4] cluster could be achieved if cluster oligomerization could be adequately suppressed. Here, we describe synthetic approaches to generating all-ferrous [Fe_4S_4] cluster for

which undesired oligomeriation can be suppressed, and the surprising finding that the cluster's unique Fe does not coordinate N_2, and instead binds nothing at all (Figure 5.1E).

Results and Discussion

We first attempted to prepare an N_2 complex of an [Fe_4S_4] cluster by abstracting Cl• from $(IMes)_3Fe_4S_4Cl$ (**1-Cl**, IMes = 1,3-bis(2,4,6-trimethylpheny)limidazol-2-ylidene)[33] using $Ti(N[^tBu]Ar)_3$ (Ar = 3,5-dimethylphenyl)[34] under an N_2 atmosphere, with the hope that the three sterically protective IMes ligands would prevent cluster oligomerization. Although such oligomerization reactions are suppressed when an analogous reaction is performed in the presence of CO (affording the previously reported CO-bound [Fe_4S_4] cluster, $IMes_3Fe_4S_4CO$ (**1-CO**)),[35] reduction of **1-Cl** in the absence of CO instead yielded an [Fe_8S_8] cluster, $(IMes)_4Fe_8S_8$ (**1-FBDC**, Figure 5.2), along with free IMes. It has previously been reported that reduction of Fe–S clusters with phosphine ligands similarly leads to oligomerization with loss of PR_3;[24,36] here, these oligomerization reactions lead to the formation of EBDCs in which the two clusters are bridged by a single edge or cubane tetramers in which two EBDCs are bridged across a second edge to

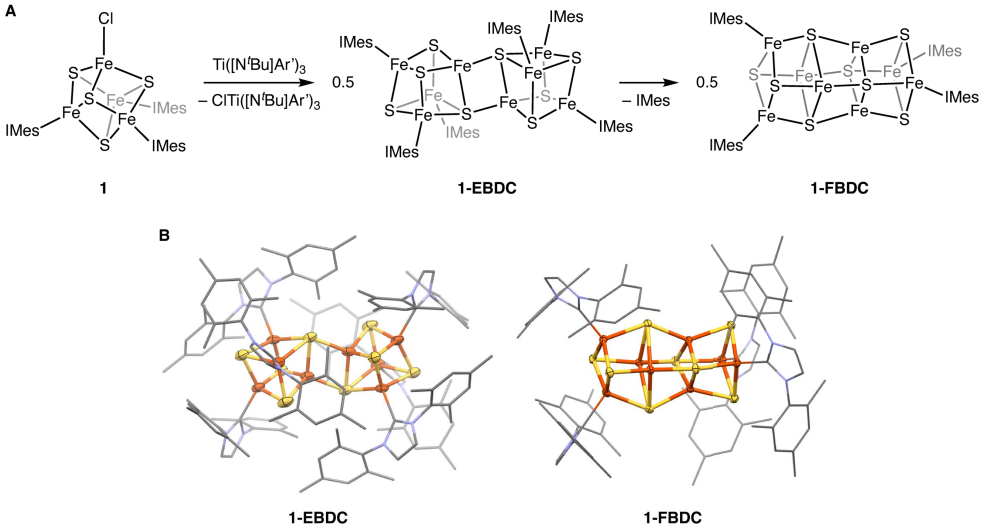

Figure 5.2. A) Reduction of **1-Cl** leads to formation of **1-FBDC** via intermediate **1-EBDC**. B) Electron crystallographic structure of **1-EBDC** (left) and X-ray crystallographic structure of **1-FBDC** (right); carbon (gray), nitrogen (blue), iron (orange), and sulfur (yellow) with ellipsoids at the 50% probability level. IMes ligands are shown as sticks for clarity.

another EBDCs.[24,37,38] Cluster **1-FBDC** can be envisioned as derived from an EBDC in which two additional ligands have been lost and replaced by intracluster Fe–S bonds, resulting in the two constituent $[Fe_4S_4]$ clusters being bridged by one face of each cubane. Therefore, we refer to **1-FBDC** as a face-bridged double cubane (FBDC).

In understanding the electronic structure of **1-FBDC**, it is useful to first understand the electronic structure of typical $[Fe_4S_4]^0$ clusters.[39–41] All-ferrous $[Fe_4S_4]^0$ clusters have an $S = 4$ ground spin state originating from antiferromagnetic coupling of a single Fe^{2+} site ($S = 2$, minority spin) with three spin-aligned Fe^{2+} ($S = 6$, majority spin) sites.[39,42–44] Studies aimed at understanding the origin of this spin state have revealed several characteristic geometric and spectroscopic signatures of this spin coupling pattern.[45,46] First, the different spin coupling constants between the spin-aligned and anti-aligned Fe centers lead to a characteristic distortion, in which the Fe center in the minority spin has long Fe–Fe distances and a short Fe–L bond (where L is the terminal ligand) compared to the majority spin Fe centers. Second, Mössbauer spectra of $[Fe_4S_4]^0$ clusters show three Fe sites with relatively small $|\Delta E_Q|$ and one Fe site with large $|\Delta E_Q|$; magnetic Mössbauer spectra reveal that the site with large $|\Delta E_Q|$ is the minority spin Fe center. EBDCs (which have an $S = 0$ ground spin state) have the same characteristic features: two Fe centers with long Fe–Fe distances compared to the others and a Mössbauer spectrum with a 3:1 ratio of sites with small $|\Delta E_Q|$ to sites with large $|\Delta E_Q|$. Based on the presence of these structural and spectroscopic signatures, EBDCs have been described as two $S = 4$ $[Fe_4S_4]^0$ clusters antiferromagnetically coupled to one another, leading to the $S = 0$ ground spin state.[47]

Cluster **1-FBDC**, like the EBDCs, has an overall $S = 0$ ground spin state determined by SQUID magnetometry (Figure S5.33). The Fe–S cluster core of **1-FBDC** has approximate C_2 symmetry, with two Fe–NHC Fe sites having much longer average Fe–Fe distances (2.760(1) Å) and shorter

average Fe–C(NHC) distances (2.020(3) Å) than the other two Fe–NHC sites (2.641(1) Å and 2.091(3) Å, respectively Figure S5.22). Additionally, the Mössbauer spectrum of **1-FBDC** (simulated with three quadrupole doublets in a 1:1:2 ratio, Figure S5.35) shows two Fe sites with a large $|\Delta E_Q|$ (2.920 mm s^{-1}) compared to the other six ($|\Delta E_Q|_{avg}$ = 1.356 mm s^{-1}). The presence of two Fe sites with elongated Fe–Fe distances and of two sites in the Mössbauer spectrum with large $|\Delta E_Q|$ suggests that **1-FBDC**, like the EBDCs, can be formulated as two $[Fe_4S_4]^0$ clusters each with $S = 4$ that are antiferromagnetically coupled to one another to yield an $S = 0$ ground spin state.

We hypothesized that **1-FBDC** might form via an intermediate EBDC with six IMes ligands, followed by spontaneous loss of IMes owing to steric clashes between the IMes ligands. Indeed, when reduction of **1-Cl** is carried out at low temperatures in toluene, a dark-brown microcrystalline solid precipitates from the reaction mixture; upon warming to room temperature and stirring for several hours this solid redissolves and formation of **1-FBDC** is observed by NMR spectroscopy. Characterization of the intermediate precipitate by microcrystal electron diffraction[48,49] reveals it to be the edge-bridged double cubane, $(IMes)_6Fe_8S_8$ (**1-EBDC**, Figure 5.2B).

As noted above, $[Fe_8S_8]^0$ EBDC clusters have been previously characterized and are generally stable. The transient stability of **1-EBDC** with respect to loss of IMes is a result of the steric congestion imparted by the six IMes ligands around **1-EBDC**; this observation suggests that dimerization of the reduced $[Fe_4S_4]$ cluster to form **1-EBDC** could be prevented if the steric profiles of the NHC ligands are further increased. To guide the design of a new, bulkier NHC, we examined the space-filling model of **1-Cl** (Figure 5.3A),[33] which shows that the *m*-H positions of the NHC mesityl substituents are positioned directly over the S atoms bound to the apical Fe site. We hypothesized that introducing bulky substituents at these meta positions would prevent intermolecular Fe–S bond formation en route to **1-EBDC**, and therefore afford access to an

$[Fe_4S_4]^0$ cluster in which one Fe site remains open to coordinate a weakly binding ligand such as N_2.

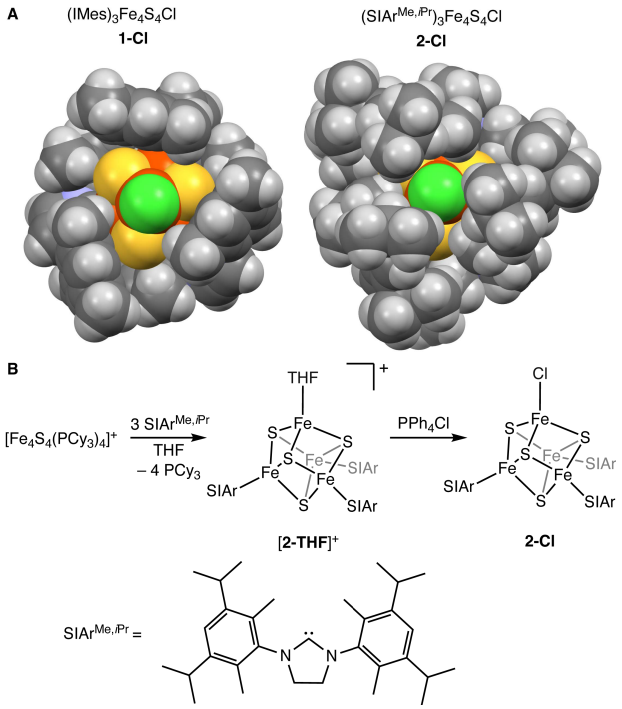

Figure 5.3. A) Space-filling models of **1** (left) and **2-Cl** (right) showing the increased steric protection of the S atoms in **2-Cl**. Carbon (gray), nitrogen (blue), iron (orange), sulfur (yellow), and chlorine (green). B) Synthesis of [**2-THF**]$^+$ and **2-Cl**.

We specifically targeted a new NHC, SIAr^{Me,iPr} (SIAr = 1,3-bis(3,5-diisopropyl-2,6-dimethylphenyl)-4,5-dihydroimidazol-2-ylidene), which features *m*-^{i}Pr and *o*-CH_3 substituents on the aryl ring. The synthesis of SIAr^{Me,iPr} is described in the SI; briefly, it is prepared via bromination of 4,6-diisopropyl-1,3-dimethylbenzene,[50] followed by a Buchwald-Hartwig amination of the resulting 3-bromo-1,5-diisopropyl-2-4-dimethylbenzene with ethylenediamine,[51–53] ring closure with triethylorthoformate,[54] and deprotonation with sodium hexamethyldisilyamide.

The reaction of four equiv. SIAr^{Me,iPr} with $[Fe_4S_4(PCy_3)_4][BPh_4]$ in tetrahydrofuran (THF) was anticipated to result in formation of $[(SIAr^{Me,iPr})_3Fe_4S_4(PCy_3)][BPh_4]$, analogous to the reactivity

observed for IMes.[55] Instead, the product obtained is [(SIAr^{Me,iPr})$_3$Fe$_4$S$_4$(THF)][BPh$_4$] ([**2-THF**]$^+$), in which, in addition to the three PCy$_3$ ligands replaced by NHCs, the fourth PCy$_3$ has been displaced by THF (Figure 5.3B). The displacement of the fourth equivalent of PCy$_3$ in [**2-THF**]$^+$ suggests that the addition of *m*-^{i}Pr substituents has indeed made the binding pocket at the fourth Fe site smaller, preventing coordination of a large ligand like PCy$_3$.

Cluster [**2-THF**]$^+$ was converted to (SIAr^{Me,iPr})$_3$Fe$_4$S$_4$Cl (**2-Cl**) by treatment with [PPh$_4$]Cl, and single crystals suitable for X-ray diffraction analysis were obtained by evaporation of a saturated pentane solution. The space-filling model of the X-ray crystallographic structure of **2-Cl** is shown in Fig. 5.3A, and comparison to that of **1-Cl** confirms that the *m*-^{i}Pr substituents are positioned above the S atoms bound to the unique Fe site. The effects of the increased steric pressure in **2-Cl** compared to **1-Cl** can also be gleaned by comparison of their ^{1}H NMR spectra. In **1-Cl**, the resonances assigned to the IMes ligands are relatively sharp and reflect effective C_{3v} symmetry and fast Fe–C(NHC) bond rotation on the NMR timescale, such that the IMes ligands give rise to four total resonances.[33] On the other hand, the SIAr^{Me,iPr} resonances in the NMR spectrum of **2-Cl** are extremely broad at room temperature. Upon cooling the solution to –20 °C, the NMR spectrum becomes sharper, and 22 resonances are apparent, each integrating for either three or nine protons (Figure S5.18). The NMR spectrum of **2-Cl** at –20 °C reflects apparent C_3 symmetry in solution due to slow rotation around the Fe–C(NHC) bond, such that the three SIAr^{Me,iPr} ligands are equivalent, but within each ligand every aryl-H, imidazolinium backbone H, ^{i}Pr methine, and methyl group is inequivalent. The solution of **2-Cl** must be heated to 60 °C to increase the rate of Fe–C(NHC) bond rotation enough to coalesce the inequivalent SIAr^{Me,iPr} protons and achieve apparent C_{3v} symmetry in solution (Figure S5.19). The much higher temperature required to render

Fe–C(NHC) bond rotation faster than the NMR timescale in **2-Cl** compared to **1-Cl** highights the additional steric congestion caused by addition of the *m*-^{i}Pr substituents.

With clusters supported by a more sterically encumbering NHC in hand, we turned to reduction of **2-Cl** and [**2-THF**]$^{+}$. The same product was observed by ^{1}H NMR spectroscopy upon either reduction of [**2-THF**]$^{+}$ with decamethylcobaltocene in cyclohexane or reduction of **2-Cl** using alkali metals including Li, Na, or K in cyclohexane (Figure S5.16); The former reaction (Figure 5.4A) is our preferred synthetic route because it avoids **2-Cl** as an additional intermediate and because the reduction is cleaner. The reduction product, **2**, is characterized by an exceptionally broad NMR spectrum with peaks at 52 and 41 ppm. Its $S = 4$ ground spin state was established by SQUID magnetometry (Figure S5.33). We synthesize and manipulate **2** in the prescence of excess SIAr^{Me,iPr} owing to its instability in the absence of SIAr^{Me,iPr} (*vide infra*).

Because the reductions of **2-Cl** and [**2-THF**]$^{+}$ were conducted under an N_2 atmosphere, we anticipated that **2** could be an N_2 adduct, analogous to the N_2 complexes reported recently with Mo-Fe-S clusters. However, we found no evidence for an N–N stretch in the thin-film IR spectrum of **2**, thus precluding the formation of a terminal N_2 complex, and crystallographic characterization of **2** revealed the absence of coordinated N_2 or any other ligand at the unique Fe site. Instead, the unique Fe site adopts a highly pyramidalized three-coordinate geometry (Figure 5.4A). Cluster **2** crystallizes with whole molecule disorder—the minor component in approximately 30% occupancy is **2** upside down relative to the major component—but can be refined wholly anisotropically with no restraints placed on the Fe–S or Fe–C(NHC) distances. The major and minor components show similar cluster core metrics (see SI). Additionally, we collected a crystallographic dataset on a sample of **2** that was crystallized under different conditions (see SI); although the diffraction data set is of lower quality, there is no cluster disorder, the core bond

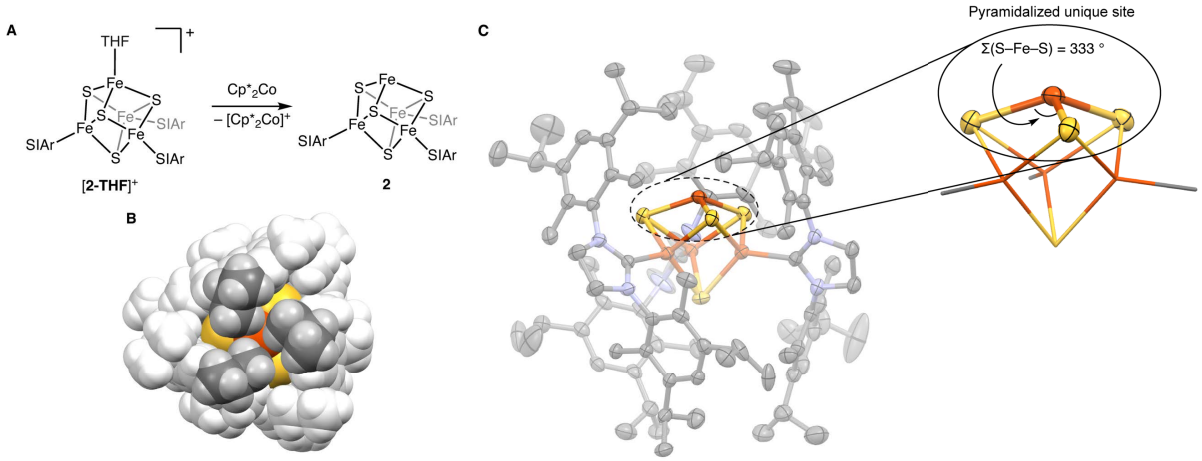

Figure 5.4. A) Synthesis of **2** via reduction of [**2-THF**]$^{+}$. B) Spacefilling model of the crystallographic structure of **2** highlighting the ^{i}Pr groups protecting the three coordinate Fe site. C) X-ray crystallographic structure of **2** with colors as in Figure 5.2B and inset showing the pyramidalization of the unique Fe site.

metrics are similar to the refinement obtained from the high-quality dataset, and again no electron density was found for any ligand at the three coordinate Fe site. We rule out the presence of a hydride ligand in **2** in part because the hypothetical hydride complex would be odd-electron and would therefore exhibit a signal in its perpendicular-mode EPR spectrum. The geometry of the unique Fe is also inconsistent with it being four-coordinate (*vide infra*). Additionally, the arrangement of the ^{i}Pr groups around the apical Fe site is consistent with the assignment of **2** as containing a three coordinate Fe site: whereas in **2-Cl** the isopropyl methine protons are oriented inwards towards the chloride ligands, in **2** the isopropyl methine protons are twisted outwards away from the cluster, bringing the isopropyl methyl groups directly above above the three-coordinate site and occupying the space where a ligand would typically reside (Figure 5.4B). Despite the twisting of the isopropyl groups, the shortest Fe–C(^{i}Pr) contact is 3.833 Å, which is sufficiently long to rule out significant agostic interactions.

Before discussing the bonding and reactivity of **2**, we note that compound **2** is synthesized and manipulated in the presence of free SIAr^{Me,iPr} because of the instability of **2** with respect to loss of

SIAr^{Me,iPr}. The excess SIAr^{Me,iPr} can be removed by recrystallization from cyclohexane/pentane followed by cyclohexane/tetramethylsilane, however this leads to significant loss of **2** due to its high solubility. The presence of free SIAr^{Me,iPr} prevents decomposition to **2-FBDC**, the structure which was confirmed by X-ray crystallography (Figure S5.45). In the absence of excess SIAr^{Me,iPr}, **2** converts partially to **2-FBDC** upon standing in solution at room temperature overnight, but in the presence of 1 equiv SIAr^{Me,iPr} **2** is stable at room temperature overnight and only converts to **2-FBDC** upon heating to 80 °C for several days.

Though the products **1-FBDC** and **2-FBDC** are structurally analogous, the observation that SIAr^{Me,iPr} stabilizes **2** indicates that the mechanisms of FBDC formation are different. Compound **2-FBDC** presumably forms via loss of SIAr^{Me,iPr} from **2** to give an intermediate with only two NHCs coordinated that then undergoes dimerization (Figure 5.5); such a mechanism explains why addition of exogenous SIAr^{Me,iPr} prevents decomposition of **2**. On the other hand, **1-FBDC** forms via initial formation of **1-EBDC**, as determined by characterization of the **1-EBDC** intermediate (Figure 5.2C). As expected for this mechanism (Figure 5.5), addition of IMes to the reaction of **1-**

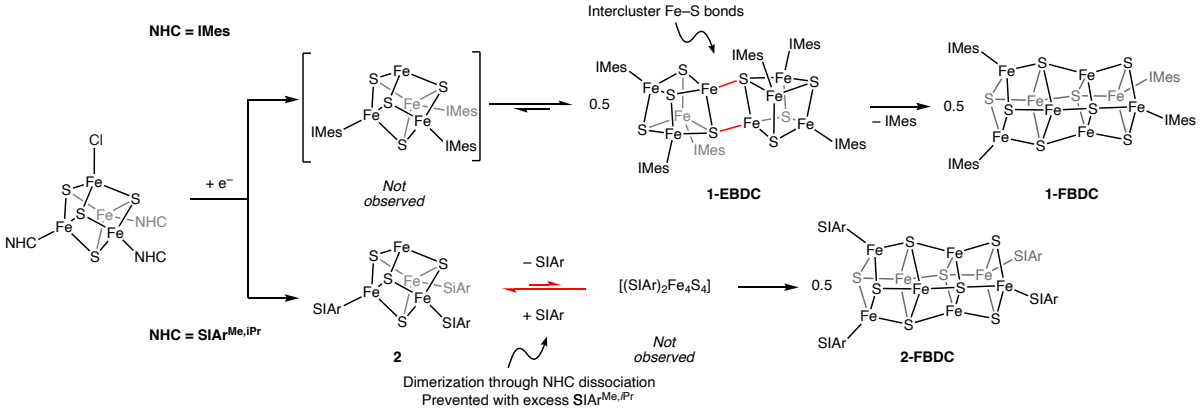

Figure 5.5. Formation of **1-FBDC** from **1-Cl** occurs via initial formation of **1-EBDC** containing Fe–S bonds between two [Fe_4S_4] clusters. Upon standing in solution, **2** converts to **2-FBDC** with loss of SIAr^{Me,iPr}. This reaction likely proceeds through an intermediate with 2 SIAr^{Me,iPr} coordinated and as such can be prevented by manipulating **2** in the presence of excess SIAr^{Me,iPr}.

Cl and Ti([N^{t}Bu]Ar)$_3$ has no effect on the rapid formation of **1-FBDC**, nor does addition of IMes to **1-FBDC** convert it back to **1-EBDC** or to any [Fe_4S_4] species. The formation of FBDC structures with both IMes and SIAr and of EBDC structures with phosphine ligands highlights that the formation of higher-nuclearity clusters is a thermodynamic sink for [Fe_4S_4]^0 clusters, but that such condensation reactions can be perturbed and controlled by design of the cluster's supporting ligands.

The three-coordinate Fe site in **2** is highly unusual (Figure 5.4C). Only one other example of a three-coordinate Fe–S site—an [Fe_4S_3] cluster with a planar three-coordinate Fe site[56]—has been reported. Moreover, the hundreds of synthetic [Fe_4S_4] clusters universally have minimally four-coordinate Fe sites.[25,26,57,58] The sum of the S–Fe–S angles around the apical Fe site is 333.68(4)° which is much closer to the value for a perfect tetrahedron (328.5°) than that for a perfectly trigonal planar center (360°). In comparison, the average sum of the S–Fe–S bond angles around the other three Fe sites in **2** is 316.0(1)°, which is typical for [Fe_4S_4] clusters[25,57] and smaller than for the unique Fe site, indicating a moderate degree of planarization relative to an Fe site in a typical Fe–S cluster (and also inconsistent with the unique site having a fourth ligand, such as a hydride). Although somewhat planarized compared with a typical Fe–S cluster site, the pyramidalization of the three coordinate Fe site is still notable from a broader coordination chemistry perspective, as pyramidalized geometries for three coordinate d^1 through d^9 metal centers are rare. In fact, the trigonal planar site in **2** is the most pyramidalized three-coordinate Fe site reported in the Cambridge Structural Database.[59] Pyramidalized geometries are often observed for d^0 and d^{10} transition-metal, lanthanide, and actinide complexes, and have been attributed to several factors including imbuing an increased dipole moment and stabilizing dispersion interactions.[60–64] In **2**, full planarization is likely disfavored by the constraints imposed by the remainder of the cluster; a

planar Fe site would be forced to be unreasonably close to the other Fe centers in the cluster and would have unreasonable bond angles at the sulfur atoms bound to the unique site.

Despite the atypical coordination environment for the unique Fe site in **2**, the cluster adopts the $S = 4$ spin state that is typical for $[Fe_4S_4]^0$ clusters (determined by SQUID magnetometry, Figure S5.33). The structural distortion that is characteristic of the $S = 4$ spin state (in which the Fe center with minority spin has relatively short Fe–C(NHC) and long Fe–Fe distances compared to the three Fe centers with majority spin) is also observed for **2**. One of the Fe centers (Fe4) bound to an $SIAr^{Me,iPr}$ ligand has modestly longer average Fe–Fe distances (2.715(1) Å) and a shorter Fe–C(NHC) distance (2.058(2) Å) compared to the other two Fe–NHC centers (d_{avg}(Fe–Fe) = 2.659(2) Å and 2.692(1) Å; Fe–C(NHC) = 2.097(2) Å and 2.082(2) Å). Therefore, we assign Fe4 as being in the minority spin, while the other three Fe centers, including the three-coordinate site, are in the majority spin; this proposal is supported by broken-symmetry density functional theory calculations (see SI). The Fe–S and Fe–Fe distances at the three-coordinate Fe site (2.269(1) Å and 2.554(1) Å, respectively) are short compared to the average Fe–S and Fe–Fe distances at the other Fe sites (2.334(2) Å and 2.689(3) Å), which are more similar those reported for other $[Fe_4S_4]^0$ clusters.[39–41] These decreasing Fe–S and Fe–Fe distances can be attributed the three-coordinate site being relatively electron deficient compared to a four-coordinate site, since it does not have a fourth donor ligand. The Mössbauer spectrum of **2** is magnetically split at 5 K and remains broad at 80 K, potentially due to slow magnetic relaxation (see SI). The magnetic splitting at 5 K and broadness at 80 K prevents assignment of the three coordinate site in the Mössbauer spectrum, however the average isomer shift of the Fe centers in **2** is 0.59 mm s^{-1}, which is higher than that observed for $[\mathbf{2\text{-}THF}]^+$ ($\delta_{avg.}$ = 0.53 mm s^{-1}) and consistent with **2** being reduced by one electron relative to $[\mathbf{2\text{-}THF}]^+$. High-field Mössbauer studies will be the subject of future work.

To investigate if **2** might bind N_2 in equilibrium in solution, we collected ^{1}H NMR spectra of **2** in cyclohexane in a sealed tube under an atmosphere of N_2 and under vacuum; if N_2 binds to **2** in equilibrium in solution, then degassing the NMR sample should result in a shift in the position of that equilibrium and induce a change in the ^{1}H NMR spectrum of **2**. Figure 5.20 shows that the ^{1}H NMR spectra collected under N_2 and vacuum are superimposable with one another, even at –40 °C, suggesting no equilibrium for binding dinitrogen in solution. On the basis of the above crystallographic and ^{1}H NMR experiments, we conclude that **2** has no measurable affinity for N_2 under the conditions we have examined (Figure 5.6A).

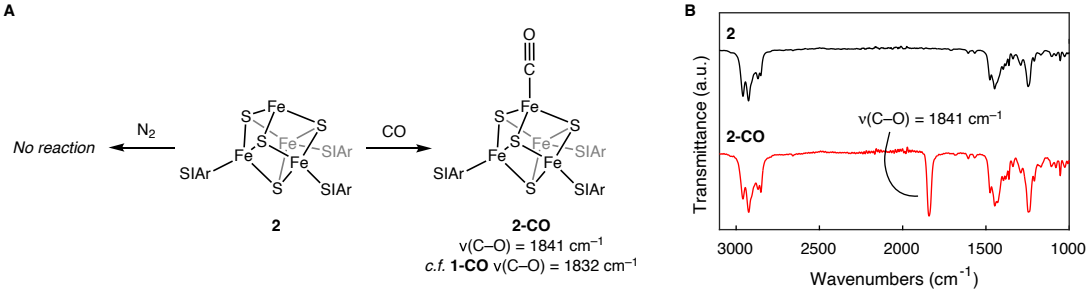

Figure 5.6. Reaction of **2** with N_2 and CO. A) Compound **2** has no reaction with N_2, even at low temperature, but reacts rapidly at room temperature with CO to form **2-CO**. B) Compound **2-CO** shows a strong CO stretch at 1841 cm^{-1}.

To determine if SIAr^{Me,iPr} was simply too bulky to allow a diatomic ligand to coordinate to the apical Fe site, we exposed **2** to ca. 2 equiv CO. Immediately upon addition of CO, the solution turned from brown-red to dark yellow-brown, and the consumption of **2** and formation of (SIAr^{Me,iPr})$_3$Fe$_4$S$_4$CO (**2-CO**) was observed by NMR spectroscopy (Figure 5.6 and S5.15). An IR spectrum of this reaction mixture showed a strong peak at 1841 cm^{-1} corresponding to ν(C–O) (Figure 5.6B), which is very similar to that previously observed for (IMes)$_3$Fe$_4$S$_4$CO (1832 cm^{-1})[35] and which supports the assignment of **2-CO**. Facile coversion of **2** to **2-CO** indicates that the SIAr^{Me,iPr} ligands in **2** are not so large as to preclude coordination of a diatomic ligand.

Several factors likely contribute to the low affinity of **2** for N_2. First, we note that of the recently reported, Fe-bound N_2 complexes of Mo-Fe-S clusters, none is a neutral, terminal N_2 complex; instead, each features N_2 as a bridging ligand between the Fe center of a cluster and either the Fe center of another cluster or an electropositive group (Ti^{3+}, Na^+, R_3Si^+). It is possible that for **2**, the steric bulk of the *m*-^{i}Pr groups on SIAr^{Me,iPr} is sufficient to prevent formation of a bridging dinitrogen complex. Since a terminally-bound N_2 is a poorer ligand than a bridging N_2, the low affinity of **2** for N_2 could be due to the imposing steric profile of SIAr^{Me,iPr}. Additionally, the overall energetics of N_2 binding could be unfavorable due to the disruption of dispersion interactions between the SIAr^{Me,iPr} ligands[65] in addition to the large, negative entropic term expected for coordination of N_2 to **2**. Lastly, it must be noted that, unlike for N_2 binding to nitrogenase cofactors, N_2 binding to **2** would occur in the absence of secondary-sphere interactions, which have been shown to promote N_2 binding and activation.[66]

In conclusion, with the aim of preparing $[Fe_4S_4]$ clusters bound to N_2, we designed an $[Fe_4S_4]$ cluster bound by three bulky NHC ligands to limit pathways to higher-nuclearity clusters that are typically thermodynamic sinks for $[Fe_4S_4]^0$ clusters. The $[Fe_4S_4]^0$ cluster, **2**, features an open coordination site that binds and activates CO analogously to the previously described $[Fe_4S_4]^0$ cluster **1-CO**.[35] However, rather than binding N_2, cluster **2** binds no ligand at the apical site, which instead adopts an unusually pyramidalized, three-coordinate geometry. The lack of reactivity of **2** with N_2—in contrast with its reactivity with CO—suggests that the lack of affinity for N_2 is specific to the strength of the interactions between N_2 and **2** and not simply because the bulky steric profile of the ligands in **2** prevents coordination of diatomic ligands. The differences between $[Fe_4S_4]$ and $[MoFe_3S_4]$ clusters that lead to a low affinity of **2** for N_2 but an accessible N_2 adduct for $[MoFe_3S_4]$ clusters will be the subject of furthur investigation.

References

(1) *Catalysts for Nitrogen Fixation: Nitrogenases, Relevant Chemical Models, and Commercial Processes*, 1st ed.; Smith, B. E., Richards, R. L., Newton, W. E., Eds.; Springer Dordrecht, 2004.

(2) Schneider, K.; Müller, A. Iron-Only Nitrogenase: Exceptional Catalytic, Structural and Spectroscopic Features. In *Catalysts for Nitrogen Fixation. Nitrogen Fixation: Origins, Applications, and Research Progress*; Smith, B. E., Richards, R. L., Newton, W. E., Eds.; 2004; Vol. 1.

(3) Harris, D. F.; Lukoyanov, D. A.; Kallas, H.; Trncik, C.; Yang, Z. Y.; Compton, P.; Kelleher, N.; Einsle, O.; Dean, D. R.; Hoffman, B. M.; Seefeldt, L. C. Mo-, V-, and Fe-Nitrogenases Use a Universal Eight-Electron Reductive-Elimination Mechanism to Achieve N_2 Reduction. *Biochemistry* **2019**, *58* (30), 3293–3301.

(4) Hoffman, B. M. .; Lukoyanov, D.; Dean, D. R.; Seefeldt, L. C. Nitrogenase: A Draft Mechanism. *Acc. Chem. Res.* **2013**, *46* (2), 587–595.

(5) Eady, R. R. Structure-Function Relationships of Alternative Nitrogenases. *Chem. Rev.* **1996**, *96* (7), 3013–3030.

(6) MacBeth, C. E.; Harkins, S. B.; Peters, J. C. Synthesis and Characterization of Cationic Iron Complexes Supported by the Neutral Ligands NPi-Pr_3, NArPi-Pr_3, and NSt-Bu_3. *Can. J. Chem.* **2005**, *83* (4), 332–340.

(7) Rutledge, H. L.; Tezcan, F. A. Electron Transfer in Nitrogenase. *Chem. Rev.* **2020**, *120* (12), 5158–5193.

(8) Seefeldt, L. C.; Yang, Z. Y.; Lukoyanov, D. A.; Harris, D. F.; Dean, D. R.; Raugei, S.; Hoffman, B. M. Reduction of Substrates by Nitrogenases. *Chem. Rev.* **2020**, *120* (12), 5082–5106.

(9) Danyal, K.; Dean, D. R.; Hoffman, B. M.; Seefeldt, L. C. Electron Transfer within Nitrogenase: Evidence for a Deficit-Spending Mechanism. *Biochemistry* **2011**, *50* (43), 9255–9263.

(10) Burgess, B. K.; Lowe, D. J. Mechanism of Molybdenum Nitrogenase. *Chem. Rev.* **1996**, *96* (7), 2983–3012.

(11) Hoffman, B. M.; Lukoyanov, D.; Yang, Z.-Y. Y.; Dean, D. R.; Seefeldt, L. C. Mechanism of Nitrogen Fixation by Nitrogenase: The next Stage. *Chem. Rev.* **2014**, *114* (8), 4041–4062.

(12) Spatzal, T.; Perez, K. A.; Einsle, O.; Howard, J. B.; Rees, D. C. Ligand Binding to the FeMo-Cofactor: Structures of Co-Bound and Reactivated Nitrogenase. *Science* **2014**, *345* (6204), 1620–1623.

(13) Buscagan, T. M.; Perez, K. A.; Maggiolo, A. O.; Rees, D. C.; Spatzal, T. Structural Characterization of Two CO Molecules Bound to the Nitrogenase Active Site. *Angew. Chem. Int. Ed.* **2021**, *60* (11), 5704–5707.

(14) Spatzal, T.; Perez, K. A.; Howard, J. B.; Rees, D. C. Catalysis-Dependent Selenium Incorporation and Migration in the Nitrogenase Active Site Iron-Molybdenum Cofactor. *Elife* **2015**, *4*, 1–11.

(15) Deardorff, C. L.; Eric Sikma, R.; Rhodes, C. P.; Hudnall, T. W. Carbene-Derived α-Acyl Formamidinium Cations: Organic Molecules with Readily Tunable Multiple Redox Processes. *Chem. Commun.* **2016**, *52* (58), 9024–9027.

(16) Sippel, D.; Rohde, M.; Netzer, J.; Trncik, C.; Gies, J.; Grunau, K.; Djurdjevic, I.;

Decamps, L.; Andrade, S. L. A.; Einsle, O. A Bound Reaction Intermediate Sheds Light on the Mechanism of Nitrogenase. *Science* **2018**, *359* (6383), 1484–1489.
(17) Kang, W.; Lee, C. C.; Jasniewski, A. J.; Ribbe, M. W.; Hu, Y. Structural Evidence for a Dynamic Metallocofactor during N_2 Reduction by Mo-Nitrogenase. *Science* **2020**, *368* (6497), 1381–1385.
(18) Lee, C. C.; Kang, W.; Jasniewski, A. J.; Stiebritz, M. T.; Tanifuji, K.; Ribbe, M. W.; Hu, Y. Evidence of Substrate Binding and Product Release via Belt-Sulfur Mobilization of the Nitrogenase Cofactor. *Nat. Catal.* **2022**, *5* (5), 443–454.
(19) Rohde, M.; Grunau, K.; Einsle, O. CO Binding to the FeV Cofactor of CO-Reducing Vanadium Nitrogenase at Atomic Resolution. *Angew. Chem. Int. Ed.* **2020**, *59* (52), 23626–23630.
(20) Burgess, B. K.; Wherland, S.; Newton, W. E.; Stiefel, E. I. Nitrogenase Reactivity: Insight into the Nitrogen-Fixing Process through Hydrogen-Inhibition and HD-Forming Reactions. *Biochemistry* **1981**, *20* (18), 5140–5146.
(21) Fisher, K.; Dilworth, M. J.; Newton, W. E. Differential Effects on N2 Binding and Reduction, HD Formation, and Azide Reduction with α-195(His)- and α-191(Gln)-Substituted MoFe Proteins of *Azotobacter Vinelandii* Nitrogenase. *Biochemistry* **2000**, *39* (50), 15570–15577.
(22) Siegbahn, P. E. M. Model Calculations Suggest That the Central Carbon in the FeMo-Cofactor of Nitrogenase Becomes Protonated in the Process of Nitrogen Fixation. *J. Am. Chem. Soc.* **2016**, *138* (33), 10485–10495.
(23) Siegbahn, P. E. M. The Mechanism for Nitrogenase Including All Steps. *Phys. Chem. Chem. Phys.* **2019**, *21* (28), 15747–15759.
(24) Goh, C.; Segal, B. M.; Huang, J.; Long, J. R.; Holm, R. H. Polycubane Clusters: Synthesis of $[Fe_4S_4(PR_3)_4]^{1+,0}$ (R = Bu(t), Cy, Pr(i)) and $[Fe_4S_4]^0$ Core Aggregation upon Loss of Phosphine. *J. Am. Chem. Soc.* **1996**, *118* (47), 11844–11853.
(25) Venkateswara Rao, P.; Holm, R. H. Synthetic Analogues of the Active Sites of Iron−Sulfur Proteins. *Chem. Rev.* **2004**, *104* (2), 527–560.
(26) Holm, R. H.; Lo, W. Structural Conversions of Synthetic and Protein-Bound Iron-Sulfur Clusters. *Chem. Rev.* **2016**, *116* (22), 13685–13713.
(27) Zhang, Y.; Zuo, J. L.; Zhou, H. C.; Holm, R. H. Rearrangement of Symmetrical Dicubane Clusters into Topological Analogues of the P Cluster of Nitrogenase: Nature's Choice? *J. Am. Chem. Soc.* **2002**, *124* (48), 14292–14293.
(28) McSkimming, A.; Suess, D. L. M. Dinitrogen Binding and Activation at a Molybdenum–Iron–Sulfur Cluster. *Nat. Chem.* **2021**, *13* (7), 666–670.
(29) Ohki, Y.; Munakata, K.; Matsuoka, Y.; Hara, R.; Kachi, M.; Uchida, K.; Tada, M.; Cramer, R. E.; Sameera, W. M. C.; Takayama, T.; Sakai, Y.; Kuriyama, S.; Nishibayashi, Y.; Tanifuji, K. Nitrogen Reduction by the Fe Sites of Synthetic $[Mo_3S_4Fe]$ Cubes. *Nature* **2022**, *607* (7917), 86–90.
(30) Chisnell, J. R.; Premakumar, R.; Bishop, P. E. Purification of a Second Alternative Nitrogenase from a NifHDK Deletion Strain of *Azotobacter Vinelandii*. *J. Bacteriol.* **1988**, *170* (1), 27–33.
(31) Müller, A.; Schneider, K.; Knüttel, K.; Hagen, W. R. EPR Spectroscopic Characterization of an Iron Only Nitrogenase S = 3/2 Spectrum of Component 1 Isolated from *Rhodobacter Capsulatus*. *FEBS Lett.* **1992**, *303* (1), 36–40.
(32) Schneider, K.; Gollan, U.; Dröttboom, M.; Selsemeier-Voigt, S.; Müller, A. Comparative

Biochemical Characterization of the Iron-Only Nitrogenase and the Molybdenum Nitrogenase from *Rhodobacter Capsulatus*. *Eur. J. Biochem.* **1997**, *244* (3), 789–800.
(33) Brown, A. C.; Suess, D. L. M. Controlling Substrate Binding to Fe_4S_4 Clusters through Remote Steric Effects. *Inorg. Chem.* **2019**, *58* (8), 5273–5280.
(34) Peters, J. C.; Johnson, A. R.; Odom, A. L.; Wanandi, P. W.; Davis, W. M.; Cummins, C. C. Assembly of Molybdenum/Titanium μ-Oxo Complexes via Radical Alkoxide C-O Cleavage. *J. Am. Chem. Soc.* **1996**, *118* (42), 10175–10188.
(35) Brown, A. C.; Thompson, N. B.; Suess, D. L. M. Evidence for Low-Valent Electronic Configurations in Iron−Sulfur Clusters. *J. Am. Chem. Soc.* **2022**, *144* (20), 9066–9073.
(36) Osterloh, F.; Segal, B. M.; Achim, C.; Holm, R. H. Reduced Mono-, Di-, and Tetracubane-Type Clusters Containing the $[MoFe_3S_4]^{2+}$ Core Stabilized by Tertiary Phosphine Ligation. *Inorg. Chem.* **2000**, *39* (5), 980–989.
(37) Zhou, H.-C.; Holm, R. H. Synthesis and Reactions of Cubane-Type Iron−Sulfur−Phosphine Clusters, Including Soluble Clusters of Nuclearities 8 and 16. *Inorg. Chem.* **2003**, *42* (1), 11–21.
(38) Deng, L.; Majumdar, A.; Lo, W.; Holm, R. H. Stabilization of 3:1 Site-Differentiated Cubane-Type Clusters in the $[Fe_4S_4]^{1+}$ Core Oxidation State by Tertiary Phosphine Ligation: Synthesis, Core Structural Diversity, and $S = 1/2$ Ground States. *Inorg. Chem.* **2010**, *49* (23), 11118–11126.
(39) Deng, L.; Holm, R. H. Stabilization of Fully Reduced Iron-Sulfur Clusters by Carbene Ligation: The $[Fe_nS_n]^0$ Oxidation Levels (n = 4, 8). *J. Am. Chem. Soc.* **2008**, *130* (30), 9878–9886.
(40) Zhang, H.; Ouyang, Z.; Liu, Y.; Zhang, Q.; Wang, L.; Deng, L. (Aminocarbene)(Divinyltetramethyldisiloxane)Iron(0) Compounds: A Class of Low-Coordinate Iron(0) Reagents. *Angew. Chem. Int. Ed.* **2014**, *53* (32), 8432–8436.
(41) Scott, T. A.; Berlinguette, C. P.; Holm, R. H.; Zhou, H. C. Initial Synthesis and Structure of an All-Ferrous Analogue of the Fully Reduced $[Fe_4S_4]^0$ Cluster of the Nitrogenase Iron Protein. *Proc. Natl. Acad. Sci. U. S. A.* **2005**, *102* (28), 9741–9744.
(42) Hans, M.; Buckel, W.; Bill, E. Spectroscopic Evidence for an All-Ferrous $[4Fe\text{-}4S]^0$ Cluster in the Superreduced Activator of 2-Hydroxyglutaryl-CoA Dehydratase from *Acidaminococcus Fermentans*. *J. Biol. Inorg. Chem.* **2008**, *13* (4), 563–574.
(43) Angove, H. C.; Yoo, S. J.; Burgess, B. K.; Münck, E. Mössbauer and EPR Evidence for an All-Ferrous Fe_4S_4 Cluster with $S = 4$ in the Fe Protein of Nitrogenase. *J. Am. Chem. Soc.* **1997**, *119* (37), 8730–8731.
(44) Yoo, S. J.; Angove, H. C.; Burgess, B. K.; Hendrich, M. P.; Münck, E. Mossbauer and Integer-Spin EPR Studies and Spin-Coupling Analysis of the $[4Fe\text{-}4S]^0$ Cluster of the Fe Protein from *Azotobacter Vinelandii* Nitrogenase. *J. Am. Chem. Soc.* **1999**, *121* (11), 2534–2545.
(45) Chakrabarti, M.; Deng, L.; Holm, R. H.; Münck, E.; Bominaar, E. L. Mössbauer, Electron Paramagnetic Resonance, and Theoretical Studies of a Carbene-Based All-Ferrous Fe_4S_4 Cluster: Electronic Origin and Structural Identification of the Unique Spectroscopic Site. *Inorg. Chem.* **2009**, *48* (7), 2735–2747.
(46) Chakrabarti, M.; Münck, E.; Bominaar, E. L. Density Functional Theory Study of an All Ferrous 4Fe-4S Cluster. *Inorg. Chem.* **2011**, *50* (10), 4322–4326.
(47) Chakrabarti, M.; Deng, L.; Holm, R. H.; Münck, E.; Bominaar, E. L. The Modular Nature of All-Ferrous Edge-Bridged Double Cubanes. *Inorg. Chem.* **2010**, *49* (4), 1647–1650.

(48) Nannenga, B. L.; Shi, D.; Leslie, A. G. W.; Gonen, T. High-Resolution Structure Determination by Continuous-Rotation Data Collection in MicroED. *Nat. Methods* **2014**, *11* (9), 927–930.
(49) Jones, C. G.; Martynowycz, M. W.; Hattne, J.; Fulton, T. J.; Stoltz, B. M.; Rodriguez, J. A.; Nelson, H. M.; Gonen, T. The CryoEM Method MicroED as a Powerful Tool for Small Molecule Structure Determination. *ACS Cent. Sci.* **2018**, *4* (11), 1587–1592.
(50) Moffett, R. B.; Tang, A. H. Skeletal Muscle Stimulants. Substituted Benzoic Acids. *J. Med. Chem.* **1968**, *11* (5), 1020–1022.
(51) Guram, A. S.; Rennels, R. A.; Buchwald, S. L. A Simple Catalytic Method for the Conversion of Aryl Bromides to Arylamines. *Angew. Chem. Int. Ed.* **1995**, *34* (12), 1348–1350.
(52) Louie, J.; Hartwig, J. F. Palladium-Catalyzed Synthesis of Arylamines from Aryl Halides. Mechanistic Studies Lead to Coupling in the Absence of Tin Reagents. *Tetrahedron Lett.* **1995**, *36* (21), 3609–3612.
(53) Aoyama, H.; Tokunaga, M.; Kiyosu, J.; Iwasawa, T.; Obora, Y.; Tsuji, Y. Kinetic Resolution of Axially Chiral 2,2′ -Dihydroxy-1,1 ′ -Biaryls By. *J. Am. Chem. Soc.* **2005**, No. 127, 10474–10475.
(54) Kuhn, K. M.; Grubbs, R. H. A Facile Preparation of Imidazolinium Chlorides. *Org. Lett.* **2008**, *10* (10), 2075–2077.
(55) Bostelaar, T. M.; Brown, A. C.; Sridharan, A.; Suess, D. L. M. A General Method for Metallocluster Site-Differentiation. *Nat. Synth.* **2023**, In press.
(56) DeRosha, D. E.; Chilkuri, V. G.; Van Stappen, C.; Bill, E.; Mercado, B. Q.; DeBeer, S.; Neese, F.; Holland, P. L. Planar Three-Coordinate Iron Sulfide in a Synthetic [4Fe-3S] Cluster with Biomimetic Reactivity. *Nat. Chem.* **2019**, *11* (11), 1019–1025.
(57) Tan, L. L.; Holm, R. H.; Lee, S. C. Structural Analysis of Cubane-Type Iron Clusters. *Polyhedron* **2013**, *58*, 206–217.
(58) Lee, S. C.; Holm, R. H. The Clusters of Nitrogenase: Synthetic Methodology in the Construction of Weak-Field Clusters. *Chem. Rev.* **2004**, *104* (2), 1135–1157.
(59) Search performed by searching for three-coordinate Fe sites with a sum of the three L–Fe–L angles below 350°.
(60) Price, A. N.; Berryman, V.; Ochiai, T.; Shephard, J. J.; Parsons, S.; Kaltsoyannis, N.; Arnold, P. L. Contrasting Behaviour under Pressure Reveals the Reasons for Pyramidalization in Tris(Amido)Uranium(III) and Tris(Arylthiolate) Uranium(III) Molecules. *Nat. Commun.* **2022**, *13* (1), 1–6.
(61) Bradley, D. C.; Ghotra, J. S.; Hart, F. A. Low Co-ordination Numbers in Lanthanide and Actinide Compounds. Part 1. The Preparation and Characterization of Tris{bis(Trimethylsilyl)-Amido)Lanthanides. *J. Chem. Soc. Dalton Trans.* **1973**, 1021–1023.
(62) Brady, E. D.; Clark, D. L.; Gordon, J. C.; Hay, P. J.; Keogh, D. W.; Poli, R.; Scott, B. L.; Watkin, J. G. Tris(Bis(Trimethylsilyl)Amido)Samarium: X-Ray Structure and DFT Study. *Inorg. Chem.* **2003**, *42* (21), 6682–6690.
(63) Andersen, R. A.; Templeton, D. H.; Zalkin, A. Structure of Tris(Bis(Trimethylsilyl)Amido)Neodymium(III), $Nd[N(Si(CH_3)_3)_2]_3$. *Inorg. Chem* **1978**, *17* (8), 2317–2319.
(64) Ghotra, J. S.; Hursthouse, M. B.; Welch, A. J. Three-co-ordinate Scandium(III) and Europium(III); Crystal and Molecular Structures of Their Trishexamethyldisilylamides. *J.*

Chem. Soc., Chem. Commun. **1973**, 923, 669–670.
(65) Liptrot, D. J.; Power, P. P. London Dispersion Forces in Sterically Crowded Inorganic and Organometallic Molecules. *Nat. Rev. Chem.* **2017**, *1*.
(66) Stripp, S. T.; Duffus, B. R.; Fourmond, V.; Léger, C.; Leimkühler, S.; Hirota, S.; Hu, Y.; Jasniewski, A.; Ogata, H.; Ribbe, M. W. Second and Outer Coordination Sphere Effects in Nitrogenase, Hydrogenase, Formate Dehydrogenase, and CO Dehydrogenase. *Chem. Rev.* **2022**, *122* (14), 11900–11973.

Supporting Information

A. Experimental Methods

General Considerations

All reactions were performed using standard Schlenk techniques or in an LC Technologies inert atmosphere glove box under an N_2 atmosphere. Glassware was dried in an oven at 160 °C prior to use. Molecular sieves (3 Å), and Celite® were activated by heating to 300 °C overnight under vacuum prior to storage under an atmosphere of nitrogen. *O*-difluorobenzene (DFB) was distilled from CaH_2, C_6D_6, C_6D_{12}, and methylcyclohexane were degassed by three freeze–pump–thaw cycles, and other solvents were degassed by sparging with argon and dried by passing through a column of activated alumina. All solvents were stored under an N_2 atmosphere over 3 Å molecular sieves.

NMR spectra were recorded on Bruker 400 and 500 MHz spectrometers. ^{1}H chemical shifts are given relative to residual solvent peaks; spectra in C_6D_{12} are referenced to residual solvent at 1.4 ppm and spectra in DFB and Et_2O were referenced to the triplet of residual *n*-pentane at 0.89 ppm. Solvent suppression for NMR in protonated solvents was carried out using WET solvent suppression.[1] FT-IR samples were taken as thin films using a Bruker Alpha Platinum ATR spectrometer with OPUS software in a glovebox under an N_2 atmosphere. EPR spectra were recorded on a Bruker EMX spectrometer at 9.37 GHz (perpendicular mode) as frozen glasses. Simulations were performed using EasySpin[2] (5.2.21) in Matlab (R2017b). UV-vis spectra were recorded on a Cary 50 spectrometer. Zero-field and 77 mT ^{57}Fe Mössbauer spectra were measured with a constant-acceleration spectrometer at 150K, 80 K, or 5 K using a SEE co. W302 constant-acceleration spectrometer. Isomer shifts are quoted relative to α-Fe foil at room temperature;

Mössbauer spectra were simulated with WMOSS v.4.[3] SQUID magnetometry data was collected on solid microcrystalline samples immobilized in gel capsules using eicosane on a Quantum Design MPMS3 SQUID magnetometer in the range of 2–300 K with a 0.5 T applied field. Elemental analyses were performed at Midwest Microlab. X-ray structural determinations were performed at the MIT diffraction facility using a Bruker X8 diffractometer with an APEX II CCD detector or a Bruker D8 Venture diffractometer with a Photon2 CPAD detector. Diffraction data was collected, integrated, and corrected for absorption using Bruker APEX3 software and its associated modules (SAINT, SADABS, TWINABS). Structural solutions and refinements (on F^2) were carried out using SHELXT and SHELXL-2018 in ShelXle.[4] Ellipsoid plots and figures were made using Mercury 2021.2.0.

$(IMes)_3Fe_4S_4Cl$,[5] $Ti(N[^tBu]Ar)_3$[6], $[Fe_4S_4(PCy_3)_4][BPh_4]$[7], and 1-bromo-3,5-diisopropyl-2,6-dimethylbenzene[8] were synthesized according to literature procedures

Statement on Compound Purity

The purity of all compounds was assessed by a variety of spectroscopic and analytical methods as detailed below. All organic compounds can be isolated in high purity as determined by ^1H and ^{13}C NMR spectroscopy and HRMS. Compounds **1-FBDC**, [**2-THF**]$^+$, and **2-Cl**, are air-sensitive but can be isolated as a crystalline solid in high purity as determined by NMR, EPR, and Mössbauer spectroscopic analysis and SQUID magnetometry as well as H and N content from elemental analysis. Low C content was obtained by elemental analysis as has been observed for other members of this class of molecules[9–12] and in other contexts.[13] Elemental analysis results are as follows: **1-FBDC**: Anal. Found: C, 49.96; H, 4.77; N, 5.32. Calcd. for $C_{84}H_{96}N_8Fe_8S_8 \cdot C_6H_6$: C,

54.07; H, 5.14; N, 5.61. [**2-THF**][BPh_4]: Anal. Found: C, 69.68; H, 8.38; N, 4.00. Calcd. for $C_{121}H_{166}N_6Fe_4S_4BO$: C, 69.77; H, 8.03; N, 4.03. **2-Cl**: Anal. Found: C, 62.37; H, 8.19; N, 4.95. Calcd. for $C_{93}H_{138}N_6Fe_4S_4Cl$: C, 64.67; H, 8.05; N, 4.87.

Compound **2** was prepared and manipulated in the presence of excess free $SIAr^{Me,iPr}$ to prevent decomposition, but is pure in terms of the Fe–S content as determined by the absence of ^{1}H NMR resonances attributable to the known decomposition product **2-FBDC**, by the conversion of all ^{1}H NMR resonances assigned to **2** to **2-CO** upon addition of CO, and by SQUID magnetometry (which gives the expected magnetic moment for an $S = 4$ compound after correction for the mass of free NHC).Therefore, we assess that **2** is pure except for added, stabilizing $SIAr^{Me,iPr}$.

$(IMes)_4Fe_8S_8$ (**1-FBDC**)

$(IMes)_3Fe_4S_4Cl$ (413 mg, 0.318 mmol) was dissolved in 4 mL of benzene. A solution of $Ti(N^tBuAr)_3$ (276 mg, 0.478 mmol) dissolved in 2 mL of benzene was added dropwise to the stirring solution of $(IMes)_3Fe_4S_4Cl$. The dark orange-brown solution was stirred for 1 h and then concentrated to a volume of 1 mL. Hexanes (10 mL) was added and the precipitate was collected on a frit. The solids were washed with hexanes (3 x 2 mL) to remove $ClTi(N^tBuAr)_3$ and IMes. The solids were redissolved in benzene (2 mL) and recrystallized by layering with hexanes (10 mL). The dark brown crystals were collected on a frit. Yield: 232 mg (75%). ^{1}H NMR (C_6D_6, 293 K) δ 7.28 (s, 8H, backbone C*H*), 6.80 (s, 16H, Mes *m*-C*H*), 3.73 (s, 48H, Mes *p*-CH_3), 1.75 (s, 24H, Mes *o*-CH_3).

N[1],*N*[2]-bis(3,5-diisopropyl-2,6-dimethylphenyl)ethane-1,2-diaminium dichloride

1-bromo-3,5-diisopropyl-2,6-dimethylbenzene (6.2 g, 23 mmol, 2.1 equiv), ethylenediamine (0.77 mL, 11 mmol, 1 equiv) $Pd(OAc)_2$ (52.1 mg, 0.232, 2 mol%), BINAP (286 mg, 0.459 mmol, 4 mol%), and NaO^{t}Bu (3.2 g, 33 mmol, 2.9 equiv) were suspended in toluene (50 mL) in a sealed tube and the mixture was heated to 120 °C for 3 d. After 3 d, the mixture was cooled to room temperature and diluted with 200 mL of THF. The solution was filtered through Celite and the solvent removed in vacuo to yield a red oil. This oil was dissolved in THF (4 mL) and 1 M HCl (100 mL) was added. The suspension was stirred for 30 min, then the precipitated solid was collected on a frit, washed with Et_2O (3 x 5 mL), and dried in vacuo. Yield: 5.1 g (87 %). ^{1}H NMR ($CDCl_3$, 293 K) δ 9.37 (s, 4H, N*H*$_2$), 7.10 (s, 2H, *p*-C*H*), 3.74 (s, 4H, NC*H*$_2$), 3.08 (sept, 4H, J = 6.9 Hz, ^{i}Pr C*H*), 2.40 (s, 12H, *o*-C*H*$_3$), 1.19 (d, 24H, J = 6.9 Hz, ^{i}Pr C*H*$_3$) ^{13}C{^{1}H} NMR ($CDCl_3$, 293 K) δ 146.1, 129.2, 128.4, 126.4, 125.4, 29.8, 23.5, 14.8. HRMS for $[M-H]^+$ calculated: m/z = 437.38903, found: 438.39017.

1,3-Bis(3,5-diisopropyl-2,6-dimethylphenyl)imidazolinium tetrafluoroborate (SIAr^{Me,iPr}·HBF_4)

N[1],*N*[2]-bis(3,5-diisopropyl-2,6-dimethylphenyl)ethane-1,2-diaminium dichloride (5.1 g, 10. mmol) was suspended in triethylorthoformate (30 mL). The suspension was heated to 120°C until distillation of ethanol ceased. The solution was concentrated to 5 mL and 50 mL of water was added. $NaBF_4$ (1.5 g, 14 mmol) dissolved in water (20 mL) was added. The solution was extracted with dichloromethane (2 x 100 mL) and the solvent removed in vacuo. Et_2O (200 mL) was added and the precipitate was collected on a frit. Yield: 4.2 g (79 %). ^{1}H NMR ($CDCl_3$, 293 K) δ 7.67 (s,

1H, Im C*H*), 7.30 (s, 2H, *p*-C*H*), 4.59 (s, 4H, NCH_2), 3.14 (sept, 4H, J = 6.75 Hz, ^{i}Pr C*H*), 2.34 (s, 12H, *o*-CH_3), 1.25 (d, 12H, J = 6.75 Hz, ^{i}Pr CH_3), 1.22 (d, 12H, J = 6.9 Hz, ^{i}Pr CH_3), ^{13}C{^{1}H} NMR ($CDCl_3$, 293 K) δ 158.1, 146.7, 132.6, 129.7, 124.1, 52.5, 29.8, 23.4, 13.7. HRMS for $[M]^+$ calculated: m/z = 447.37338, found: 447.37465.

1,3-Bis(3,5-diisopropyl-2,6-dimethylphenyl)-4,5-dihydroimidazol-2-ylidene ($SIAr^{Me,iPr}$)

$SIAr^{Me,iPr}$·HBF_4 (2.003 g, 3.747 mmol) was suspended in benzene (20 mL). A solution of NaHMDS (652 mg, 3.56 mmol) in benzene (20 mL) was added dropwise. The resulting solution was stirred for 30 min, filtered through Celite, and lyophilized. Yield: 1.552 g (97 %). ^{1}H NMR (C_6D_6, 293 K) δ 7.28 (s, 2H, *p*-C*H*), 3.36 (s, 4H, NCH_2), 3.11 (sept, 4H, J = 6.87, ^{i}Pr C*H*), 2.40 (s, 12H, *o*-CH_3), 1.25 (d, 12H, J = 6.87 Hz, ^{i}Pr CH_3), 1.20 (d, 12H, J = 6.87 Hz, ^{i}Pr CH_3). ^{13}C{^{1}H} NMR ($CDCl_3$, 293 K) δ 244.6, 145.2, 142.2, 131.2, 128.4, 120.3, 51.7, 30.2, 23.7, 23.6, 13.8.

$[(SIAr^{Me,iPr})_3Fe_4S_4(THF)][BPh_4]$ ([**2-THF**]$^+$)

$[Fe_4S_4(PCy_3)_4][BPh_4]$ (1.88 g, 1.05 mmol) was dissolved in THF (30 mL). $SIAr^{Me,iPr}$ (1.61 g, 3.60 mmol, 3.4 equiv) dissolved in THF (10 mL) was added slowly. The resulting solution was stirred for 1 h, filtered through Celite, and concentrated in vacuo to 5 mL. Hexanes (50 mL) was added and the precipitate collected on a frit, washed with hexanes (3 x 15 mL) and Et_2O (3 x 15 mL), and dried in vacuo. Yield: 1.98 g (90%). ^{1}H NMR (THF, 293 K) δ 8.50 (s, 12H, NCH_2), 7.20 (br t, 8H, $[BPh_4]$), 7.02 (s, 6H, *p*-C*H*), 6.77 (t, 8H, $[BPh_4]$), 6.63 (t, 4H, $[BPh_4]$), 3.21 (br s, 12H, ^{i}Pr C*H*), 2.44 (br s, 36H, *o*-CH_3), 1.19 (br s, 72 H, ^{i}Pr CH_3). ^{1}H NMR (DFB, 293 K) δ 16.09 (s, 4 H, THF), 8.35 (s, 12H, NCH_2), 8.34 (s, 4H, THF), 7.28 (br t and singlet, 8H + 6H, $[BPh_4]$ and *p*-

C*H*), 7.13 (t, 8H, [BPh_4]), 3.44 (br s, 12H, ^{i}Pr C*H*), 2.72 (br s, 36H, *o*-CH_3), 1.36 (br s, 72 H, ^{i}Pr CH_3). The NMR spectrum of [**2-THF**]$^+$ was recorded in both THF and DFB to ensure peaks that overlapped with the suppressed solvent resonances could be integrated. In DFB solutions, the bound THF can be observed but in THF solutions the bound THF ligand exchanges rapidly with free THF. EPR: $g_1 = 2.074$, $g_2 = 1.960$, $g_3 = 1.920$ (10:1 toluene:THF, 15 K, 9.37 GHz).

($SIAr^{Me,iPr}$)$_3Fe_4S_4Cl$ (**2-Cl**)

Compound [**2-THF**]$^+$ (203 mg, 0.0975 mmol) was dissolved in THF (50 mL). PPh_4Cl (42 mg, 0.11 1.1 equiv) was suspended in THF (2 mL) and added to the solution of [**2-THF**]$^+$. The resulting solution was stirred for 2 h, filtered through Celite, and the solvent removed in vacuo. Acetonitrile (1 mL) was added and the precipitate collected on a frit and washed with additional acetonitrile (3 x 5 mL). The black solid was recrystallized by diffusion of *n*-pentane into Et_2O. Yield: 96 mg (58%). ^{1}H NMR (C_6D_6 293 K) δ 9.33 (s, 6H, NCH_2), 7.25 (s, 3H, *p*-C*H*), 4.31 (br s, 18H, *o*-CH_3), 3.48 (br s, 12H, ^{i}Pr C*H*), 1.40 and 1.23 (br s, 72H, ^{i}Pr CH_3). Some resonances are not apparent at room temperature because Fe–C(NHC) bond rotation is close to the NMR timescale. EPR: $g_1 = 2.085$, $g_2 = 1.975$, $g_3 = 1.943$ (toluene, 20 K, 9.37 GHz).

($SIAr^{Me,iPr}$)$_3Fe_4S_4$ (**2**)

Compound [**2-THF**]$^+$ (106 mg, 0.0511 mmol) was suspended in cyclohexane (4 mL). To that solution were added $SIAr^{Me,iPr}$ (21.4 mg, 0.0479 mmol) in cyclohexane (1 mL) and Cp^*_2Co (14.2 mg, 0.043 mmol, 0.9 equiv) in cyclohexane (1 mL). The resulting solution was stirred for 30 min, filtered through Celite to remove a yellow-gray precipitate, and lyophilized. Yield: 87.6 mg.

Corrected for 21.4 mg of $SIAr^{Me,iPr}$: 66.2 mg of **2** (91%). ^1H NMR (C_6D_{12}, 293 K) δ 51.3, 40.8, 5.54.

$(SIAr^{Me,iPr})_4Fe_8S_8$ (**2-FBDC**)

Compound [**2-THF**]$^+$ (25 mg, 0.010 mmol) was suspended in cyclohexane (1 mL). To that solution was added Cp^*_2Co (2.9 mg, 0.009 mmol, 0.9 equiv) in cyclohexane (1 mL). The solution was filtered through Celite, pumped down, and washed with TMS. The yield of this procedure was low (< 40 %) and the NMR spectrum contains free $SIAr^{Me,iPr}$, but it was suitable to identify the NMR spectrum of **2-FBDC**. Crystals suitable for X-ray diffraction were grown from diffusion of TMS into cyclohexane. ^1H NMR (C_6D_{12}, 293 K) δ 8.02 (s, 16H, NCH_2), 7.21 (s, 8H, *p*-C*H*), 4.09 (br s, 48H, *o*-CH_3), 2.75 (s, 16H, ^{i}Pr C*H*), 1.30 and –0.41 (s, 96H, ^{i}Pr CH_3).

$(SIAr^{Me,iPr})_3Fe_4S_4$ (**2-CO**)

To a solution of **2** (20 mg, 0.012 mmol) with $SIAr^{Me,iPr}$ (1.5 equiv) in cyclohexane (0.7 mL) was added CO (1 mL) via syringe. ^1H NMR spectroscopy indicated quatitative conversion to **2-CO**. ^1H NMR (C_6D_{12} 293 K) δ 22.53 (s, 3H, NCH_2), 19.93 (s, 3H, NCH_2), 18.95 (s, 3H, NCH_2), 18.01 (s, 3H, NCH_2), 7.71 (s, 3H, *p*-C*H*), 7.65 (s, 3H, *p*-C*H*), 5.83 (s, 6H), 5.15 (s, 2 x 6H), 4.06 (s, 2 x 6H), 1.49 (s, 2 x 6H). Some resonances overlap with resonances of $SIAr^{Me,iPr}$. FT-IR (DFB solution, cm^{-1}): 1841 cm^{-1}.

B. NMR Spectra

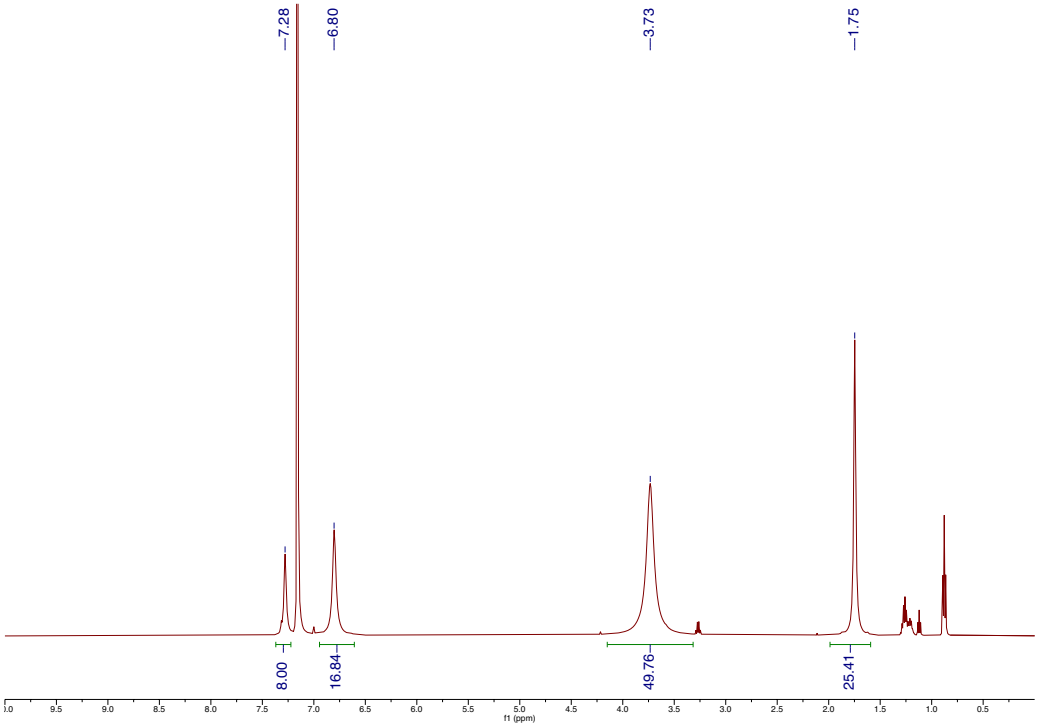

Figure S5.1: ^{1}H NMR spectrum of **1-FBDC** in C_6D_6 at 293 K.

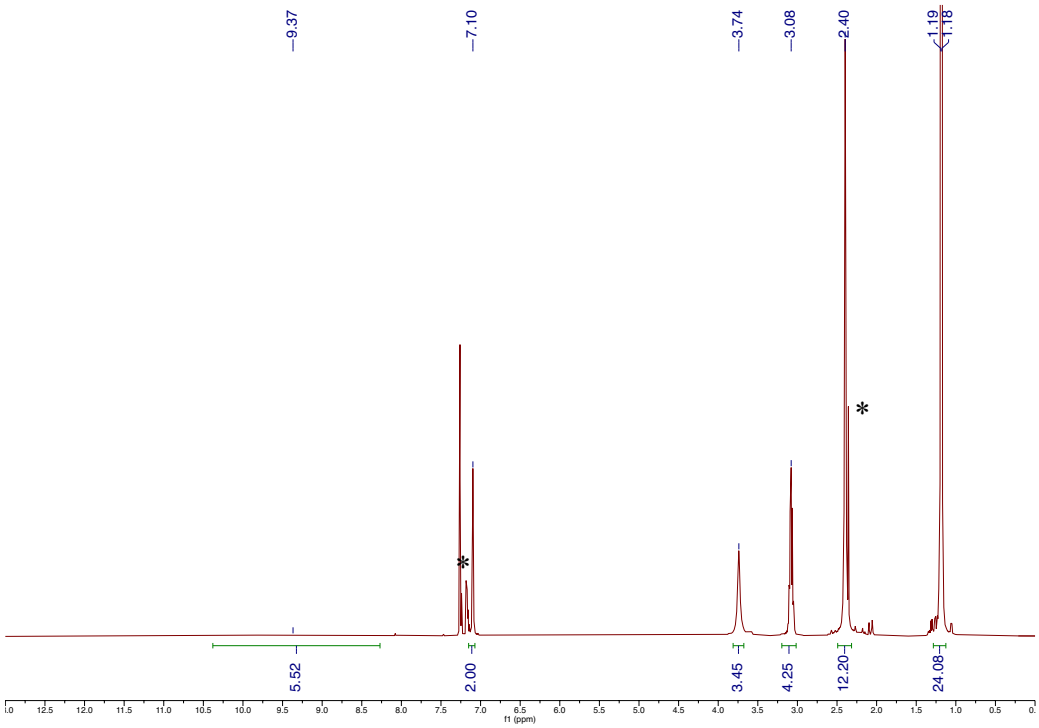

Figure S5.2: ^{1}H NMR spectrum of N^1,N^2-bis(3,5-diisopropyl-2,6-dimethylphenyl)ethane-1,2-diaminium dichloride in $CDCl_3$ at 293 K. (*) toluene

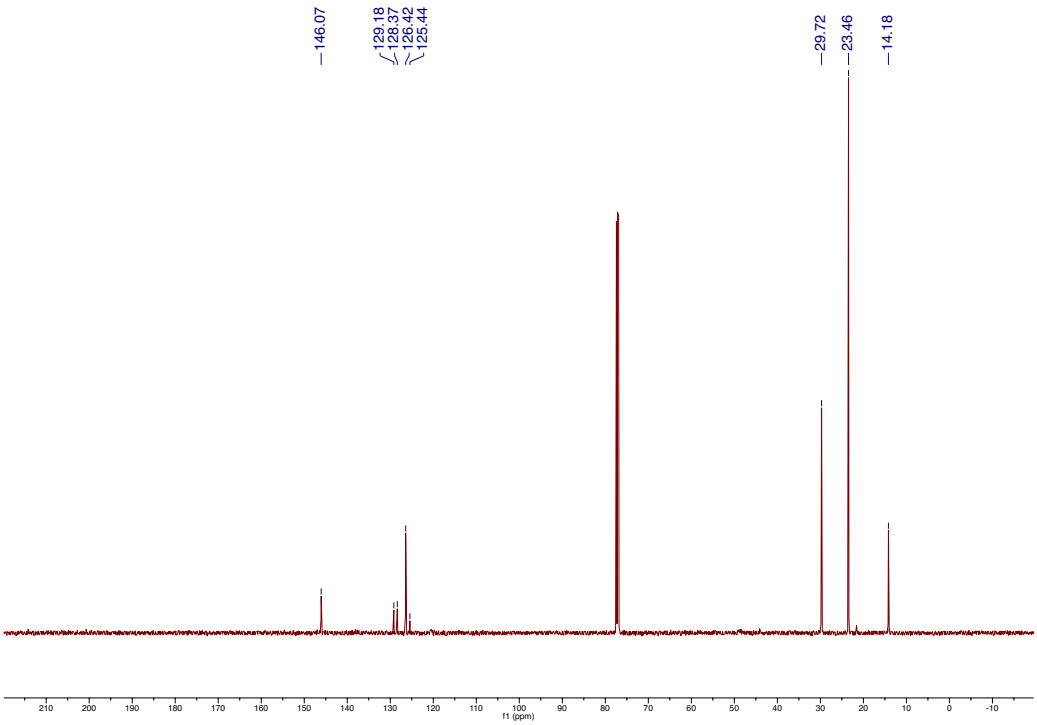

Figure S5.3: $^{13}C\{^{1}H\}$ NMR spectrum of N^1,N^2-bis(3,5-diisopropyl-2,6-dimethylphenyl)ethane-1,2-diaminium dichloride in $CDCl_3$ at 293 K.

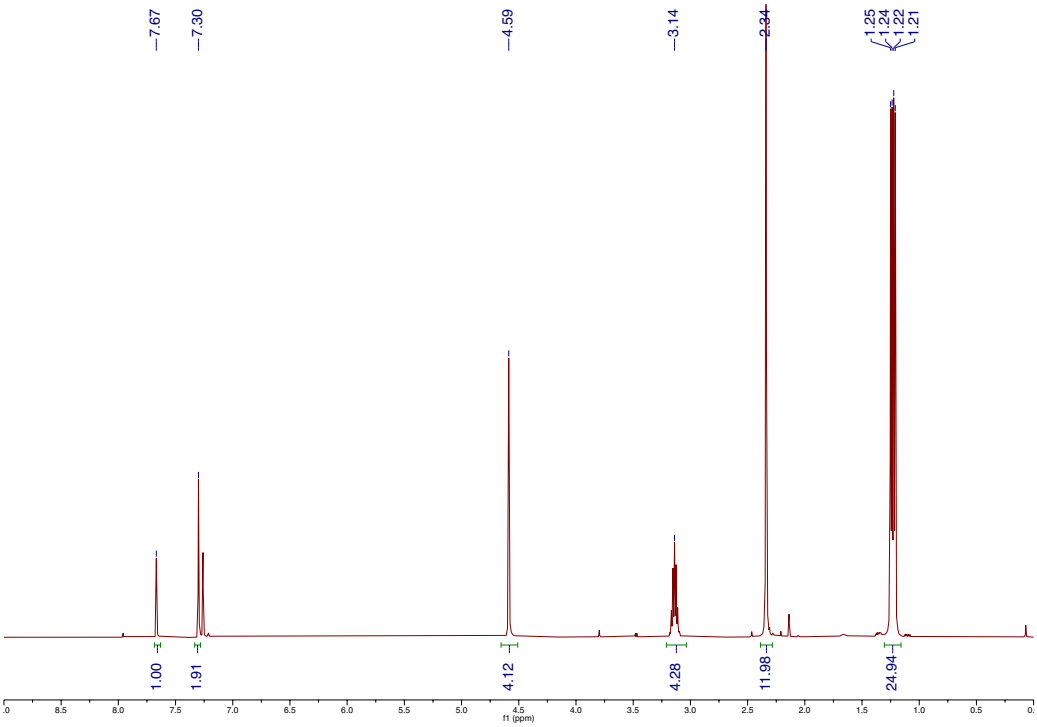

Figure S5.4: ^{1}H NMR spectrum of $SIAr^{Me,iPr}\cdot HBF_4$ in $CDCl_3$ at 293 K.

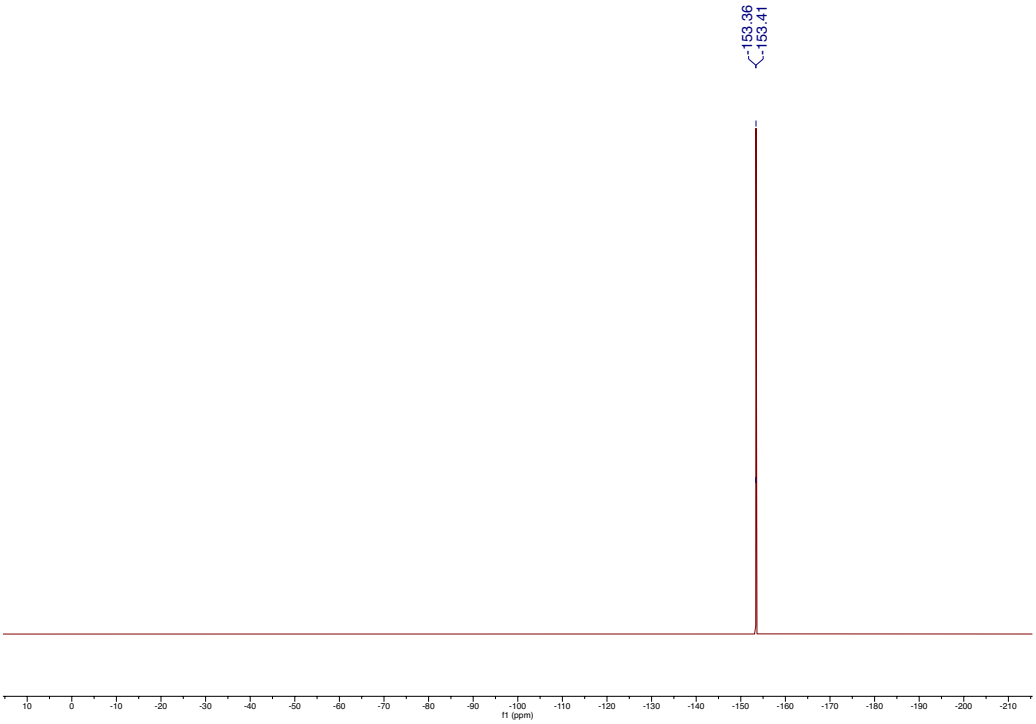

Figure S5.5: ^{19}F NMR spectrum of $SIAr^{Me,iPr}\cdot HBF_4$ in $CDCl_3$ at 293 K.

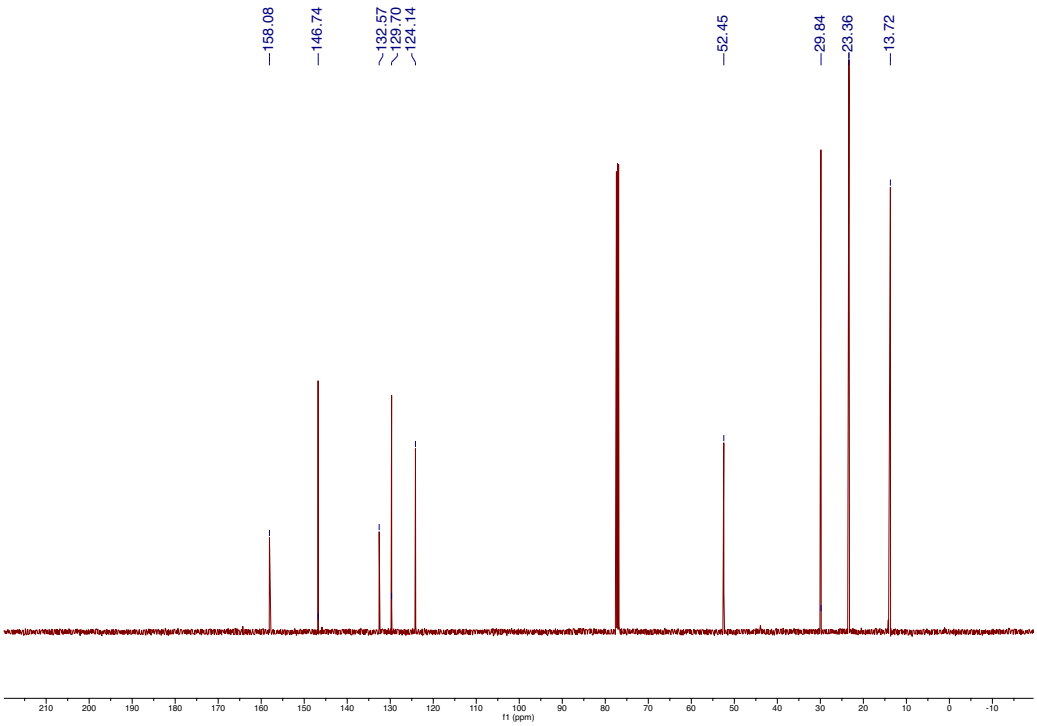

Figure S5.6: $^{13}C\{^1H\}$ NMR spectrum of $SIAr^{Me,iPr}\cdot HBF_4$ in $CDCl_3$ at 293 K.

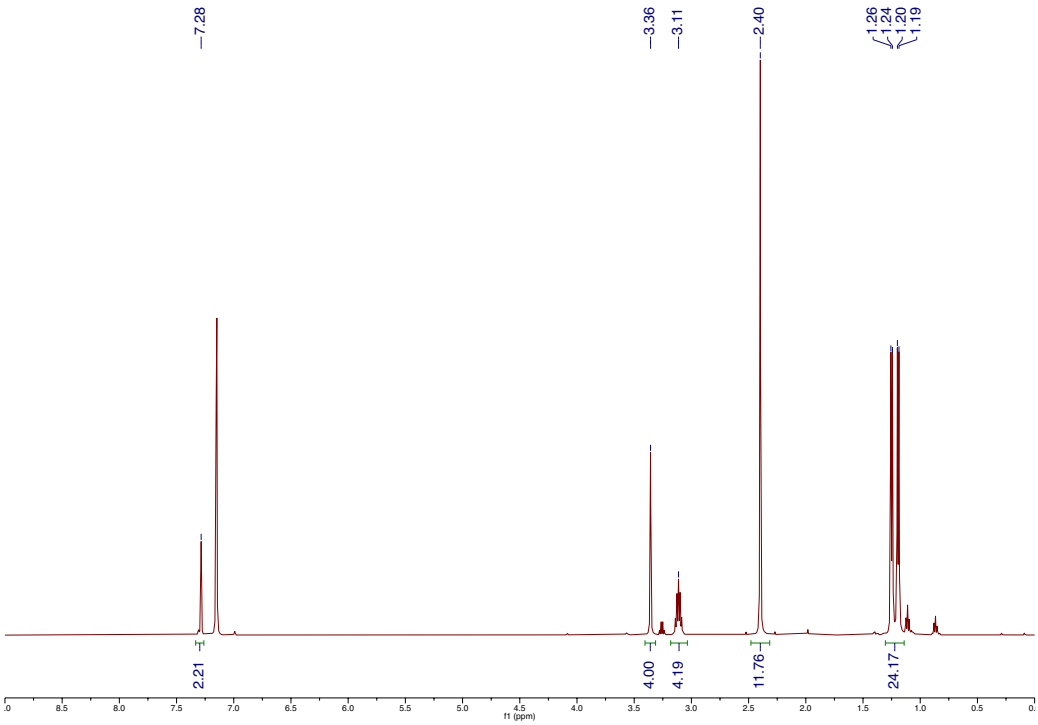

Figure S5.7: ^{1}H NMR spectrum of $SIAr^{Me,iPr}$ in C_6D_6 at 293 K.

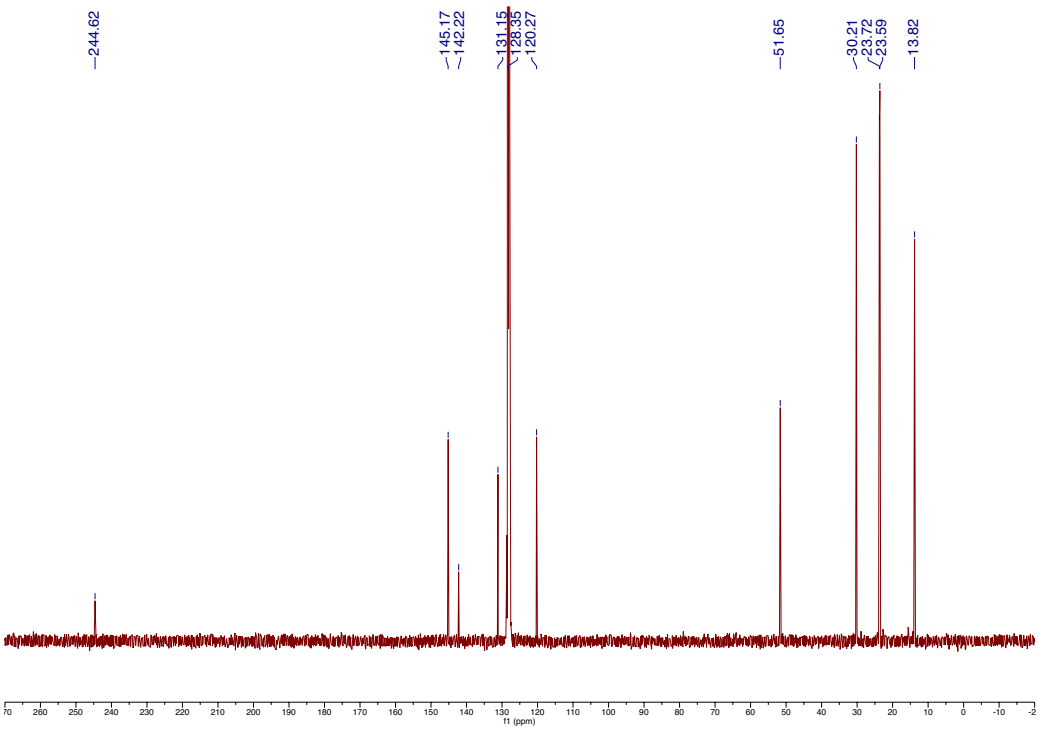

Figure S5.8: $^{13}C\{^{1}H\}$ NMR spectrum of $SIAr^{Me,iPr}$ in C_6D_6 at 293 K.

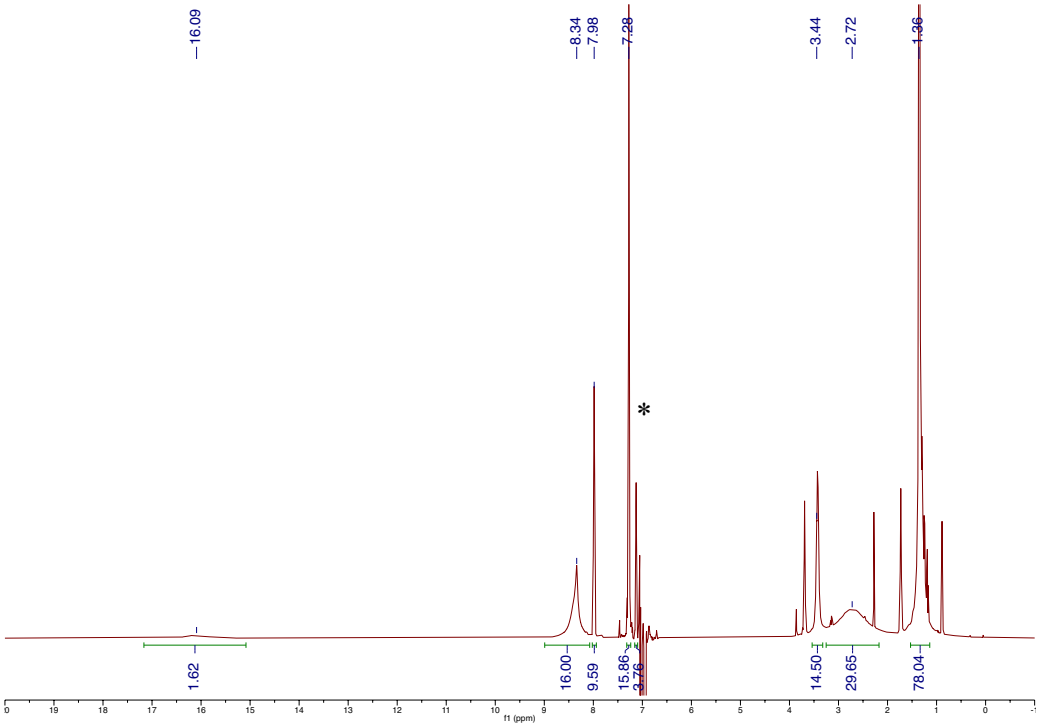

Figure S5.9: ^{1}H NMR spectrum of [**2-THF**][BPh_4] in DFB at 293 K. (*) residual signals from suppressed solvent

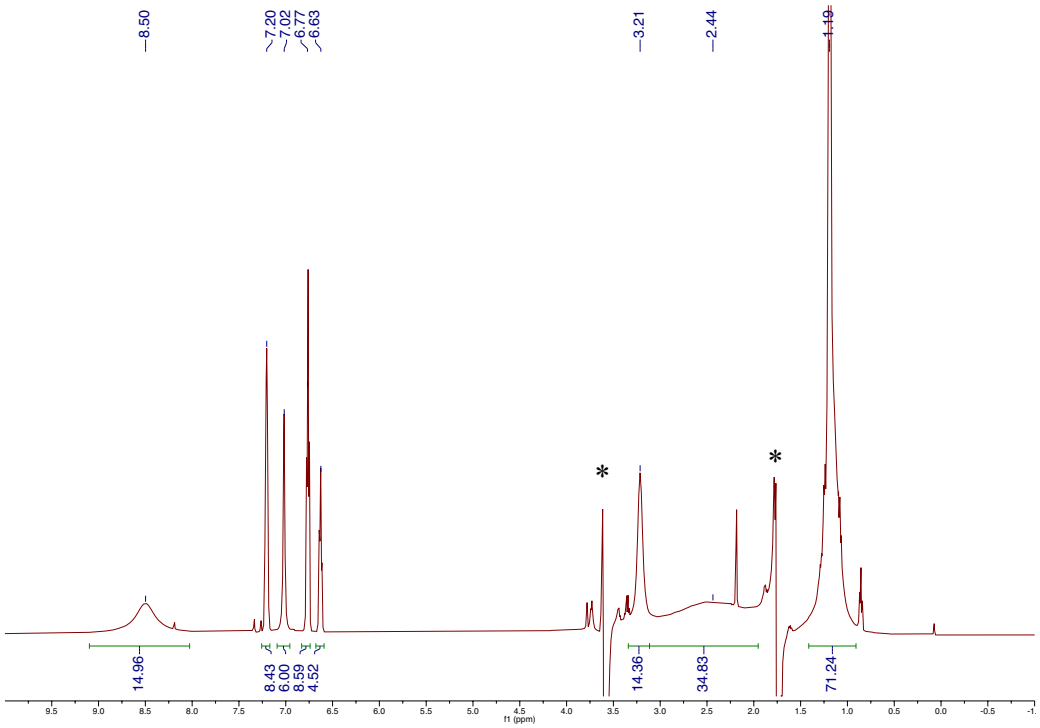

Figure S5.10: ^{1}H NMR spectrum of [**2-THF**][BPh_4] in THF at 293 K. (*) residual signals from suppressed solvent

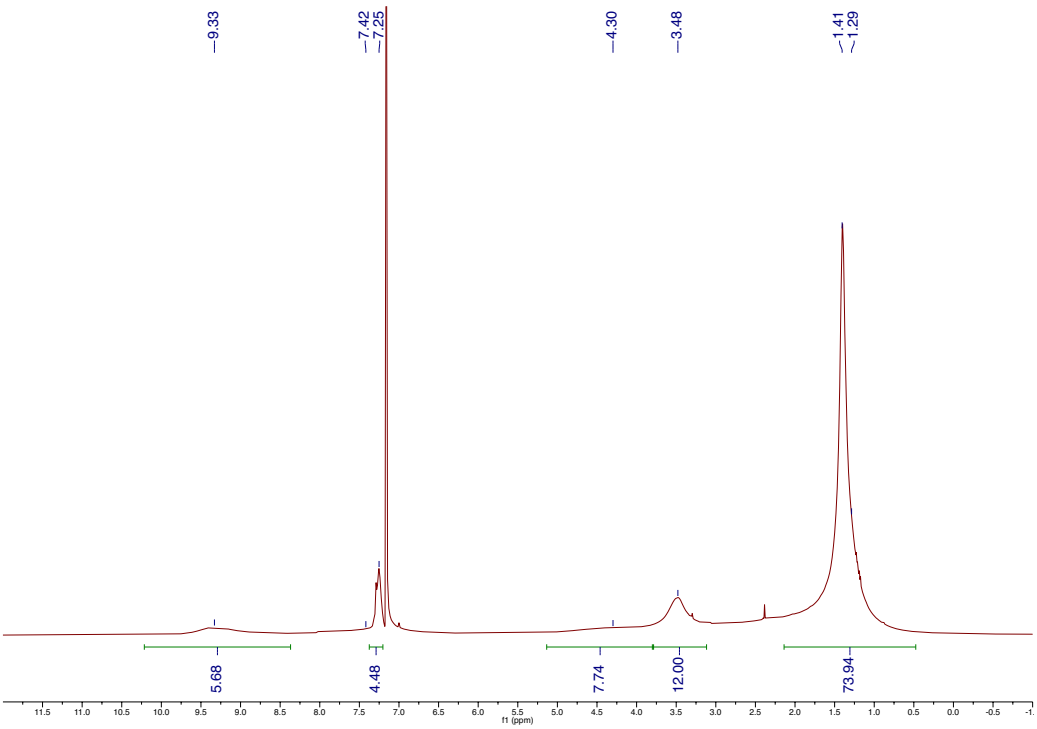

Figure S5.11: ^{1}H NMR spectrum of **2-Cl** in C_6D_6 at 293 K.

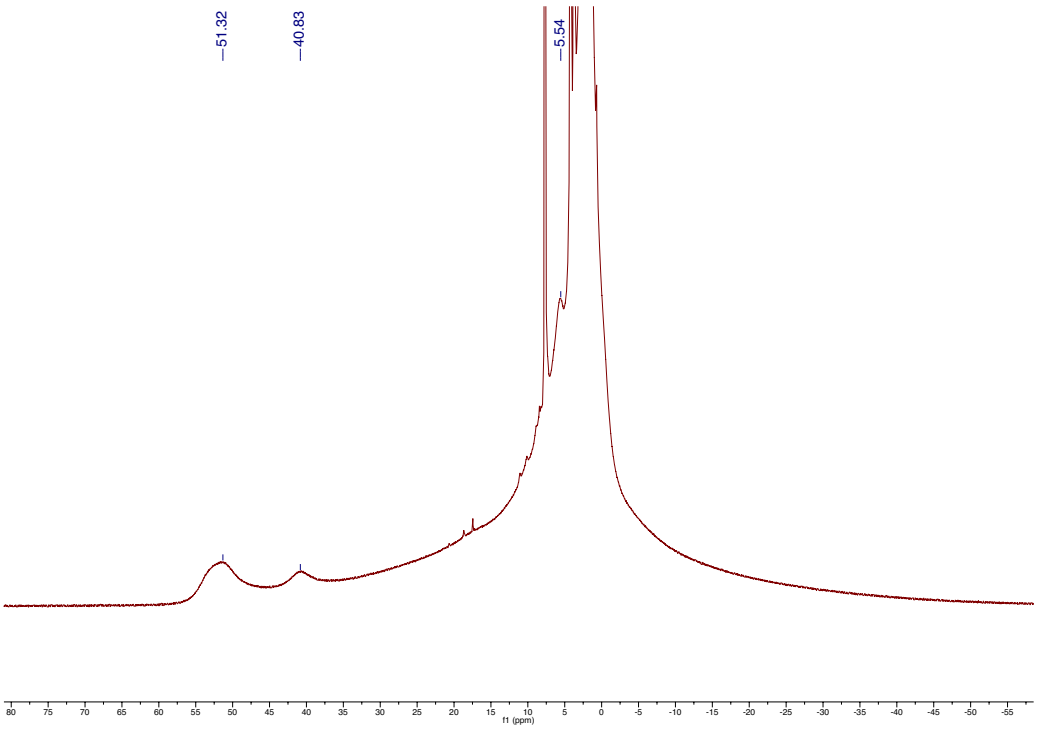

Figure S5.12: ^{1}H NMR spectrum of **2** in C_6D_{12} at 293K highlighting the characteristic peaks of **2** at 51, 41, and 5.5 ppm.

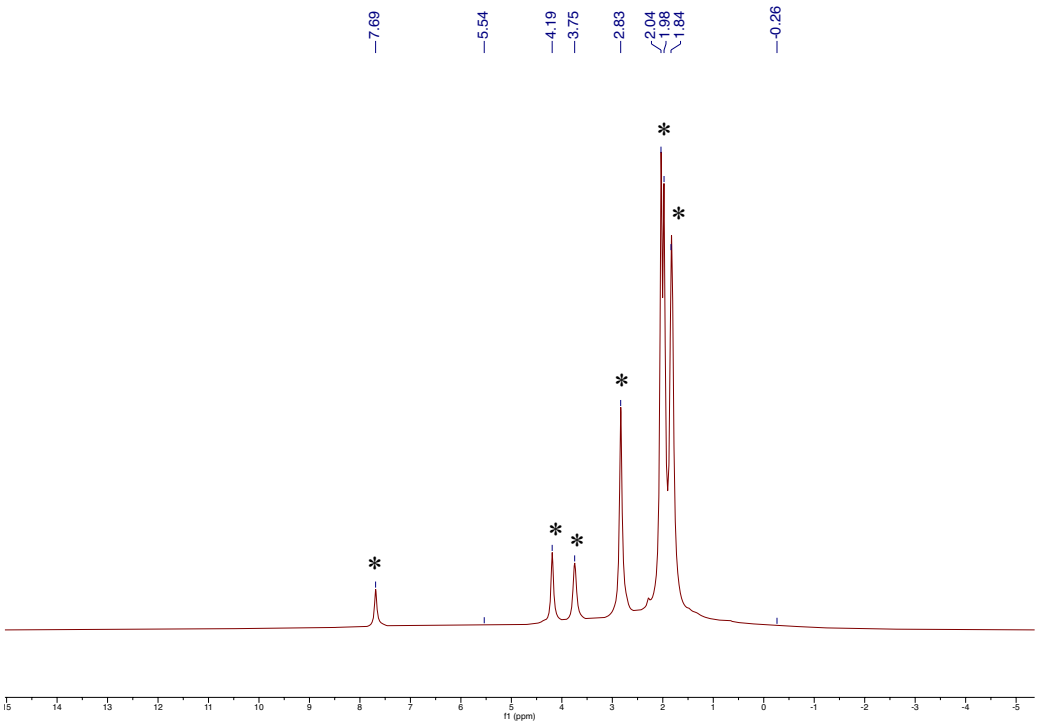

Figure S5.13: ^{1}H NMR spectrum of **2** in C_6D_{12} at 293K. Because the resonances of **2** are so broad, the only visible peaks in the diamagnetic region are SIAr^{Me,iPr} (*).

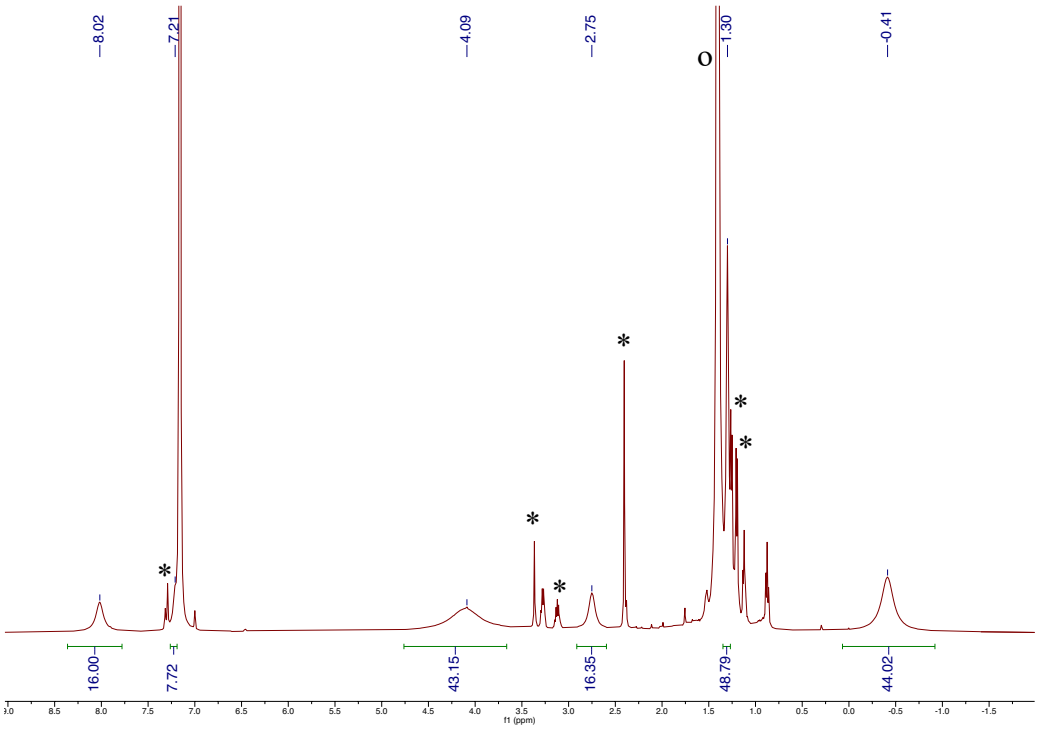

Figure S5.14: ^{1}H NMR spectrum of **2-FBDC** in C_6D_6 at 293 K. (*) free SIAr^{Me,iPr}, (o) cyclohexane

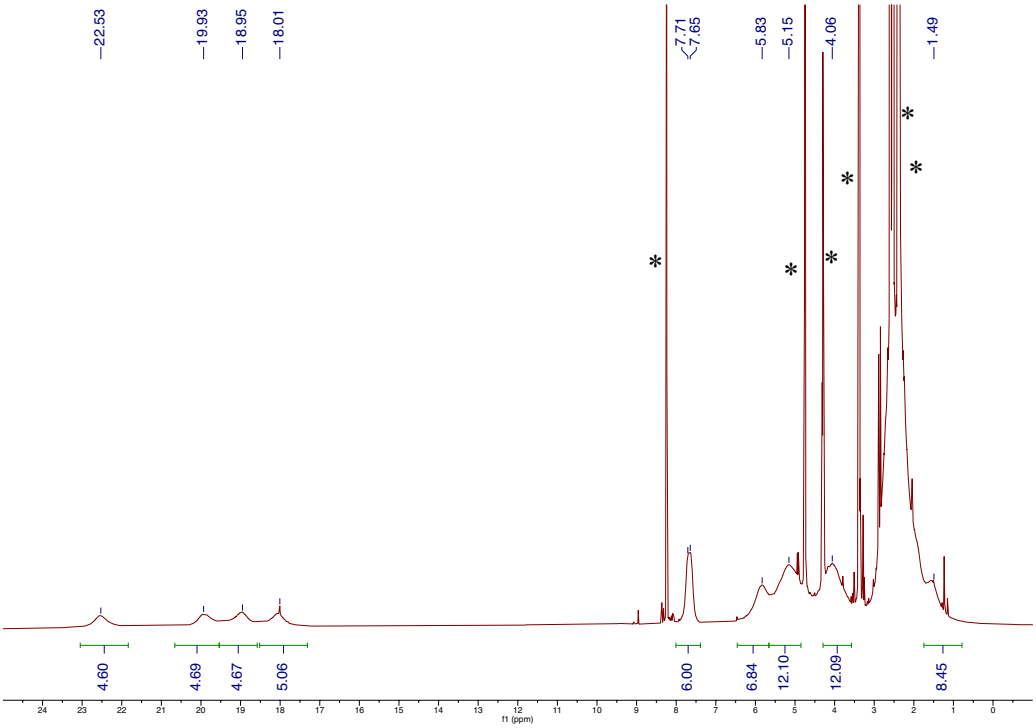

Figure S5.15: ^{1}H NMR spectrum of **2-CO** in C_6D_{12} at 293 K. (*) free SIAr^{Me,iPr}

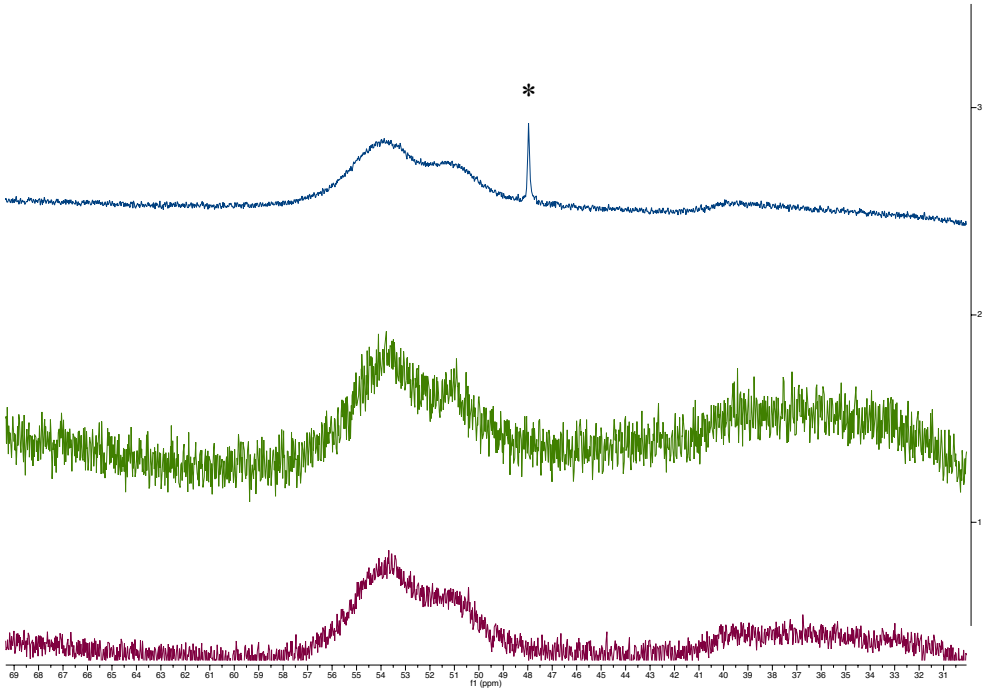

Figure S5.16: crude ^{1}H NMR spectrum of **2** in C_6H_{12} generated by reduction with Cp*$_2$Co (top), Na (middle) and K (bottom) showing the same characteristic peaks at ca. 50 ppm are formed each reaction (*) Cp*$_2$Co

C. VT NMR spectra of 1-Cl

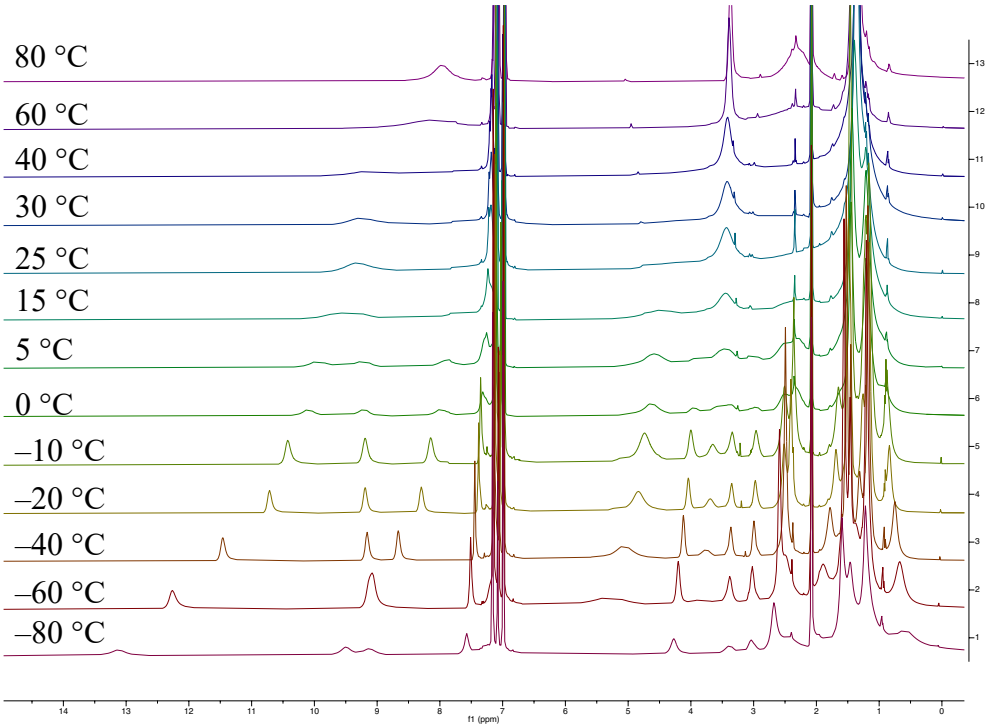

Figure S5.17: VT NMR spectra of **1-Cl** in d^8-toluene between 80 °C and –80 °C showing the decoalescence of the $SIAr^{Me,iPr}$ peaks at low temperatures

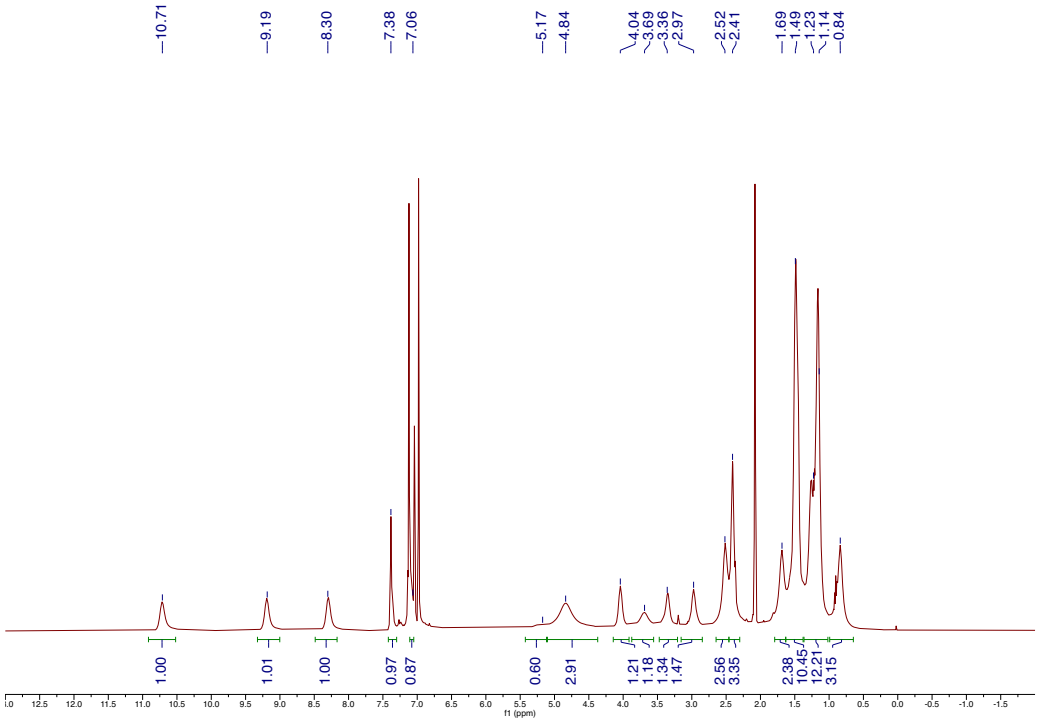

Figure S5.18: NMR spectrum of **1-Cl** in d^8-toluene at –20 °C. At this temperature, rotation around the Fe–C(NHC) bond is slow, leading to C_3 symmetry on the NMR timescale

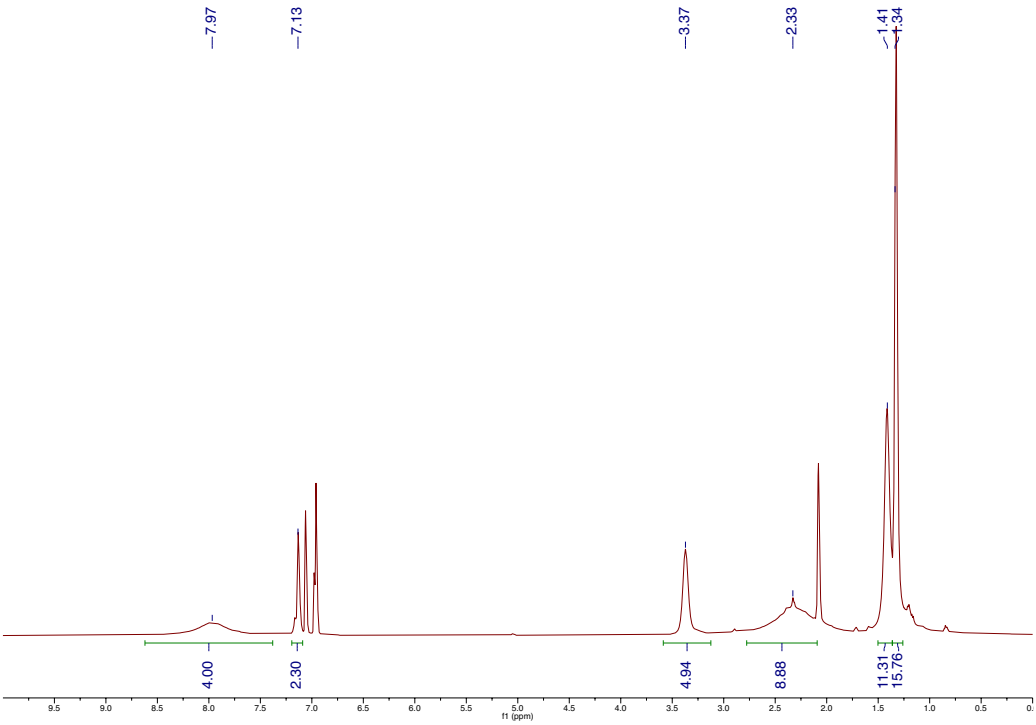

Figure S5.19: NMR spectrum of **1-Cl** in d^8-toluene at 80 °C. At this temperature, Fe–C(NHC) bond rotation is faster than the NMR timescale, leading to approximate C_{3v} symmetry

D. VT NMR spectra of 2 under N_2 and under vacuum

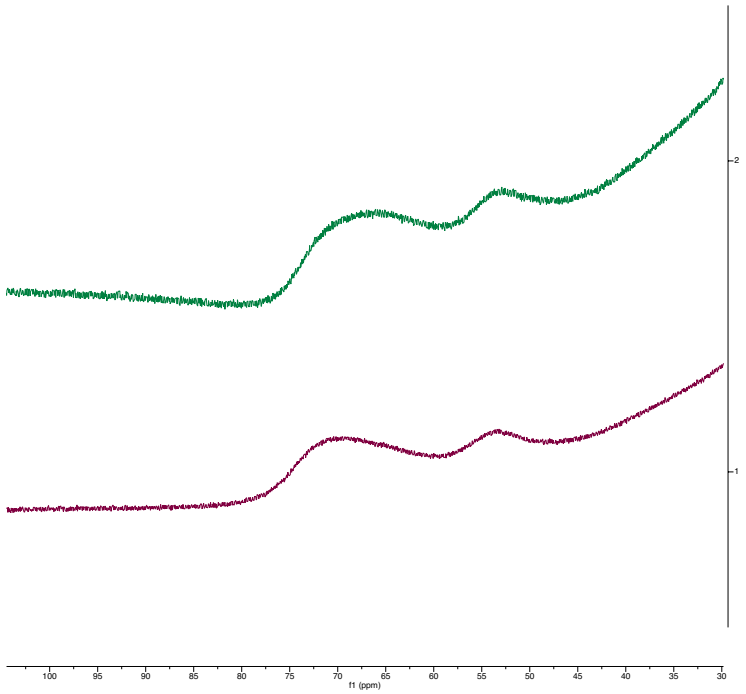

Figure S5.20: NMR spectrum of **2** in C_7D_{14} at –40 °C in the absence (top) and presence (bottom) of N_2. Even at low temperatures, the NMR spectrum of **2** is not affected by the presence or absence of N_2.

E. Cartoons of the electronic structure of EBDC and FBDC

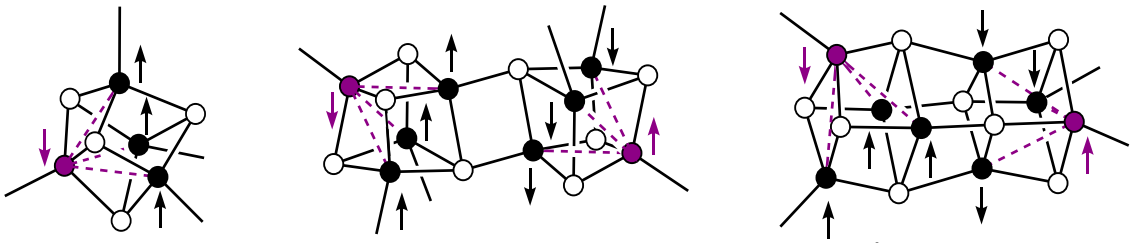

Figure S5.21: Cartoon depicting the spin coupling pattern in an $[Fe_4S_4]^0$ cluster that leads to the $S = 4$ ground spin state (left), cartoon depicting how EBDCs (middle) and the FBDC (right) can be described as two antiferromagnetically coupled $[Fe_4S_4]^0$ clusters. The purple Fe center is antiferromagnetically coupled to its neighboring three Fe centers; the antiferromagnetically coupled Fe can be recognized in the crystal structure by its long Fe–Fe distances. (purple dashed lines)

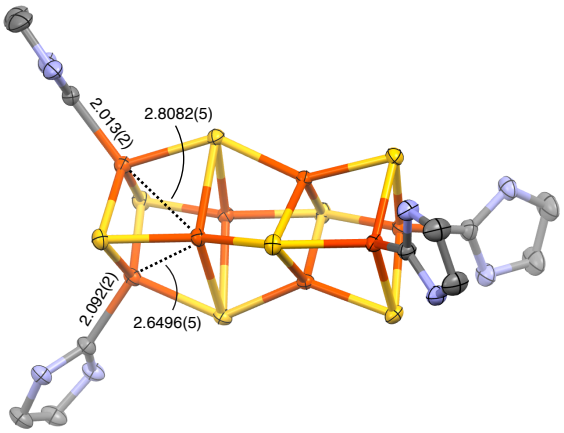

Figure S5.22: Crystallographic structure of **1-FBDC** highlighting the longer Fe–Fe distances (2.8082(5) Å vs. 2.6496(5) Å) and shorter Fe–C distance (2.013(2) Å vs. 2.092(2) Å) at the Fe site that is antiferromagnetically coupled to the adjacent Fe centers. The cluster has approximate C_2 symmetry, so the other pair of NHC-ligated Fe centers is very similar, as is the pattern of distances to the other bridging Fe center.

F. IR spectra

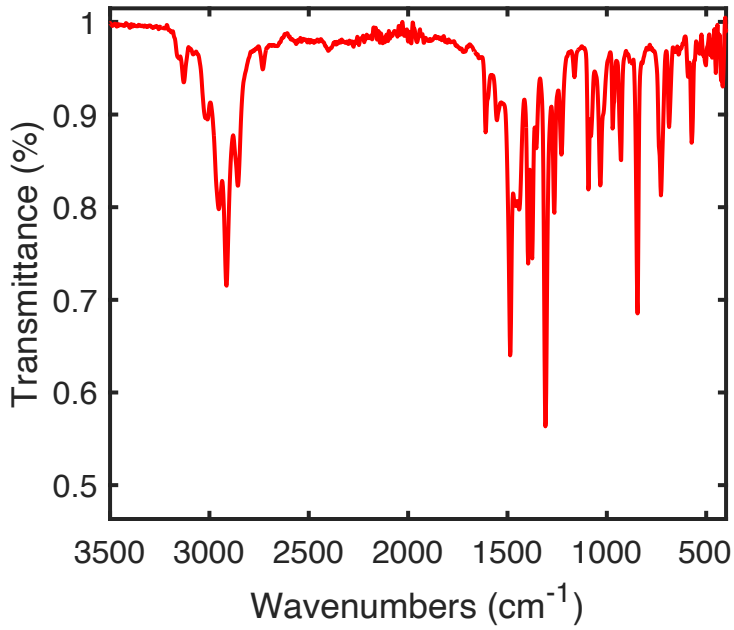

Figure S5.23: IR spectrum of **1-FBDC**

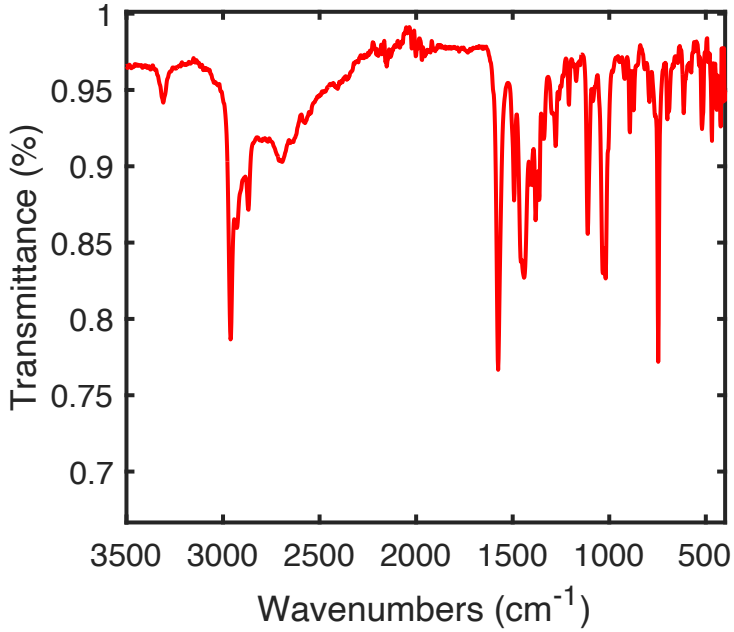

Figure S5.24: IR spectrum of N^1,N^2-bis(3,5-diisopropyl-2,6-dimethylphenyl)ethane-1,2-diaminium dichloride

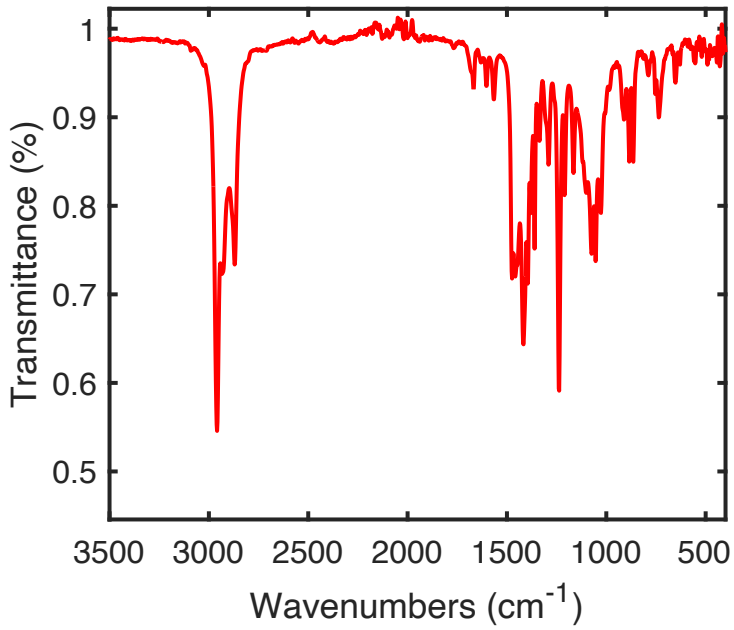

Figure S5.25: IR spectrum of $SIAr^{Me,iPr}\cdot HBF_4$

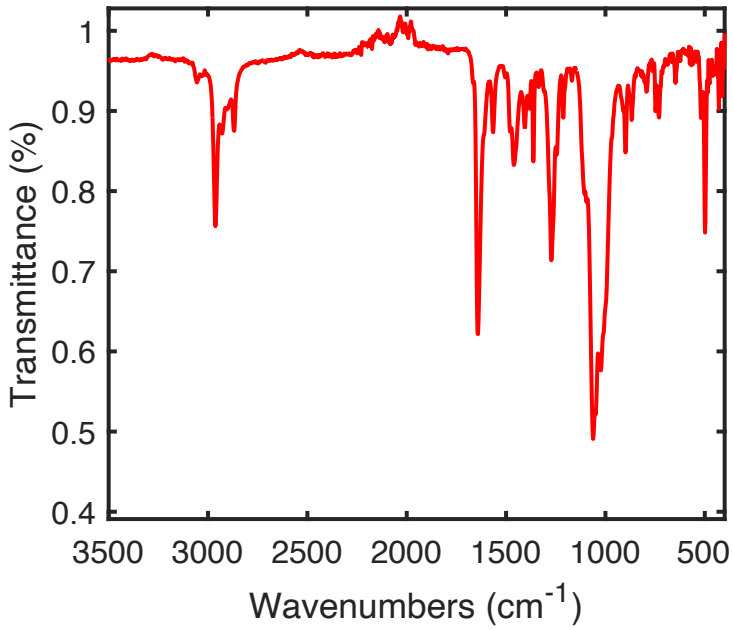

Figure S5.26: IR spectrum of $SIAr^{Me,iPr}$

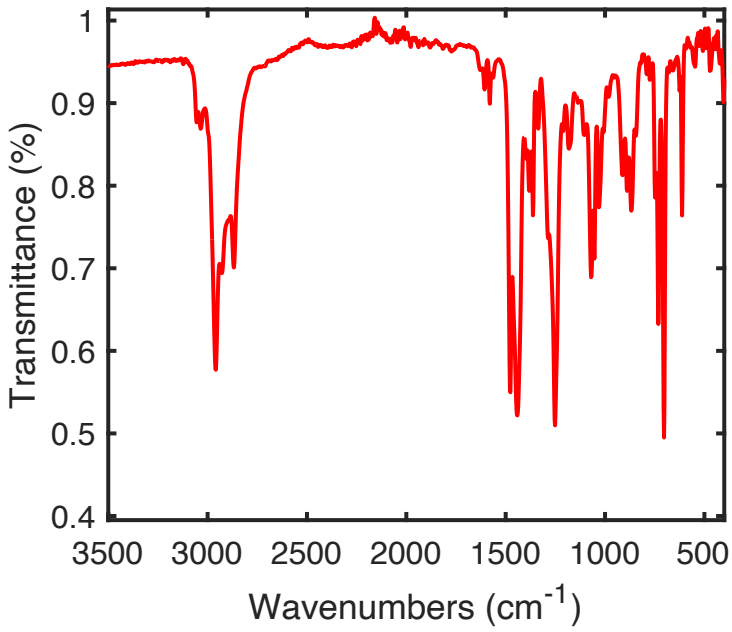

Figure S5.27: IR spectrum of [**2-THF**][BPh_4]

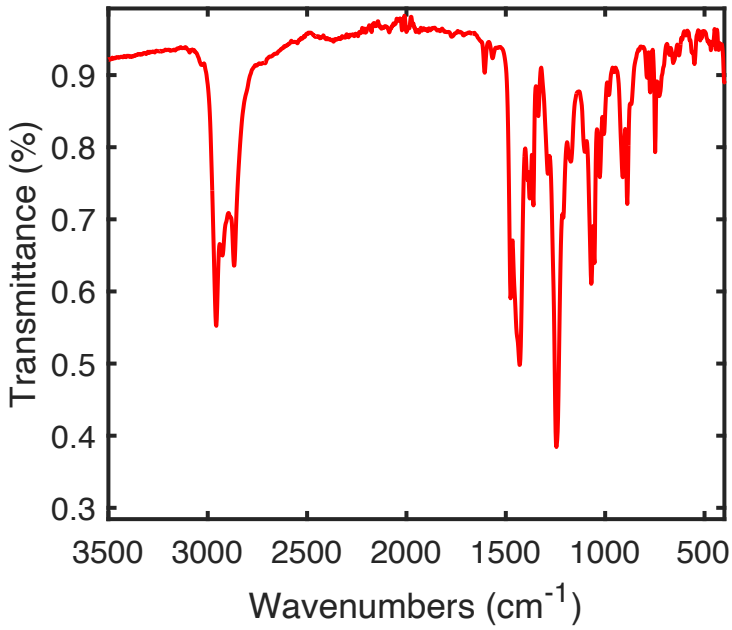

Figure S5.28: IR spectrum of **2-Cl**

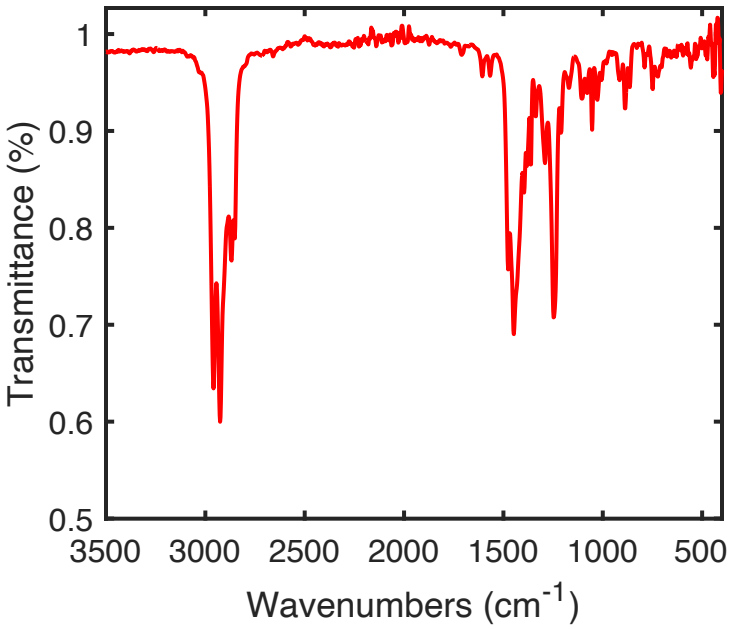

Figure S5.29: IR spectrum of **2**. No stretches derived from a terminal N_2 ligand are apparent.

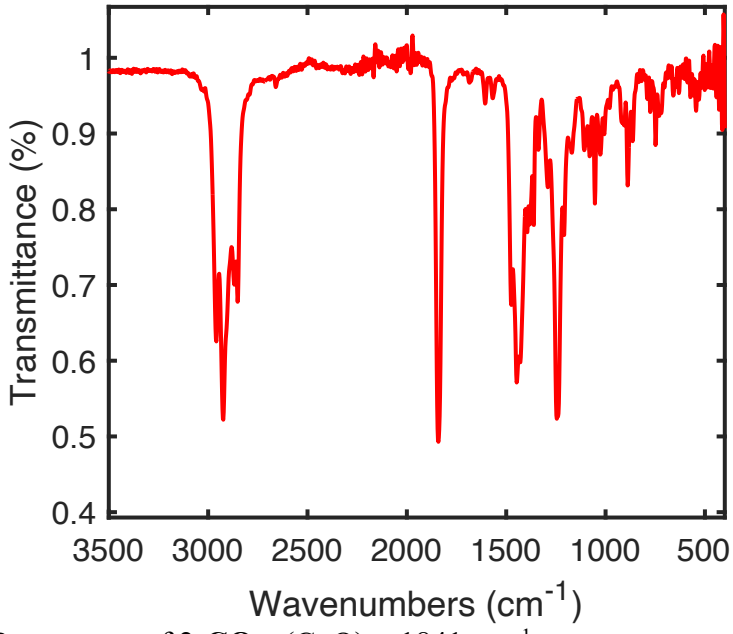

Figure S5.30: IR spectrum of **2-CO**. ν(C–O) = 1841 cm^{-1}

G. EPR spectra

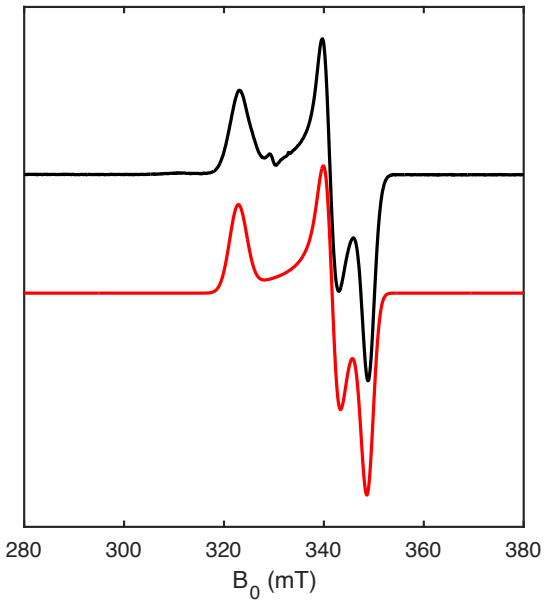

Figure S5.31: EPR spectrum of [**2-THF**][BPh_4] in THF/Tol (10:1) at 15 K (perpendicular mode, black) and simulation (red). Microwave power: 63 μW; microwave frequency: 9.3697 GHz; simulation parameters: g = [2.074 1.960 1.920], g-strain = [0.025 0.017 0.015].

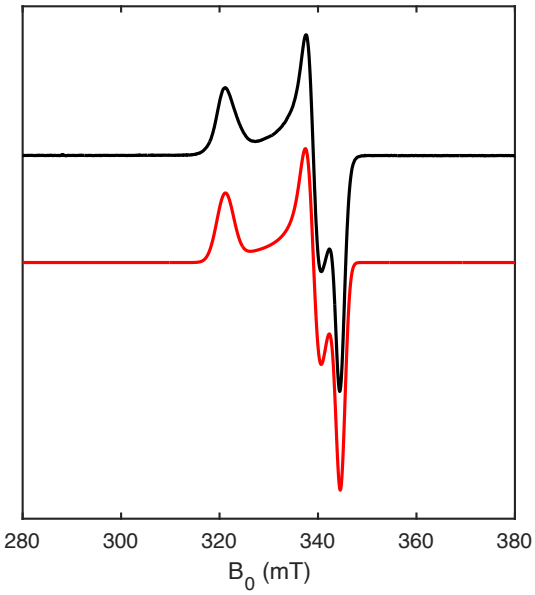

Figure S5.32: EPR spectrum of **2-Cl** in toluene at 15 K (perpendicular mode, black) and simulation (red). Microwave power: 63 μW; microwave frequency: 9.3698 GHz; simulation parameters: g = [2.085 1.975 1.943], g-strain = [0.025 0.016 0.011].

H. SQUID magnetometry

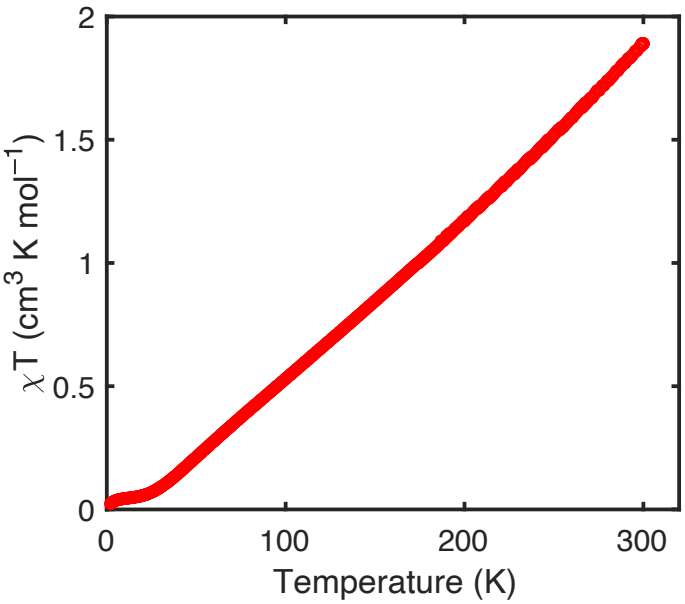

Figure S5.33: SQUID magnetometry data (χT vs. T) for **1-FBDC** collected at a field of 1 T. Data are corrected for diamagnetic contributions using Pascal's constants. The values of χT at low temperature (below 50 K, ca. 0.04 cm^3 K mol^{-1}) are close to the expectation value for an $S = 0$ system (0 cm^3 K mol^{-1}). The increase in χT with increasing temperature may be attributed to temperature independent paramagnetism (TIP) or population of higher spin excited states.

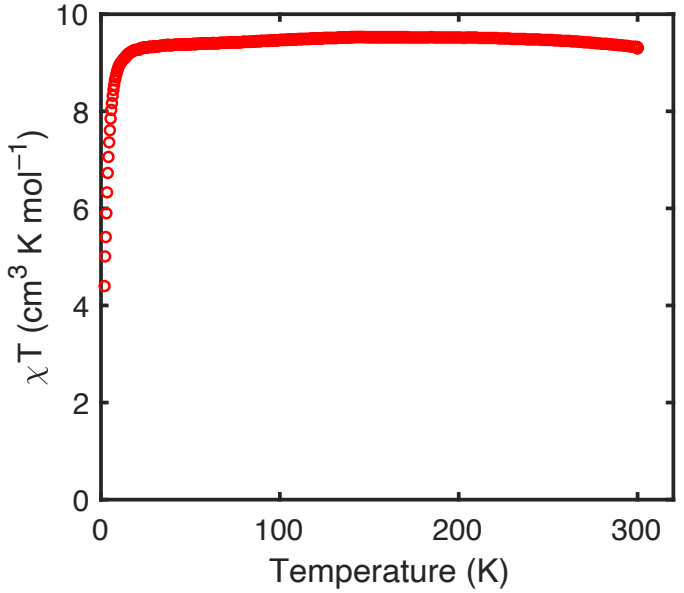

Figure S5.34: SQUID magnetometry data (χT vs. T) for **2** collected at a field of 1 T. Data are corrected for diamagnetic contributions using Pascal's constants. The values of χT ca. 9.5 cm^3 K mol^{-1}) are close to the expectation value for an $S = 4$ system (10 cm^3 K mol^{-1}).

I. Mössbauer spectra

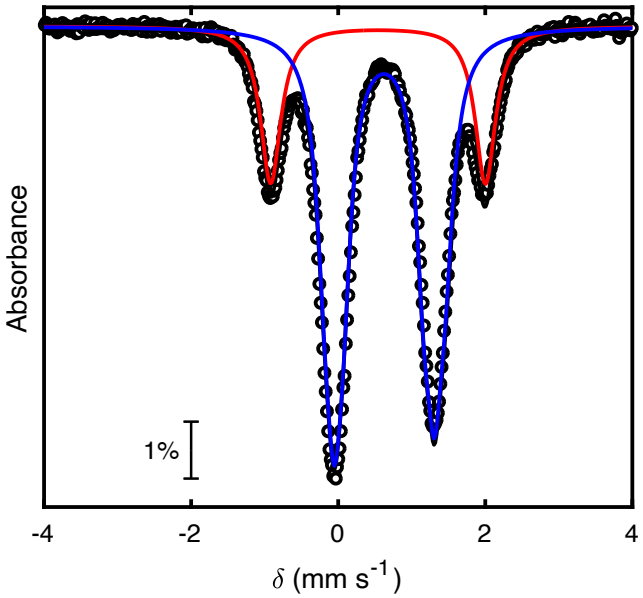

Figure S5.35: Mössbauer spectrum of **1-FBDC** at 80 K with parameters as in table S5.1. The red site is the site with large $|\Delta E_Q|$, the sum of the other three sites is plotted in blue.

Table S5.1: Fit parameters for Mössbauer spectrum of **1-FBDC**

Compound		δ (mm·s^{-1})	$\|\Delta E_Q\|$ (mm·s^{-1})	Γ (mm·s^{-1})	Rel. Area
1-FBDC	Site 1	0.542	2.920	0.346	1
	Site 2	0.520	1.338	0.279	1
	Site 3	0.684	1.365	0.332	2
	Avg δ	**0.608**	–	–	

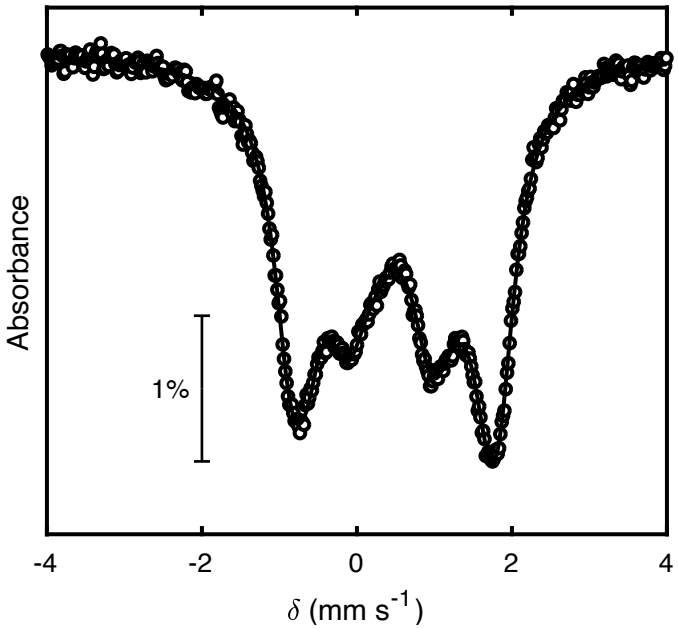

Figure S5.36: Mössbauer spectrum of [**2-THF**]$^+$ at 80 K with parameters as in table S5.2. The spectrum is broad at 80 K, and so the individual site parameters are not reliable: only the average δ is discussed and only the total fit is plotted.

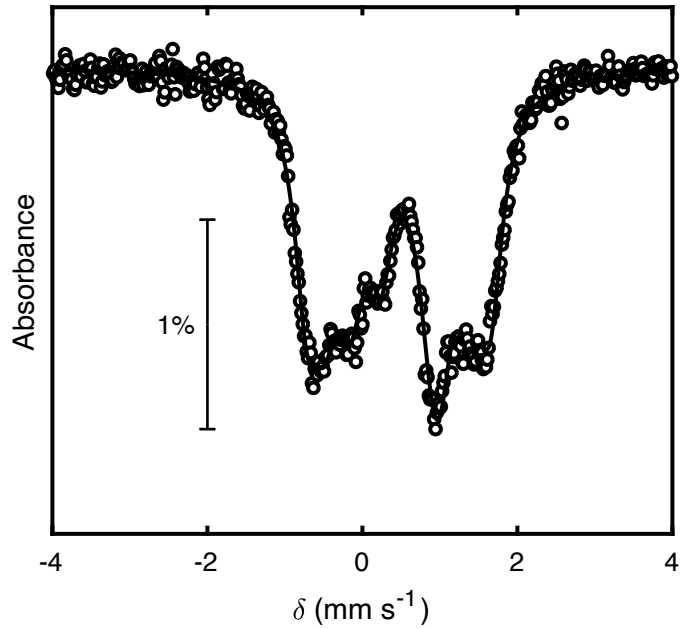

Figure S5.37: Mössbauer spectrum of [**2-THF**]$^+$ at 150 K with parameters as in table S5.2.

Table S5.2: Fit parameters for Mössbauer spectrum of [**2-THF**]$^{+}$

Temp		δ (mm·s^{-1})	$\lvert\Delta E_Q\rvert$ (mm·s^{-1})	Γ (mm·s^{-1})	Rel. Area
80 K	Site 1	0.704	0.982	1.000	1
	Site 2	0.412	1.096	0.634	1
	Site 3	0.515	2.346	0.576	1
	Site 4	0.483	2.708	0.525	1
	Avg δ	**0.528**	–	–	
150 K	Site 1	0.550	0.679	0.445	1
	Site 2	0.422	1.169	0.418	1
	Site 3	0.449	1.876	0.417	1
	Site 4	0.467	2.375	0.372	1
	Avg δ	**0.472**	–	–	–

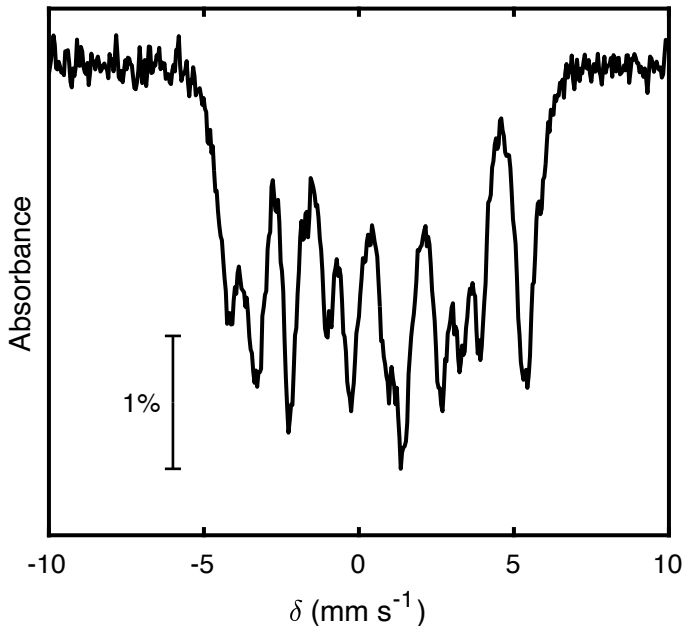

Figure S5.38: Mössbauer spectrum of **2** at 5 K with a magnetic field of 77 mT oriented parallel to the sample. The spectrum is magnetically split and, due to the number of parameters required, cannot be reliably simulated in the absence of high magnetic field data.

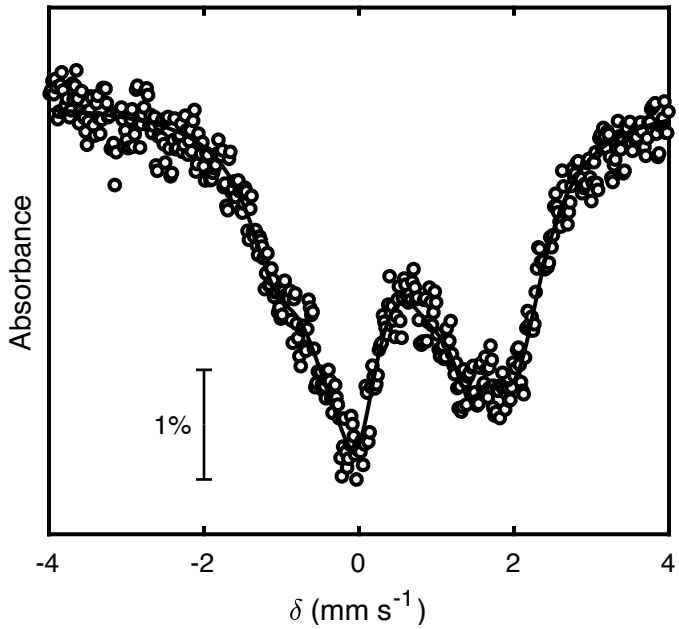

Figure S5.39: Mössbauer spectrum of **2** at 80 K with parameters as in table S5.3. The spectrum is broad at 80 K, and so the individual site parameters are not reliable: only the average δ is discussed and only the total fit is plotted.

Table S5.3: Fit parameters for Mössbauer spectrum of **2**

Compound		δ (mm·s^{-1})	$\lvert\Delta E_Q\rvert$ (mm·s^{-1})	Γ (mm·s^{-1})	Rel. Area
	Site 1	0.458	3.072	0.908	1
	Site 2	0.404	1.024	1.000	1
1-FBDC	Site 3	0.708	1.437	0.681	1
	Site 4	0.786	2.479	0.954	1
	Avg δ	**0.589**	–	–	

J. Computational Details

General Considerations

All calculations were carried out using version 5.0.3 of the ORCA program package[14] using the broken-symmetry (BS) approach to approximate the multireference electronic states of Fe–S clusters. BS solutions were constructed using the FlipSpin feature of ORCA.

Coordinates for non-H atoms were taken from X-ray crystallographic coordinates for **2**; H atom positions were optimized. To improve the efficiency of the calculations, the mesityl substituents on the IMes ligands were simplified to H. The ZORA-def2-TZVP basis set was used for all atoms.[15] For all calculations, the ZORA relativistic correction[16] and the general-purpose Coulomb fitting basis set SARC/J were used;[17] all basis sets were fully decontracted. Solid-state effects were approximated using the CPCM solvation model with an infinite dielectric.[18] All calculations were conducted along M_S = 4 or 0 broken-symmetry surfaces, generated from an initial high-spin reference by flipping the spins on one or more Fe sites.

For **2** surface, 10 BS determinants were calculated: four on the S = 4 surface flipping the spins on one Fe atom, and six on the S = 0 surface flipping the spins on two Fe atoms. Fe0 is the three coordinate Fe site and Fe3 is the site identified crystallographically as being in the minority spin. The BS-DFT results support the conclusion from the crystallographic analysis: the S = 4 determinant in which Fe3 is in the minority spin is the lowest in energy.

Table S5.4: Relative energies of BS states for **2**

	S	Rel. energy (kcal/mol)
BS0	4	–[a]
BS1	4	+3.81
BS2	4	+1.60
BS3	4	0
BS01	0	+6.75
BS02	0	+7.30
BS03	0	+8.66
BS12	0	+9.71
BS13	0	+7.30
BS23	0	+8.11

[a]: converged to the BS4 solution

K. Crystallographic Details

1-FBDC: Crystallized from benzene/pentane in P–1 with a mixture of lattice benzene and pentane. The lattice solvent were disordered, and the disorder was modeled using similarity restraints on 1-2 and 1-3 distances and displacement parameters and rigid bond restraints.

1-EBDC: Microcrystals were examined using electron diffraction. The data sets (6) were indexed and merged using XDS, solved using ShelXS, and refined using ShelXL using scattering factors from the International tables.[19]

2-Cl: Crystallized from pentane in Pbca with pentane in the lattice. The lattice solvent was severely disordered and so solvent contributions to the diffraction pattern were removed with SQUEEZE.[20] The cluster core was additionally disordered over two positions, with the minor component being the cluster upside down; the cluster disorder was refine with similarity restraints on displacement parameters and rigid bond restraints. Several $SIAr^{Me,iPr}$ ligands were partially or entirely disordered, this disorder was modeled using similarity restraints on 1-2 and 1-3 distances and displacement parameters and rigid bond restraints.

[2-THF][BPh_4]: Crystallized from DFB/pentane in P–1 with solvent in the lattice. The lattice solvent was severely disordered and so solvent contributions to the diffraction pattern were removed with SQUEEZE.[20] The cluster core and coordinated THF ligand were disordered over two positions; the cluster disorder was refine with similarity restraints on displacement parameters

and rigid bond restraints. One $SIAr^{Me,iPr}$ ligand and the $[BPh_4]^-$ anion were entirely disordered, this disorder was modeled using similarity restraints on 1-2 and 1-3 distances and displacement parameters and rigid bond restraints.

2: One crystal was grown from cyclohexane/TMS and crystallized in P–1 with TMS in the lattice. Two of the lattice solvents were severely disordered and so solvent contributions to the diffraction pattern were removed with SQUEEZE.[20] The entire molecule was disordered over two positions, with the minor component being the cluster upside down; the cluster disorder was refined with similarity restraints on displacement parameters and rigid bond restraints on the entire molecule and similarity restraints on 1-2 and 1-3 distances for the $SIAr^{Me,iPr}$ ligands.

An additional crystal ($P2_1/n$) was grown from cooling a pentane solution of **2**, this crystal was of poorer quality but confirms the composition of **2**. In this structure, the lattice solvents were severely disordered and so solvent contributions to the diffraction pattern were removed with SQUEEZE.[20] Additionally, three ^{i}Pr groups on the $SIAr^{Me,iPr}$ ligand are disordered, this disorder was modeled using similarity restraints on 1-2 and 1-3 distances and displacement parameters and rigid bond restraints.

2-FBDC: Crystallized from cyclohexane/TMS in P–1 with TMS in the lattice. The structure shows some Q-peaks near the cluster (ca. 1 e^-) attributed to minor unresolved twin components.

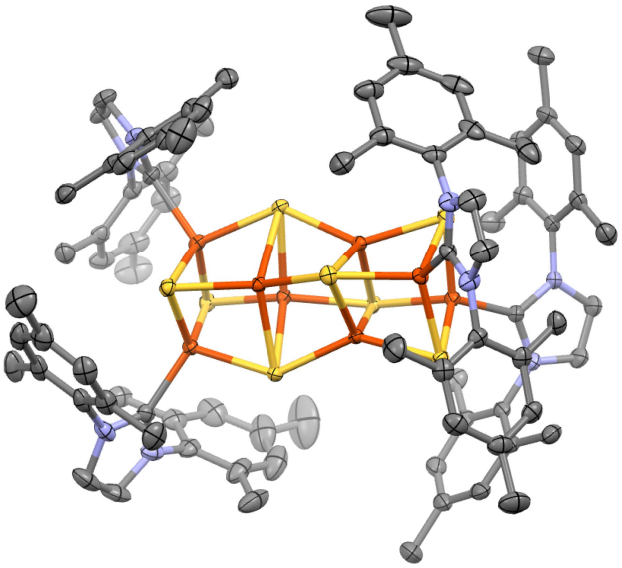

Figure S5.40: Crystallographic structure of **1-FBDC** with ellipsoids at the 50% probability level. Carbon (gray), nitrogen (blue), iron (orange), sulfur (yellow).

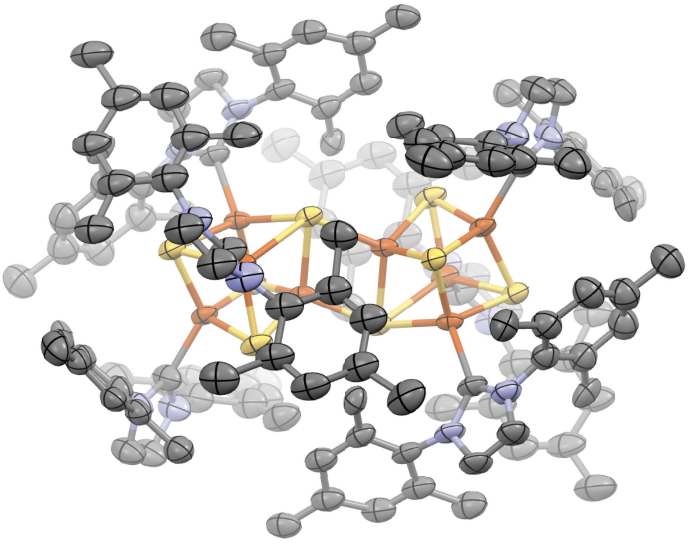

Figure S5.41: Crystallographic structure of **1-EBDC**with ellipsoids at the 50% probability level. Carbon (gray), nitrogen (blue), iron (orange), sulfur (yellow).

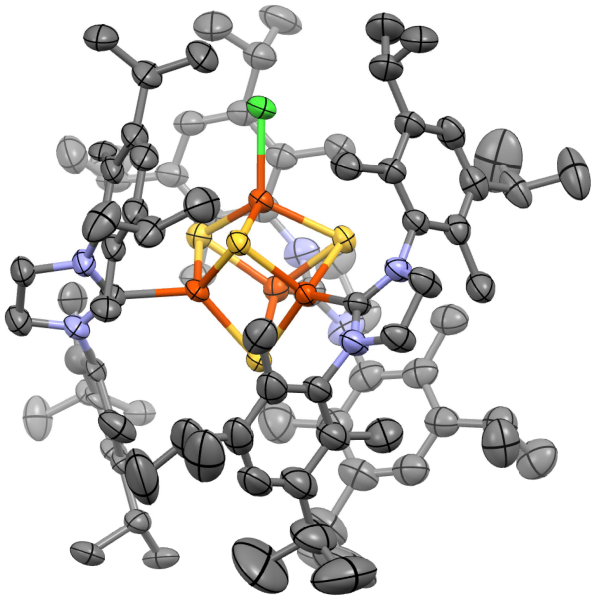

Figure S5.42: Crystallographic structure of **2-Cl** with ellipsoids at the 50% probability level. Carbon (gray), nitrogen (blue), iron (orange), sulfur (yellow).

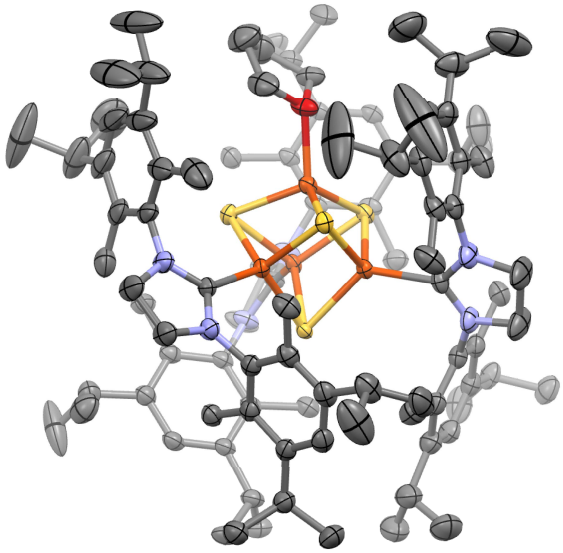

Figure S5.43: Crystallographic structure of [**2-THF**]$^{+}$ with ellipsoids at the 50% probability level. Carbon (gray), nitrogen (blue), iron (orange), sulfur (yellow), oxygen (red).

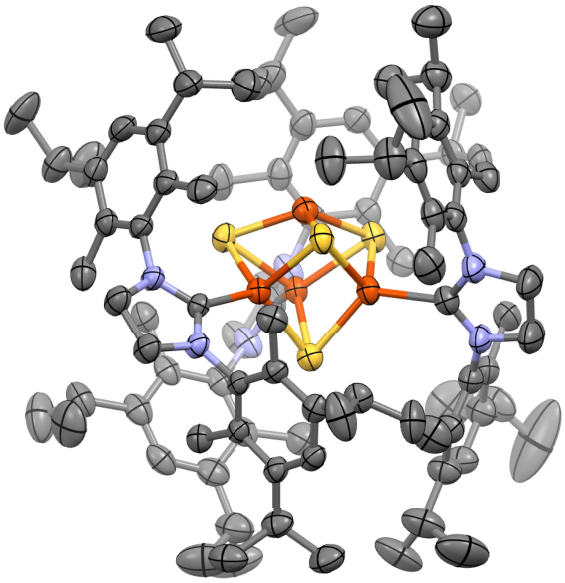

Figure S5.44: Crystallographic structure of **2** from cyclohexane/pentane with ellipsoids at the 50% probability level. Carbon (gray), nitrogen (blue), iron (orange), sulfur (yellow).

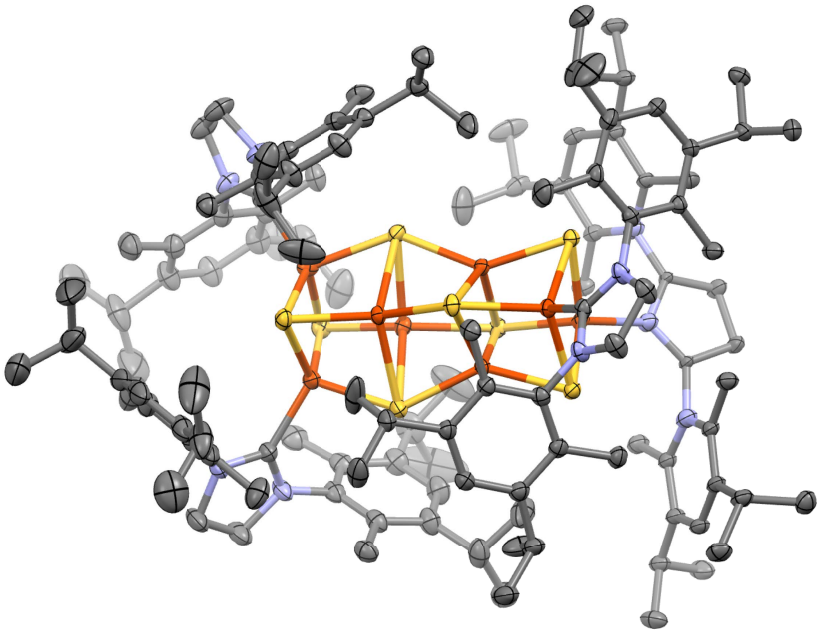

Figure S5.45: Crystallographic structure of **2-FBDC** with ellipsoids at the 50% probability level. Carbon (gray), nitrogen (blue), iron (orange), sulfur (yellow).

L. References

(1) Smallcombe, S. H.; Patt, S. L.; Keifer, P. A. WET Solvent Suppression and Its Applications to LC NMR and High-Resolution NMR Spectroscopy. *J. Magn. Reson. Ser. A* **1995**, *117* (2), 295–303.

(2) Stoll, S.; Schweiger, A. EasySpin, a Comprehensive Software Package for Spectral Simulation and Analysis in EPR. *J. Magn. Reson.* **2006**, *178* (1), 42–55.

(3) Prisecaru, I. WMOSS4 Mössbauer Spectral Analysis Software, www.wmoss.org.

(4) Hübschle, C. B.; Sheldrick, G. M.; Dittrich, B. ShelXle: A Qt Graphical User Interface for SHELXL. *J. Appl. Crystallogr.* **2011**, *44* (6), 1281–1284.

(5) Brown, A. C.; Suess, D. L. M. Controlling Substrate Binding to Fe_4S_4 Clusters through Remote Steric Effects. *Inorg. Chem.* **2019**, *58* (8), 5273–5280.

(6) Peters, J. C.; Johnson, A. R.; Odom, A. L.; Wanandi, P. W.; Davis, W. M.; Cummins, C. C. Assembly of Molybdenum/Titanium μ-Oxo Complexes via Radical Alkoxide C-O Cleavage. *J. Am. Chem. Soc.* **1996**, *118* (42), 10175–10188.

(7) Goh, C.; Segal, B. M.; Huang, J.; Long, J. R.; Holm, R. H. Polycubane Clusters: Synthesis of $[Fe_4S_4(PR_3)_4]^{1+,0}$ (R = Bu(t), Cy, Pr(i)) and $[Fe_4S_4]^0$ Core Aggregation upon Loss of Phosphine. *J. Am. Chem. Soc.* **1996**, *118* (47), 11844–11853.

(8) Moffett, R. B.; Tang, A. H. Skeletal Muscle Stimulants. Substituted Benzoic Acids. *J. Med. Chem.* **1968**, *11* (5), 1020–1022.

(9) Sridharan, A.; Brown, A. C.; Suess, D. L. M. A Terminal Imido Complex of an Iron–Sulfur Cluster. *Angew. Chem. Int. Ed.* **2021**, *60* (23), 12802–12806.

(10) McSkimming, A.; Suess, D. L. M. Dinitrogen Binding and Activation at a Molybdenum–Iron–Sulfur Cluster. *Nat. Chem.* **2021**, *13* (7), 666–670.

(11) Brown, A. C.; Suess, D. L. M. Valence Localization in Alkyne and Alkene Adducts of Synthetic $[Fe_4S_4]^+$ Clusters. *Inorg. Chem.* **2022**.

(12) Kim, Y.; Sridharan, A.; Suess, D. L. M. The Elusive Mononitrosylated $[Fe_4S_4]$ Cluster in Three Redox States. *Angew. Chem. Int. Ed.* **2022**.

(13) Kuveke, R. E. H. H.; Barwise, L.; Ingen, Y. Van; Vashisth, K.; Roberts, N.; Chitnis, S. S.; Dutton, J. L.; Martin, C. D.; Melen, R. L.; Van Ingen, Y.; Vashisth, K.; Roberts, N.; Chitnis, S. S.; Dutton, J. L.; Martin, C. D.; Melen, R. L. An International Study Evaluating Elemental Analysis. *ACS Cent. Sci.* **2022**, *8* (7), 855–863.

(14) Neese, F. The ORCA Program System. *Wiley Interdiscip. Rev. Comput. Mol. Sci.* **2012**, *2* (1), 73–78.

(15) Pantazis, D. A.; Chen, X. Y.; Landis, C. R.; Neese, F. All-Electron Scalar Relativistic Basis Sets for Third-Row Transition Metal Atoms. *J. Chem. Theory Comput.* **2008**, *4* (6), 908–919.

(16) Van Wüllen, C. Molecular Density Functional Calculations in the Regular Relativistic Approximation: Method, Application to Coinage Metal Diatomics, Hydrides, Fluorides and Chlorides, and Comparison with First-Order Relativistic Calculations. *J. Chem. Phys.* **1998**, *109* (2), 392–399.

(17) Weigend, F. Accurate Coulomb-Fitting Basis Sets for H to Rn. *Phys. Chem. Chem. Phys.* **2006**, *8* (9), 1057–1065.

(18) Barone, V.; Cossi, M. Conductor Solvent Model. *J. Phys. Chem. A* **1998**, *102* (97), 1995–2001.
(19) *International Tables for Crystallography Volume C: Mathematical, Physical and Chemical Tables*; Prince, E., Ed.; 2006.
(20) Spek, A. L. PLATON SQUEEZE: A Tool for the Calculation of the Disordered Solvent Contribution to the Calculated Structure Factors. *Acta Crystallogr. Sect. C Struct. Chem.* **2015**, *71*, 9–18.

Chapter 6. Redox Delocalization in [$MoFe_3S_4$] Clusters Mediated by Mo–Fe Bonding

Introduction:

The proliferation of life on Earth requires conversion of the most abundant form of nitrogen, N_2, to a bioavailable form, NH_3.[1] This essential reaction is mediated by the three nitrogenase isozymes: the Mo, V, and Fe-only nitrogenases (Figure 6.1).[1] The catalytic cofactors of the three isozymes are structurally similar Fe–S clusters but they differ in the identity of the homocitrate-bound metal center—FeMo-co contains Mo, FeV-co contains V, and FeFe-co contains only Fe.[1–4] These isozymes have different activities for their native reaction, N_2 reduction,[4–8] and also for non-native reactions such as acetylene and CO reduction (Figure 6.1).[9–14] Although the Mo nitrogenase is the most active and preferentially expressed when Mo is available,[8,15,16] all three are biologically relevant.[17–19]

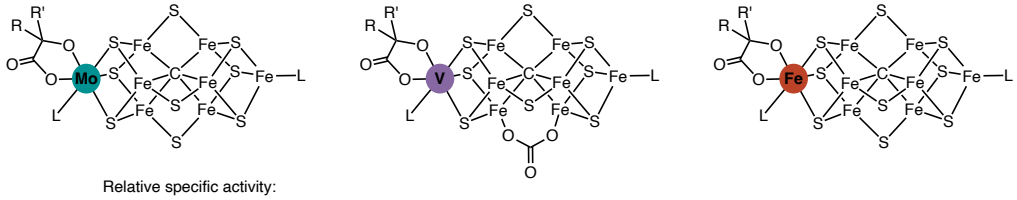

Figure 6.1. Nitrogenase isozymes containing FeMo-co, FeV-co, and FeFe-co have similar cofactor structures but different activities for substrate reduction.

Of the three isozymes, Mo nitrogenase was the first discovered[20,21] and remains the most thoroughly studied;[22,23] the role of the Mo center in catalysis has been debated and remains poorly understood. That Mo nitrogenase is the most well studied, combined with the proliferation of Mo-based N_2 complexes and N_2 reduction catalysts,[24–28] led to early hypotheses that Mo was important to N_2 fixation because Mo is the site of N_2 binding.[29,30] However, structural characterization of the MoFe protein,[31] as well as the existence of V and Fe-only nitrogenases, complicated this assumption. It is now more broadly thought that N_2 coordination likely occurs at one or more 'belt' Fe

sites. Evidence for N_2 binding at Fe includes (i) mutagenesis of residues proximal to the Fe sites perturbs dinitrogen reduction,[32] (ii) CO coordinates at the belt Fe sites,[11,33,34] (iii) the belt S atoms are exchangeable,[35] and (iv) several states with putative N_2 reduction intermediates bound to the belt Fe sites have been crystallographically characterized.[36–38] The plausibility of N_2 binding at one or more Fe sites in nitrogenase cofactors has been additionally bolstered by model chemistry, including mononuclear Fe–N_2 complexes,[39–41] Fe-based catalysts for N_2 reduction,[42] and Mo-Fe-S clusters that bind and activate N_2 at Fe.[43,44]

The building consensus that the belt Fe sites are the location of N_2 binding re-introduces questions of why Mo and V are incorporated into the nitrogenase cofactors. For example, how does the incorporation of these heterometals change the electronic structure of an Fe–S cluster relative to an all-Fe cluster, and how might these changes be responsible for the observed differences in N_2 reduction activity? Comparative studies of FeMo-co and FeV-co, as well as synthetic analogues, have suggested that the Fe centers in FeMo-co are more oxidized than the Fe centers in FeV-co.[45,46] In addition, it has been proposed that Mo forms stronger bonds to Fe than does V, leading to greater stability in turnover states with open coordination sites and weakly coordinating ligands.[45] However, it remains unclear how Mo and V may perturb the electronic structure relative to an all-Fe cluster and how this affects binding and activation of nitrogenase substrates.

To understand the fundamental differences in the electronic structure of a Fe-S cluster and Mo-Fe-S clusters, it is necessary to have a series of Mo-Fe-S and Fe-S clusters that are accessible in multiple oxidation states, where the Fe centers have the same coordination sphere, and the coordination sphere of Mo is occupied by a substitutionally inert ligand, so that the effects of varying a ligand on Fe can be assessed. We were particularly interested in how binding π-acidic ligands to $[MoFe_3S_4]$ and $[Fe_4S_4]$ clusters leads to unusual electronic structures, and therefore to explore the

differences in binding and activation of π-acidic ligands at a Fe–S clusters containing Mo compared to those containing only Fe, we pursued the synthesis of [$MoFe_3S_4$] clusters in which one of the Fe centers is coordinated to CO. These clusters may be directly compared to [Fe_4S_4]–CO clusters, which we recently reported contain low-valent Fe sites.[47]

Results

Our approach to synthesizing [$MoFe_3S_4$]–CO clusters began with the synthesis of $Cp^*MoFe_3S_4(IMes)_2Cl$ (**1-Cl**, IMes = 1,3-bis(2,4,6-trimethylphenyl)imidazol-2-ylidene) by treatment of $[PPh_4][Cp^*MoFe_3S_4Cl_3]$ with IMes and Cp_2Co in tetrahydrofuran (THF), analogous to the previously reported preparation of $Cp^*MoFe_3S_4(IPr)_2Cl$ (IPr = 1,3-bis(2,6-diisopropylphenyl)imidazol-2-ylidene).[43] To bind CO at one of the Fe sites, we took an analogous approach to that used for preparation of CO-bound [Fe_4S_4] clusters:[47] abstracting either Cl· or Cl^- from **1-Cl**. Reduction of **1-Cl** with $Ti(N[^tBu]Ar)_3$ (Ar = 3,5-dimethylphenyl)[48] in the presence of CO affords $Cp^*MoFe_3S_4(IMes)_2CO$ (**1-CO**) in 90% yield (Figure 6.2A); **1-CO** has an $S = 1/2$ ground spin state as established by EPR spectroscopy (Figure S6.11). Alternatively, abstraction of Cl^- from **1-CO** with $Na[BAr^F_4]$ (Ar^F = 3,5-bis(trifluoromethyl)phenyl) followed by treatment with CO yields the cationic, $[MoFe_3S_4]^{2+}$ CO-bound cluster $[Cp^*MoFe_3S_4(IMes)_2CO][BAr^F_4]$ ([**1-CO**][BAr^F_4],

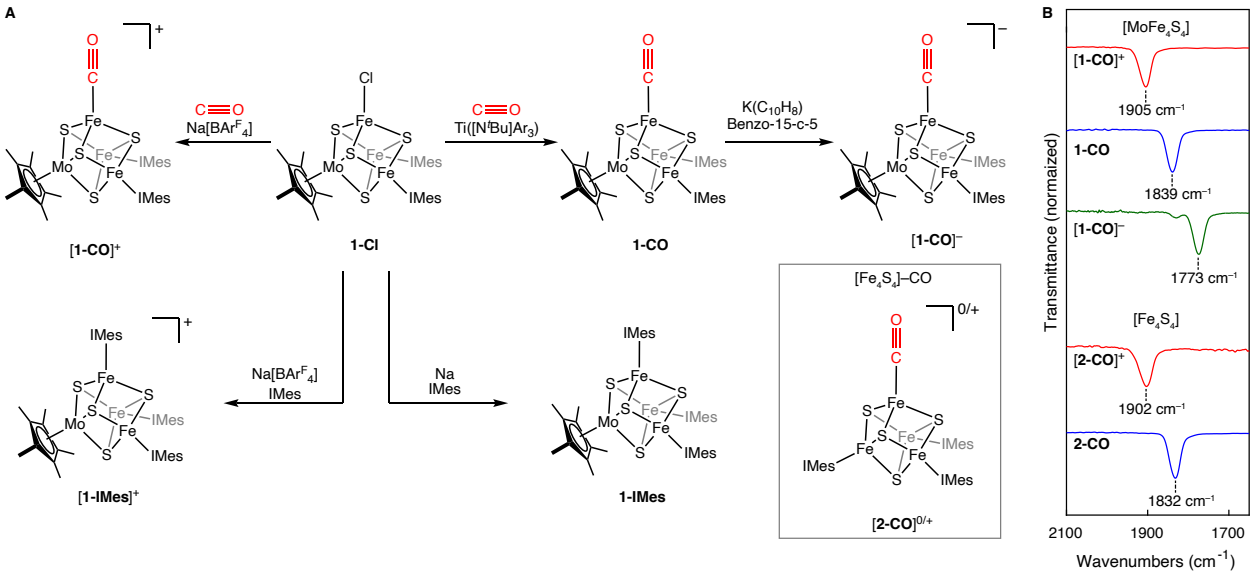

Figure 6.2. Synthesis and IR spectroscopy of [$MoFe_3S_4$] clusters. A) Synthesis of [**1-CO**]$^{-/0/+}$ and [**1-IMes**]$^{0/+}$ and structure of [**2-CO**]$^{0/+}$. B) IR spectra of [**1-CO**]$^{-/0/+}$ and [**2-CO**]$^{0/+}$ showing the similarity of ν(C–O) for **1-CO**/**2-CO** and [**1-CO**]$^+$/[**2-CO**]$^+$.

henceforth referred to as [**1-CO**]$^{+}$; Figure 6.2A), which has an $S = 0$ ground spin state established by SQUID magnetometry (Figure S6.12).

The infrared C–O stretching frequencies of **1-CO** and [**1-CO**]$^{+}$ are 1839 and 1905 cm^{-1} (Figure 6.2B), respectively, and are striking similar to those of the previously reported $[Fe_4S_4]^0$ and $[Fe_4S_4]^{+}$ analogues: $(IMes)_3Fe_4S_4CO$ (**2-CO**, 1832 cm^{-1}, Figure 6.2B and S6.7) and $[(IMes)_3Fe_4S_4CO][BAr^F{}_4]$ ([**2-CO**]$^{+}$, 1902 cm^{-1}, Figure 6.2B and S6.8). For **2-CO** and [**2-CO**]$^{+}$, it was shown that the high degree of C–O bond weakening is due to adoption of states in which the Fe_{CO} site has at least partial low-valent character;[47] the extremely similar C–O stretching frequencies for **1-CO** and [**1-CO**]$^{+}$ suggest a similar local electronic structure for the Fe_{CO} site in these $[MoFe_3S_4]$ clusters.

Cyclic voltammetry of **1-CO** showed a reversible oxidation at –1.45 V (vs. Fc/Fc^{+}, compared to –1.54 V for **2-CO**) and, unlike for **2-CO**, shows reversible reduction (at –2.40 V, Figure S6.20). Accordingly, we set out to reduce **1-CO**. Mixing **1-CO** with $K(C_{10}H_8)$ in THF followed by addition of 2 equiv benzo-15-crown-5 yields the anionic $[MoFe_3S_4]^0$ cluster $[K(Benzo\text{-}15\text{-}c\text{-}5)_2][Cp^*MoFe_3S_4(IMes)_2CO]$ ([**1-CO**]$^{-}$), which has a C–O stretching frequency of 1773 cm^{-1}, lower than that of **1-CO** by 66 cm^{-1} and consistent with increased π-backbonding to the CO ligand upon reduction of **1-CO** to [**1-CO**]$^{-}$ (Figure S6.9). Compound [**1-CO**]$^{-}$ has an $S = 0$ ground spin state determined by SQUID magnetometry.

To better understand the effects of CO coordination to [**1-CO**]$^{0/+}$, we used a similar strategy to that used to characterize the low valent sites in [**2-CO**]$^{0/+}$, comparing [**1-CO**]$^{0/+}$ to $[MoFe_3S_4]$ clusters in which the Fe centers are bound by only NHCs, and observing how the spectroscopic and structural properties of the clusters are affected by replacement of an NHC with CO, in particular looking at the differences between the NHC ligated sites in [**1-CO**]$^{0/+}$ and in all-NHC ligated

clusters. Therefore, we needed to synthesize [$MoFe_3S_4$] clusters that are structurally analogous [**1-CO**]$^{0/+}$ but with only NHC ligands. We prepared two clusters in which all three Fe sites are ligated by IMes; the first, Cp*$MoFe_3S_4$(IMes)$_3$ (**1-IMes**), was synthesized by addition of Na and IMes to **1-Cl** in benzene (Figure 6.2A). Its one-electron oxidized counterpart, [Cp*$MoFe_3S_4$(IMes)$_3$][$BAr^F{}_4$] ([**1-IMes**][$BAr^F{}_4$]), was synthesized by treatment of **1-Cl** with Na[$BAr^F{}_4$] and IMes in THF (Figure 6.2A). Compound **1-IMes** has an $S = 1/2$ ground spin state like **2-CO** and [**1-IMes**]$^+$ has an $S = 2$ ground spin state (typical for [$MoFe_3S_4$]$^{2+}$ clusters).

With the CO-bound [$MoFe_3S_4$] clusters and all-NHC ligated [Fe_4S_4] clusters in hand, we turned to structural characterization to assess how CO coordination affects the electronic structure of [**1-CO**]$^{-/0/+}$ (Figure 6.3A). To do so, we examined the structural differences between CO-bound clusters and homoleptic clusters in the same charge state. For example, the structural hallmarks of the intramolecular electron transfer that leads to low-valent Fe–CO configurations in [**2-CO**]$^{0/+}$ are contraction of the Fe(NHC)–S bond lengths (by ca. 0.06 Å) and the Fe–C(NHC) bond lengths (by

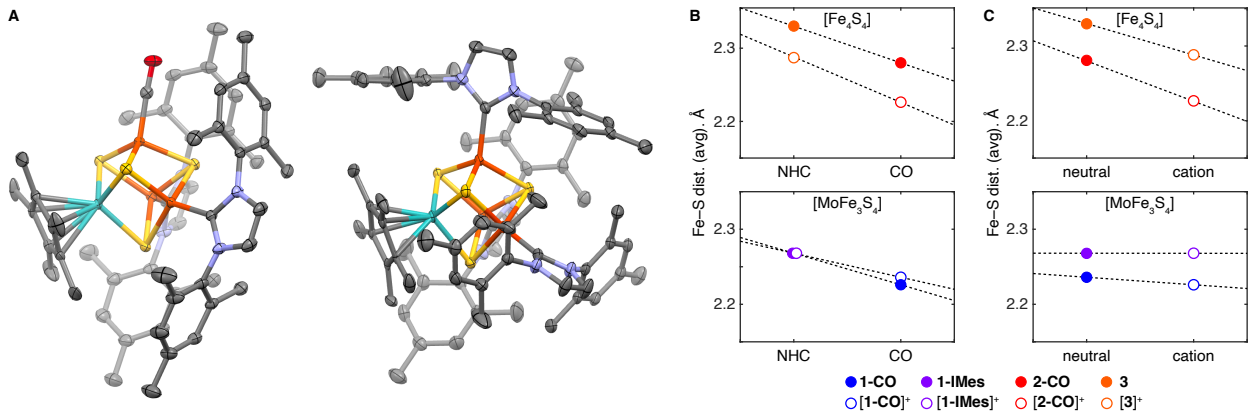

Figure 6.3. Structural characterization of [$MoFe_3S_4$] clusters. A) Crystallographic structures of **1-CO** (left) and **1-IMes** (right) with ellipsoids at the 50% probability level. Carbon (gray), nitrogen (blue), iron (orange), sulfur (yellow), molybdenum (teal), and oxygen (red). B) Plot of how Fe–S distances change upon replacement of a sulfur for CO in [Fe_4S_4] clusters ([**2-CO**]$^{0/+}$ and [**3**]$^{0/+}$, top) and in [$MoFe_3S_4$] clusters ([**1-CO**]$^{0/+}$ and [**1-IMes**]$^{0/+}$, bottom). C) Plot of how Fe–S distances change upon oxidation in [Fe_4S_4] clusters ([**2-CO**]$^{0/+}$ and [**3**]$^{0/+}$, top) and in [$MoFe_3S_4$] clusters ([**1-CO**]$^{0/+}$ and [**1-IMes**]$^{0/+}$, bottom).

ca. 0.04 Å) relative to homoleptic analogues in the same charge state ([(I^iPr^{Me})$_4$Fe$_4$S$_4$]$^{0/+}$, [**3**]$^{0/+}$, Table 6.1 and Figure 6.3B).[47,49] Similarly, the average Fe(NHC)–S bond length in **1-CO** (2.226(1) Å) is 0.042 Å shorter than the average Fe(NHC)–S bond length in **1-IMes** (2.268(6) Å, Table 6.1 and Figure 6.3B) and the average Fe(NHC)–S bond length in [**1-CO**]$^+$ (2.236 Å), is 0.032 Å shorter than the average Fe(NHC)–S bond length in **1-IMes** (2.268(6) Å, table 6.1). For **1-CO**, no contraction in the Fe–C(NHC) distance is observed (the average Fe–C(NHC) distance in **1-CO** (2.011(3)) and **1-IMes** (2.011(1)) are the same) but for [**1-CO**]$^+$ the Fe–C(NHC) distance contracts from 2.076(3) Å in [**1-IMes**]$^+$ to 2.043 in [**1-CO**]$^+$. There is no homoleptic comparison for the structure of anion [**1-CO**]$^-$, but compared to **1-IMes** it has longer Fe(NHC)–S bond lengths (2.249(3) Å) and shorter Fe–C(NHC) bond lengths (1.970(6) Å), consistent with reduction of the cluster. Across all five compounds ([**1-CO**]$^{-/0/+}$ and [**1-IMes**]$^{0/+}$) only minor changes in the Mo–C(Cp*) and Mo–S distances were observed (Table 6.1). Overall, the contraction of the average Fe–S(NHC) and Fe–C(NHC) distances upon coordination of CO suggests that, like seen in [**2-**

Table 6.1. Structural Parameters for [**1-CO**]$^{-/0/+}$, [**1-IMes**]$^{0/+}$, [**2-CO**]$^{0/+}$, and [**3**]$^{0/+}$

	NHC-bound Fe (avg.)		CO-bound Fe (avg.)		Mo (avg).	
	Fe–C (Å)	Fe–S (Å)	Fe–C (Å)	Fe–S (Å)	Mo–C (Å)	Mo–S (Å)
[**1-CO**]$^-$	1.970(6)	2.249(3)	1.740(5)	2.237(2)	2.41(1)	2.346(2)
[**1-CO**]^0	2.011(3)	2.226(1)	1.759(4)	2.207(2)	2.38(2)	2.344(1)
[**1-CO**]$^+$	2.043	2.236	1.796	2.194	2.37	2.338
[**1-IMes**]^0	2.011(1)	2.2679(7)	–	–	2.41(2)	2.3517(4)
[**1-IMes**]$^+$	2.076(3)	2.268(6)	–	–	2.37(1)	2.341(1)
[**2-CO**]^0	2.053(2)	2.280(2)	1.772(2)	2.259(1)	–	–
[**2-CO**]$^+$	2.029(2)	2.226(2)	1.789(2)	2.199(1)	–	–
[**3**]^0	2.109(5)	2.330(3)	–	–	–	–
[**3**]$^+$	2.060(5)	2.288(2)	–	–	–	–

CO]$^{0/+}$, coordination of CO to the [$MoFe_3S_4$] clusters results in formation of low-valent Fe–CO sites.

Although the comparisons between the CO-bound and homoleptic [$MoFe_3S_4$] clusters in the same charge states (*i.e.*, between **1-CO** and **1-IMes** and between [**1-CO**]$^+$ and [**1-IMes**]$^+$) follow the same general trends reported for the [Fe_4S_4] clusters, the trends *within* a redox series (i.e. [**1-CO**]$^-$/**1-CO**/[**1-CO**]$^+$ and **1-IMes**/[**1-IMes**]$^+$) are quite different from those seen for [Fe_4S_4] clusters (Figure 6.3C). In the [Fe_4S_4] clusters examined above, the average Fe–S distances generally contract upon oxidation. In **2-CO**, the average Fe–S distance (2.274(4) Å) decreases by 0.054 Å upon oxidation to [**2-CO**]$^+$ (2.219(4) Å). Similarly, the average Fe–S distance in **3** (2.330(3) Å) decreases by 0.042 Å upon oxidation to [**3**]$^+$ (2.288(2) Å, Figure 6.3B). These trends are consistent with the typical behavior of [Fe_4S_4] clusters: oxidation generally leads to contraction of the Fe–S bonds.[50] Unlike the [Fe_4S_4] clusters, among the [$MoFe_3S_4$] clusters reported herein the core bond metrics do not respond predictably to redox events. For example, between [**1-CO**]$^{0/+}$, the average Fe–S bond length only varies by 0.025 Å (from 2.236(4) Å to 2.226(4) Å) and in fact the average Fe–S bond lengths in **1-IMes** and [**1-IMes**]$^+$ are not distinguishable (2.2679(7) and 2.268(6) Å, respectively, Figure 6.3C). That the structural changes of the [$MoFe_3S_4$] clusters following redox events are attenuated compared to those of the [Fe_4S_4] clusters—even for clusters containing only NHC ligands—suggests that, although [Fe_4S_4] and [$MoFe_3S_4$] clusters activate CO via formation of low-valent Fe_{CO} sites, the distribution of added electrons/holes across the [Fe_4S_4] and [$MoFe_3S_4$] clusters are quite different. As a result, while the [Fe_4S_4] and [$MoFe_3S_4$] bond metrics change similarly when an NHC is replaced by CO, [Fe_4S_4] and [$MoFe_3S_4$] clusters respond very differently to changing oxidation states.

Mössbauer spectroscopy provides additional insight into the changes in bonding within Fe-S clusters upon successive redox events and upon replacement of an NHC with CO. The [Fe_4S_4] clusters display typical trends, with oxidation of either **2-CO** or **3** leading to a change in $\delta_{avg.}$ of 0.12 mm s^{-1}. Additionally, replacement of an NHC by CO led to a change in δ_{avg} of 0.12 mm s^{-1} for the NHC-bound Fe sites, comparing clusters in the same oxidation state,[47] which was attributed to oxidation of the NHC-bound sites upon formation of a low-valent Fe–CO site.

The Mössbauer spectra of [**1-CO**]$^{-/0/+}$ and [**1-IMes**]$^{0/+}$ display the same disparities as the structural parameters for comparisons between different coordination spheres in the same charge state versus comparisons between different charge states with the same coordination sphere (Figure 6.4A and 6.4B). The isomer shifts of the [$MoFe_3S_4$] clusters in the same charge state follow the expected trends upon replacement of an NHC with CO: the NHC-ligated sites in **1-CO** have a lower $\delta_{avg.}$ (0.41 mm s^{-1}) than those in **1-IMes** ($\delta_{avg.}$ = 0.48 mm s^{-1}) and the NHC-ligated sites in [**1-CO**]$^+$ have a lower $\delta_{avg.}$ (0.36 mm s^{-1}) than those in [**1-IMes**]$^+$ ($\delta_{avg.}$ = 0.49 mm s^{-1}). However, across the series [**1-CO**]$^{-/0/+}$ the average isomer shift of the NHC-bound sites varies by only 0.05 mm s^{-1}, less than half the variance observed over a one electron oxidation from **2-CO** to [**2-CO**]$^+$. We considered that in [**1-CO**]$^{-/0/+}$ perhaps increased π-backbonding with CO or Fe–CO centered redox events could explain the attenuation of the changes in the isomer shift upon oxidation. However, the changes in ν(C–O) across both redox series are comparable (ca. 70 cm^{-1} per electron oxidation) and there are no clear structural changes at the Fe–CO unit that would support this hypothesis, since the Fe–CO bond distance changes in [**1-CO**]$^{-/0/+}$ are similar to those seen for [**2-CO**]$^{0/+}$.

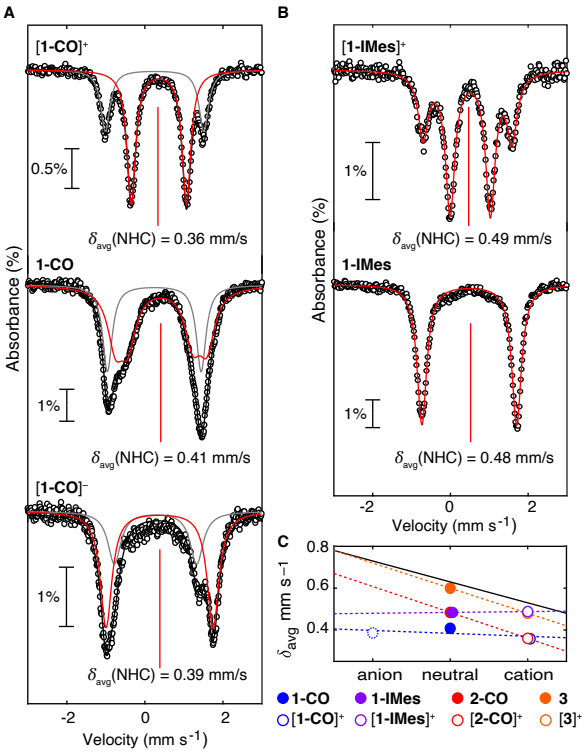

Figure 6.4. Mössbauer characterization of [$MoFe_3S_4$] clusters. A) Mössbauer spectra of [**1-CO**]$^+$ (top), **1-CO** (middle), [**1-CO**]$^-$ (bottom) with the Fe–NHC sites in red and the Fe–CO site in gray. B) Mössbauer spectra of [**1-IMes**]$^+$ (top), and **1-IMes** (bottom) with simulation (red). C) Plot of δ_{avg} (Fe–NHC) for [$MoFe_3S_4$] clusters **1-IMes**/[**1-IMes**]$^+$ (purple), [**1-CO**]$^-$/ [**1-CO**]/ [**1-CO**]$^+$ (blue), **2-CO**/[**2-CO**]$^+$ (red), and **3**/ [**3**]$^+$ (orange). The black line is the linear relationship between isomer shift and oxidation state reported in ref. 50.

Table 6.2. Mössbauer parameters for [**1-CO**]$^{-/0/+}$ and [**3**]$^{0/+}$

	NHC-bound Fe (avg.)		CO-bound Fe	
Compound	δ (mm s^{-1})	$\lvert\Delta E_Q\rvert$ (mm s^{-1})	δ (mm s^{-1})	$\lvert\Delta E_Q\rvert$ (mm s^{-1})
[**1-CO**]$^-$	0.39	2.741	0.28	2.109
[**1-CO**]^0	0.41	2.003	0.24	2.402
[**1-CO**]$^+$	0.36	1.414	0.25	2.520
[**3**]^0	0.48	2.438	–	–
[**3**]$^+$	0.49	1.452	–	–

Even more strikingly, in **1-IMes** and [**1-IMes**]$^+$—in which all the Fe centers are ligated by NHC ligands, removing any complications from variable Fe–CO backbonding—the Fe centers have nearly identical δ_{avg}. In fact, oxidation from **1-IMes** ($\delta_{avg.}$ = 0.48 mm s^{-1}) to [**1-IMes**]$^+$ ($\delta_{avg.}$

= 0.49 mm s^{-1}) actually leads to a small *increase* in $\delta_{avg.}$ instead of the predicted ca. 0.1 mm s^{-1} decrease (Figure 6.4C). Here, it is more difficult to rationalize the lack of a change in the Mössbauer isomer shifts by changes in the extent of π-backbonding because NHCs are relatively poor π-acceptors compared to CO. Despite the apparent lack of change in the average isomer shift, $|\Delta E_Q|_{avg.}$ appears highly responsive to the change in oxidation state, decreasing by 1.3 mm s^{-1} over the series [**1-CO**]$^{-/0/+}$ and 0.99 mm s^{-1} from [**1-IMes**]^0 to [**1-IMes**]$^+$. In comparison, the changes in $|\Delta E_Q|_{avg}$ for the [Fe_4S_4] clusters are much smaller: $|\Delta E_Q|_{avg}$ decreases by 0.63 mm s^{-1} from **1-IMes** to [**1-IMes**]$^+$ but only by 0.07 mm s^{-1} from **2-CO** to [**2-CO**]$^+$.

The Mössbauer spectra of the [$MoFe_3S_4$] clusters suggest that, unlike [Fe_4S_4] clusters, redox events in the cluster are not localized to the Fe sites, so we turned to X-ray absorption spectroscopies (specifically Mo K-edge HERFD-XAS and Fe-and S K-edge XAS) to assess if the redox events in the series [**1-CO**]$^{-/0/+}$ and [**1-IMes**]$^{0/+}$ could be occurring primarily on the Mo or S centers. We first considered the relevant XAS spectra for the [Fe_4S_4] complexes **2-CO** and [**4**]$^{0/+}$ to assess if the systematic bond-length changes we observed by X-ray crystallographic analysis and δ_{avg} changes we observed from Mössbauer spectroscopic analysis are consistent with the changes seen in the XAS spectra (collection of XAS spectra for [**2-CO**]$^+$ was precluded by its instability under vacuum).

The challenges in directly relating Fe K-edge energies to oxidation state in multimetallic clusters with metal-metal interactions, such as Fe–S clusters, are well documented,[51,52] and thus we expected the Fe K-edge XAS spectra to be of limited utility. Comparisons of the three [Fe_4S_4] clusters (**2-CO**, **3**, and [**3**]$^+$) demonstrate the complexities of interpreting the XAS spectra across Fe–S cluster oxidation states. The Fe K-edge XAS spectra of **3** shows two pre-edge features at 7111.4 eV and 7113.2 eV and a rising edge at 7116.8 eV (Figure 6.5A, Table 6.3). Oxidation of **3**

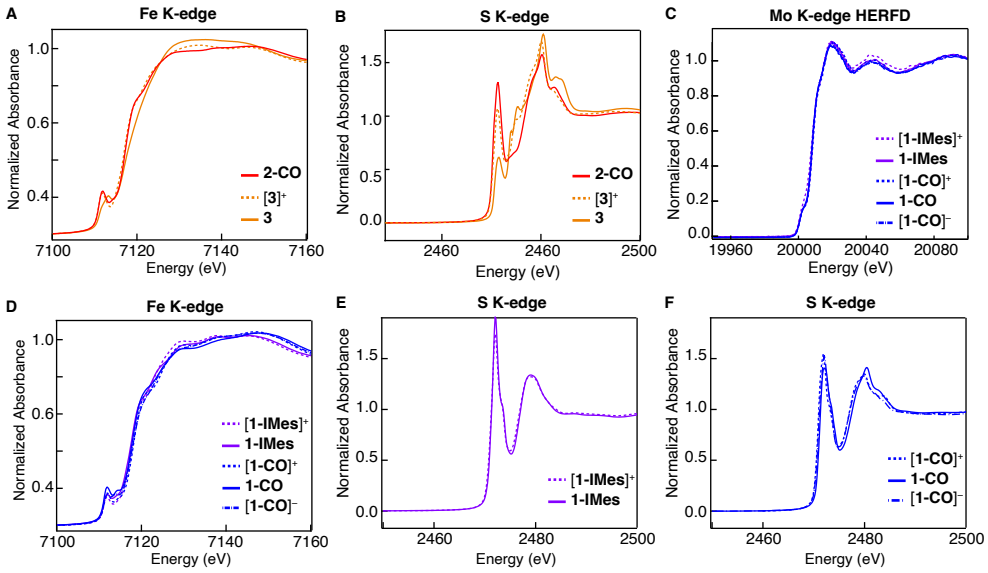

Figure 6.5. XAS spectra for [Fe_4S_4] and [$MoFe_3S_4$] compounds. A) Fe K-edge XAS for for **2-CO**, [**3**]$^+$ and **3**. B) S K-edge XAS for **2-CO**, [**3**]$^+$ and **3**. C) Mo K-edge HERFD-XAS for [**1-IMes**]$^+$, **1-IMes**, [**1-CO**]$^+$, **1-CO**, and [**1-CO**]$^-$. D) Fe K-edge XAS for [**1-IMes**]$^+$, **1-IMes**, [**1-CO**]$^+$, **1-CO**, and [**1-CO**]$^-$. E) S K-edge XAS for [**1-IMes**]$^+$ and **1-IMes** F) S K-edge XAS for [**1-CO**]$^+$, **1-CO**, and [**1-CO**]$^-$.

to [**3**]$^+$ results in a change in the pre-edge to a single feature at 7111.4 eV; the rising edge remains constant at 7116.8 eV. That there is no change in the rising edge energy contradicts simple trends in rising edge energies,[53] since oxidation is expected to increase the energy of the rising edge, but is consistent with previous work on Fe–S clusters in which it was found that oxidation does not predictably lead to changes in the rising edge position.[51] The white line intensity in Fe K-edge XAS at 7125 eV has previously been observed to decrease upon oxidation of Fe–S clusters; the origin of this trend is not yet understood.[51,52,54] We note, however, that no difference in the white line intensity for **3** and [**3**]$^+$ at 7125 eV is observed. Complex **2-CO** has a nearly identical Fe K-edge spectrum to [**3**]$^+$, with only a single pre-edge feature at 7111.5 eV (Table 6.3).

S K-edge XAS spectroscopy has previously been demonstrated to be an excellent marker of oxidation state and Fe–S covalency in Fe–S clusters.[55] The S K-edge spectra of the [Fe_4S_4] compounds **2-CO**, **3**, and [**3**]$^+$ can be interpreted in a straightforward manner (Figure 6.5B, Table

Table 6.3. XAS data for $[Fe_4S_4]$ and $[MoFe_3S_4]$ clusters

	Mo		Fe		S		
	Pre-edge energy (eV)	Edge energy (eV)	Pre-edge energy (eV)	Edge energy (eV)	Pre-edge energy (eV)	Area	% covalency
2-CO	–	–	7111.5	7116.9	2471.95	2.10(1)	32%
3	–	–	7111.4 7113.2	7116.8	2472.23	1.00(1)	15%
[**3**]$^+$	–	–	7111.4	7116.8	2472.06	1.62(1)	25%
[**1-CO**]$^-$	20002.2	20008.0	7111.6 7113.5	7117.2	2472.25	3.59(1)	55%
1-CO	20002.3	20008.0	7111.7 7113.9	7117.8	2472.56	3.79(4)	58%
[**1-CO**]$^+$	20002.3	20009.0	7111.5 7114.3	7118.2	2472.29	3.6(1)	55%
1-IMes	20002.0	20008.0	7111.5	7117.8	2477.05	3.5(1)	53%
[**1-IMes**]$^+$	20002.0	20008.0	7111.6	7117.9	2577.10	3.56(4)	54%

6.3). In particular, the intensity of the pre-edge feature (corresponding to a 1s to 3p transition that gains intensity from mixing the filled S 3p orbitals with partially filled metal d-orbitals) can be directly related to the average percent S 3p character in the d-manifold and therefore to the covalency of the M–S bonds.[56,57] As such, as the oxidation state of the cluster increases, the M–S covalency typically increases, leading to an increase in the integrated area of the pre-edge feature in the S K-edge spectra.[56] Examination of the XAS spectra of **3** and [**3**]$^+$ demonstrate this exact trend: the intensity of the pre-edge feature in the S K-edge spectrum of **3** is relatively weak (1.00(1) integrated area, corresponding to 15% covalency per Fe–S bond). Upon oxidation to [**3**]$^+$, the intensity of the pre-edge feature increases dramatically to 1.62(1) integrated area, corresponding to 25% covalency—a 10% increase in covalency at each Fe–S bond. Both **3** and [**3**]$^+$ have lower Fe–S covalency than reported for $[Fe_4S_4Cl_4]^{2-}$ ($[Fe_4S_4]^{2+}$ cluster, 39% covalency),[56] consistent with their lower oxidation states. In **2-CO**, the intensity of the pre-edge feature is even greater at 2.10(1) integrated area (32 % covalency); this further increase in intensity is attributed both to oxidation of the NHC-bound Fe sites, as observed from Mössbauer spectroscopy, leading to increased

Fe_{NHC}–S covalency, as well as increased covalency of the Fe–S bonds at the Fe_{CO} site due to the highly electron withdrawing CO ligand. The increased Fe–S covalency at the Fe_{CO} site is also apparent in the X-ray crystallographic structure of **2-CO** by the shortening of the Fe–S bonds at that site relative to the NHC-ligated sites (Table 6.1).

Having demonstrated from analysis of the XAS spectra of **2-CO**, **3**, and [**3**]$^{+}$ that both increasing the oxidation state of $[Fe_4S_4]$ clusters and coordination of an electron withdrawing CO ligand reliably lead to predictable changes the S K-edge XAS spectra in particular, we returned to analysis of the $[MoFe_3S_4]$ clusters.

First, examination of Mo K-edge data reveals that all five compounds ([**1-CO**]$^{-/0/+}$ and [**1-IMes**]$^{0/+}$) have nearly superimposable spectra (Figure 6.5C, Table 6.3), characterized by a weak pre-edge feature between 20,002.0 and 20,002.3 eV (the weakness being consistent with a pseudo-octahedral coordination environment) and a rising edge at 20,008.0 eV. These features are extremely similar to those observed for $[TpMoFe_3S_4Cl_3]^{-}$, for which the Mo HERFD XAS shows a rising edge at 20,009.1 eV and a weak pre-edge feature at 20,002.1 eV.[58] The nearly identical Mo K-edge HERFD-XAS spectra for $[MoFe_3S_4]$ clusters across four redox states—from $[MoFe_3S_4]^{3+}$ in $[TpMoFe_3S_4Cl_3]^{-}$ to $[MoFe_3S_4]^{0}$ in [**1-CO**]$^{-}$—suggests that Mo remains in approximately the same oxidation state in $[MoFe_3S_4]$ clusters over many redox states. This is consistent with the minor changes in the Mo–C(Cp*) and Mo–S distances (Table 6.1) over the series of compounds reported herein and inconsistent with redox events occurring at Mo.

There are minor changes to the Fe K-edge XAS spectra between the five $[MoFe_3S_4]$ cluster: the rising edge energies are very similar across oxidation states, and the energy of the rising edge increases slightly with increasing oxidation state (Table 6.3, Figure 6.5D). Similarly to **3** and [**3**]$^{+}$, the white line intensity at 7125 eV does not appear to trend with oxidation state for either the [**1-**

CO]$^{-/0/+}$ redox series or the [**1-IMes**]$^{0/+}$ redox series; in both series, the white line intensity is approximately constant. Due to the difficulty in interpreting the Fe XAS spectra of multimetallic Fe complexes, as noted for the [Fe_4S_4] clusters, we do not comment further on the Fe XAS spectra.

As described above, S K-edge XAS spectra provide more reliable insight into oxidation state and Fe–S covalency in Fe–S clusters than Fe K-edge XAS spectra. Based on the changes to the S K-edge XAS spectra observed for [**3**]$^{0/+}$ and [**2-CO**], we predicted that as the [$MoFe_3S_4$] compounds become more oxidized, the S-K edge intensity would increase. Beginning with [**1-IMes**]$^{0/+}$, the S-K edge intensity (3.5(1) and 3.56(4) integrated area, respectively) is significantly higher than seen for the [Fe_4S_4] compounds (Table 6.3, Figure 6.5E), corresponding to higher M–S covalency in the [$MoFe_3S_4$] compounds (53% and 54% covalency, respectively). There is no change in the covalency (1%) upon oxidation of **1-IMes** to [**1-IMes**]$^+$; for comparison upon oxidation of **3** to [**3**]$^+$ the covalency increases significantly (10%). Turning to the CO-bound clusters [**1-CO**]$^{-/0/+}$, all three complexes have similar pre-edge intensity to [**1-IMes**]$^{0/+}$ (integrated areas of 3.59(1) for [**1-CO**]$^-$, 3.79(4) for **1-CO**, and 3.6(1) for [**1-CO**]$^+$, Table 6.3 and Figure 6.5E). The pre-edge intensities correlate to high covalencies similar to those observed for **1-IMes** to [**1-IMes**]$^+$: 55% for [**1-CO**]$^-$, 58% for **1-CO**, and 55% for [**1-CO**]$^+$. In comparison, for the [Fe_4S_4] clusters, **2-CO** has a much more intense pre-edge feature in the S K-edge XAS than [**3**]$^{0/+}$ (Table 6.3). Additionally, the magnitude of the difference between clusters in the same charge state is much smaller; indeed, the M-S covalency is invariant across the [**1-CO**]$^{-/0/+}$ series. In comparison, the difference in covalency between **3** and **2-CO** is 17%. Overall, the magnitude of changes in the S K-edge XAS spectra of the [$MoFe_3S_4$] clusters, both (A) across several redox events and (B) upon substitution of an NHC for CO, is greatly attenuated compared the magnitude of changes observed for [Fe_4S_4] complexes.

At this point, we can synthesize the information gleaned from the structural parameters, Mössbauer spectra, and Mo/Fe/S XAS spectra of [**1-IMes**]$^{0/+}$ and [**1-CO**]$^{-/0/+}$. Replacement of an NHC with CO in the same cluster charge state (*i.e.,* comparing **1-CO** with **1-IMes** and [**1-CO**]$^{+}$ with [**1-IMes**]$^{+}$) leads to similar contraction in the Fe–S bonds and increase in $\delta_{avg.}(Fe_{IMes})$ as observed for [Fe_4S_4] clusters (**2-CO**/**3** and [**2-CO**]$^{+}$/[**3**]$^{+}$); these changes are hallmarks of formation of low-valent Fe_{CO} sites. Consistent with the formation of low-valent Fe_{CO} sites, the degree of CO bond weakening is very similar in **1-CO**/**2-CO** and [**1-CO**]$^{+}$/[**2-CO**]$^{+}$. However, the CO-bound clusters [**1-CO**]$^{-/0/+}$ and the homoleptic NHC-bound clusters [**1-IMes**]$^{0/+}$ both show greatly attenuated structural/spectroscopic changes within a redox series compared to the [Fe_4S_4] clusters: there is little contraction of the core structural metrics and little change in $\delta_{avg.}$ upon oxidation of [**1-CO**]$^{-}$ to **1-CO** to [**1-CO**]$^{+}$ or upon oxidation of **1-IMes** to [**1-IMes**]$^{+}$. Overall, it appears that addition of redox equivalents to the [$MoFe_3S_4$] clusters reported herein do not lead to the major structural and spectroscopic changes that are well documented for the addition of redox equivalents to [Fe_4S_4] clusters.

Discussion

Structural and spectroscopic analyses of [$MoFe_3S_4$] compounds with and without CO ligands reveal that low-valent states are accessible in MoFe–S clusters just like in Fe–S clusters, enabling coordination and activation of π-acidic ligands like CO. Such low-valent states may also be relevant to activation of N_2 and CO in the recently reported [$MoFe_3S_4$]–N_2, [Mo_3FeS_4]–N_2, and [Mo_3FeS_4]–CO complexes.[43,44]

More curiously, this study has also revealed that these [$MoFe_3S_4$] clusters, even when supported by relatively innocent ligands such as NHCs (*i.e.*, in **1-IMes** and [**1-IMes**]$^+$), do not show significant structural or spectroscopic changes over addition of redox equivalents. The structures of **1-IMes** and [**1-IMes**]$^+$ are unusually similar: upon oxidation the Fe–S distances do not change, the Mo–S distances contract by 0.01 Å and the Fe–C(NHC) distances lengthen by 0.065 Å. In contrast, the structures of [Fe_4S_4] clusters obey well-established trends, with Fe–S distances and Fe–C(NHC) distances typically decreasing upon oxidation. The structures of the [Fe_4S_4] clusters **3** and [**3**]$^+$ are likewise consistent with such trends; upon oxidation the Fe–S distances contract by 0.042 Å and the Fe–C(NHC) distances by 0.049 Å.

The same absence of significant redox trends is apparent in the Mössbauer spectra and the Mo/Fe/S K-edge XAS spectra of **1-IMes** and [**1-IMes**]$^+$ (as well as [**1-CO**]$^{-/0/+}$)—there are very minor differences between structurally analogous clusters in different oxidation states. Again, the [Fe_4S_4] clusters display more typical redox trends, with $\delta_{avg.}$ decreasing by 0.12 mm s^{-1} and the Fe–S covalency (calculated from the the S K-edge XAS spectrum) increasing by 10% upon oxidation of **3** to [**3**]$^+$.

Compared to [Fe_4S_4] clusters, less is reported about the redox trends in structural and spectroscopic parameters of [$MoFe_3S_4$] clusters. However, the reported redox series for isostructural

[$MoFe_3S_4$] clusters demonstrate typical behavior intermediate between typical [Fe_4S_4] clusters and the [$MoFe_3S_4$] clusters reported herein. For example, for the one oxidation redox couple relating $[TpMoFe_3S_3Cl_3]^{2-}$ and $[TpMoFe_3S_3Cl_3]^{-}$, the average Fe–S distance decreases by 0.018 Å (from 2.282 Å to 2.264 Å) and $\delta_{avg.}$ decreases by 0.11 mm s^{-1} (whereas a change of 0.16 mm s^{-1} would be predicted for one electron distributed over three Fe sites).[59]

The results reported herein demonstrate that the trends delineated for [Fe_4S_4] clusters are either attenuated or break down when translated to [$MoFe_3S_4$] clusters. Moreover, the characterization of [$MoFe_4S_4$] clusters reported herein established the difficulty in understanding the redox behavior of [$MoFe_3S_4$] clusters: no clear trends in metal oxidation state for either Mo or Fe or in M–S bonding are observed by Mo/Fe/S XAS spectroscopy, Mössbauer spectroscopy, or X-ray structural analysis of [**1-CO**]$^{-/0/+}$ and [**1-IMes**]$^{0/+}$. If all spectroscopic and structural data indicate no change to the effective oxidation state of the core atoms over successive redox events, then where are the electrons coming from/going to?

We hypothesize that the lack of observable spectroscopic changes and structural changes over the redox series of [$MoFe_3S_4$] compounds compared to [Fe_4S_4] complexes may be due to increased metal-metal bonding in the [$MoFe_3S_4$] clusters, mediated by the larger and relatively diffuse d-orbitals of Mo compared to Fe. Typical [Fe_4S_4] clusters containing tetrahedral Fe sites have largely been described using an exchange-coupled system framework; that is, the cluster is described as four metal centers interacting primarily via superexchange coupling mediated by the bridging sulfur atoms (as well as double exchange within mixed-valent Fe^{3+}/Fe^{2+} pairs). In this case, activation of strong π-acids such as CO requires a discrete electron transfer from one Fe site to another (Figure 6.6A). However, for Mo, we argue that incorporation of a larger transition metal increases the importance of direct metal-metal bonding, pushing the [$MoFe_3S_4$] cluster towards a

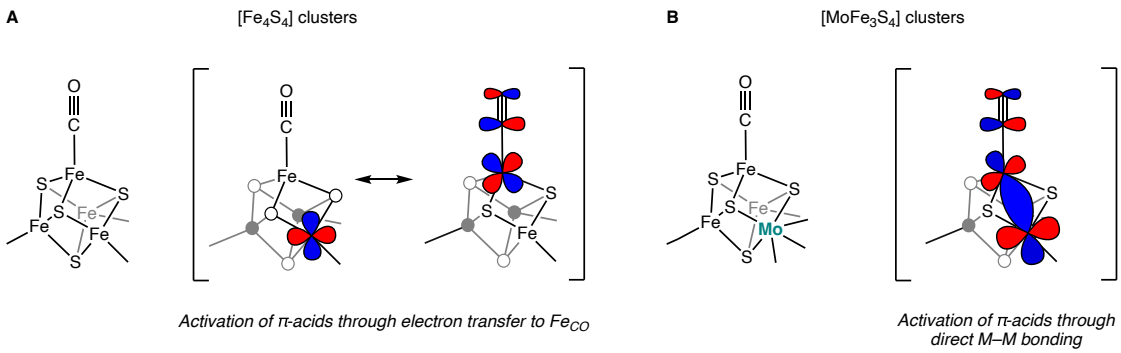

Figure 6.6. Bonding description for activation of π-acids at Fe–S clusters. A) In Fe–S clusters, bonding with π-acids is driven by electron hopping between Fe sites. B) In MoFe–S clusters, increased direct metal-metal bonding contributes electron density towards activation of π-acidic ligands.

regime best described as containing covalent metal-metal bonds and away from a regime that can be described strictly though Heisenberg exchange coupling and electron hopping (Figure 6.6B). That Mo-S clusters exhibit greater covalency has been previously demonstrated for open-cuboidal $[Mo_3S_4]$ clusters, which calculations show are best described as metal-metal bonded rather than coupled via superexchange.[60] This covalency explains the disparities between the trends observed for $[Fe_4S_4]$ clusters (here, and extensively in the literature) and those for $[MoFe_3S_4]$ clusters—the exchange coupling that results in the well-understood redox behavior of $[Fe_4S_4]$ clusters is not sufficient to describe the bonding in $[MoFe_3S_4]$ clusters.

That highly covalent systems display unexpected redox trends in their structural parameters is well established in mononuclear systems. For example, it has been demonstrated that for Fe–N_2 and Fe–CO complexes supported by phosphine ligands, over three redox states $[Fe–L]^{-/0/+}$, the Mössbauer isomer shift becomes higher as the system is oxidized—opposite the typical trend, in which isomer shift decreases upon oxidation.[61–65] This has been explained as a competing effect where the Fe–L bond becomes longer upon oxidation (owing to strong Fe–L π-backbonding that is weaker for a more oxidized metal center), leading to expansion of the Fe 4s orbitals and a resultant increase in the isomer shift.[61] For metals supported by σ and π donor ligands, the metal-

ligand bond length always decreases upon oxidation, such that the two factors contributing to the isomer shift (M–L bond distance and oxidation state) move in concert with one another. Such competing trends are apparent in the Fe–CO bonding in both the [$MoFe_3S_4$] and [Fe_4S_4] clusters, contributions from M–L π-backbonding explain why δ(Fe–CO) changes very slightly with increasing oxidation state. We hypothesize that a similar effect is at play in [**1-CO**]$^{-/0/+}$ and [**1-IMes**]$^{0/+}$: the highly covalent nature of the cluster bonding leads to redox events occurring in delocalized Mo–Fe and Fe–Fe bonding orbitals, which manifests as very small effective changes to the valence at each metal site. This in turn leads to very little change at the bonding at each metal site, and therefore very little structural and spectroscopic change apparent over the [**1-CO**]$^{-/0/+}$ and [**1-IMes**]$^{0/+}$ redox series.

One piece of structural evidence that points towards entering a highly covalent bonding regime in the [$MoFe_3S_4$] clusters is that the Fe–C(NHC) bond distances contract upon reduction, reaching a very short distance of 1.970(6) Å in [**1-CO**]$^{-}$. In contrast, for all redox series of [Fe_4S_4] clusters supported by NHC ligands, the Fe–C(NHC) bond length *increases* upon reduction; for example, the Fe–C(NHC) bond length in [**3**]$^{+}$ (2.060(5) Å) increases to 2.109(5) Å upon reduction to **3**. As discussed above, increasing M–L bond length upon reduction is typical for systems characterized primarily by σ and/or π donation from the ligand to the metal—as the metal becomes more electron rich, the metal receives less electron density from the ligand and the M–L bond lengthens. In contrast, M–L bond distances that contract upon oxidation are characteristic of systems in which π-backbonding is an important component of M–L bonding—as the metal becomes more electron rich, it becomes more proficient at π-backbonding to the ligand and thus the M–L bond becomes stronger upon reduction. That the Fe–C(NHC) bond lengths in [**1-CO**]$^{-/0/+}$ and [**1-IMes**]$^{0/+}$ becomes shorter upon oxidation indicates that π-backbonding to the NHC is more

important in describing the bonding in [**1-CO**]$^{-/0/+}$ and [**1-IMes**]$^{0/+}$ than it is to describe the Fe–NHC bonding in [**2-CO**]$^{0/+}$ and [**4**]$^{0/+}$. That is, the Fe centers in the [$MoFe_3S_4$] clusters are more π-basic than in analogous [Fe_4S_4] clusters, enabling the formation of more covalent Fe–C(NHC) bonds. This may result from the generally increased covalency within the cluster, leading to the [$MoFe_3S_4$] clusters having shorter Fe–S bond lengths than the [Fe_4S_4] clusters, increasing the strength of the Fe–S bonds, and finally resulting in higher energy d-orbitals at the Fe centers that provide a better energetic match for the π-accepting orbitals on the NHC ligand.

We speculate that the differences in covalency between [$MoFe_3S_4$] and [Fe_4S_4] clusters may be related to why [$MoFe_3S_4$]–N_2 and [Mo_3FeS_4]–N_2 complexes have been prepared and isolated[43] and, at least so far, [Fe_4S_4] clusters appear to have negligible affinity for N_2, and may even be isolated with a three-coordinate Fe site (Chapter 5 of this thesis). With the less covalent bonding in [Fe_4S_4] clusters, there is a greater difference in relative orbital energies at adjacent Fe sites needed to access the low-valent states that enable activation of π-acidic ligands. N_2 is not a strong enough π-acid to make this electron transfer energetically accessible in [Fe_4S_4] clusters, while CO is.[47] The [$MoFe_3S_4$] clusters, with their higher covalency, can smoothly donate varying amounts of electron density to different substrates, without the abrupt electron transfer and spin isomerism events required for activation of π-acidic substrates in [Fe_4S_4] clusters (Chapter 4 of this thesis).

Conclusion

We have reported herein the synthesis of [$MoFe_3S_4$]–CO clusters in three oxidation states, including an anionic state with a highly activated CO ligand (ν(C–O) = 1773 cm^{-1}). Analysis of these compounds by similar methods used previously [Fe_4S_4]–CO complexes (*i.e.* comparison to [$MoFe_3S_4$] clusters in the same charge state with only NHC ligands) demonstrates that [$MoFe_3S_4$] clusters access the same mechanism to achieve high degrees of CO activation: formation of low-valent Fe–CO states. In the course of this work, we have additionally found that [$MoFe_3S_4$] and [Fe_4S_4] clusters respond differently to oxidation and reduction events. The trends in the structural and spectroscopic parameters (Mössbauer isomer shifts and XAS spectra) that have been well-documented for redox series of [Fe_4S_4] clusters are not clear across the redox series of the [$MoFe_3S_4$] clusters reported herein. Specifically, in [Fe_4S_4] clusters over successive oxidation events, the Fe–S bond distances contract, the average Mössbauer isomer shift decreases, and the intensity of the pre-edge feature in S K-edge XAS spectra increases. None of these trends are observed for the [$MoFe_3S_4$] clusters reported herein, which is attributed to increased Mo–Fe covalency for the [$MoFe_3S_4$] clusters due to the increased covalent radius of Mo compared to Fe, which enables better orbital overlap. In the more covalent [$MoFe_3S_4$] clusters, redox equivalents are distributed across the cluster in Mo–Fe bonding orbitals, leading to little change to the structure and spectroscopic parameters across oxidation states. The effects on the electronic structure of replacing Fe with Mo are expected to be general; that is, we hypothesize that incorporation of Mo into FeMo-co might increase the overall covalency of the cluster, potentially improving how readily the cluster can access electron rich states that can activate substrates.

References

(1) *Catalysts for Nitrogen Fixation: Nitrogenases, Relevant Chemical Models, and Commercial Processes*, 1st ed.; Smith, B. E., Richards, R. L., Newton, W. E., Eds.; Springer Dordrecht, 2004.

(2) Schneider, K.; Gollan, U.; Dröttboom, M.; Selsemeier-Voigt, S.; Müller, A. Comparative Biochemical Characterization of the Iron-Only Nitrogenase and the Molybdenum Nitrogenase from *Rhodobacter Capsulatus*. *Eur. J. Biochem.* **1997**, *244* (3), 789–800.

(3) Müller, A.; Schneider, K.; Knüttel, K.; Hagen, W. R. EPR Spectroscopic Characterization of an Iron Only Nitrogenase $S = 3/2$ Spectrum of Component 1 Isolated from *Rhodobacter Capsulatus*. *FEBS Lett.* **1992**, *303* (1), 36–40.

(4) Schneider, K.; Müller, A. Iron-Only Nitrogenase: Exceptional Catalytic, Structural and Spectroscopic Features. In *Catalysts for Nitrogen Fixation. Nitrogen Fixation: Origins, Applications, and Research Progress*; Smith, B. E., Richards, R. L., Newton, W. E., Eds.; 2004; Vol. 1.

(5) Eady, R. R. Structure-Function Relationships of Alternative Nitrogenases. *Chem. Rev.* **1996**, *96* (7), 3013–3030.

(6) Miller, R. W.; Eady, R. R. Molybdenum and Vanadium Nitrogenases of *Azotobacter Chroococcum*. Low Temperature Favours N_2 Reduction by Vanadium Nitrogenase. *Biochem. J.* **1988**, *256* (2), 429–432.

(7) Harris, D. F.; Lukoyanov, D. A.; Kallas, H.; Trncik, C.; Yang, Z. Y.; Compton, P.; Kelleher, N.; Einsle, O.; Dean, D. R.; Hoffman, B. M.; Seefeldt, L. C. Mo-, V-, and Fe-Nitrogenases Use a Universal Eight-Electron Reductive-Elimination Mechanism to Achieve N_2 Reduction. *Biochemistry* **2019**, *58* (30), 3293–3301.

(8) Seefeldt, L. C.; Yang, Z. Y.; Lukoyanov, D. A.; Harris, D. F.; Dean, D. R.; Raugei, S.; Hoffman, B. M. Reduction of Substrates by Nitrogenases. *Chem. Rev.* **2020**, *120* (12), 5082–5106.

(9) Lee, C. C.; Tanifuji, K.; Newcomb, M.; Liedtke, J.; Hu, Y.; Ribbe, M. W. A Comparative Analysis of the CO-Reducing Activities of MoFe Proteins Containing Mo- and V-Nitrogenase Cofactors. *ChemBioChem* **2018**, *19* (7), 649–653.

(10) Lee, C. C.; Fay, A. W.; Weng, T. C.; Krest, C. M.; Hedman, B.; Hodgson, K. O.; Hu, Y.; Ribbe, M. W. Uncoupling Binding of Substrate CO from Turnover by Vanadium Nitrogenase. *Proc. Natl. Acad. Sci. U. S. A.* **2015**, *112* (45), 13845–13849.

(11) Spatzal, T.; Perez, K. A.; Einsle, O.; Howard, J. B.; Rees, D. C. Ligand Binding to the FeMo-Cofactor: Structures of CO-Bound and Reactivated Nitrogenase. *Science* **2014**, *345* (6204), 1620–1623.

(12) Lee, C. C.; Hu, Y.; Ribbe, M. W. Vanadium Nitrogenase Reduces CO. *Science* **2010**, *329* (5992), 642.

(13) Harris, D. F.; Jimenez-Vicente, E.; Yang, Z. Y.; Hoffman, B. M.; Dean, D. R.; Seefeldt, L. C. CO as a Substrate and Inhibitor of H+ Reduction for the Mo-, V-, and Fe-Nitrogenase Isozymes. *J. Inorg. Biochem.* **2020**, *213* (September), 111278.

(14) Yang, Z. Y.; Dean, D. R.; Seefeldt, L. C. Molybdenum Nitrogenase Catalyzes the Reduction and Coupling of CO to Form Hydrocarbons. *J. Biol. Chem.* **2011**, *286* (22), 19417–19421.

(15) Premakumar, R.; Pau, R. N.; Mitchenall, L. A.; Easo, M.; Bishop, P. E. Regulation of the Transcriptional Activators AnfA and VnfA by Metals and Ammonium in *Azotobacter Vinelandii*. *FEMS Microbiol. Lett.* **1998**, *164* (1), 63–68.

(16) Kutsche, M.; Leimkuhler, S. Promoters Controlling Expression of the Alternative Nitrogenase and the Molybdenum Uptake System in *Rhodobacter capsulatus* Are Activated by NtrC, Independent of σ54 and Repressed by Molybdenum *J. Bact.* **1996**, *178* (7), 2010–2017.
(17) Harwood, C. S. Iron-Only and Vanadium Nitrogenases: Fail-Safe Enzymes or Something More? *Annu. Rev. Microbiol.* **2020**, *74*, 247–266.
(18) Darnajoux, R.; Magain, N.; Renaudin, M.; Lutzoni, F.; Bellenger, J. P.; Zhang, X. Molybdenum Threshold for Ecosystem Scale Alternative Vanadium Nitrogenase Activity in Boreal Forests. *Proc. Natl. Acad. Sci. U. S. A.* **2019**, *116* (49), 24682–24688.
(19) McRose, D. L.; Zhang, X.; Kraepiel, A. M. L.; Morel, F. M. M. Diversity and Activity of Alternative Nitrogenases in Sequenced Genomes and Coastal Environments. *Front. Microbiol.* **2017**, *8* (FEB), 1–13.
(20) Bulen, W. A.; LeComte, J. R. The Nitrogenase System from Azotobacter: Two-Enzyme Requirement for N_2 Reduction, ATP-Dependent H_2 Evolution, and ATP Hydrolysis. *Proc. Natl. Acad. Sci. U. S. A.* **1966**, *56* (3), 979–986.
(21) Mortenson, L. E. Components of Cell-Free Extracts of *Clostridium Pasteurianum* Required for ATP-Dependent H_2 Evolution from Dithionite and for N_2 Fixation. *BBA - Gen. Subj.* **1966**, *127* (1), 18–25.
(22) Burgess, B. K.; Lowe, D. J. Mechanism of Molybdenum Nitrogenase. *Chem. Rev.* **1996**, *96* (7), 2983–3012.
(23) Hoffman, B. M. .; Lukoyanov, D.; Dean, D. R.; Seefeldt, L. C. Nitrogenase: A Draft Mechanism. *Acc. Chem. Res.* **2013**, *46* (2), 587–595.
(24) Yandulov, D. V; Schrock, R. R. Catalytic Reduction of Dinitrogen to Ammonia at a Single Molybdenum Center. *Science* **2003**, *301* (5629), 76–78.
(25) Hidai, M. Chemical Nitrogen Fixation by Molybdenum and Tungsten Complexes. *Coord. Chem. Rev.* **1999**, *185–186*, 99–108.
(26) Richards, R. L. Reactions of Small Molecules at Transition Metal Sites: Studies Relevant to Nitrogenase, an Organometallic Enzyme. *Coord. Chem. Rev.* **1996**, *154*, 83–97.
(27) Hidai, M.; Mizobe, Y. Recent Advances in the Chemistry of Dinitrogen Complexes. *Chem Rev.* **1995**, *95*, 1115–1133.
(28) Chatt, J.; Dilworth, J. R.; Richards, R. L. Recent Advances in the Chemistry of Nitrogen Fixation. *Chem Rev.* **1978**, *78* (6), 589–625.
(29) Grönberg, K. L. C.; Gormal, C. A.; Durrant, M. C.; Smith, B. E.; Henderson, R. A. Why R-Homocitrate Is Essential to the Reactivity of FeMo-Cofactor of Nitrogenase: Studies on NifV--Extracted FeMo-Cofactor. *J. Am. Chem. Soc.* **1998**, *120* (41), 10613–10621.
(30) Pickett, C. J. The Chatt Cycle and the Mechanism of Enzymic Reduction of Molecular Nitrogen. *J. Biol. Inorg. Chem.* **1996**, *1* (6), 601–606.
(31) Kim, J.; Rees, D. C. Structural Models for the Metal Centers in the Nitrogenase Molybdenum-Iron Protein. *Science* **1992**, *257* (5077), 1677–1682.
(32) Barney, B. M.; Igarashi, R. Y.; Dos Santos, P. C.; Dean, D. R.; Seefeldt, L. C. Substrate Interaction at an Iron-Sulfur Face of the FeMo-Cofactor during Nitrogenase Catalysis. *J. Biol. Chem.* **2004**, *279* (51), 53621–53624.
(33) Buscagan, T. M.; Perez, K. A.; Maggiolo, A. O.; Rees, D. C.; Spatzal, T. Structural Characterization of Two CO Molecules Bound to the Nitrogenase Active Site. *Angew. Chem. Int. Ed.* **2021**, *60* (11), 5704–5707.
(34) Rohde, M.; Grunau, K.; Einsle, O. CO Binding to the FeV Cofactor of CO-Reducing

Vanadium Nitrogenase at Atomic Resolution. *Angew. Chem. Int. Ed.* **2020**, *59* (52), 23626–23630.
(35) Spatzal, T.; Perez, K. A.; Howard, J. B.; Rees, D. C. Catalysis-Dependent Selenium Incorporation and Migration in the Nitrogenase Active Site Iron-Molybdenum Cofactor. *Elife* **2015**, *4*, 1–11.
(36) Sippel, D.; Rohde, M.; Netzer, J.; Trncik, C.; Gies, J.; Grunau, K.; Djurdjevic, I.; Decamps, L.; Andrade, S. L. A.; Einsle, O. A Bound Reaction Intermediate Sheds Light on the Mechanism of Nitrogenase. *Science* **2018**, *359* (6383), 1484–1489.
(37) Lee, C. C.; Kang, W.; Jasniewski, A. J.; Stiebritz, M. T.; Tanifuji, K.; Ribbe, M. W.; Hu, Y. Evidence of Substrate Binding and Product Release via Belt-Sulfur Mobilization of the Nitrogenase Cofactor. *Nat. Catal.* **2022**, *5* (5), 443–454.
(38) Kang, W.; Lee, C. C.; Jasniewski, A. J.; Ribbe, M. W.; Hu, Y. Structural Evidence for a Dynamic Metallocofactor during N2 Reduction by Mo-Nitrogenase. *Science* **2020**, *368* (6497), 1381–1385.
(39) Betley, T. A.; Peters, J. C. Dinitrogen Chemistry from Trigonally Coordinated Iron and Cobalt Platforms. *J. Am. Chem. Soc.* **2003**, *125* (36), 10782–10783.
(40) Hendrich, M. P.; Gunderson, W.; Behan, R. K.; Green, M. T.; Mehn, M. P.; Betley, T. A.; Lu, C. C.; Peters, J. C. On the Feasibility of N_2 Fixation via a Single-Site FeI/FeIV Cycle: Spectroscopic Studies of FeI(N_2)FeI, FeIV≡N, and Related Species. *Proc. Natl. Acad. Sci. U. S. A.* **2006**, *103* (46), 17107–17112.
(41) Smith, J. M.; Lachicotte, R. J.; Pittard, K. A.; Cundari, T. R.; Lukat-Rodgers, G.; Rodgers, K. R.; Holland, P. L. Stepwise Reduction of Dinitrogen Bond Order by a Low-Coordinate Iron Complex. *J. Am. Chem. Soc.* **2001**, *123* (37), 9222–9223.
(42) Anderson, J. S.; Rittle, J.; Peters, J. C. Catalytic Conversion of Nitrogen to Ammonia by an Iron Model Complex. *Nature* **2013**, *501* (7465), 84–87.
(43) McSkimming, A.; Suess, D. L. M. Dinitrogen Binding and Activation at a Molybdenum–Iron–Sulfur Cluster. *Nat. Chem.* **2021**, *13* (7), 666–670.
(44) Ohki, Y.; Munakata, K.; Matsuoka, Y.; Hara, R.; Kachi, M.; Uchida, K.; Tada, M.; Cramer, R. E.; Sameera, W. M. C.; Takayama, T.; Sakai, Y.; Kuriyama, S.; Nishibayashi, Y.; Tanifuji, K. Nitrogen Reduction by the Fe Sites of Synthetic [Mo3S4Fe] Cubes. *Nature* **2022**, *607* (7917), 86–90.
(45) Rees, J. A.; Bjornsson, R.; Kowalska, J. K.; Lima, F. A.; Schlesier, J.; Sippel, D.; Weyhermüller, T.; Einsle, O.; Kovacs, J. A.; DeBeer, S. Comparative Electronic Structures of Nitrogenase FeMoco and FeVco. *Dalton Trans.* **2017**, *46* (8), 2445–2455.
(46) Carney, M. J.; Kovacs, J. A.; Zhang, Y. P.; Papaefthymiou, G. C.; Spartalian, K.; Frankel, R. B.; Holm, R. H. Comparative Electronic Properties of Vanadium-Iron-Sulfur and Molybdenum-Iron-Sulfur Clusters Containing Isoelectronic Cubane-Type $[VFe3S4]^{2+}$ and $[MoFe3S4]^{3+}$ Cores. *Inorg. Chem.* **1987**, *26* (5), 719–724.
(47) Brown, A. C.; Thompson, N. B.; Suess, D. L. M. Evidence for Low-Valent Electronic Configurations in Iron−Sulfur Clusters. *J. Am. Chem. Soc.* **2022**, *144* (20), 9066–9073.
(48) Peters, J. C.; Johnson, A. R.; Odom, A. L.; Wanandi, P. W.; Davis, W. M.; Cummins, C. C. Assembly of Molybdenum/Titanium μ-Oxo Complexes via Radical Alkoxide C-O Cleavage. *J. Am. Chem. Soc.* **1996**, *118* (42), 10175–10188.
(49) Deng, L.; Holm, R. H. Stabilization of Fully Reduced Iron-Sulfur Clusters by Carbene Ligation: The $[Fe_nS_n]^0$ Oxidation Levels (n = 4, 8). *J. Am. Chem. Soc.* **2008**, *130* (30), 9878–9886.

(50) Venkateswara Rao, P.; Holm, R. H. Synthetic Analogues of the Active Sites of Iron−Sulfur Proteins. *Chem. Rev.* **2004**, *104* (2), 527–560.
(51) Kowalska, J. K.; Hahn, A. W.; Albers, A.; Schiewer, C. E.; Bjornsson, R.; Lima, F. A.; Meyer, F.; DeBeer, S. X-Ray Absorption and Emission Spectroscopic Studies of $[L_2Fe_2S_2]^n$ Model Complexes: Implications for the Experimental Evaluation of Redox States in Iron-Sulfur Clusters. *Inorg. Chem.* **2016**, *55* (9), 4485–4497.
(52) Kowalska, J.; DeBeer, S. The Role of X-Ray Spectroscopy in Understanding the Geometric and Electronic Structure of Nitrogenase. *Biochim. Biophys. Acta - Mol. Cell Res.* **2015**, *1853* (6), 1406–1415.
(53) *Physical Methods in Bioinorganic Chemistry: Spectroscopy and Magnetism*; Que, L., Ed.; University Science Books: Sausalito, CA.
(54) Musgrave, K. B.; Angove, H. C.; Burgess, B. K.; Hedman, B.; Hodgson, K. O.; V, S. U. All-Ferrous Titanium (III) Citrate Reduced Fe Protein of Nitrogenase : An XAS Study of Electronic and Metrical Structure. *J. Am. Chem. Soc.* **1998**, *7863* (120), 5325–5326.
(55) Solomon, E. I.; Hedman, B.; Hodgson, K. O.; Dey, A.; Szilagyi, R. K. Ligand K-Edge X-Ray Absorption Spectroscopy: Covalency of Ligand-Metal Bonds. *Coord. Chem. Rev.* **2005**, *249* (1–2), 97–129.
(56) Glaser, T.; Rose, K.; Shadle, S. E.; Hedman, B.; Hodgson, K. O.; Solomon, E. I. S K-Edge X-Ray Absorption Studies of Tetranuclear Iron-Sulfur Clusters: **2001**, 442–454.
(57) Hedman, B.; Hodgson, K. O.; Solomon, E. I. X-Ray Absorption Edge Spectroscopy of Ligands Bound to Open-Shell Metal Ions: Chlorine K-Edge Studies of Covalency in $CuCl_4^{2-}$. *J. Am. Chem. Soc.* **1990**, *112* (4), 1643–1645.
(58) Bjornsson, R.; Lima, F. A.; Spatzal, T.; Weyhermüller, T.; Glatzel, P.; Bill, E.; Einsle, O.; Neese, F.; DeBeer, S.; Hoffman, B. M. Identification of a Spin-Coupled Mo(III) in the Nitrogenase Iron–Molybdenum Cofactor. *Chem. Sci.* **2014**, *5* (8), 3096–3103.
(59) Fomitchev, D. V.; McLauchlan, C. C.; Holm, R. H. Heterometal Cubane-Type MFe_3S_4 Clusters (M = Mo, V) Trigonally Symmetrized with Hydrotris(Pyrazolyl)Borate(1-) and Tris(Pyrazolyl)Methanesulfonate(1-) Capping Ligands. *Inorg. Chem.* **2002**, *41* (4), 958–966.
(60) Bahn, C. S.; Tan, A.; Harris, S. Bonding in Mo3M'S4 Cubane-Type Clusters: Variations in Electronic Structure When M' Is a Main Group or Transition Metal. *Inorg. Chem.* **1998**, *37* (11), 2770–2778.
(61) Ye, S.; Bill, E.; Neese, F. Electronic Structures of the $[Fe(N_2)(SiP^iPr_3)]^{+1/0/-1}$ Electron Transfer Series: A Counterintuitive Correlation between Isomer Shifts and Oxidation States. *Inorg. Chem.* **2016**, *55* (7), 3468–3474.
(62) Lee, Y.; Peters, J. C. Silylation of Iron-Bound Carbon Monoxide Affords a Terminal Fe Carbyne. *J. Am. Chem. Soc.* **2011**, *133* (12), 4438–4446.
(63) Lee, Y.; Mankad, N. P.; Peters, J. C. Triggering N2 Uptake via Redox-Induced Expulsion of Coordinated NH_3 and N_2 Silylation at Trigonal Bipyramidal Iron. *Nat. Chem.* **2010**, *2* (7), 558–565.
(64) Mankad, N. P.; Whited, M. T.; Peters, J. C. Terminal FeI–N_2 and FeII···H–C Interactions Supported by Tris(Phosphino)Silyl Ligands. *Angew. Chem.* **2007**, *119* (30), 5870–5873.
(65) Whited, M. T.; Mankad, N. P.; Lee, Y.; Oblad, P. F.; Peters, J. C. Dinitrogen Complexes Supported by Tris(Phosphino)Silyl Ligands. *Inorg. Chem.* **2009**, *48* (6), 2507–2517.

Supporting Information

A. Experimental Methods

General Considerations

All reactions were performed using standard Schlenk techniques or in an LC Technologies inert atmosphere glove box under an N_2 atmosphere. Glassware was dried in an oven at 160 °C prior to use. Molecular sieves (3 Å), and Celite® were activated by heating to 300 °C overnight under vacuum prior to storage under an atmosphere of nitrogen. *O*-difluorobenzene (DFB) was distilled from CaH_2, C_6D_6 was degassed by three freeze–pump–thaw cycles, and other solvents were degassed by sparging with argon and dried by passing through a column of activated alumina. All solvents were stored under an N_2 atmosphere over 3 Å molecular sieves.

NMR spectra were recorded on Bruker 400 and 500 MHz spectrometers. ^{1}H chemical shifts are given relative to residual solvent peaks; spectra in DFB and Et_2O are referenced to the triplet of residual *n*-pentane at 0.89 ppm. Solvent suppression for NMR in protonated solvents was carried out using WET solvent suppression.[1] FT-IR samples were taken as thin films using a Bruker Alpha Platinum ATR spectrometer with OPUS software in a glovebox under an N_2 atmosphere. EPR spectra were recorded on a Bruker EMX spectrometer at 9.37 GHz (perpendicular mode) as frozen glasses. Simulations were performed using EasySpin[2] (5.2.21) in Matlab (R2017b). UV-vis spectra were recorded on a Cary 50 spectrometer. Zero-field ^{57}Fe Mössbauer spectra were measured with a constant-acceleration spectrometer at 80 K using a SEE co. W302 constant-acceleration spectrometer. Isomer shifts are quoted relative to α-Fe foil at room temperature; Mössbauer spectra were simulated with WMOSS v.4.[3] Elemental analyses were performed at Midwest Microlab. X-ray structural determinations were performed at the MIT diffraction facility using a Bruker X8 diffractometer with an APEX II CCD detector or a Bruker D8 Venture diffractometer with a

Photon2 CPAD detector. Diffraction data was collected, integrated, and corrected for absorption using Bruker APEX3 software and its associated modules (SAINT, SADABS, TWINABS). Structural solutions and refinements (on F^2) were carried out using SHELXT and SHELXL-2018 in ShelXle.[4] Ellipsoid plots and figures were made using Mercury 2021.2.0.

$(I^iPr^{Me})_4Fe_4S_4$,[5] $[(I^iPr^{Me})_4Fe_4S_4][BPh_4]$,[6] $(IMes)_3Fe_4S_4CO$,[7] IMes,[8,9] $Ti(N(^tBu)Ar)_3$[10], $Na[BAr^F_4]$[11], K(napthalenide)·$(THF)_{0.5}$,[12] and $[PPh_4][Cp^*MoFe_3S_4Cl_3]$[13] were prepared according to literature procedures.

Statement on Compound Purity

The purity of all compounds was assessed by a variety of spectroscopic and analytical methods as detailed below. All compounds are air-sensitive and [**1-CO**]$^-$ and [**1-CO**]$^+$ are unstable towards dynamic vacuum, but all compounds can be isolated as crystalline solids in high purity as determined by NMR, EPR, and Mössbauer spectroscopic analysis, SQUID magnetometry, and as H and N content from elemental analysis. Low C content was obtained by elemental analysis as has been observed for other members of this class of molecules[14–16] and in other contexts.[17] Elemental analysis results are as follows:

$Cp^*MoFe_3S_4(IMes)_2Cl$ (**1-Cl**): Anal. Found: C, 51.54; H, 5.25; N, 4.40. Calcd. for $C_{52}H_{63}ClN_4Fe_3S_4Mo$: C, 53.32; H, 5.42; N, 4.78

$Cp^*MoFe_3S_4(IMes)_2CO$ (**1-CO**): Anal. Found: C, 49.85; H, 5.22; N, 4.35. Calcd. for $C_{53}H_{63}N_4Fe_3S_4MoO$: C, 54.70; H, 5.46; N, 4.81

$[Cp^*MoFe_3S_4(IMes)_2CO][BAr^F_4]$ ([**1-CO**]$^+$): Anal. Found: C, 49.72; H, 3.73; N, 2.79. Calcd. for $C_{85}H_{75}BF_{24}N_4Fe_3S_4MoO$: C, 50.73; H, 3.73; N, 2.76

[K(Benzo-15-crown-5)$_2$][Cp*MoFe$_3$S$_4$(IMes)$_2$CO] ([**1-CO**]$^-$): Anal. Found: C, 50.78; H, 5.55; N, 2.89. Calcd. for $C_{81}H_{103}N_4Fe_3S_4MoO_{11}K$: C, 55.93; H, 5.97; N, 3.22

[Cp*MoFe$_3$S$_4$(IMes)$_3$][BAr$^F{}_{24}$] ([**1-IMes**]$^+$): Anal. Found: C, 54.37; H, 4.30; N, 3.67. Calcd. for $C_{105}H_{99}BF_{24}N_6Fe_3S_4Mo$: C, 54.75; H, 4.33; N, 3.65

Cp*MoFe$_3$S$_4$(IMes)$_2$Cl (**1-Cl**)

This compound was prepared using a procedure adapted from that employed for the synthesis of Cp*MoFe$_3$S$_4$(IPr)$_2$Cl.[15] A solution of IMes (687 mg, 2.26 mmol, 2.2 equiv) in THF (10 mL) was added to a suspension of [PPh$_4$][Cp*MoFe$_3$S$_4$Cl$_3$] (1.00 g, 1.03 mmol) in THF (10 mL). The solution was stirred for 2 min and a solution of Cp$_2$Co (214 mg, 1.13 mmol, 1.1 equiv) in THF (2 mL) was added dropwise. The solution was stirred for 30 min then filtered through Celite and concentrated to 10 mL. Et$_2$O (100 mL) was added and the mixture was stirred for 5 min. The dark precipitates were collected on a frit and washed with additional Et$_2$O (3 x 10 mL). The solids were dried in vacuo. Yield: 999 mg (83%). Crystals suitable for X-ray diffraction were grown by diffusion of *n*-pentane into at THF solution of **1-Cl**. ^{1}H NMR (400 MHz, CD_2Cl_2, 293 K) δ 7.55 (s, 4H IMes), 7.41 (s, 4H, IMes), 5.03 (s, 4H, IMes), 3.07 (s, 12H, Mes C*H$_3$*), 2.72 (s, 12H, Mes C*H$_3$*), 2.27 (s, 12H, Mes C*H$_3$*), –6.47 (s, 15H, Cp*).

Cp*MoFe$_3$S$_4$(IMes)$_2$CO (**1-CO**)

Cp*MoFe$_3$S$_4$(IMes)$_2$Cl (250. mg 0.213 mmol) was dissolved in THF (5 mL) and frozen in a Schlenk flask in liquid N_2. A solution of Ti(N(^{t}Bu)Ar)$_3$ (185 mg, 0.320 mmol, 1.5 equiv) in THF (5 mL) was layered on top and frozen. The flask was capped with a septum and removed from the glovebox, maintaining the temperature at –196 °C. The flask was evacuated and CO (8 mL) was

added via syringe. The flask was warmed to room temperature and the solution stirred vigorously for 5 min. The solution was concentrated to 2 mL and pentane (20 mL) was added. The black precipitates were collected on a frit and washed with pentane (3 x 5 mL). Yield: 223 mg (90%). Crystals suitable for X-ray diffraction were grown by vapor diffusion of *n*-pentane into a solution of **1-CO** in THF at room temperature. ^{1}H NMR (400 MHz, C_6D_6, 293 K) δ 9.50 (s, 4H, IMes), 7.95 (s, 4H, IMes), 7.32 (s, 4H, IMes), 3.05 (s, 12H, Mes C*H*$_3$) 2.88 (s, 12H, Mes C*H*$_3$), 2.38 (s, 15H, Cp*), 2.02 (s, 12H, Mes C*H*$_3$).

$[Cp^*MoFe_3S_4(IMes)_2CO][BAr^F{}_4]$ ($[\mathbf{1\text{-}CO}]^+$)

A solution of $Na[BAr^F{}_4]$ (38 mg, 0.043 mmol) in Et_2O (1 mL) was added dropwise to a stirred suspension of $Cp^*MoFe_3S_4(IMes)_2Cl$ (50. mg, 0.043 mmol) in Et_2O (2 mL). The solution was stirred for 10 min, then filtered through Celite, concentrated to 1 mL, and placed in a septum capped vial. To this vial, 6 mL of CO was added via syringe. The solution was stirred for 5 min, then pentane (10 mL) was added to induce crystallization of the product. The mixture was allowed to stand for 15 min, then the solvent was decanted from the crystals and the crystals were washed with additional pentane (1 x 2 mL). The crystals were dried under a stream of N_2 because compound $[\mathbf{1\text{-}CO}]^+$ is unstable to dynamic vacuum. Yield: 59 mg (67%). Crystals suitable for X-ray diffraction were grown by layering *n*-pentane onto an Et_2O solution of $[\mathbf{1\text{-}CO}]^+$ and storage at –35 °C overnight. ^{1}H NMR (400 MHz, DFB, 293 K) δ 8.30 (s, 8H, $[BAr^F{}_4]^-$), 7.69 (s, 4H, IMes), 7.65 (s, 4H, $[BAr^F{}_4]^-$), 5.05 (s, 4H, IMes), 3.09 (s, 15H, Cp*), 2.87 (s, 12H, Mes C*H*$_3$), 2.74 (s, 12H, Mes C*H*$_3$), 1.77 (s, 12H, Mes C*H*$_3$). One IMes aryl resonance is obscured by the suppressed DFB resonances.

[K(Benzo-15-crown-5)$_2$][Cp*MoFe$_3$S$_4$(IMes)$_2$CO] ([**1-CO**]$^-$)

A solution of K(napthalenide)·(THF)$_{0.5}$ (9.6 mg, 0.048 mmol) in THF (1 mL) was added dropwise to a solution of Cp*MoFe$_3$S$_4$(IMes)$_2$CO (50. mg, 0.043 mmol) in THF (2 mL). The solution was stirred for 5 min, then filtered through Celite, added to a solution of benzo-15-crown-5 (25 mg, 0.094 mmol) in THF (1 mL), and the resultant mixture stirred for 5 min. The solution was concentrated to 1 mL and 10 mL of pentane were added to precipitate the product. The solvent was decanted and the black solids washed with additional pentane (3 x 2 mL). The solids were dried under a stream of a stream of N_2 because [**1-CO**]$^-$ is unstable to dynamic vacuum. Yield: 37.9 mg (50%). Crystals suitable for X-ray diffraction were grown by layering *n*-pentane onto a THF solution of [**1-CO**]$^-$ and storage at –35 °C overnight. ^{1}H NMR (400 MHz, THF, 293 K) δ (s, 4H, IMes), 6.84 (s, 8H, 2 x IMes or benzo-15-c-5), 6.76 (s, 4H, IMes or benzo-15-c-5), 6.72 (s, 4H, IMes or benzo-15-c-5), 4.01 (8H, benzo-15-c-5), 3.79 (8H, benzo-15-c-5), 2.37 (s, 12H, IMes), 2.00 (s, 12H, IMes), 1.45 (s, 15H, Cp*). Two benzo-15-c-5 resonances and one IMes resonance are obscured by the suppressed THF solvent.

Cp*MoFe$_3$S$_4$(IMes)$_3$ (**1-IMes**)

Sodium (10. mg) was added to solution of Cp*MoFe$_3$S$_4$(IMes)$_2$Cl (102 mg, 0.085 mmol) and IMes (26 mg, 0.085 mmol) in benzene (10 mL). The reaction was stirred for 4 h until the color had changed from yellow-brown to dark red. The solution was filtered through Celite and concentrated to 2 mL and the product was precipitated with pentane (10 mL). Crystals suitable for X-ray diffraction were grown by diffusion of pentane into a benzene solution of **1-IMes**. ^{1}H NMR (400 MHz, C_6D_6, 293 K) δ 13.14 (s, 6H, IMes backbone), 6.50 (s, 12H, IMes *m*-C*H*), 2.40 (s, 18H, IMes *p*-CH_3), 1.72 (s, 36H, Mes *o*-CH_3), –0.28 (s, 15H, Cp*).

$[Cp^*MoFe_3S_4(IMes)_3][BAr^F{}_{24}]$ ([**1-IMes**]$^+$)

A solution of $Na[BAr^F{}_4]$ (38 mg, 0.043 mmol) in THF (2 mL) was added dropwise to a solution of $Cp^*MoFe_3S_4(IMes)_2Cl$ (50. mg, 0.043 mmol) and IMes (17 mg, 0.056 mmol) in THF (2 mL). The solution was stirred for 5 min and then filtered through Celite. The solution was concentrated to 0.5 mL and pentane (10 mL) was added to precipitate the product. The dark solids were washed with pentane (3 x 2 mL) and dried in vacuo. Yield: 69 mg (70%). ^{1}H NMR (400 MHz, DFB 293 K) δ 8.32 (s, 8H, $[BAr^F{}_4]^-$), 7.68 (s, 4H, $[BAr^F{}_4]^-$), 7.66 (s, 12H, IMes *m*-C*H*), 6.49 (s, 6H, IMes backbone C*H*) 2.85 (s, 18H, Mes *p*-CH_3), 2.72 (s, 36H, Mes *o*-CH_3), 1.40 (s, 15H, Cp*). Crystals suitable for X-ray diffraction were grown by layering HMDSO onto a DFB solution of [**1-IMes**]$^+$ and storage at –35 °C overnight.

B. NMR Spectra

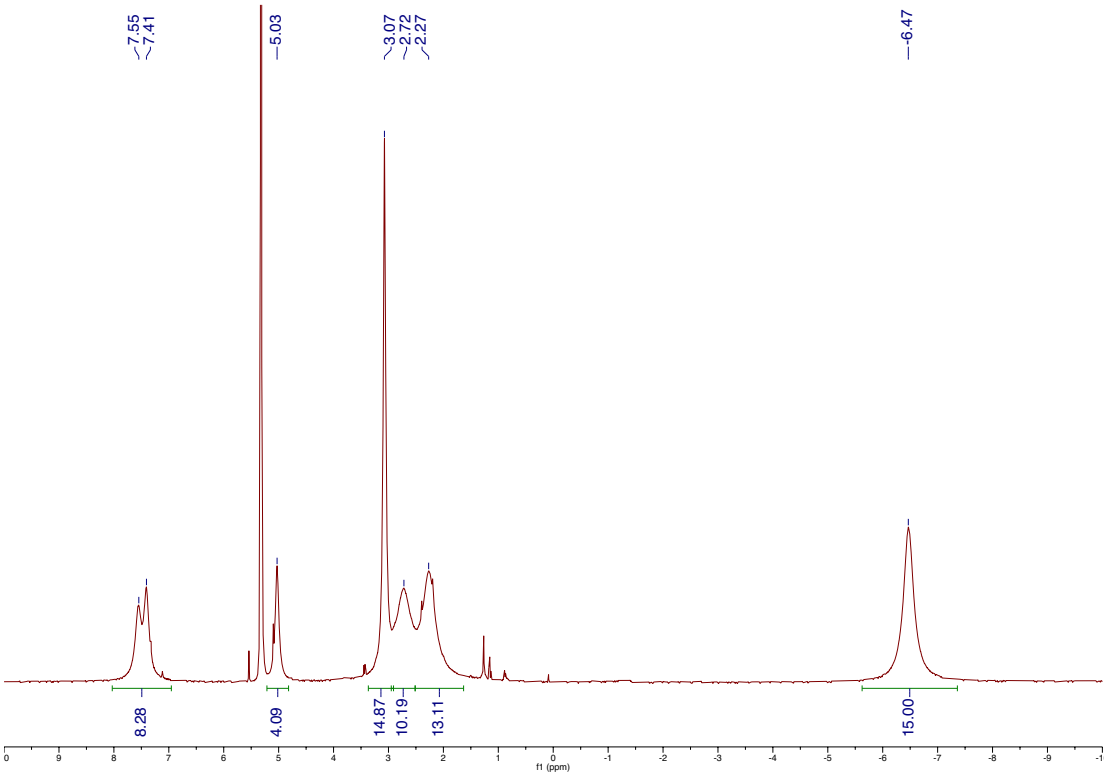

Figure S6.1: ^{1}H NMR spectrum of **1-Cl** in CD_2Cl_2 at 293 K

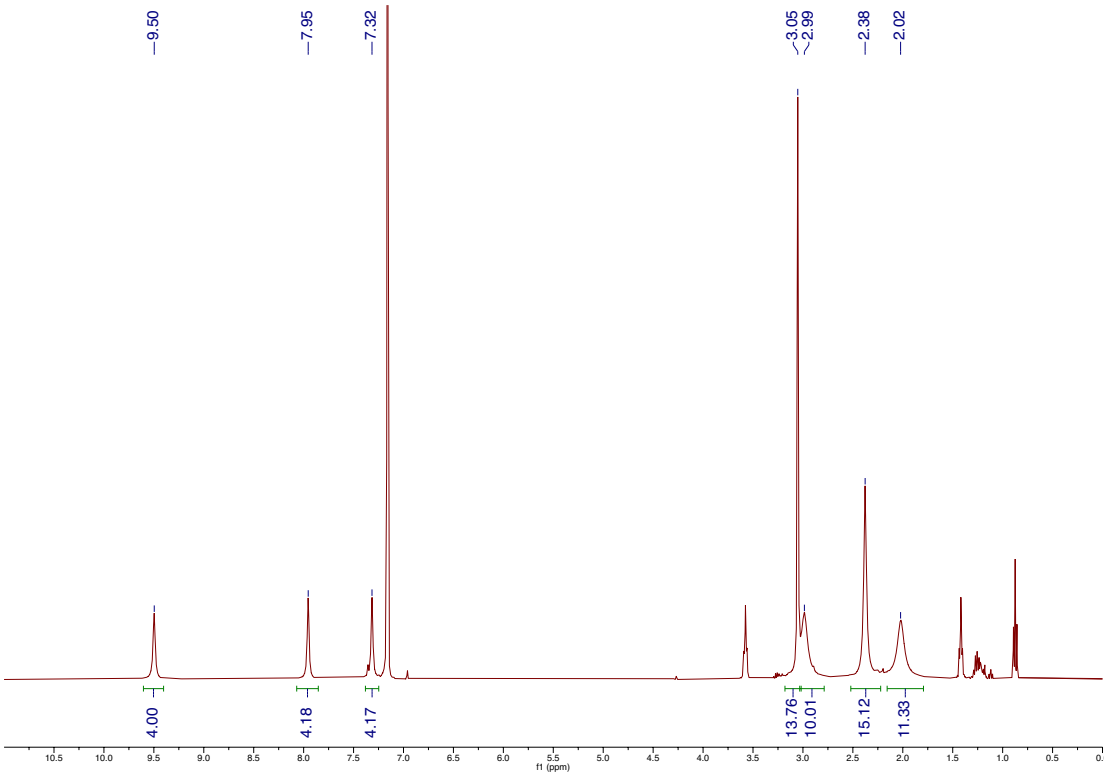

Figure S6.2: ^{1}H NMR spectrum of **1-CO** in C_6D_6 at 293 K

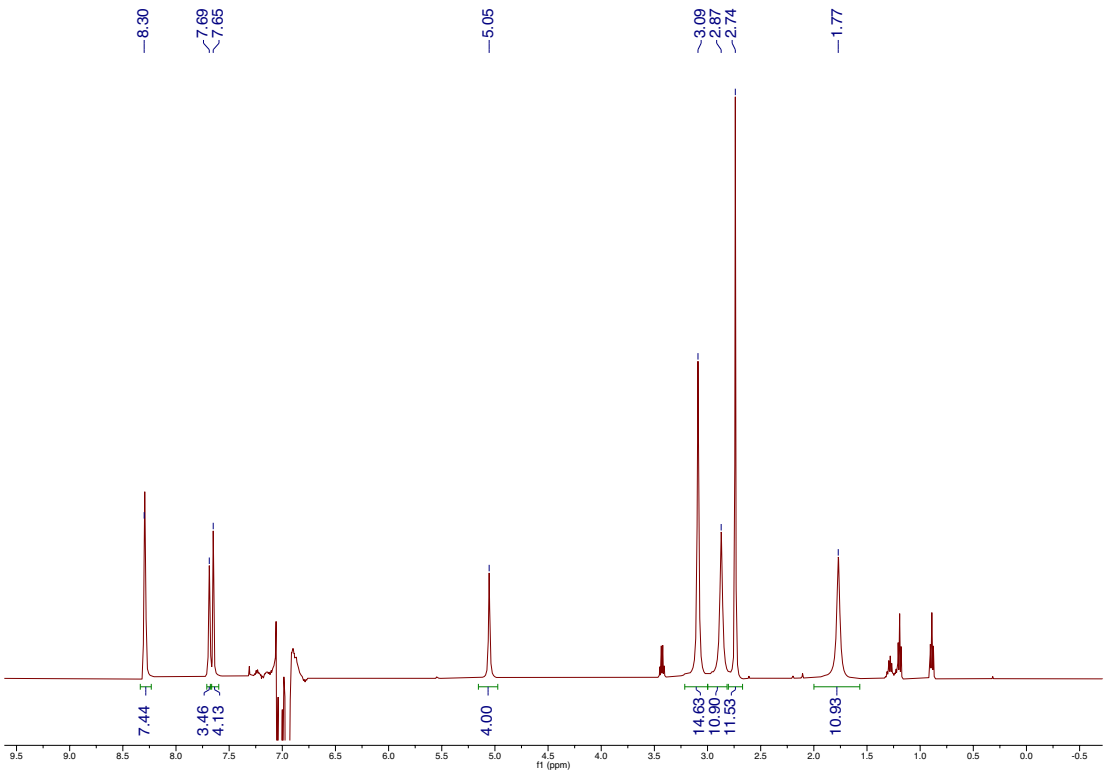

Figure S6.3: ^{1}H NMR spectrum of [**1-CO**][BAr^{F}_{4}] in DFB at 293 K

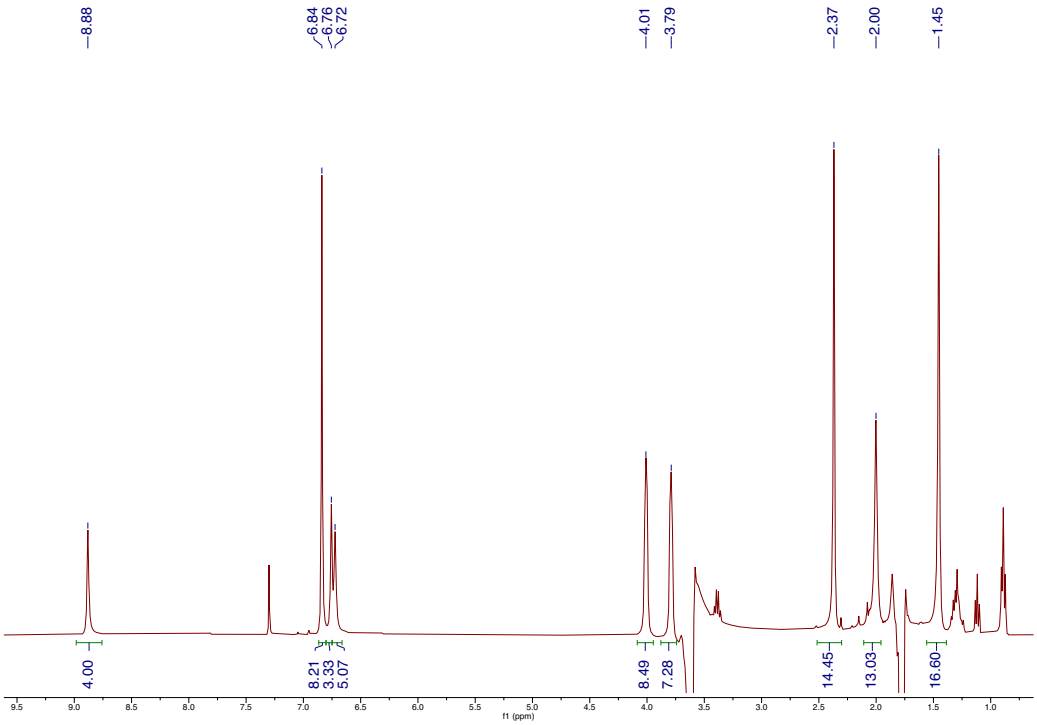

Figure S6.4: ^{1}H NMR spectrum of [K(Benzo-15-crown-5)$_2$][**1-CO**] in THF at 293 K

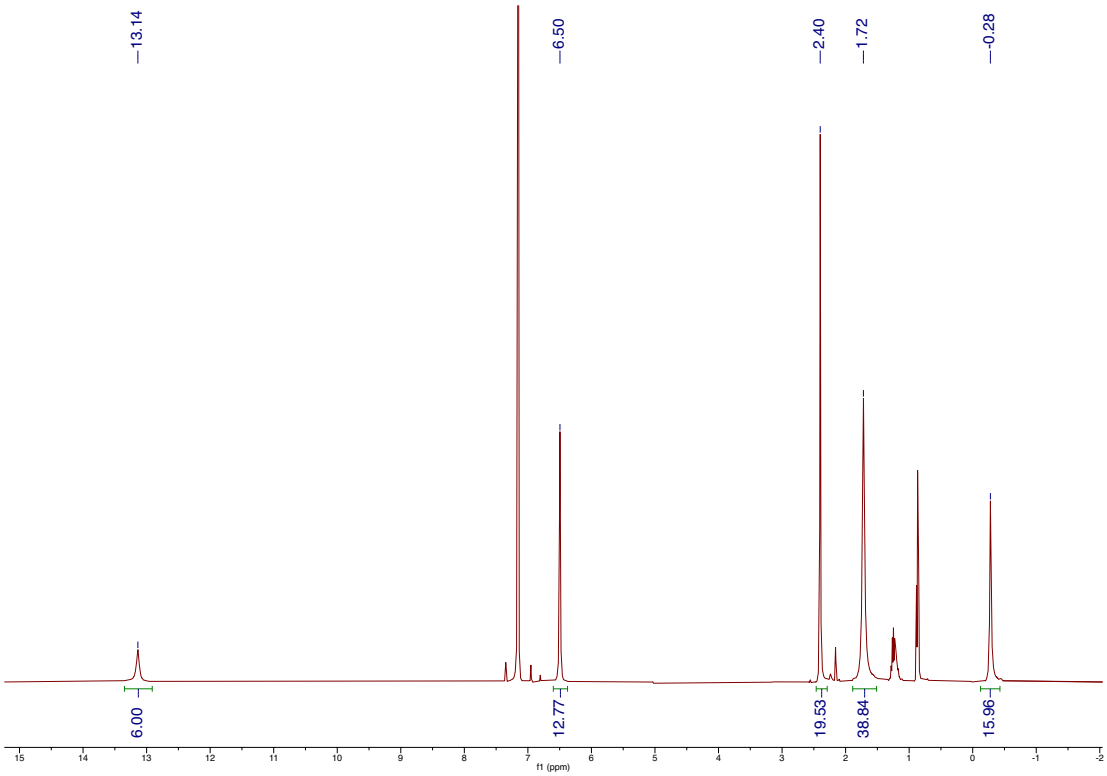

Figure S6.5: ^{1}H NMR spectrum of **1-IMes** in DFB at 293 K

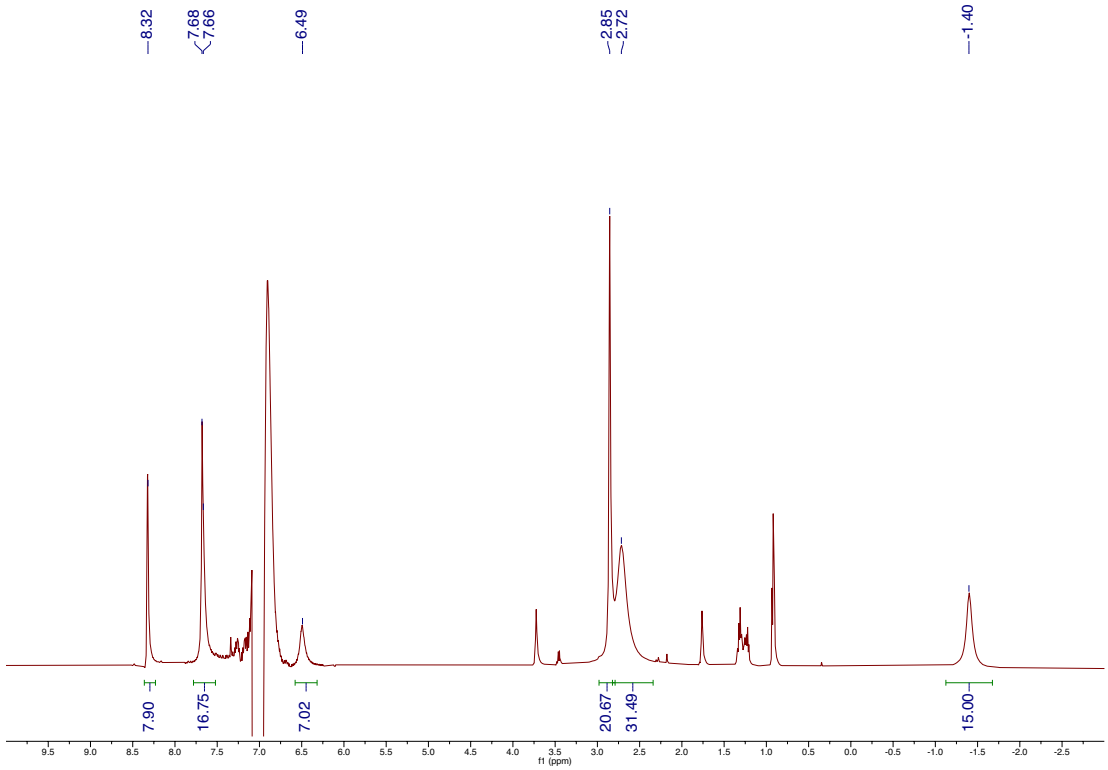

Figure S6.6: ^{1}H NMR spectrum of [**1-IMes**][BAr^{F}_{24}] in DFB at 293 K

C. IR Spectra

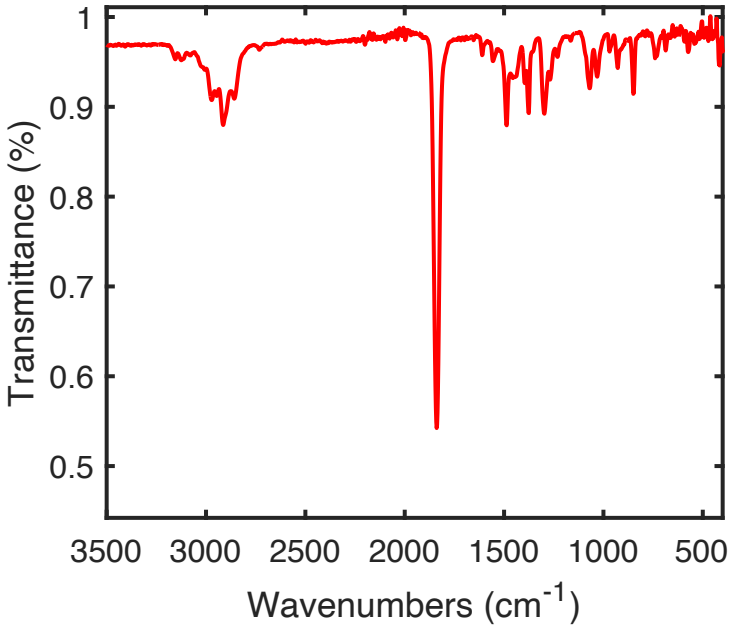

Figure S6.7: IR spectrum of **1-CO**. ν(C–O) = 1841 cm^{-1}

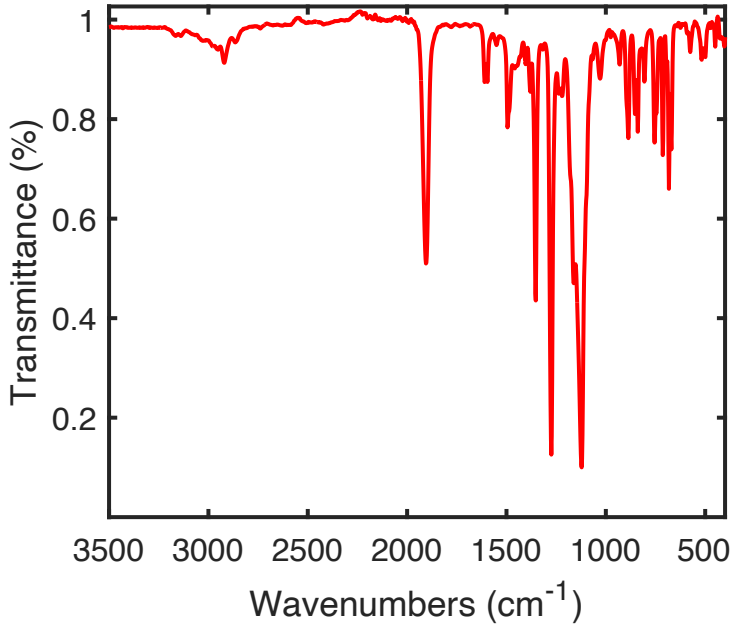

Figure S6.8: IR spectrum of [**1-CO**][BAr^F_4]. ν(C–O) = 1905 cm^{-1}

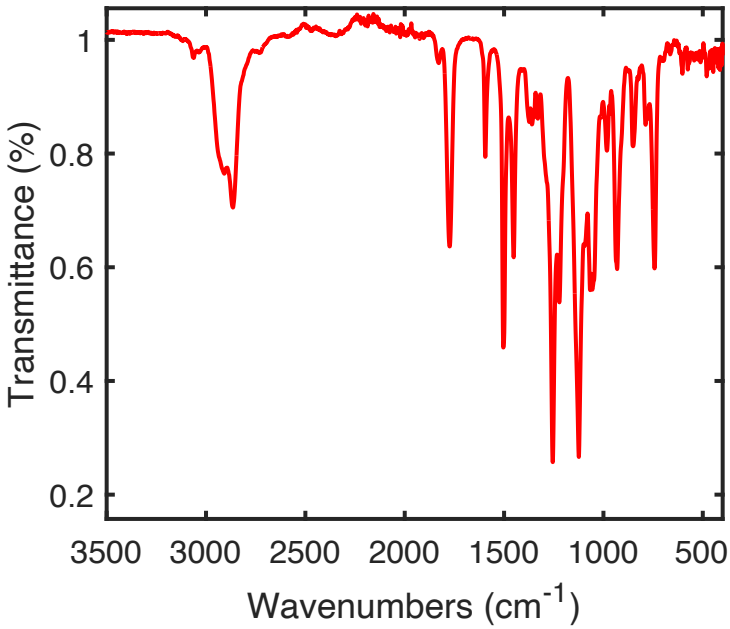

Figure S6.9: IR spectrum of [K(Benzo-15-crown-5)$_2$][**1-CO**]. ν(C–O) = 1773 cm^{-1}

D. EPR Spectra

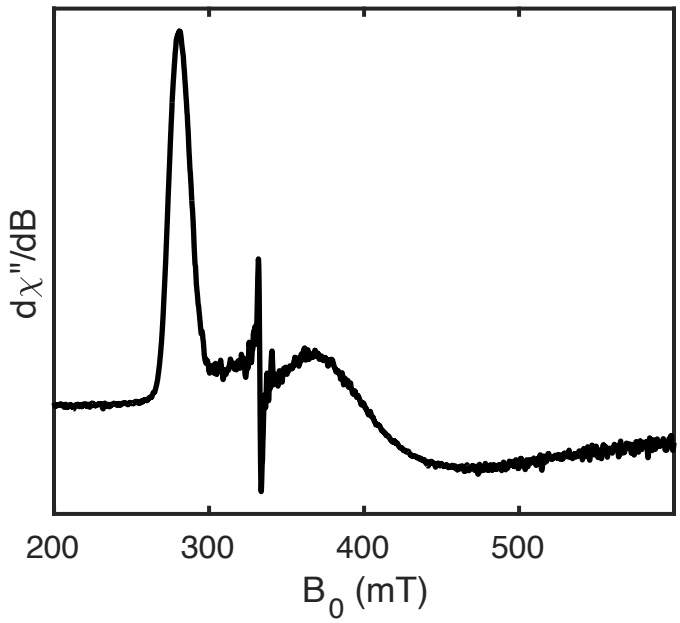

Figure S6.10: EPR spectrum of **1-IMes** in toluene at 5 K (perpendicular mode, black). Microwave power: 250 μW; microwave frequency: 9.3732 GHz. $g_1 \sim 2.39$, $g_2 \sim 1.65$.

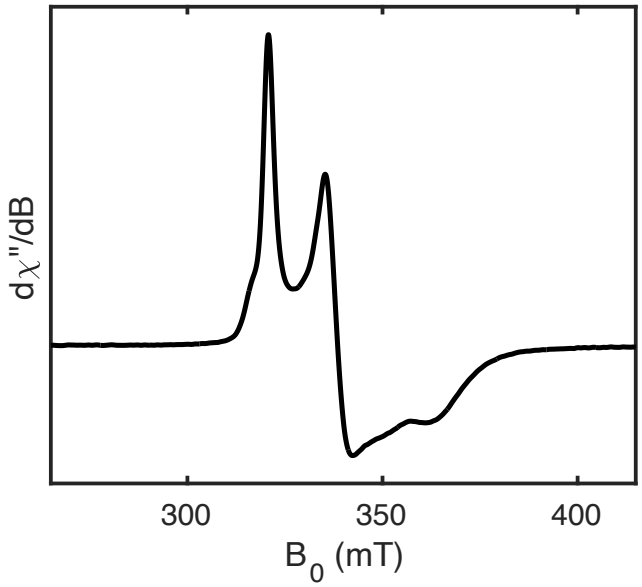

Figure S6.11: EPR spectrum of **1-CO** in toluene at 15 K (perpendicular mode, black). Microwave power: 63 μW; microwave frequency: 9.3678 GHz. $g_1 = 2.08$, $g_2 = 1.98$, $g_3 = 1.85$.

E. SQUID magnetometry

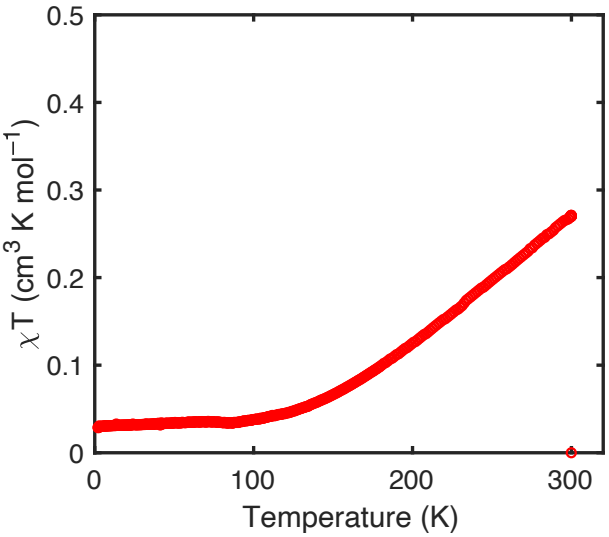

Figure S6.12: SQUID magnetometry data (χT vs. T) for [**1-CO**][$BArF_4$] collected at a field of 0.5 T. Data are corrected for diamagnetic contributions using Pascal's constants. The values of χT at low temperature (below 100 K, ca. 0.02 cm^3 K mol^{-1}) are close to the expectation value for an $S = 0$ system (0 cm^3 K mol^{-1}). The increase in χT with increasing temperature may be attributed to temperature independent paramagnetism (TIP) or population of higher spin excited states.

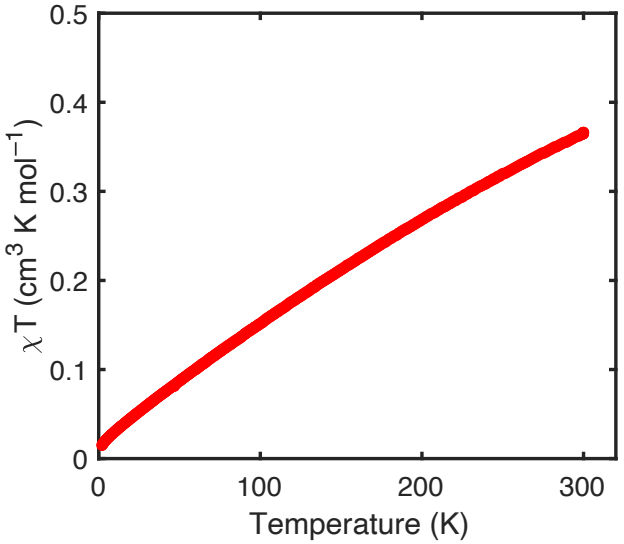

Figure S6.13: SQUID magnetometry data (χT vs. T) for [K(benzo-15-c-5)$_2$][**1-CO**] collected at a field of 0.5 T. Data are corrected for diamagnetic contributions using Pascal's constants. The values of χT at low temperature (below 100 K, ca. 0.02 cm^3 K mol^{-1}) are close to the expectation value for an $S = 0$ system (0 cm^3 K mol^{-1}). The increase in χT with increasing temperature may be attributed to temperature independent paramagnetism (TIP) or population of higher spin excited states.

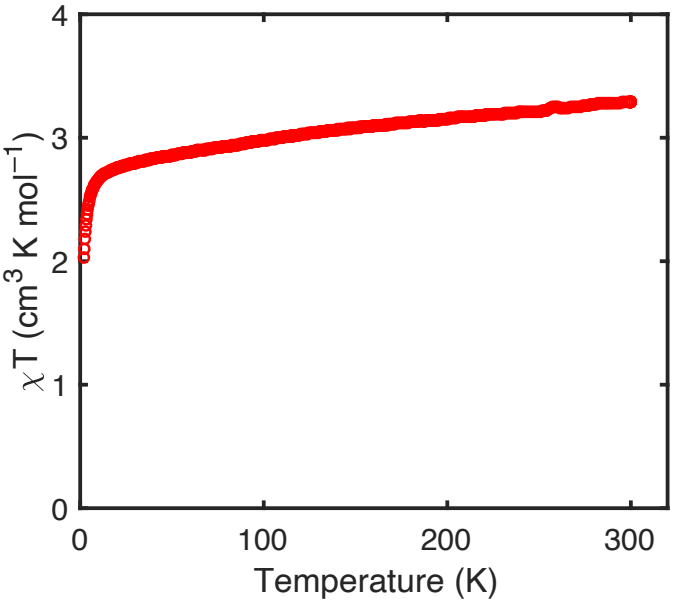

Figure S6.14: SQUID magnetometry data (χT vs. T) for [**1-IMes**][BAr^F_4] collected at a field of 0.5 T. Data are corrected for diamagnetic contributions using Pascal's constants. The values of χT (ca. 3 cm^3 K mol^{-1}) are close to the expectation value for an $S = 2$ system (3.0 cm^3 K mol^{-1}).

F. Mössbauer spectra

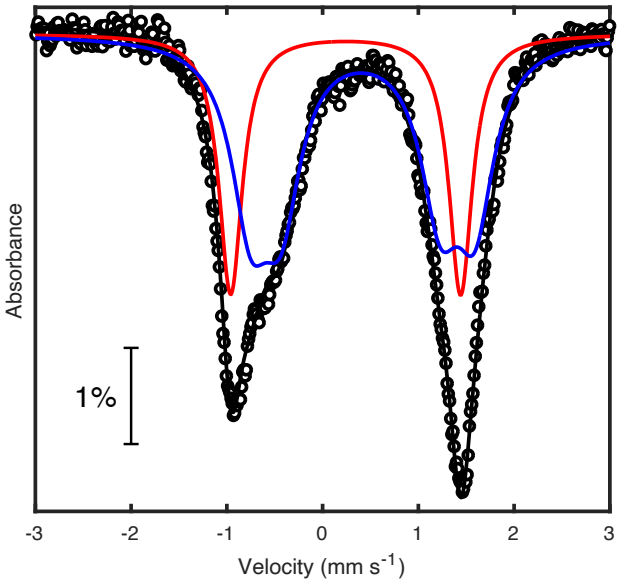

Figure S6.15: Mössbauer spectrum of **1-CO** at 80 K (dots) and total simulation using the parameters in table S6.1 (black). The Fe–CO site is shown in red and the sum of the two Fe–NHC sites is shown in blue.

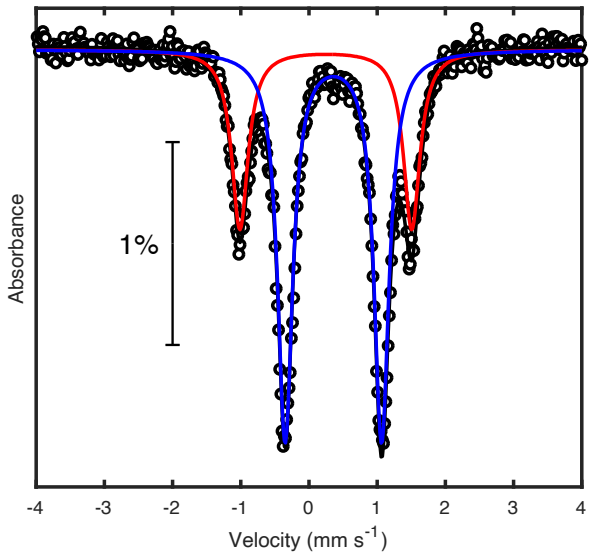

Figure S6.16: Mössbauer spectrum of [**1-CO**]$^{+}$ at 80 K (dots) and total simulation using the parameters in table S6.1 (black). The Fe–CO site is shown in red and the sum of the two Fe–NHC sites is shown in blue.

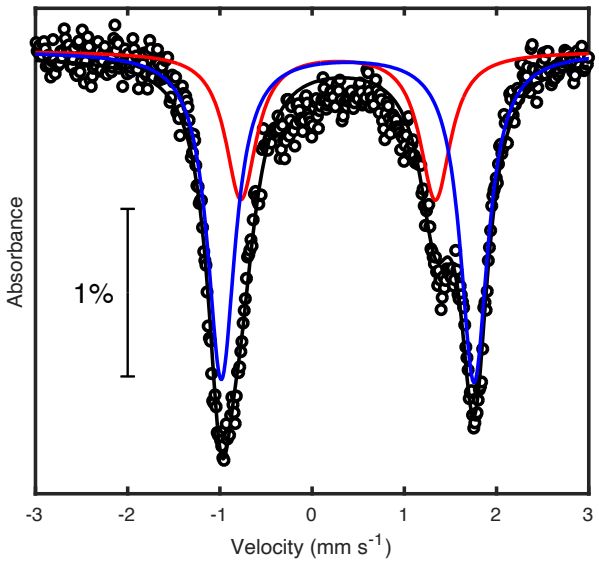

Figure S6.17: Mössbauer spectrum of [**1-CO**]$^{-}$ at 80 K (dots) and total simulation using the parameters in table S6.1 (black). The Fe–CO site is shown in red and the sum of the two Fe–NHC sites is shown in blue.

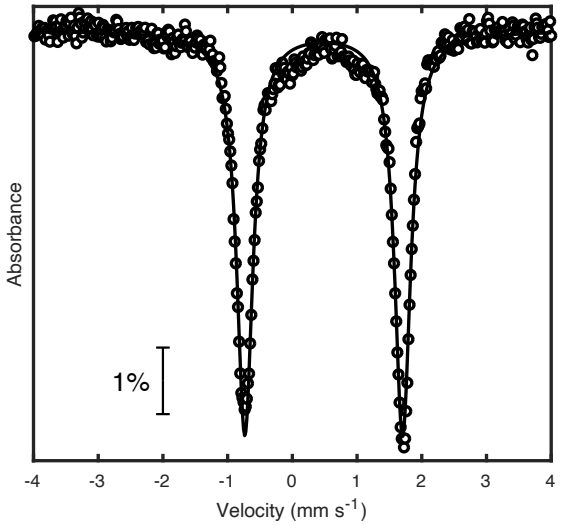

Figure S6.18: Mössbauer spectrum of **1-IMes** at 80 K (dots) and total simulation using the parameters in table S6.1 (black). All three Fe–NHC sites are simulated with one quadrupole doublet.

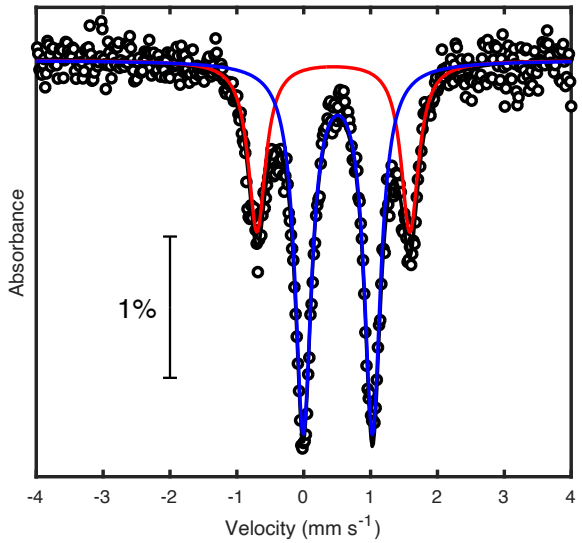

Figure S6.19: Mössbauer spectrum of [**1-IMes**]$^{+}$ at 80 K (dots) and total simulation using the parameters in table S6.1 (black). Two NHC sites are simulated with small $|\Delta E_Q|$ (blue) and one Fe–NHC site with large $|\Delta E_Q|$ (red).

Table S6.1: Fit parameters for Mössbauer spectrum of [**1-CO**]$^{-/0/+}$ and [**1-IMes**]$^{0/+}$

		δ (mm·s^{-1})	$\lvert\Delta E_Q\rvert$ (mm·s^{-1})	Γ (mm·s^{-1})	Rel. Area
1-CO	Fe–CO	0.241	2.402	0.295	1
	Fe–NHC (1)	0.397	1.664	0.500	1
	Fe–NHC (2)	0.419	2.342	0.485	1
[**1-CO**]$^{+}$	Fe–CO	0.247	2.520	0.292	1
	Fe–NHC	0.358	1.414	0.268	2
[**1-CO**]$^{-}$	Fe–CO	0.282	2.109	0.405	1
	Fe–NHC	0.386	2.741	0.364	2
1-IMes	Fe–NHC	0.484	2.438	0.302	1
[**1-IMes**]$^{+}$	Fe–NHC (1)	0.444	2.287	0.317	1
	Fe–NHC (2)	0.510	1.035	0.295	2

G. Cyclic Voltammetry

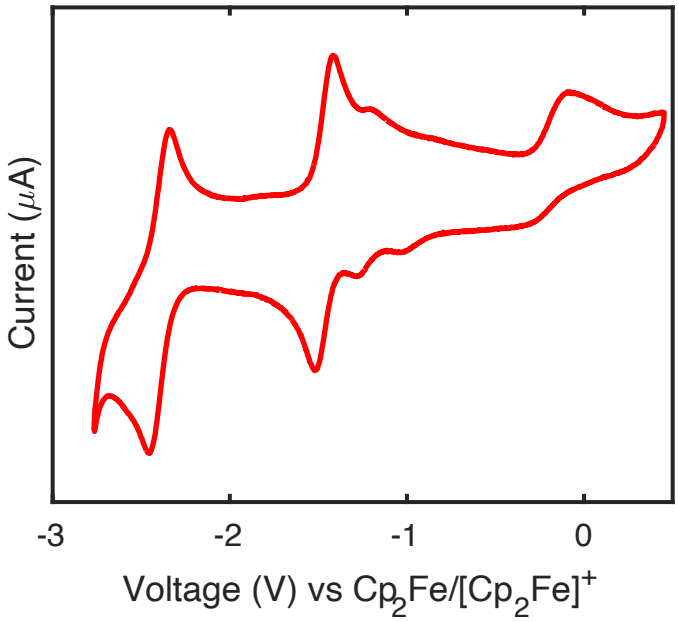

Figure S6.20: Cyclic voltammogram of **1-CO** in DFB with 0.2 M $TPABAr^{F}{}_{4}$ using a glassy carbon working electrode, a silver wire counter electrode, and a silver wire reference electrode at a scan rate of 200 mv/s. Compound **1-CO** undergoes a reduction to [**1-CO**]$^{-}$ at –2.40 V and an oxidation to [**1-CO**]$^{+}$ at –1.45 V vs Fc/Fc^{+}.

H. Crystallographic Details

1-CO: Crystallizes in $P2_1/m$ from THF and pentane with pentane in the lattice. The lattice solvent was disordered; this disorder was modeled using similarity restraints on 1-2 and 1-3 distances and displacement parameters and rigid bond restraints. The cluster resides on a mirror plane; the Cp* ring was refined as disordered 50/50 over this mirror plane.

[**1-CO**]$^+$: Crystallizes in P1 from DFB and pentane with four molecules in the asymmetric unit. It additionally crystallized as a non-merohedral twin. A second domain was found using cell_now, twinning was taken into account during data integration, scaling was done with TWINABS, and the data was refined against the HKLF5 file.

[**1-CO**]$^-$: Crystallizes in P–1 from THF and pentane with pentane in the lattice. The lattice solvent was disordered; this disorder was modeled using similarity restraints on 1-2 and 1-3 distances and displacement parameters and rigid bond restraints.

1-IMes: Crystallizes in P–3c1 from THF and pentane. The cluster lies on a 3-fold rotational axis and is generally well-ordered on this axis except for the Cp* ring, which was modelled in part -1; 3-fold staggered over the rotational axis. The lattice solvent was severely disordered and so solvent contributions to the diffraction pattern were removed with SQUEEZE.[18]

[**1-IMes**]$^+$: Crystallizes in $P2_1/n$ from DFB and HMSO with DFB in the lattice. The lattice solvent, the [$BAr^F{}_4$] anion, the Cp* ring, one IMes ligand, and one cluster Fe and 2 S atoms were disordered;

The disorder in the lattice solvent, [BAr^F_4] anion, Cp* ring, and IMes ligand was modeled using similarity restraints on 1-2 and 1-3 distances and displacement parameters and rigid bond restraints. The disorder in the Fe and S positions was modeled using only similarity restraints on the displacement parameters and rigid bond restraints.

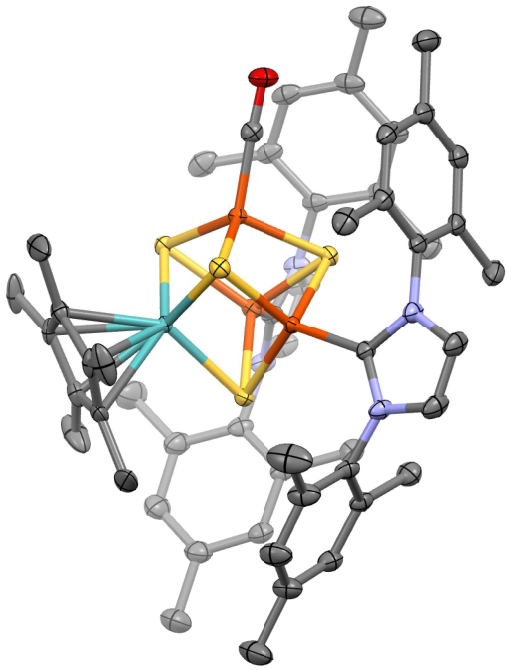

Figure S6.21: Crystallographic structure of **1-CO** with ellipsoids at the 50% probability level. Carbon (gray), nitrogen (blue), iron (orange), sulfur (yellow), molybdenum (teal) and oxygen (red).

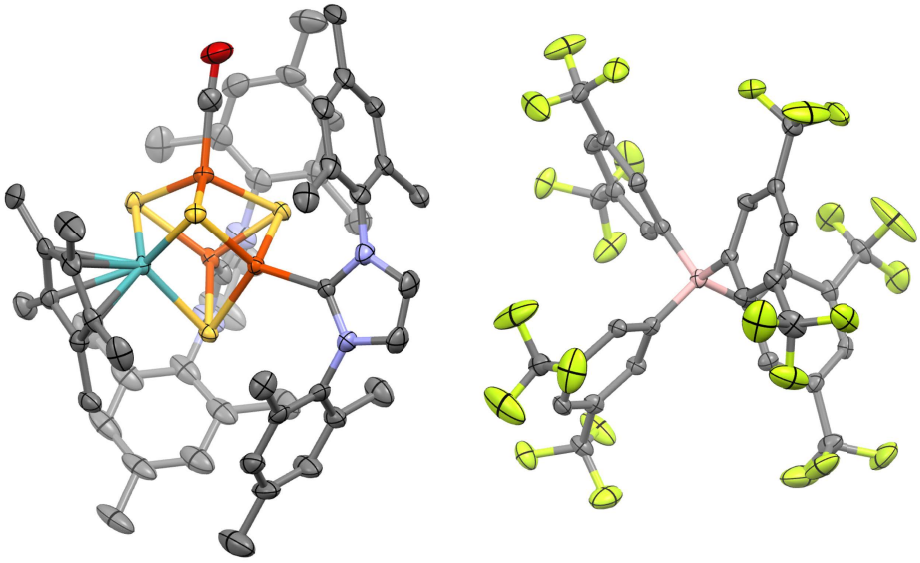

Figure S6.22: Crystallographic structure of [**1-CO**]$^{+}$ with ellipsoids at the 50% probability level. Carbon (gray), nitrogen (blue), iron (orange), sulfur (yellow), molybdenum (teal), oxygen (red), boron (pink), and fluorine (green).

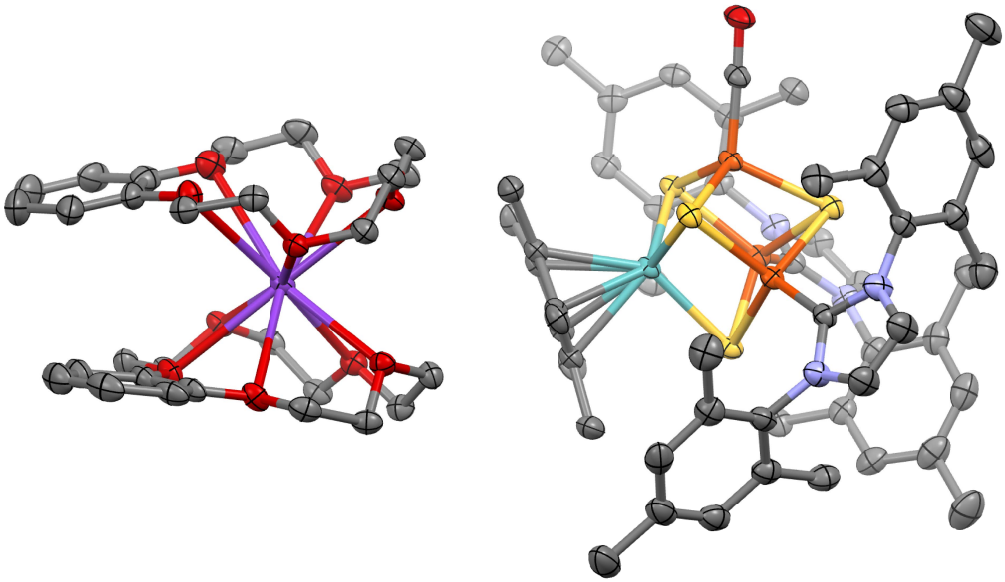

Figure S6.23: Crystallographic structure of [**1-CO**]$^{+}$ with ellipsoids at the 50% probability level. Carbon (gray), nitrogen (blue), iron (orange), sulfur (yellow), molybdenum (teal), oxygen (red), and potassium (purple).

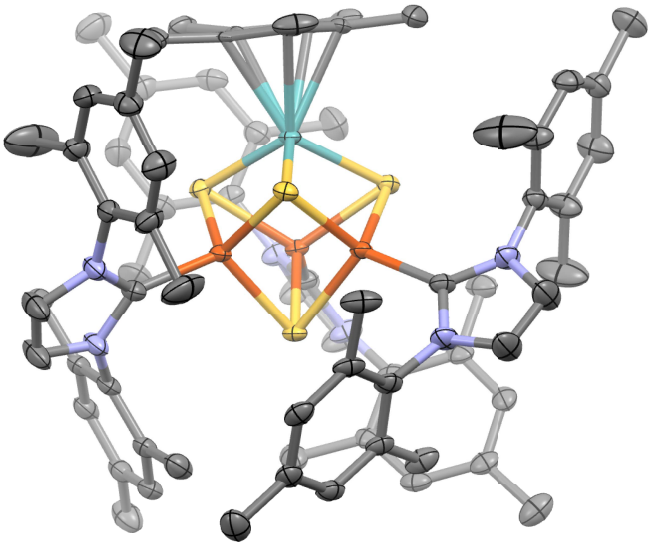

Figure S6.24: Crystallographic structure of **1-IMes** with ellipsoids at the 50% probability level. Carbon (gray), nitrogen (blue), iron (orange), sulfur (yellow), molybdenum (teal).

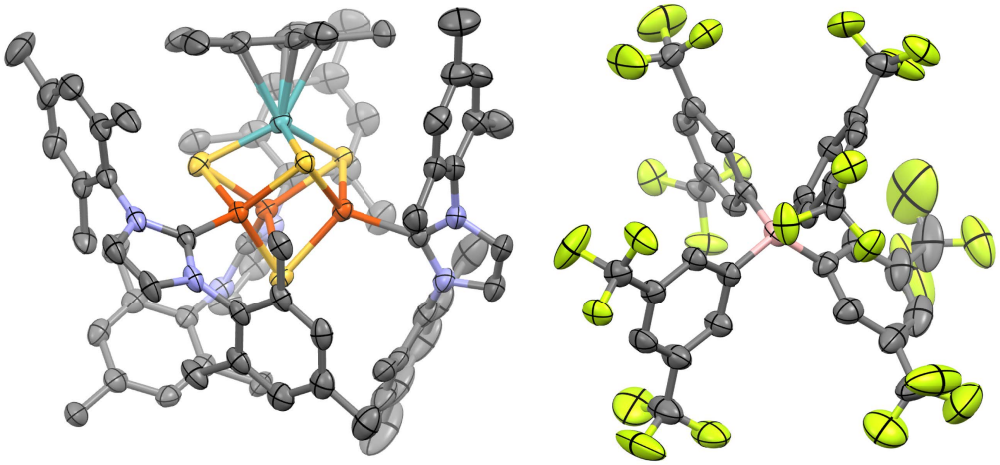

Figure S6.25: Crystallographic structure of [**1-IMes**][BAr^{F}_{4}] with ellipsoids at the 50% probability level. Carbon (gray), nitrogen (blue), iron (orange), sulfur (yellow), molybdenum (teal), boron (pink), and fluorine (green).

I. References

(1) Smallcombe, S. H.; Patt, S. L.; Keifer, P. A. WET Solvent Suppression and Its Applications to LC NMR and High-Resolution NMR Spectroscopy. *J. Magn. Reson. Ser. A* **1995**, *117* (2), 295–303.

(2) Stoll, S.; Schweiger, A. EasySpin, a Comprehensive Software Package for Spectral Simulation and Analysis in EPR. *J. Magn. Reson.* **2006**, *178* (1), 42–55.

(3) Prisecaru, I. WMOSS4 Mössbauer Spectral Analysis Software, www.wmoss.org.

(4) Hübschle, C. B.; Sheldrick, G. M.; Dittrich, B. ShelXle: A Qt Graphical User Interface for SHELXL. *J. Appl. Crystallogr.* **2011**, *44* (6), 1281–1284.

(5) Deng, L.; Holm, R. H. Stabilization of Fully Reduced Iron-Sulfur Clusters by Carbene Ligation: The $[Fe_nS_n]^0$ Oxidation Levels (n = 4, 8). *J. Am. Chem. Soc.* **2008**, *130* (30), 9878–9886.

(6) Brown, A. C.; Suess, D. L. M. Controlling Substrate Binding to Fe_4S_4 Clusters through Remote Steric Effects. *Inorg. Chem.* **2019**, *58* (8), 5273–5280.

(7) Brown, A. C.; Thompson, N. B.; Suess, D. L. M. Evidence for Low-Valent Electronic Configurations in Iron–Sulfur Clusters. *J. Am. Chem. Soc.* **2022**, *144* (20), 9066–9073.

(8) Bantreil, X.; Nolan, S. P. Synthesis of N-Heterocyclic Carbene Ligands and Derived Ruthenium Olefin Metathesis Catalysts. *Nat. Protoc.* **2011**, *6* (1), 69–77.

(9) Hintermann, L. Expedient Syntheses of the N-Heterocyclic Carbene Precursor Imidazolium Salts IPr·HCl, IMes·HCl and IXy·HCl. *Beilstein J. Org. Chem.* **2007**, *3* (22).

(10) Peters, J. C.; Johnson, A. R.; Odom, A. L.; Wanandi, P. W.; Davis, W. M.; Cummins, C. C. Assembly of Molybdenum/Titanium μ-Oxo Complexes via Radical Alkoxide C-O Cleavage. *J. Am. Chem. Soc.* **1996**, *118* (42), 10175–10188.

(11) Yakelis, N. A.; Bergman, R. G. Safe Preparation and Purification of Sodium Tetrakis[(3,5-Trifluoromethyl)Phenyl]Borate ($NaBArF_{24}$): Reliable and Sensitive Analysis of Water in Solutions of Fluorinated Tetraarylborates. *Organometallics* **2005**, *24* (14), 3579–3581.

(12) Scott, T. A.; Ooro, B. A.; Collins, D. J.; Shatruk, M.; Yakovenko, A.; Dunbar, K. R.; Zhou, H. C. After 118 Years, the Isolation of Two Common Radical Anion Reductants as Simple, Stable Solids. *Chem. Commun.* **2009**, No. 1, 65–67.

(13) Komuro, T.; Kawaguchi, H.; Lang, J.; Nagasawa, T.; Tatsumi, K. $[MoFe_3S_4]^{3+}$ and $[MoFe_3S_4]^{2+}$ Cubane Clusters Containing a Pentamethylcyclopentadienyl Molybdenum Moiety. *J. Organomet. Chem.* **2007**, *692* (1–3), 1–9.

(14) Sridharan, A.; Brown, A. C.; Suess, D. L. M. A Terminal Imido Complex of an Iron–Sulfur Cluster. *Angew. Chem. Int. Ed.* **2021**, *60* (23), 12802–12806.

(15) McSkimming, A.; Suess, D. L. M. Dinitrogen Binding and Activation at a Molybdenum–Iron–Sulfur Cluster. *Nat. Chem.* **2021**, *13* (7), 666–670.

(16) Brown, A. C.; Suess, D. L. M. Valence Localization in Alkyne and Alkene Adducts of Synthetic $[Fe_4S_4]^+$ Clusters. *Inorg. Chem.* **2022**, *62* (5) 1911-1918.

(17) Kuveke, R. E. H. H.; Barwise, L.; Ingen, Y. Van; Vashisth, K.; Roberts, N.; Chitnis, S. S.; Dutton, J. L.; Martin, C. D.; Melen, R. L.; Van Ingen, Y.; Vashisth, K.; Roberts, N.; Chitnis, S. S.; Dutton, J. L.; Martin, C. D.; Melen, R. L. An International Study Evaluating Elemental Analysis. *ACS Cent. Sci.* **2022**, *8* (7), 855–863.

(18) Spek, A. L. PLATON SQUEEZE: A Tool for the Calculation of the Disordered Solvent Contribution to the Calculated Structure Factors. *Acta Crystallogr. Sect. C Struct. Chem.* **2015**, *71*, 9–18.

Chapter 7. Reversible Formation of Alkyl Radicals at [Fe_4S_4] Clusters and Its Implications for Selectivity in Radical SAM Enzymes

Introduction

Nature utilizes radical chemistry for a wide range of challenging reactions including cofactor maturation, antibiotic synthesis, and secondary metabolism.[1–4] The most common radical initiator is the 5′-deoxyadenosyl radical (5′-dAdo•), which is generated in adenosylcobalamin and radical *S*-adenosylmethionine (SAM) enzymes.[1,3] Because the 5′-dAdo• is a primary carbon radical, it can abstract H atoms from strong X–H bonds and initiate reactions that proceed through high-energy intermediates.[5] Although this enables thermodynamically and kinetically challenging reactions to proceed, it introduces an additional difficulty: how to generate and utilize the 5′-dAdo• in a controlled fashion so as to avoid unproductive reactivity.

The 5′-dAdo• is derived from relatively unreactive precursors, either by homolysis of the Co–C bond in adenosylcobalamin[1] or by reductive cleavage of an S–C bond in SAM (Figure 7.1).[3,6,7] In both adenosylcobalamin and radical SAM enzymes, a dramatic rate enhancement for production of the 5′-dAdo• is observed only when all reaction components are present (i.e., substrate and adenosylcobalamin for adenosylcobalamin enzymes[8–11] or substrate, SAM, and a reduced [Fe_4S_4] cluster for radical SAM enzymes[12]). But even with this safety mechanism operative, it is possible for the 5′-dAdo• to react unproductively, for example by abstracting the wrong H atom from the substrate or the protein. How selective H-atom abstraction occurs upon generation of the 5′-dAdo• is therefore a critical subject of investigation. Structural modeling and spectroscopic studies of adenosylcobalamin enzymes suggest that the 5′ carbon must traverse several ångstroms (ca. 6 Å) between the Co center and the target substrate H atom.[13–16] In contrast, structural and spectroscopic studies of radical SAM enzymes with SAM and substrate bound reveal that the substrate X–H bond is positioned in

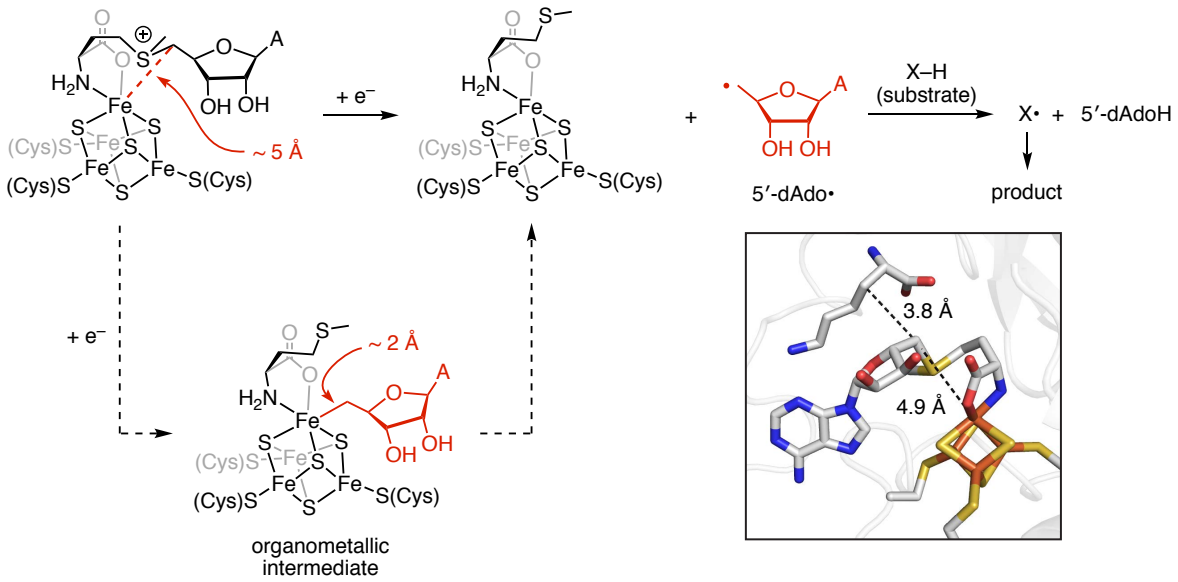

Figure 7.1. Proposed mechanism for 5′-dAdo• formation in radical SAM enzymes showing the bond-distance changes incurred upon Fe–C bond formation and homolysis. (Inset) Structure of the lysine 2,3-aminomutase active site (PDB ID: 2A5H). From the available structural and spectroscopic data, the 5′ carbon appears to be primed for selective H-atom abstraction, but formation and homolysis of an Fe–C bond would require significant rearrangement in the active site with the 5′ carbon moving away from the substrate X–H bond to form an Fe–C bond and back toward the substrate to undergo H-atom abstraction.

close proximity to the 5′-dAdo carbon (ca. 4 Å, corresponding to only ca. 3 Å to the target H atom; Figure 7.1, inset).[17,18] Based on these findings, it was proposed[17] that the closer proximity of the substrate's target H atom and the 5′-carbon in radical SAM enzymes compared to adenosylcobalamin enzymes may explain why radical SAM enzymes outnumber[19,20] adenosylcobalamin enzymes by a factor of ~10^4: because radical SAM enzymes position the substrate X–H bond adjacent to the nascent 5′-dAdo•, their active sites are predisposed to perform selective H-atom abstraction upon generation of the 5′-dAdo•.

This narrative has been somewhat complicated by the discovery of an unexpected intermediate in 5′-dAdo• formation: an organometallic species—observed in a wide range of radical SAM enzymes—that features a bond between an Fe of the [Fe_4S_4] cluster and the 5′-dAdo carbon, akin to the Co–C bond in adenosylcobalamin (Figure 7.1).[21,22] Efforts to understand this species' precise geometric and electronic structure are ongoing and its role as an intermediate in 5′-dAdo• generation raises several questions. First, because Fe–C bond

homolysis is an unprecedented reaction for Fe–S clusters, it is unclear if and how the Fe–C bond in an alkylated [Fe_4S_4] cluster can be sufficiently weakened to generate primary carbon radicals. Second, the careful positioning of the 5′ carbon near the target H atom—certainly an important factor for selectivity—must also be considered in light of the geometric changes required to form and break an Fe–C bond (Figure 7.1);[23] if such dramatic rearrangements occur during catalysis, then rigid positioning of the substrate and SAM cannot fully account for the selectivity of radical SAM enzymes. Therefore, other mechanisms for achieving selectivity must be considered, particularly those that take into account the dynamic nature of the active site.

We herein address these questions with a combination of model chemistry and kinetic simulations. In contrast to synthetic models of adenosylcobalamin enzymes, which have provided insights into the structure and reactivity of adenosylcobalamin,[24–33] there are no functional models of the organometallic intermediate in radical SAM enzymes (i.e., alkylated [Fe_4S_4] clusters that generate alkyl radicals). Using synthetic [Fe_4S_4]–alkyl clusters, we show that even highly reactive, primary carbon radicals can be generated from [Fe_4S_4]–alkyl clusters and in doing so delineate the coordination-chemistry requirements for Fe–C bond homolysis. Notably, we find that Fe–C bond homolysis is both facile and reversible. Using kinetic simulations, we then evaluate the circumstances in which reversible Fe–C bond homolysis can affect the selectivity of H-atom abstraction. Our findings suggest that, by slowing the rates of all reactions of the 5′-dAdo•, an organometallic intermediate may be key to achieving selective reactivity in radical SAM enzymes.

Results and Discussion

Synthesis of alkylated [Fe_4S_4] clusters

We recently reported the first [Fe_4S_4]–alkyl cluster, which is stable with respect to Fe–C bond homolysis at room temperature.[34] Our current study centers on the chemistry of

alkylated [Fe_4S_4] clusters supported by the *N*-heterocyclic carbene IMes (IMes = 1,3-dimesitylimidazol-2-ylidene); the complement of three strongly binding IMes ligands increases the stability of these clusters and makes them suitable for reactivity and mechanistic studies.

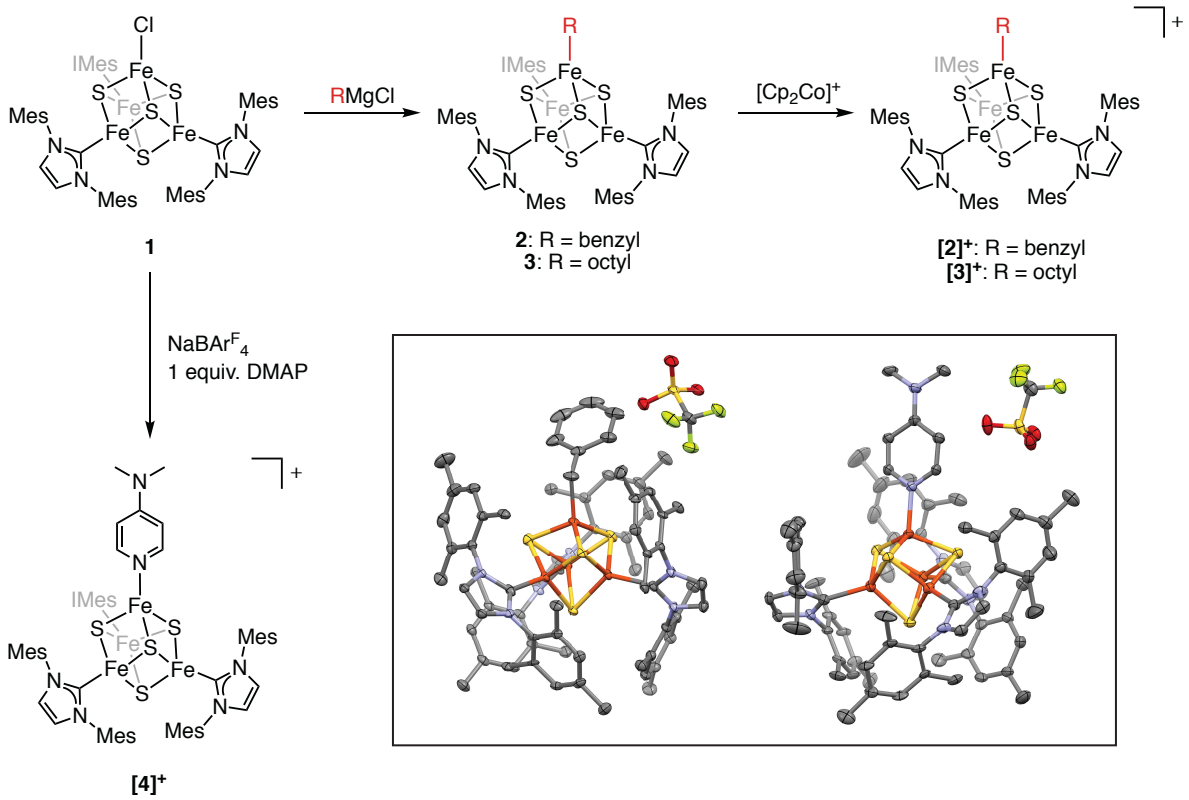

Figure 7.2. Synthesis of alkylated [Fe_4S_4]$^{+/2+}$ clusters and an [Fe_4S_4]$^{+}$–DMAP adduct**.** (Inset) Thermal ellipsoid (50%) plot of **[2][OTf]** (left) and **[4][OTf]** (right). Color scheme: carbon (gray), iron (orange), sulfur (yellow), nitrogen (blue), oxygen (red), fluorine (green).

Synthetic access to IMes-supported [Fe_4S_4]–alkyl clusters is afforded by treatment of (IMes)$_3$$Fe_4S_4$Cl (**1**)[35] with the appropriate Grignard reagent to provide (IMes)$_3$$Fe_4S_4$(benzyl) (**2**) and (IMes)$_3$$Fe_4S_4$(octyl) (**3**) in 64% and 66% yield, respectively (Figure 7.2). The ^{1}H NMR resonances from the IMes ligands in **2** and **3** are similar to those observed for **1**. The α protons of the benzyl and octyl groups are observed at 223 and 258 ppm for **2** and **3**, respectively; the β protons of the octyl group in **3** are observed at 22 ppm. EPR spectroscopic analysis establishes that both clusters have an S = ½ ground spin state (Figures S7.53 and S7.54). The one-electron oxidized clusters [(IMes)$_3$$Fe_4S_4$(benzyl)][$BAr^F_4$] (**[2]**$^+$, [$BAr^F_4$] = [tetrakis(3,5-trifluoromethyl)phenyl]borate)]**)** and [(IMes)$_3$$Fe_4S_4$(octyl)][$BAr^F_4$] (**[3]**$^+$) were synthesized by

reaction of **2** or **3** with $[Cp_2Co][BAr^F_4]$. Upon oxidation, the resonances in the ^{1}H NMR spectrum corresponding to the α protons of the benzyl and octyl groups shift upfield to 68 ppm for $\mathbf{[2]}^+$ and 75 ppm for $\mathbf{[3]}^+$; the β protons in $\mathbf{[3]}^+$ also shift upfield to –3.5 ppm. These shifts are similar to the ^{1}H NMR shifts observed in the previously reported $[Fe_4S_4]^{2+}$–Et cluster[34] and are indicative of a diamagnetic ground state with thermally populated, paramagnetic excited states. Clusters **2** and $\mathbf{[2]}^+$ have been crystallographically characterized (Figure 7.2 (inset) and S7.80); their metrical parameters are similar to those of **1** and of the previously reported alkyl cluster.[34]

Observation of Fe–C bond homolysis

In comparison to the organometallic intermediate characterized in radical SAM enzymes—which is consumed in minutes at 170 K[21]—the alkylated clusters described above are strikingly stable. We attribute this to the coordination number of the alkylated Fe site: homolysis of the Fe–C bond would lead to a high-energy intermediate with a three-coordinate Fe site. In contrast, homolysis of the Fe–C bond in the organometallic intermediate in radical SAM enzymes, which is thought to have a six-coordinate Fe site, would generate an energetically feasible, five-coordinate Fe site. We therefore hypothesized that addition of an exogenous ligand to the synthetic clusters could lead to Fe–C bond homolysis through an intermediate with a five-coordinate Fe site. Indeed, reaction of $\mathbf{[2]}^+$ with an excess of a pyridine, such as 4-*N*,*N*-dimethylaminopyridine (DMAP), results in a rapid reaction at room temperature to generate the reduced $[Fe_4S_4]^+$ cluster $[(IMes)_3Fe_4S_4(DMAP)][BAr^F_4]$ ($\mathbf{[4]}^+$, 95 ± 3%) and bibenzyl (92 ± 3 % yield) (Scheme 7.1A). The identity of $\mathbf{[4]}^+$ was confirmed by its independent synthesis and characterization (Figure 7.2). Fe–C bond homolysis extends to other alkyl groups including those whose corresponding radicals are much more reactive than the benzyl radical. For example, when DMAP is added to $\mathbf{[3]}^+$, $\mathbf{[4]}^+$ (92 ± 3 %) and hexadecane (75 ± 8 % yield)

are rapidly formed (Scheme 7.1B). The rate of C–C bond formation scales with the substituent Hammett parameters;[36] when DMAP ($\sigma_p = -0.83$) is added to $[\mathbf{2}]^+$, the reaction is complete in less than 10 min, whereas the reaction of $\mathbf{[2]}^+$ with pyridine ($\sigma_p = 0.0$) results in ca. 90% conversion in 15 min and that of $\mathbf{[2]}^+$ with 4-trifluoromethylpyridine (CF_3-py, $\sigma_p = 0.54$) takes over 24 h to reach 90% completion (Scheme 7.1C). The rates increase with the donicity of the substituted pyridine, consistent with pyridine coordination preceding Fe–C bond homolysis. Fe–C bond homolysis is not limited to pyridinyl donors; addition of quinuclidine generates the quinuclidine adduct (98 ± 3 %) and bibenzyl (90 ± 4 %).

The reactions of $\mathbf{[2]}^+$ and $\mathbf{[3]}^+$ with exogenous ligands are consistent with donor-induced Fe–C bond homolysis followed by combination of the radical with another benzyl or alkyl group to form bibenzyl or hexadecane (the C–C bond-forming step could occur by one or more pathways involving a radical; see SI p. S39). Such mechanisms involving M–C bond

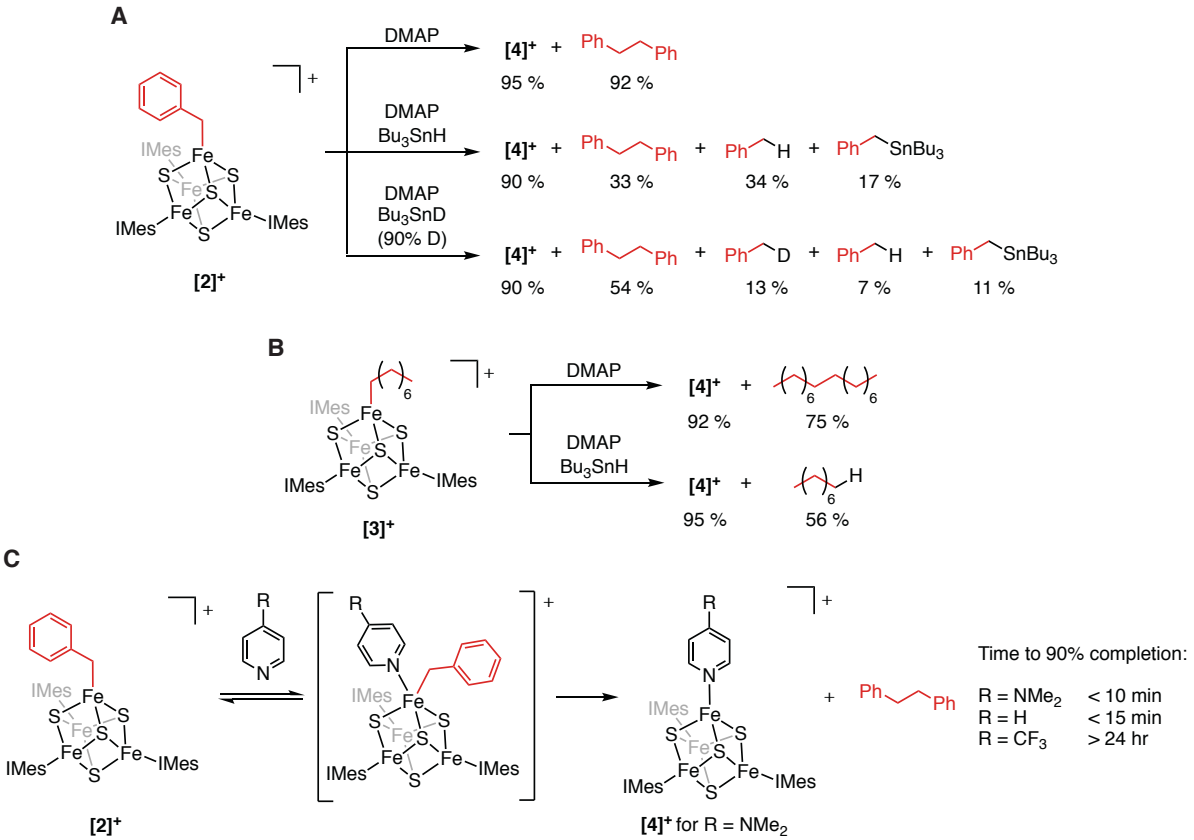

Scheme 7.1. Formation of alkyl radicals from [Fe_4S_4] clusters. (A) Generation and trapping of benzyl radicals upon treatment of **[2]**$^+$ with DMAP. (B) Generation and trapping of octyl radicals upon treatment of **[3]**$^+$ with DMAP. (C) Reaction of **[2]**$^+$ with substituted pyridines.

homolysis would align our findings with those observed for adenosylcobalamin model complexes[24,29,33,37] and those proposed for organometallic intermediates in radical SAM enzymes.[21,22,38] However, these observations do not rule out other conceivable mechanisms that proceed without formation of organic radicals (i.e., those in which bibenzyl or hexadecane is formed through concomitant Fe–C bond cleavage and C–C bond formation). No intermediates were observable by NMR or EPR spectroscopies, so to distinguish between these mechanistic possibilities we performed a series of experiments to assay for the generation of organic radicals.

As an initial test, we carried out the reaction of **[2]**$^+$ and **[3]**$^+$ with DMAP in the presence of a radical trap. We chose Bu_3SnH because it does not react with either cluster in the absence of DMAP and the expected organic products (toluene for **[2]**$^+$ and octane for **[3]**$^+$) are

readily detected by ^{1}H NMR spectroscopy and GC–MS, respectively. When DMAP is added to **[2]**$^+$ in the presence of 20 equiv. of Bu_3SnH, the reduced cluster **[4]**$^+$ is formed in less than 10 minutes. Alkyl groups are detected as a mixture of toluene (34 ± 3%), bibenzyl (33 ± 3%), and Bu_3SnBn (17 ± 3%) (Scheme 7.1A). That both bibenzyl and toluene were observed in this reaction indicates incomplete trapping of the benzyl radicals by Bu_3SnH and suggests that the pathways that lead to bibenzyl and toluene occur with competitive rates. Addition of DMAP to **[3]**$^+$ in the presence of Bu_3SnH induces similar reactivity with production of octane (56 ± 6%; Scheme 7.1B). The reaction of **[2]**$^+$ with DMAP was also carried out in the presence of Bu_3SnD (90% D), which resulted in the formation of bibenzyl (54 ± 3%), toluene (7 ± 3%), d^1-toluene (13 ± 3%) and Bu_3SnBn (11 ± 3%) (Scheme 7.1A). Formation of d^1-toluene indicates that Bu_3SnD is the deuterium-atom source and the lower deuterium incorporation into toluene (1:1.9 H:D) compared to Bu_3SnH/D (1:9 H:D) is indicative of a kinetic isotope effect for H/D-atom abstraction from Bu_3SnH/D.

Because radical traps can alter the major mechanistic pathway of the reaction—and therefore not provide definitive evidence of free-radical intermediates—we pursued the use of radical clocks as a complementary test for the generation of free radicals. For these purposes, we wanted a radical clock that rearranges on a timescale similar to or faster than the rate of other reactions involving organic radicals, which we estimated based on the following observations. In the reaction of **[2]**$^+$ with DMAP, the benzyl radical is only partially trapped by Bu_3SnH, suggesting that other reactions leading to bibenzyl formation are competitive with trapping. Because H–$SnBu_3$ abstraction by an organic radical occurs at ~10^6 s^{-1},[39] we predicted that a radical clock with a similar rate constant would exhibit at least partial rearrangement under the Fe–C bond homolysis conditions. We therefore selected the 5-hexenyl radical clock, which rearranges to the cyclopentylmethyl radical with a rate constant of 1.8 x 10^5 s^{-1} (20

°C),[40,41,42] and assayed for organic products derived from the 5-hexenyl and/or cyclopentylmethyl radicals.

To test these predictions, we prepared $(IMes)_3Fe_4S_4$(5-hexenyl) (**5**) and $[(IMes)_3Fe_4S_4(5\text{-hexenyl})][BAr^F{}_4]$ (**[5]**$^+$) using the methodology described above. The ^{1}H NMR spectra of **5** and **[5]**$^+$ are similar to those of **3** and **[3]**$^+$; the α and β protons of the 5-hexenyl group shift from 256 ppm and 24.5 ppm, respectively, to 74 ppm and -4.0 ppm, respectively, upon oxidation of **5** to **[5]**$^+$. Addition of excess DMAP to **[5]**$^+$ leads to immediate formation of **[4]**$^+$ and coupled organic fragments. Integration of the ^{1}H NMR spectrum suggests that approximately 72 ± 2 % of the alkyl groups are cyclized, while 28 ± 2% of the alkyl groups still contain alkene resonances (Figures S7.50 and S7.51). The observation of both cyclized and uncyclized organic products strongly supports that the Fe–C bond undergoes homolysis upon addition of DMAP to **[5]**$^+$ and suggests that the rates of subsequent steps involving the organic radical are indeed competitive with cyclization.

Evidence for reversible Fe–C bond homolysis

We also carried out the reaction of **[5]**$^+$ with an excess of CF_3-py. As expected, addition of CF_3-py induces consumption of **[5]**$^+$ and formation of the CF_3-py adduct, **[6]**$^+$. This reaction takes more than 24 h to reach completion (much slower than when DMAP is added) because of the diminished equilibrium for CF_3-py binding. Intriguingly, a second species, characterized by peaks in the ^{1}H NMR spectrum at 75 ppm and –3 ppm, increases in intensity over the course of this reaction (Figure 7.3). Given the similarity of the ^{1}H NMR resonances to those of the other $[Fe_4S_4]^{2+}$–alkyl clusters described herein, we hypothesized that this new species was $[(IMes)_3Fe_4S_4(\text{cyclopentylmethyl})][BAr^F{}_4]$ (**[7]**$^+$), containing a cyclopentylmethyl group derived from the 5-hexenyl radical; its identity was confirmed by independent synthesis of **[7]**$^+$. We note that **[5]**$^+$ does not convert to **[7]**$^+$ in the absence of added pyridine. The conversion of

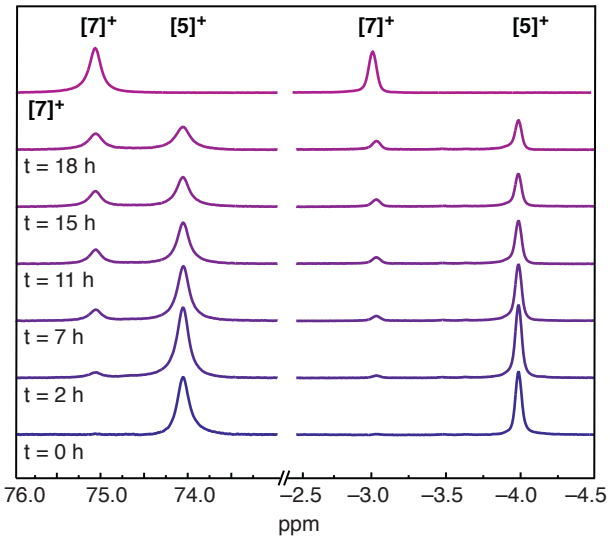

Figure 7.3. Partial ^{1}H NMR spectrum of the reaction between **[5]**$^{+}$ and CF_3-py showing the decay of **[5]**$^{+}$ and the growth of **[7]**$^{+}$ during the course of the reaction. The top trace is an authentic sample of **[7]**$^{+}$.

[5]$^{+}$ to **[7]**$^{+}$ via organic radicals demonstrates that Fe–C bond homolysis is reversible, whereby pyridine binding to **[5]**$^{+}$ induces formation of the transient 5-hexenyl radical, which rearranges to the cyclopentylmethyl radical and recombines with **[6]**$^{+}$ to give **[7]**$^{+}$ (Scheme 7.2A).

Based on these findings, we predicted that Fe–C bond homolysis in the reaction of **[2]**$^{+}$ with pyridines should also be reversible, and that if this was the case, [(IMes)$_3$Fe$_4$S$_4$(pyridine)][BAr$^{F}_4$] (**[8]**$^{+}$) would inhibit the radical termination steps that lead to bibenzyl. To test this, we added pyridine to **[2]**$^{+}$ in the presence and absence of additional **[8]**$^{+}$ (Scheme 7.2B); we chose to perform this test with pyridine and **[8]**$^{+}$ rather than DMAP and **[4]**$^{+}$ to slow the reaction so that the effect of the additional pyridine adduct would be easier to observe by ^{1}H NMR spectroscopy. In the absence of added **[8]**$^{+}$, the reaction of **[2]**$^{+}$ and pyridine to yield **[8]**$^{+}$ and bibenzyl is ca. 90% complete in 15 minutes. Strikingly, in the presence of 10 equiv. of added **[8]**$^{+}$, the reaction is only ca. 50% complete after 2 h. Taken together, these observations demonstrate rapid and reversible alkyl radical formation from [Fe$_4$S$_4$] clusters. That [Fe$_4$S$_4$] clusters exhibit this reactivity, which has also been observed in

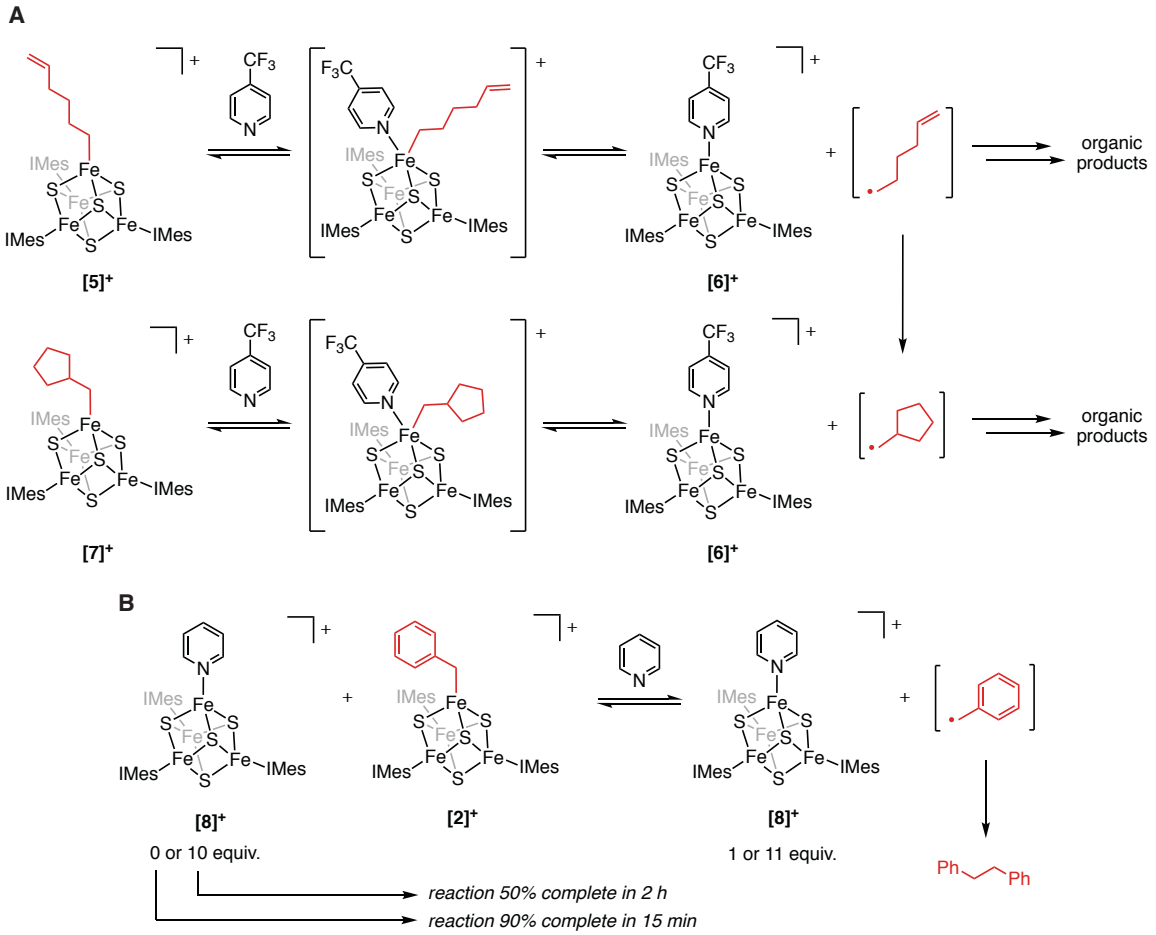

Scheme 7.2. Evidence for reversible Fe–C bond homolysis. (A) Proposed mechanism for the conversion of **[5]**$^+$ to **[7]**$^+$. (B) Reaction of **[2]**$^+$ with pyridine in the presence of an excess of **[8]**$^+$ decreases the rate of bibenzyl formation.

other open-shell metal complexes[37,43–46]—most notably adenosylcobalamin models—further deepens the connections between the chemistry of adenosylcobalamin and radical SAM enzymes.

Kinetic simulations of reversible Fe–C bond homolysis in radical SAM enzymes

Our results demonstrate that even primary alkyl radicals can be produced from [Fe_4S_4]–alkyl clusters, providing support for the intermediacy of organometallic species in radical SAM enzymes.[21,22,38] We now consider how an organometallic intermediate that generates an alkyl radical can impact catalysis in radical SAM enzymes. First, an organometallic precursor to the

5′-dAdo• would clearly decrease the population of the 5′-dAdo•, with a stronger Fe–C bond shifting the homolysis equilibrium towards the organometallic species. An Fe–C bond that is too strong could shut down 5′-dAdo• production entirely, but our results suggest that radical SAM enzymes may avoid this scenario by virtue of the coordination geometry at the unique Fe site: coordination of the amine (and likely the carboxylate) of methionine renders the apical Fe site five- or six-coordinate. As we have shown here, coordination numbers greater than four for the alkylated Fe results in a dramatically weakened Fe–C bond.

However, even a weak Fe–C bond would significantly deplete the population of the 5′-dAdo•. This would decrease the rates of all subsequent steps, but how would it impact selectivity for productive versus unproductive reactions? Of course, if the 5′-dAdo• and substrate are perfectly positioned for abstraction of only the desired H atom, the selectivity for the productive pathway would be perfect, and an organometallic intermediate would have no impact on selectivity. Even if the 5′-dAdo• can undergo unproductive reactions, such as abstracting the wrong H atom from the substrate or protein, the selectivity would depend only on the relative rates of the productive and unproductive pathways (Figure 7.4A and 7.4B).
An organometallic intermediate can only affect the selectivity of the H-atom abstraction step if an additional, kinetically coupled process is operative. Multiple selectivity-influencing processes can be envisioned including bond rotations, rearrangements in the active site, or larger conformational changes. Regardless of their precise nature, such processes will affect the selectivity of the reaction only if they can outcompete X–H bond activation. Under these conditions, an organometallic intermediate can affect selectivity by slowing the rates of X–H bond activation to allow these processes to occur.

We evaluated this hypothesis using a simplified kinetic model consisting of a radical SAM enzyme for which the selectivity of X–H bond activation is dictated by whether the protein is in a productive state (denoted P and representing states leading to the substrate

radical) or an unproductive state (denoted U and representing states leading to any other reaction of the 5′-dAdo•) (Figure 7.4C). In choosing rate constants for these simulations, we assumed that recombination of the 5′-dAdo• with the cluster is rapid ($k_{-1} = 10^{11}$ s^{-1}), that interconversion between protein states is slow ($k_2 = 10^2$ s^{-1} and $k_{-2} = 1$ s^{-1}, favoring

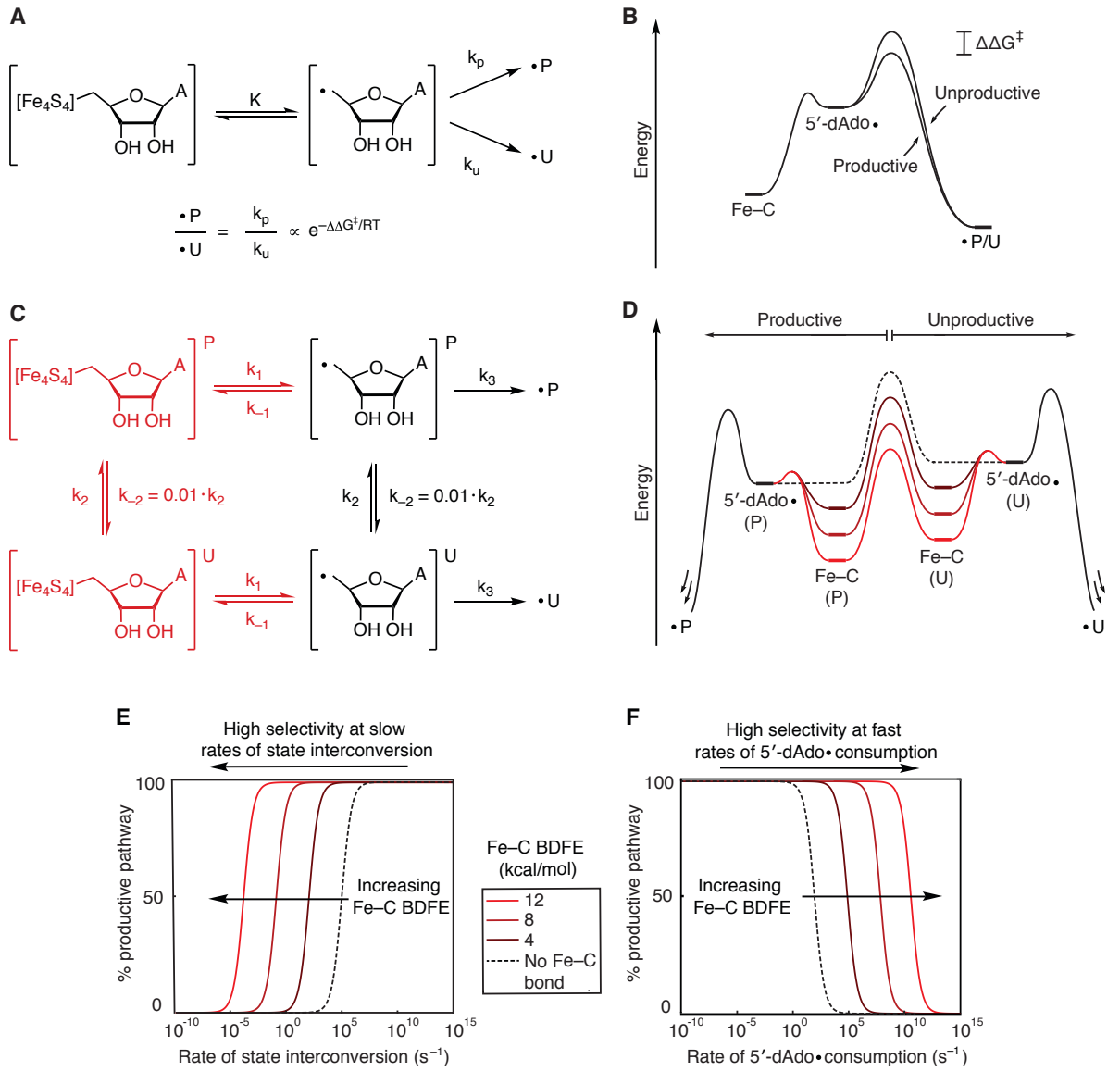

Figure 7.4. (A) Kinetic model and (B) energy diagram for a system in which the 5′-dAdo• reacts through a branching path with fixed rates of X–H abstraction. The presence of the organometallic intermediate has no effect on the selectivity. (C) Kinetic model that invokes interconversion between productive (P) and unproductive (U) states in the absence (black) and presence (black and red) of an organometallic intermediate. (D) Quantitative energy diagram for the system depicted in C showing the effect of the organometallic intermediate using barriers calculated from the rate constants listed below. As the Fe–C bond strength increases, the barrier to state interconversion becomes lower than the barrier to homolysis and X–H bond activation. (E) Simulations showing the selectivity of the reaction as a function of the rate of state interconversion and Fe–C bond strength. (F) Simulations showing the selectivity of the reaction as a function of the rate of X–H bond activation and Fe–C bond strength. k_{-1} (10^{11} s^{-1}), k_2 (10^2 s^{-1}), and k_3 (10^5 s^{-1}) were held constant and k_1 was varied to give the indicated Fe–C bond strengths.

the productive state by ~ 2 kcal/mol), and that Fe–C bond homolysis occurs slower than X–H bond activation ($k_1 = 10^3\ s^{-1}$, $k_3 = 10^5\ s^{-1}$). Further discussion of these rate constants is in the SI. Under these conditions, the slow rate of state interconversion favors X–H bond activation from the initial state; if the radical is formed in the unproductive state, state interconversion must outcompete unproductive X–H bond activation for productive reactivity to occur. We therefore initialized our simulations with the 5′-dAdo• in the unproductive state as a worst-case scenario to determine if an organometallic intermediate can recover selectivity for the productive reaction.

With these rate constants and in the absence of the organometallic intermediate, 99% of the radical is funneled to undesired pathways because, as noted above, H-atom abstraction is much faster than state interconversion. However, if an organometallic intermediate is formed, the H-atom abstraction step is sufficiently slowed such that the reaction occurs with 99% selectivity for the *productive* pathway (note that given the difference in energy of the productive and unproductive states, the maximum selectivity under thermodynamic control is 99%). Thus, if SAM is cleaved when the protein is in an unproductive state (e.g., if the initial substrate positioning is somehow perturbed), formation of the Fe–C bond could buy time for the protein to convert to a state that yields productive reactivity. Figure 7.4D illustrates the energetics of this process: introducing an Fe–C bond raises the barrier to X–H bond activation relative to state interconversion. This shifts the reaction from being under kinetic control, in which X–H bond activation outcompetes state interconversion, to being under Curtin-Hammett control, in which the relative X–H bond activation barriers control the selectivity.

We also probed how selectivity is affected by the individual kinetic parameters. Figure 7.4E shows the reaction outcome as a function of the rate of state interconversion with a range of Fe–C bond strengths; as the Fe–C bond strength is increased, higher selectivity for the productive reaction can be obtained at slower rates of state interconversion. This demonstrates

how even a weak Fe–C bond in an organometallic intermediate can allow for relatively slow processes to impact the selectivity of the reaction. An analogous effect is observed when the rate of (both productive and unproductive) X–H bond activation is varied (Figure 7.4F); increasing the Fe–C bond strength allows for high selectivity even with very fast rates of X–H bond activation.

Overall, these results support a mechanism by which reversible formation of an organometallic intermediate can affect the selectivity in radical SAM reactions: it increases the range of kinetic parameters (X–H abstraction rates and state interconversion rates) for which interconversion between productive and unproductive states can occur, allowing these processes to outcompete what may be intrinsically very fast unproductive reactions.

Connection between reversible M–C bond homolysis in radical SAM and adenosylcobalamin enzymes

The protective mechanism described above is agnostic with respect to the identity of the metal fragment, and therefore may apply equally well to adenosylcobalamin enzymes for which reversible Co–C bond cleavage has been observed.[45-47] Evidence for reversible Co–C bond homolysis was provided by rate measurements using protiated and deuterated substrate, which showed an H/D kinetic isotope effect on the apparent rate of Co–C bond homolysis that results from kinetic coupling of Co–C bond homolysis and H-atom abstraction.[47–50] Similar kinetic experiments carried out with radical SAM enzymes could determine if reversible Fe–C bond cleavage occurs during turnover of radical SAM enzymes. The observation of a kinetic isotope effect for consumption of the organometallic intermediate when the substrate is deuterated would simultaneously provide evidence that the organometallic intermediate is on-path for productive chemistry and that Fe–C bond homolysis is reversible in enzymatic systems.

Conclusion

The observation of facile Fe–C bond homolysis from [Fe_4S_4]–alkyl clusters demonstrates the feasibility of 5′-dAdo• formation from organometallic intermediates in radical SAM enzymes and links the chemistry of radical SAM and adenosylcobalamin model systems. Similarly to Co–C bond homolysis in adenosylcobalamin model systems, Fe–C bond homolysis from [Fe_4S_4]–alkyl clusters occurs reversibly to generate primary carbon radicals, but unlike in adenosylcobalamin models, homolysis of Fe–C bonds in [Fe_4S_4]-alkyl clusters is facile at room temperature. Overall, these findings suggest that in both adenosylcobalamin enzymes and radical SAM enzymes, reversible homolysis of M–C bonds can allow for selective X–H bond activation by kinetically coupling reactions of the 5′-dAdo• to dynamic processes within or beyond the protein active site. Studies of the dynamics of these proteins will help illuminate how radical SAM and adenosylcobalamin enzymes utilize reversible M–C bond homolysis as a strategy to control the 5′-dAdo• and will contribute to our understanding of the differences between these two enzyme families.

References

(1) Banerjee, R.; Ragsdale, S. W. The Many Faces of Vitamin B_{12} : Catalysis by Cobalamin-Dependent Enzymes. *Annu. Rev. Biochem.* **2003**, *72* (1), 209–247.

(2) Booker, S. J.; Grove, T. L. Mechanistic and Functional Versatility of Radical SAM Enzymes. *F1000 Biology Reports*. **2010** *2* (52).

(3) Broderick, J. B.; Duffus, B. R.; Duschene, K. S.; Shepard, E. M. Radical *S*-Adenosylmethionine Enzymes. *Chem. Rev.* **2014**, *114* (8), 4229–4317.

(4) Landgraf, B. J.; McCarthy, E. L.; Booker, S. J. Radical *S*-Adenosylmethionine Enzymes in Human Health and Disease. *Annu. Rev. Biochem.* **2016**, *85* (1), 485–514.

(5) Owing to its high reactivity, the 5′-dAdo• radical has only recently been observed. For details, see Yang, H.; McDaniel, E. C.; Impano, S.; Byer, A. S.; Jodts, R. J.; Yokoyama, K.; Broderick, W. E.; Broderick, J. B.; Hoffman, B. M. The Elusive 5′-Deoxyadenosyl Radical: Captured and Characterized by Electron Paramagnetic Resonance and Electron Nuclear Double Resonance Spectroscopies. *J. Am. Chem. Soc.* **2019**, *141* (30), 12139–12146. and Sayler, R. I.; Stich, T. A.; Joshi, S.; Cooper, N.; Shaw, J. T.; Begley, T. P.; Tantillo, D. J.; Britt, R. D. Trapping and Electron Paramagnetic Resonance Characterization of the 5′dAdo• Radical in a Radical S-Adenosyl Methionine Enzyme Reaction with a Non-Native Substrate. *ACS Cent. Sci.* **2019**, *5* (11), 1777–1785.

(6) Frey, P. A. Lysine 2,3-Aminomutase: Is Adenosylmethionine a Poor Man's Adenosylcobalamin? *FASEB J.* **1993**, *7* (8), 662–670.

(7) Frey, P. A.; Magnusson, O. T. *S*-Adenosylmethionine: A Wolf in Sheep's Clothing, or a Rich Man's Adenosylcobalamin? *Chem. Rev.* **2003**, *103* (6), 2129–2148.

(8) Tamao, Y.; Blakley, R. L. Direct Spectrophotometric Observation of an Intermediate Formed from Deoxyadenosylcobalamin in Ribonucleotide Reduction. *Biochemistry* **1973**, *12* (1), 24–34.

(9) Finlay, T. H.; Valinsky, J.; Mildvan, A. S.; Abeles, R. H. Electron Spin Resonance Studies with Dioldehydrase. Evidence for Radical Intermediates in Reactions Catalyzed by Coenzyme B_{12}. *J. Biol. Chem.* **1973**, *248* (4), 1285–1290.

(10) Berkovitch, F.; Behshad, E.; Tang, K. H.; Enns, E. A.; Frey, P. A.; Drennan, C. L. A Locking Mechanism Preventing Radical Damage in the Absence of Substrate, as Revealed by the X-Ray Structure of Lysine 5,6-Aminomutase. *Proc. Nat. Acad. Sci. USA* **2004**, *101* (45), 15870–15875.

(11) Zelder, O.; Beatrix, B.; Leutbecher, U.; Buckel, W. Characterization of the Coenzyme-B_{12}–Dependent Glutamate Mutase from Clostridium Cochlearium Produced in Escherichia Coli. *Eur. J. Biochem.* **1994**, *226* (2), 577–585.

(12) Lieder, K. W.; Booker, S.; Ruzicka, F. J.; Beinert, H.; Reed, G. H.; Frey, P. A. S-Adenosylmethionine-Dependent Reduction of Lysine 2,3-Aminomutase and Observation of the Catalytically Functional Iron-Sulfur Centers by Electron Paramagnetic Resonance. *Biochemistry* **1998**, *37* (8), 2578–2585.

(13) Gruber, K.; Reitzer, R.; Kratky, C. Radical Shuttling in a Protein: Ribose Pseudorotation Controls Alkyl-Radical Transfer in the Coenzyme B_{12} Dependent Enzyme Glutamate Mutase. *Angew. Chemie - Int. Ed.* **2001**, *40* (18), 3377–3380. 3

(14) Shibata, N.; Tamagaki, H.; Hieda, N.; Akita, K.; Komori, H.; Shomura, Y.; Terawaki, S. I.; Mori, K.; Yasuoka, N.; Higuchi, Y., Toraya, T.. Crystal Structures of Ethanolamine Ammonia-Lyase Complexed with Coenzyme B_{12} Analogs and Substrates. *J. Biol. Chem.* **2010**, *285* (34), 26484–26493.

(15) LoBrutto, R.; Bandarian, V.; Magnusson, O. T.; Chen, X.; Schramm, V. L.; Reed, G. H. 5′-Deoxyadenosine Contacts the Substrate Radical Intermediate in the Active Site

of Ethanolamine Ammonia-Lyase: ^{2}H and ^{13}C Electron Nuclear Double Resonance Studies. *Biochemistry* **2001**, *40* (1), 9–14.
(16) Canfield, J. M.; Warncke, K. Geometry of Reactant Centers in the Co^{II}-Substrate Radical Pair State of Coenzyme B_{12}-Dependent Ethanolamine Deaminase Determined by Using Orientation-Selection-ESEEM Spectroscopy. *J. Phys. Chem. B* **2002**, *106* (34), 8831–8841.
(17) Horitani, M.; Byer, A. S.; Shisler, K. A.; Chandra, T.; Broderick, J. B.; Hoffman, B. M. Why Nature Uses Radical SAM Enzymes so Widely: Electron Nuclear Double Resonance Studies of Lysine 2,3-Aminomutase Show the 5′-DAdo• "Free Radical" Is Never Free. *J. Am. Chem. Soc.* **2015**, *137* (22), 7111–7121.
(18) Vey, J. L.; Drennan, C. L. Structural Insights into Radical Generation by the Radical SAM Superfamily. *Chem. Rev.* **2011**, *111* (4), 2487–2506.
(19) Sofia, H. J.; Chen, G.; Hetzler, B. G.; Reyes-Spindola, J. F.; Miller, N. E. Radical SAM, a Novel Protein Superfamily Linking Unresolved Steps in Familiar Biosynthetic Pathways with Radical Mechanisms: Functional Characterization Using New Analysis and Information Visualization Methods. *Nucleic Acids Res.* **2001**, *29* (5), 1097–1106.
(20) Holliday, G. L.; Akiva, E.; Meng, E. C.; Brown, S. D.; Calhoun, S.; Pieper, U.; Sali, A.; Booker, S. J.; Babbitt, P. C. Atlas of the Radical SAM Superfamily: Divergent Evolution of Function Using a "Plug and Play" Domain. In *Methods in Enzymology*, Vahe Bandarian, Eds.; Academic Press Inc., 2018; Vol. 606, 1–71.
(21) Horitani, M.; Shisler, K.; Broderick, W. E.; Hutcheson, R. U.; Duschene, K. S.; Marts, A. R.; Hoffman, B. M.; Broderick, J. B. Radical SAM Catalysis via an Organometallic Intermediate with an Fe-[5'-C]-Deoxyadenosyl Bond. *Science* **2016**, *352* (6287), 822–825.
(22) Byer, A. S.; Yang, H.; McDaniel, E. C.; Kathiresan, V.; Impano, S.; Pagnier, A.; Watts, H.; Denler, C.; Vagstad, A. L.; Piel, J., Duschene, K.S.; Shepard, E. M.; Shields, T. P.; Scott, L. G.; Lilla, E. A.; Yokoyama, K.; Broderick, W. E.; Hoffman, B. M.; Broderick, J. B.. Paradigm Shift for Radical S-Adenosyl-L-Methionine Reactions: The Organometallic Intermediate Ω Is Central to Catalysis. *J. Am. Chem. Soc.* **2018**, *140* (28), 8634-8638.
(23) Nicolet, Y. Structure–Function Relationships of Radical SAM Enzymes. *Nat. Catal.* **2020**, *3* (4), 337–350.
(24) Daikh, B. E.; Finke, R. G. Unprecedented and Reversible Cobalt-to-Carbon Alkyl Bond Rearrangement in the Coenzyme B_{12} Model Complex $C_6H_5CH_2Co^{III}[C_2(DO)(DOH)_{Pn}]I$: Synthesis, Structural Characterization, and Mechanistic Studies. *J. Am. Chem. Soc.* **1991**, *113* (11), 4160–4172.
(25) Garr, C. D.; Finke, R. G. Adocobalamin (AdoCbl or Coenzyme B_{12}) Co-C Bond Homolysis Radical-Cage Effects: Product, Kinetic, Mechanistic, and Cage Efficiency Factor (Fc) Studies, plus the Possibility That Coenzyme B_{12}-Dependent Enzymes Function as "Ultimate Radical Cages" and "Ultimate Radical Traps". *Inorg. Chem.* **1993**, *32* (20), 4414–4421.
(26) Hay, B. P.; Finke, R. G. Thermolysis of the Co–C Bond of Adenosylcobalamin. 2. Products, Kinetics, and Co–C Bond Dissociation Energy in Aqueous Solution. *J. Am. Chem. Soc.* **1986**, *108* (16), 4820–4829.
(27) Koenig, T.; Finke, R. G. The Cage Effect and Apparent Activation Parameters for Bond Homolysis. *J. Am. Chem. Soc.* **1988**, *110* (8), 2657–2658.
(28) Finke, R. G.; Hay, B. P. Thermolysis of Adenosylcobalamin: A Product, Kinetic, and Cobalt-Carbon (C5') Bond Dissociation Energy Study. *Inorg. Chem.* **1984**, *23* (20), 3041–3043.
(29) Halpern, J. Some Aspects of Organocobalt Chemistry Related to Vitamin B_{12}. *Ann. N.*

Y. Acad. Sci. **1974**, *239* (1), 2–21.
(30) Tsou, T. T.; Loots, M.; Halpern, J. Kinetic Determination of Transition Metal-Alkyl Bond Dissociation Energies: Application to Organocobalt Compounds Related to B_{12} Coenzymes. *J. Am. Chem. Soc.* **1982**, *104* (2), 623–624.
(31) Ng, F. T. T.; Rempel, G. L.; Halpern, J. Ligand Effects on Transition-Metal-Alkyl Bond Dissociation Energies. *J. Am. Chem. Soc.* **1982**, *104* (2), 621-623.
(32) Halpern, J. Determination of Transition Metal-Alkyl Bond Dissociation Energies from Kinetic Measurements. *Polyhedron* **1988**, *7* (16–17), 1483–1490.
(33) Halpern, J. Determination and Significance of Transition Metal-Alkyl Bond Dissociation Energies. *Acc. Chem. Res.* **1982**, *15* (8), 238–244.
(34) Ye, M.; Thompson, N. B.; Brown, A. C.; Suess, D. L. M. A Synthetic Model of Enzymatic $[Fe_4S_4]$-Alkyl Intermediates. *J. Am. Chem. Soc.* **2019**, *141* (34), 13330–13335.
(35) Brown, A. C.; Suess, D. L. M. Controlling Substrate Binding to Fe_4S_4 Clusters through Remote Steric Effects. *Inorg. Chem.* **2019**, *58* (8), 5273–5280.
(36) Hansch, C.; Leo, A.; Taft, R. W. A Survey of Hammett Substituent Constants and Resonance and Field Parameters. *Chem. Rev.* **1991**, *91* (2), 165–195.
(37) Daikh, B. E.; Finke, R. G. The Persistent Radical Effect: A Prototype Example of Extreme, 10^5 to 1, Product Selectivity in a Free-Radical Reaction Involving Persistent $\cdot Co^{II}$[Macrocycle] and Alkyl Free Radicals. *J. Am. Chem. Soc.* **1992**, *114* (8), 2938–2943.
(38) Dong, M.; Kathiresan, V.; Fenwick, M. K.; Torelli, A. T.; Zhang, Y.; Caranto, J. D.; Dzikovski, B.; Sharma, A.; Lancaster, K. M.; Freed, J. H.; Ealick, S. E.; Hoffman, B. M.; Lin, H. Organometallic and Radical Intermediates Reveal Mechanism of Diphthamide Biosynthesis. *Science* **2018**, *359* (6381), 1247–1250.
(39) Newcomb, M. Competition Methods and Scales for Alkyl Radical Reaction Kinetics. *Tetrahedron* **1993**, *49* (6), 1151–1176.
(40) Newcomb, M. Radical Kinetics and Clocks. In *Encyclopedia of Radicals in Chemistry, Biology and Materials*; John Wiley & Sons, Ltd: Chichester, UK, 2012.
(41) Walling, C.; Cioffari, A. Cyclization of 5-Hexenyl Radicals. *J. Am. Chem. Soc.* **1972**, *94* (17), 6059–6064.
(42) Ash, C. E.; Hurd, P. W.; Darensbourg, M. Y.; Newcomb, M. Competing Nucleophilic Displacement and Radical Chain Reduction in Reactions of Transition-Metal Hydride Anions with Alkyl Bromides. *J. Am. Chem. Soc.* **1987**, *109* (11), 3313–3317.
(43) Fischer, H. The Persistent Radical Effect: A Principle for Selective Radical Reactions and Living Radical Polymerizations. *Chem. Rev.* **2001**, *101* (12), 3581–3610.
(44) Fischer, H. Unusual Selectivities of Radical Reactions by Internal Suppression of Fast Modes. *J. Am. Chem. Soc.* **1986**, *108* (14), 3925–3927.
(45) Branchaud, B. P.; Yu, G. X. An Example of the Persistent Radical Effect in Cobaloxime-Mediated Radical Alkyl-Alkenyl Cross Coupling. *Organometallics* **1993**, *12* (11), 4262–4264.
(46) Byungho, S.; Goff, H. M. Free Radical-Mediated Electron Transfer in Organometallic Complexes: Homolysis and Alkyl Group Crossover Reactions for Alkyliron(II) Porphyrins. *Inorganica Chim. Acta* **1994**, *226* (1–2), 231–235.
(47) Chen, D.; Abend, A.; Stubbe, J. A.; Frey, P. A. Epimerization at Carbon-5′ of (5′R)-[5′-^{2}H]Adenosylcobalamin by Ribonucleoside Triphosphate Reductase: Cysteine 408-Independent Cleavage of the Co-C5′ Bond. *Biochemistry* **2003**, *42* (15), 4578–4584.
(48) Marsh, E. N. G.; Meléndez, G. D. R. R. Adenosylcobalamin Enzymes: Theory and Experiment Begin to Converge. *Biochim. Biophys. Acta - Proteins Proteomics* **2012**, *1824* (11), 1154–1164.

(49) Marsh, E. N. G.; Ballou, D. P. Coupling of Cobalt-Carbon Bond Homolysis and Hydrogen Atom Abstraction in Adenosylcobalamin-Dependent Glutamate Mutase. *Biochemistry* **1998**, *37* (34), 11864–11872.
(50) Cheng, M. C.; Marsh, E. N. G. Isotope Effects for Deuterium Transfer between Substrate and Coenzyme in Adenosylcobalamin-Dependent Glutamate Mutase. *Biochemistry* **2005**, *44* (7), 2686–2691.

Supporting information:

Synthetic protocols

General Considerations: Unless otherwise noted, all reactions were performed using standard Schlenk techniques or in an LC Technologies inert atmosphere glove box under an atmosphere of nitrogen (< 1 ppm O_2/H_2O). All compounds are air and water sensitive and were manipulated and stored to avoid exposure to air and water. Glassware was dried in an oven at 160 °C prior to use. Molecular sieves (3 Å), neutral alumina, and Celite® were activated by heating to 300 °C overnight under vacuum prior to storage under an atmosphere of nitrogen. Diethyl ether (Et_2O), benzene and pentane were degassed by sparging with argon, dried by passing through a column of activated alumina, and stored under an atmosphere of nitrogen over 3 Å molecular sieves. Tetrahydrofuran (THF) was distilled from sodium/benzophenone and stored under an atmosphere of nitrogen over 3 Å molecular sieves. Hexamethyldisiloxane (HMDSO) was degassed by sparing with nitrogen and stored under an atmosphere of nitrogen over 3 Å molecular sieves. C_6D_6 was degassed by three freeze–pump–thaw cycles and stored under an atmosphere of nitrogen over 3 Å activated molecular sieves. $(IMes)_3Fe_4S_4Cl$ was prepared according to previously reported procedures.[1] 4-CF_3-pyridine, pyridine, and $^nBu_3SnH$ were dried over CaH_2 and distilled under nitrogen. Grignard reagents (octylmagnesium bromide, 6-hexenylmagnesium bromide, and cyclopentylmethylmagnesium bromide) were prepared by addition of the halide to activated magnesium turnings in THF. Bromomethylcyclopentane was prepared by dropwise addition of elemental bromine to a solution of cyclopentylmethanol and PPh_3 in CH_2Cl_2.[2] $NaBAr^F_4$ (sodium tetrakis[(3,5-trifluoromethyl)phenyl]borate) was prepared according to literature procedure.[3] $[Cp_2Co][BAr^F_4]$ was synthesized by salt metathesis from $[Cp_2Co][PF_6]$ using the procedure reported for $[Cp_2Fe][BAr^F_4]$.[4] All other reagents were purchased and used as received. NMR spectra were recorded on Bruker 400 and 500 MHz spectrometers. ^1H and $^{13}C\{^1H\}$ chemical shifts are given relative to residual solvent peaks,

$^{119}Sn\{^{1}H\}$ shifts are relative to neat Me_4Sn (0 ppm). FT-IR samples were taken as thin films using a Bruker Alpha Platinum ATR spectrometer with OPUS software in a glovebox under an N_2 atmosphere. EPR spectra were recorded on a Bruker EMX spectrometer at 9.37 GHz as frozen glasses. Simulations were performed using EasySpin[5] (5.2.21) in MATLAB (R2017b). UV-vis spectra were taken on a Cary 50 spectrometer. GC/MS experiments were carried out on an Agilent 5973N gas chromatograph/mass spectrometer using EI–MS ionization. X-ray structural determinations were performed at the MIT diffraction facility using a Bruker X8 diffractometer with an APEX II CCD detector or a Bruker D8 Venture diffractometer with a Photon2 CPAD detector. Diffraction data was collected, integrated, and corrected for absorption using Bruker APEX3 software and its associated modules (SAINT, SADABS, TWINABS). Structural solutions and refinements (on F^2) were carried out using SHELXT and SHELXL-2018 in ShelXle.[6] Ellipsoid plots and figures were made using Mercury.

General preparation of alkylated clusters: $(IMes)_3Fe_4S_4Cl$ (1 eq) was suspended in Et_2O (ca. 0.03 M). A solution of Grignard reagent (0.09–0.14 M in THF, 1.05 eq) was added dropwise. The dark red-brown solution was stirred for 5 min and filtered through Celite. The filtrate was added to a column of neutral alumina (2.5 g of alumina per 100 mg of $(IMes)_3Fe_4S_4Cl$, packed as a suspension in Et_2O) to remove residual Mg salts. The product was eluted from the column with one column volume of Et_2O and the solvent was removed in vacuo.

$(IMes)_3Fe_4S_4$(benzyl) (2): 500 mg of $(IMes)_3Fe_4S_4Cl$, 0.14 M benzylmagnesium chloride. The resulting orange-brown solids were washed with pentane (3 x 2 mL). Yield: 334 mg (64%). ^{1}H NMR (500 MHz, C_6D_6, 293 K) δ 224 (s, 2H, Fe-C*H*$_2$), 11.36 (s, 2H, benzyl *m*-C*H*), 6.98 (s, 12H, Mes C*H*), 5.98 (s, 6H, backbone C*H*), 2.37 (s, 18H, Mes *p*-C*H*$_3$), 1.98 (s, 36H, Mes *o*-C*H*$_3$), –4.68 (s, 2H, benzyl *o*-C*H*), –6.50 (s, 1H, benzyl *p*-C*H*); $^{13}C\{^{1}H\}$ NMR (125 MHz,

C_6D_6): δ 193.8 (benzyl), 193.3 (benzyl), 143.4 (IMes), 139.1 (IMes), 132.9 (IMes), 131.4 (IMes), 126.4 (IMes), 71.9 (benzyl), 37.1 (IMes), 21.4 (IMes). EPR: g = [2.123 1.953 1.931] (toluene, 15 K, 9.37 GHz). X-ray quality crystals were grown by diffusion of pentane into Et_2O at room temperature.

$(IMes)_3Fe_4S_4$(octyl) (3): 100 mg of $(IMes)_3Fe_4S_4Cl$, 0.1 M octylmagnesium bromide. The resulting orange-brown solids were washed with pentane (2 x 1 mL) to give 57.9 mg of product. A second crop of crystals were collected by cooling the pentane washes to –40 °C for 16 h. Total yield: 70.2 mg (66%). ^{1}H NMR (400 MHz, C_6D_6, 293 K) δ 258 (s, 2H, Fe-CH_2), 21.81 (s, 2H, Fe-CH_2CH_2), 7.02 (s, 12H, Mes CH), 6.14 (s, 6H, backbone CH), 2.41 (s, 2H, Fe-$(CH_2)_3$CH_2) 2.33 (s, 18H, Mes *p*-CH_3), 2.07 (s, 36H, Mes *o*-CH_3), 1.66 (s, 2H, Fe-$(CH_2)_4$CH_2), 1.39 (m, 4H, Fe-$(CH_2)_5$CH_2CH_2), 0.93 (t, 3H, J = 5.94 Hz, Fe-$(CH_2)_7$CH_3), 0.67 (s, 2H, Fe-$(CH_2)_2$CH_2); ^{13}C{^{1}H} NMR (125 MHz, C_6D_6): δ 145.7 (IMes), 138.6 (IMes), 132.9 (IMes), 130.9 (IMes), 127.7 (IMes), 41.1 (Fe-$(CH_2)_3$CH_2) 37.3 (IMes), 37.0 (Fe-$(CH_2)_4$CH_2), 34.6, 23.3 (Fe-$(CH_2)_5$CH_2CH_2), 21.0 (IMes), 14.7 (Fe-$(CH_2)_7$CH_3). EPR: g = [2.122 1.954 1.933] (toluene, 15 K, 9.37 GHz).

$(IMes)_3Fe_4S_4$(5-Hexenyl) (5): 100 mg of $(IMes)_3Fe_4S_4Cl$, 0.12 M 5-hexenylmagnesium bromide. The resulting orange-brown solids were washed with pentane (3 x 2 mL). Yield: 53.1 mg (51%). ^{1}H NMR (400 MHz, C_6D_6, 293 K) δ 256 (s, 2H, Fe-CH_2), 24.5 (s, 2H, Fe-CH_2CH_2), 7.00 (s, 12H, Mes CH), 6.18 (m, 1H, Fe-$(CH_2)_4$CHCH_2), 6.12 (s, 6H, backbone CH), 4.94 (m, 2H, Fe-$(CH_2)_4$CHCH_2), 2.87 (s, 2H, Fe-$(CH_2)_3$CH_2) 2.32 (s, 18H, Mes *p*-CH_3), 2.05 (s, 36H, Mes *o*-CH_3), 0.54 (s, 2H, Fe-$(CH_2)_2$CH_2); ^{13}C{^{1}H} NMR (125 MHz, C_6D_6): 147.4 (Fe-$(CH_2)_4$CHCH_2), 146.0 (IMes), 139.0 (IMes), 133.3 (IMes), 131.2 (IMes),

127.5 (IMes), 115.6 (Fe-$(CH_2)_4CHCH_2$), 44.5 (Fe-$(CH_2)_3CH_2$) , 37.5 (IMes), 21.3 (IMes). EPR: g = [2.121 1.953 1.932] (toluene, 15 K, 9.37 GHz).

$(IMes)_3Fe_4S_4$(cyclopentylmethyl) (7): 100 mg of $(IMes)_3Fe_4S_4Cl$, 0.09 M cyclopentylmethylmagnesium bromide. The resulting orange-brown solids were washed with pentane (3 x 2 mL). Yield: 36.8 mg (36%). ^{1}H NMR (400 MHz, C_6D_6, 293 K) δ 256 (s, 2H, Fe-CH_2), 21.3 (s, 1H, Fe-CH_2CH), 7.01 (s, 12H, Mes CH), 6.15 (s, 6H, backbone CH), 4.27 (s, 2H, cyclopent), 2.85 (s, 2H, cyclopent) 2.33 (s, 18H, Mes p-CH_3), 2.06 (s, 36H, Mes o-CH_3), 1.84 (s, 2H, cyclopent), –1.63 (s, 2H, cyclopent); ^{13}C{^{1}H} NMR (125 MHz, C_6D_6): δ 145.7 (IMes), 138.6 (IMes), 132.9 (IMes), 130.9 (IMes), 127.8 (IMes), 37.3 (IMes), 34.0 (cyclopent), 21.0 (IMes). EPR: g = [2.123 1.954 1.933] (toluene, 15 K, 9.37 GHz).

General method for oxidation of alkylated clusters: The alkylated cluster (1 eq) was mixed with $[Cp_2Co][BAr^F_4]$ (1.2 eq). The solids were suspended in pentane or HMDSO and stirred for 5 min. The solution was filtered to remove cobaltocene. The dark solids were extracted into benzene and filtered through Celite to remove $[Cp_2Co][BAr^F_4]$. The solvent was removed in vacuo and the residual solids were washed again with pentane. Oxidized clusters, particularly those with β-hydrogens, exhibited some thermal instability and so were freshly generated for each experiment.

$[(IMes)_3Fe_4S_4Bn][BAr^F_4]$ ($[2]^+$): The reaction was carried out in pentane. The product was isolated as a red-brown solid. Yield: 28.1 mg (12.7 μmol) on a 27.1 mg (20.0 μmol) scale (64%). ^{1}H NMR (500 MHz, C_6D_6, 293 K) δ 67.5 (s, 2H, Fe-CH_2), 8.44 (s, 8H, $[BAr^F_4]$), 7.71 (s, 4H, $[BAr^F_4]$), 7.17 (s, 2H, benzyl m-CH), 6.98 (d, 2H, J = 7.6 Hz, benzyl o-CH), 6.90 (t, 1H, J = 7.6 Hz, benzyl p-CH), 6.85 (s, 12H, Mes CH), 5.63 (s, 6H, backbone CH), 2.31 (s,

18H, Mes *p*-CH_3), 1.99 (s, 36H, Mes *o*-CH_3); $^{13}C\{^1H\}$ NMR (125 MHz, C_6D_6): 162.5 (q, [BAr^F_4]), 140.0 (IMes), 138.8 (IMes), 135.2 ([BAr^F_4]), 134.7 (IMes), 130.0 (IMes), 129.6 (q, [BAr^F_4]), 129.6 (benzyl *m*-*C*H) 128.2, 127.4 (IMes), 125.4 (benzyl *o*–*C*H), 125.0 ([BAr^F_4]), 122.1, 121.4 (benzyl *p*-*C*H), 117.7 ([BAr^F_4]), 23.9 (IMes), 20.5 (IMes). Crystallographic characterization of this complex was obtained by oxidation of $(IMes)_3Fe_4S_4Cl$ with [Cp*$_2$Fe][OTf] and crystallization by vapor diffusion of pentane into THF at room temperature. [$(IMes)_3Fe_4S_4Bn$][OTf] can be converted to the [BAr^F_4] salt by addition of $NaBAr^F_4$ to a THF solution of [$(IMes)_3Fe_4S_4Bn$][OTf], followed by removal of the solvent in vacuo, extraction into benzene, and filtration through Celite.

[$(IMes)_3Fe_4S_4$(octyl)][BAr^F_4] ([3]$^+$): The reaction was carried out in HMDSO. The product was isolated as a brown solid. Yield: 11.2 mg (5.00 μmol) on a 12.3 mg (9.03 μmol) scale (56%). ^1H NMR (500 MHz, C_6D_6, 293 K) δ 74.7 (s, 2H, Fe-CH_2), 8.45 (s, 8H, [BAr^F_4]), 7.71 (s, 4H, [BAr^F_4]), 6.90 (s, 12H, Mes CH), 5.64 (s, 6H, backbone CH), 2.31 (s, 18H, Mes *p*-CH_3), 2.05 (s, 36H, Mes *o*-CH_3), 1.92 (s, 2H, Fe-$(CH_2)_3CH_2$), 1.55 (s, 2H, Fe-$(CH_2)_2CH_2$), 1.46 (m, 6H, Fe-$(CH_2)_4CH_2CH_2CH_2$), 1.00 (t, 3H, J = 6.71 Hz, Fe-$(CH_2)_7CH_3$), –3.57 (s, 2H, Fe-CH_2CH_2); $^{13}C\{^1H\}$ NMR (125 MHz, C_6D_6): 162.5 (q, [BAr^F_4]), 140.0 (IMes), 139.0 (IMes), 135.2 ([BAr^F_4]), 134.7 (IMes), 130.0 (IMes), 129.6 (q, [BAr^F_4]), 127.8 (IMes), 125.0 ([BAr^F_4]), 121.6, 117.7 ([BAr^F_4]), 32.2 (octyl), 31.0 (octyl), 28.8 (Fe-$(CH_2)_3CH_2$), 24.2 (IMes), 23.4 (Fe-$(CH_2)_2CH_2$), 23.3 (octyl), 20.9 (IMes), 14.4 (Fe-$(CH_2)_7CH_3$).

[$(IMes)_3Fe_4S_4$(5-hexenyl)][BAr^F_4] ([5]$^+$): The reaction was carried out in HMDSO. The product was isolated as a brown solid. Yield: 20.5 mg (9.27 μmol) on a 21.5 mg (15.9 μmol) scale (59%). ^1H NMR (500 MHz, C_6D_6, 293 K) δ 74.2 (s, 2H, Fe-CH_2), 8.45 (s, 8H, [BAr^F_4]), 7.71 (s, 4H, [BAr^F_4]), 6.89 (s, 12H, Mes CH), 5.95 (m, 1H, Fe-$(CH_2)_4CHCH_2$), 5.64 (s, 6H,

backbone CH), 5.22 (d, 1H, J = 17.1 Hz, Fe-$(CH_2)_4CHCH_2$ trans), 5.14 (d, 1H, J = 10 Hz, Fe-$(CH_2)_4CHCH_2$ cis), 2.60, (q, 2H, J = 6 Hz, Fe-$(CH_2)_3CH_2$), 2.30 (s, 18H, Mes *p*-CH_3), 2.04 (s, 36H, Mes *o*-CH_3), 1.51 (s, 2H, Fe-$(CH_2)_2CH_2$), –4.00 (s, 2H, Fe-CH_2CH_2). $^{13}C\{^1H\}$ NMR (125 MHz, C_6D_6): 162.8 (q, [BAr^F_4]), 141.1 (Fe-$(CH_2)_4CHCH_2$) 140.3 (IMes), 139.3 (IMes), 135.5 ([BAr^F_4]), 135.1 (IMes), 130.3 (IMes), 129.9 (q, [BAr^F_4]), 127.9 (IMes), 125.3 ([BAr^F_4]), 121.9, 118.1 ([BAr^F_4]), 114.5 (Fe-$(CH_2)_4CHCH_2$), 33.5, (Fe-$(CH_2)_3CH_2$) 25.0 (Fe-$(CH_2)_2CH_2$), 24.5 (IMes), 20.9 (IMes).

[$(IMes)_3Fe_4S_4$(cyclopentymethyl)][BAr^F_4] ([7]$^+$): The reaction was carried out in HMDSO. The product was isolated as a brown solid. Yield: 37.4 mg (16.9 μmol) on a 30 mg (22.3 μmol) scale (76%). ^1H NMR (500 MHz, C_6D_6, 293 K) δ 75.0 (s, 2H, Fe-CH_2), 8.40 (s, 8H, [BAr^F_4]), 7.70 (s, 4H, [BAr^F_4]), 6.89 (s, 12H, Mes CH), 5.77 (s, 6H, backbone CH), 2.30 (s, 18H, Mes *p*-CH_3), 2.16 (s, 2H, cyclopent), 2.05 (s, 36H, Mes *o*-CH_3), 1.90 (s, 2H, cyclopent), 1.80 (s, 2H, cyclopent), 1.11 (s, 2H, cyclopent), –3.05 (s, 1H, Fe-CH_2CH); ^{13}C NMR (125 MHz, C_6D_6): 163.3 (q, [BAr^F_4]), 140.3 (IMes), 139.3 (IMes), 135.5 ([BAr^F_4]), 135.1 (IMes), 130.4 (IMes), 129.9 (q, [BAr^F_4]), 128.0 (IMes), 125.3 ([BAr^F_4]), 123.0, 118.1 ([BAr^F_4]), 27.6 (cyclopent), 27.4 (cyclopent), 24.5 (IMes), 20.9 (IMes).

General preparation for pyridine-bound clusters: [$(IMes)_3Fe_4S_4(Et_2O)$][BAr^F_4] was generated in situ by a modification of a previously reported procedure.[1] $(IMes)_3Fe_4S_4Cl$ (100 mg, 0.0769 mmol) was dissolved in benzene (10 mL). A solution of $NaBAr^F_4$ (68.2 mg, 0.0769 mmol) in Et_2O (2 mL) was added dropwise. The solution was stirred for 5 minutes and then filtered through Celite. The solvent was removed in vacuo to obtain a dark-brown powder. Yield: 117.5 mg (70%). These solids were redissolved in Et_2O and treated with a 1 eq. of a

pyridine as a benzene stock solution (0.1 M). Removal of the solvent in vacuo provided the pyridine adducts.

$[(IMes)_3Fe_4S_4(DMAP)][BAr^F{}_4]$ ($[4]^+$): From 20.5 mg (9.31 μmol) of $[(IMes)_3Fe_4S_4(Et_2O)][BAr^F{}_4]$. The dark yellow-brown solids were washed with hexanes to remove residual DMAP. Yield: 21 mg (99%). ^{1}H NMR (500 MHz, C_6D_6/THF (10:1), 293 K) δ 22.8 (s, 2H, DMAP), 14.3 (s, 2H, DMAP), 8.39 (s, 8H, $[BAr^F{}_4]$), 7.68 (s, 4H, $[BAr^F{}_4]$), 7.27 (s, 6H, DMAP) 6.81 (s, 12H, Mes CH), 6.08 (s, 6H, backbone CH), 2.23 (s, 18H, Mes *p*-CH_3), 2.05 (s, 36H, Mes *o*-CH_3); $^{13}C\{^1H\}$ NMR (125 MHz, C_6D_6/THF (10:1): 162.8 (q, $[BAr^F{}_4]$), 144.8 (IMes), 139.6 (IMes), 135.5 ($[BAr^F{}_4]$), 133.5 (IMes), 133.1 (IMes), 131.8 (IMes), 129.9 (q, $[BAr^F{}_4]$), 125.3 ($[BAr^F{}_4]$), 118.1 ($[BAr^F{}_4]$), 36.3 (IMes), 20.9 (IMes). This compound was crystallized as the [OTf] salt. $[(IMes)_3Fe_4S_4(THF)][OTf]$ was formed by addition of an excess of NaOTf to $(IMes)_3Fe_4S_4Cl$ in THF. The solvent was removed in vacuo, the solid was extracted into benzene, the mixture was filtered and the solvent was removed again. The solids were extracted into THF, the solution was filtered, an excess of DMAP was added, and the product was crystallized by vapor diffusion of pentane into the THF solution.

$[(IMes)_3Fe_4S_4(pyridine)][BAr^F{}_4]$ ($[8]^+$): From 27.5 mg (12.5 μmol) of $[(IMes)_3Fe_4S_4(Et_2O)][BAr^F{}_4]$. The product was isolated as a dark red-brown solid. Yield: 25.3 mg (92%). ^{1}H NMR (500 MHz, C_6D_6/THF (10:1), 293 K) δ 18.9 (s, 2H, pyridine), 16.7 (s, 2H, pyridine), 8.41 (s, 8H, $[BAr^F{}_4]$), 7.69 (s, 4H, $[BAr^F{}_4]$), 6.77 (s, 12H, Mes CH), 6.09 (s, 6H, backbone CH), 2.22 (s, 18H, Mes *p*-CH_3), 2.09 (s, 36H, Mes *o*-CH_3), –0.61 (s, 1H, pyridine); $^{13}C\{^1H\}$ NMR (125 MHz, C_6D_6/THF (10:1): 162.3 (q, $[BAr^F{}_4]$), 144.5 (IMes), 139.4 (IMes), 135.1 ($[BAr^F{}_4]$), 134.9 (IMes), 133.2 (IMes), 131.4 (IMes), 129.5 (q, $[BAr^F{}_4]$), 125.3 ($[BAr^F{}_4]$), 117.7 ($[BAr^F{}_4]$), 35.5 (IMes), 20.4 (IMes).

[(IMes)$_3$Fe$_4$S$_4$(4-CF$_3$-pyridine)][BAr$^F{}_4$] ([6]$^+$): From 24.3 mg (11.0 μmol) of [(IMes)$_3$Fe$_4$S$_4$(Et$_2$O)][BAr$^F{}_4$]. The product was isolated as a dark green-brown solid. Yield: 24.3 mg (99%). ^{1}H NMR (500 MHz, C$_6$D$_6$/THF (10:1), 293 K) δ 17.2 (s, 2H, pyridine), 16.8 (s, 2H, pyridine), 8.37 (s, 8H, [BAr$^F{}_4$]), 7.68 (s, 4H, [BAr$^F{}_4$]), 6.76 (s, 12H, Mes CH), 6.11 (s, 6H, backbone CH), 2.21 (s, 18H, Mes *p*-CH$_3$), 2.15 (s, 36H, Mes *o*-CH$_3$); ^{1313}C{^{1}H} NMR (125 MHz, C$_6$D$_6$/THF (10:1): 162.3 (q, [BAr$^F{}_4$]), 144.5 (IMes), 139.4 (IMes), 137.1 (IMes) 135.1 ([BAr$^F{}_4$]), 133.2 (IMes), 131.3 (IMes), 129.5 (q, [BAr$^F{}_4$]), 125.3 ([BAr$^F{}_4$]), 117.6 ([BAr$^F{}_4$]), 34.7 (IMes), 20.3 (IMes).

NMR spectra of compounds

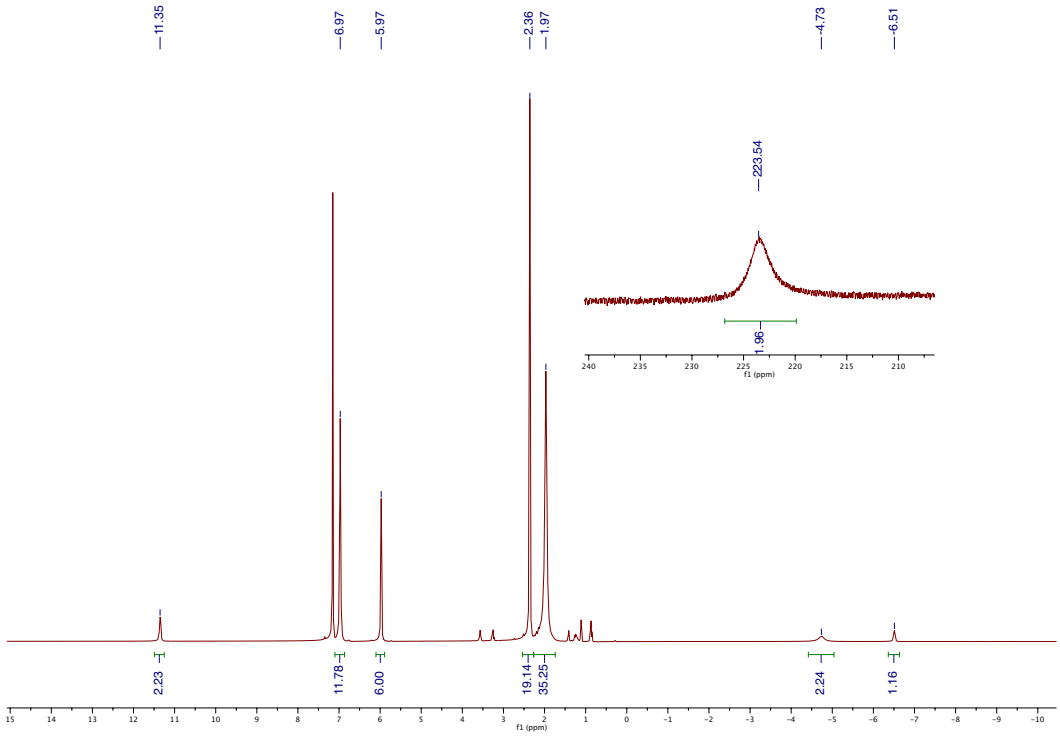

Figure S7.1: ^{1}H NMR spectrum of **2** in C_6D_6 at 293 K.

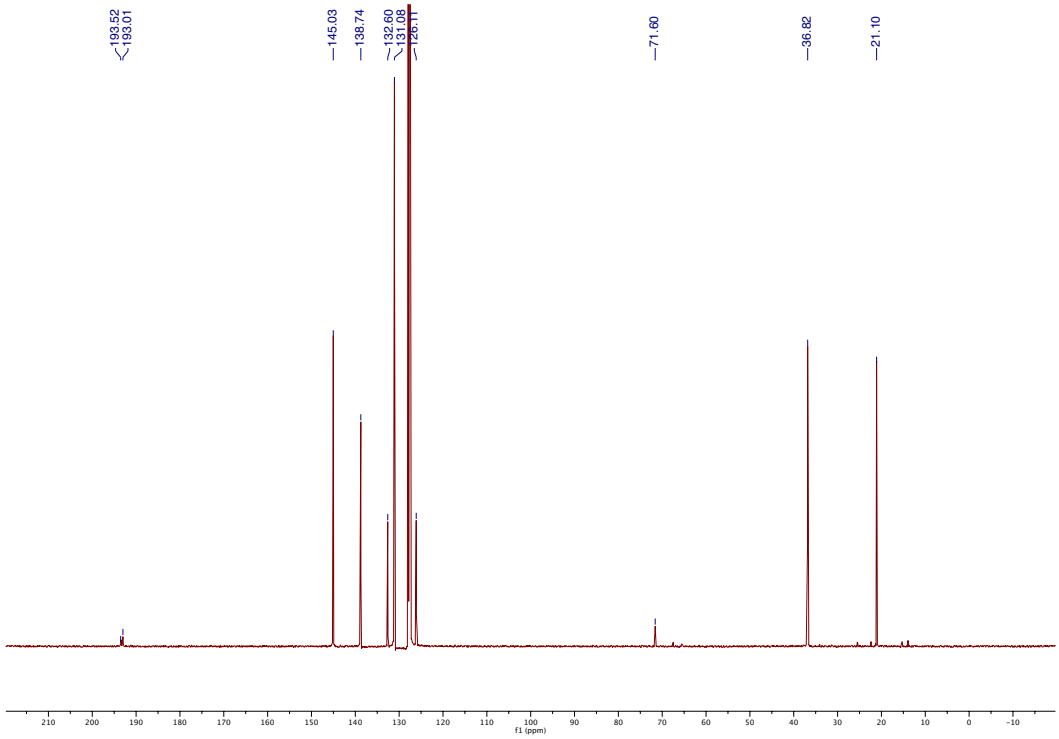

Figure S7.2: $^{13}C\{^{1}H\}$ NMR spectrum of **2** in C_6D_6 at 293 K.

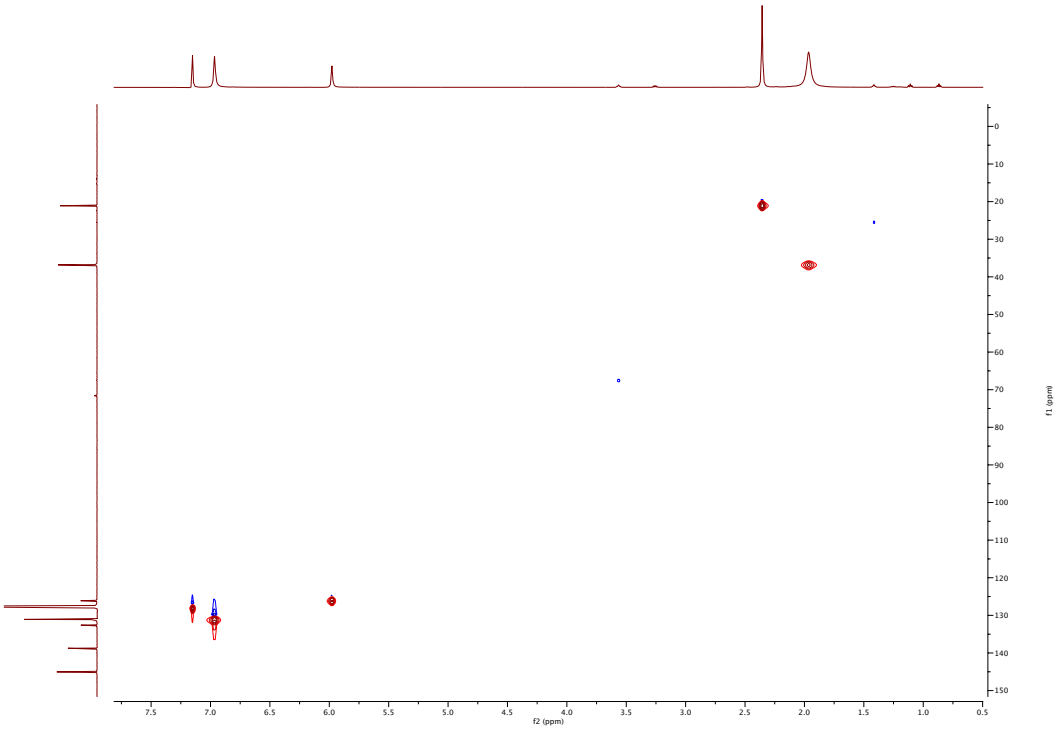

Figure S7.3: ^{1}H-^{13}C multiplicity edited HSQC spectrum of **2** in C_6D_6 at 293 K.

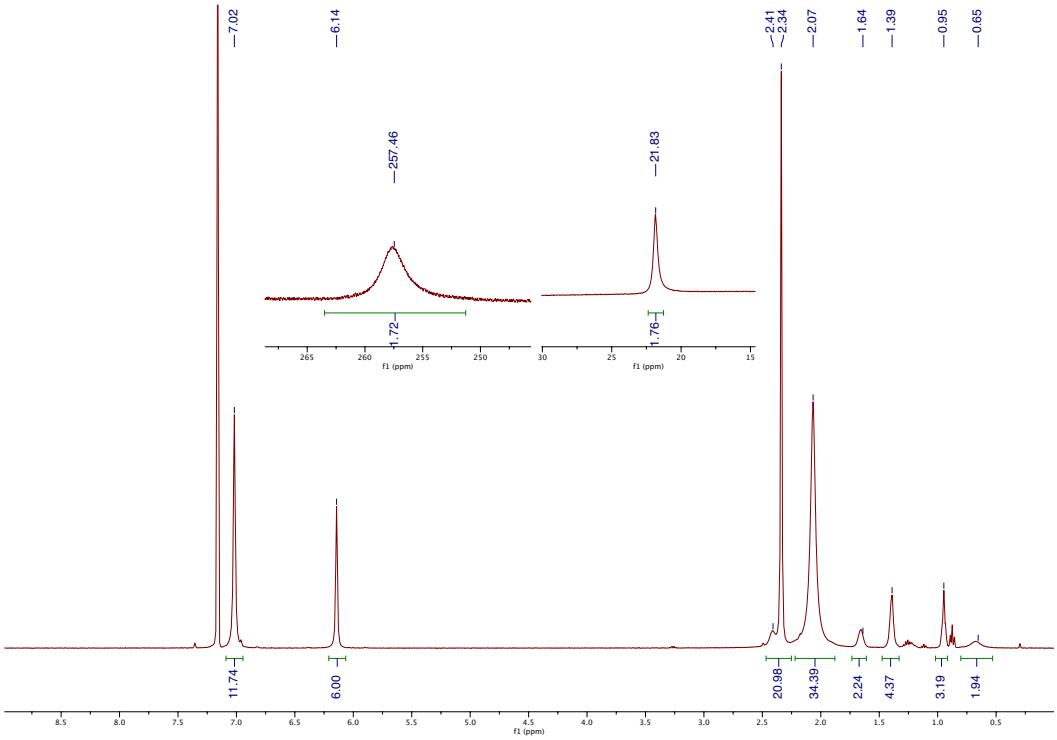

Figure S7.4: ^{1}H NMR spectrum of **3** in C_6D_6 at 293 K.

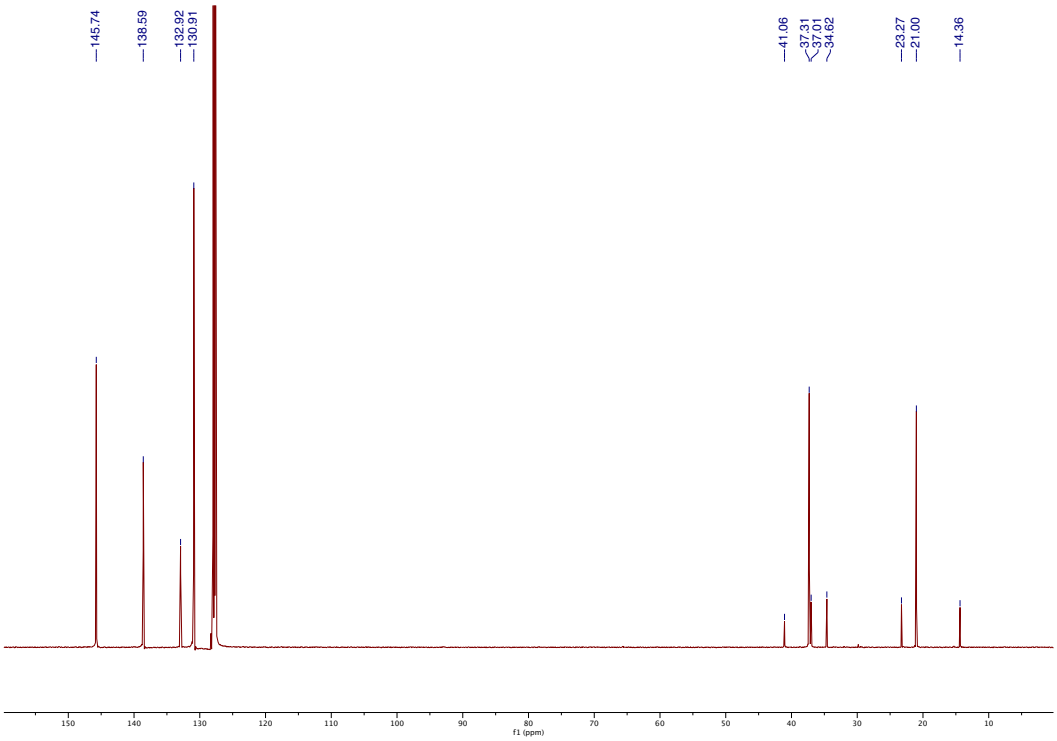

Figure S7.5: $^{13}C\{^{1}H\}$ NMR spectrum of **3** in C_6D_6 at 293 K.

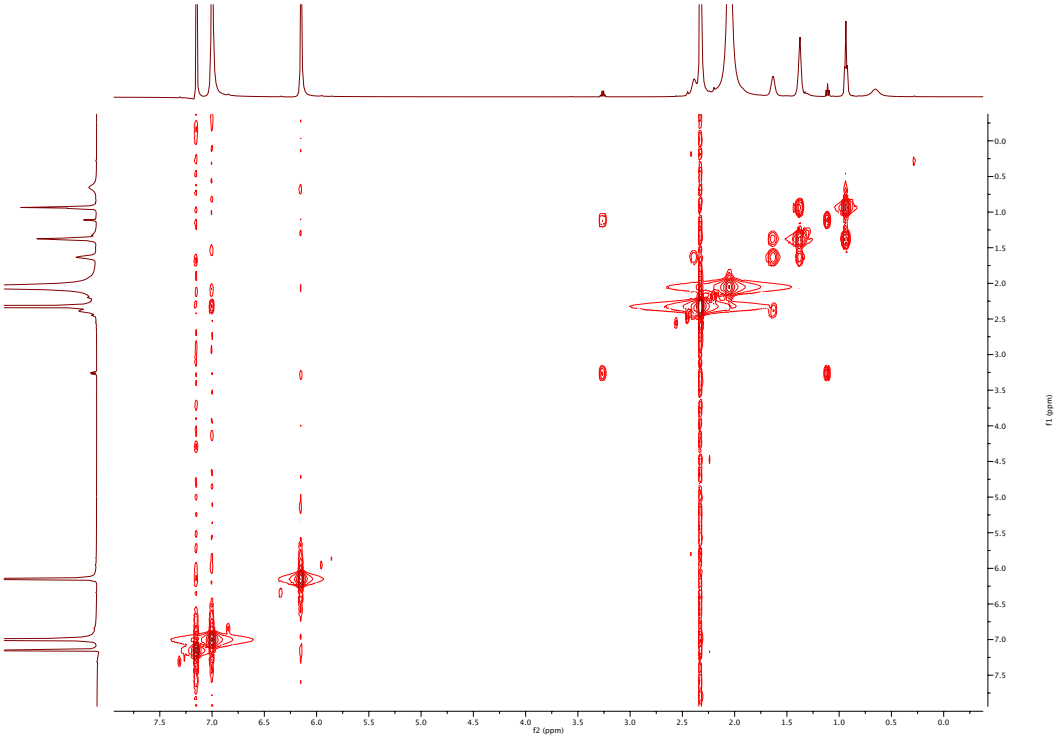

Figure S7.6: ^{1}H-^{1}H COSY spectrum of **3** in C_6D_6 at 293 K.

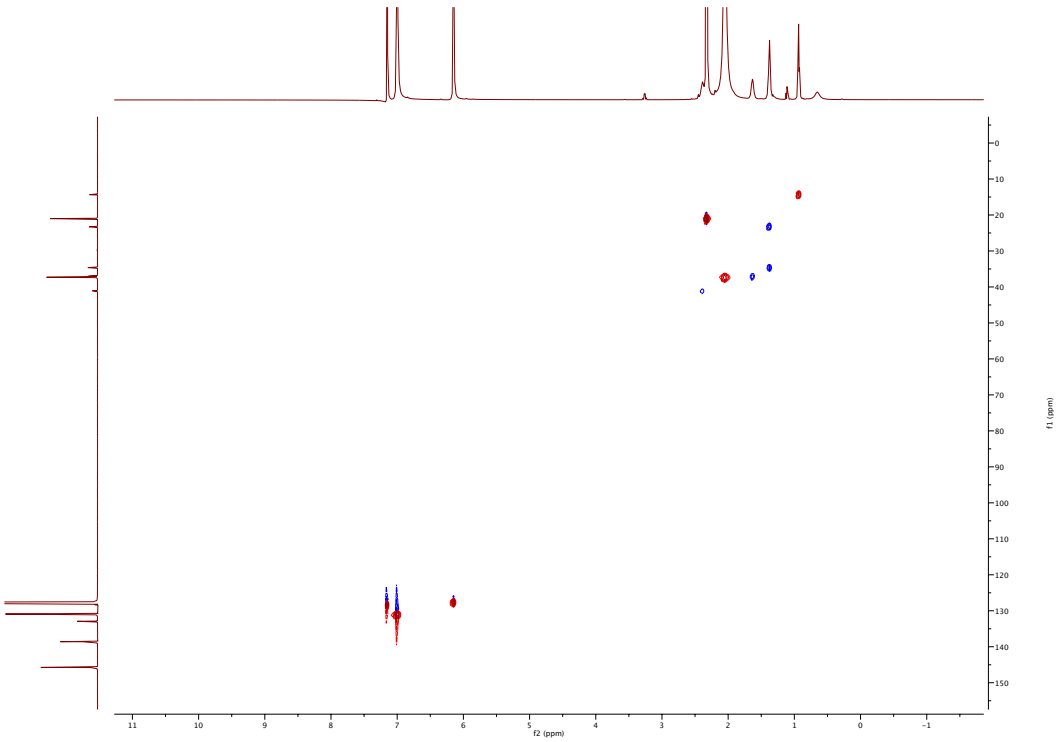

Figure S7.7: ^{1}H-^{13}C multiplicity edited HSQC spectrum of **3** in C_6D_6 at 293 K.

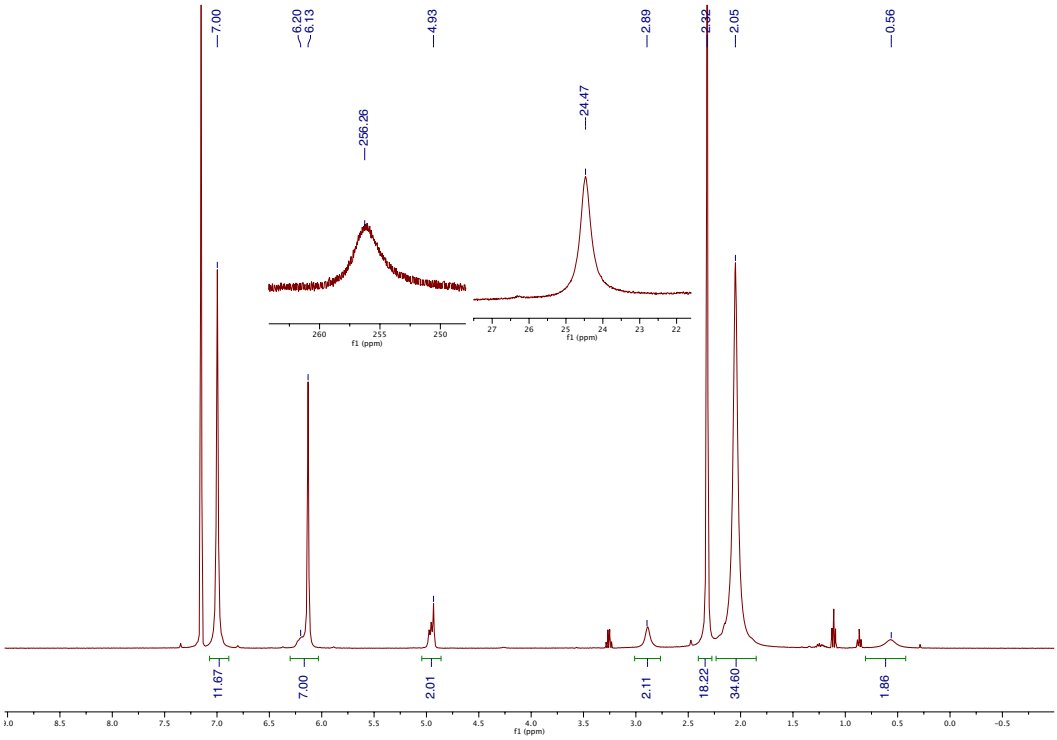

Figure S7.8: ^{1}H NMR spectrum of **5** in C_6D_6 at 293 K.

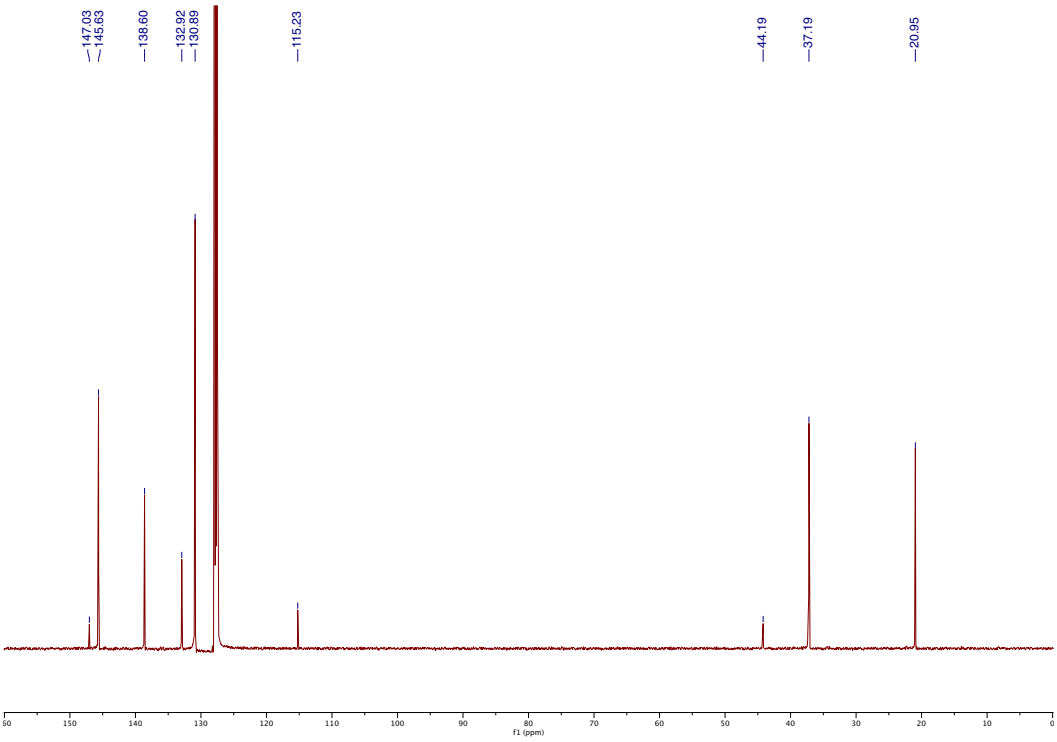

Figure S7.9: $^{13}C\{^{1}H\}$ NMR spectrum of **5** in C_6D_6 at 293 K.

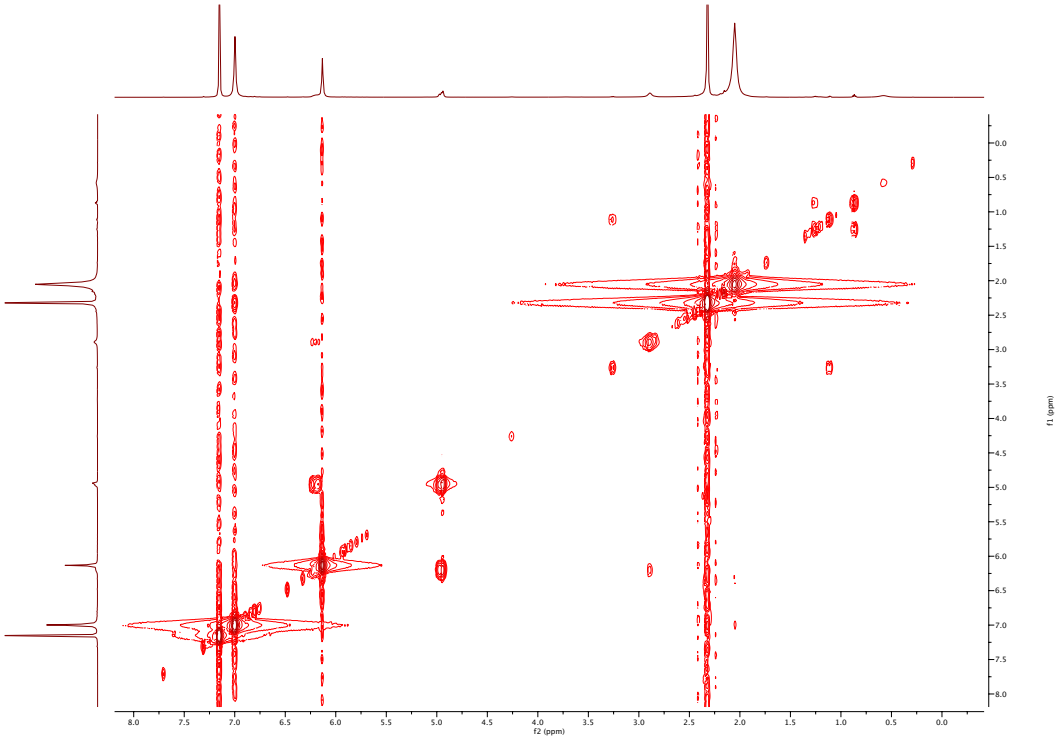

Figure S7.10: ^{1}H-^{1}H COSY spectrum of **5** in C_6D_6 at 293 K.

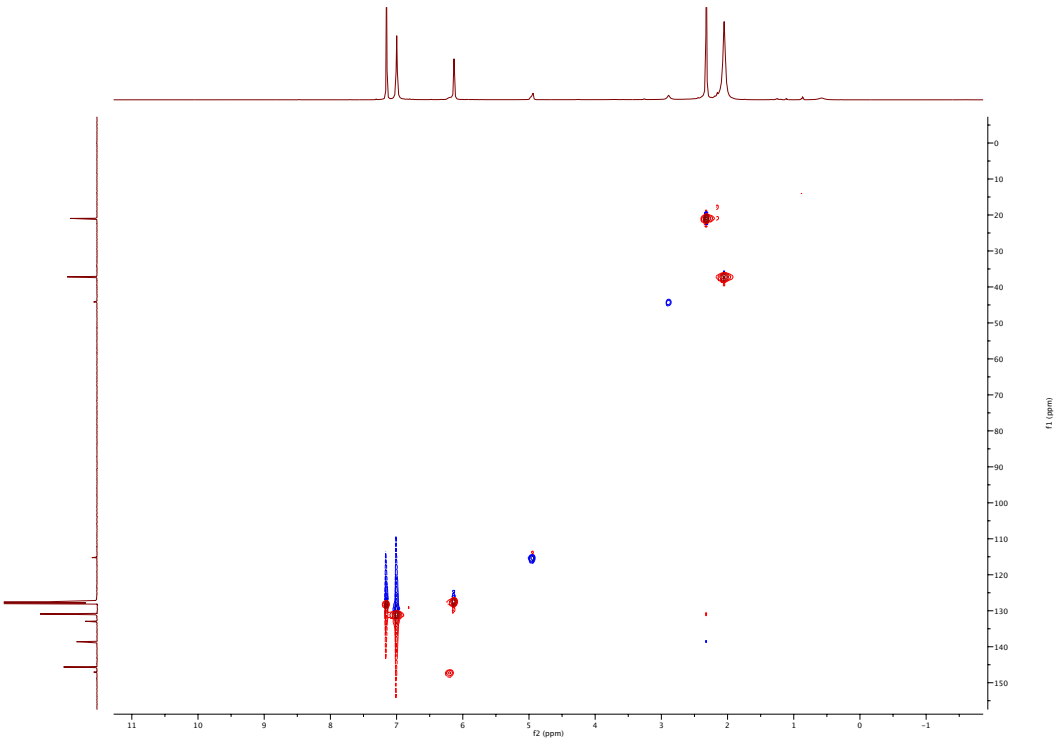

Figure S7.11: ^{1}H-^{13}C multiplicity edited HSQC spectrum of **5** in C_6D_6 at 293 K.

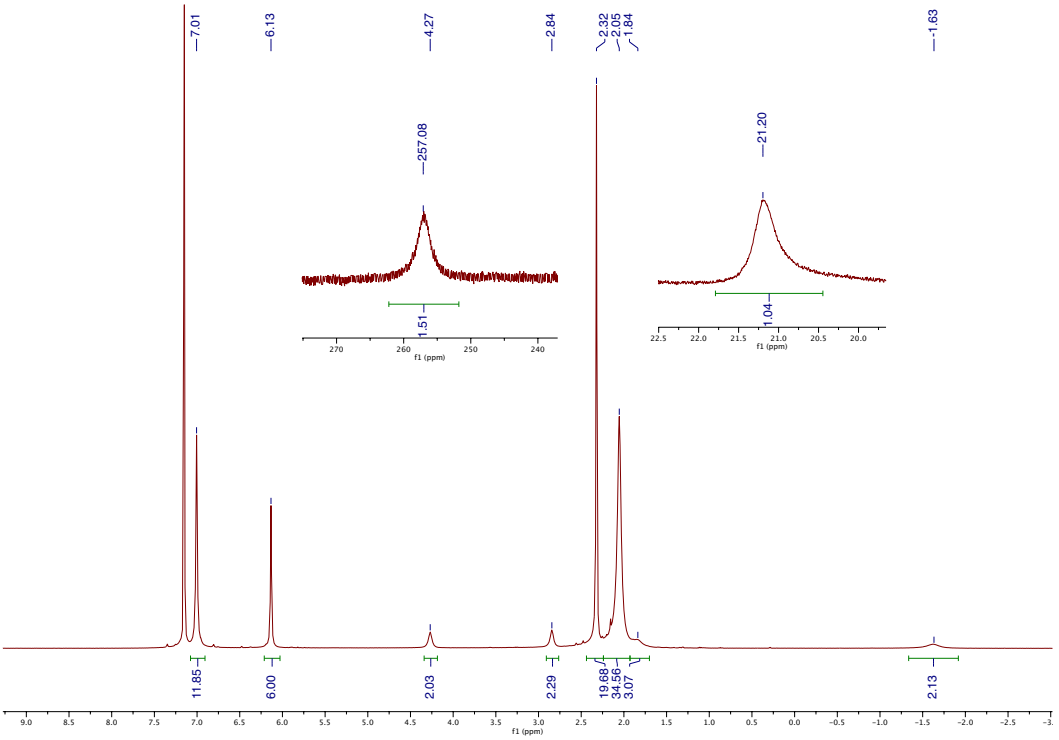

Figure S7.12: ^{1}H NMR spectrum of **7** in C_6D_6 at 293 K.

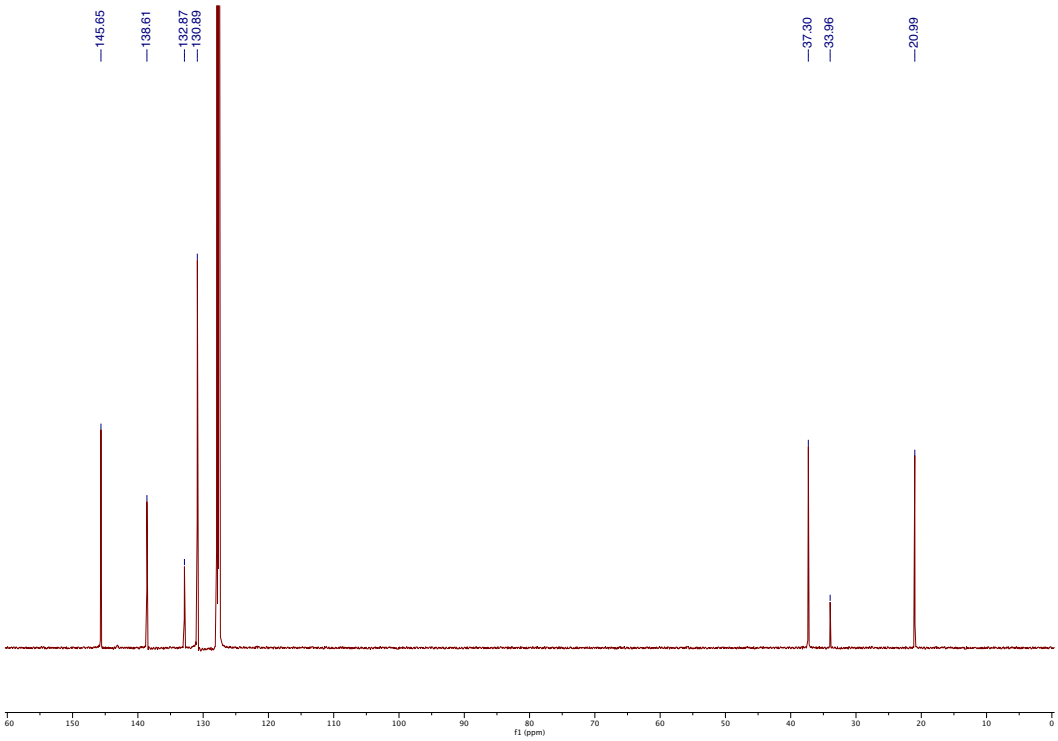

Figure S7.13: $^{13}C\{^{1}H\}$ NMR spectrum of **7** in C_6D_6 at 293 K.

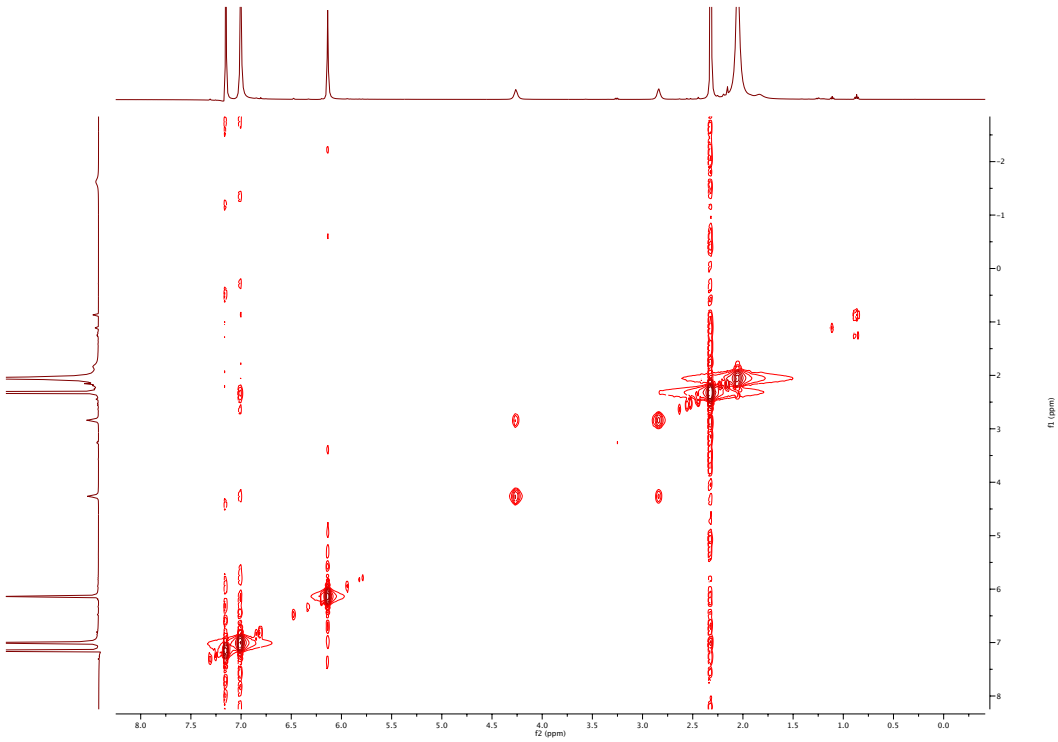

Figure S7.14: ^{1}H-^{1}H COSY spectrum of **7** in C_6D_6 at 293 K.

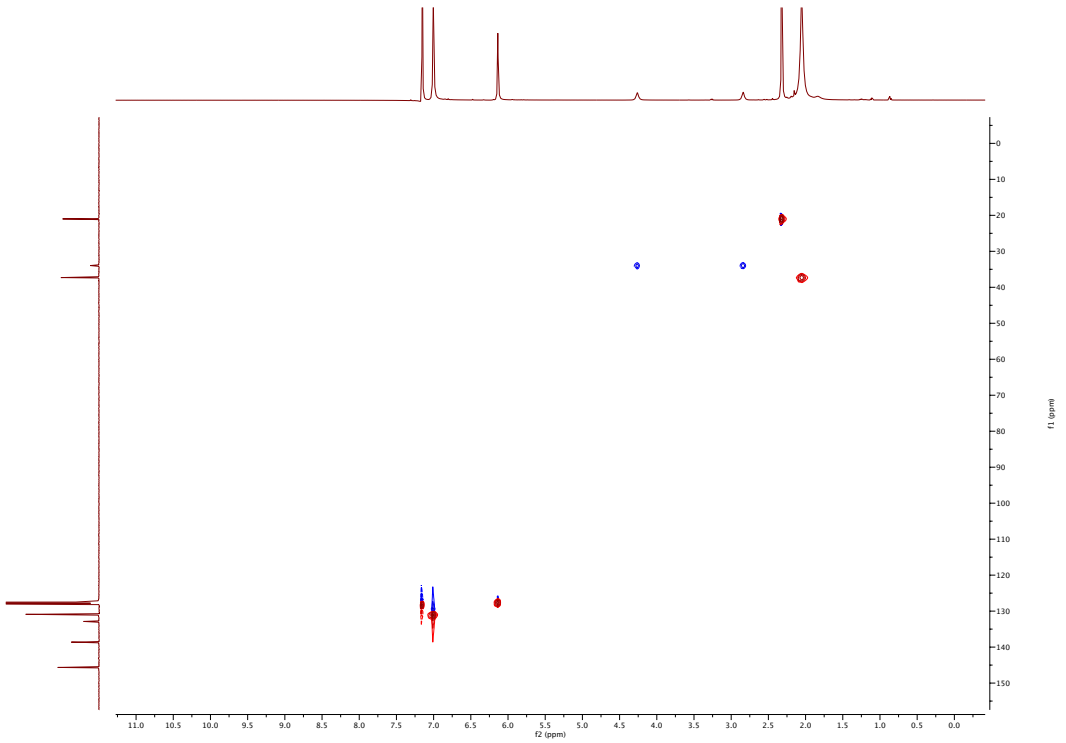

Figure S7.15: ^{1}H-^{13}C multiplicity edited HSQC spectrum of **7** in C_6D_6 at 293 K.

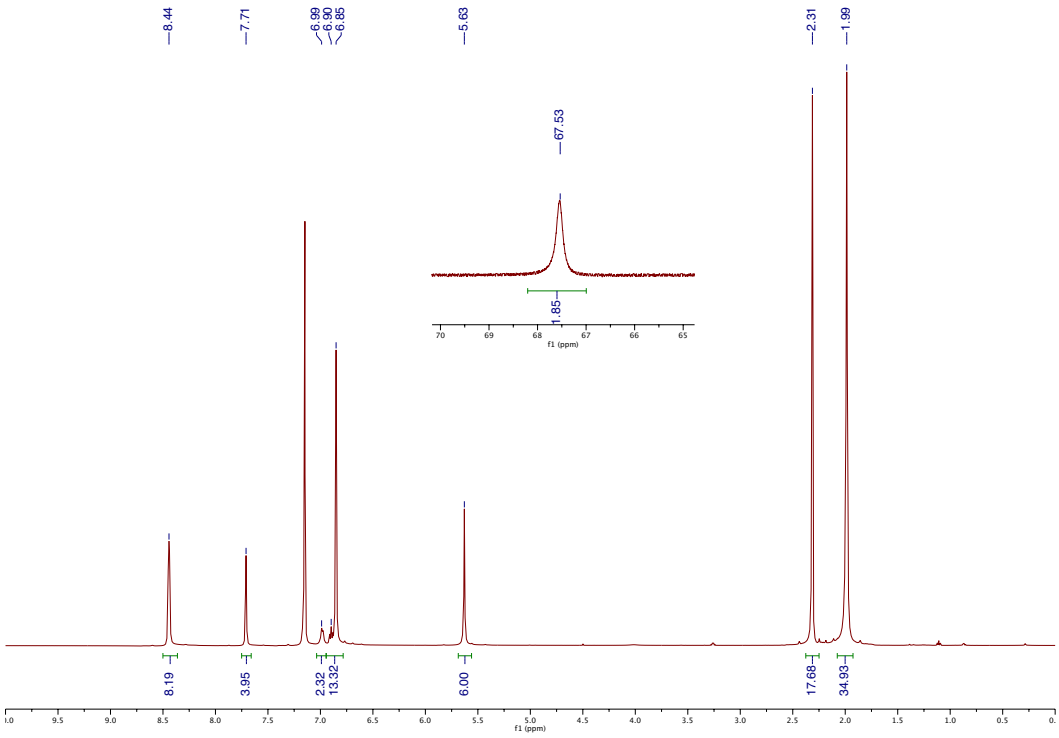

Figure S7.16: ^{1}H NMR spectrum of **[2]**$^{+}$ in C_6D_6 at 293 K.

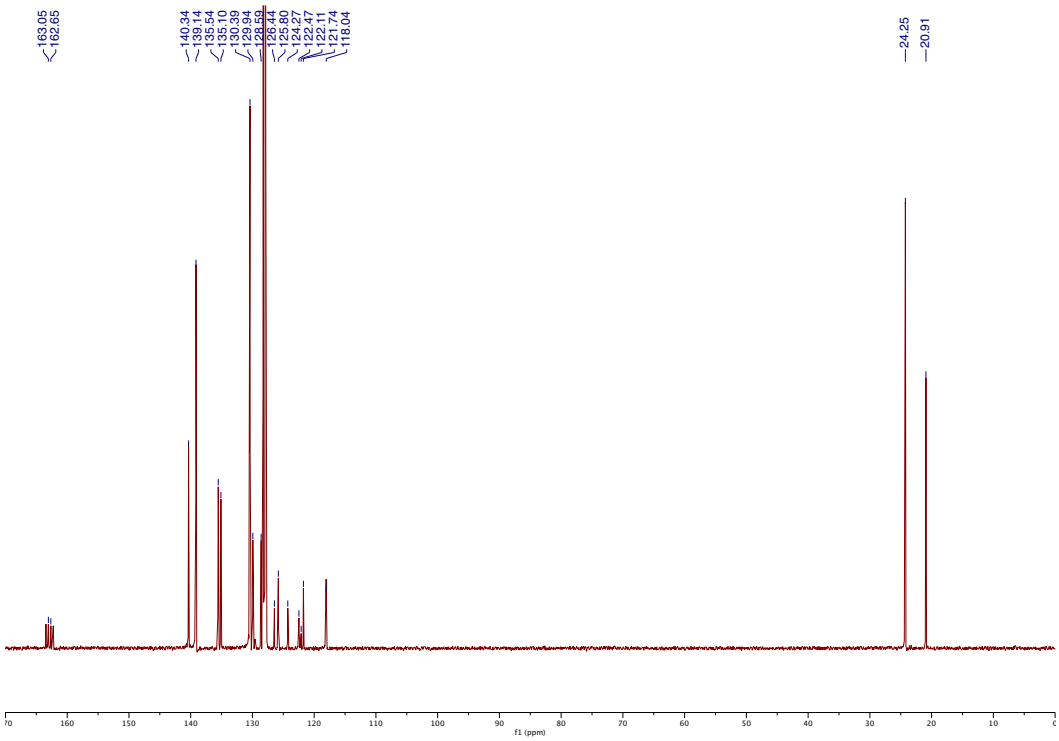

Figure S7.17: $^{13}C\{^{1}H\}$ NMR spectrum of **[2]**$^{+}$ in C_6D_6 at 293 K.

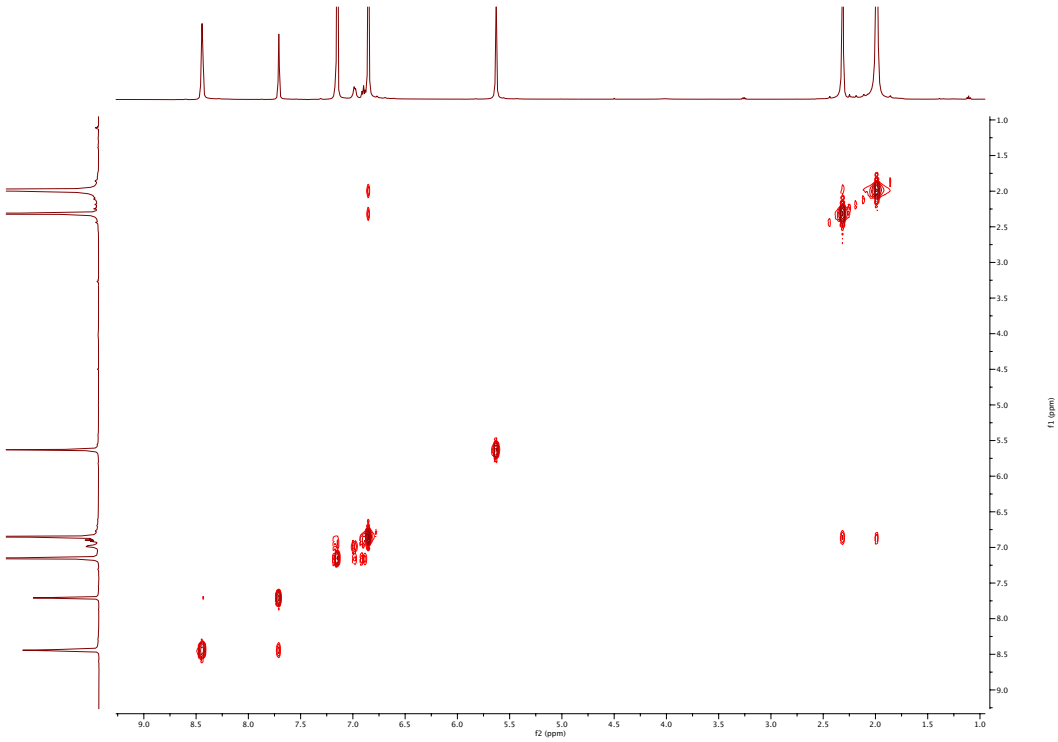

Figure S7.18: ^{1}H-^{1}H COSY spectrum of **[2]**$^{+}$ in C_6D_6 at 293 K.

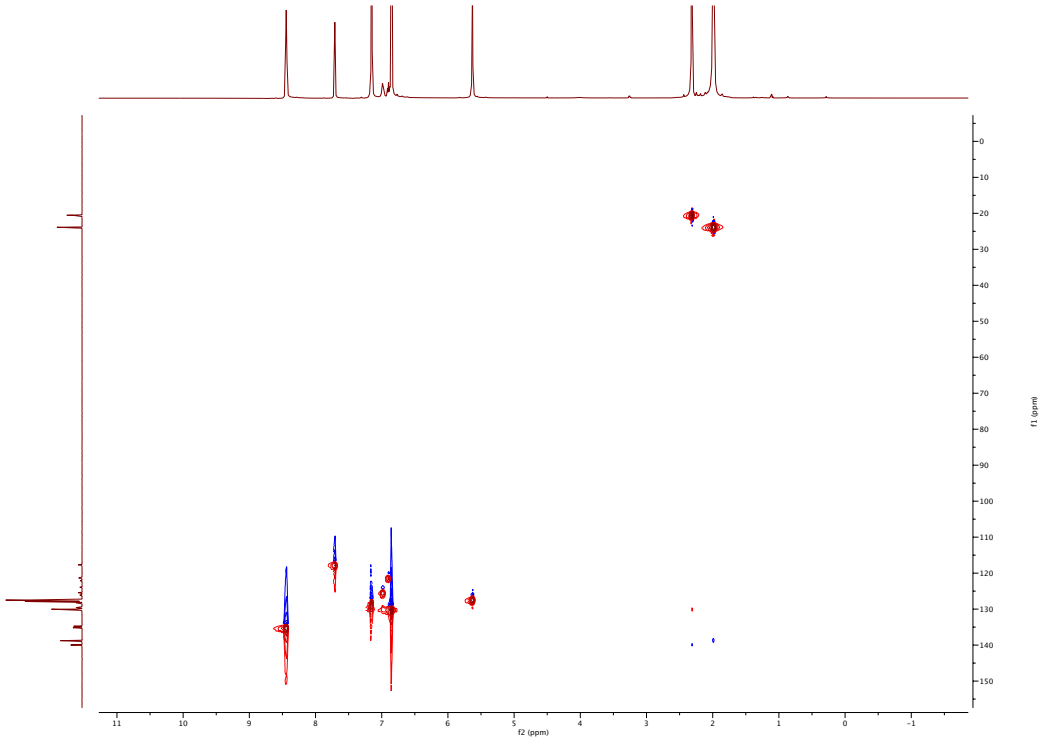

Figure S7.19: ^{1}H-^{13}C multiplicity edited HSQC spectrum of **[2]**$^{+}$ in C_6D_6 at 293 K.

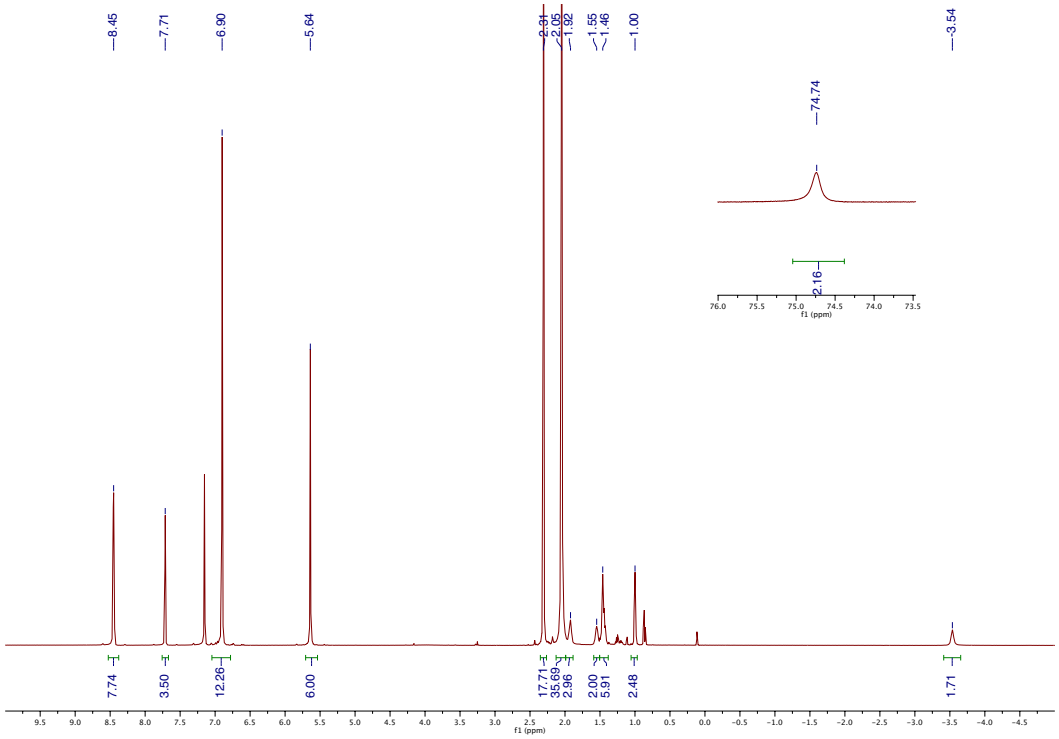

Figure S7.20: ^{1}H NMR spectrum of **[3]**$^{+}$ in C_6D_6 at 293 K.

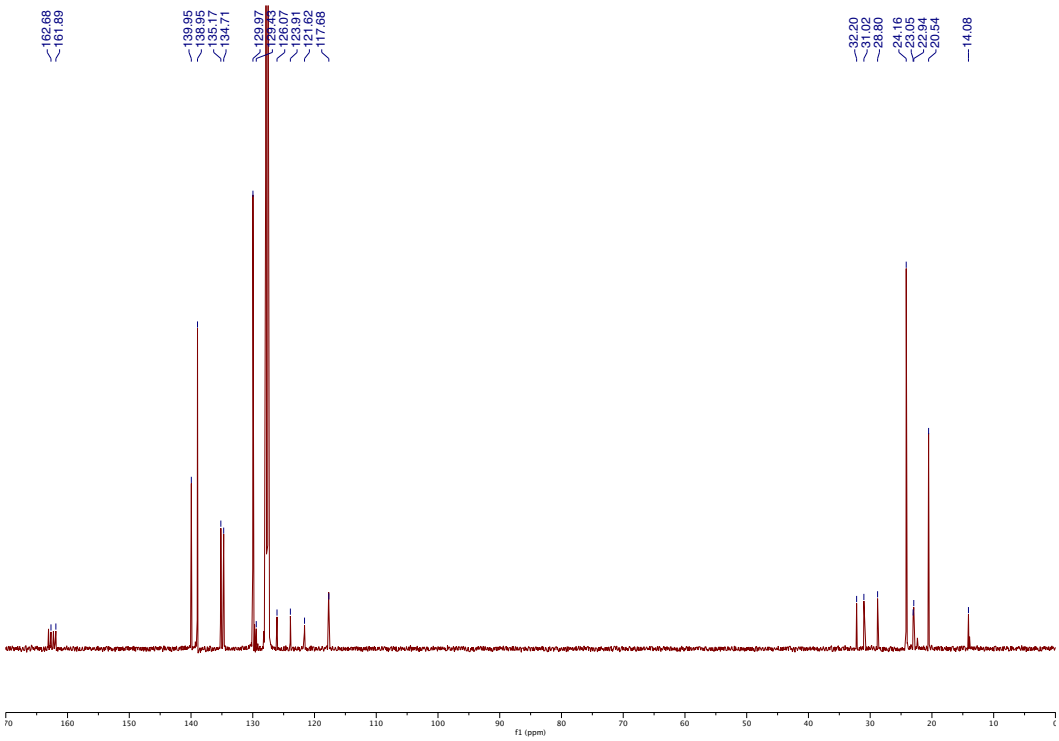

Figure S7.21: $^{13}C\{^{1}H\}$ NMR spectrum of **[3]**$^{+}$ in C_6D_6 at 293 K.

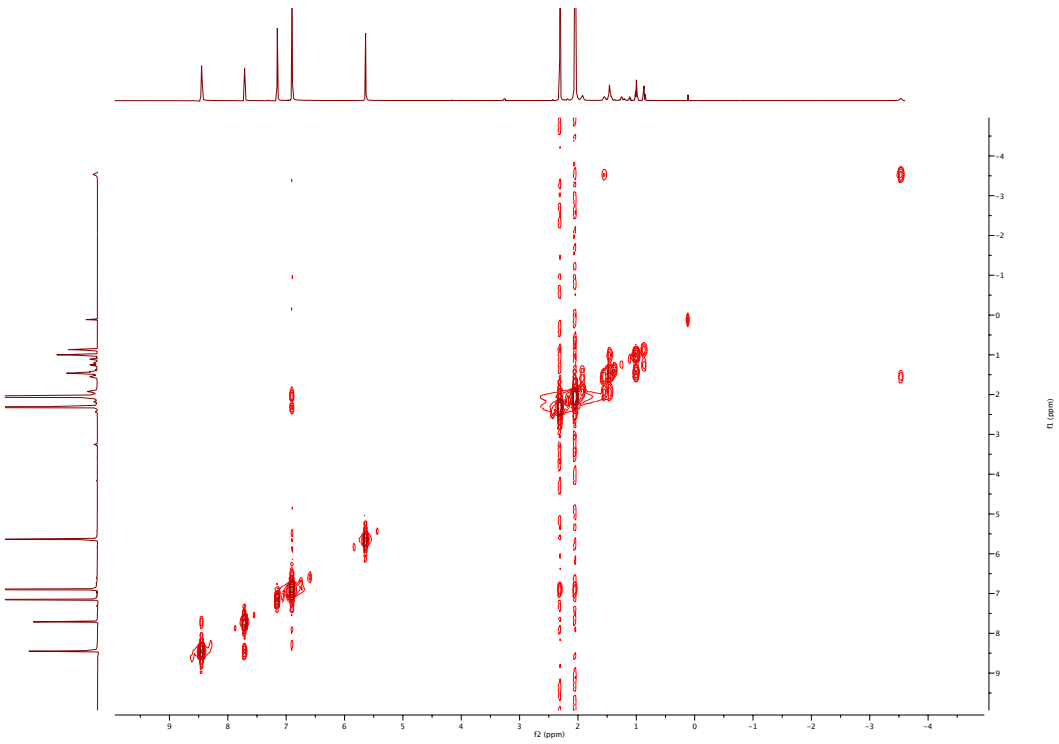

Figure S7.22: ^{1}H-^{1}H COSY spectrum of **[3]**$^{+}$ in C_6D_6 at 293 K.

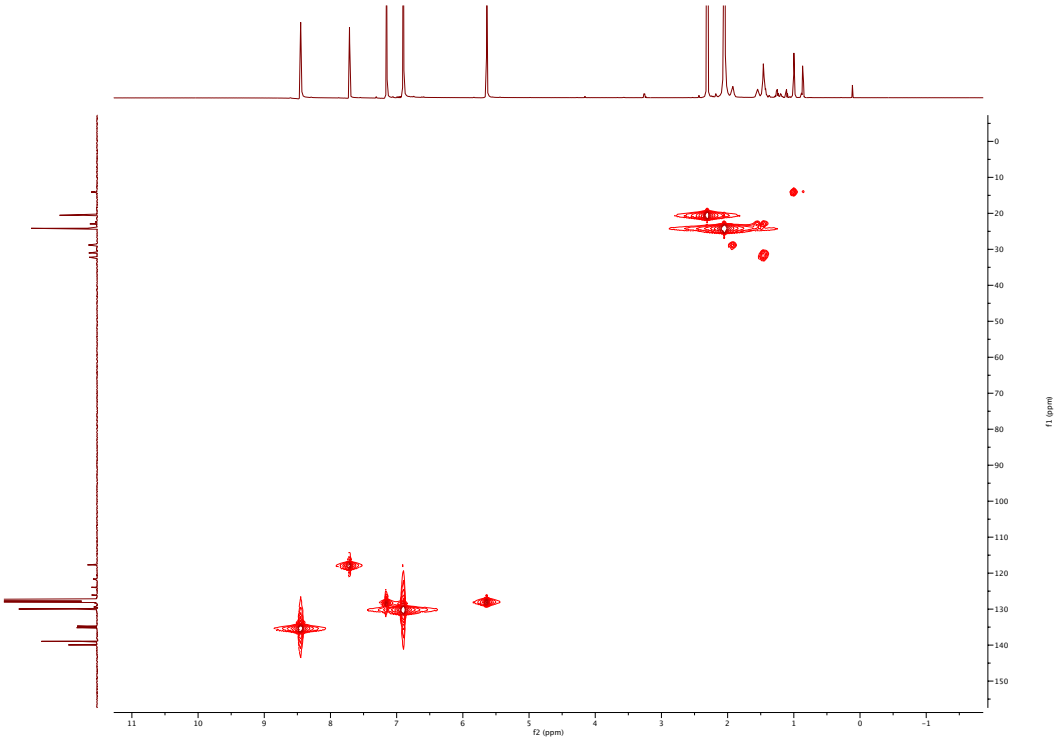

Figure S7.23: ^{1}H-^{13}C HSQC spectrum of **[3]**$^{+}$ in C_6D_6 at 293 K.

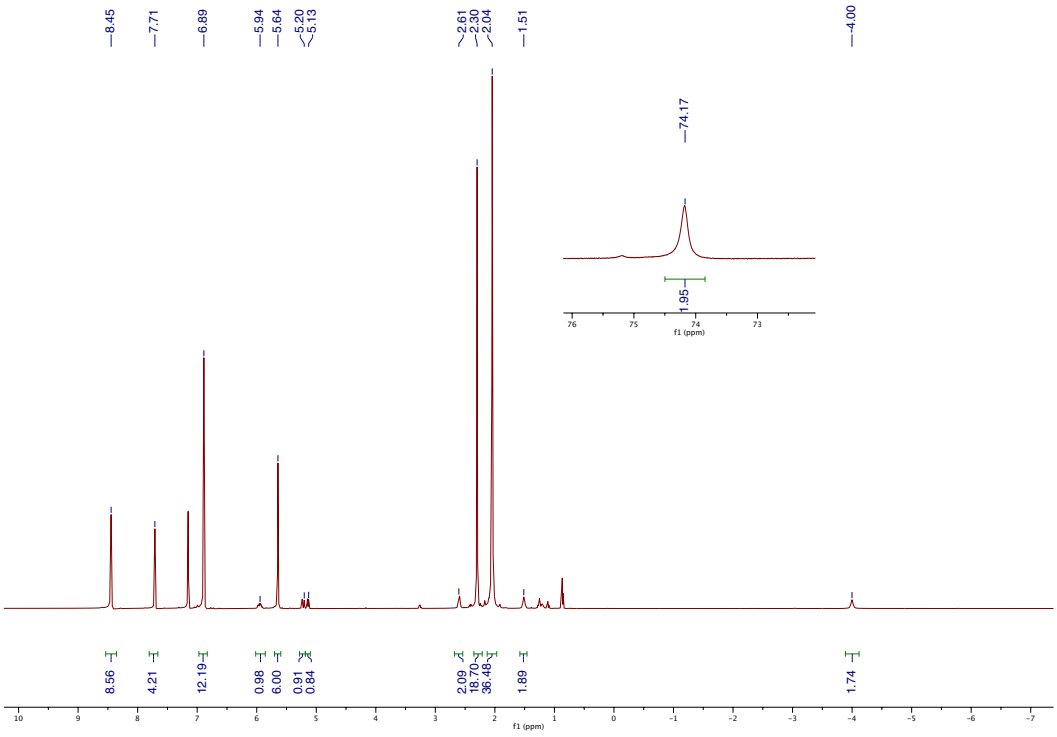

Figure S7.24: ^{1}H NMR spectrum of **[5]**$^{+}$ in C_6D_6 at 293 K.

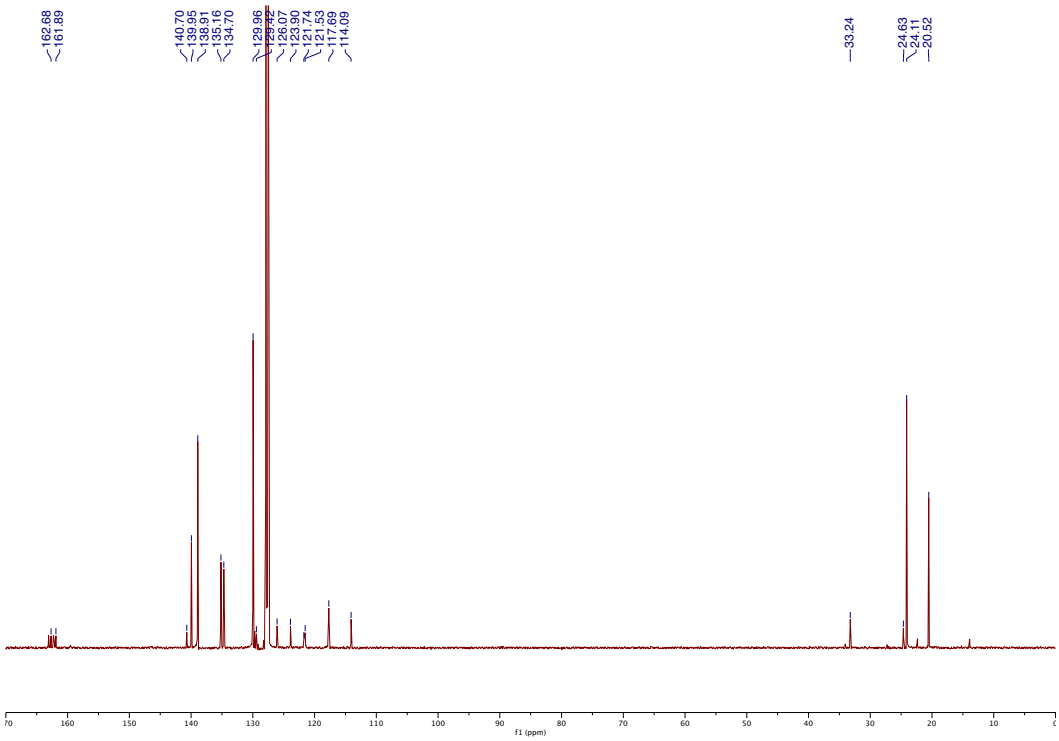

Figure S7.25: $^{13}C\{^{1}H\}$ NMR spectrum of **[5]**$^{+}$ in C_6D_6 at 293 K.

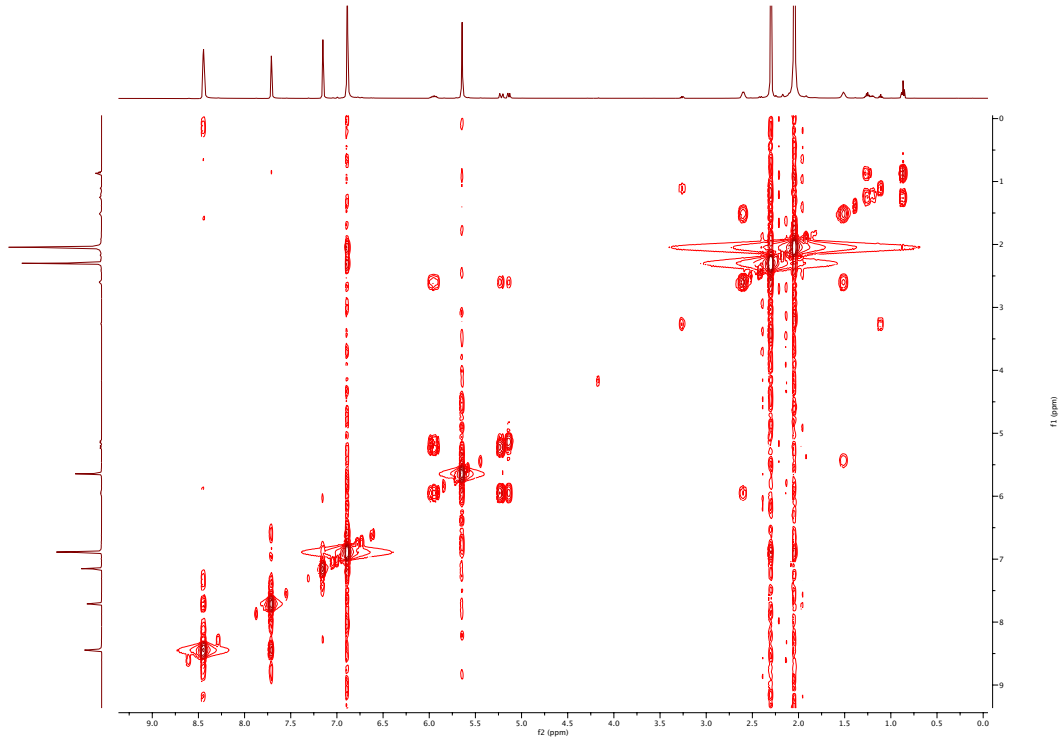

Figure S7.26: ^{1}H-^{1}H COSY spectrum of **[5]**$^{+}$ in C_6D_6 at 293 K.

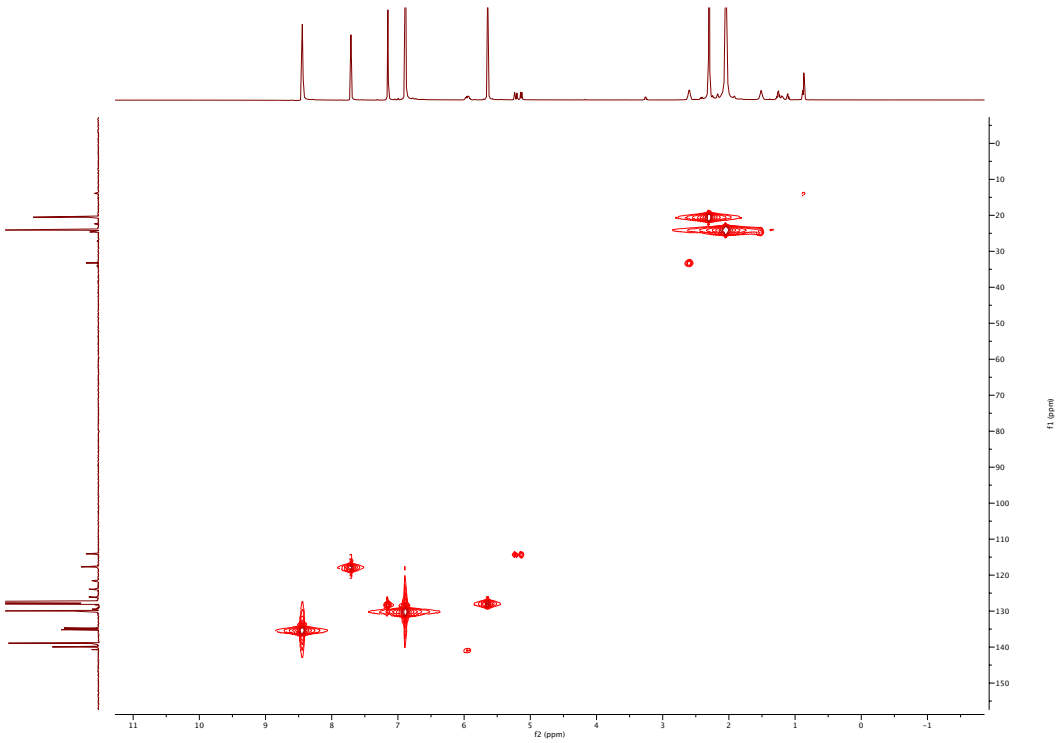

Figure S7.27: ^{1}H-^{13}C HSQC spectrum of **[5]**$^{+}$ in C_6D_6 at 293 K.

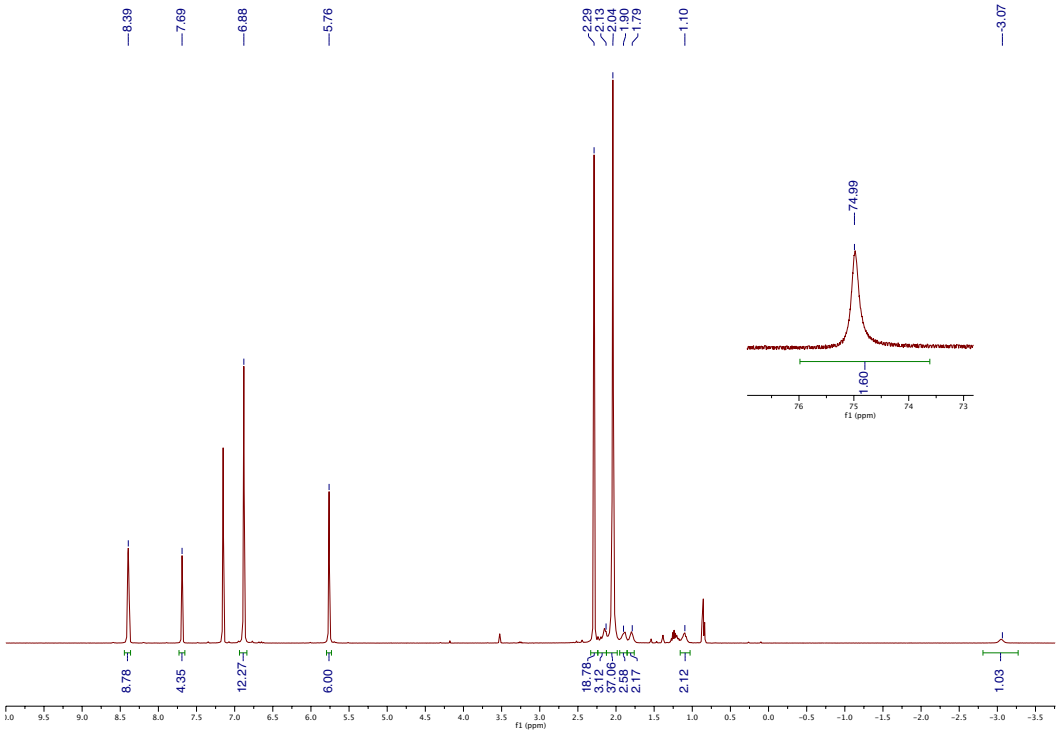

Figure S7.28: ^{1}H NMR spectrum of **[7]**$^{+}$ in C_6D_6/d^{8}-THF 15:1 at 293 K.

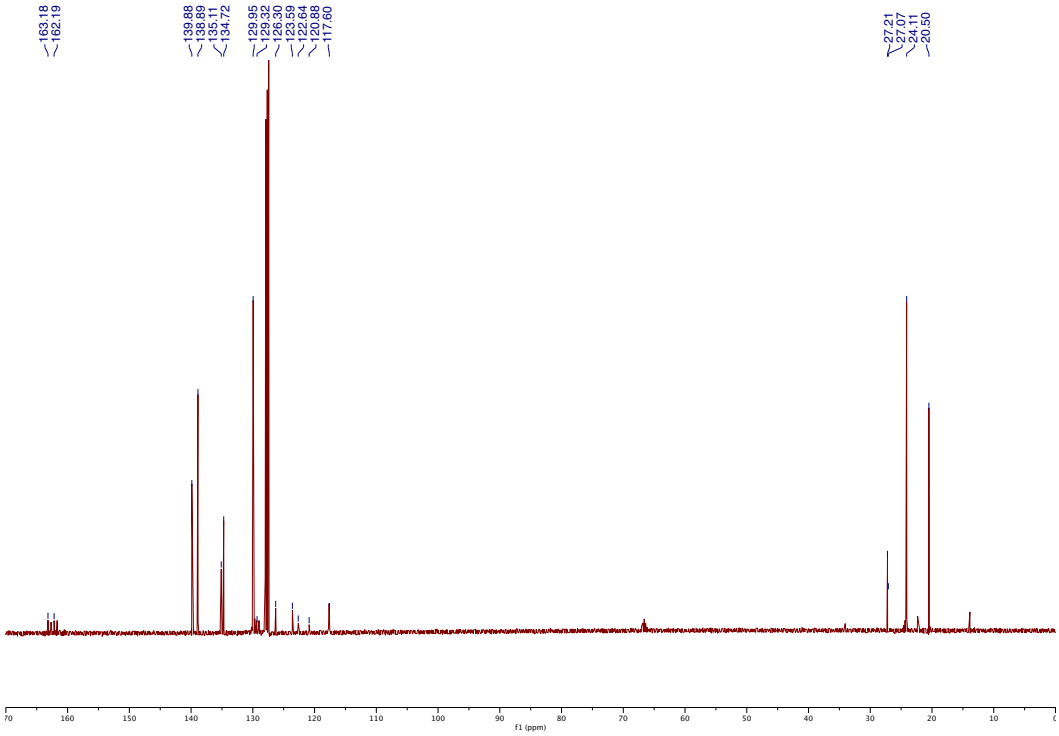

Figure S7.29: $^{13}C\{^{1}H\}$ NMR spectrum of **[7]**$^{+}$ in C_6D_6/d^8-THF 15:1 at 293 K.

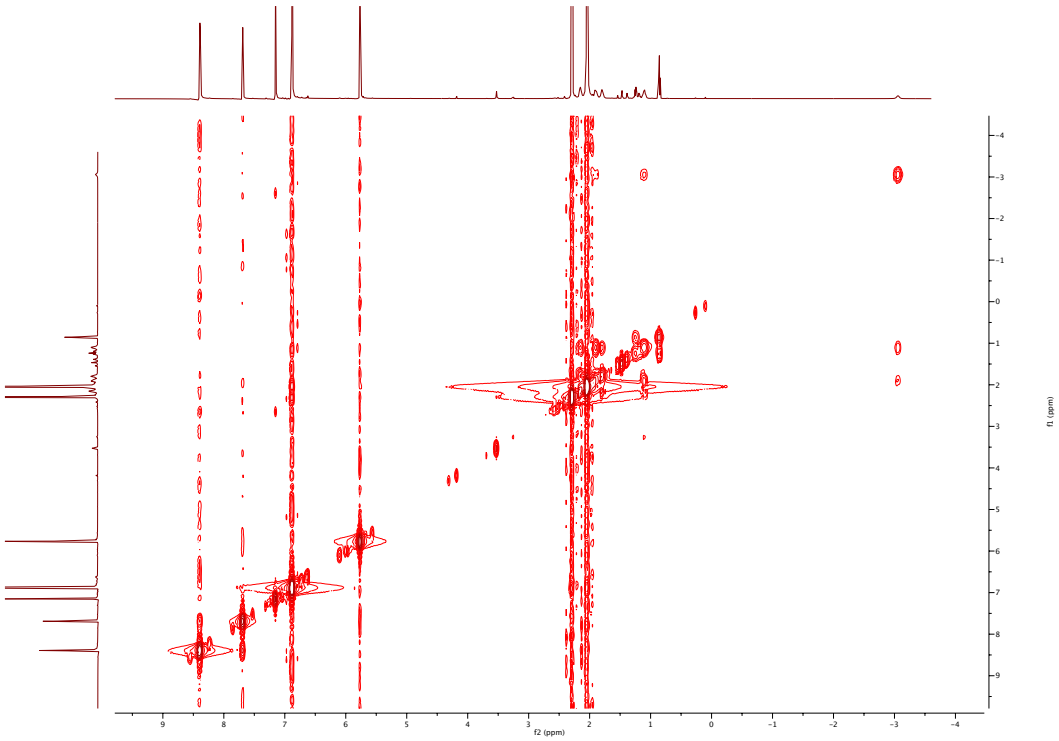

Figure S7.30: ^{1}H-^{1}H COSY spectrum of **[7]**$^{+}$ in C_6D_6/d^8-THF 15:1 at 293 K.

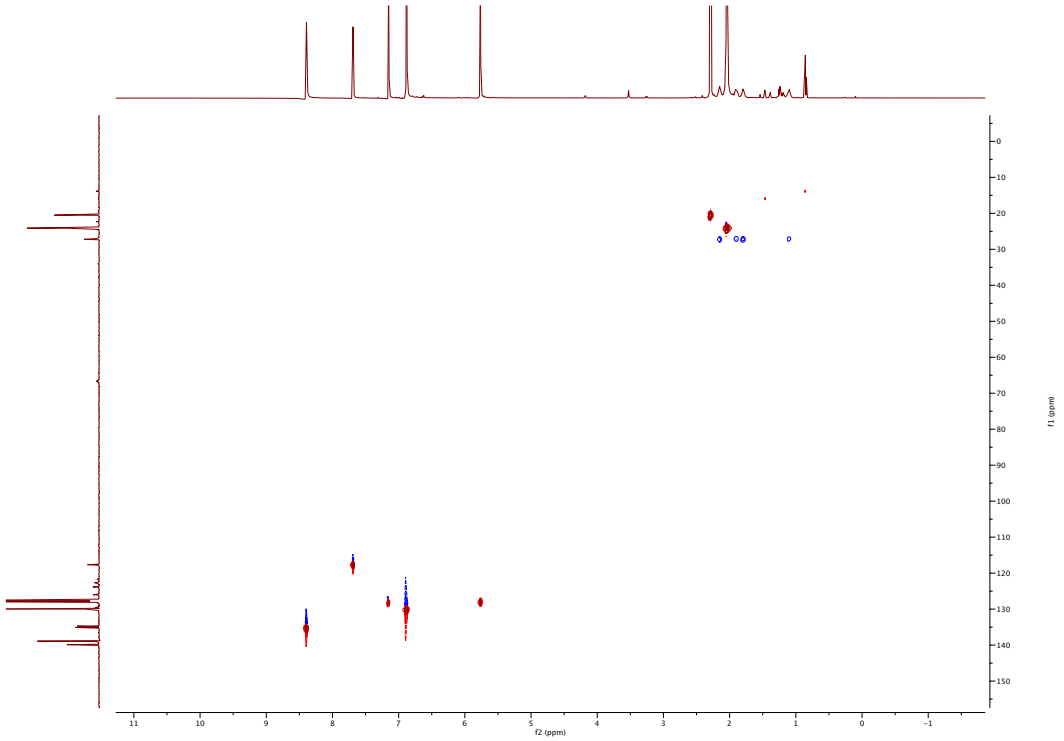

Figure S7.31: ^{1}H-^{13}C multiplicity edited HSQC spectrum of **[7]**$^{+}$ in C_6D_6/d^8-THF 15:1 at 293 K.

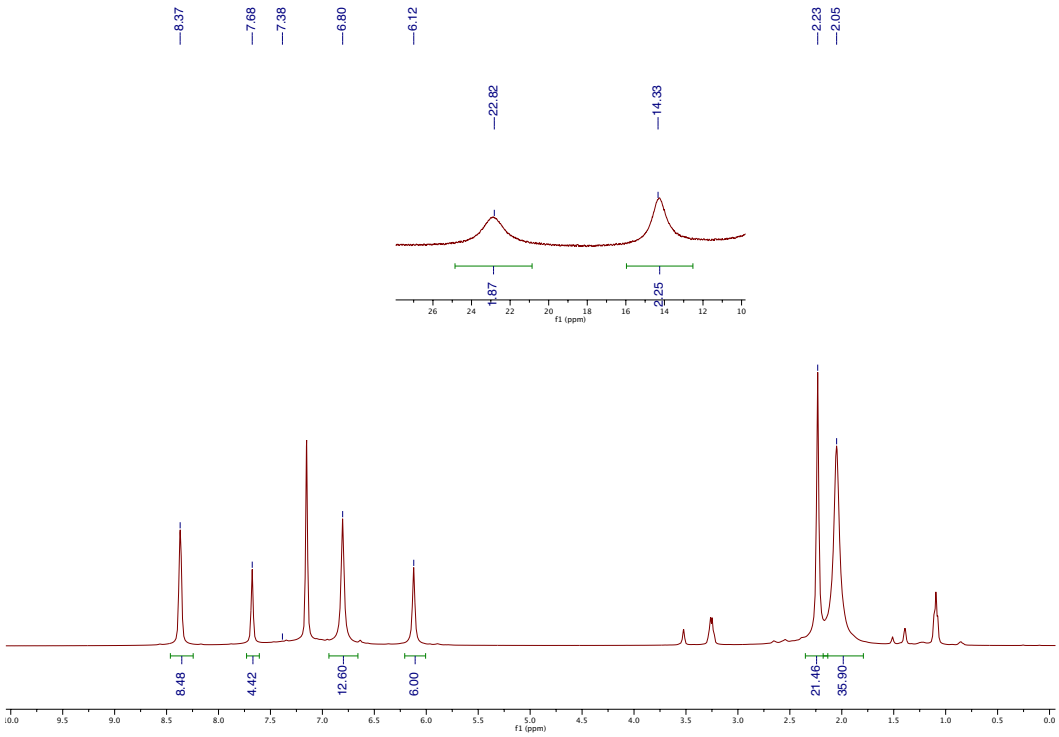

Figure S7.32: ^{1}H NMR spectrum of **[4]**$^{+}$ in C_6D_6/d^8-THF 15:1 at 293 K.

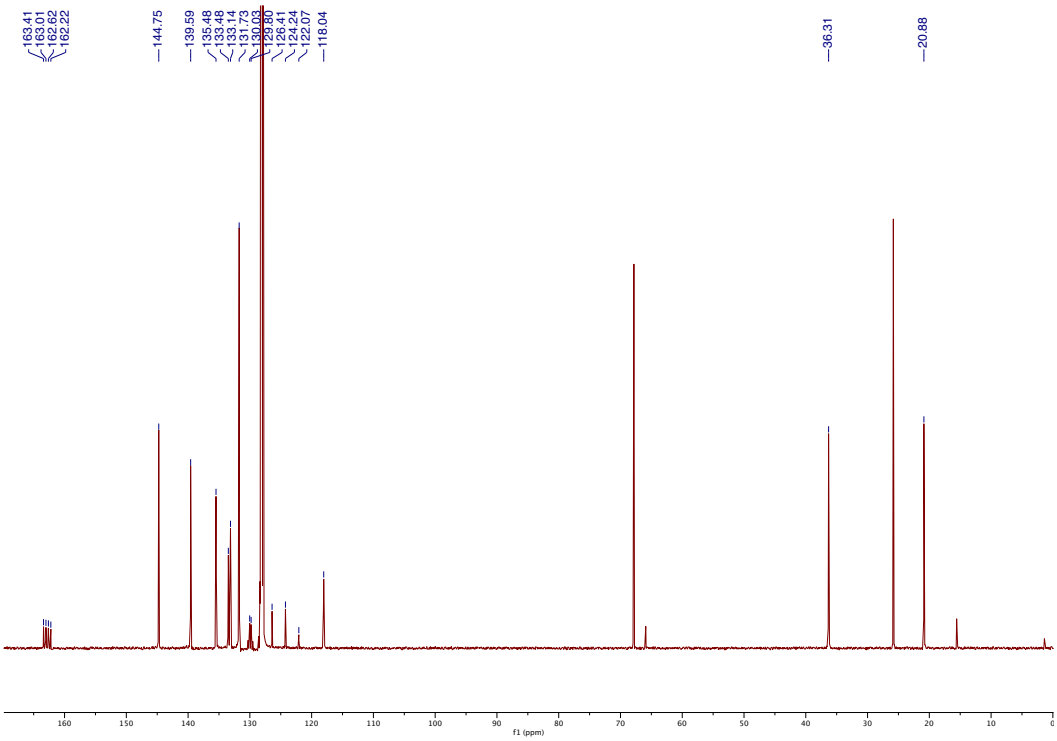

Figure S7.33: $^{13}C\{^{1}H\}$ NMR spectrum of **[4]**$^{+}$ in C_6D_6/THF 15:1 at 293 K.

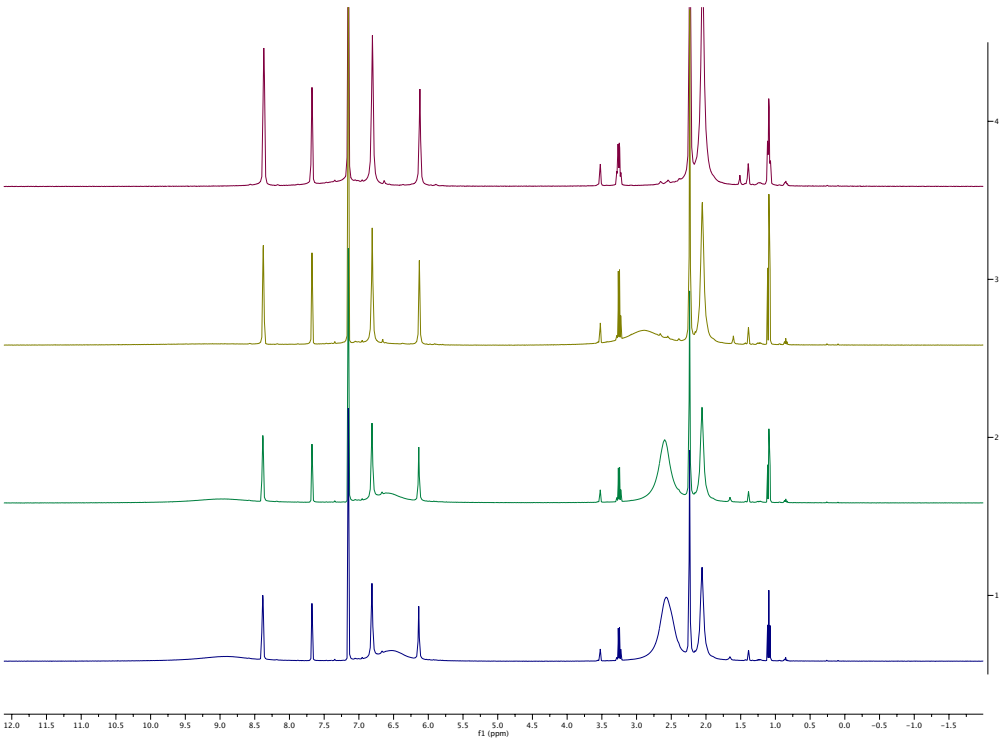

Figure S7.34: ^{1}H NMR spectrum of **[4]**$^{+}$ in C_6D_6/d^8-THF 15:1 at 293 K with 1, 5, 10 and 20 equiv. (top to bottom) of DMAP added.

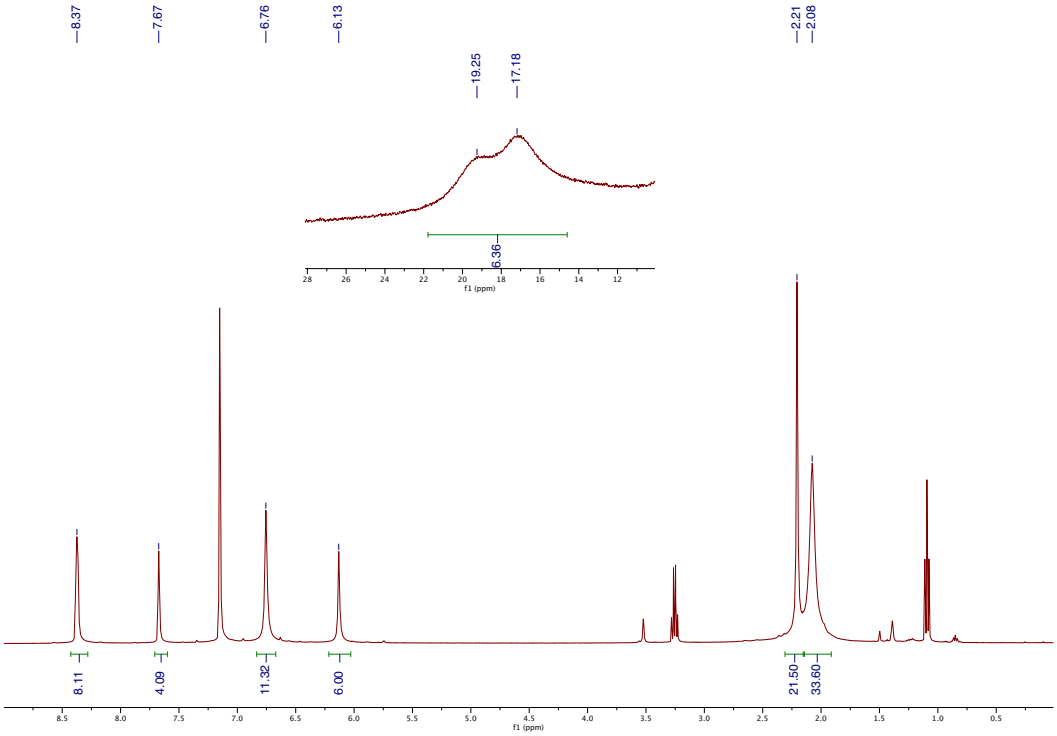

Figure S7.35: ^{1}H NMR spectrum of **[8]**$^{+}$ in C_6D_6/d^8-THF 15:1 at 293 K.

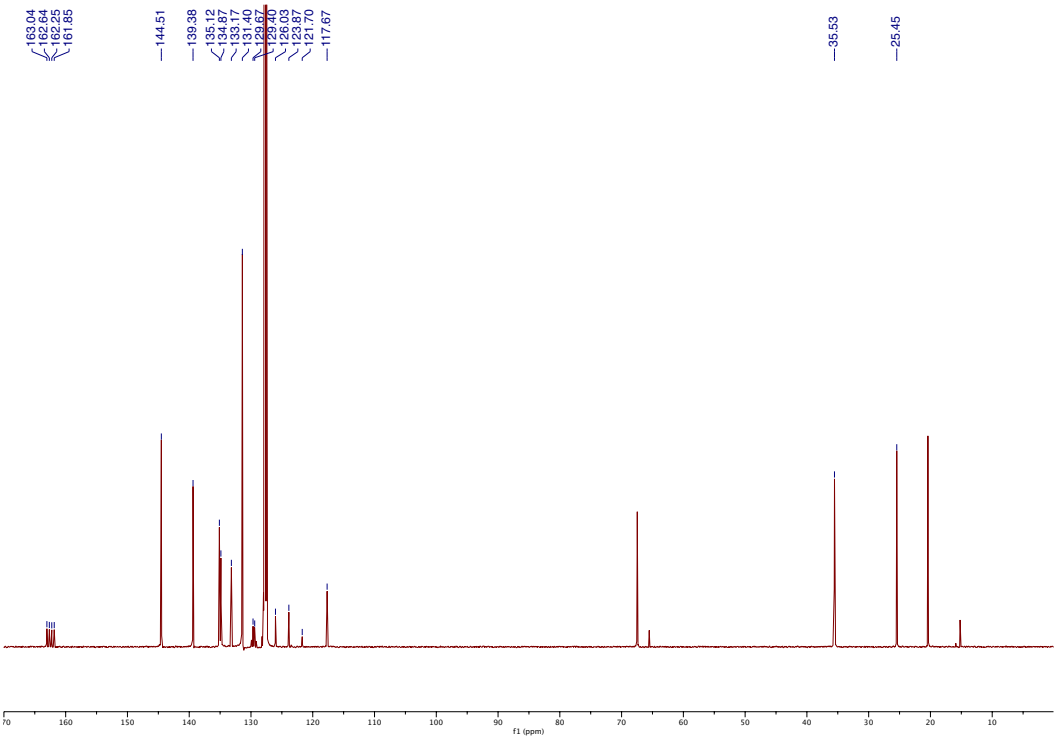

Figure S7.36: $^{13}C\{^{1}H\}$ NMR spectrum of **[8]**$^{+}$ in C_6D_6/THF 15:1 at 293 K.

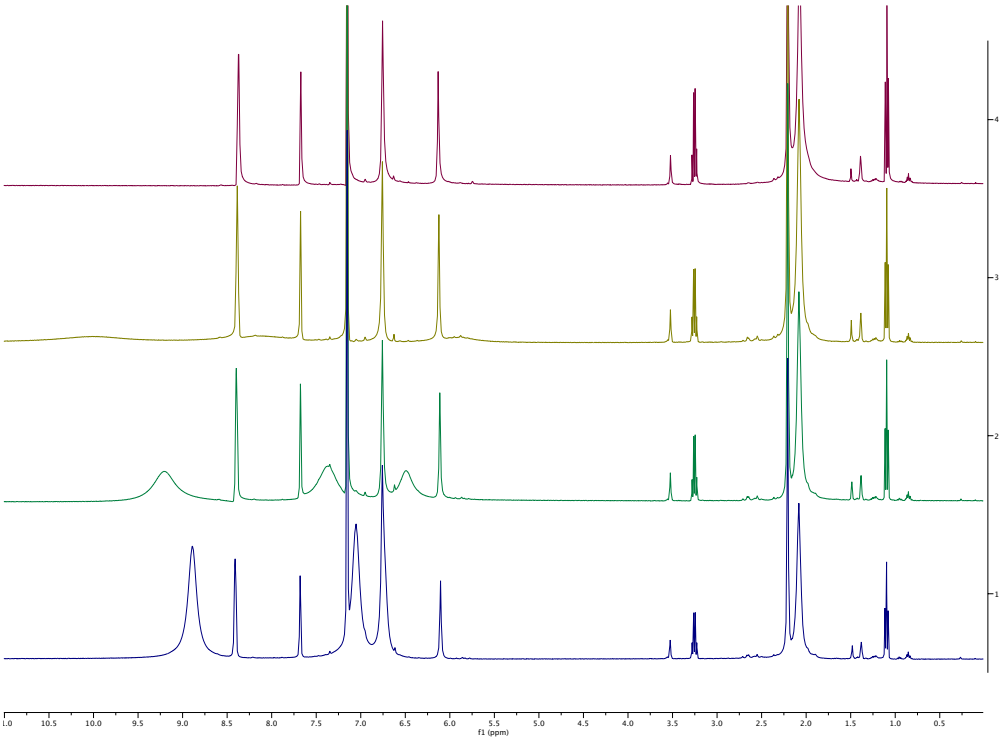

Figure S7.37: ^{1}H NMR spectrum of **[8]**$^{+}$ in C_6D_6/d^8-THF 15:1 at 293 K with 1, 5, 10 and 20 equiv. (top to bottom) of pyridine added

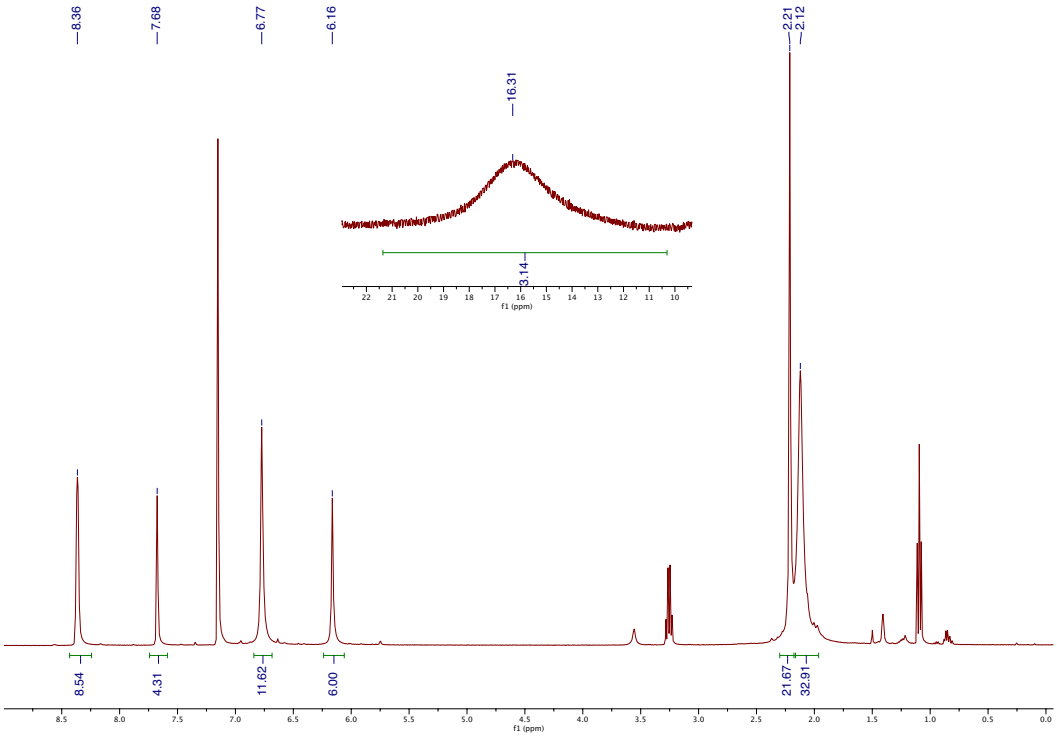

Figure S7.38: ^{1}H NMR spectrum of **[6]**$^{+}$ in C_6D_6/d^8-THF 15:1 at 293 K.

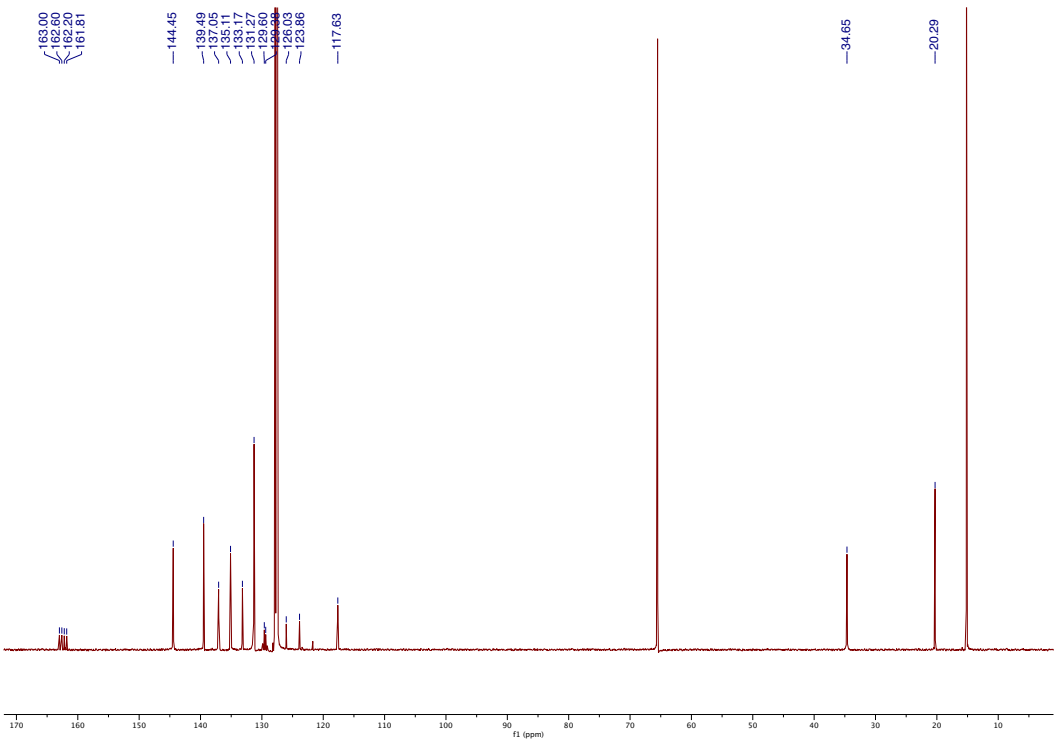

Figure S7.39: $^{13}C\{^{1}H\}$ NMR spectrum of **[6]**$^{+}$ in C_6D_6/THF 15:1 at 293 K.

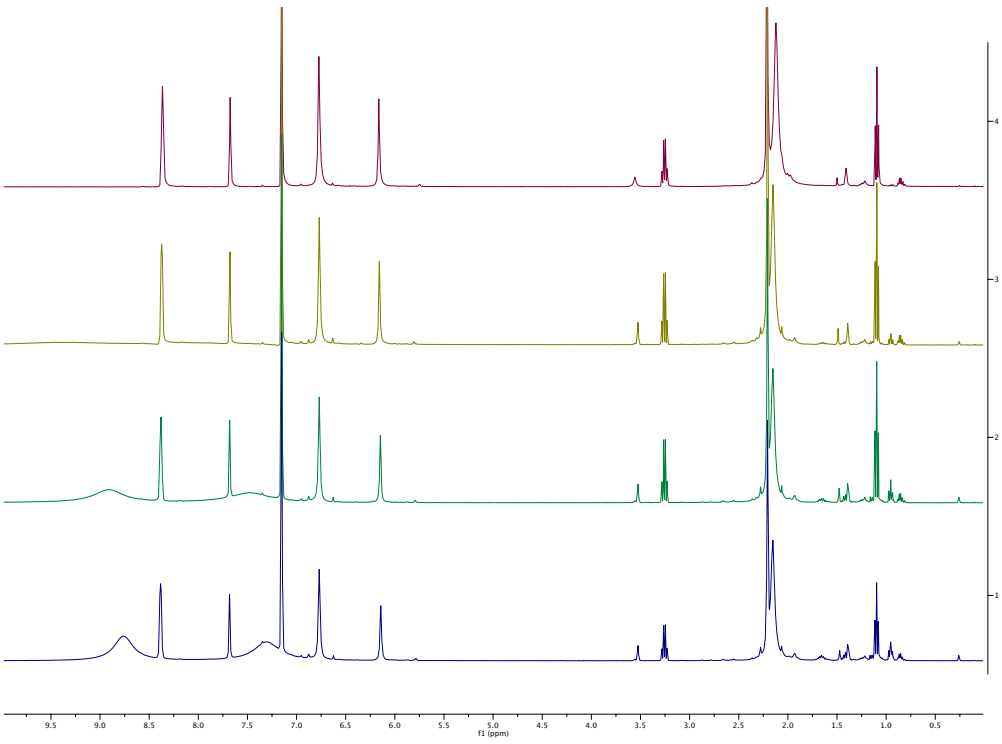

Figure S7.40: ^{1}H NMR spectrum of **[6]**$^{+}$ in C_6D_6/d^8-THF 15:1 at 293 K with 1, 5, 10 and 20 equiv. (top to bottom) of 4-CF_3-pyridine added.

Experimental details and NMR spectra for radical reactions

The products of the reaction between alkylated $[Fe_4S_4]^{2+}$ clusters and pyridines were analyzed by ^1H NMR spectroscopy and/or gas chromatography (GC). The GC was calibrated using standards of octane and hexadecane with concentrations between 0.04 and 0.8 mg/mL. An internal standard of HMDSO was added to each trial and a ^1H NMR spectrum was obtained prior to addition of the pyridine to ensure accurate integration of the starting material relative to HMDSO. All NMR spectra were recorded with long delays between scans (30 s) to ensure accurate integrations. Each reaction was performed in triplicate and the reported yields are the average across the three trials. Note that the ^1H NMR features corresponding to the cationic pyridine adducts shift due to fast exchange with excess pyridine (see Fig. S34).

Table S7.1. Summary of reactions between $[(IMes)_3Fe_4S_4R]^+$ clusters and pyridines in the presence or absence of a radical trap.

R	Base	Trap	R-R (%)	R-H (%)	R-D (%)	R-Sn (%)	Total (%)
Benzyl	DMAP	-	92(3)	4(3)	-	-	96(4)
	DMAP	Bu_3SnH	33(3)	34(3)	-	17(3)	84(5)
	DMAP	Bu_3SnD	54(3)	7(3)	13(3)	11(3)	85(6)
	CF_3py	Bu_3SnH	n.d.	55(3)	-	43(3)	98(4)
	quinuclidine	-	90(4)	8(3)	-	-	98(5)
Octyl	DMAP	Bu_3SnH	75(8)	n.d.	-	-	75(8)
	DMAP	Bu_3SnH	n.d.	56(6)	-	-	56(6)
	CF_3py	Bu_3SnH	n.d.	52(2)	-	-	52(2)
5-Hexenyl	DMAP	-	99(4) of which 28(2) is uncyclized		-	-	99(4)

1. **[2]**$^{+}$ + 20 equiv. DMAP

   The reactions were analyzed by ^{1}H NMR spectroscopy. The amount of bibenzyl was determined using the curve fitting program available in MNova.

2. **[2]**$^{+}$ + 20 equiv. DMAP + 20 equiv. Bu_3SnH

   The reactions were analyzed by ^{1}H NMR spectroscopy. The amounts of bibenzyl, toluene, and Bu_3SnBn were determined using the curve fitting program available in MNova.

3. **[2]**$^{+}$ + 20 equiv. DMAP + 20 equiv. Bu_3SnD

   The reactions were analyzed by ^{1}H NMR spectroscopy. The amounts of bibenzyl, toluene, d^{1}-toluene, and Bu_3SnBn were determined using the curve fitting program available in MNova.

4. **[2]**$^{+}$ + 20 equiv. CF_3-py + 20 equiv. Bu_3SnH

   The reactions were analyzed by ^{1}H NMR spectroscopy. The amounts of toluene and Bu_3SnBn were determined using the curve fitting program available in MNova.

5. **[2]**$^{+}$ + 20 equiv. quinuclidine

   The reactions were analyzed by ^{1}H NMR spectroscopy. The reaction mixture was passed through a plug of silica to remove iron-containing species and quinuclidine. The amounts of toluene and bibenzyl were determined using the curve fitting program available in MNova.

6. **[3]**$^{+}$ + 20 equiv. DMAP

   The reactions were analyzed first by ^{1}H NMR spectroscopy. The reaction mixture was then passed through a plug of silica to remove iron-containing species and the silica was washed with benzene to dilute the sample to a total volume of 5 mL. Product yields were determined by GC.

7. **[3]**$^{+}$ + 20 equiv. DMAP + 20 equiv. Bu_3SnH

   The reactions were analyzed first by ^{1}H NMR spectroscopy. The reaction mixture was then passed through a plug of silica to remove iron-containing species and the silica was washed with benzene to dilute the sample to a total volume of 5 mL. Product yields were determined by GC.

8. **[3]**$^{+}$ + 20 equiv. CF_3-py + 20 equiv. Bu_3SnH

   The reactions were analyzed first by ^{1}H NMR spectroscopy. The reaction mixture was passed through a plug of silica to remove iron-containing species and the silica was washed with benzene to dilute the sample to a total volume of 5 mL. Product yields were determined by GC.

9. **[5]**$^{+}$ + 20 equiv. DMAP

   The reactions were analyzed first by ^{1}H NMR spectroscopy. The reaction mixture was passed through a plug of silica to remove iron-containing species and a second NMR spectrum was obtained.

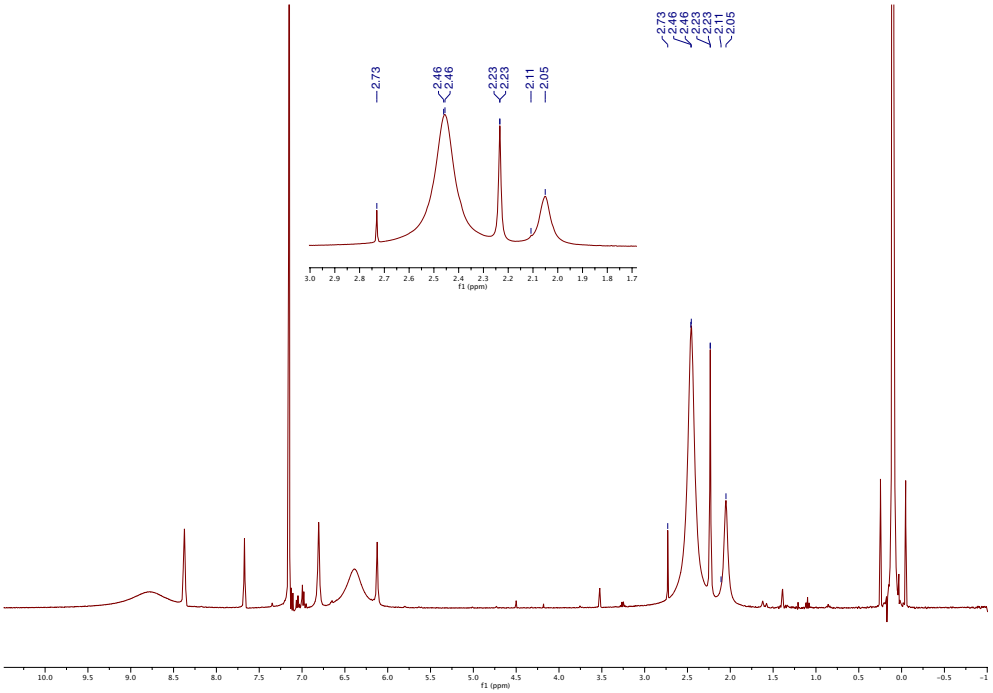

Figure S7.41: ^{1}H NMR spectrum of reaction 1: addition of DMAP to **[2]**$^{+}$. Inset shows toluene (2.11 ppm) and bibenzyl (2.73 ppm).

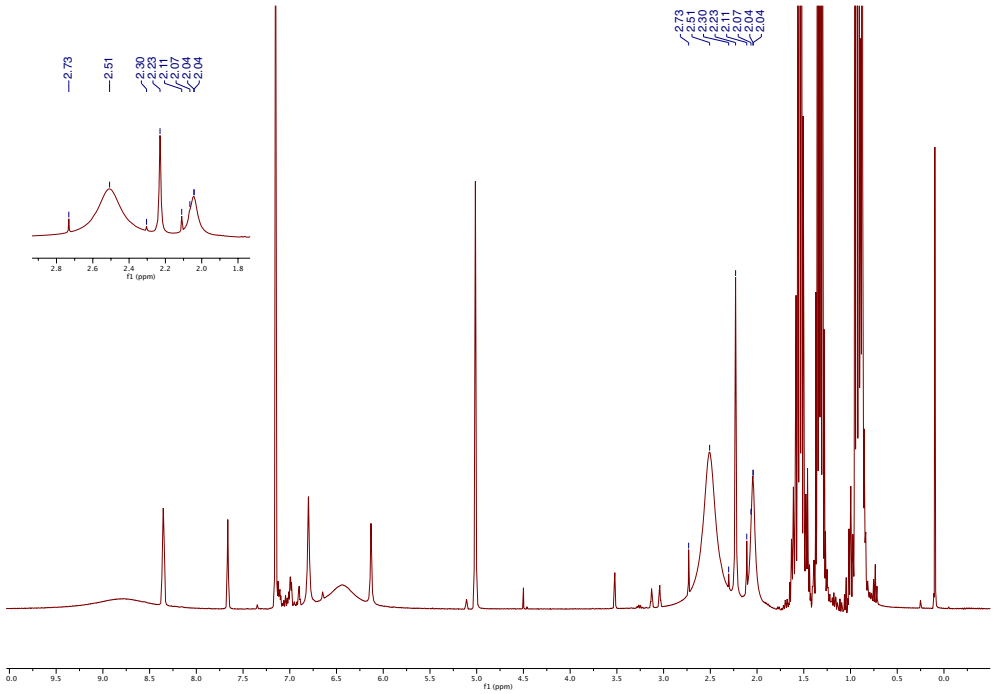

Figure S7.42: ^{1}H NMR spectrum of reaction 2: addition of DMAP to **[2]**$^{+}$ in the presence of Bu_3SnH. Inset shows toluene (2.11 ppm), Bu_3SnBn (2.30 ppm) and bibenzyl (2.74 ppm).

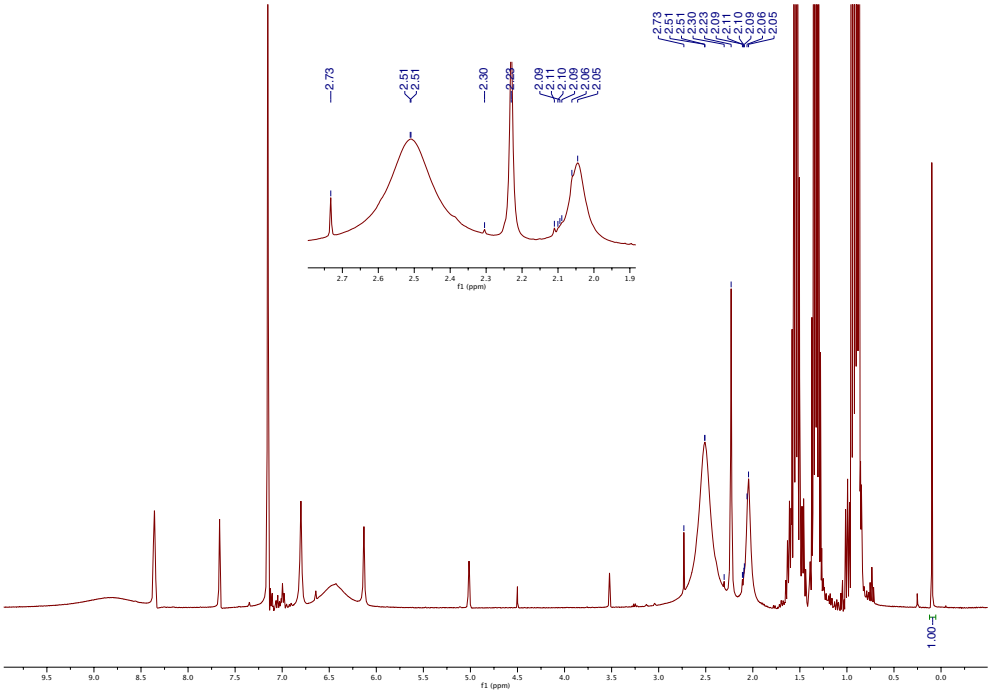

Figure S7.43: ^{1}H NMR spectrum of reaction 3: addition of DMAP to **[2]**$^{+}$ in the presence of Bu_3SnD. Inset shows toluene (2.11 ppm), d^{1}-toluene (2.09 ppm) Bu_3SnBn (2.30 ppm) and bibenzyl (2.74 ppm).

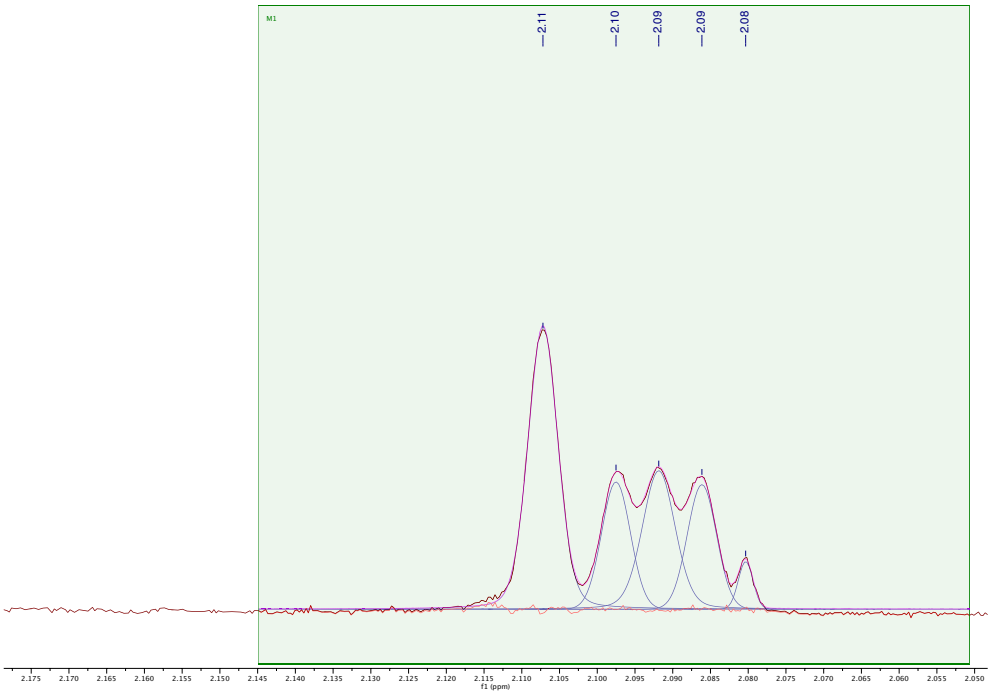

Figure S7.44: ^{1}H NMR spectrum of reaction 3 after vacuum transfer of the volatile material. Toluene (2.11 ppm) and d^{1}-toluene (1:1:1 triplet, 2.09 ppm) are visible. The peak at 2.08 ppm is a ^{13}C satellite peak from residual DMAP.

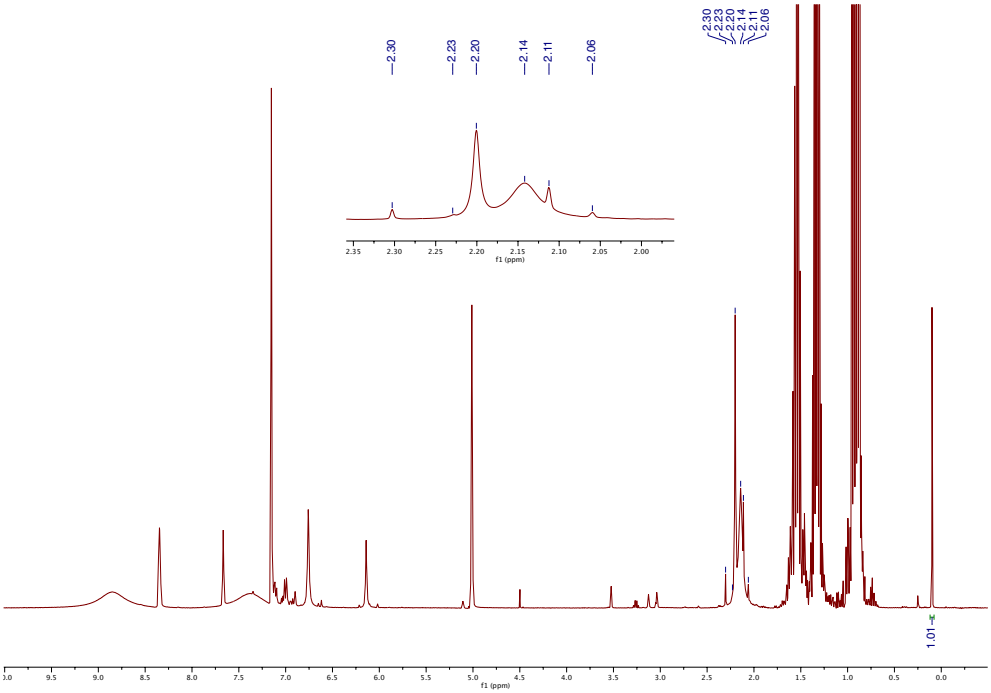

Figure S7.45: ^{1}H NMR spectrum of reaction 4: addition of 4-CF_3-py to **[2]**$^{+}$ in the presence of Bu_3SnH. Inset shows toluene (2.11 ppm).

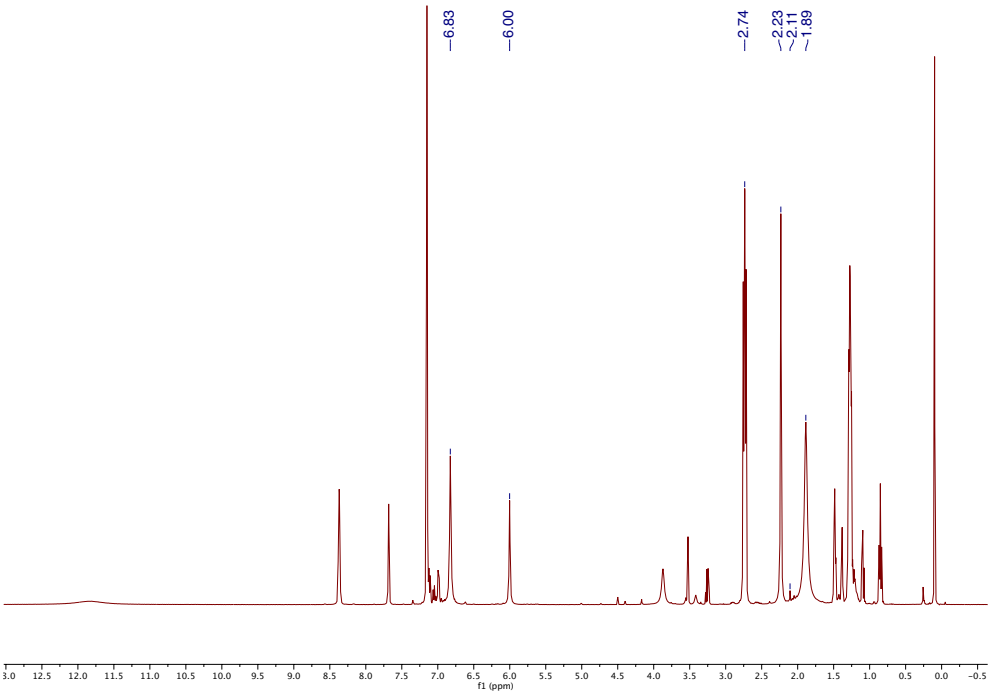

Figure S7.46: ^{1}H NMR spectrum of reaction 5: addition of quinuclidine to **[2]**$^{+}$. Resonances from excess quinuclidine overlap with those of bibenzyl (2.75 ppm).

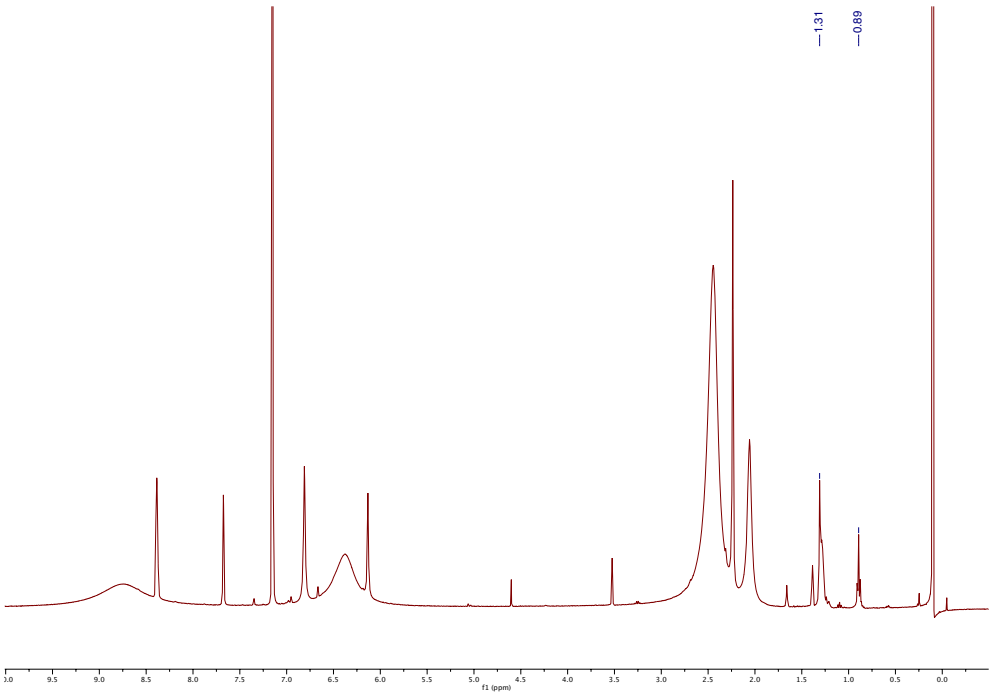

Figure S7.47: ^{1}H NMR spectrum of reaction 6: addition of DMAP to **[3]**$^{+}$. Hexadecane appears as overlapping peaks at 0.89 and 1.31 ppm.

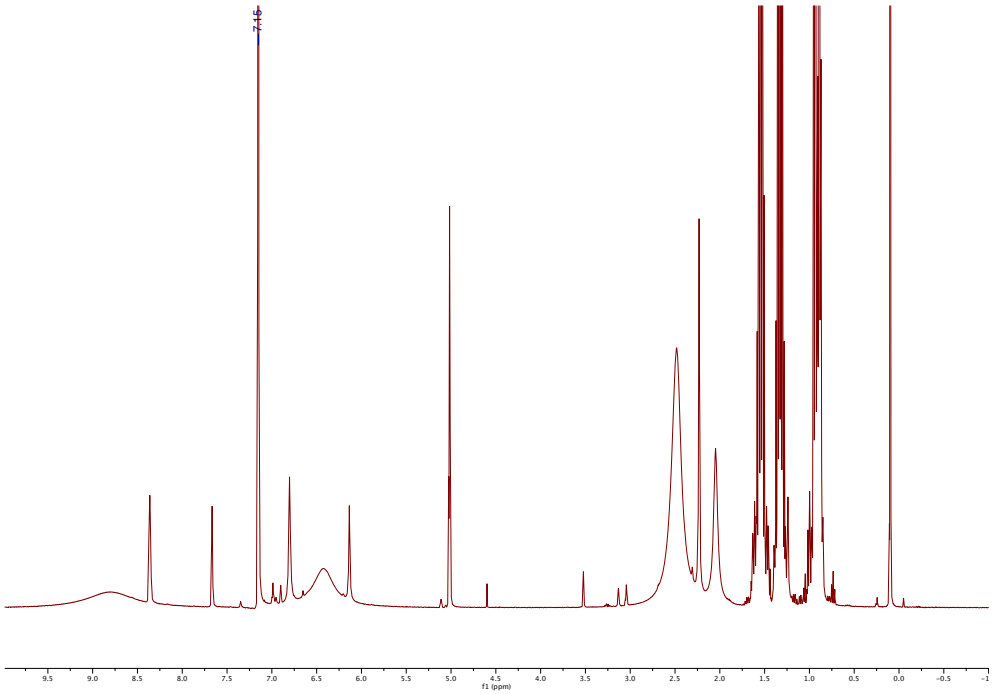

Figure S7.48: ^{1}H NMR spectrum of reaction 7: addition of DMAP to **[3]**$^{+}$ in the presence of Bu_3SnH. Hexadecane and octane are obscured by excess Bu_3SnH.

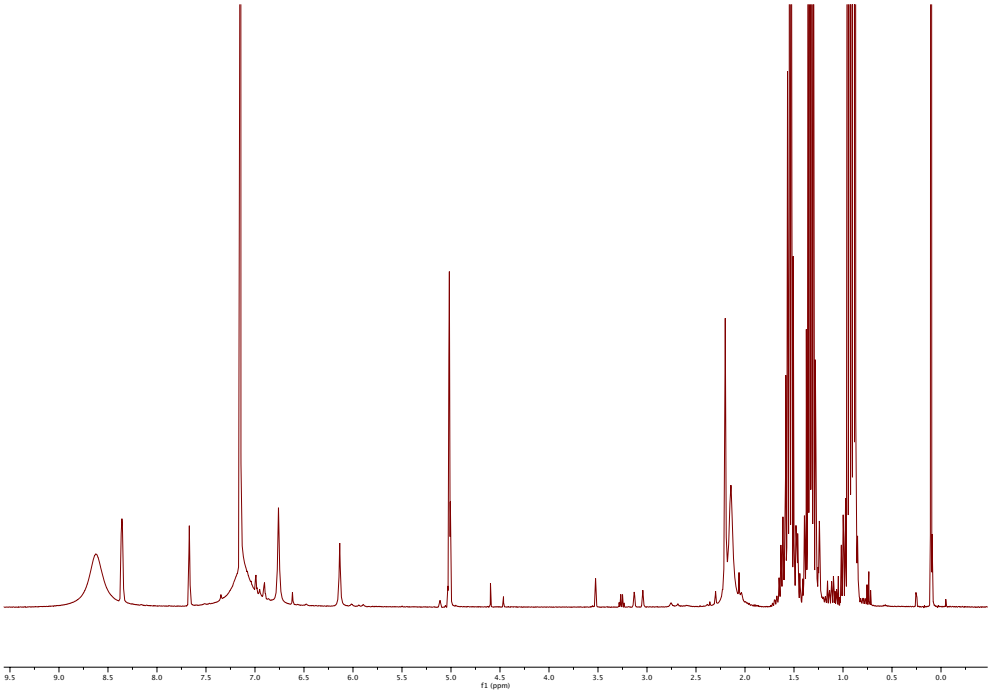

Figure S7.49: ^{1}H NMR spectrum of reaction 8: addition of 4-CF_3-py to **[3]**$^{+}$ in the presence of Bu_3SnH. Hexadecane and octane are obscured by excess Bu_3SnH.

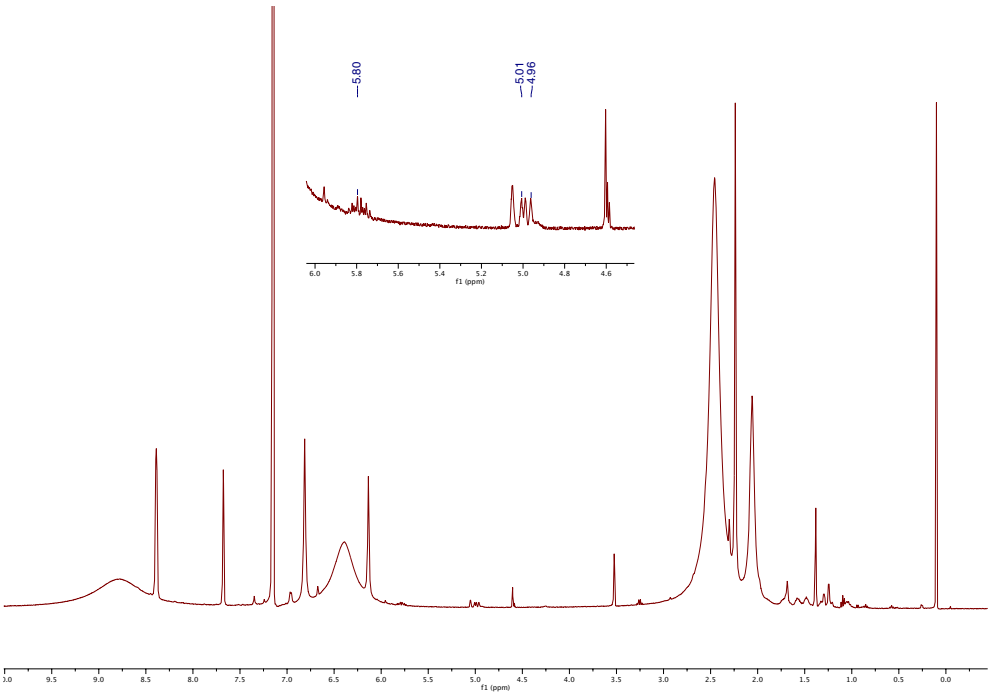

Figure S7.50: ^{1}H NMR spectrum of reaction 9: addition of DMAP to **[5]**$^{+}$. Inset shows the alkene resonances.

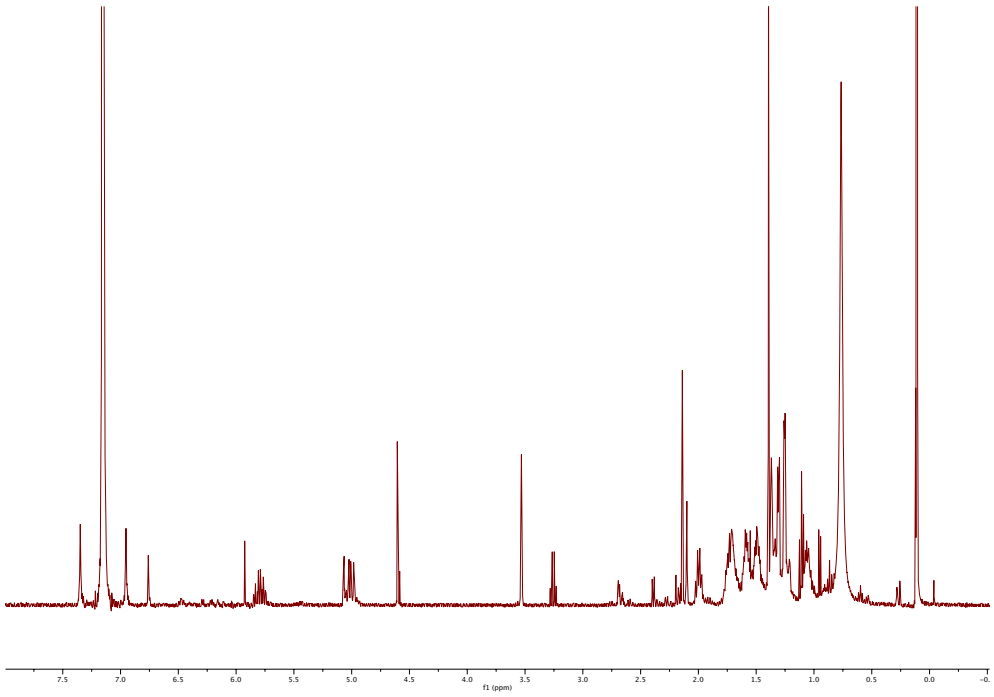

Figure S7.51: ^{1}H NMR spectrum of reaction 9 after running the reaction mixture through a plug of silica. Integration of the alkene resonances at 5.8 and 5.0 ppm relative to the alkyl region (1.9 through 0.9 ppm) and the internal standard gave the percentage of alkyl groups that still contained alkene resonances.

Discussion of the mechanism of the radical release reaction

The radicals generated by Fe–C bond homolysis from the pyridine-bound intermediate discussed in the main text (Scheme 7.2) can undergo subsequent reactions to generate C–C coupled organic fragments by several conceivable mechanisms:

A) Reaction with the starting material, **[2]**$^+$

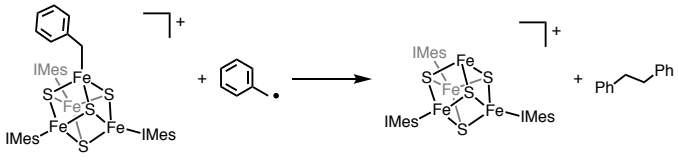

B) Reaction with the 5-coordinate intermediate

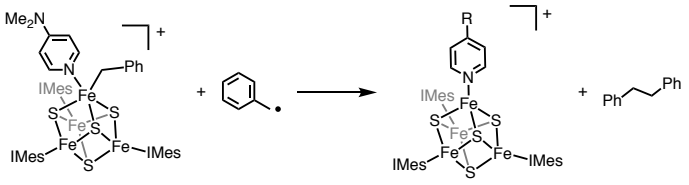

C) Free-radical coupling with a second free alkyl radical

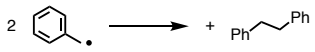

Reaction C is unlikely because free radicals are reactive and are expected to be present at a very low concentration, disfavoring direct second-order coupling. Additionally, only hexadecane was formed in the reaction of **[3]**$^+$ with DMAP; if reaction C was occurring we would expect to observe octane and octene (resulting from H-atom abstraction from one octyl radical by another) in addition to hexadecane.[7] Based on these observations, reaction C can be ruled out.

Between reactions A and B, we consider reaction A unlikely because it would entail generating a three-coordinate apical Fe site. For these reasons, reaction B most likely accounts for the formation of coupled organic products. Moreover, reaction B, but not A, is consistent with the following observations:

- The reaction of **[2]**$^+$ with DMAP occurs more cleanly for more donating pyridines. This is because there is a higher concentration of the 5-coordinate intermediate present when the pyridine is a stronger ligand, resulting in faster C–C coupling.
- With more donating pyridines (DMAP), C–C coupling occurs at a competitive rate to Sn–H abstraction. With a weakly donating pyridine (CF_3-py), Sn–H abstraction completely outcompetes C–C coupling. This is consistent with having a lower concentration of the 5-coordinate intermediate present with less donating pyridines, leading to slower C–C coupling. The rate of Sn–H activation is independent of the pyridine used.

For mechanism B, C–C coupling could occur by either an S_H2 mechanism or by oxidative addition and reductive elimination (see below). Experimentally differentiating between these possibilities is challenging.

1) S_H2 mechanism (concomitant Fe–C bond cleavage and C–C bond formation)

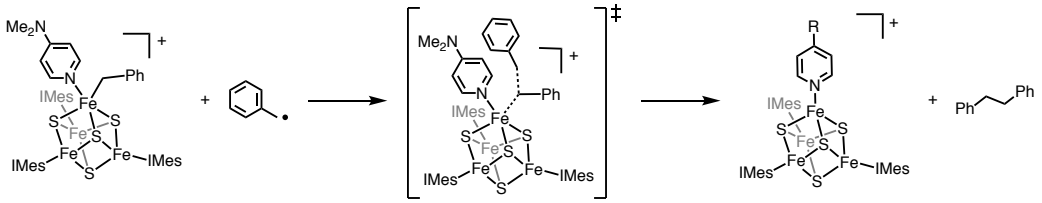

2) Oxidative addition/reductive elimination

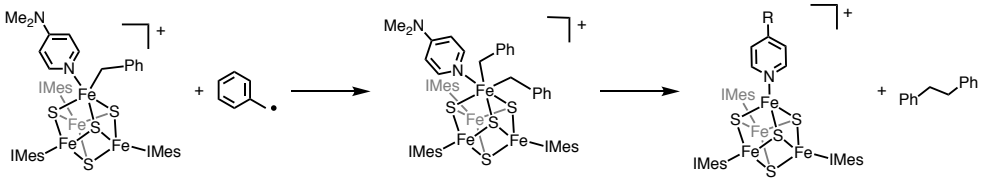

Finally, we note that additional, radical-derived products are observed in reactions involving Bu_3SnH. These include the expected H-atom abstraction product(s), and, in the case of **[2]**$^+$, Bu_3SnBn, which may form by:

i) Reaction of $Bu_3Sn\cdot$ or Bu_6Sn_2 with benzyl radicals

ii) Reaction of $Bu_3Sn\cdot$ or Bu_6Sn_2 with **[2]**$^+$ or the 5-coordinate intermediate

Reaction ii seems more likely than reaction i since benzyl radicals, $Bu_3Sn\cdot$, and Bu_6Sn_2 are all present at small concentrations in this reaction. However, further differentiation of these mechanisms is beyond the scope of this discussion.

Kinetic simulations

To simulate the reaction outcomes for our model system, we used MATLAB to symbolically solve the system of differential equations that describes the kinetic model in the presence and the absence of the organometallic intermediate.

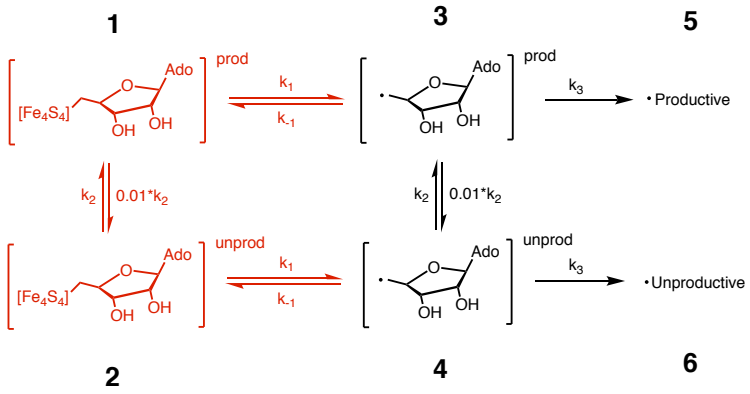

In the presence of the organometallic intermediate:

$$\frac{d[1]}{dt} = -k_1[1] + k_{-1}[3] - 0.01 * k_2[1] + k_2[2]$$

$$\frac{d[2]}{dt} = -k_1[2] + k_{-1}[4] + 0.01 * k_2[1] - k_2[2]$$

$$\frac{d[3]}{dt} = k_1[1] - k_{-1}[3] - 0.01 * k_2[3] + k_2[4] - k_3[3]$$

$$\frac{d[4]}{dt} = k_1[2] - k_{-1}[4] + 0.01 * k_2[3] + k_2[4] - k_3[4]$$

$$\frac{d[5]}{dt} = k_3[3]$$

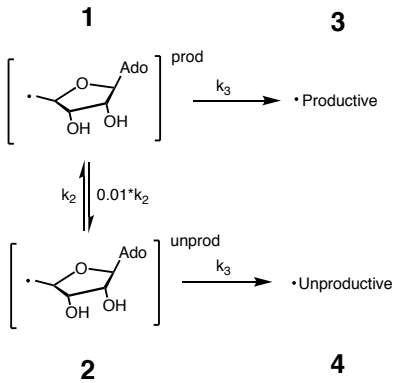

$$\frac{d[1]}{dt} = -0.01 * k_2[1] + k_2[2] - k_3[1]$$

$$\frac{d[2]}{dt} = 0.01 * k_2[1] - k_2[2] - k_3[2]$$

$$\frac{d[3]}{dt} = k_3[1]$$

$$\frac{d[4]}{dt} = k_3[2]$$

Carrying out these simulations requires assumptions for the rate constants k_1, k_{-1}, k_2, k_{-2}, and k_3. The initial choices for rate constants are outlined below:

k_{-1}: The reactions of open-shell metal fragments with organic radicals have been widely studied,[8,9] and the rate constant for recombination of the metal center with the organic radical consistently approaches the diffusion limit (10^{10} s^{-1}). This allows us to estimate that reformation of the Fe–C bond (k_{-1}) occurs at least as fast as the diffusion limit. As such, we set k_{-1} to 10^{11} s^{-1}; the absolute rate constant is unimportant in our simulations so long as this process is the fastest in the system.

k_1: The percentage of the 5′-dAdo• that is masked as an Fe–C bond is dictated by the equilibrium constant between Fe-bound and "free" 5′-dAdo•, which is equivalent to the bond dissociation free energy (BDFE) for the Fe–C bond. Estimating the BDFE from the half–life of the organometallic intermediate in pyruvate-formate lyase activating enzyme (~10^0 min at 170 K)[10] conflates the barrier to Fe–C homolysis and the barrier for X–H activation. Nevertheless, with the assumption that Fe–C bond homolysis is rate limiting (i.e., that the X–H activation barrier does not contribute to the observed half-life) and that the barrier for recombination is small, we approximate the BDFE as ~11 kcal/mol using the Eyring equation and $t_{1/2}$=ln(2)/k for a first-order reaction. A bond strength of ~11 kcal/mol corresponds to a

difference in forward and reverse rate constants on the order of 10^8, and we can therefore approximate $k_1 = 10^3\ s^{-1}$.

k_3: For the reasons outlined above, it is difficult to estimate the barrier for X–H activation from the available data. Consistent with the assumption that Fe–C bond homolysis is rate-limiting, we set the rate of H-atom abstraction ($k_3 = 10^5\ s^{-1}$) such that X–H activation is faster than Fe–C bond homolysis ($k_1 = 10^3\ s^{-1}$). We use the same rate of X–H activation in the "productive" and "unproductive" states; any difference in these rates will quantitatively change the selectivity of the reaction but not affect the qualitative conclusions of these simulations.

k_2 and k_{-2}: The dynamical processes that affect the selectivity in radical SAM enzymes could occur on a wide range of time scales, from 10^0 to $10^{15}\ s^{-1}$.[11,12] It is difficult to determine *a priori* which processes are important for X–H abstraction selectivity and therefore which time scales to consider. As such, we varied the rates of state interconversion in our simulations, initially with $k_2 = 10^2\ s^{-1}$ and $k_{-2} = 1\ s^{-1}$ (both being slower than X–H activation and Fe–C bond homolysis). In all simulations, we set $k_{-2} = 0.01 \cdot k_2$ such that the "productive" state is thermodynamically favored by ~2 kcal/mol and we allowed the system to convert between productive and unproductive states with either the organometallic species or the 5′-dAdo• present.

In addition to the figures discussed in the text, contour plots can be generated that explore the interdependence of the rate constants, in particular how the rates of state interconversion and X–H activation simultaneously contribute to product selectivity.

We began with Fe–C homolysis rates as defined above ($k_1 = 10^3\ s^{-1}$ and $k_{-1} = 10^{11}\ s^{-1}$). Each trace (Fig. S7.52) is drawn as a 50/50 selectivity contour with the region above and to the left of the trace corresponding to the region of selectivity for the productive reaction and the region below and to the right of the trace corresponding to the region of selectivity

for the unproductive reaction. The black line shows the selectivity in the absence of the organometallic intermediate.

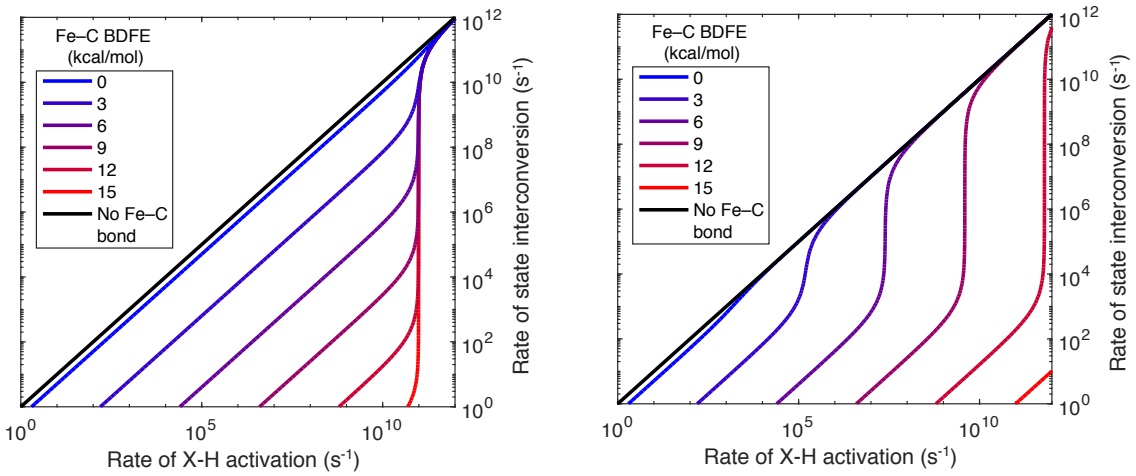

Figure S7.52: Contour plots for the kinetic model showing the interdependence of the modelled rate constants. On the left k_1 was varied ($k_{-1} = 10^{11}$ s^{-1}) and on the right k_{-1} was varied ($k_1 = 10^3$ s^{-1}) to give the desired bond strength. Contours were drawn at 50% selectivity. The black lines show the 50% selectivity level in the absence of the organometallic species.

The region between each trace and the black line is the range of kinetic parameters for which the presence of the organometallic intermediate is expected to increase selectivity.

From these plots we can see that a stronger Fe–C bond leads to a larger range of kinetic parameters for which high selectivity can be achieved. In Figure S7.51 (left), the selectivity contours in the presence of the organometallic intermediate depart from the black line at the point where the Fe–C bond reformation is faster than X–H activation. This emphasizes that the low barrier to Fe–C bond reformation following homolysis is critical for allowing the organometallic intermediate to function as a protective mechanism during catalysis.

Matlab script for solving the system of differential equations and plotting figures 7.4E, 7.4F and S7.51

1. Solve differential eq, with organometallic intermediate

```
clear

GC=1.987e-3; %gas constant

%Defining system of equations and solving it symbolically
syms a(t) b(t) c(t) d(t) e(t) f(t) m n o k p
cond=[a(0)==0,b(0)==0,c(0)==0,d(0)==1,e(0)==0,f(0)==0];
eqns= [diff(a,t)== -(m*a - k*c) - (p*n*a - n*b),...
    diff(b,t)== -(m*b - k*d) + (p*n*a - n*b),...
    diff(c,t)== (m*a - k*c) - o*c - (p*n*c -n*d),...
    diff(d,t)== (m*b - k*d) - o*d + (p*n*c - n*d),...
    diff(e,t)== o*c,...
    diff(f,t)== o*d];
sol=dsolve(eqns,cond);
% saves functions so they can be called later
a=matlabFunction(sol.a);
b=matlabFunction(sol.b);
c=matlabFunction(sol.c);
d=matlabFunction(sol.d);
e=matlabFunction(sol.e);
f=matlabFunction(sol.f);

% a is organometallic in productive state
% b is organometallic in unproductive state
% c is 5'-dAdo in productive state
% d is 5'-dAdo in unproductive state
% e is productive product
% f is unproductive product

% m is homolysis rate (k1)
% n is unproductive to productive conversion rate (k2)
% o is abstraction rate (k3)
% k is Fe-C bond formation rate (k-1)
% p is productive to unproductive conversion rate divided by k2 (k-2/k2)
```

---

2. Plot 1D traces for varying the interconversion rate (4E)

```
%sets figure up
FigHandle = figure;
set(FigHandle,'Position', [1000, 1000, 240, 200]);
box on

%sets range and points for x-values
range=30;
increment=0.1;
offset=-10;
loopsize=range/increment;
points=zeros(loopsize,5);

%loops over different values of Fe-C bond strength
for r=0:4:12
    BDFE=r; %each value of Fe-C BDFE
    s=r/4+1; %indexing values
    BDFEf(s,1)=BDFE; %saving BDFEs
```

```
        Keq=exp(-BDFE/(GC*298)); %converting from BDFE to equilibrium
                 constant (k1/k-1=keq)

        k=1*10.^11; %value for k-1
        m=k*Keq; %getting homolysis rate from equilibrium constant
(keq*k-                  1=k1)
        mx(s,1)=m; %saving values of homolysis rate

        o=1*10^5; %value for k3
        p=0.01; % energy difference between productive and unproductive
                 state
        t=1e100000000; %evaluates solution at steady state

        %evaluates equation for each value of interconversion rate
        for i=1:loopsize
            j=(i*increment)+offset; %generates values for state
                     interconversion rate
            n=1*10^j; %varying the rate of state interconversion
            points(i,1)=n; %saving rates of interconversion
            subrad=e(k,m,n,o,p,t); %solving diff eq for each set of
                     parameters, for productive product
            v=s+1; %creating an index for each point
            points(i,v)=subrad*100; %converting to percent and saving
        end

        semilogx(points(:,1),points(:,v),'-',
                 'MarkerSize',0.25,'linewidth',0.5,'color',[(r+2)/15 0
0]);
        hold on
    end

    %sets plot parameters
    axis([10^-10 10^15 0 100]);
    h=gca;
    h.FontSize=6;
    xlabel('rate of state interconversion (s-1)')
    ylabel('Percentage productive radical')
```

---

3. Plot 1D traces for varying the abstraction rate (4F)

```
    %sets figure up
    FigHandle = figure;
    set(FigHandle,'Position', [1000, 1000, 240,200]);
    box on

    %sets range and points for x-values
    range=30;
    increment=0.1;
    offset=-10;
    loopsize=range/increment;
    points=zeros(loopsize,2);

    %loops over different values of Fe-C bond strength
    for r=0:4:12
        BDFE=r; %each value of Fe-C BDFE
        s=r/4+1; %indexing to save values
        BDFEf(s,1)=BDFE; %saving BDFEs
```

```
            Keq=exp(-BDFE/(GC*298)); %converting back from BDFE to
equilibrium                    constant (k1/k-1=keq)

            k=1*10.^11; %value for k-1
            m=k*Keq; %getting homolysis rate from equilibrium constant
              (keq*k-1=k1)
            mx(s,1)=m; %saving values of homolysis rate

            n=1*10^2; %setting rate of state interconversion
            p=0.01; % energy difference between productive and unproductive
                    state
            t=1e100000000; %timeline for simulation

            %evaluates equation for each value of interconversion rate
            for i=1:loopsize %indexing
                j=(i*increment)+offset; %generates values for C-H activation
                          rate
                o=1*10^j; %varying rate of C-H activation
                points(i,1)=o; %saving values for rate of C-H activation
                subrad=e(k,m,n,o,p,t); %solving diff eq for each set of
                          parameters, for productive product
                v=s+1; %creating an index for each point
                points(i,v)=subrad*100; %converting to percent and saving
            end
            semilogx(points(:,1),points(:,v),'-',
                    'MarkerSize',0.25,'linewidth',0.5,'color',[(r+2)/15 0
0]);
            hold on
        end

        %plot parameters
        box on
        h=gca;
        h.FontSize=6;
        axis([10^-10 10^15 0 100]);
        xlabel('rate of C-H activation (s-1)')
        ylabel('Percentage productive radical')
```

---

4. Plot first contour plot (S51 left)

```
        %sets figure parameters
        FigHandle = figure;
        set(FigHandle,'Position', [1000, 1000, 360, 300]);
        box off

        %Sets range of parameters to look over
        for r=0:3:15
            % generating values for parameters
            r=15-r;
            s=(r/3)+1;
            v=0:0.1:12;

            %Generates a matrix of points with spacing and range defined by v
            [X,Y]=meshgrid(v);

            %stores BDFE and converts to Keq
            BDFE=r;
            BDFEf(s,1)=BDFE;
            Keq=exp(-BDFE/(GC*298));
```

```
        %model parameters, generates m from Keq
        k=1*10.^11;
        m=k*Keq;
        n=1*10.^Y;
        o=1*10.^X;
        t=1e100000;
        p=0.01;

        %evaluates differential equation
        subrad=e(k,m,n,o,p,t);
        hold on
        %plots only the 50% selectivity contour
        contour(o,n,subrad,[0.5 0.5],'color',[r/15 0 1-
                r/15],'linewidth',1.5);
    end

    %defines plot parameters
    ax=gca;
    set(ax,'xscale','log','yscale','log','YAxisLocation','right');
    box on
    ax.FontSize=12;

    %plots the line corresponding to no organometallic intermediate
    nofecx=0:0.1:13;
    nofecx=1.*10.^nofecx;
    nofecy=nofecx;
    axis([10^0 10^12 10^0 10^12]);
    plot(nofecx,nofecy,'color',[0 0 0],'linewidth',1.5);

    xlabel('Rate of X-H activation (s-1)')
    ylabel('Rate of state interconversion (s-1)')
    legend('0','3','6','9','12','15','No Fe-C
                bond','location','northwest');
```

---

5. Plot second contour plot (S51 right)

```
    FigHandle = figure;
    set(FigHandle,'Position', [1000, 1000, 360, 300]);
    box off

    %Sets range of parameters to look over
    for r=0:3:15

        % generating values for parameters
        s=r/3+1;
        v=0:0.1:12;

        %Generates a matrix of points with spacing and range defined by v
        [X,Y]=meshgrid(v);

        %stores BDFE and converts to Keq
        BDFE=r;
        BDFEr(s,1)=BDFE;
        Keq=exp(-BDFE/(GC*298));

        %model parameters, generates k from Keq
        m=1*10.^3;
        k=m/Keq;
        kr(s,1)=k;
```

```
        n=1*10.^Y;
        o=1*10.^X;
        t=1e1000;
        p=0.01;

        %evaluates differential equation
        subrad=e(k,m,n,o,p,t);
        hold on

        %plots only the 50% selectivity contour
        contour(o,n,subrad,[0.5,0.5],'color',[r/15 0 1-
                r/15],'linewidth',1.5);
    end

    %plots the line corresponding to no organometallic intermediate
    nofecx=0:0.1:12;
    nofecx=1.*10.^nofecx;
    nofecy=nofecx;
    plot(nofecx,nofecy,'color',[0 0 0],'linewidth',1.5);

    %defines plot parameters
    box on
    axis([10^0 10^12 10^0 10^12]);
    h=(gca);
    h.FontSize=12;
    set(h,'xscale','log','yscale','log','YAxisLocation','right');
    xlabel('Rate of X-H activation (s-1)')
    ylabel('Rate of state interconversion (s-1)')
    legend('0','3','6','9','12','15','No Fe-C
                bond','location','northwest');
```

---

6. Solve differential eq, without organometallic intermediate

```
    clear

    %Defining system of equations and solving it symbolically
    syms  c(t) d(t) e(t) f(t) n o p
    cond=[c(0)==0,d(0)==1,e(0)==0,f(0)==0];
    eqns= [diff(c,t)== - o*c - (p*n*c -n*d),...
        diff(d,t)== - o*d + (p*n*c - n*d),...
        diff(e,t)== o*c,...
        diff(f,t)== o*d];
    % saves functions so they can be called later
    sol=dsolve(eqns,cond);
    c=matlabFunction(sol.c);
    d=matlabFunction(sol.d);
    e=matlabFunction(sol.e);
    f=matlabFunction(sol.f);

    % c is 5'-dado in productive state
    % d is 5'-dado in unproductive state
    % e is productive product
    % f is unproductive product

    % n is unproductive to productive conversion rate (k2)
    % o is abstraction rate (k3)
    % p is productive to unproductive conversion rate divided by k2
    (k-2/k2)
```

---

7. Plot 1D traces for varying the interconversion rate

```
%sets range and points for x-values
range=20;
increment=0.1;
offset=-9;
loopsize=range/increment;
points=zeros(loopsize,3);

%evaluates equation for each value of interconversion rate
for i=1:loopsize
  j=(i*increment)+offset; %index values of n

  n=1*10^j; %varying the rate of state interconversion
  o=1*10^5; %set the abstraction rate
  p=0.01; %energy difference between productive and unproductive
  state
  points(i,1)=n; %saves the values of n

  t=1e1000; %evaluates solution at steady state

  subrad=e(n,o,p,t);%solves for productive product
  points(i,2)=subrad*100; %saves percent productive radical
 end

semilogx(points(:,1),points(:,2),'-
  ','color','black','linewidth',0.5);
%plots on same plot as other script
axis([10^-10 10^15 0 100])
hold on
```

---

8. Plot 1D traces for varying the X–H abstraction rate

```
%sets range and points for x-values
range=20;
increment=0.1;
offset=-9;
loopsize=range/increment;
points=zeros(loopsize,3);

%evaluates equation for each value of abstraction rate
for i=1:loopsize %index
j=(i*increment)+offset; %indexes values for o

n=1*10^2; %sets state interconversion rate
o=1*10^j; %varies abstraction rate
points(i,1)=o; %saves values of abstraction rate

t=1e1000; %evaluates solution at steady state

subrad=e(n,o,t); %evaluates diff eq for each value
points(i,2)=subrad*100; %saves percent productive radical
end
semilogx(points(:,1),points(:,2),'-
  ','color','black','linewidth',0.5); %plots on same plot as other
  script
axis([10^-10 10^15 0 100])
hold on
```

EPR Spectra

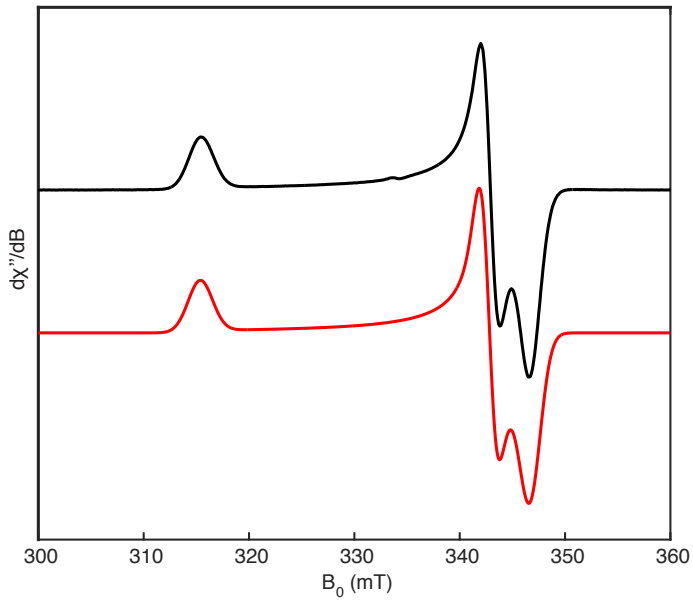

Figure S7.53: X-Band CW EPR spectrum of **2** (1 mM) in toluene at 15 K (black) and simulation (red). Microwave power: 16 µW, microwave frequency: 9.370 GHz. Simulation parameters: *g* = [2.123 1.953 1.931], *g*-strain = [0.017 0.008 0.012].

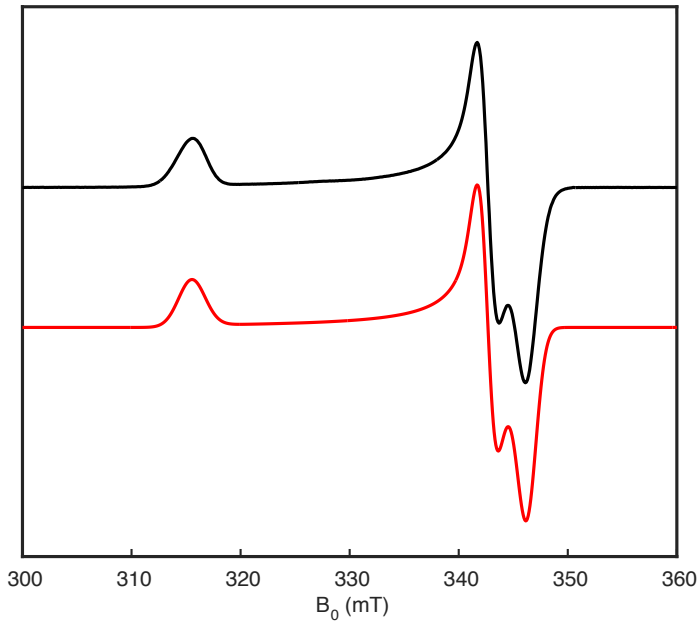

Figure S7.54: X-Band CW EPR spectrum of **3** (1 mM) in toluene at 15 K (black) and simulation (red). Microwave power: 16 µW, microwave frequency: 9.370 GHz. Simulation parameters: *g* = [2.122 1.954 1.934], *g*-strain = [0.018 0.008 0.010].

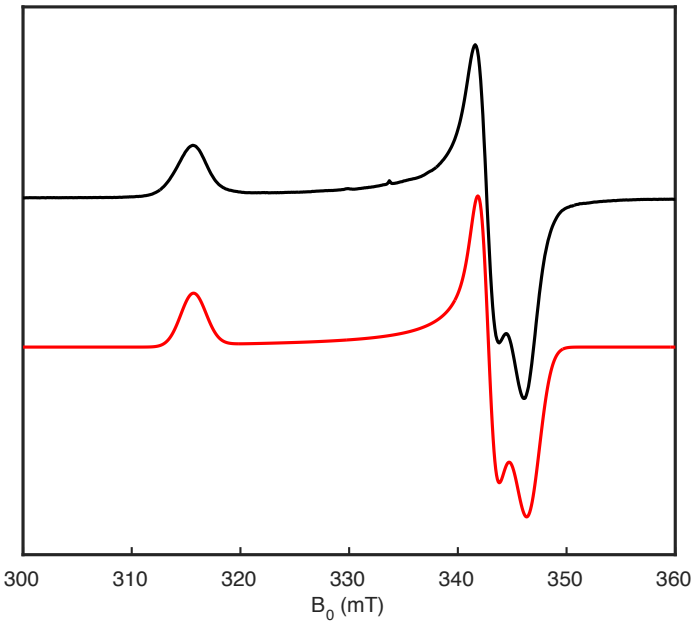

Figure S7.55: X-Band CW EPR spectrum of **5** (1 mM) in toluene at 15 K (black) and simulation (red). Microwave power: 16 µW, microwave frequency: 9.369 GHz. Simulation parameters: *g* = [2.121 1.953 1.932], *g*-strain = [0.017 0.008 0.013].

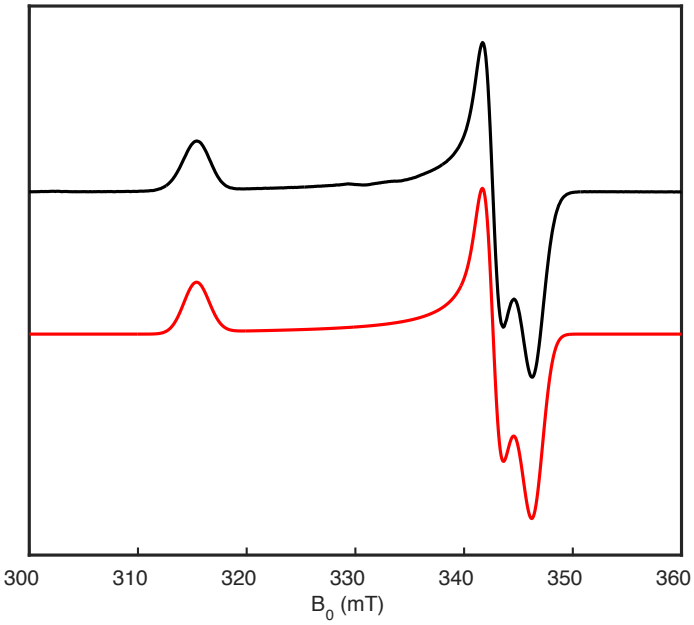

Figure S7.56: X-Band CW EPR spectrum of **7** (1 mM) in toluene at 15 K (black) and simulation (red). Microwave power: 16 µW, microwave frequency: 9.371 GHz. Simulation parameters: *g* = [2.123 1.954 1.933], *g*-strain = [0.017 0.008 0.011].

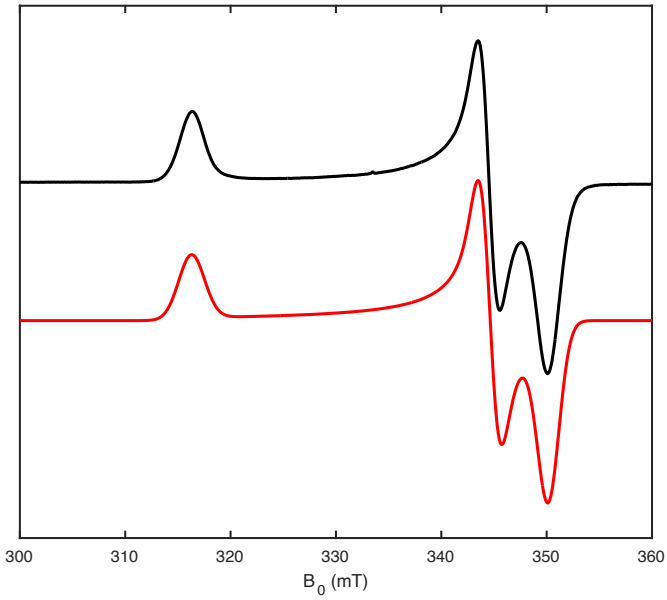

Figure S7.57: X-Band CW EPR spectrum of **[4]**$^{+}$ (1 mM) in 10:1 toluene:THF at 15 K (black) and simulation (red). Microwave power: 63 µW, microwave frequency: 9.369 GHz. Simulation parameters: *g* = [2.117 1.943 1.912], *g*-strain = [0.018 0.010 0.012].

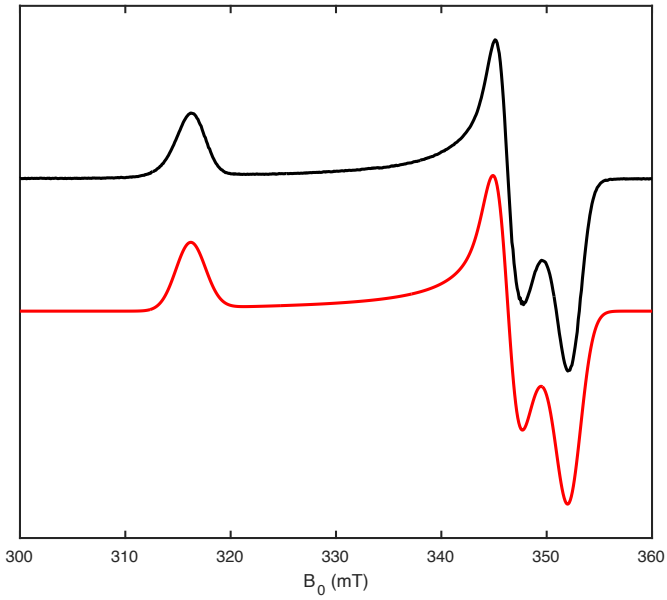

Figure S7.58: X-Band CW EPR spectrum of **[6]**$^{+}$ (1 mM) in 10:1 toluene:THF at 15 K (black) and simulation (red). Microwave power: 16 µW, microwave frequency: 9.368 GHz. Simulation parameters: *g* = [2.117 1.933 1.901], *g*-strain = [0.021 0.013 0.014].

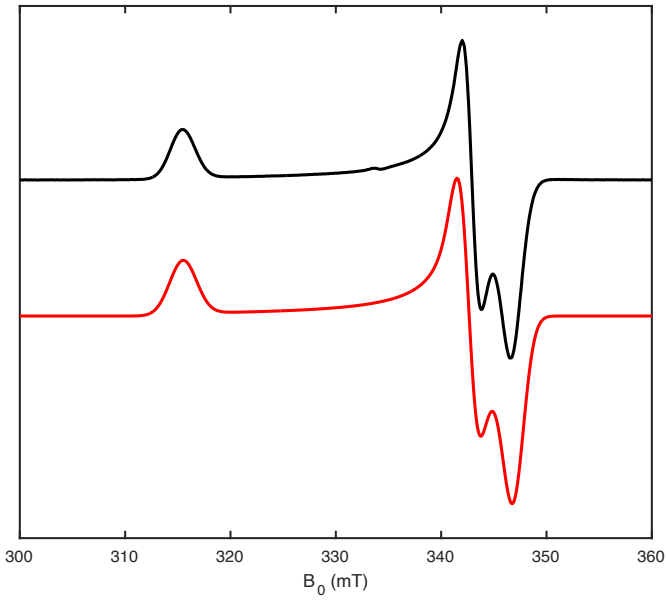

Figure S7.59: X-Band CW EPR spectrum of **[8]**$^{+}$ (1 mM) in 10:1 toluene:THF at 15 K (black) and simulation (red). Microwave power: 16 µW, microwave frequency: 9.370 GHz. Simulation parameters: g = [2.122 1.954 1.930], g-strain = [0.019 0.01 0.012].

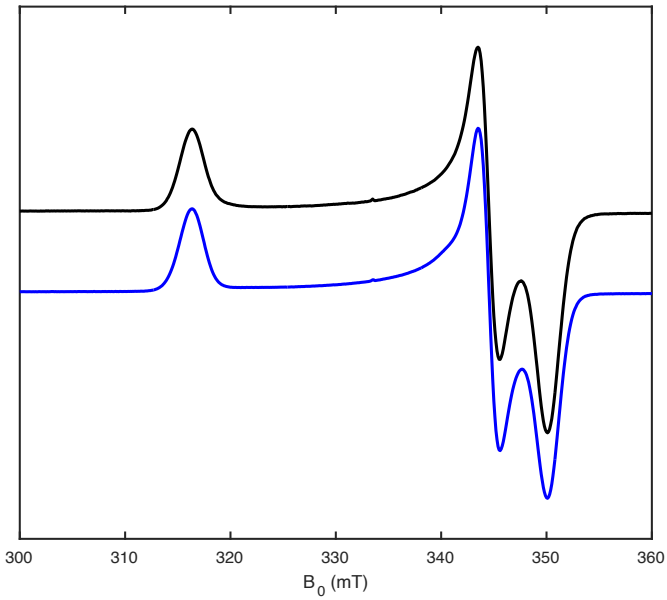

Figure S7.60: Overlaid X-Band CW EPR spectrum of **[4]**$^{+}$ (1 mM) (black) and the product of the reaction between **[2]**$^{+}$ and DMAP (blue) in 10:1 toluene:THF at 15 K (black). Microwave power: 16 µW, microwave frequency: 9.369 GHz.

IR spectra

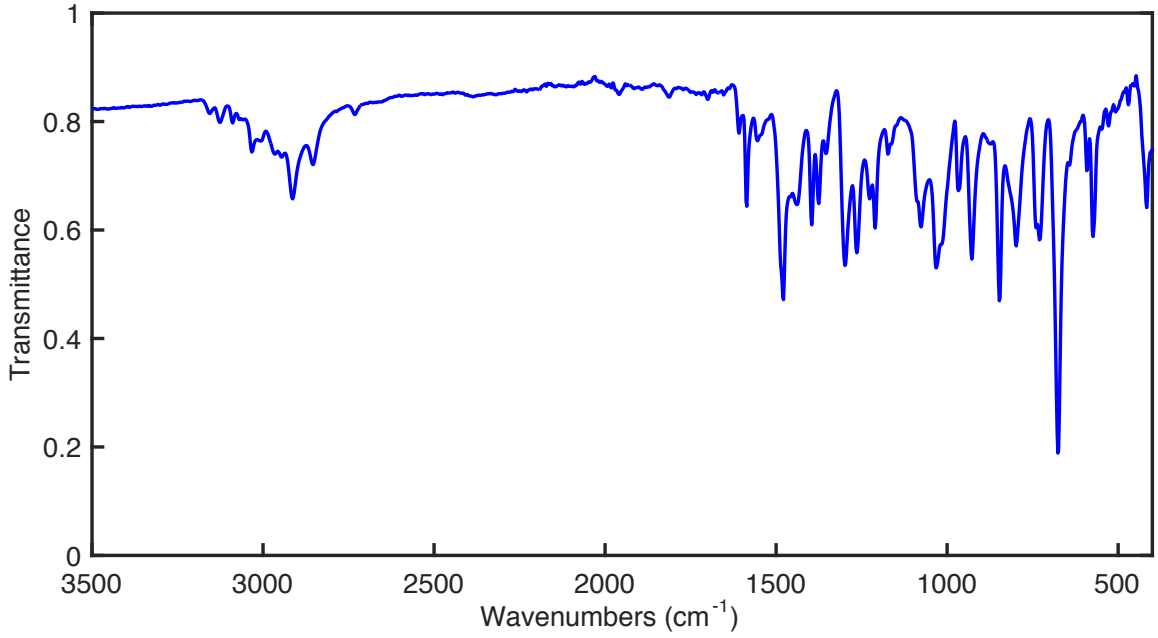

Figure S7.61: IR spectrum of **2**

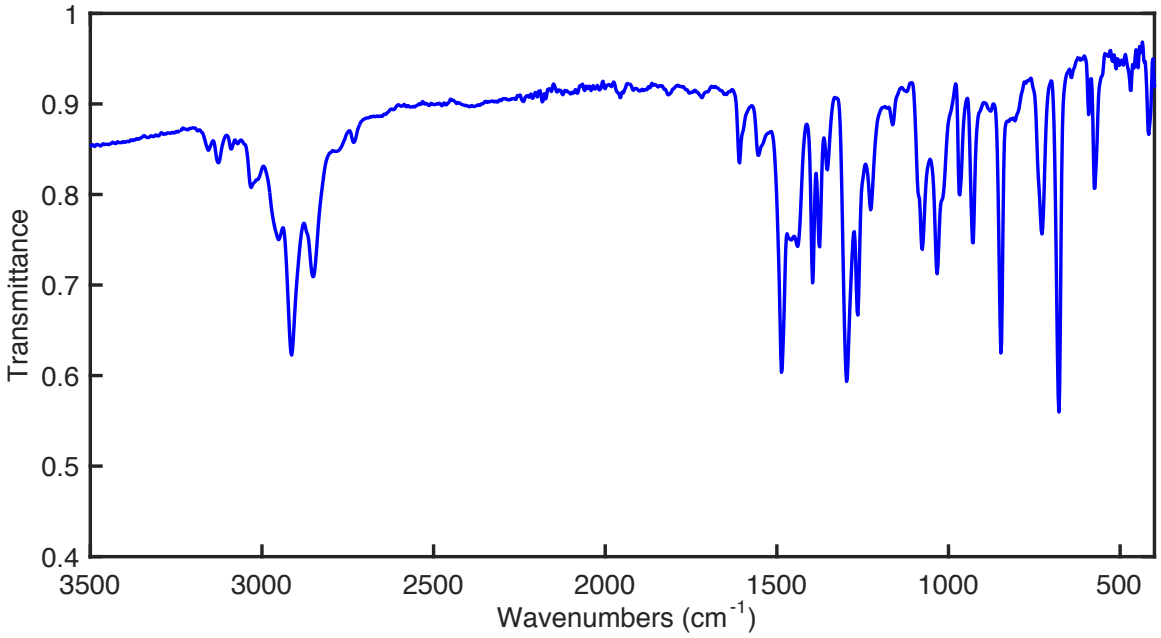

Figure S7.62: IR spectrum of **3**

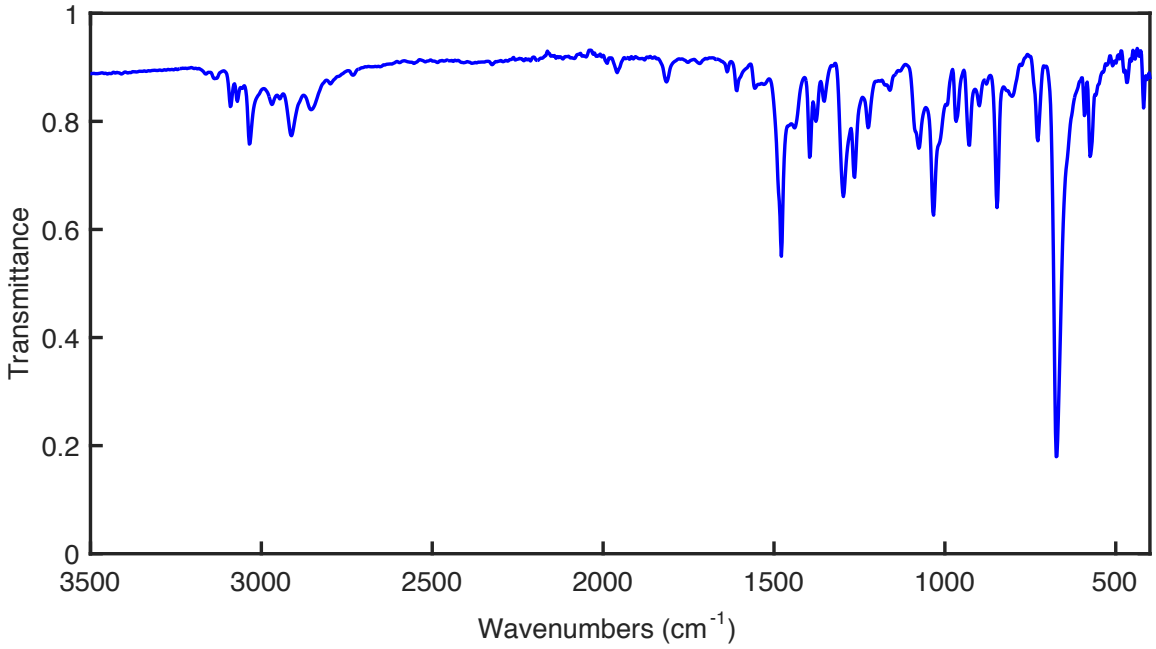

Figure S7.63: IR spectrum of **5**

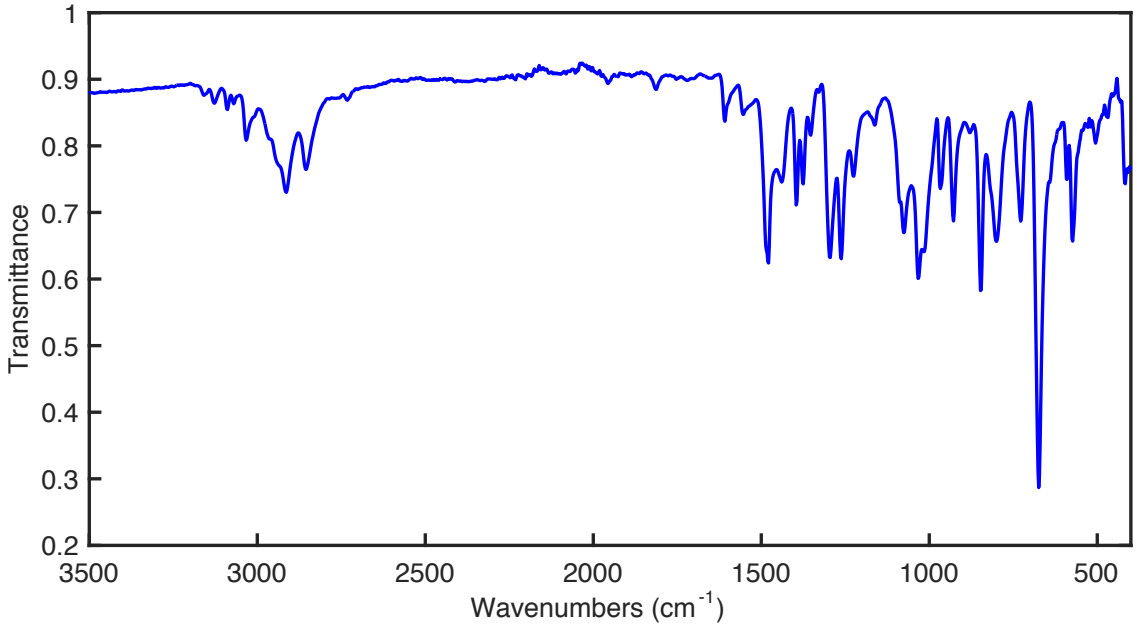

Figure S7.64: IR spectrum of **6**

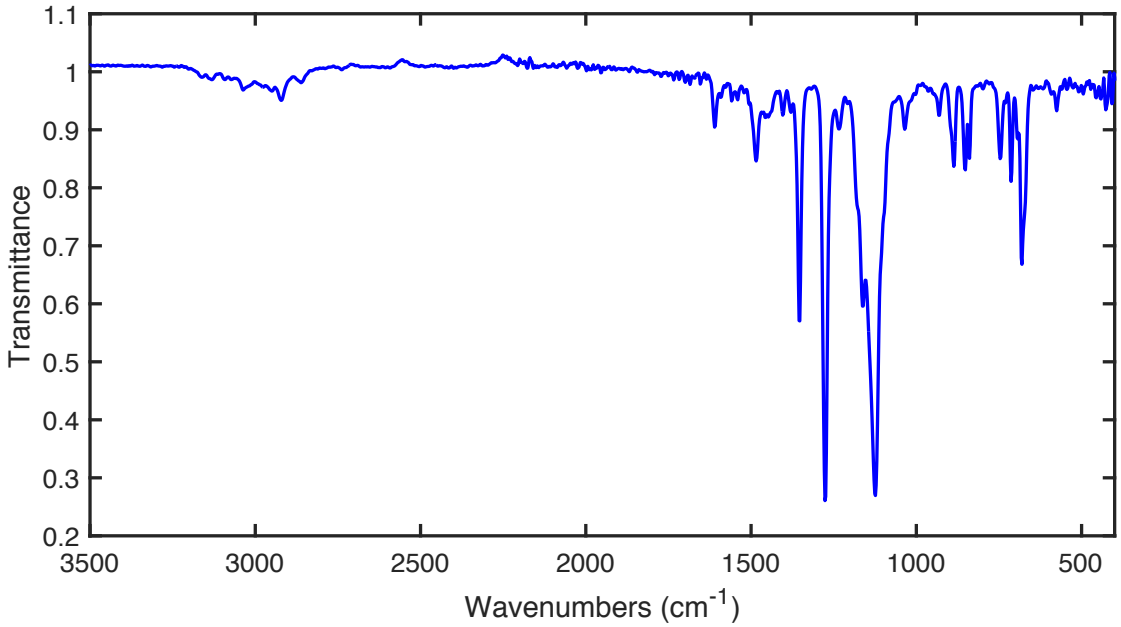

Figure S7.65: IR spectrum of **[2]**$^{+}$.

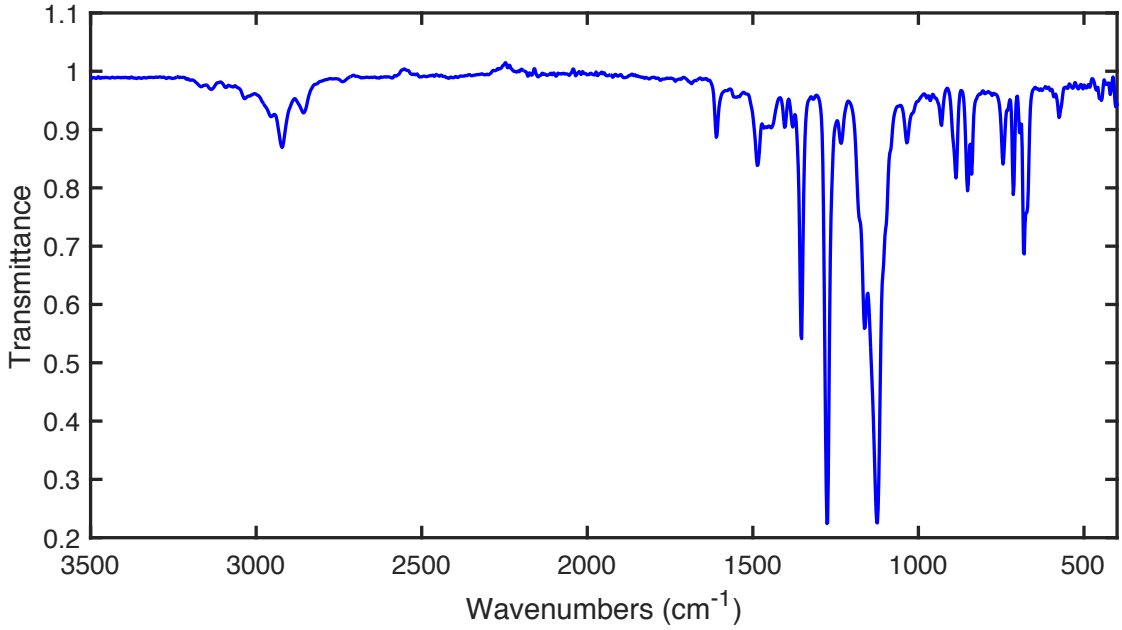

Figure S7.66: IR spectrum of **[3]**$^{+}$.

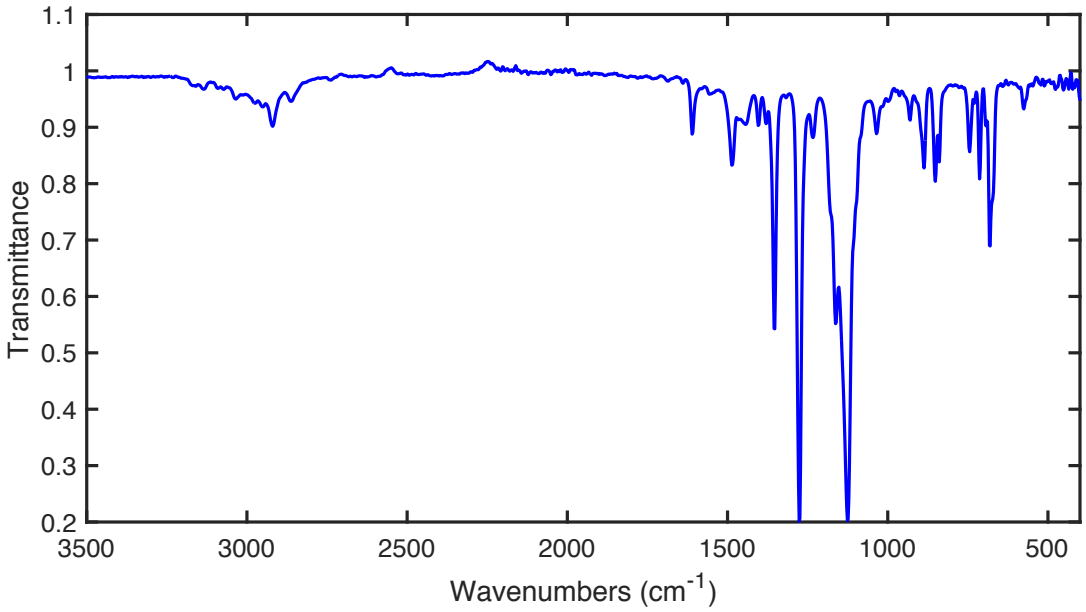

Figure S7.67: IR spectrum of **[5]**$^{+}$.

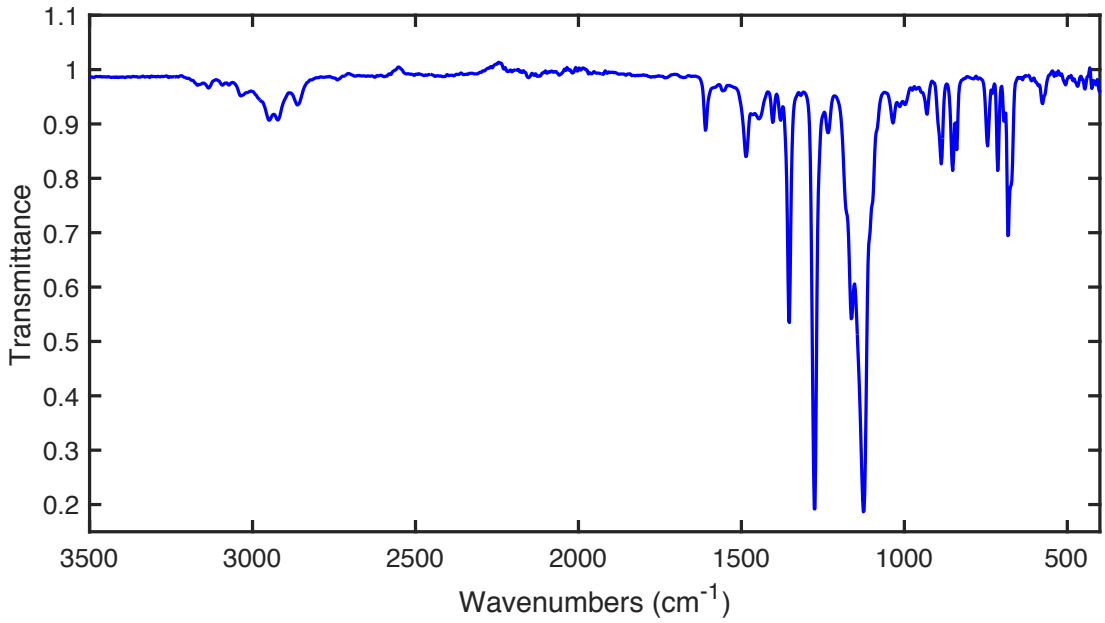

Figure S7.68: IR spectrum of **[7]**$^{+}$.

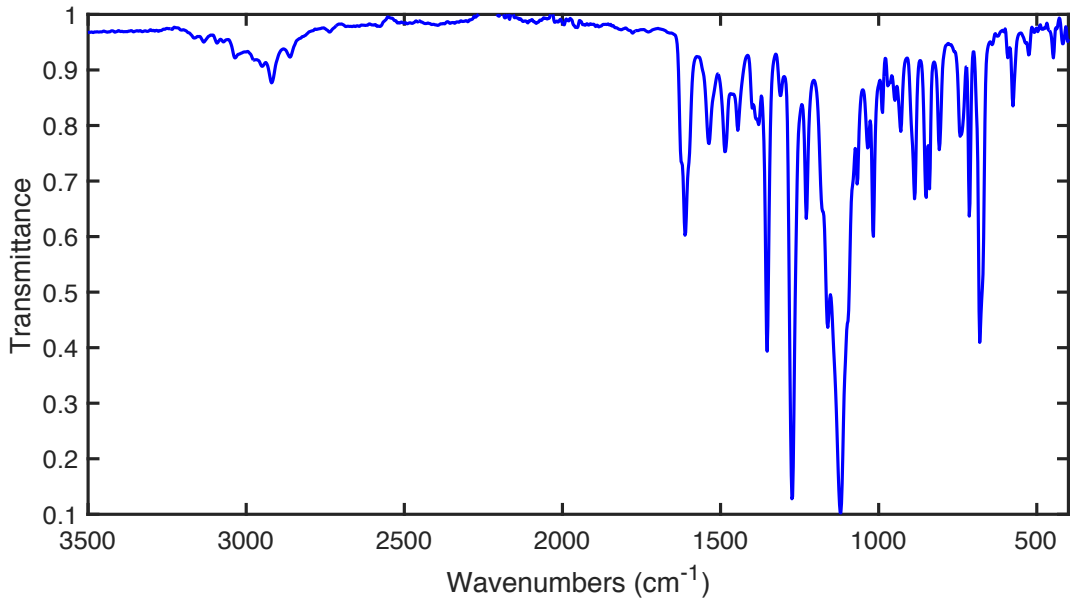

Figure S7.69: IR spectrum of **[4]**$^{+}$.

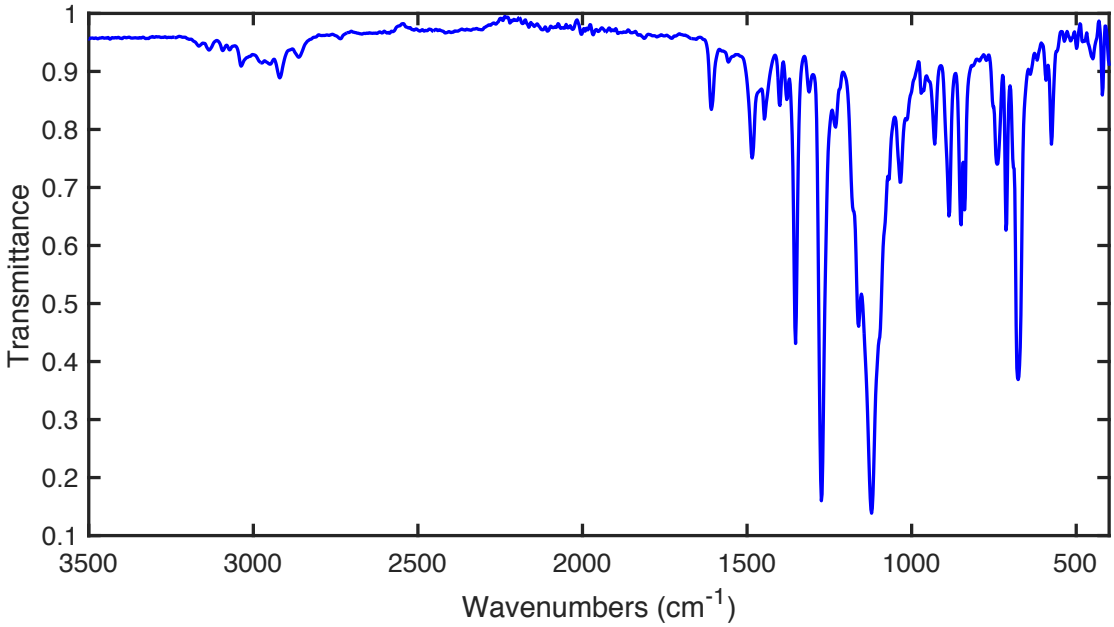

Figure S7.70: IR spectrum of **[8]**$^{+}$.

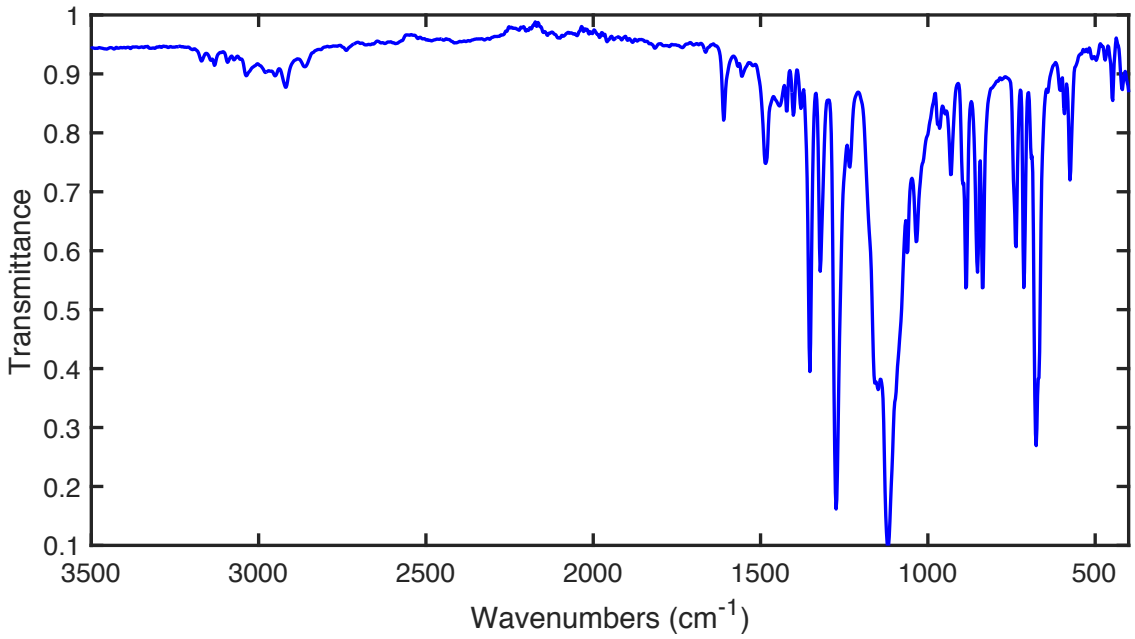

Figure S7.71: IR spectrum of **[6]**$^{+}$.

UV-Vis spectra

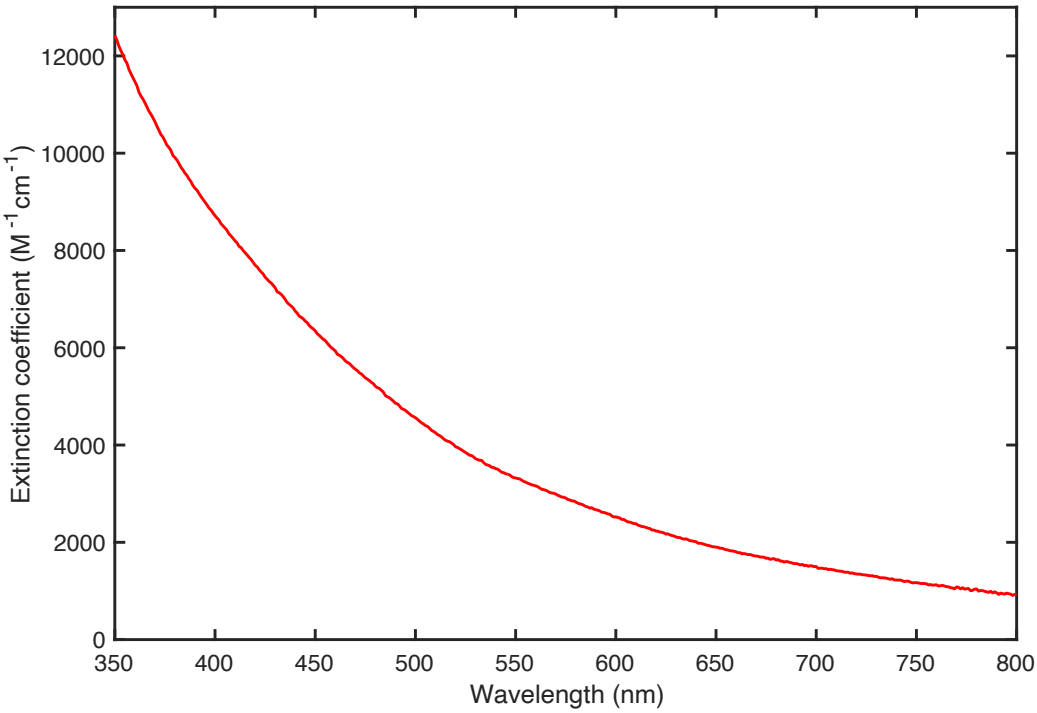

Figure S7.72: UV-Vis spectrum of **2** in THF.

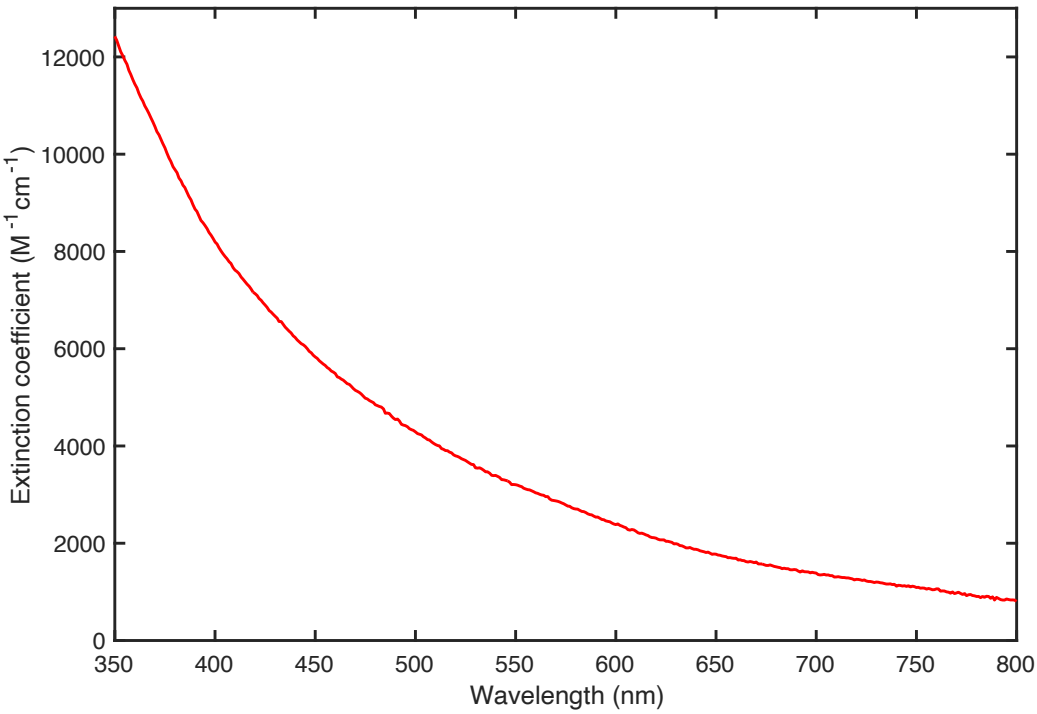

Figure S7.73: UV-Vis spectrum of **3** in THF.

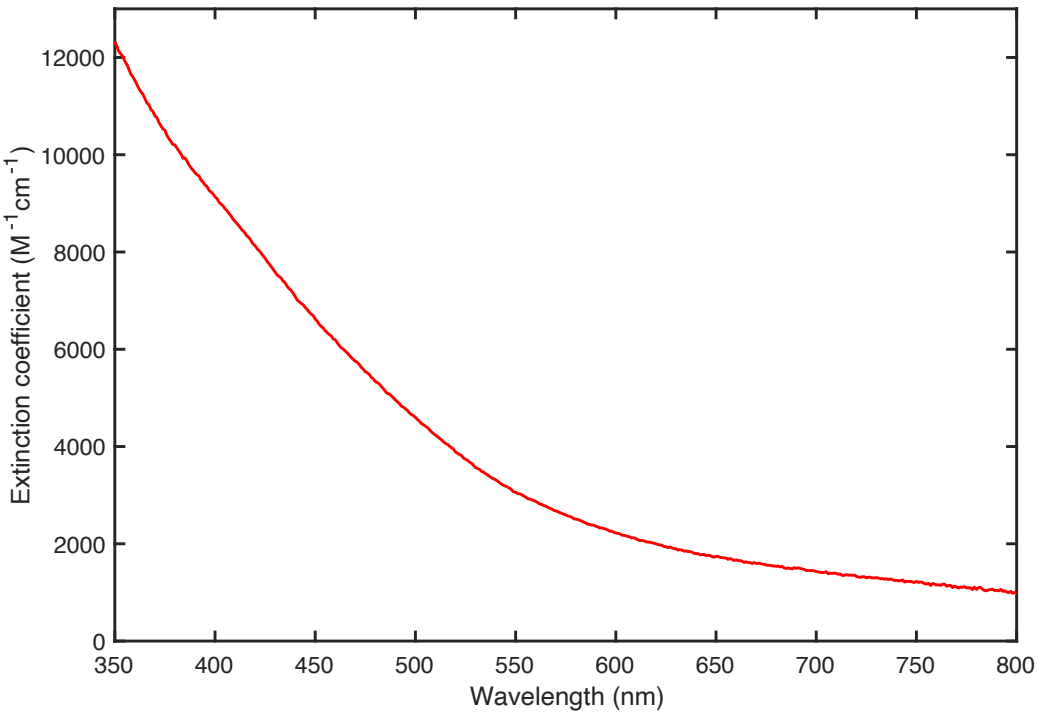

Figure S7.74: UV-Vis spectrum of **5** in THF.

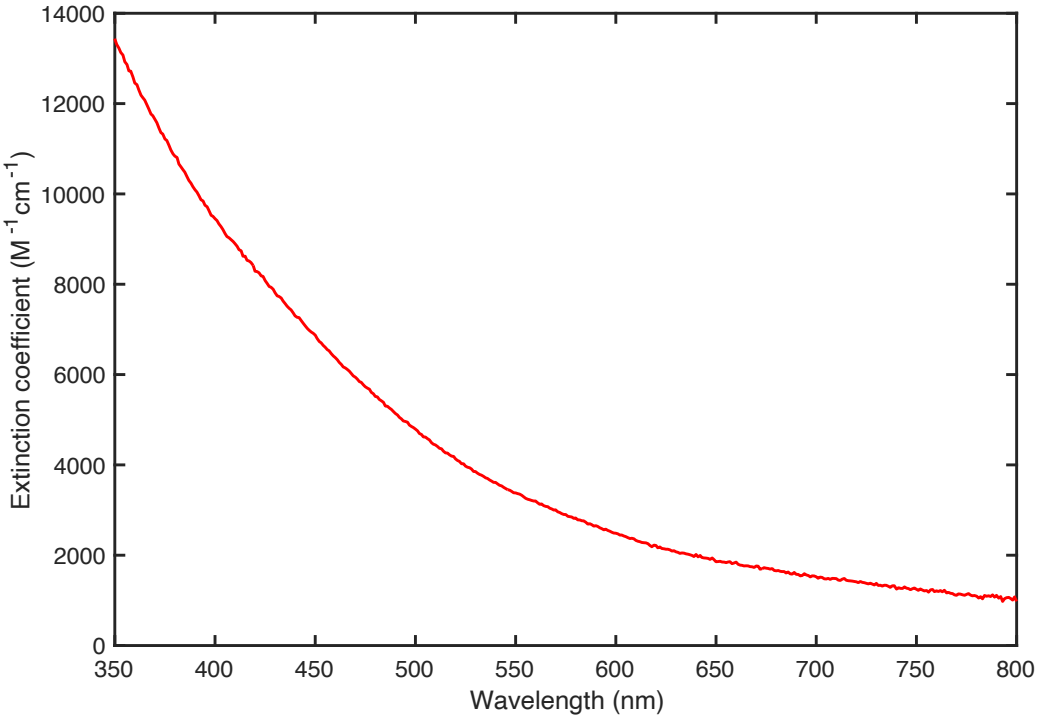

Figure S7.75: UV-Vis spectrum of **7** in THF.

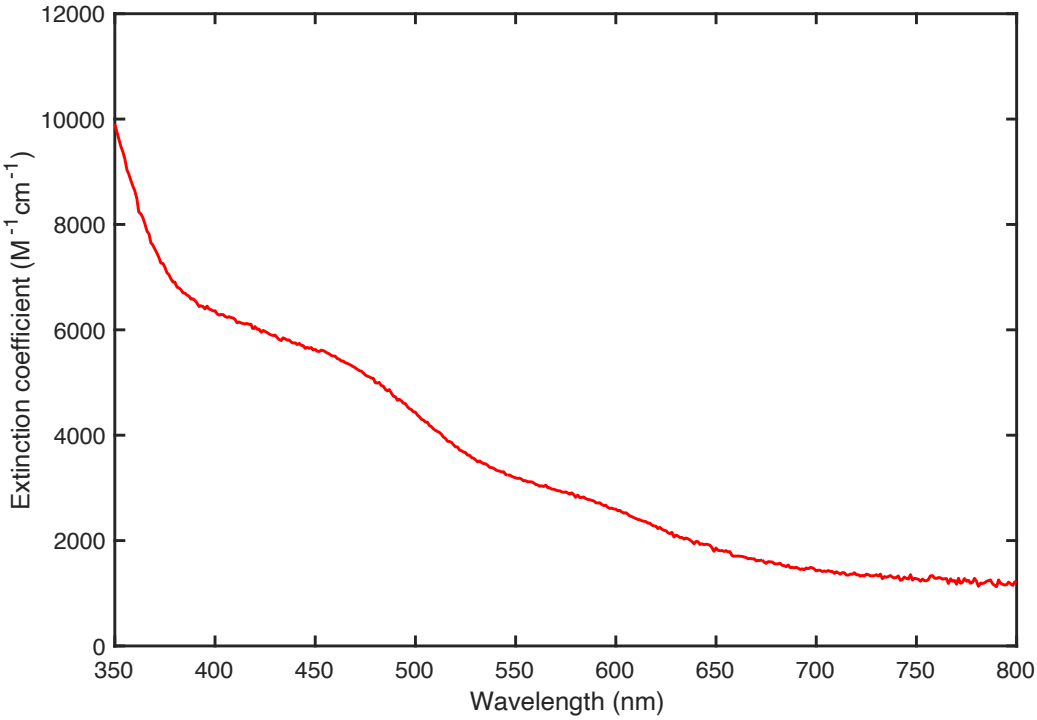

Figure S7.76: UV-Vis spectrum of **[2]**$^{+}$ in toluene.

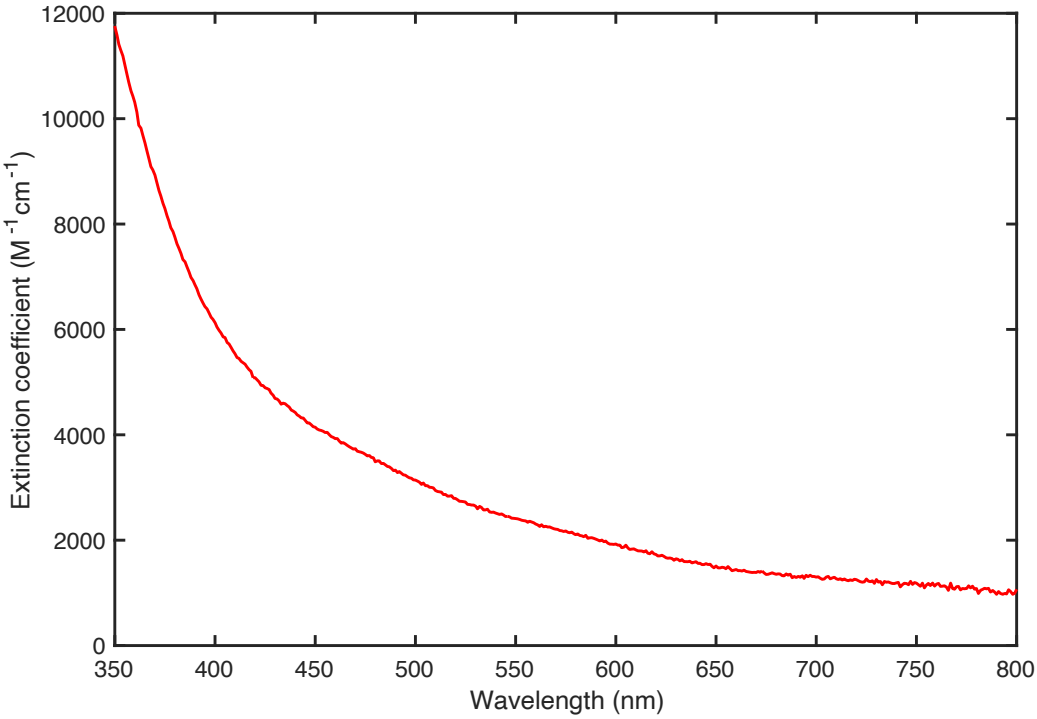

Figure S7.77: UV-Vis spectrum of **[3]**$^{+}$ in toluene.

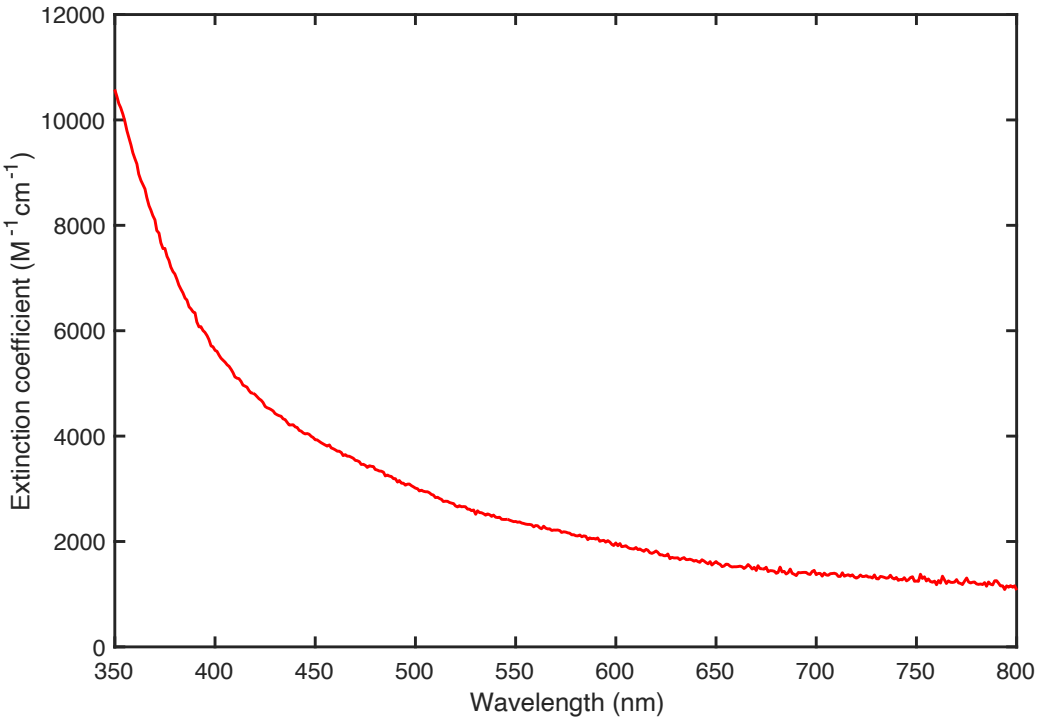

Figure S7.78: UV-Vis spectrum of **[5]**$^{+}$ in toluene.

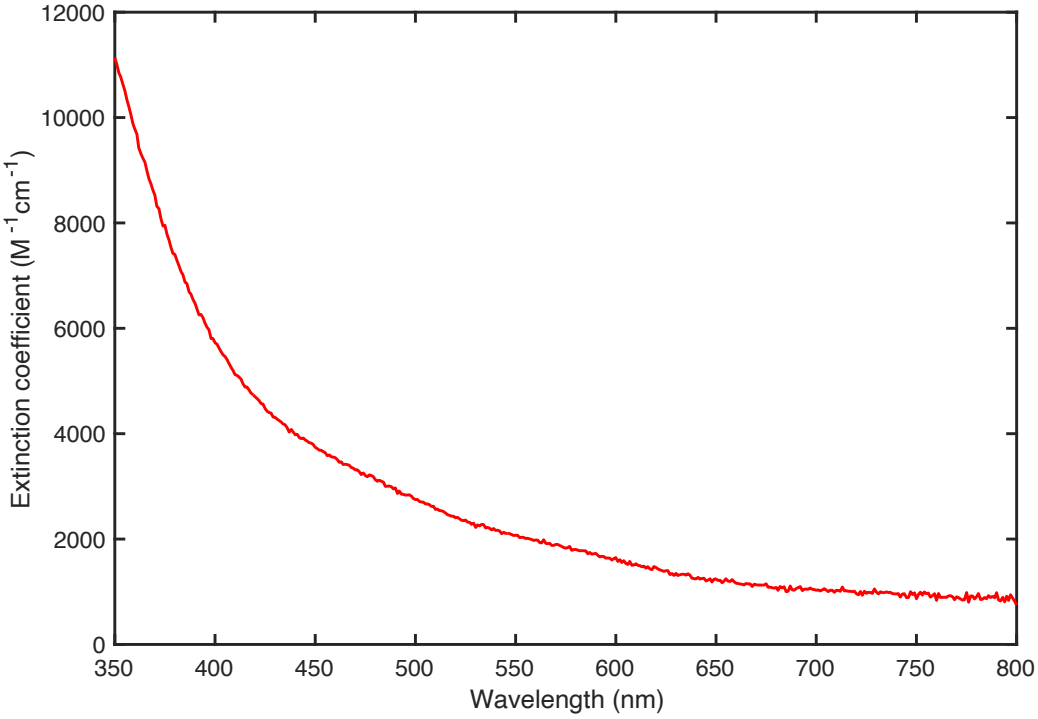

Figure S7.79: UV-Vis spectrum of **[7]**$^{+}$ in toluene.

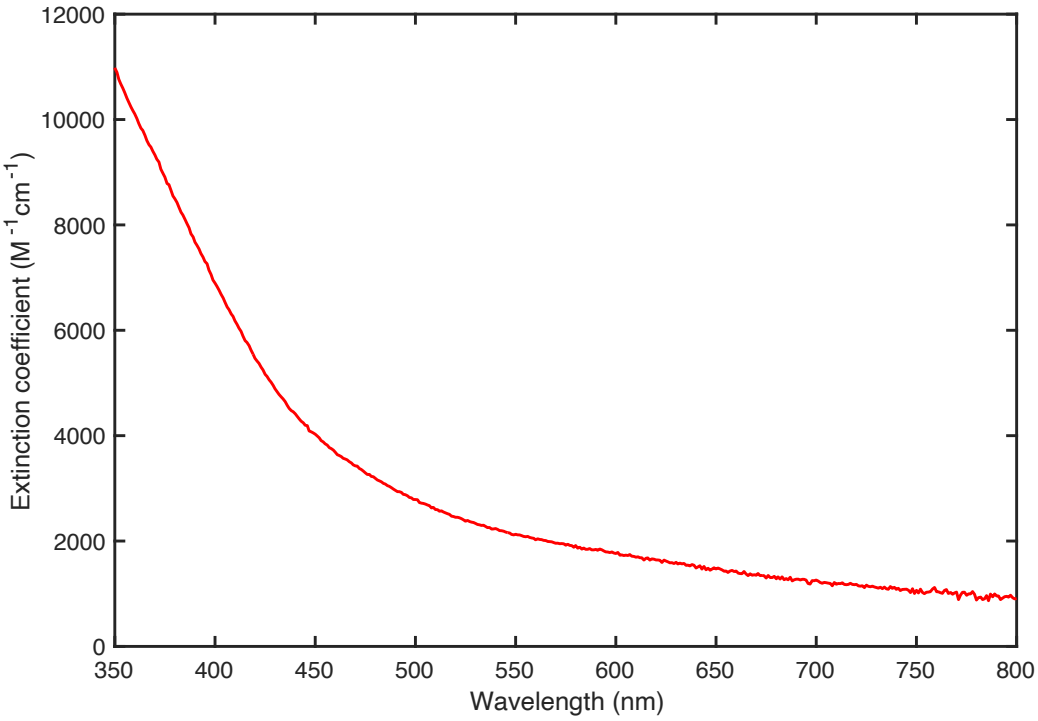

Figure S7.80: UV-Vis spectrum of **[4]**$^{+}$ in toluene.

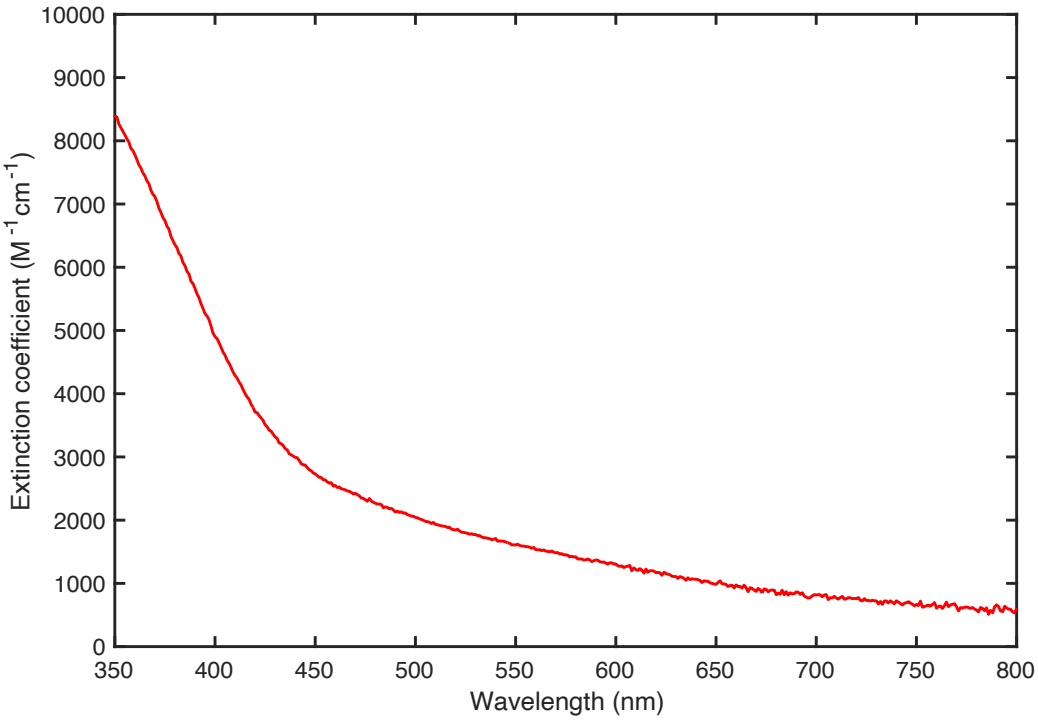

Figure S7.81: UV-Vis spectrum of **[8]**$^{+}$ in toluene.

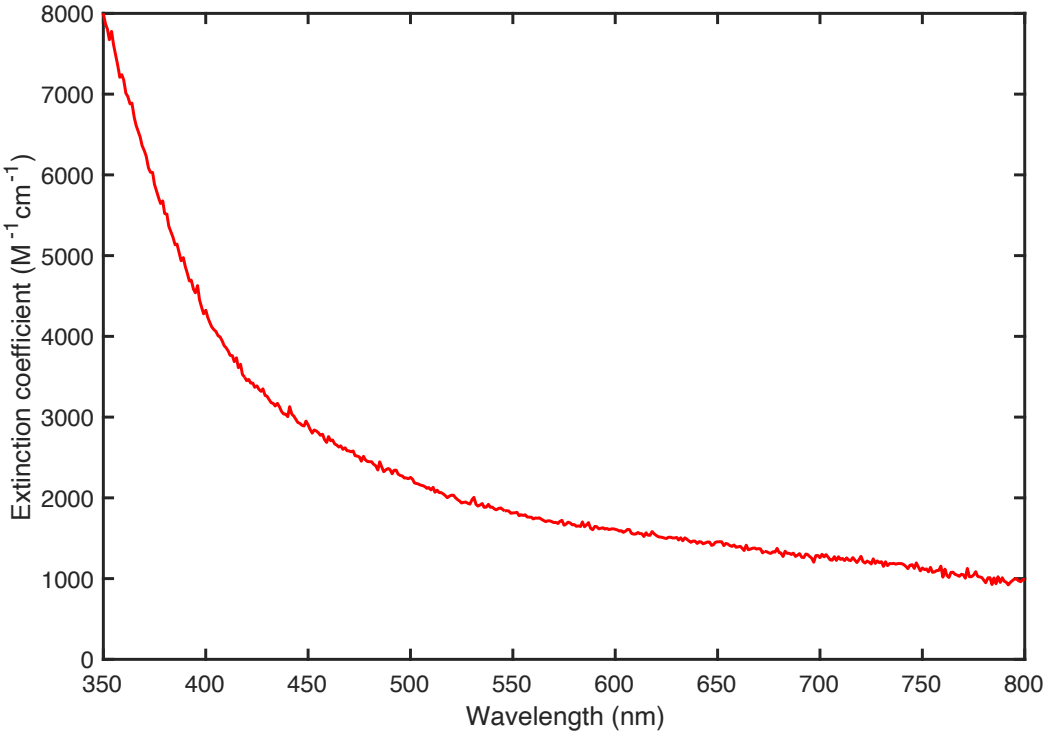

Figure S7.82: UV-Vis spectrum of **[6]**$^{+}$ in toluene.

Cyclic Voltammetry

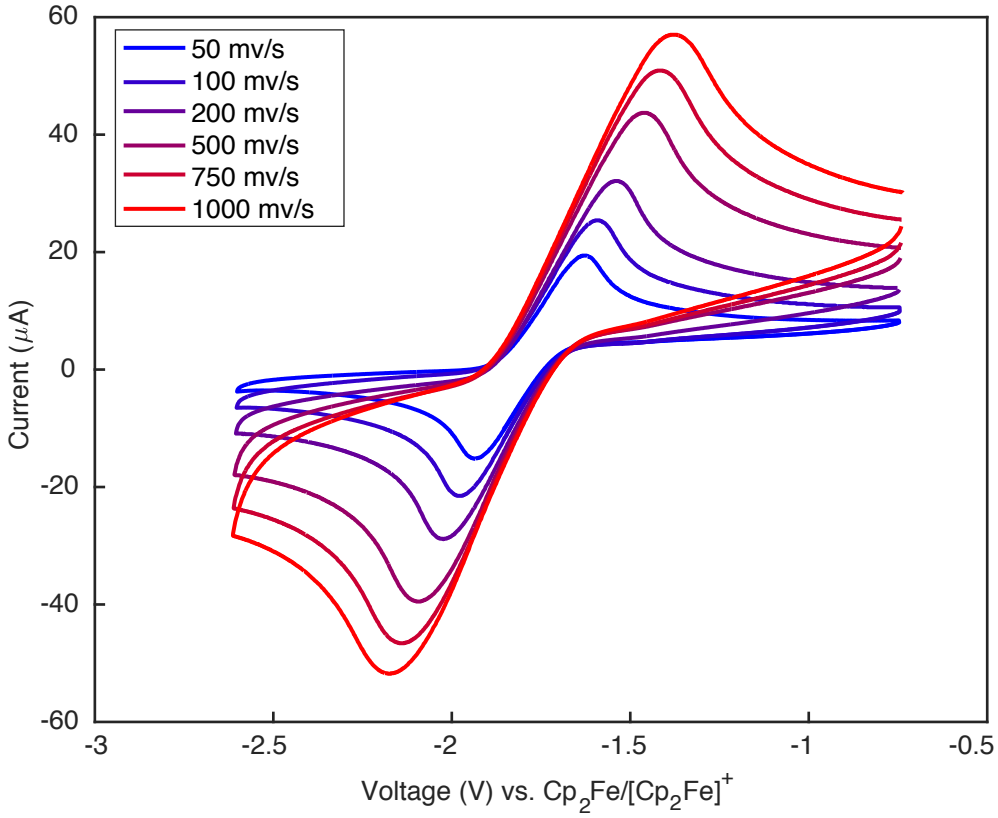

Figure S7.83: Cyclic voltammogram of **2** (5 mM) in PhF (0.1 M [NPr$_4$][BAr$^F{}_4$]) showing the **2**/**[2]**$^+$ redox couple at -1.78 V vs $Cp_2Fe/[Cp_2Fe]^+$

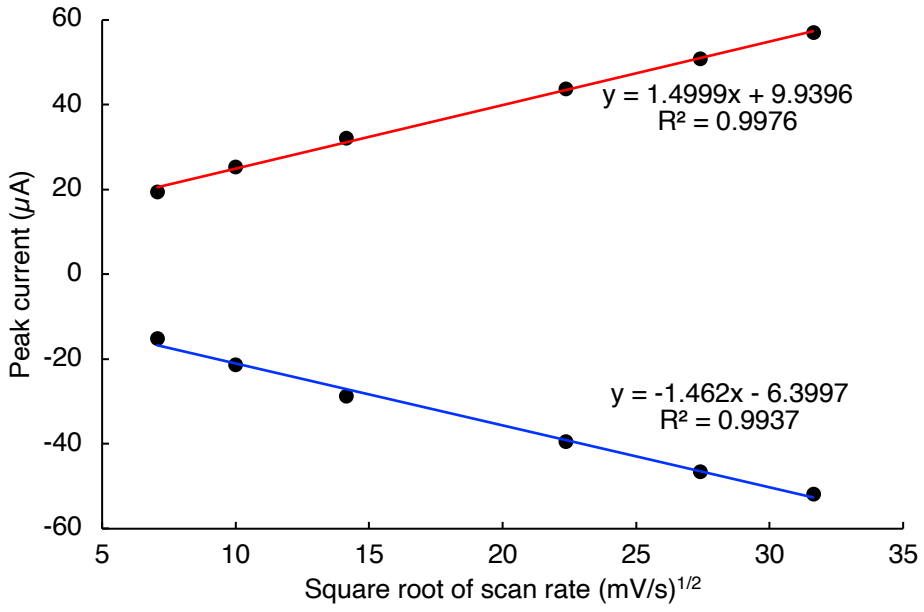

Figure S7.84: Plot of peak current vs. the square root of the scan rate, showing the reversibility of the **2**/**[2]**$^+$ redox couple.

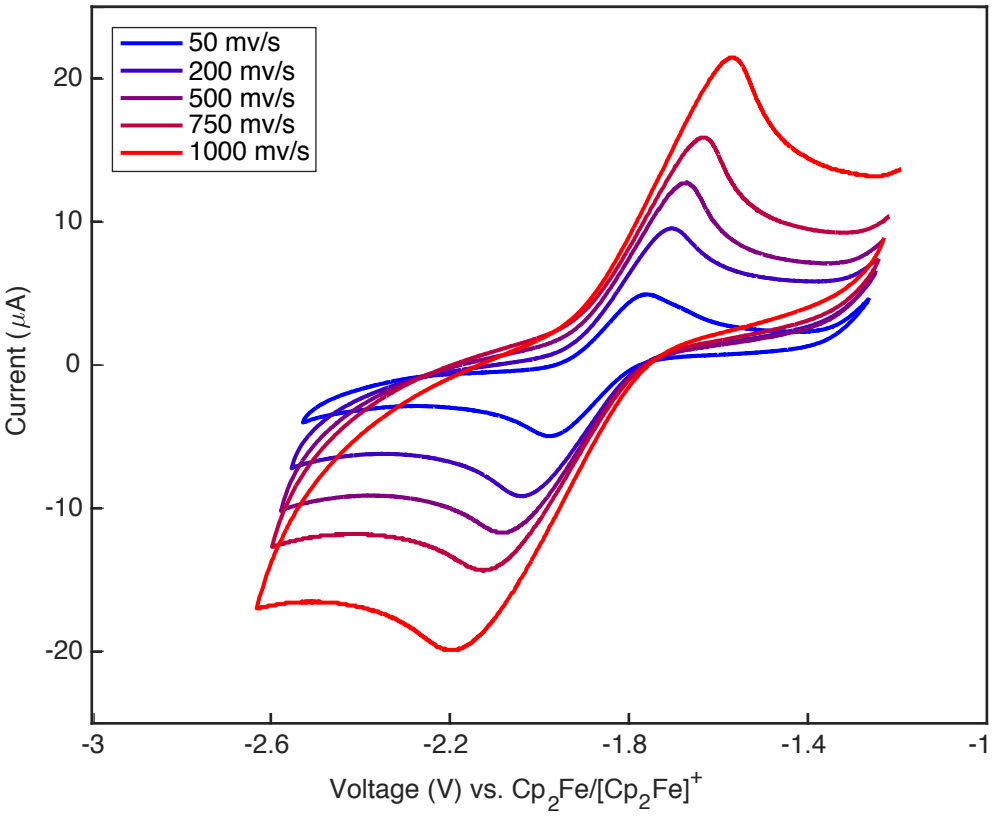

Figure S7.85: Cyclic voltammogram of **3** (5 mM) in PhF (0.1 M $[NPr_4][BAr^F{}_4]$) showing the **3**/**[3]**$^+$ redox couple at -1.88 V vs $Cp_2Fe/[Cp_2Fe]^+$

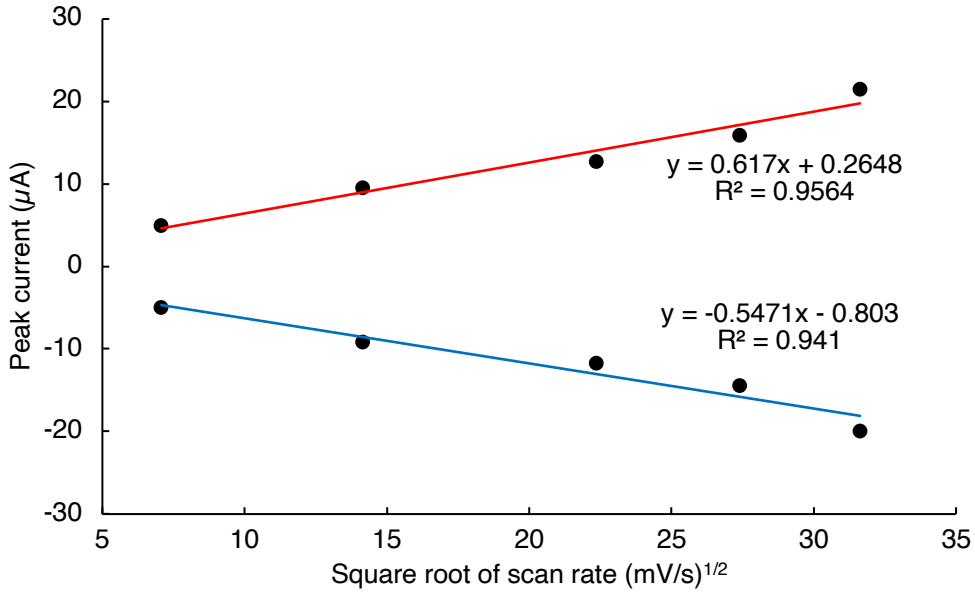

Figure S7.86: Plot of peak current vs. the square root of the scan rate, showing the reversibility of the **3**/**[3]**$^+$ redox couple.

Crystallographic Details

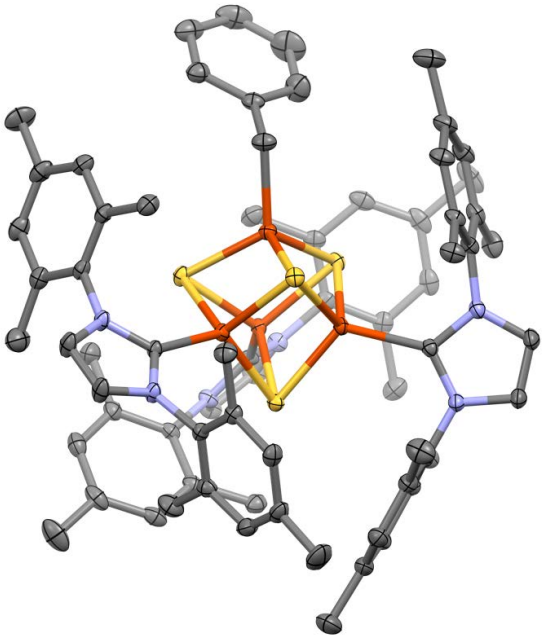

Figure S7.87: Thermal ellipsoid (50%) plot of **2**. Hydrogen atoms omitted for clarity

[2]$^{+}$: Disorder was present in the benzyl group and in THF and pentane in the lattice. The disordered atoms were refined with appropriate distance and angle restraints and rigid bond restraints.

[4]$^{+}$: Crystallized on a 3-fold symmetric axis. The triflate anion was disordered with THF over the 3-fold axis; the occupancy of the triflate was fixed at 0.333 for charge balance. The S and IMes atoms were modelled as disordered over two positions, in a 2:1 ratio. The disordered atoms were refined with appropriate distance and angle restraints and rigid bond restraints. Modeling the S atoms over two positions generates several potential cluster geometries. The atomic positions we displayed were chosen such that the cluster metrics were consistent with other $[Fe_4S_4]^{+}$ clusters (i.e., Fe–S distances between 2.20 and 2.35 Å, L–Fe–S angles > 90 °). The atomic positions for the NHCs were chosen so that the Fe atoms bonded to equivalent sulfurs had equivalent IMes ligands.

References

(1) Brown, A. C.; Suess, D. L. M. Controlling Substrate Binding to Fe_4S_4 Clusters through Remote Steric Effects. *Inorg. Chem.* **2019**, *58* (8), 5273–5280.

(2) Samsel, E. G.; Kochi, J. K. Oxidative Alkylation of Cobalt Complexes with Hydrazines. *Inorg. Chem.* **1986**, *25* (14), 2450–2457.

(3) Yakelis, N. A.; Bergman, R. G. Safe Preparation and Purification of Sodium Tetrakis[(3,5-Trifluoromethyl) Phenyl]Borate ($NaBArF_{24}$): Reliable and Sensitive Analysis of Water in Solutions of Fluorinated Tetraarylborates. *Organometallics* **2005**, *24* (14), 3579–3581.

(4) Chávez, I.; Alvarez-Carena, A.; Molins, E.; Roig, A.; Maniukiewicz, W.; Arancibia, A.; Arancibia, V.; Brand, H.; Manuel Manríquez, J. Selective Oxidants for Organometallic Compounds Containing a Stabilising Anion of Highly Reactive Cations: $(3,5(CF_3)_2C_6H_3)_4B^-)Cp_2Fe^+$ and $(3,5(CF_3)_2C_6H_3)_4B^-)Cp^*_2Fe^+$. *J. Organomet. Chem.* **2000**, *601* (1), 126–132.

(5) Stoll, S.; Schweiger, A. EasySpin, a Comprehensive Software Package for Spectral Simulation and Analysis in EPR. *J. Magn. Reson.* **2006**, *178* (1), 42–55.

(6) Hübschle, C. B.; Sheldrick, G. M.; Dittrich, B. ShelXle: A Qt Graphical User Interface for SHELXL. *J. Appl. Crystallogr.* **2011**, *44* (6), 1281–1284.

(7) Gibian, M. J.; Corley, R. C. Organic Radical-Radical Reactions. Disproportionation vs. Combination. *Chem. Rev.* **1973**, *73* (5), 441–464.

(8) Halpern, J. Determination of Transition Metal-Alkyl Bond Dissociation Energies from Kinetic Measurements. *Polyhedron* **1988**, *7* (16–17), 1483–1490.

(9) Halpern, J. Determination and Significance of Transition Metal-Alkyl Bond Dissociation Energies. *Acc. Chem. Res.* **1982**, *15* (8), 238–244.

(10) Horitani, M.; Shisler, K.; Broderick, W. E.; Hutcheson, R. U.; Duschene, K. S.; Marts, A. R.; Hoffman, B. M.; Broderick, J. B. Radical SAM Catalysis via an Organometallic Intermediate with an Fe-[5'-C]-Deoxyadenosyl Bond. *Science* **2016**, *352* (6287), 822–825.

(11) Kandt, C.; Monticelli, L. Membrane Protein Dynamics from Femtoseconds to Seconds. *Methods Mol. Biol.* **2010**, *654*, 423–440.

(12) Ben-Nissan, G.; Sharon, M. Capturing Protein Structural Kinetics by Mass Spectrometry. *Chem. Soc. Rev*. **2011**, *40* (7), 3627-3637.

Chapter 8. Valence Localization in Alkyne and Alkene Adducts of Synthetic $[Fe_4S_4]^+$ Clusters

Introduction

The Fe–S cluster enzymes IspG (GcpE) and IspH (LytB) catalyze the final steps in the isoprenoid biosynthesis pathway used by most bacteria and malaria parasites, the methylerythritol phosphate pathway.[1,2] IspG carries out the two-electron, two-proton reduction of 2-*C*-methyl-D-erythritol-2,4-cyclodiphosphate (MEcPP) to 4-hydroxy-3-methylbut-2-enyl 1-diphosphate (HMBPP) (Fig. 8.1A). The latter is further reduced by IspH

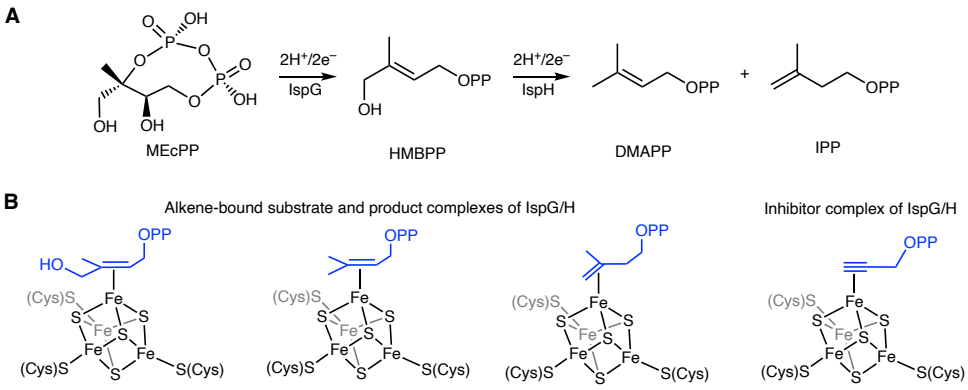

Figure 8.1. Substrates, products, and inhibitors that form π complexes with $[Fe_4S_4]$ clusters in the methylerythritol phosphate pathway of isoprenoid biosynthesis. A) Reactions catalyzed by IspG and IspH. B) Proposed structures of π complexes formed at the active sites of IspG and IspH.

to yield the key precursors to isoprenoid natural products: isopentenyl diphosphate (IPP) and dimethylallyl diphosphate (DMAPP).[3–5] IspG and IspH are attractive drug targets because the methylerythritol phosphate pathway is not used by humans,[6] and as such there has been interest in identifying inhibitors for these enzymes (Fig. 8.1).[7–11] Approaches to inhibitor design take inspiration from how substrates and products are thought to bind. Specifically, in the native IspG and IspH reactions, several species with alkenes bound to the unique Fe site of the $[Fe_4S_4]$ cluster have been proposed[12–14] (Fig. 8.1B), and alkyne inhibitors have been designed that likewise feature proposed Fe–π interactions between the unique Fe center of the cluster and the inhibitor.[7,15]

The mechanisms of IspG and IspH have been extensively studied by EPR spectroscopy,[12–14,16–21] and the key spectroscopic signatures for these π-complexes are their unusual *g*-tensors. Whereas the $S = 1/2$ spin states of $[Fe_4S_4]^+$ clusters typically give rise to signals with $g_{iso} < 2$ (*e.g.*, as observed for clusters ligated by four thiolates),[22,23] the proposed alkene complexes in IspG and IspH feature $g_{iso} > 2$.[12] Alkyne inhibitor-bound samples show similar EPR signals with $g_{iso} > 2$,[12] suggesting analogous modes of substrate, product, and inhibitor binding. Given that thiolate-ligated $[Fe_4S_4]^{3+}$ clusters display $g_{iso} > 2$, one explanation for the unusual *g*-tensors for the π-complexes of $[Fe_4S_4]^+$ clusters is that their electronic structures are dominated by resonance structures consisting of $[Fe_4S_4]^{3+}$ clusters with metallacyclopropene/metallacyclopropane ligands[24,25] (Fig. 8.2). However, evaluating this and

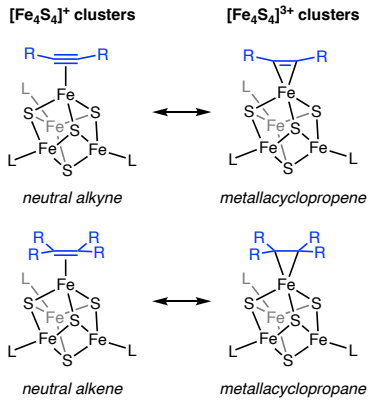

Figure 8.2. Limiting resonance structures describing the bonding between $[Fe_4S_4]^+$ clusters and alkynes/alkenes.

related proposals has been challenging because of a lack of high-resolution crystallographic data for π-complexes of IspG and IspH; the only crystallographically characterized π-complex of either enzyme is IspH bound to a pyridine-based inhibitor that binds in an η^2 C–N fashion with partial occupancy of the unique Fe site.[14] Given this backdrop, as well as proposed alkyne binding to synthetic $[Fe_4S_4]$ clusters during alkyne reduction to alkenes[26–28] and the importance of alkyne- and alkene-bound intermediates in reduction of alternative substrates by nitrogenases,[29,30] we set out to synthesize and characterize alkyne- and alkene-bound $[Fe_4S_4]^+$ clusters.

Results and Discussion

To synthesize alkyne and alkene adducts of $[Fe_4S_4]^+$ clusters, we used the $(IMes)_3Fe_4S_4$ platform (IMes = 1,3-dimesitylimidazol-2-ylidene),[35] which features three bulky IMes ligands that enforce 3:1 site-differentiation of the cluster and allow for the installation of labile, neutral ligands at the unique Fe site. We first prepared the previously reported cluster[35] $[(IMes)_3Fe_4S_4(OEt_2)][BAr^F{}_4]$ ($[\mathbf{1\text{-}OEt_2}]^+$; Ar^F = 3,5-bis(trifluoromethyl)phenyl) by treatment of $[(IMes)_3Fe_4S_4Cl][BAr^F{}_4]$ ($[\mathbf{1\text{-}Cl}]^+$) with $Ti(N[^tBu]Ar)_3$ (Ar=3,5-dimethylphenyl)[36] in diethyl ether (Et_2O). Subsequent treatment of $[\mathbf{1\text{-}OEt_2}]^+$ with an excess of PhCCH or COE in Et_2O afforded the alkyne and alkene adducts $[(IMes)_3Fe_4S_4(PhCCH)][BAr^F{}_4]$ ($[\mathbf{1\text{-}PhCCH}]^+$) or $[(IMes)_3Fe_4S_4(COE)][BAr^F{}_4]$ ($[\mathbf{1\text{-}COE}]^+$), respectively, as black, microcrystalline solids after crystallization from Et_2O and *n*-pentane (Scheme 8.1). Both complexes possess C_{3v} symmetry on the NMR timescale, consistent with relatively fast rotation of the PhCCH and COE ligands around the apical Fe site. The ^1H NMR spectrum of $[\mathbf{1\text{-}COE}]^+$ reveals that the methylene

Scheme 8.1. Synthesis of $[\mathbf{1\text{-}PhCCH}]^+$ and $[\mathbf{1\text{-}COE}]^+$. $[BAr^F{}_4]$ anions omitted for clarity.

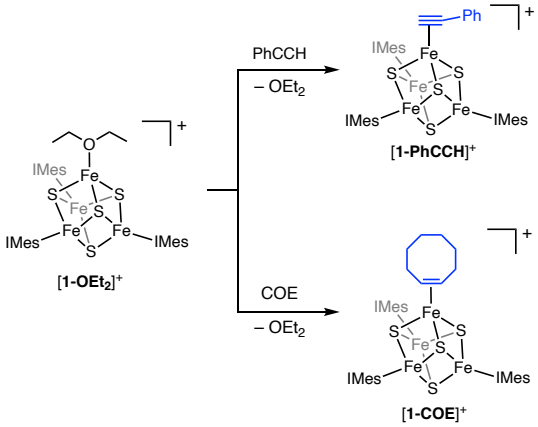

protons on the COE ligand are diastereotopic, indicating that the COE ligand does not dissociate and recoordinate on the NMR timescale. The alkyne and alkene ligands are weakly bound to the clusters and can be displaced by Et_2O. In Et_2O solutions, both $[\mathbf{1\text{-}PhCCH}]^+$ and $[\mathbf{1\text{-}COE}]^+$ exist in equilibrium with $[\mathbf{1\text{-}OEt_2}]^+$ in the absence of excess PhCCH or COE, respectively; even in the presence of excess COE, $[\mathbf{1\text{-}COE}]^+$ is observed in equilibrium with

[**1-OEt$_2$**]$^+$ in Et_2O (Fig. S8.5). However, no equilibrium with a solvent adduct is observed for [**1-PhCCH**]$^+$ or [**1-COE**]$^+$ in *o*-difluorobenzene (DFB), which is more weakly coordinating than Et_2O (Fig. 8.3, S8.1, and S8.2).

Both [**1-PhCCH**]$^+$ and [**1-COE**]$^+$ have $S = 1/2$ ground spin states as determined by EPR spectroscopy (Fig. 8.3) with g_{iso} = 2.066 for [**1-PhCCH**]$^+$ and g_{iso} = 2.059 for [**1-COE**]$^+$. Comparatively, all other reported $[Fe_4S_4]^+$ clusters with IMes ligands[35,39] have $g_{iso} \sim 2$ (*cf.* g_{iso} = 1.990 for [**1-THF**]$^+$).[35] Thus, the unusually high g_{iso} values for [**1-PhCCH**]$^+$ and [**1-COE**]$^+$ mirror those observed for proposed alkyne and alkene adducts of the $[Fe_4S_4]$ clusters in IspH

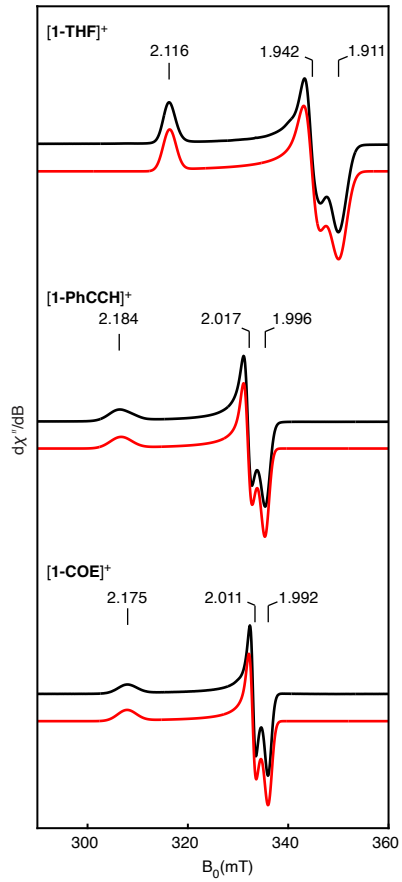

Figure 8.3. X-band EPR spectra (black) and simulations (red) of [**1-THF**]$^+$ (top, 15 K, 63 μW, 9.370 GHz, 10:1 THF/toluene, *g*-strain = [0.019 0.015 0.018]), [**1-PhCCH**]$^+$ (middle, 15 K, 63 μW, 9.374 GHz, 10:1 Et_2O/toluene, *g*-strain = [0.035 0.007 0.009]) and [**1-COE**]$^+$ (bottom, 15 K, 16 μW, 9.374 GHz, 10:1 DFB/toluene, *g*-strain = [0.030 0.005 0.008].).

and IspG (*vide supra*),[12,13] supporting that [**1-PhCCH**]$^+$ and [**1-COE**]$^+$ are appropriate models for π-complexes of protein-bound [Fe_4S_4] clusters.

As noted above, the unusual g_{iso} values observed for alkene- and alkyne-bound [Fe_4S_4]$^+$ clusters have raised interest in the electronic structures of these adducts, particularly as to what extent they are best described as [Fe_4S_4]$^{3+}$ clusters featuring metallacyclopropene/metallacyclopropane ligands.[13] Structural analysis of the Fe–C and C–C (alkyne/alkene) distances as well as the metrics of the [Fe_4S_4] core could speak to this issue, with short Fe–C bonds, long C–C bonds, and contracted [Fe_4S_4] cores being the hallmarks of a dominant [Fe_4S_4]$^{3+}$ resonance structure. However, analysis of such parameters for enzymatic alkyne and alkene adducts of [Fe_4S_4] clusters is hampered by a lack of high-resolution X-ray crystallographic data for these species, and we therefore undertook structural studies of [**1-PhCCH**]$^+$ and [**1-COE**]$^+$.

Compound [**1-PhCCH**]$^+$ was crystallized as its triflate salt (prepared as described in the SI) by diffusion of *n*-pentane into a THF solution, and [**1-COE**]$^+$ was crystallized with a [$BAr^F{}_4$] anion by layering *n*-pentane onto an Et_2O solution. Their structures were determined by single-crystal X-ray diffraction (Fig. 8.4), which verified their identities as π-complexes of [Fe_4S_4] clusters. The C–C distance in [**1-PhCCH**]$^+$ (1.253(3) Å) is between that of a free C≡C bond (1.17–1.20 Å)[43] and that of a C=C bond (1.31–1.34 Å),[43] and the C–C distance in [**1-COE**]$^+$ (1.390(2) Å) is closer to that of a free C=C bond than that of a C–C bond (1.53–1.55 Å).[43] Both complexes can also be compared to structurally characterized high-spin Fe^{1+}–alkyne and –alkene complexes,[44–54] which show average C–C bond lengths of 1.271(7) Å (alkyne) and 1.40(2)Å (alkene). High-spin Fe^{1+} compounds would be expected to have a greater resonance contribution from the metallacyclopropene/metallacyclopropane structures than the formally Fe^{2+}/Fe^{3+} centers in an [Fe_4S_4]$^+$ cluster, though even the former are typically dominated by the neutral alkyne/alkene resonance structure.[48] That the C–C distances in [**1-PhCCH**]$^+$ and [**1-**

COE]$^+$ are similar to or shorter than those in the analogous Fe^{1+} compounds supports the description of the cluster complexes as neutral alkyne and alkene adducts of $[Fe_4S_4]^+$ clusters. Consistent with the structural analysis of the C–C distances, the IR spectrum of [**1-PhCCH**]$^+$ reveals that its PhCCH ligand is less activated than in analogous Fe^{1+} compounds (ν(C≡C) = 1812 cm^{-1} in [**1-PhCCH**]$^+$ compared to 1730(10) cm^{-1} on average for Fe^{1+}–(PhCCH) compounds[44,45,50,52]). Furthermore, the relatively long average Fe–C(alkyne/alkene) distances in [**1-PhCCH**]$^+$ (2.003(3) Å) and [**1-COE**]$^+$ (2.128(2) Å) compared to the corresponding distances in high-spin Fe^{1+}–alkyne (1.96(2) Å) and –alkene (2.04(3) Å) complexes demonstrate that the clusters engage in weaker backbonding to the π-accepting ligand.

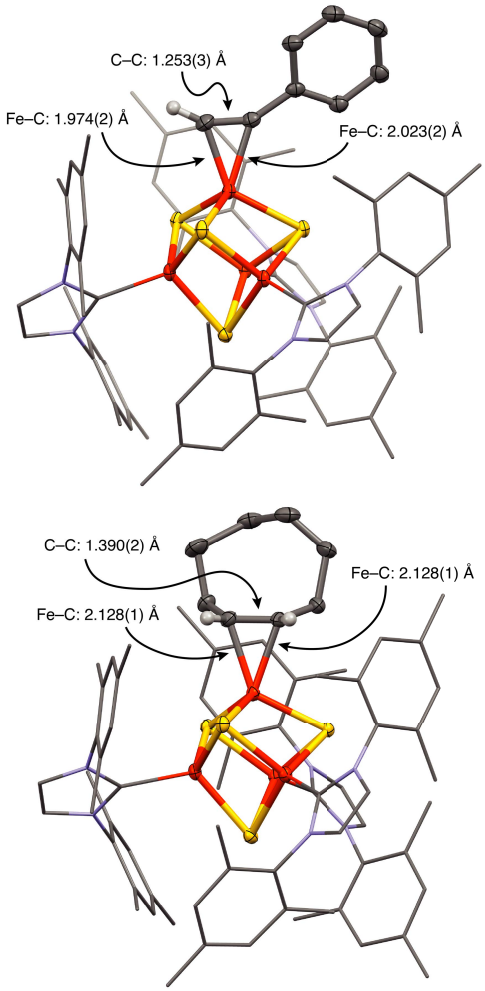

Figure 8.4. Single-crystal X-ray diffraction structures of [**1-PhCCH**]$^+$ (top) and [**1-COE**]$^+$ (bottom). Thermal ellipsoids shown at 50% probability with carbon (gray), iron (orange), sulfur (yellow), and nitrogen (blue). IMes ligands are shown as sticks and solvent molecules, anions and H-atoms except for the alkynyl and alkenyl H-atoms are omitted for clarity.

Additionally, the core Fe–S bond metrics indicate that the [Fe_4S_4] cores of [**1-PhCCH**]$^+$ and [**1-COE**]$^+$ are more reduced than would be expected for an [Fe_4S_4]$^{3+}$ cluster. Although no crystal structures of IMes-supported [Fe_4S_4]$^{3+}$ clusters have been reported, the Fe–S bond metrics of [**1-PhCCH**]$^+$ and [**1-COE**]$^+$ can be compared to those of [**1-OEt$_2$**]$^+$ (an [Fe_4S_4]$^+$ cluster)[35] and [**1-Cl**]$^+$ (an [Fe_4S_4]$^{2+}$ cluster). The average Fe–S distance in [**1-OEt$_2$**]$^+$ is 2.282(1) Å, which is 0.007 Å shorter than the average Fe–S distance in [**1-Cl**]$^+$ (2.275(5) Å). This decrease, although modest, is consistent with well-established trends in Fe–S structures, which tend to show decreases in Fe–S distances upon oxidation.[55] The average Fe–S bond distance in

both [**1-PhCCH**]$^+$ and [**1-COE**]$^+$ is 2.279(2) Å, which is between that of [**1-OEt$_2$**]$^+$ and [**1-Cl**]$^+$, and, therefore, longer than would be predicted for an $[Fe_4S_4]^{3+}$ cluster.

A similar picture emerges from Mössbauer studies of [**1-PhCCH**]$^+$ and [**1-COE**]$^+$. Mössbauer spectra of [**1-PhCCH**]$^+$, [**1-COE**]$^+$, and [**1-OEt$_2$**]$^+$ were collected at 150 K due to magnetic broadening at lower temperatures (Fig S12–S14). Additionally, in these spectra, the quadrupole doublet for the unique Fe site cannot be resolved, and as such many simulations of the data are possible. For this reason, we limit our discussion to the average Mössbauer isomer shift (δ_{avg}). For reference, δ_{avg} for [**1-OEt$_2$**]$^+$ is 0.49 mm/s at 150 K; if swapping the π-neutral Et_2O ligand for a π-acceptor ligand such as PhCCH or cyclooctene were to result in a two-electron oxidation of the cluster core to the $[Fe_4S_4]^{3+}$ state, we would expect δ_{avg} to decrease by ~0.17 mm s^{-1} to ~0.32 mm s^{-1}.[56] Instead, the observed δ_{avg} values for [**1-PhCCH**]$^+$ and [**1-COE**]$^+$ are only modestly lower than for [**1-OEt$_2$**]$^+$, at 0.41 and 0.45 mm s^{-1} respectively. A decease in δ_{avg} of 0.08 and 0.04 mm s^{-1}, respectively, is consistent with increased Fe–L covalency via backbonding to the π-acceptor ligands and minor contributions from resonance structures involving electron transfer to the unsaturated ligands (*i.e.*, an $[Fe_4S_4]^{3+}$ description and/or resonance structures involving one-electron transfer to generate an alkyne or alkene radical anion and an $[Fe_4S_4]^{2+}$ cluster; analogous resonance structures involving single-electron transfer have been used to describe the bonding in high-spin Fe^{1+}-alkyne complexes[48]). Thus, the Mössbauer, structural, and vibrational analysis (*vide supra*), as well as the compounds' cyclic voltammograms (which show that the redox couples for [**1-PhCCH**]$^+$ and [**1-COE**]$^+$ are shifted positively compared with those of [**1-OEt$_2$**]$^+$; Fig. S8.24 and S8.25 and Table S8.4), all indicate modest backbonding from the cluster to the π-acidic ligands.

We additionally considered the possibility that, despite alkyne and alkene binding not leading to complete, two-electron oxidation of the cluster, these π-acidic ligands could induce localization of ferrous character at the unique Fe site, and that such localization could be

experimentally probed using ^{1}H NMR spectroscopy. As has been previously demonstrated, $[Fe_4S_4]^+$ clusters can be described as a pair of spin-aligned $Fe^{2.5+}$ centers (S = 9/2, majority spin) anti-ferromagnetically coupled to a pair of spin-aligned Fe^{2+} centers (S = 4, minority spin) to give an overall S = 1/2 spin state, as is experimentally observed for many $[Fe_4S_4]^+$ clusters.[57] For homoleptic, synthetic clusters such as $[Fe_4S_4(I^iPr^{Me})_4]^+$ (I^iPr^{Me} = 1,3-diisopropyl-4,5-dimethylimidazol-2-ylidene), all four Fe valences within the cluster rapidly exchange on the NMR timescale, such that each Fe site has an effective valence of $Fe^{2.25+}$ and net majority spin. As a result, only one set of ligand resonances is observed in the ^{1}H NMR spectrum.[35] Valence averaging is likewise observed for the three IMes-bound sites in [**1-PhCCH**]$^+$ and [**1-COE**]$^+$. However, exchange of valences between chemically inequivalent sites, such as between the IMes- and alkyne/alkene-bound sites in [**1-PhCCH**]$^+$ and [**1-COE**]$^+$, may or may not occur. That is, the difference in the Fe coordination spheres could lead to preferential localization of different valences at different sites[40,58,59]—here, localization of Fe^{2+} at the Fe sites coordinated by the more π-accepting alkyne and alkene ligands. If, in the spectrum of thermally populated states, the unique Fe sites adopts primarily an Fe^{2+} valence, then its local spin density will not be averaged, it will reside preferentially in the S = 4, 2×Fe^{2+} pair, and it will have net minority spin density. On the other hand, if no valence localization occurs at a given temperature and on a given timescale, then all four sites will adopt Fe^{2+} and $Fe^{2.5+}$ valences with equal probability and thus all four Fe centers will appear to have majority spin density. Therefore, if it is determined that the alkyne- or alkene-bound Fe sites have minority spin density, it follows that these sites adopt localized Fe^{2+} valences.

The sign of the spin density at the unique Fe site can be predicted from the ^{1}H NMR chemical shifts of the ligands bound to the unique site if the mechanism of spin transfer from the metal center to the H-atoms on the ligand is understood,[60] because the sign of the spin density on an H atom can be directly read out from the variable temperature behavior of the ^{1}H

NMR resonance; at reasonably high temperatures (*i.e.*, near room temperature), positive spin density on a ^{1}H center is manifested as the resonance shifting downfield with decreasing temperature, and negative spin density on a ^{1}H center is manifested as the resonance shifting upfield with decreasing temperature.[59,61–63]

To determine how the sign of the spin density at the unique Fe site is reflected in the paramagnetic NMR shifts of the alkyne/alkene ligands, we computationally analyzed the molecular orbitals and spin densities of the Fe^{2+} model complexes $[FeCl_3–C_2H_2]^-$ and $[FeCl_3–C_2H_4]^-$. In both complexes, the spin on the alkyne or alkene ligand is dominated by the β-spin electron involved in Fe–alkyne/alkene π-bonding; the β-spin π-backbonding orbital is more delocalized over the alkyne/alkene than the α-spin π-backbonding orbital due to spin polarization induced by the unpaired α-spin electrons localized on the Fe center. For $[FeCl_3–C_2H_2]^-$, the Fe d orbital involved in backbonding is mixed with both the C–C π-symmetry orbital and the C–H σ-symmetry orbitals, resulting in delocalization of β-spin from Fe to the alkynyl H atoms (Fig. 8.5A, left). We would therefore expect the Fe and alkynyl H atoms to have opposite spin, since the Fe spin is dominated by the five unpaired d electrons in the α manifold and the H spin is dominated by the π-backbonding electron in the β manifold. In contrast, a similar analysis of the alkene adduct $[FeCl_3–C_2H_4]^-$ shows that the dominant spin-transfer mechanism to the alkenyl H is via spin polarization[60] of the C–H bond by the β-spin density in the C–C π system (Fig. 8.5A, right). This results in the Fe center and alkenyl H atoms bearing spin density of the same sign in alkene adducts of high-spin, tetrahedral Fe^{2+}. Thus, if we observe that the alkynyl proton in [**1-PhCCH**]$^+$ shifts downfield with decreasing

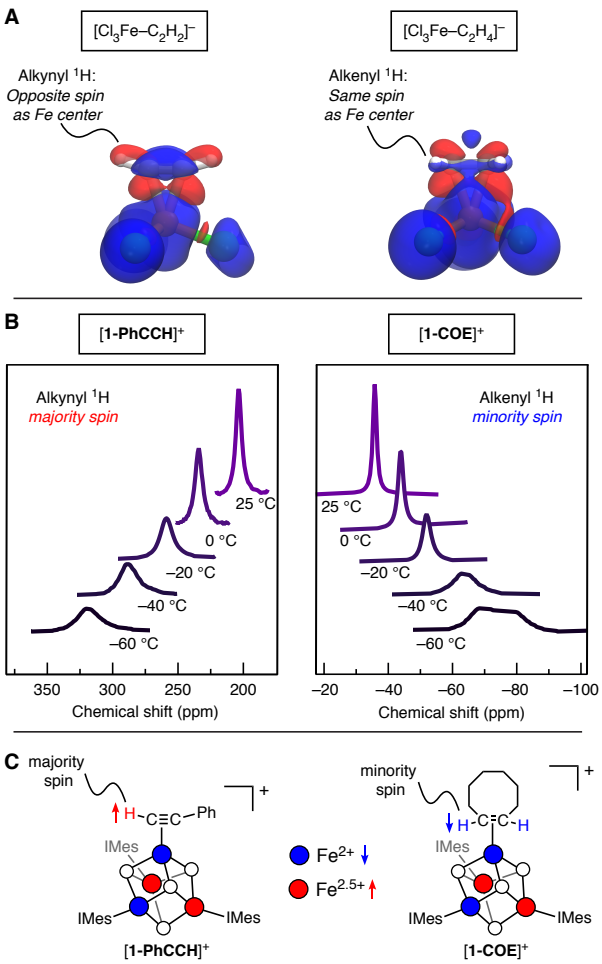

Figure 8.5. Spin density analysis of $[Cl_3Fe–L]^–$ model complexes and $[Fe_4S_4]^+$ cluster π complexes. A) Calculated spin density plots of (left) $[Cl_3Fe–C_2H_2]^–$ (0.001 au) showing β-spin density on the alkynyl H-atom and (right) $[Cl_3Fe–C_2H_4]^–$ (0.0005 au) showing α-spin density on the alkenyl H-atom. Blue is α-spin and red is β-spin. B) VT NMR spectra of (left) the alkynyl proton in [**1-PhCCH**]$^+$, demonstrating that the resonance shifts downfield with decreasing temperature and (right) the alkenyl protons in [**1-COE**]$^+$, demonstrating that the resonance shifts upfield with decreasing temperature. The change in lineshape around –60 °C is due to a decrease in molecular symmetry to C_3. C) Experimentally deduced spin densities of (left) [**1-PhCCH**]$^+$ and (right) [**1-COE**]$^+$.

temperature and the alkenyl protons in [**1-COE**]$^+$ shift upfield with decreasing temperature, we would conclude that the Fe center bears minority spin density and therefore adopts a localized Fe^{2+} valence in both clusters. [Note that in cases where there is no valence localization (all Fe centers are spin averaged to yield net majority spin) or there is localization of the majority spin $Fe^{2.5+}$ pair, we would expect the opposite trends in the ^{1}H NMR spectra.]

The chemical shift of the alkynyl proton in [**1-PhCCH**]$^+$ follows approximately Curie behavior and shifts downfield from 203 ppm at 25 ˚C to 318 ppm at –60 °C (Fig. 8.5B, left and

S19). Thus, the alkynyl proton bears positive spin density, and based on the above analysis, we conclude that the alkyne-bound Fe site bears minority spin density (Fig. 8.5C). The alkenyl protons in [**1-COE**]$^{+}$ shift in the opposite direction, moving upfield with decreasing temperature from –36 ppm at 25 °C to –73 ppm at –60 °C (Fig. 8.5B, right and S8.20). Since the alkenyl protons are expected to bear spin of the same sign as the alkene-bound Fe, this finding is likewise consistent with minority spin at the unique Fe site (Fig. 8.5C). The experimental data therefore demonstrate valence localization of Fe^{2+} at the alkyne- and alkene-bound sites in both [**1-PhCCH**]$^{+}$ and [**1-COE**]$^{+}$. Broken-symmetry density functional theory analysis on [**1-PhCCH**]$^{+}$ and [**1-COE**]$^{+}$ reveals the same sign of the spin distribution onto the alkyne/alkene ligands as observed for the mononuclear model complexes (*vide supra*) and likewise supports the favorability of localizing Fe^{2+} at the alkyne-/alkene-bound site (Fig. S8.22 and Table S8.2).

Conclusion

We reported herein the first well-defined alkyne and alkene adducts of $[Fe_4S_4]^+$ clusters. EPR spectroscopic analysis demonstrated that [**1-PhCCH**]$^+$ and [**1-COE**]$^+$, like the $[Fe_4S_4]^+$–alkyne/alkene adducts proposed in IspG and IspH, have unusual *g*-tensors, with $g_{iso} > 2$. Examination of the clusters' structural and spectroscopic properties revealed that [**1-PhCCH**]$^+$ and [**1-COE**]$^+$ are best described as $[Fe_4S_4]^{1+}$ clusters with covalent π-backbonding to alkyne/alkene ligands. The unusual *g*-tensors observed in both the synthetic and biogenic clusters likely arise from factors other than the presence of an $[Fe_4S_4]^{3+}$ cluster, such as changes in the degree of spin canting and/or changes in the local site *g*-tensors. Variable-temperature ^{1}H NMR spectroscopy revealed that binding π-accepting alkynes and alkenes to the unique Fe site of a site differentiated $[Fe_4S_4]^+$ cluster results in localization of ferrous character at the unique Fe site, and we propose this phenomenon also occurs in IspG and IspH intermediates and inhibitor-bound species, as well as in intermediates in reduction of organic substrates by nitrogenases. Lastly, we note that, in addition to being structurally faithful models for the proposed alkyne- and alkene-bound species in IspH and IspG, [**1-PhCCH**]$^+$ and [**1-COE**]$^+$ are rare examples of alkynes or alkenes bound to high-spin, formally Fe^{2+} sites.[64–66] This work therefore illustrates the utility of Fe–S clusters in studying high-spin, electron-rich Fe^{2+} sites with the ability to bind weakly donating ligands.

References

(1) Rohmer, M. From Molecular Fossils of Bacterial Hopanoids to the Formation of Isoprene Units: Discovery and Elucidation of the Methylerythritol Phosphate Pathway. *Lipids* **2008**, *43* (12), 1095–1107.

(2) Frank, A.; Groll, M. The Methylerythritol Phosphate Pathway to Isoprenoids. *Chem. Rev.* **2017**, *117* (8), 5675–5703.

(3) Wolff, M.; Seemann, M.; Tse Sum Bui, B.; Frapart, Y.; Tritsch, D.; Garcia Estrabot, A.; Rodríguez-Concepción, M.; Boronat, A.; Marquet, A.; Rohmer, M. Isoprenoid Biosynthesis via the Methylerythritol Phosphate Pathway: The (E)-4-Hydroxy-3-Methylbut-2-Enyl Diphosphate Reductase (LytB/IspH) from *Escherichia coli* Is a [4Fe-4S] Protein. *FEBS Lett.* **2003**, *541* (1–3), 115–120.

(4) Seemann, M.; Bui, B. T. S.; Wolff, M.; Tritsch, D.; Campos, N.; Boronat, A.; Marquet, A.; Rohmer, M. Isoprenoid Biosynthesis through the Methylerythritol Phosphate Pathway: The (E)4-Hydroxy-3-Methylbut-2-Enyl Diphosphate Synthase (GcpE) Is a [4Fe-4S] Protein. *Angew. Chem. Int. Ed.* **2002**, *41* (22), 4337–4339.

(5) Altincicek, B.; Duin, E. C.; Reichenberg, A.; Hedderich, R.; Kollas, A. K.; Hintz, M.; Wagner, S.; Wiesner, J.; Beck, E.; Jomaa, H. LytB Protein Catalyzes the Terminal Step of the 2-C-Methyl-D-Erythritol-4-Phosphate Pathway of Isoprenoid Biosynthesis. *FEBS Lett.* **2002**, *532* (3), 437–440.

(6) Rohmer, M.; Grosdemange Billiard, C.; Seemann, M.; Tritsch, D. Isoprenoid Biosynthesis as a Novel Target for Antibacterial and Antiparasitic Drugs. *Curr. Opin. Investig. Drugs* **2004**, *5* (2), 154–162.

(7) Wang, K.; Wang, W.; No, J. H.; Zhang, Y.; Zhang, Y.; Oldfield, E. Inhibition of the Fe_4S_4-Cluster-Containing Protein IspH (LytB): Electron Paramagnetic Resonance, Metallacycles, and Mechanisms. *J. Am. Chem. Soc.* **2010**, *132* (19), 6719–6727.

(8) Van Hoof, S.; Lacey, C. J.; Röhrich, R. C.; Wiesner, J.; Jomaa, H.; Van Calenbergh, S. Synthesis of Analogues of (E)-1-Hydroxy-2-Methylbut-2-Enyl 4-Diphosphate, an Isoprenoid Precursor and Human Γδ T Cell Activator. *J. Org. Chem.* **2008**, *73* (4), 1365–1370.

(9) Ahrens-Botzong, A.; Janthawornpong, K.; Wolny, J. A.; Tambou, E. N.; Rohmer, M.; Krasutsky, S.; Poulter, C. D.; Schünemann, V.; Seemann, M. Biosynthesis of Isoprene Units: Mössbauer Spectroscopy of Substrate and Inhibitor Binding to the [4Fe-4S] Cluster of the LytB/IspH Enzyme. *Angew. Chem. Int. Ed.* **2011**, *50* (50), 11976–11979.

(10) Wang, W.; Wang, K.; Liu, Y. L.; No, J. H.; Li, J.; Nilges, M. J.; Oldfield, E. Bioorganometallic Mechanism of Action, and Inhibition, of IspH. *Proc. Natl. Acad. Sci. U. S. A.* **2010**, *107* (10), 4522–4527.

(11) Wang, W.; Li, J.; Wang, K.; Huang, C.; Zhang, Y.; Oldfield, E. Organometallic Mechanism of Action and Inhibition of the 4Fe-4S Isoprenoid Biosynthesis Protein GcpE (IspG). *Proc. Natl. Acad. Sci. U. S. A.* **2010**, *107* (25), 11189–11193.

(12) Wang, W.; Oldfield, E. Bioorganometallic Chemistry with IspG and IspH: Structure, Function, and Inhibition of the [Fe_4S_4] Proteins Involved in Isoprenoid Biosynthesis. *Angew. Chem. Int. Ed.* **2014**, *53* (17), 4294–4310.

(13) Wang, W.; Wang, K.; Span, I.; Jauch, J.; Bacher, A.; Groll, M.; Oldfield, E. Are Free Radicals Involved in IspH Catalysis? An EPR and Crystallographic Investigation. *J. Am. Chem. Soc.* **2012**, *134* (27), 11225–11234.

(14) Span, I.; Wang, K.; Eisenreich, W.; Bacher, A.; Zhang, Y.; Oldfield, E.; Groll, M. Insights into the Binding of Pyridines to the Iron-Sulfur Enzyme IspH. *J. Am. Chem. Soc.* **2014**, *136* (22), 7926–7932.

(15) Guerra, F.; Wang, K.; Li, J.; Wang, W.; Liu, Y. L.; Amin, S.; Oldfield, E. Inhibition of the 4Fe-4S Proteins IspG and IspH: An EPR, ENDOR and HYSCORE Investigation. *Chem. Sci.* **2014**, *5* (4), 1642–1649.
(16) Xu, W.; Lees, N. S.; Hall, D.; Welideniya, D.; Hoffman, B. M.; Duin, E. C. A Closer Look at the Spectroscopic Properties of Possible Reaction Intermediates in Wild-Type and Mutant (E)-4-Hydroxy-3-Methylbut-2-Enyl Diphosphate Reductase. *Biochemistry* **2012**, *51* (24), 4835–4849.
(17) Xu, W.; Lees, N. S.; Adedeji, D.; Wiesner, J.; Jomaa, H.; Hoffman, B. M.; Duin, E. C. Paramagnetic Intermediates of (E)-4-Hydroxy-3-Methylbut-2-Enyl Diphosphate Synthase (GcpE/IspG) under Steady-State and Pre-Steady-State Conditions. *J. Am. Chem. Soc.* **2010**, *132* (41), 14509–14520.
(18) Adedeji, D.; Hernandez, H.; Wiesner, J.; Köhler, U.; Jomaa, H.; Duin, E. C. Possible Direct Involvement of the Active-Site [4Fe-4S] Cluster of the GcpE Enzyme from *Thermus thermophilus* in the Conversion of MEcPP. *FEBS Lett.* **2007**, *581* (2), 279–283.
(19) Wang, W.; Wang, K.; Li, J.; Nellutla, S.; Smirnova, T. I.; Oldfield, E. An ENDOR and HYSCORE Investigation of a Reaction Intermediate in IspG (GcpE) Catalysis. *J. Am. Chem. Soc.* **2011**, *133* (22), 8400–8403.
(20) Liu, Y. L.; Guerra, F.; Wang, K.; Wang, W.; Li, J.; Huang, C.; Zhu, W.; Houlihan, K.; Li, Z.; Zhang, Y.; Nair, S. K.; Oldfield, E. Structure, Function and Inhibition of the Two- and Three-Domain 4Fe-4S IspG Proteins. *Proc. Natl. Acad. Sci. U. S. A.* **2012**, *109* (22), 8558–8563.
(21) Li, J.; Wang, K.; Smirnova, T. I.; Khade, R. L.; Zhang, Y.; Oldfield, E. Isoprenoid Biosynthesis: Ferraoxetane or Allyl Anion Mechanism for IspH Catalysis? *Angew. Chem. Int. Ed.* **2013**, *52* (25), 6522–6525.
(22) Middleton, P.; Dickson, D. P. E.; Johnson, C. E.; Rush, J. D. Interpretation of the Mössbauer Spectra of the Four-Iron Ferredoxin from *Bacillus stearothermophilus*. *Eur. J. Biochem.* **1978**, *88* (1), 135–141.
(23) Mouesca, J. M.; Lamotte, B. Iron-Sulfur Clusters and Their Electronic and Magnetic Properties. *Coord. Chem. Rev.* **1998**, *178–180* (Part 2), 1573–1614.
(24) Shriver, D. F.; Atkins, P.; Langford, C. H. *Inorganic Chemistry*, 2nd.; Oxford University Press, 1994.
(25) Chatt, J.; Duncanson, L. A. Olefin Co-Ordination Compounds. Part III. Infra-Red Spectra and Structure: Attempted Preparation of Acetylene Complexes. *J. Chem. Soc.* **1953**, 2939–2947.
(26) Itoh, T.; Nagano, T.; Hirobe, M. The $[Fe_4S_4(SR)_4]^{2-}$ Catalytic Reduction of Diphenylacetylene to Cis-Stilbene in the Presence of $NaBH_4$. *Tetrahedron Lett.* **1980**, *21* (14), 1343–1346.
(27) McMillan, R. S.; Renaud, J.; Reynolds, J. G.; Holm, R. H. Biologically Related Iron-Sulfur Clusters as Reaction Centers. Reduction of Acetylene to Ethylene in Systems Based on $[Fe_4S_4(SR)_4]^{3-}$. *J. Inorg. Biochem.* **1979**, *11* (3), 213–227.
(28) Tanaka, K.; Nakamoto, M.; Tsunomori, M.; Tanaka, T. Raman Spectra of the Adducts of Reduced Species of $[Fe_4S_4(SPh)_4]^{2-}$ and $[Mo_2Fe_6S_8(SPh)_9]^{3-}$ with Acetylene. *Chem. Lett.* **1987**, 613–616.
(29) Lee, H. I.; Igarashi, R. Y.; Laryukhin, M.; Doan, P. E.; Dos Santos, P. C.; Dean, D. R.; Seefeld, L. C.; Hoffman, B. M. An Organometallic Intermediate during Alkyne Reduction by Nitrogenase. *J. Am. Chem. Soc.* **2004**, *126* (31), 9563–9569.
(30) Seefeldt, L. C.; Yang, Z. Y.; Duval, S.; Dean, D. R. Nitrogenase Reduction of Carbon-Containing Compounds. *Biochim. Biophys. Acta - Bioenerg.* **2013**, *1827* (8–9), 1102–1111.

(31) Smallcombe, S. H.; Patt, S. L.; Keifer, P. A. WET Solvent Suppression and Its Applications to LC NMR and High-Resolution NMR Spectroscopy. *J. Magn. Reson. Ser. A* **1995**, *117* (2), 295–303.
(32) Stoll, S.; Schweiger, A. EasySpin, a Comprehensive Software Package for Spectral Simulation and Analysis in EPR. *J. Magn. Reson.* **2006**, *178* (1), 42–55.
(33) Prisecaru, I. WMOSS4 Mössbauer Spectral Analysis Software, www.wmoss.org.
(34) Hübschle, C. B.; Sheldrick, G. M.; Dittrich, B. ShelXle: A Qt Graphical User Interface for SHELXL. *J. Appl. Crystallogr.* **2011**, *44* (6), 1281–1284.
(35) Brown, A. C.; Suess, D. L. M. Controlling Substrate Binding to Fe_4S_4 Clusters through Remote Steric Effects. *Inorg. Chem.* **2019**, *58* (8), 5273–5280.
(36) Peters, J. C.; Johnson, A. R.; Odom, A. L.; Wanandi, P. W.; Davis, W. M.; Cummins, C. C. Assembly of Molybdenum/Titanium μ-Oxo Complexes via Radical Alkoxide C-O Cleavage. *J. Am. Chem. Soc.* **1996**, *118* (42), 10175–10188.
(37) Yakelis, N. A.; Bergman, R. G. Safe Preparation and Purification of Sodium Tetrakis[(3,5-Trifluoromethyl)Phenyl]Borate ($NaBArF_{24}$): Reliable and Sensitive Analysis of Water in Solutions of Fluorinated Tetraarylborates. *Organometallics* **2005**, *24* (14), 3579–3581.
(38) Chávez, I.; Alvarez-Carena, A.; Molins, E.; Roig, A.; Maniukiewicz, W.; Arancibia, A.; Arancibia, V.; Brand, H.; Manuel Manríquez, J. Selective Oxidants for Organometallic Compounds Containing a Stabilising Anion of Highly Reactive Cations: $(3,5(CF_3)_2C_6H_3)_4B^-)Cp_2Fe^+$ and $(3,5(CF_3)_2C_6H_3)_4B^-)Cp^*_2Fe^+$. *J. Organomet. Chem.* **2000**, *601* (1), 126–132.
(39) Brown, A. C.; Suess, D. L. M. Reversible Formation of Alkyl Radicals at $[Fe_4S_4]$ Clusters and Its Implications for Selectivity in Radical SAM Enzymes. *J. Am. Chem. Soc.* **2020**, *142* (33), 14240–14248.
(40) Sridharan, A.; Brown, A. C.; Suess, D. L. M. A Terminal Imido Complex of an Iron–Sulfur Cluster. *Angew. Chem. Int. Ed.* **2021**, *60* (23), 12802–12806.
(41) McSkimming, A.; Suess, D. L. M. Dinitrogen Binding and Activation at a Molybdenum–Iron–Sulfur Cluster. *Nat. Chem.* **2021**, *13* (7), 666–670.
(42) Kuveke, R. E. H.; Barwise, L.; Ingen, Y. Van; Vashisth, K.; Roberts, N.; Chitnis, S. S.; Dutton, J. L.; Martin, C. D.; Melen, R. L. An International Study Evaluating Elemental Analysis. *ChemRxiv* **2022**, 10.26434/chemrxiv-2022-k5xvx.
(43) Anslyn, E. V.; Dougherty, D. A. *Modern Physical Organic Chemistry*, 1st ed.; University Science Books, 2006.
(44) Stoian, S. A.; Yu, Y.; Smith, J. M.; Holland, P. L.; Bominaar, E. L.; Munck, E. Mössbauer, Electron Paramagnetic Resonance, and Crystallographic Characterization of a High-Spin Fe(I) Diketiminate Complex with Orbital Degeneracy. *Inorg. Chem.* **2005**, *44* (14), 4915–4922.
(45) Yu, Y.; Smith, J. M.; Flaschenriem, C. J.; Holland, P. L. Binding Affinity of Alkynes and Alkenes to Low-Coordinate Iron. *Inorg. Chem.* **2006**, *45* (15), 5742–5751.
(46) Nieto, I.; Ding, F.; Bontchev, R. P.; Wang, H.; Smith, J. M. Thermodynamics of Hydrogen Atom Transfer to a High-Valent Iron Imido Complex. *J. Am. Chem. Soc.* **2008**, *130* (9), 2716–2717.
(47) Mock, M. T.; Popescu, C. V.; Yap, G. P. A.; Dougherty, W. G.; Riordan, C. G. Monovalent Iron in a Sulfur-Rich Environment. *Inorg. Chem.* **2008**, *47* (6), 1889–1891.
(48) Müller, I.; Munz, D.; Werncke, C. G. Reactions of Alkynes with Quasi-Linear 3d Metal(I) Silylamides of Chromium to Cobalt: A Comparative Study. *Inorg. Chem.* **2020**, *59* (14), 9521–9537.
(49) Lutz, S. A.; Hickey, A. K.; Gao, Y.; Chen, C. H.; Smith, J. M. Two-State Reactivity in

Iron-Catalyzed Alkene Isomerization Confers σ-Base Resistance. *J. Am. Chem. Soc.* **2020**, *142* (36), 15527–15535.
(50) Ott, J. C.; Wadepohl, H.; Gade, L. H. Metalloradical Reactivity, Charge Transfer, and Atom Abstractions in a T-Shaped Iron(I) Complex. *Inorg. Chem.* **2021**, *60* (6), 3927–3938.
(51) Weller, R.; Müller, I.; Duhayon, C.; Sabo-Etienne, S.; Bontemps, S.; Werncke, C. G. Quasilinear 3d-Metal(I) Complexes [KM(N(Dipp)SiR_3)$_2$] (M = Cr-Co) - Structural Diversity, Solution State Behaviour and Reactivity. *Dalton Trans.* **2021**, *50* (14), 4890–4903.
(52) Richards, C. A.; Rath, N. P.; Neely, J. M. Iron-Catalyzed Alkyne Carboamination via an Isolable Iron Imide Complex. *Organometallics* **2021**, *40* (17), 2945–2950.
(53) Bai, G.; Wei, P.; Das, A. K.; Stephan, D. W. P–H and P–P Bond Activation by Ni(I) and Fe(I) β-Diketiminato-Complexes. *J. Chem. Soc. Dalt. Trans.* **2006**, *60* (99), 11411141–11461146.
(54) Horitani, M.; Grubel, K.; McWilliams, S. F.; Stubbert, B. D.; Mercado, B. Q.; Yu, Y.; Gurubasavaraj, P. M.; Lees, N. S.; Holland, P. L.; Hoffman, B. M. ENDOR Characterization of an Iron-Alkene Complex Provides Insight into a Corresponding Organometallic Intermediate of Nitrogenase. *Chem. Sci.* **2017**, *8* (9), 5941–5948.
(55) Tan, L. L.; Holm, R. H.; Lee, S. C. Structural Analysis of Cubane-Type Iron Clusters. *Polyhedron* **2013**, *58*, 206–217.
(56) Venkateswara Rao, P.; Holm, R. H. Synthetic Analogues of the Active Sites of Iron−Sulfur Proteins. *Chem. Rev.* **2004**, *104* (2), 527–560.
(57) Noodleman, L.; Peng, C. Y.; Case, D. A.; Mouesca, J. M. Orbital Interactions, Electron Delocalization and Spin Coupling in Iron-Sulfur Clusters. *Coord. Chem. Rev.* **1995**, *144* (C), 199–244.
(58) Ye, M.; Thompson, N. B.; Brown, A. C.; Suess, D. L. M. A Synthetic Model of Enzymatic [Fe_4S_4]-Alkyl Intermediates. *J. Am. Chem. Soc.* **2019**, *141* (34), 13330–13335.
(59) McSkimming, A.; Sridharan, A.; Thompson, N. B.; Müller, P.; Suess, D. L. M. An [Fe_4S_4]$^{3+}$-Alkyl Cluster Stabilized by an Expanded Scorpionate Ligand. *J. Am. Chem. Soc.* **2020**, *142* (33), 14314–14323.
(60) Bertini, I.; Luchinat, C. NMR of Paramagnetic Substances. *Coord. Chem. Rev.* **1996**, *150*, 1–292.
(61) Bertini, I.; Briganti, F.; Scozzafava, A.; Luchinat, C.; Sola, M. 1H NMR Spectroscopy and the Electronic Structure of the High Potential Iron-Sulfur Protein from *Chromatium vinosum*. *J. Am. Chem. Soc.* **1991**, *113* (4), 1237–1245.
(62) Banci, L.; Bertini, I.; Briganti, F.; Scozzafava, A.; O1iver, M. V.; Luchinat, C. 1H NMR Spectra of Oxidized High-Potential Iron-Sulfur Protein (HiPIP) from *Rhodocyclus gelatinosus*. A Model for Oxidized HiPIPs. *Inorg. Chem.* **1991**, *30* (24), 4517–4524.
(63) Banci, L.; Bertini, I.; Piccioli, M.; Ciurli, S.; Ferretti, S.; Luchinat, C. The Electronic Structure of [Fe_4S_4]$^{3+}$ Clusters in Proteins. An Investigation of the Oxidized High-Potential Iron-Sulfur Protein II from *Ectothiorhodospira vacuolata*. *Biochemistry* **1993**, *32* (36), 9387–9397.
(64) Bloch, E. D.; Queen, W. L.; Krishna, R.; Zadrozny, J. M.; Brown, C. M.; Long, J. R. Hydrocarbon Separations in a Metal-Organic Framework with Open Iron(II) Coordination Sites. *Science* **2012**, *335* (6076), 1606–1610.
(65) MacLeod, K. C.; McWilliams, S. F.; Mercado, B. Q.; Holland, P. L. Stepwise N-H Bond Formation from N2-Derived Iron Nitride, Imide and Amide Intermediates to Ammonia. *Chem. Sci.* **2016**, *7* (9), 5736–5746.

(66) King, A. K.; Gallagher, K. J.; Mahon, M. F.; Webster, R. L. Markovnikov versus Anti-Markovnikov Hydrophosphination: Divergent Reactivity Using an Iron(II) β-Diketiminate Pre-Catalyst. *Chem. Eur. J.* **2017**, *23* (38), 9039–9043.

Supporting information

General Considerations

All reactions were performed using standard Schlenk techniques or in an LC Technologies inert atmosphere glove box under an N_2 atmosphere. Glassware was dried in an oven at 160 °C prior to use. Molecular sieves (3 Å), and Celite® were activated by heating to 300 °C overnight under vacuum prior to storage under an atmosphere of nitrogen. *O*-difluorobenzene (DFB) was distilled from CaH_2, C_6D_6 was degassed by three freeze–pump–thaw cycles, and other solvents were degassed by sparging with argon and dried by passing through a column of activated alumina. All solvents were stored under an N_2 atmosphere over 3 Å molecular sieves.

NMR spectra were recorded on Bruker 400 and 500 MHz spectrometers. ^1H chemical shifts are given relative to residual solvent peaks; spectra in Et_2O and DFB are referenced to the triplet of residual *n*-pentane at 0.89 ppm. Solvent suppression for NMR in protonated solvents was carried out using WET solvent suppression.[31] FT-IR samples were taken as thin films using a Bruker Alpha Platinum ATR spectrometer with OPUS software in a glovebox under an N_2 atmosphere. EPR spectra were recorded on a Bruker EMX spectrometer at 9.37 GHz as frozen glasses. Simulations were performed using EasySpin[32] (5.2.21) in Matlab (R2017b). UV-vis spectra were recorded on a Cary 50 spectrometer. Zero-field ^{57}Fe Mössbauer spectra were measured with a constant-acceleration spectrometer at 150 K. Isomer shifts are quoted relative to α-Fe foil at room temperature. Mössbauer spectra were simulated with WMOSS v.4.[33] Elemental analyses were performed at Midwest Microlab. X-ray structural determinations were performed at the MIT diffraction facility using a Bruker X8 diffractometer with an APEX II CCD detector or a Bruker D8 Venture diffractometer with a Photon2 CPAD detector. Diffraction data was collected, integrated, and corrected for absorption using Bruker APEX3 software and its associated modules (SAINT, SADABS, TWINABS). Structural

solutions and refinements (on F^2) were carried out using SHELXT and SHELXL-2018 in ShelXle.[34] Ellipsoid plots and figures were made using Mercury 2021.2.0.

$(IMes)_3Fe_4S_4Cl$,[35] $Ti(N[^tBu]Ar)_3$,[36] $Na[BAr^F{}_4]$,[37] and $[Cp_2Fe][BAr^F{}_4]$[38] were prepared according to literature procedures. [**1-OEt$_2$**][$BAr^F{}_4$] was prepared by a modification of the literature procedure (*vide infra*).[39] Phenylacetylene (PhCCH) and *cis*-cyclooctene (COE) were degassed by three freeze-pump-thaw cycles.

Statement on Compound Purity

The purity of all compounds was assessed by a variety of spectroscopic and analytical methods as detailed below. Compounds [**1-Cl**]$^+$, [**1-PhCCH**]$^+$, and [**1-COE**]$^+$ are air-sensitive but can be isolated as crystalline solids in high purity as determined by NMR, EPR, and Mössbauer spectroscopic analysis (see Fig. 8.3 and the SI) as well as H and N content from elemental analysis; low C content was obtained by elemental analysis as has been observed for other members of this class of molecules[40,41] and in other contexts.[42] Elemental analysis results are as follows: [**1-Cl**][$BAr^F{}_4$]: Anal. Found: C, 51.84; H, 4.04; N, 4.19. Calcd. for $C_{95}H_{84}N_6Fe_4S_4BF_{24}Cl$: C, 52.74; H, 3.91; N, 3.88; [**1-PhCCH**][$BAr^F{}_4$]: Anal. Found: C, 51.09; H, 4.05; N, 3.72. Calcd. for $C_{103}H_{90}N_6Fe_4S_4BF_{24}$: C, 55.47; H, 4.07; N, 3.77; [**1-COE**][$BAr^F{}_4$]: Anal. Found: C, 54.34; H, 4.82; N, 3.92. Calcd. for $C_{103}H_{98}N_6Fe_4S_4BF_{24}$: C, 55.27; H, 4.41; N, 3.75. ^{1}H NMR spectra for [**1-PhCCH**]$^+$ and [**1-COE**]$^+$ are reported in both DFB and Et_2O because in DFB the solvent resonances from DFB obscure some of the aryl resonances of [**1-PhCCH**]$^+$ and [**1-COE**]$^+$, whereas in Et_2O both [**PhCCH**]$^+$ and [**1-COE**]$^+$ exist in equilibrium with [**1-OEt$_2$**]$^+$ in the absence of excess PhCCH or COE. As such, the ^{1}H NMR spectra in DFB demonstrate that as-prepared [**1-PhCCH**]$^+$ and [**1-COE**]$^+$ are pure and free of [**1-OEt$_2$**]$^+$, and the ^{1}H NMR spectra in Et_2O allow the aryl resonances to be assigned. In combination, the spectra support the purity and NMR assignments of [**1-PhCCH**]$^+$ and [**1-COE**]$^+$.

$[(IMes)_3Fe_4S_4Cl][BAr^F{}_4]$ ($[\mathbf{1\text{-}Cl}]^+$):

$(IMes)_3Fe_4S_4Cl$ (500 mg, 0.385 mmol) was suspended in 5 mL Et_2O. A solution of $[Cp_2Fe][BAr^F{}_4]$ (403 mg, 0.385 mmol, 1 equiv.) in 5 mL Et_2O was added dropwise. The mixture was stirred for 5 min and concentrated to 2 mL. The product was precipitated upon addition of *n*-pentane (15 mL). The solids were collected on a frit and washed thoroughly with *n*-pentane (3 x 5 mL) to remove Cp_2Fe. Yield: 722 mg (87%). ^{1}H NMR (400 MHz, Et_2O, 293 K) δ 7.77 (s, 8H, $[BAr^F{}_4]^-$), 7.51 (s, 4H, $[BAr^F{}_4]^-$), 7.00 (s, 6H, backbone C*H*), 6.91 (s, 12H, Mes *m*-C*H*), 2.39 (s, 18H, Mes *p*-C*H*$_3$), 2.16 (s, 36H, Mes *o*-C*H*$_3$). Crystals suitable for X-ray diffraction were grown by layering *n*-pentane onto a solution of [**1-Cl**][$BAr^F{}_4$] in Et_2O and storage at –35 °C overnight.

$[(IMes)_3Fe_4S_4(OEt_2)][BAr^F{}_4]$ ($[\mathbf{1\text{-}OEt_2}]^+$):

The preparation reported here is a modification of previously reported procedures.[35,39] $[(IMes)_3Fe_4S_4Cl][BAr^F{}_4]$ (148 mg, 0.068 mmol) was dissolved in 2 mL Et_2O. A solution of $Ti(N[^tBu]Ar)_3$ (79 mg, 0.136 mmol) in 2 mL Et_2O was added dropwise. The solution was concentrated to 0.5 mL and *n*-pentane (10 mL) was added to precipitate the product. The precipitate was collected and recrystallized from Et_2O/*n*-pentane a second time. Yield: 126 mg (84%). Spectroscopic data were consistent with previous reports.[35]

$[(IMes)_3Fe_4S_4(PhCCH)][BAr^F{}_4]$ ($[\mathbf{1\text{-}PhCCH}]^+$):

$[(IMes)_3Fe_4S_4(OEt_2)][BAr^F{}_4]$ (77 mg, 0.035 mmol) was dissolved in 1 mL Et_2O. An excess (ca. 100 mg) of PhCCH was added. The product was precipitated with *n*-pentane and recrystallized from Et_2O/*n*-pentane in the presence of excess (ca. 1 mM) PhCCH. Yield: 78 mg (99 %). ^{1}H NMR (400 MHz, DFB, 293 K) δ 203 (s, 1H, PhCC*H*), 10.84 (s, 2H, PhCCH *o*-H), 8.82 (t, 1H, PhCCH *p*-H), 8.77 (d, 2H, PhCCH *m*-H), 8.29 (s, 8H, $[BAr^F{}_4]^-$), 7.65 (s, 4H, $[BAr^F{}_4]^-$), 2.47

(s, 18H, Mes *p*-C*H*$_3$), 2.39 (br s, 36H, Mes *o*-C*H*$_3$). IMes aryl resonances are obscured by overlap with DFB resonances. ^{1}H NMR (400 MHz, Et_2O, 293 K, recorded in the presence of excess PhCCH to prevent formation of [**1-OEt$_2$**]$^+$) δ 200 (s, 1H, PhCC*H*), 10.71 (s, 2H, PhCCH *o*-H), 8.74 (t, 1H, PhCCH *p*-H), 8.67 (d, 2H, PhCCH *m*-H), 7.75 (s, 8H, [BAr$^F_4$]$^-$), 7.50 (s, 4H, [BAr$^F_4$]$^-$), 7.28 (s, 6H, backbone C*H*), 6.98 (s, 12H, Mes *m*-C*H*) 2.42 (s, 18H, Mes *p*-C*H*$_3$), 2.37 (br s, 36H, Mes *o*-C*H*$_3$). EPR: $g_1 = 2.184$, $g_2 = 2.017$, $g_3 = 1.996$ (15 K, 63 μW, 9.37 GHz). FT-IR (thin film, cm^{-1}): 1812 (C≡C stretch). This compound was crystallized as the triflate salt by addition of an excess of PhCCH to a solution of [(IMes)$_3$Fe$_4$S$_4$(THF)][OTf][39] in THF followed by vapor diffusion of *n*-pentane into the THF solution at room temperature overnight.

[(IMes)$_3$Fe$_4$S$_4$(C_8H_{14})][BAr$^F_4$] ([**1-COE**]$^+$):

[(IMes)$_3$Fe$_4$S$_4$(OEt_2)][BAr$^F_4$] (77 mg, 0.035 mmol) was dissolved in 1 mL Et_2O. An excess (ca. 100 mg) of COE was added. The product was precipitated with *n*-pentane and recrystallized from Et_2O/*n*-pentane in the presence of excess (ca. 1 mM) COE. Yield: 56 mg (72 %). ^{1}H NMR (400 MHz, DFB, 293 K, recorded in the presence of excess COE) δ 13.31 (s, 2H, C_8H_{14}), 8.29 (s, 8H, [BAr$^F_4$]$^-$), 7.65 (s, 4H, [BAr$^F_4$]$^-$), 7.44 (s, 2H, C_8H_{14}), 7.29 (s, 6H, backbone C*H*), 6.52 (s, 2H, C_8H_{14}), 3.17 (s, 2H, C_8H_{14}), 2.78 (s, 2H, C_8H_{14}) 2.50 (s, 18H, Mes *p*-C*H*$_3$), 2.44 (br s, 36H, Mes *o*-C*H*$_3$), 1.82 (s, 2H, C_8H_{14}), –35.8 (s, 2H, C_8H_{14}). IMes *m*-H resonances are obscured by overlap with DFB resonances. ^{1}H NMR (400 MHz, Et_2O, 293 K, recorded in the presence of excess cyclooctene, [**1-OEt$_2$**]$^+$ is present due to an equilibrium between Et_2O and COE coordination in Et_2O solutions) δ 13.36 (s, 2H, C_8H_{14}), 7.74 (s, 8H, [BAr$^F_4$]$^-$), 7.65 (s, 6H, backbone C*H*), 7.57 (br s, 2H, C_8H_{14}, overlaps with [BAr$^F_4$]$^-$ resonances), 7.49 (s, 4H, [BAr$^F_4$]$^-$), 7.04 (s, 12H, IMes *m*-H), 6.46 (s, 2H, C_8H_{14}), 3.12 (s, 2H, C_8H_{14}), 2.70 (s, 2H, C_8H_{14}) 2.48 (s, 18H, Mes *p*-C*H*$_3$), 2.40 (br s, 36H, Mes *o*-C*H*$_3$), 1.68 (s, 2H, C_8H_{14}), –36.4 (s, 2H, C_8H_{14}). EPR: $g_1 = 2.175$, $g_2 = 2.011$, $g_3 = 1.992$ (15K, 16 μW, 9.37 GHz). Crystals suitable for

X-ray diffraction were grown by layering *n*-pentane onto a solution of [**1-COE**][BAr^F_4] in Et_2O and storage at –35 °C overnight.

A. NMR spectra

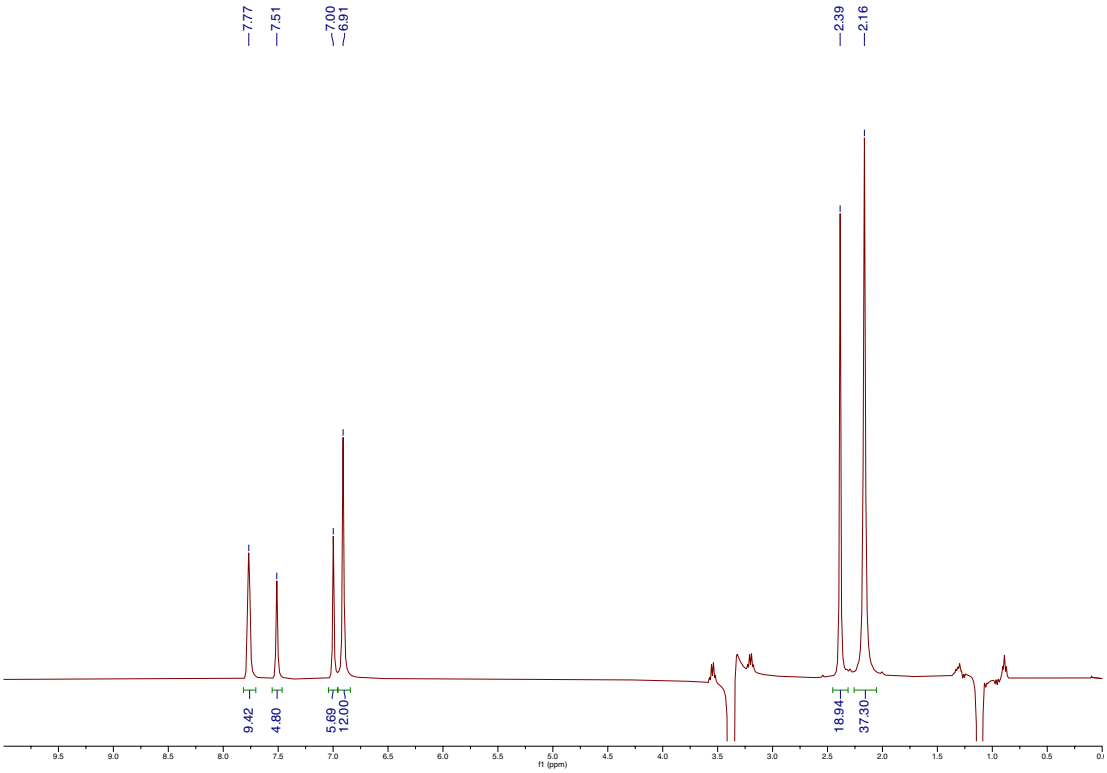

Figure S8.1: ^{1}H NMR spectrum of $[(IMes)_3Fe_4S_4Cl][BAr^F{}_4]$ in Et_2O at 293 K.

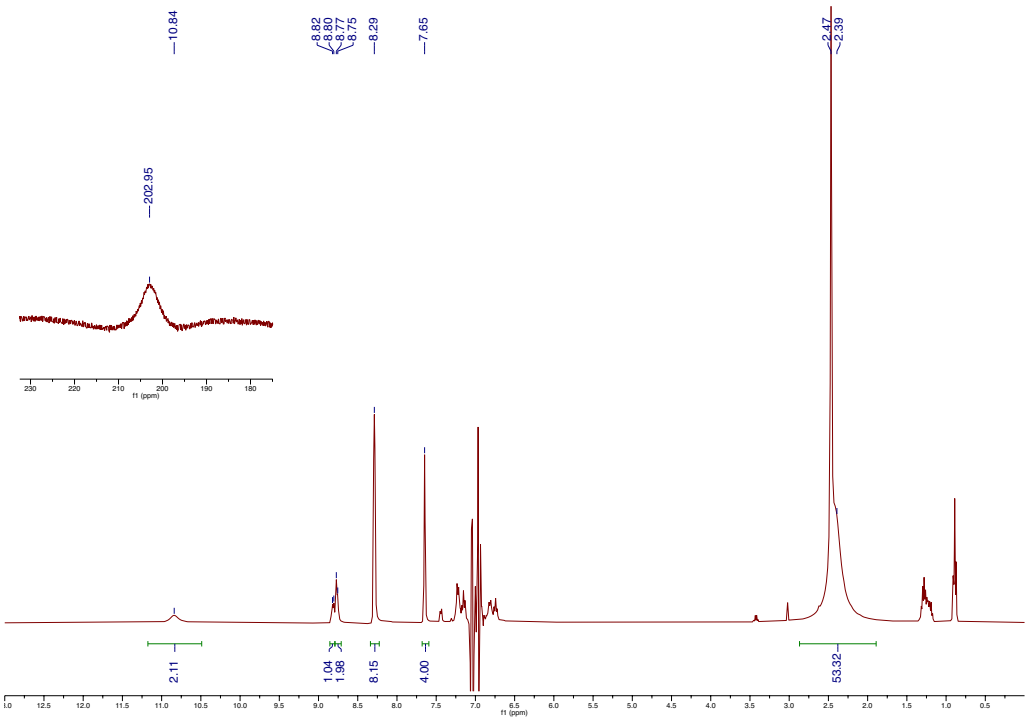

Figure S8.2: ^{1}H NMR spectrum of [**1-PhCCH**]$^{+}$ in DFB at 293 K. The region between 6.6 and 7.3 ppm contains two IMes resonances that are obscured by suppressed DFB resonances.

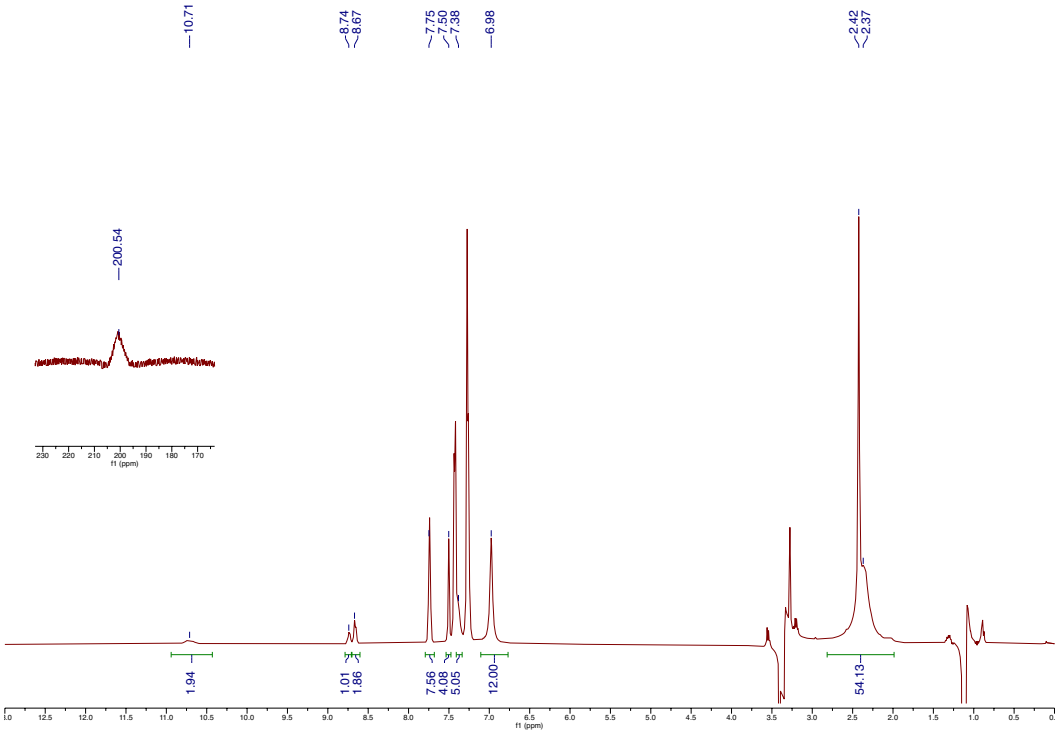

Figure S8.3: ^{1}H NMR spectrum of [**1-PhCCH**]$^{+}$ in Et_2O at 293 K. The NMR was recorded in the presence of excess PhCCH to prevent formation of $[(IMes)_3Fe_4S_4(Et_2O)][BAr^F{}_4]$.

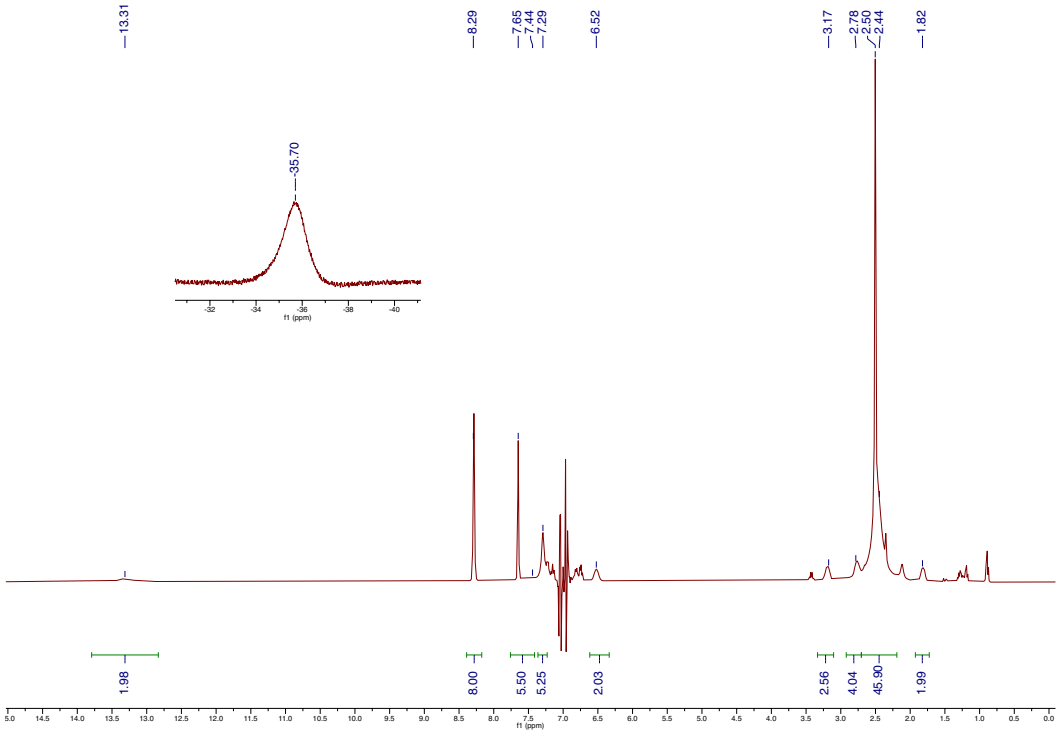

Figure S8.4: ^{1}H NMR spectrum of [**1-COE**]$^{+}$ in DFB at 293 K. The region between 6.6 and 7.3 ppm contains one IMes resonance that is obscured by suppressed DFB resonances.

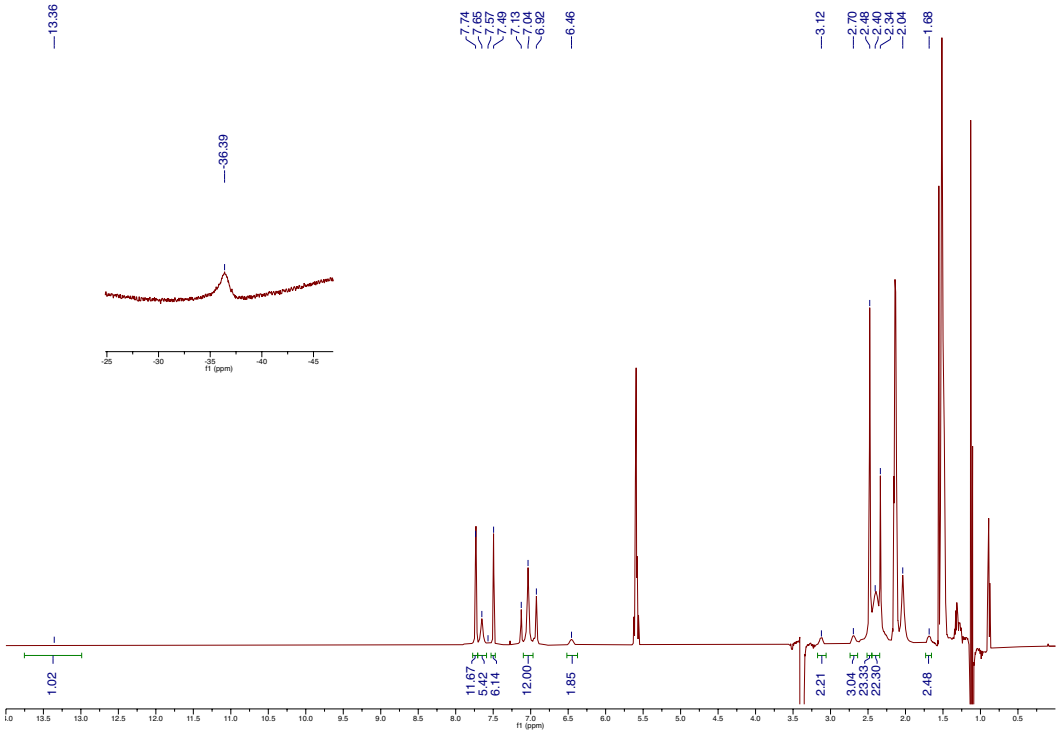

Figure S8.5: ^{1}H NMR spectrum of [**1-COE**]$^{+}$ in Et_2O at 293 K. The NMR spectrum was recorded in the presence of excess cyclooctene to limit formation of [**1-OEt$_2$**]$^{+}$. Even in the presence of excess cyclooctene, [**1-OEt$_2$**]$^{+}$ is present (peaks at 7.13, 6.92, 2.34 and 2.04 ppm).

B. IR spectra

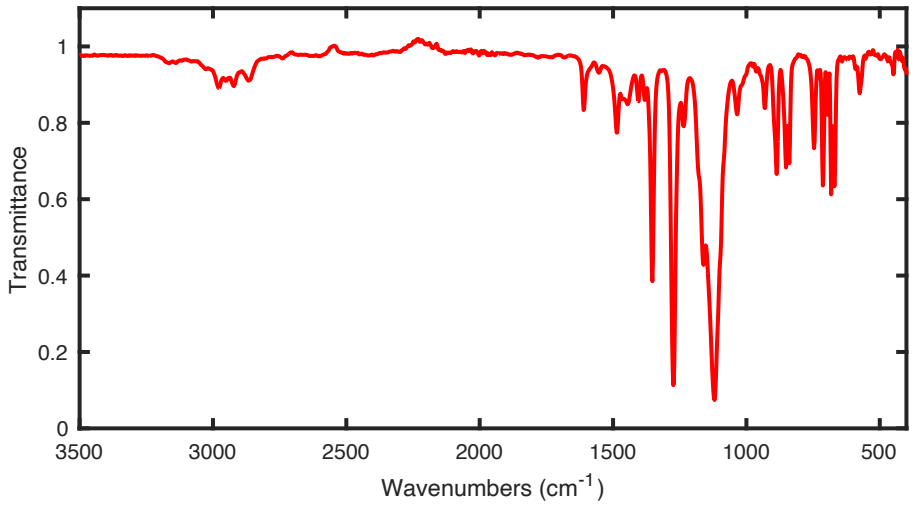

Figure S8.6: IR spectrum of [**1-Cl**]$^+$

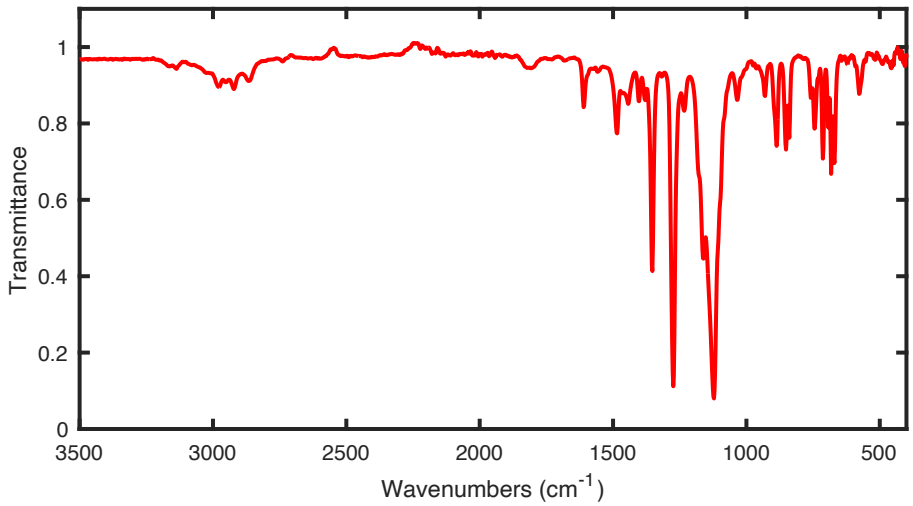

Figure S8.7: IR spectrum of [**1-PhCCH**]$^+$

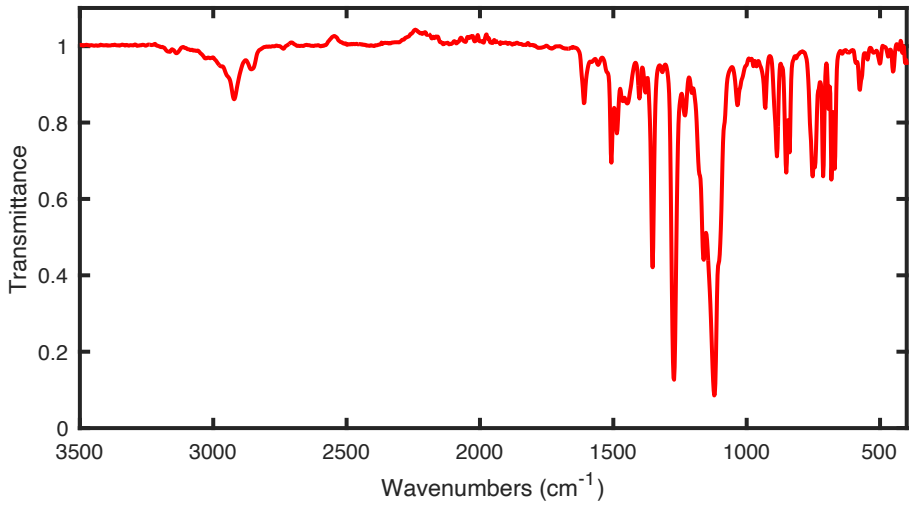

Figure S8.8: IR spectrum of [**1-COE**]$^+$

C. UV-vis spectra

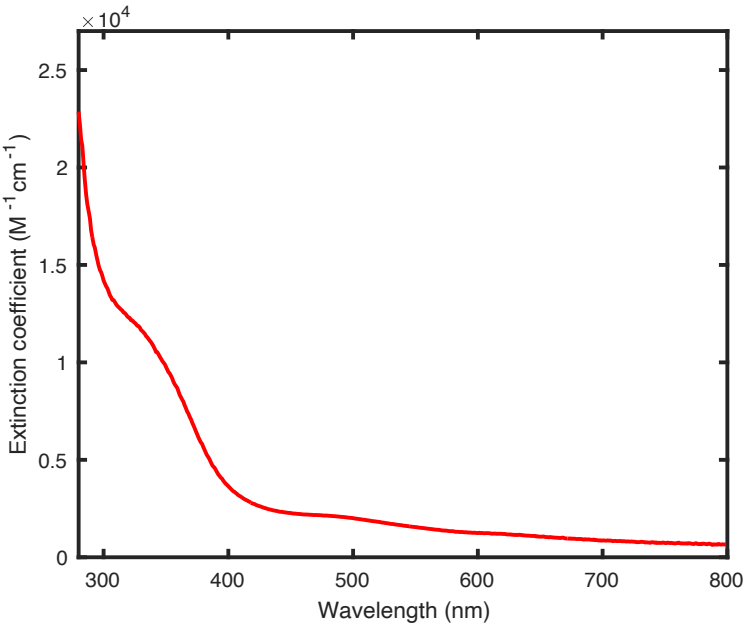

Figure S8.11: UV-vis spectrum of [**1-Cl**]$^+$ in THF.

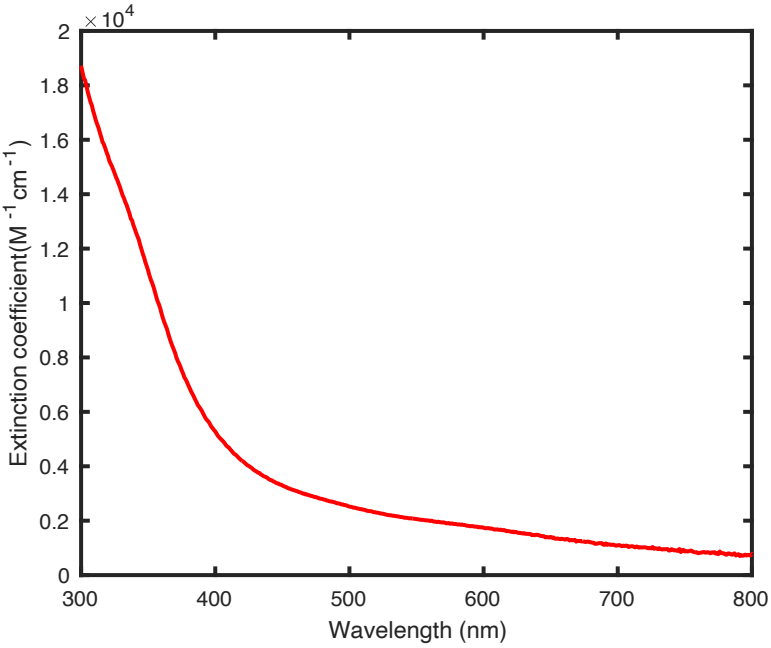

Figure S8.12: UV-vis spectrum of [**1-PhCCH**]$^+$ in DFB with 0.1 mM PhCCH .

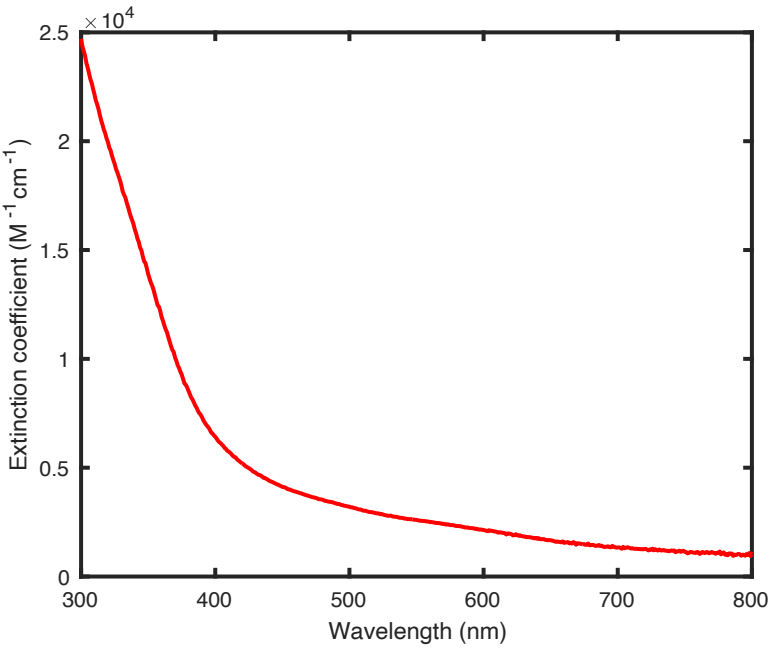

Figure S8.13: UV-vis spectrum of [**1-COE**]$^+$ in DFB with 0.1 mM COE.

D. Mössbauer spectra

Mössbauer spectra were collected at 150 K due to magnetic broadening at lower temperatures. The spectra were simulated using four quadrupole doublets with equal intensity according to the parameters summarized in Table 8.1. Due to overlap of multiple quadrupole doublets, the signals arising from the unique Fe site and the NHC-bound Fe sites cannot be readily distinguished. For this reason, we discuss the average isomer shift, δ_{avg}, because it does not depend on the model used to fit spectra composed of multiple quadrupole doublets.

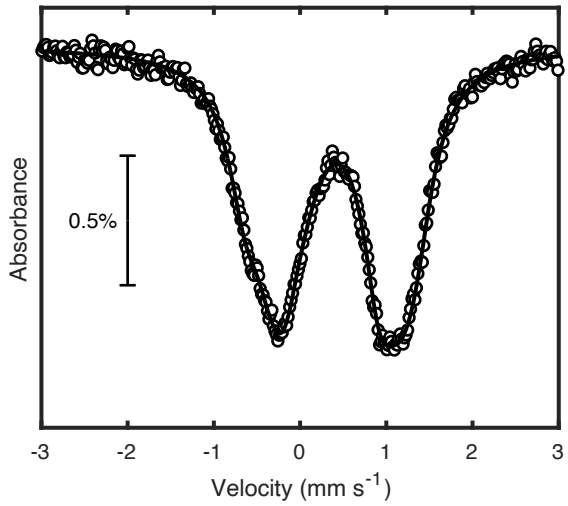

Figure S8.14: Mössbauer spectrum of [**1-PhCCH**]$^+$ at 150 K (dots) and simulation (black) using parameters in table 8.1.

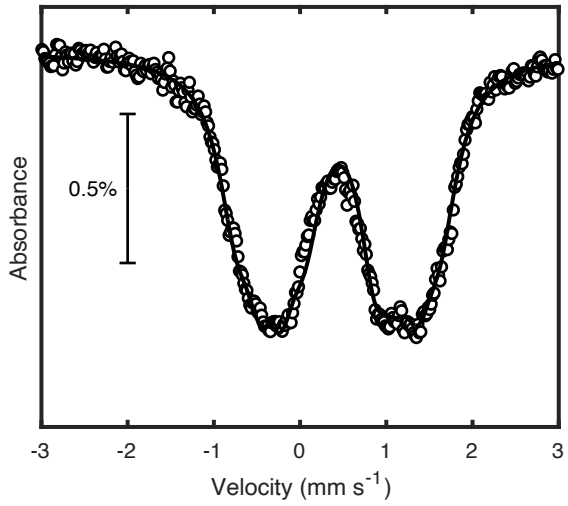

Figure S8.15: Mössbauer spectrum of [**1-COE**]$^+$ at 150 K (dots) and simulation (black) using parameters in table 8.1.

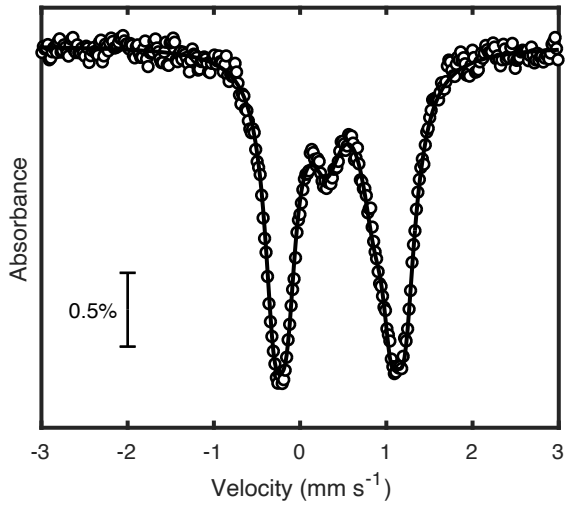

Figure S8.16: Mössbauer spectrum of [**1-OEt₂**]$^+$ at 150 K (dots) and simulation (black) using parameters in table 8.1.

Table S8.1: Mössbauer simulation parameters for [**1-PhCCH**]$^+$, [**1-COE**]$^+$, and [**1-OEt₂**]$^+$.[a]

Compound	Site	δ (mm·s^{-1})	$\lvert\Delta E_Q\rvert$ (mm·s^{-1})	Γ (mm·s^{-1})
[**1-PhCCH**]$^+$	1	0.406	1.521	0.500
	2	0.498	0.971	0.706
	3	0.355	1.976	0.500
	4	0.364	1.100	0.445
	Average	**0.406**		
[**1-COE**]$^+$	1	0.321	1.079	0.430
	2	0.449	1.846	0.445
	3	0.440	2.375	0.497
	4	0.578	1.049	0.500
	Average	**0.447**		
[**1-OEt₂**]$^+$	1	0.300	1.108	0.356
	2	0.452	1.203	0.248
	3	0.452	1.519	0.261
	4	0.758	0.904	0.432
	Average	**0.491**		

[a]: Note that the parameters for the individual quadrupole doublets are not physically meaningful because the spectra are too broad to obtain a unique, reliable simulation.

E. **Variable Temperature NMR spectra**

VT NMR spectra of [**1-PhCCH**]$^+$ and [**1-COE**]$^+$ were recorded at five temperatures between 25 °C and –60 °C. Spectra were collected in Et_2O in the presence of excess PhCCH and COE, respectively, to limit formation of [**1-OEt$_2$**]$^+$. Figures S8.17 and S8.19 show the region between 20 and 0 ppm and figures S8.18 and S8.20 show the downfield region below 6 ppm. The resonances attributes alkynyl and alkenyl protons are shown in the main text (Figure 8.5). The alkynyl and alkenyl protons shift according to the Curie law (Figure S8.21 and S8.22).

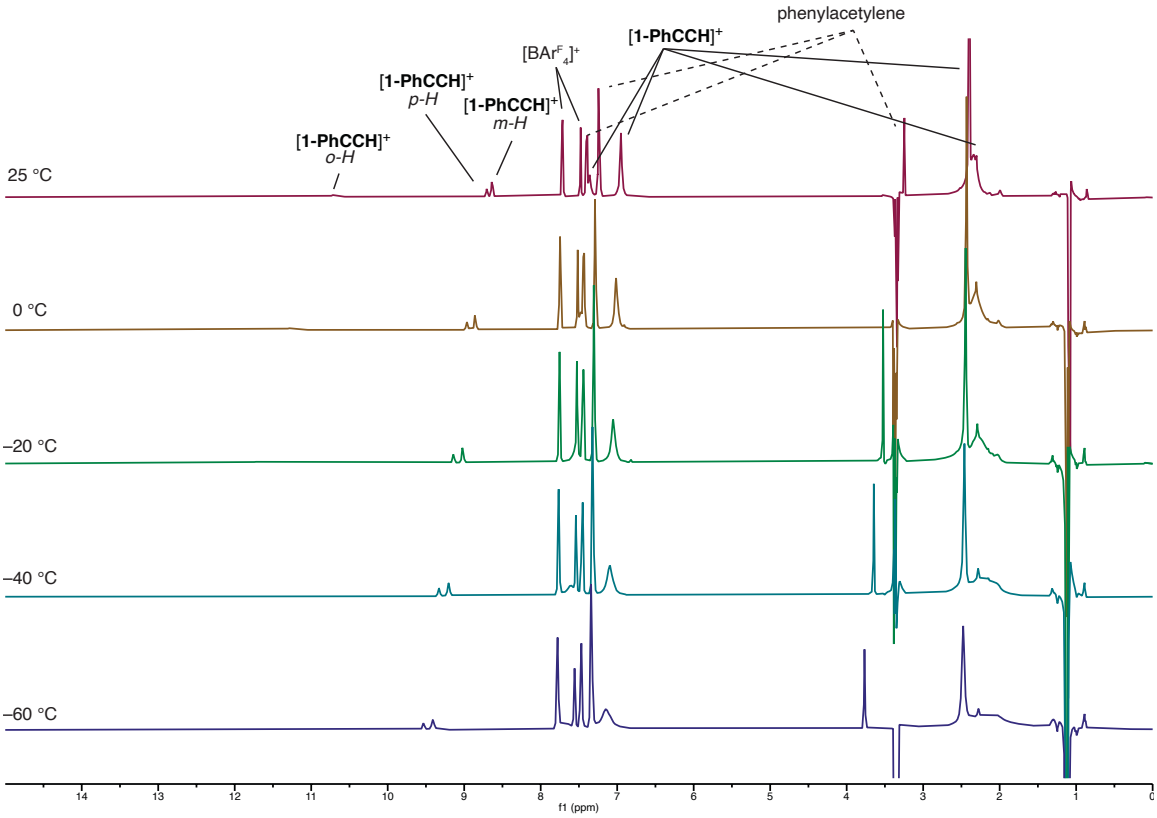

Figure S8.17: VT ^{1}H NMR spectra of [**1-PhCCH**]$^+$.

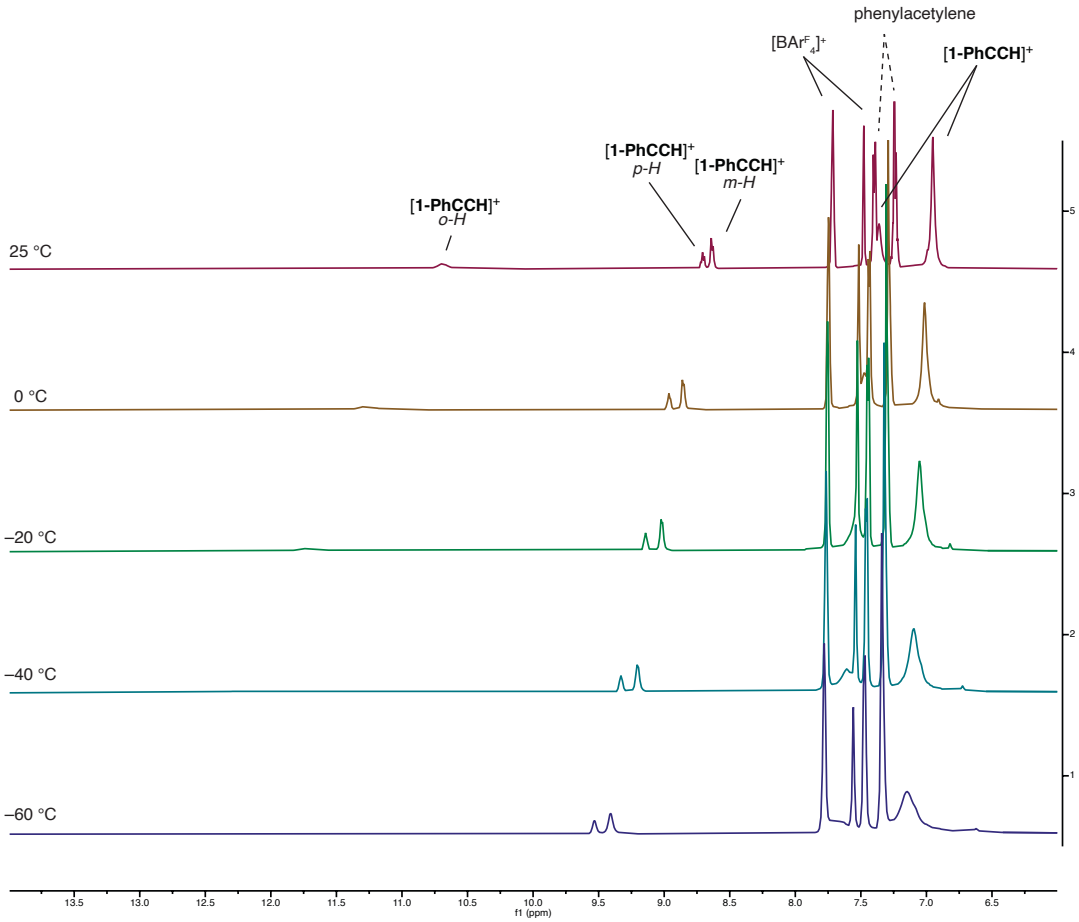

Figure S8.18: VT ^{1}H NMR spectra of [**1-PhCCH**]$^{+}$ between 6 and 14 ppm.

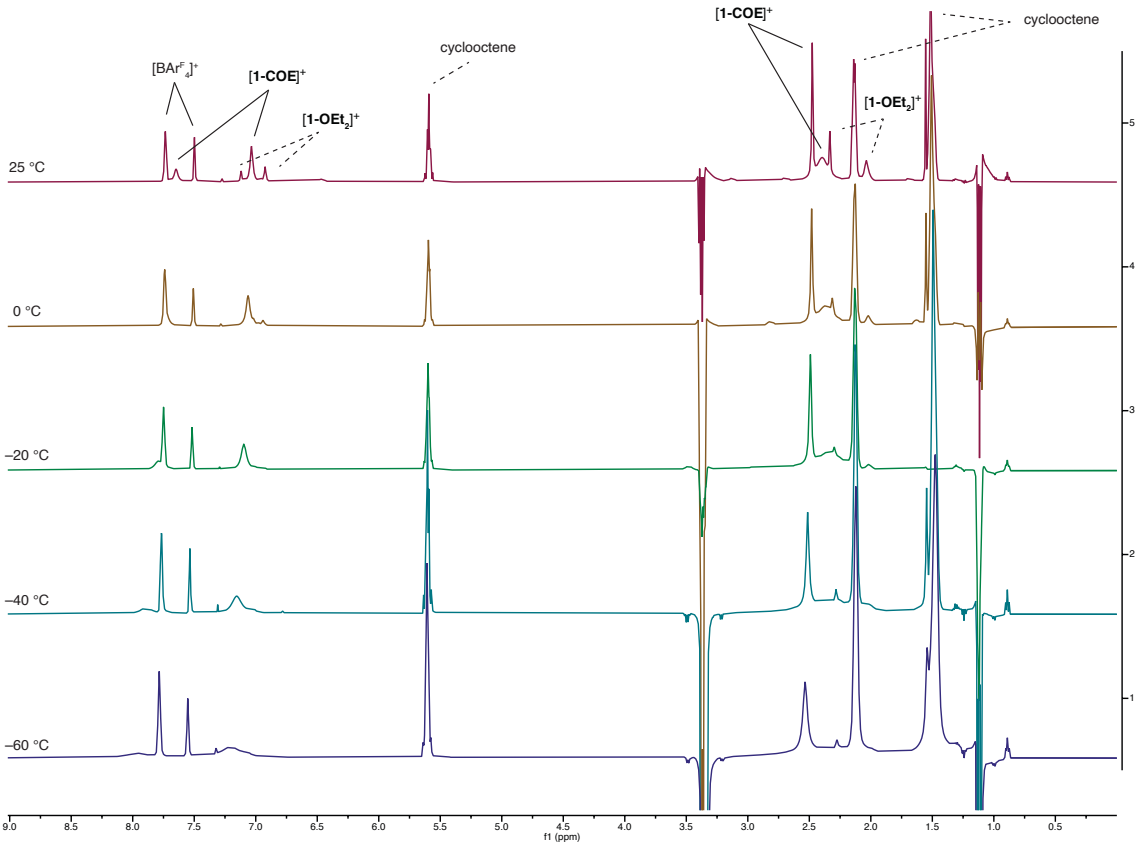

Figure S8.19: VT ^{1}H NMR spectra of [**1-COE**]$^{+}$ between 0 and 9 ppm.

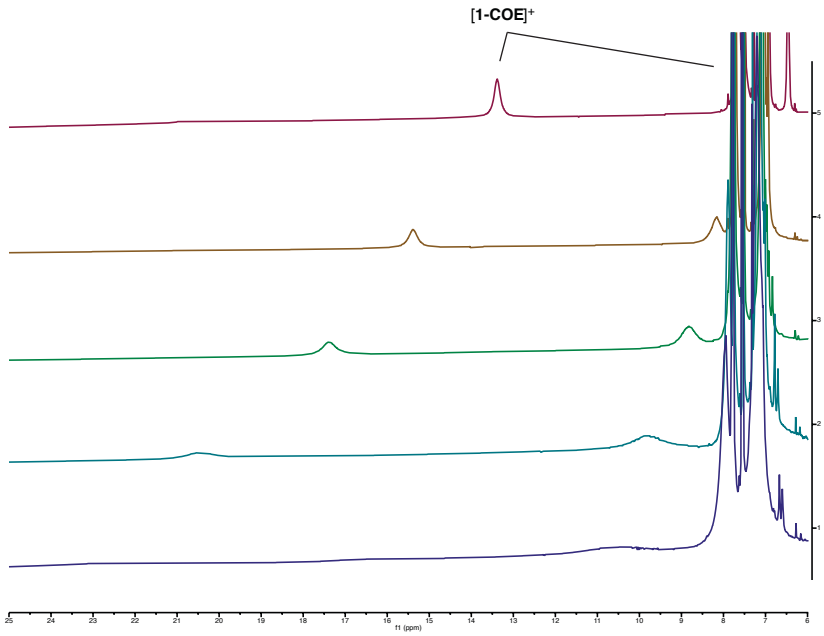

Figure S8.20: VT ^{1}H NMR spectra of [**1-COE**]$^{+}$ between 9 and 25 ppm.

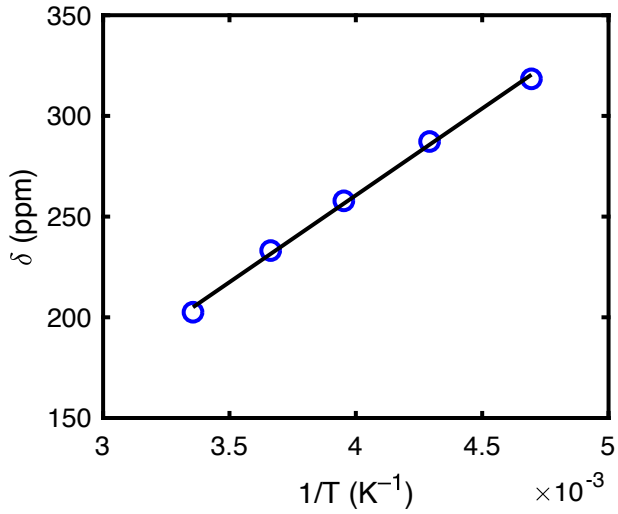

Figure S8.21: Plot of chemical shift vs. 1/T (K) for alkynyl protons in [**1-PhCCH**]$^{+}$.

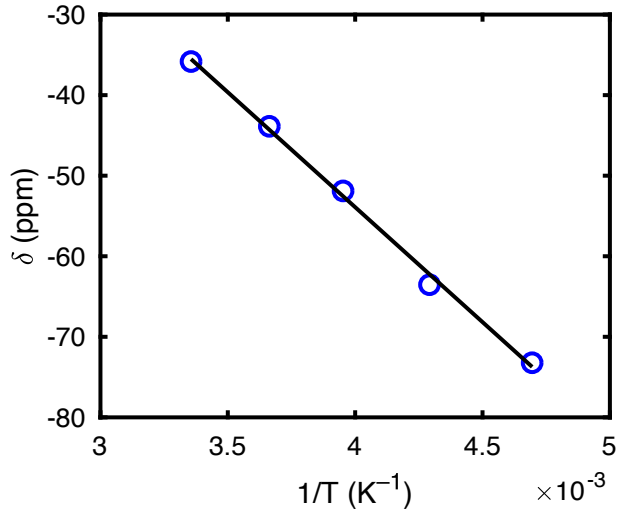

Figure S8.22: Plot of chemical shift vs. 1/T (K) for alkenyl protons in [**1-COE**]$^{+}$.

F. Computational Details

All calculations were carried out using version 4.1.2 of the ORCA program package[1] using the broken-symmetry (BS) approach to approximate the multireference electronic states of Fe–S clusters. BS solutions were constructed using the FlipSpin feature of ORCA.

Coordinates for non-H atoms in [**1-PhCCH**]$^+$ and [**1-COE**]$^+$ were taken from X-ray crystallographic coordinates. To improve the efficiency of the calculations, the mesityl substituents on the IMes ligands were simplified to H. The positions of all H atoms were optimized.

Single point calculations on [**1-PhCCH**]$^+$ and [**1-COE**]$^+$ and geometry optimizations on $[FeCl_3–C_2H_2]^-$ and $[FeCl_3–C_2H_4]^-$ were performed using the TPSSh (10% Hartree-Fock) functional.[2,3] For Fe, S, C, Cl, and N atoms, the DKH-def2-TZVP basis set was used;[4] for H atoms, the DKH-def2-SVP basis set was used. For all calculations, the DKH2 relativistic correction[5] and the general-purpose Coulomb fitting basis set SARC/J were used;[6] all basis sets were fully decontracted. Solid-state effects were approximated using the CPCM solvation model with an infinite dielectric.[7] Wavefunctions were optimized along a low-spin BS surface generated from an initial high-spin calculation by flipping the spins on atoms i,j; BS determinants are named as BSij. Calculations were accelerated through the use of the RIJCOSX approximation with a fine auxiliary integration grid (GridX7).[8]

To analyze localized orbitals, we employed the intrinsic bond orbital (IBO) method developed by Knizia,[9] which applies Pipek-Mezey localization[10] in a basis of so-called intrinsic atomic orbitals (IAOs) and analyzed the resultant orbitals using a Löwdin population analysis. Valences were calculated by summing the Löwdin population analyses for electrons delocalized between two Fe sites and for orbitals involved in Fe–alkyne/–alkene π-backbonding; orbitals localized >80% on one Fe center were assigned entirely to that Fe center.

As described in the main text, $[Fe_4S_4]^+$ clusters are described as a pair of spin-aligned $Fe^{2.5+}$ centers (S = 9/2, majority spin) anti-ferromagnetically coupled to a pair of spin-aligned Fe^{2+} centers (S = 4, minority spin) to give an overall S = 1/2 spin state. For both [**1-PhCCH**]$^+$ and [**1-COE**]$^+$, the Fe center that is spin-aligned with the alkyne or alkene bound Fe center can be readily identified by the presence of a tetragonal compression—four parallel Fe–S bonds which are contracted relative to the cluster's average Fe–S bond length—such that the $[Fe_4S_4]$ cluster can be described as two $[Fe_2S_2]$ rhombs connected by the short Fe–S bonds. The Fe centers are spin-aligned within each rhomb and anti-aligned between rhombs. In the case of [**1-PhCCH**]$^+$, the Fe center spin-aligned with the unique Fe center is Fe3 (crystal structure numbering); in the case of [**1-COE**]$^+$ the Fe center spin-aligned with the unique Fe center is Fe4.

We computed BS determinants for S = 1/2 states with the unique Fe center (Fe1) in the minority spin pair (expected to result in the unique Fe center being in the S = 4, Fe^{2+} pair) or majority spin pair (expected to result in the unique Fe center being in the S = 9/2, $Fe^{2.5+}$ pair). For both [**1-PhCCH**]$^+$ and [**1-COE**]$^+$, the BS determinant in which the unique Fe site was in the minority spin pair was calculated to be lower in energy by 17.5 kcal/mol (Table S8.2). Localized orbital analysis of the lower energy determinant for both complexes reflects the canonical electronic structure for $[Fe_4S_4]^+$ clusters with localization of Fe^{2+} at the alkyne or alkene-bound Fe site (An S = 4 pair of Fe^{2+} centers (1x alkyne-/alkene-bound Fe and 1 x NHC-

Table S8.2: Relative energies of calculated BS-DFT determinants for [**1-PhCCH**]$^+$ and [**1-COE**]$^+$

Compound	BS determinant	Alkyne-/alkene-bound Fe spin	Rel. energy (kca/mol)
[**1-PhCCH**]$^+$	BS13	minority	0
	BS24	majority	+17.5
[**1-COE**]$^+$	BS14	minority	0
	BS23	majority	+17.5

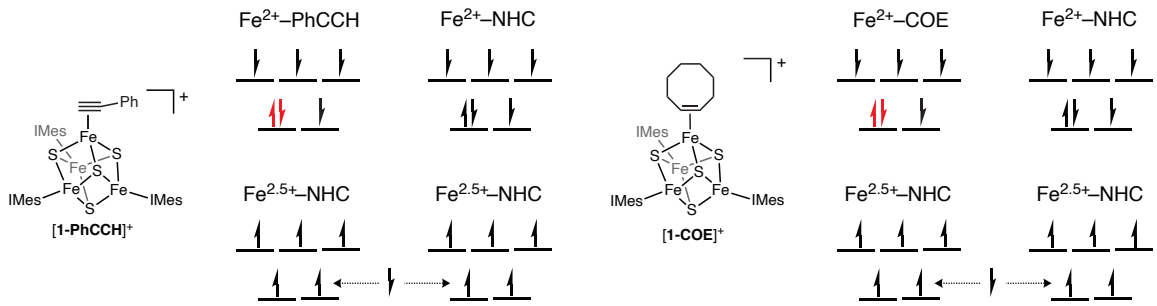

Figure S8.23: Localized orbital, qualitative electronic structure of [**1-PhCCH**]$^+$ and [**1-COE**]$^+$ for the lower energy BS determinant (BS13 for [**1-PhCCH**]$^+$ and BS14 for [**1-COE**]$^+$). Electrons highlighted in red are in orbitals involved in Fe–alkyne/–alkene backbonding; population analyses are summarized in table S8.3.

bound Fe) antiferromagnetically coupled to an $S = 9/2$ pair of $Fe^{2.5+}$ centers (2x NHC-bound Fe). Fig. S8.23), supporting the assignment of the alkyne-/alkene-bound Fe site as localized Fe^{2+} as described in the main text.

A Löwdin population analysis of the orbitals (1 x α-spin and 1x β-spin) involved in Fe–alkyne/alkene backbonding indicates modest π-backbonding to the alkyne or alkene, resulting in transfer of ca. 0.4 e^- to PhCCH, and transfer of ca. 0.2 e^- to COE (Table S8.3). In terms of the limiting resonance structures discussed in the main text, a neutral alkyne/alkene adduct would represent transfer of 0 e^-, and a metallacyclopropene/metallacyclopropane would represent transfer of 2 e^-. As such, the BS-DFT calculations support description of [**1-PhCCH**]$^+$ and [**1-COE**]$^+$ as $[Fe_4S_4]^+$ neutral alkene adducts, with modest contributions from

Table S8.3: Löwdin population analysis of orbitals involved in π-backbonding in [**1-PhCCH**]$^+$ and [**1-COE**]$^+$.

Compound	Orbital	Fe	Alkene/alkyne
[**1-PhCCH**]$^+$	161a	0.671	0.251
	104b	0.828	0.124
	Total	**1.499**	**0.375**
[**1-COE**]$^+$	106a	0.784	0.150
	94b	0.875	0.071
	Total	**1.659**	**0.221**

resonance structures representing 1 e^- reduction of the alkyne/alkene and formation of an $[Fe_4S_4]^{2+}$ cluster and/or 2 e^- reduction and formation of an $[Fe_4S_4]^{3+}$ cluster.

The spin densities on both [**1-PhCCH**]$^+$ and [**1-COE**]$^+$ reflect the same trends observed for the model mononuclear complexes $[Cl_3Fe–C_2H_2]^-$ and $[Cl_3Fe–C_2H_4]^-$. The alkynyl protons have the opposite spin density as alkyne-bound Fe center, while the alkenyl protons have the same spin as the alkene-bound Fe center. Since the Fe center adopts minority spin density in both [**1-PhCCH**]$^+$ and [**1-COE**]$^+$, this means that the alkynyl protons are expected to possess majority spin and the alkenyl protons are expected to possess minority spin (Figure S8.24).

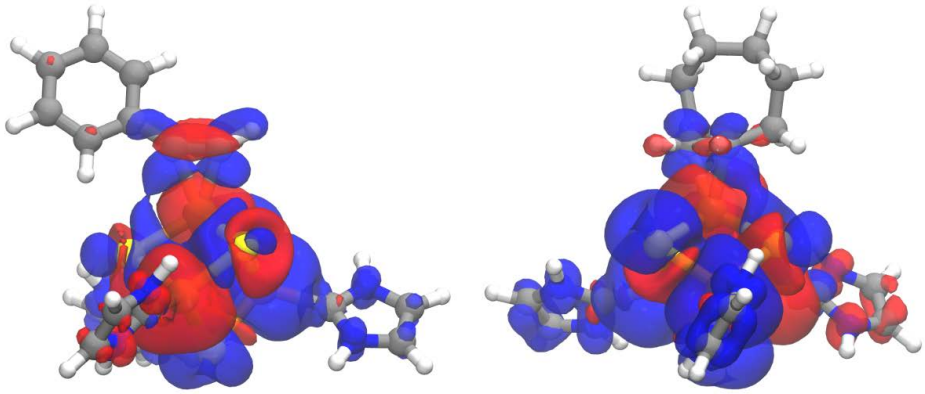

Figure S8.24: Spin density calculated for [**1-PhCCH**]$^+$ (BS13) and [**1-COE**]$^+$ (BS14). Isosurface: 0.001 au ([**1-PhCCH**]$^+$) and 0.0005 au ([**1-COE**]$^+$) Blue is α-spin and red is β-spin. The Fe center bound to the alkyne/alkene bears β-spin, the alkynyl protons have α-spin and the alkenyl protons have β-spin.

G. **Crystallographic Details**

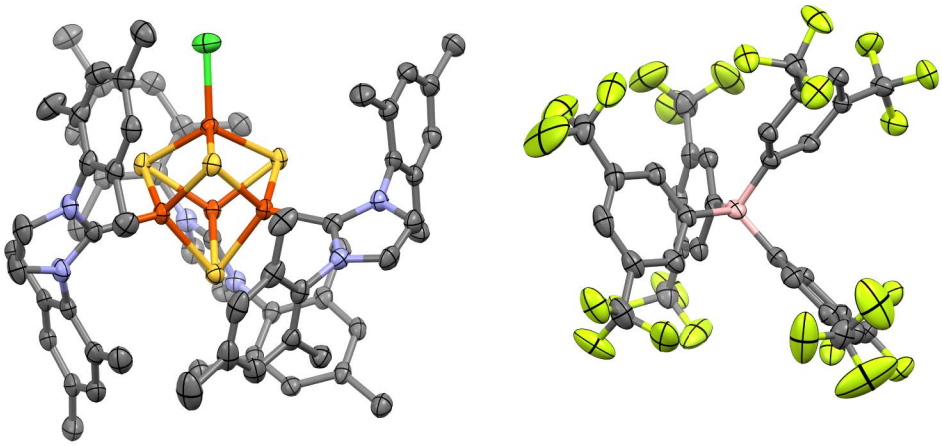

Figure S8.25: Single-crystal X-ray diffraction structure of [**1-Cl**]$^{+}$ (Thermal ellipsoids shown at 50% probability with carbon (gray), iron (orange), sulfur (yellow), chlorine (dark green), nitrogen (blue), boron (pink) and fluorine (light green). Solvent molecules and H-atoms are omitted for clarity.

[**1-Cl**]$^{+}$: Disorder was present in Et_2O in the lattice and in the -CF_3 groups of the [$BAr^F{}_4$] anion. The disorder was modeled using similarity restraints on 1-2 and 1-3 distances and displacement parameters and rigid bond restraints.

[**1-PhCCH**]$^{+}$: Disorder was present in THF in the lattice. The disorder was modeled using similarity restraints on 1-2 and 1-3 distances and displacement parameters and rigid bond restraints.

[**1-COE**]$^{+}$: Disorder was present in the cyclooctene ligand (ring flip) and in the -CF_3 groups of the [$BAr^F{}_4$] anion. The disorder was modeled using similarity restraints on 1-2 and 1-3 distances and displacement parameters and rigid bond restraints. One reflection was omitted due to interference from the beamstop.

H. References

(1) Neese, F. The ORCA Program System. *Wiley Interdiscip. Rev. Comput. Mol. Sci.* **2012**, *2* (1), 73–78.

(2) Tao, J.; Perdew, J. P.; Staroverov, V. N.; Scuseria, G. E. Climbing the Density Functional Ladder: Nonempirical Meta–Generalized Gradient Approximation Designed for Molecules and Solids. *Phys. Rev. Lett.* **2003**, *91* (14), 3–6.

(3) Staroverov, V. N.; Scuseria, G. E.; Tao, J.; Perdew, J. P. Comparative Assessment of a New Nonempirical Density Functional: Molecules and Hydrogen-Bonded Complexes. *J. Chem. Phys.* **2003**, *119* (23), 12129–12137.

(4) Pantazis, D. A.; Chen, X. Y.; Landis, C. R.; Neese, F. All-Electron Scalar Relativistic Basis Sets for Third-Row Transition Metal Atoms. *J. Chem. Theory Comput.* **2008**, *4* (6), 908–919.

(5) Reiher, M. Relativistic Douglas-Kroll-Hess Theory. *Wiley Interdiscip. Rev. Comput. Mol. Sci.* **2012**, *2* (1), 139–149.

(6) Weigend, F. Accurate Coulomb-Fitting Basis Sets for H to Rn. *Phys. Chem. Chem. Phys.* **2006**, *8* (9), 1057–1065.

(7) Barone, V.; Cossi, M. Conductor Solvent Model. *J. Phys. Chem. A* **1998**, *102* (97), 1995–2001.

(8) Neese, F.; Wennmohs, F.; Hansen, A.; Becker, U. Efficient, Approximate and Parallel Hartree-Fock and Hybrid DFT Calculations. A “chain-of-Spheres” Algorithm for the Hartree-Fock Exchange. *Chem. Phys.* **2009**, *356* (1–3), 98–109.

(9) Knizia, G. Intrinsic Atomic Orbitals: An Unbiased Bridge between Quantum Theory and Chemical Concepts. *J. Chem. Theory Comput.* **2013**, *9* (11), 4834–4843.

(10) Pipek, J.; Mezey, P. G. A Fast Intrinsic Localization Procedure Applicable for Ab Initio and Semiempirical Linear Combination of Atomic Orbital Wave Functions. *J. Chem. Phys.* **1989**, *90* (9), 4916–4926.

Chapter 9. An Open-Cuboidal [Fe_3S_4] Cluster Characterized in Both Biologically Relevant Redox States

Main text

Iron-sulfur (Fe–S) clusters serve as redox-active cofactors in hundreds of thousands of proteins.[1] The structures most commonly found in biology are diamond-core [Fe_2S_2] clusters, open-cuboidal [Fe_3S_4] clusters (Figure 9.1A), and cuboidal [Fe_4S_4] clusters, each of which

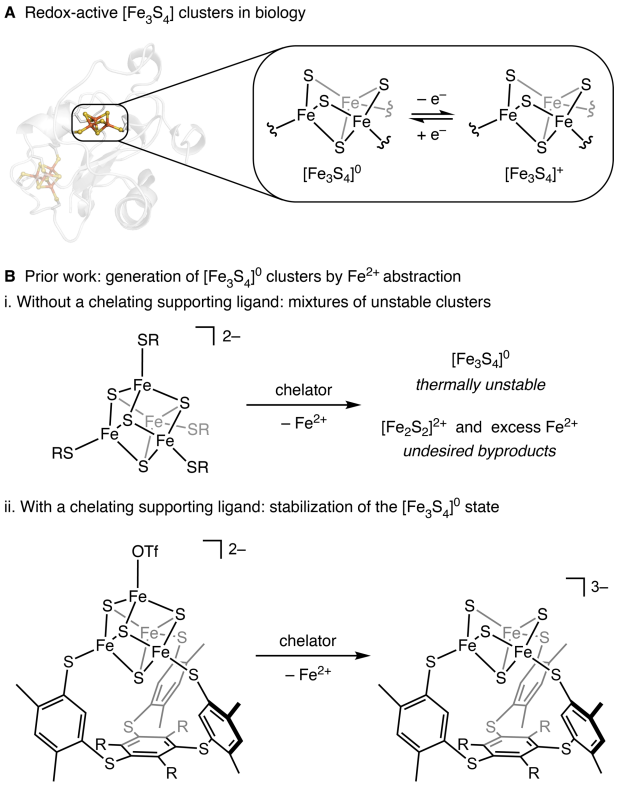

Figure 9.1. Synthetic models of [Fe_3S_4] proteins. A) Structure of *Azotobacter vinelandii* ferredoxin I (PDB: 7FDI), highlighting the biologically relevant redox states. B) Fe^{2+} abstraction from synthetic $[Fe_4S_4]^{2+}$ clusters typically affords mixtures of thermally unstable Fe–S clusters (i) unless stabilized by a chelating supporting ligand (ii).

has been characterized in multiple redox states.[1–3] Synthetic analogues of biological Fe–S clusters have been studied for more than fifty years,[4–6] and the initial reports[7,8] describing the preparation and structural characterization of [Fe_2S_2] and [Fe_4S_4] clusters appeared shortly after the discovery and characterization of their biological counterparts. The two complete

series of biorelevant redox states ($[Fe_2S_2]^{2+/+}$ and $[Fe_4S_4]^{3+/2+/+/0}$) have since been fully characterized.[9,10]

The development of synthetic models of open-cuboidal $[Fe_3S_4]$ clusters has been slower, with the sole structurally characterized example being an $[Fe_3S_4]^0$ cluster reported in 1996.[11,12] The dearth of synthetic, open-cuboidal $[Fe_3S_4]$ clusters can be attributed to the instability of the open-cuboidal structure in the absence of a protein scaffold. To illustrate: whereas $[Fe_2S_2]$ and $[Fe_4S_4]$ clusters can be readily self-assembled in organic solvents,[7,8] only linear $[Fe_3S_4]$ clusters have been generated via self-assembly.[13] And although open-cuboidal $[Fe_3S_4(SR)_3]^{n-}$ clusters have been generated via Fe^{2+} abstraction from $[Fe_4S_4(SR)_4]^{m-}$ clusters, the mixtures thus obtained are unstable at ambient temperature and contaminated by other cluster forms (Figure 9.1B).[11,12,14,15] The only open-cuboidal cluster obtained in pure form was stabilized by a chelating, trithiolate ligand, and even then in only one of the two biorelevant redox states: $[Fe_3S_4]^0$ (Figure 9.1B).[11,12]

The paucity of synthetic $[Fe_3S_4]$ clusters stands in contrast to enduring interest in the properties and functions of $[Fe_3S_4]$ proteins.[16,17] Following the discovery of biological $[Fe_3S_4]$ clusters[18–20] and the assignment of the cluster's Fe–S ratio[21] and open-cuboidal structure,[22–25] additional studies have characterized the interconversion between $[Fe_3S_4]$ and $[Fe_4S_4]$ forms,[26–30] the biological functions of $[Fe_3S_4]$ proteins,[31–34] and the unique spectroscopic features[18,20,35–37] and electronic structures[38–40] of both redox states. The oxidized, $[Fe_3S_4]^+$ state continues to be of particular theoretical and experimental interest for several reasons.[16] First, the triangular arrangement of antiferromagnetically coupled Fe^{3+} ions leads to spin frustration,[41] which is relieved by spin canting that gives rise to an $S = 1/2$ ground state with unusual spectroscopic properties.[18,35,38] Second, the high-resolution crystal structures of the *Azotobacter vinelandii* ferredoxin I (*Av* FdI) have shown that the cluster structure in the oxidized ($[Fe_3S_4]^+$) state is indistinguishable from that in the reduced ($[Fe_3S_4]^0$) state[42–45] (in contrast to other Fe–S

clusters, for which redox-state changes are accompanied by large structural changes[4]). This observation has led to the proposal that for $[Fe_3S_4]$ proteins, the polypeptide enforces an entatic state, which could promote rapid electron transfer.[42]

One challenge in evaluating this and related hypotheses is the lack of $[Fe_3S_4]^+$ model compounds, characterization of which would reveal if, in the absence of a protein scaffold, (i) the $[Fe_3S_4]^+$ state adopts the unusual spin-canted electronic structure, and (ii) if the $[Fe_3S_4]^0$ and $[Fe_3S_4]^+$ states have similar structural metrics (thereby testing the notion of the protein enforcing an entatic state). We therefore targeted the synthesis of a pair of isostructural $[Fe_3S_4]$ clusters in both biorelevant redox states.

Our synthetic strategy entailed (i) stabilizing the open-cuboidal $[Fe_3S_4]$ structure using strongly binding,[46] sterically encumbering *N*-heterocyclic carbene supporting ligands to prevent formation of other cluster structures;[47,48] and (ii) using a chelator to abstract Fe^{2+} from an $[Fe_4S_4]^{2+}$ cluster to yield an $[Fe_3S_4]^0$ cluster, by analogy to the preparation of the previously reported $[Fe_3S_4]^0$ cluster (Figure 9.1B)[11] and to Fe^{2+} removal from isolated nitrogenase cofactors.[49,50]

Specifically, we treated $[(IMes)_3Fe_4S_4Cl][PF_6]$[51] (IMes = 3,5-dimesitylimidazol-2-ylidene) with 2 equiv KTp (Tp = tris(pyrazolyl)borate), generating the inner-sphere KPF_6 complex, $(IMes)_3Fe_4S_4KPF_6$ (**1**·KPF_6), along with Tp_2Fe and KCl (Scheme 1). Although **1**·KPF_6 was not isolated (and instead served as an intermediate to the targeted open-cuboidal

Scheme 9.1. Preparation of open-cuboidal $[Fe_3S_4]^+$ and $[Fe_3S_4]^0$ clusters.

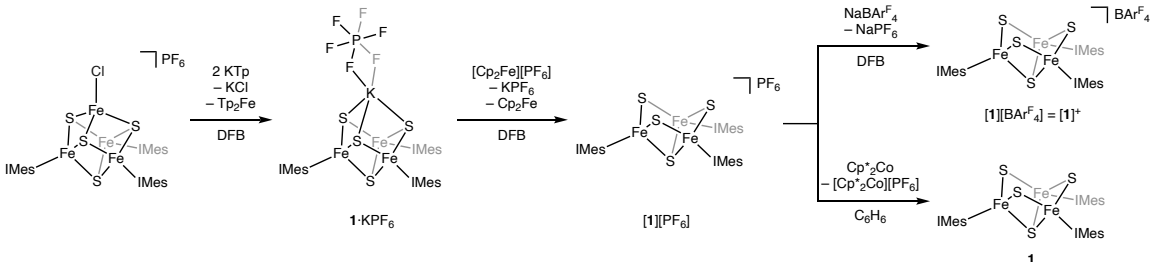

[Fe_3S_4] clusters, as discussed below), single crystals were obtained from the reaction mixture, and the X-ray crystal structure revealed binding of K^+ to the three μ_2-sulfides of the $[Fe_3S_4]^0$ cluster and two fluorides from the [PF_6] anion (Figure S9.15). We hypothesized that oxidation would decrease the affinity of the $[Fe_3S_4]^0$ cluster for K^+, and indeed found that mixing in-situ generated **1**·KPF_6 with [Cp_2Fe][PF_6] resulted in KPF_6 precipitation and generation of [$(IMes)_3Fe_3S_4$][PF_6] ([**1**][PF_6]), which was separated from Tp_2Fe and Cp_2Fe by precipitation from 1,2-difluorobenzene (DFB) with *n*-pentane (Scheme 1). As-isolated, [**1**][PF_6] typically contains small amounts (≤ 10%) of [$(IMes)_3Fe_4S_4Cl$][PF_6]. However, pure samples of the $[Fe_3S_4]^+$ cluster [**1**][BAr^F_4] (henceforth denoted $[\mathbf{1}]^+$; BAr^F_4 = tetrakis(3,5-trifluoromethylphenyl)borate) can be obtained following salt metathesis using $NaBAr^F_4$ and precipitation from Et_2O with *n*-pentane. Alternatively, reduction of [**1**][PF_6] with decamethylcobaltocene affords the reduced, $[Fe_3S_4]^0$ cluster $(IMes)_3Fe_3S_4$ (**1**; Scheme 1) in pure form following precipitation from DFB with *n*-pentane. The cyclic voltammogram of **1** in DFB features the **1**/$[\mathbf{1}]^+$ redox couple at –1.17 V vs. Fc/Fc^+ and a reduction wave corresponding to the $[\mathbf{1}]^-$/**1** redox couple at –2.32 V (Figure S9.11); these potentials are similar to those observed for the aforementioned thiolate-ligated [Fe_3S_4] cluster (–1.19 V and –2.12 V, in MeCN),[11] though caution should be exercised in comparing the two because the effects from NHC vs thiolate ligation (where NHC ligation is expected to render the cluster less electron-rich[46,52]) are conflated with those arising from differences in electrochemical conditions. Despite the electrochemical reversibility of the $[\mathbf{1}]^-$/**1** couple, we have not yet been able to isolate $[\mathbf{1}]^-$.

With an isostructural pair of $[Fe_3S_4]^0$ and $[Fe_3S_4]^+$ clusters in hand, we undertook a comparative analysis of their properties. Similarly to biological $[Fe_3S_4]^0$ clusters,[16,17,26] the ground spin state of **1** is a quintet (as determined by SQUID magnetometry; Figure S9.10) that arises from antiferromagnetic coupling between a pair of spin-aligned $Fe^{2.5+}$ centers

(themselves coupled via the double-exchange mechanism) and a high-spin Fe^{3+} center.[39] This electronic structure is reflected in the 80 K Mössbauer spectrum of **1**, which can be simulated using three quadrupole doublets fixed in a 1:1:1 ratio (Figure 9.2A and Table S9.1): two

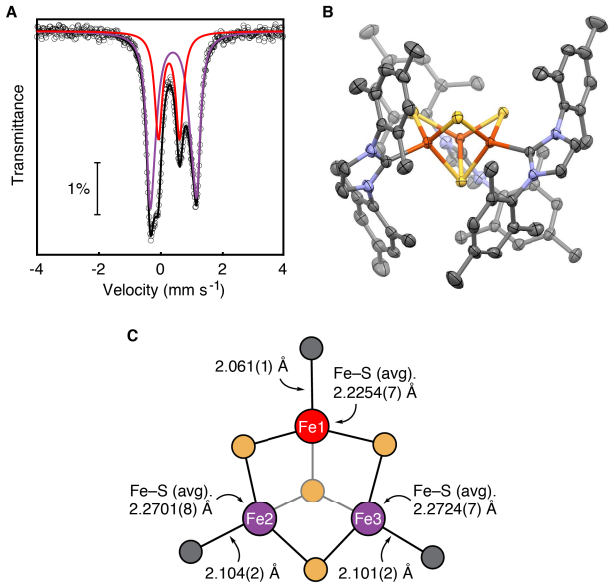

Figure 9.2. Characterization of **1**. A) Mössbauer spectrum (circles, 80 K, microcrystalline powder) and simulation (black, total; purple, $Fe^{2.5+}$ sites; red, Fe^{3+} site) using the parameters described in the text and Table S9.1. B) X-ray crystallographic structure of **1**·$[Cp_2Co][PF_6]$; carbon (gray), nitrogen (blue), iron (orange), and sulfur (yellow) with ellipsoids at the 50% probability level. The co-crystallized $[Cp_2Co][PF_6]$ and solvent molecules have been omitted for clarity. C) Metrics of the cluster core with Fe valences colored as in Figure 9.2A.

reflective of $Fe^{2.5+}$ centers (δ = 0.40 and 0.42 mm s^{-1} and ΔE_Q = 1.52 and 1.24 mm s^{-1}, respectively, purple),[53] and a third with a much lower isomer shift (0.28 mm s^{-1}) and smaller quadrupole splitting (0.68 mm s^{-1}) that is thus readily identified as the ferric site in **1** (red). The Mössbauer spectrum of **1** is similar to those of protein-bound, Cys-ligated $[Fe_3S_4]^0$ clusters.[16,39,53,54]

Under most conditions, **1** crystallizes in the rhombohedral space group R–3c on a C_3 axis, leading to severe disorder that prohibits detailed structural analysis (see SI page S18). Fortuitously, when **1** is synthesized with Cp_2Co instead of Cp^*_2Co, it co-crystallizes with $[Cp_2Co][PF_6]$ from crude reaction mixtures in the triclinic space group P–1 with no crystallographic symmetry imposed on the cluster. The high-quality structure thus obtained

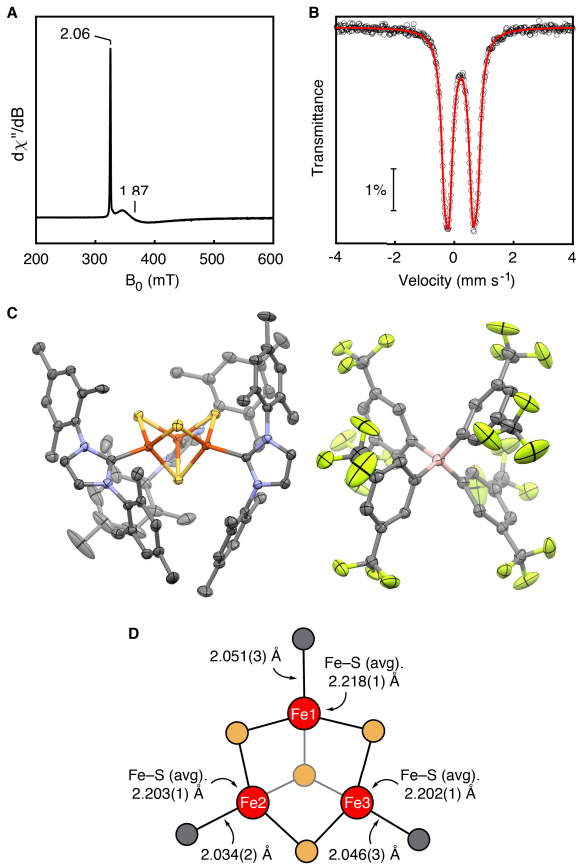

Figure 9.3. Characterization of [**1**]$^{+}$. A) 9.37 GHz EPR spectrum (9:1 toluene/DFB, 5 K, 250 μW). B) Mössbauer spectrum (circles, 80 K, microcrystalline powder) and total simulation (red) using the parameters described in the text and Table S9.2. C) X-ray crystallographic structure; graphics as in Figure 9.2B with boron (pink) and fluorine (green). D) Metrics of the cluster core.

(Figure 9.2B) allows for the reliable determination of structural parameters. Clear hallmarks for the localization of Fe^{3+} at the Fe1 site are observed: the average Fe–S distances for Fe2 (2.2701(8) Å) and Fe3 (2.2724(7) Å) are longer than for Fe1 (2.2254(7) Å) (Figure 9.2C; analogous differences in the Fe–C distances are observed). The Fe–S distances in **1** are very similar to those observed in high-resolution crystal structures of protein-bound $[Fe_3S_4]^0$ clusters, which have average Fe–S distances of 2.28(4) Å for the $Fe^{2.5+}$ sites and 2.24(3) Å for the Fe^{3+} sites.[42] In the one structurally characterized synthetic, open-cuboidal $[Fe_3S_4]^0$ cluster,[11] the Fe–S distances are somewhat longer and more evenly distributed (2.260(7), 2.278(6), and 2.286(6) Å; Table S9.6); the S–Fe–S and Fe–S–Fe angles are similar amongst **1**, **1**·KPF_6, and the thiolate-ligated cluster,[11] and are compiled in table S9.7. Broken-symmetry density

functional theory (BS DFT) calculations on **1** (TPSSh/def2-TZVP) using its crystallographic coordinates support localization of Fe^{3+} at the Fe1 site (Table S9.4).

We now turn to characterization of $[\mathbf{1}]^+$. Its X-band EPR spectrum (Figure 9.3A) features an $S = {}^1/_2$ signal that is sharp at $g_{\|} = 2.06$ and exceptionally broad at $g_{\perp} \sim 1.87$. Both features—the g-values and broadness at $g_{\perp}$—are spectroscopic signatures of biological $[Fe_3S_4]^+$ clusters[16,17,35,38] and have been attributed to antisymmetric exchange that mixes the $|3\ {}^5/_2\ {}^1/_2\rangle$ and $|2\ {}^5/_2\ {}^1/_2\rangle$ states (where $|S_{12}\ S_3\ S_{tot}\rangle$ is the state having total spin, S_{tot}, in which two Fe^{3+} sites (1 and 2) together adopt a canted spin of S_{12}; antiferromagnetic coupling of this pair with the remaining Fe^{3+} center (having S_3) gives S_{tot}).[40] We therefore conclude that, like its biological counterparts, $[\mathbf{1}]^+$ adopts the spin-canted electronic structure that is characteristic of $[Fe_3S_4]^+$ clusters.

The 80 K Mössbauer spectrum of $[\mathbf{1}]^+$ was simulated using two quadrupole doublets (Figure 9.3B, Table S9.2) fixed in a 2:1 ratio with low isomer shifts (0.22 and 0.23 mm s^{-1}, respectively) and relatively small quadrupole splittings (1.04 and 0.72 mm s^{-1}, respectively), both of which are hallmarks of high-spin Fe^{3+} in a tetrahedral coordination environment.[53] The average parameters are similar to those of biological $[Fe_3S_4]^+$ clusters (the Mössbauer spectra of which are often simulated using a single quadrupole doublet),[16,17,35,53] and, together with the EPR data, reveal that $[\mathbf{1}]^+$ faithfully models the electronic structures of biological $[Fe_3S_4]^+$ clusters.

The X-ray crystal structure of $[\mathbf{1}]^+$ (Figure 9.3C/D) reveals quite similar average Fe–S and Fe–C distances among the three Fe sites, all metrics being similar to those for the Fe^{3+} site identified in **1** and shorter than those of the mixed-valence pair in **1** (Figure 9.2C). The Fe–Fe distances (2.6386(5), 2.6202(5), and 2.6422(5) Å) likewise span a narrow range. Overall, the cluster core of $[\mathbf{1}]^+$ is substantially contracted and closer to C_3 symmetry than that of **1**. In contrast, structural studies of *Av* FdI (the only $[Fe_3S_4]$ protein for which high-resolution

structures are available in both the reduced and oxidized states),[42–45] showed that the clusters in the $[Fe_3S_4]^0$ and $[Fe_3S_4]^+$ states have nearly identical metrics. Within experimental error, the average Fe–S distance in *Av* FdI (2.26(6) Å for $[Fe_3S_4]^0$ and 2.26(3) for $[Fe_3S_4]^+$) is the same as in **1** (2.256(1) Å) and longer than that observed in $[\mathbf{1}]^+$ (2.207(2) Å). We therefore conclude that, in the absence of constraints imposed by the polypeptide, the structures of $[Fe_3S_4]$ clusters are highly responsive to their redox state. Whether or not biological $[Fe_3S_4]$ clusters are, as a rule, poised in an entatic state awaits a larger number of high-resolution structures of oxidized $[Fe_3S_4]$ proteins.

In summary, with the synthesis of $[\mathbf{1}]^+$, synthetic analogues of the three common Fe–S cluster structures have now been reported in each biologically relevant redox state. Both $[\mathbf{1}]^+$ and **1** have similar electronic structures as their biological counterparts, but the bond lengths in the synthetic clusters' $[Fe_3S_4]$ cores are more responsive to changes in redox state. This finding supports the hypothesis[42] that *Av* FdI (and potentially other $[Fe_3S_4]$ proteins) enforces an entatic state on its $[Fe_3S_4]$ cluster, preventing typical contraction of the cluster core upon oxidation. Additionally, the stabilization of the open-cuboidal $[Fe_3S_4]$ structure in the absence of a chelating ligand or a protein scaffold highlights the utility of bulky, monodentate ligands in constructing a protective coordination sphere that can facilitate access to otherwise recalcitrant cluster structures.

References

(1) Beinert, H.; Holm, R. H.; Münck; Eckard. Iron-Sulfur Clusters: Nature's Modular, Multipurpose Structures. *Science* **1997**, *277* (5326), 653–659.

(2) Sticht, H.; Rösch, P. The Structure of Iron–Sulfur Proteins. *Prog. Biophys. Mol. Biol.* **1998**, *70*, 95–136.

(3) Johnson, D. C.; Dean, D. R.; Smith, A. D.; Johnson, M. K. Structure, Function and Formation of Biological Iron-Sulfur Clusters. *Annu. Rev. Biochem.* **2005**, *74*, 247–281.

(4) Venkateswara Rao, P.; Holm, R. H. Synthetic Analogues of the Active Sites of Iron−Sulfur Proteins. *Chem. Rev.* **2004**, *104* (2), 527–560.

(5) Lee, S. C.; Holm, R. H. The Clusters of Nitrogenase: Synthetic Methodology in the Construction of Weak-Field Clusters. *Chem. Rev.* **2004**, *104* (2), 1135–1157.

(6) Lee, S. C.; Lo, W.; Holm, R. H. Developments in the Biomimetic Chemistry of Cubane-Type and Higher Nuclearity Iron-Sulfur Clusters. *Chem. Rev.* **2014**, *114* (7), 3579–3600.

(7) Herskovitz, T.; Averill, B. A.; Holm, R. H.; Ibers, J. A.; Phillips, W. D.; Weiher, J. F. Structure and Properties of a Synthetic Analogue of Bacterial Iron--Sulfur Proteins. *Proc. Natl. Acad. Sci. U. S. A.* **1972**, *69* (9), 2437–2441.

(8) Mayerle, J. J.; Frankel, R. B.; Holm, R. H.; Ibers, J. A.; Phillips, W. D.; Weiher, J. F. Synthetic Analogs of the Active Sites of Iron Sulfur Proteins. Structure and Properties of Bis[o-xylyldithiolato-μ_2-sulfidoferrate(III)], an Analog of the 2Fe-2S Proteins. *Proc. Natl. Acad. Sci. U. S. A.* **1973**, *70* (8), 2429–2433.

(9) Albers, A.; Demeshko, S.; Dechert, S.; Bill, E.; Bothe, E.; Meyer, F. The Complete Characterization of a Reduced Biomimetic [2Fe-2S] Cluster. *Angew. Chem. Int. Ed.* **2011**, *50* (39), 9191–9194.

(10) Scott, T. A.; Berlinguette, C. P.; Holm, R. H.; Zhou, H. C. Initial Synthesis and Structure of an All-Ferrous Analogue of the Fully Reduced $[Fe_4S_4]^0$ Cluster of the Nitrogenase Iron Protein. *Proc. Natl. Acad. Sci. U. S. A.* **2005**, *102* (28), 9741–9744.

(11) Zhou, J.; Hu, Z.; Münck, E.; Holm, R. H. The Cuboidal Fe_3S_4 Cluster: Synthesis, Stability, and Geometric and Electronic Structures in a Non-Protein Environment. *J. Am. Chem. Soc.* **1996**, *118* (8), 1966–1980.

(12) Zhou, J.; Holm, R. H. Synthesis and Metal Ion Incorporation Reactions of the Cuboidal Fe_3S_4 Cluster. *J. Am. Chem. Soc.* **1995**, *117* (45), 11353–11354.

(13) Hagen, K. S.; Watson, A. D.; Holm, R. H. Synthetic Routes to Fe_2S_2, Fe_3S_4, Fe_4S_4, and Fe_6S_9 Clusters From the Common Precursor $[Fe(SC_2H_5)_4]^{2-}$: Structures and Properties of $[Fe_3S_4(SR)_4]^{3-}$ and $[Fe_6S_9(SC_2H_5)_2]^{4-}$, Examples of the Newest Types of Fe-S-SR Clusters. *J. Am. Chem Soc.* **1983**, *4* (15), 3905–3913.

(14) Weterings, J. P.; Kent, T. A.; Prins, R. Low-Temperature Oxidation of [4Fe-4S] Analogues. Generation of an Fe/S Cluster Spectroscopically Similar to the 3-Fe Clusters in the 3-Fe Ferredoxins. *Inorg. Chem.* **1987**, *26* (2), 324–329.

(15) Roth, E. K. H.; Jordanov, J. Oxidation Reactions of $[Fe_4S_4(S\text{-}2,4,6\text{-}(i\text{-}Pr)_3C_6H_2)_4]^{2-}$ and an Oxidative Conversion of the Fe_4S_4 Core into an Fe_3S_4 Center. *Inorg. Chem.* **1993**, 31, 240–243.

(16) Johnson, M. K.; Duderstadt, R. E. Biological and Synthetic $[Fe_3S_4]$ Clusters. *Adv. Inorg. Chem.* **1999**, *47*, 1–82.

(17) Beinert, H.; Thomson, A. J. Three-Iron Clusters in Iron-Sulfur Proteins. *Arch. Biochem. Biophys.* **1983**, *222* (2), 333–361.

(18) Emptage, M. H.; Kent, T. A.; Huynh, B. H.; Rawlings, J.; Orme-Johnson, W. H.; Münck, E. On the Nature of the Iron-Sulfur Centers in a Ferredoxin from *Azotobacter vinelandii*. Mossbauer Studies and Cluster Displacement Experiments. *J. Biol. Chem.*

1980, *255* (5), 1793–1796.
(19) Stout, C. D.; Ghosh, D.; Pattabhi, V.; Robbins, A. H. Iron-Sulfur Clusters in *Azotobacter* Ferredoxin at 2.5 Å Resolution. *J. Biol. Chem.* **1980**, *255* (5), 1797–1800.
(20) Sweeney, W. V.; Rabinowitz, J. C.; Yoch, D. C. High and Low Reduction Potential 4Fe-4S Clusters in *Azotobacter vinelandii* (4Fe-4S)2 Ferredoxin I. Influence of the Polypeptide on the Reduction Potentials. *J. Biol. Chem.* **1975**, *250* (19), 7842–7847.
(21) Beinert, H.; Emptage, M. H.; Dreyer, J. L.; Scott, R. A.; Hahn, J. E.; Hodgson, K. O.; Thomson, A. J. Iron-Sulfur Stoichiometry and Structure of Iron-Sulfur Clusters in Three-Iron Proteins: Evidence for [3Fe-4S] Clusters. *Proc. Natl. Acad. Sci. U. S. A.* **1983**, *80* (2), 393–396.
(22) Antonio, M. R.; Averill, B. A.; Moura, I.; Orme-Johnson, W. H.; Teo, B. K.; Xavier, A. V. Core Dimensions in the 3Fe Cluster of *Desulfovibrio gigas* Ferredoxin II by Extended X-Ray Absorption Fine Structure Spectroscopy. *J. Biol. Chem.* **1982**, *257* (12), 6646–6649.
(23) Johnson, M. K.; Czernuszewicz, R. S.; Spiro, T. G.; Fee, J. A.; Sweeney, W. V. Resonance Raman Spectroscopic Evidence for a Common [3Fe-4S] Structure among Proteins Containing Three-Iron Centers. *J. Am. Chem. Soc.* **1983**, *105* (22), 6671–6678.
(24) Stout, G. H.; Turley, S.; Sieker, L. C.; Jensen, L. H. Structure of Ferredoxin I from *Azotobacter vinelandii*. *Proc. Natl. Acad. Sci. U. S. A.* **1988**, *85* (4), 1020–1022.
(25) Kissinger, C. R.; Adman, E. T.; Sieker, L. C.; Jensen, L. H. Structure of the 3Fe-4S Cluster in *Desulfovibrio gigas* Ferredoxin II. *J. Am. Chem. Soc.* **1988**, *110* (26), 8721–8723.
(26) Thomson, A. J.; Robinson, A. E.; Johnson, M. K.; Cammack, R.; Rao, K. K.; Hall, D. O. Low-Temperature Magnetic Circular Dichroism Evidence for the Conversion of Four-Iron-Sulphur Clusters in a Ferredoxin from *Clostridium pasteurianum* into Three-Iron-Sulphur Clusters. *BBA - Bioenerg.* **1981**, *637* (3), 423–432.
(27) Johnson, M. K.; Spiro, T. G.; Mortenson, L. E. Resonance Raman and Electron Paramagnetic Resonance Studies on Oxidized and Ferricyanide-Treated *Clostridium pasteurianum* Ferredoxin. Vibrational Assignments from ^{34}S Shifts and Evidence for Conversion of 4 to 3 Iron-Sulfur Clusters via Oxidative Damage. *J. Biol. Chem.* **1982**, *257* (5), 2447–2452.
(28) Bell, S. H.; Dickson, D. P. E.; Johnson, C. E.; Cammack, R.; Hall, D. O.; Rao, K. K. Mossbauer Spectroscopic Evidence for the Conversion of [4Fe-4S] Clusters in *Bacillus stearothermophilus* Ferredoxin Into [3Fe-3S] Clusters. *FEBS Lett.* **1982**, *142* (1), 143–146.
(29) Kent, T. A.; Dreyer, J. L.; Kennedy, M. C. Mossbauer Studies of Beef Heart Aconitase: Evidence for Facile Interconversions of Iron Sulfur Clusters. *Proc. Natl. Acad. Sci. U. S. A.* **1982**, *79* (4), 1096–1100.
(30) Moura, J. J. G.; Moura, I.; Kent, T. A.; Lipscomb, J. D.; Huynh, B. H.; LeGall, J.; Xavier, A. V.; Münck, E. Interconversions of [3Fe-3S] and [4Fe-4S] Clusters. Mossbauer and Electron Paramagnetic Resonance Studies of *Desulfovibrio gigas* Ferredoxin II. *J. Biol. Chem.* **1982**, *257* (11), 6259–6267.
(31) Bruschi, M.; Guerlesquin, F. Structure, Function, and Evolution of Bacterial Ferredoxins. *FEMS Microbiol. Rev.* **1988**, *54*, 155–176.
(32) Beinert, H.; Kennedy, M. C.; Stout, C. D. Aconitase as Iron−Sulfur Protein, Enzyme, and Iron-Regulatory Protein. *Chem. Rev.* **1996**, *96* (7), 2335–2374.
(33) Crack, J. C.; Le Brun, N. E. Redox-Sensing Iron-Sulfur Cluster Regulators. *Antioxidants Redox Signal.* **2018**, *29* (18), 1809–1829.
(34) Johnson, M. K.; Smith, A. D. Iron-Sulfur Proteins. In *Encyclopedia of Inorganic*

Chemistry; John Wiley & Sons, Ltd, 2006.
(35) Huynh, B. H.; Moura, J. J.; Moura, I.; Kent, T. A.; LeGall, J.; Xavier, A. V.; Münck, E. Evidence for a Three-Iron Center in a Ferredoxin from *Desulfovibrio gigas*. Mössbauer and EPR Studies. *J. Biol. Chem.* **1980**, *255* (8), 3242–3244.
(36) Zhengguo, H.; Jollie, D.; Burgess, B. K.; Stephens, P. J.; Münck, E. Möessbauer and EPR Studies of *Azotobacter vinelandii* Ferredoxin I. *Biochemistry* **1994**, *33* (48), 14475–14485.
(37) Macedo, A. L.; Moura, I.; Surerus, K. K.; Papaefthymiou, V.; Liu, M. Y.; LeGall, J.; Münck, E.; Moura, J. J. G. Thiol/Disulfide Formation Associated with the Redox Activity of the [Fe_3S_4] Cluster of *Desulfovibrio gigas* Ferredoxin II. ^{1}H NMR and Mossbauer Spectroscopic Study. *J. Biol. Chem.* **1994**, *269* (11), 8052–8058.
(38) Kent, T. A.; Huynh, B. H.; Münck, E. Iron-Sulfur Proteins: Spin-Coupling Model for Three-Iron Clusters. *Proc. Natl. Acad. Sci. U. S. A.* **1980**, *77* (11), 6574–6576.
(39) Papaefthymiou, V.; Girerd, J. J.; Moura, I.; Moura G, J.; Münck, E. Mossbauer Study of *D. Gigas* Ferredoxin II and Spin-Coupling Model for the Fe_3S_4 Cluster with Valence Delocalization. *J. Am. Chem. Soc.* **1987**, *109* (15), 4703–4710.
(40) Sanakis, Y.; Macedo, A. L.; Moura, I.; Moura, J. J. G.; Papaefthymiou, V.; Münck, E. Evidence for Antisymmetric Exchange in Cuboidal [3Fe-4S]$^+$ Clusters *J. Am. Chem. Soc.* **2000**, *122* (48), 11855–11863.
(41) Boudalis, A. K. Half-Integer Spin Triangles: Old Dogs, New Tricks. *Chem. Eur. J.* **2021**, *27* (24), 7022–7042.
(42) Schipke, C. G.; Goodin, D. B.; McRee, D. E.; Stout, C. D. Oxidized and Reduced *Azotobacter vinelandii* Ferredoxin I at 1.4 Å Resolution: Conformational Change of Surface Residues without Significant Change in the [3Fe-4S]$^{(+/0)}$ Cluster. *Biochemistry* **1999**, *38* (26), 8228–8239.
(43) Stout, C. D.; Stura, E. A.; McRee, D. E. Structure of *Azotobacter vinelandii* 7Fe Ferredoxin at 1.35 Å Resolution and Determination of the [Fe-S] Bonds with 0.01 Å Accuracy. *J. Mol. Biol.* **1998**, *278* (3), 629–639.
(44) Stout, C. D. Crystal Structures of Oxidized and Reduced *Azotobacter vinelandii* Ferredoxin at pH 8 and 6. *J. Biol. Chem.* **1993**, *268* (34), 25920–25927.
(45) Here, we include only structures of [Fe_3S_4] clusters with relatively high (better than 1.5 Å) resolution and for which the oxidation state of the cluster is clearly established. In the case of [Fe_3S_4]$^+$ clusters, the authors have conducted EPR experiments to address the possibility of photoreduction upon X-ray irradiation and have demonstrated that the [Fe_3S_4]$^+$ cluster remains in the oxidized state.
(46) Deng, L.; Holm, R. H. Stabilization of Fully Reduced Iron-Sulfur Clusters by Carbene Ligation: The [Fe_nS_n]^0 Oxidation Levels (n = 4, 8). *J. Am. Chem. Soc.* **2008**, *130* (30), 9878–9886.
(47) Brown, A. C.; Suess, D. L. M. Controlling Substrate Binding to Fe_4S_4 Clusters through Remote Steric Effects. *Inorg. Chem.* **2019**, *58* (8), 5273–5280.
(48) McSkimming, A.; Suess, D. L. M. Dinitrogen Binding and Activation at a Molybdenum–Iron–Sulfur Cluster. *Nat. Chem.* **2021**, *13* (7), 666–670.
(49) Srisantitham, S.; Badding, E. D.; Suess, D. L. M. Postbiosynthetic Modification of a Precursor to the Nitrogenase Iron-Molybdenum Cofactor. *Proc. Natl. Acad. Sci. U. S. A.* **2021**, *118* (11), 1–6.
(50) Badding, E. D.; Srisantitham, S.; Lukoyanov, D. A.; Hoffman, B. M.; Suess, D. L. M. Connecting the Geometric and Electronic Structures of the Nitrogenase Iron-Molybdenum Cofactor through Site-Selective Labeling. *Chemrxiv* **2022**. https://doi.org/10.26434/chemrxiv-2022-m57j9.
(51) Brown, A. C.; Suess, D. L. M. Valence Localization in Alkyne and Alkene Adducts of

Synthetic $[Fe_4S_4]^+$ Clusters. *Inorg. Chem.* **2022**. https://doi.org/10.1021/acs.inorgchem.2c01353.
(52) Brown, A. C.; Thompson, N. B.; Suess, D. L. M. Evidence for Low-Valent Electronic Configurations in Iron−Sulfur Clusters. *J. Am. Chem. Soc.* **2022**, *144* (20), 9066–9073.
(53) Pandelia, M. E.; Lanz, N. D.; Booker, S. J.; Krebs, C. Mössbauer Spectroscopy of Fe/S Proteins. *Biochim. Biophys. Acta - Mol. Cell Res.* **2015**, *1853* (6), 1395–1405.
(54) Zhang, B.; Arcinas, A. J.; Radle, M. I.; Silakov, A.; Booker, S. J.; Krebs, C. First Step in Catalysis of the Radical S-Adenosylmethionine Methylthiotransferase MiaB Yields an Intermediate with a $[3Fe\text{-}4S]^0$-Like Auxiliary Cluster. *J. Am. Chem. Soc.* **2020**, *142* (4), 1911–1924.

Supporting information:

A. Experimental Methods

General Considerations

All reactions were performed using standard Schlenk techniques or in an LC Technologies inert atmosphere glove box under an N_2 atmosphere. Glassware was dried in an oven at 160 °C prior to use. Molecular sieves (3 Å), and Celite® were activated by heating to 300 °C overnight under vacuum prior to storage under an atmosphere of nitrogen. *O*-difluorobenzene (DFB) was distilled from CaH_2, C_6D_6 was degassed by three freeze–pump–thaw cycles, and other solvents were degassed by sparging with argon and dried by passing through a column of activated alumina. All solvents were stored under an N_2 atmosphere over 3 Å molecular sieves.

NMR spectra were recorded on Bruker 400 and 500 MHz spectrometers. ^{1}H chemical shifts are given relative to residual solvent peaks; spectra in DFB and Et_2O are referenced to the triplet of residual *n*-pentane at 0.89 ppm. Solvent suppression for NMR in protonated solvents was carried out using WET solvent suppression.[1] FT-IR samples were taken as thin films using a Bruker Alpha Platinum ATR spectrometer with OPUS software in a glovebox under an N_2 atmosphere. EPR spectra were recorded on a Bruker EMX spectrometer at 9.37 GHz (perpendicular mode) as frozen glasses. Simulations were performed using EasySpin[2] (5.2.21) in Matlab (R2017b). UV-vis spectra were recorded on a Cary 50 spectrometer. Zero-field ^{57}Fe Mössbauer spectra were measured with a constant-acceleration spectrometer at 80 K using a SEE co. W302 constant-acceleration spectrometer. Isomer shifts are quoted relative to α-Fe foil at room temperature; Mössbauer spectra were simulated with WMOSS v.4.[3] SQUID magnetometry data was collected on solid microcrystalline samples immobilized in gel capsules using icosane on a Quantum Design MPMS3 SQUID magnetometer in the range of 2–300 K with a 0.5 T applied field. Electrochemical experiments were performed using a GAMRY Reference 600 potentiostat with a glassy carbon working electrode, a Ag wire

auxiliary electrode, and a Ag wire pseudoreference electrode. The electrolyte, [TPA][BAr^F_4], (TPA = tetra-*n*-propylammonium) was prepared according to literature procedures[4] and recrystallized twice from Et_2O/*n*-pentane prior to use. Elemental analyses were performed at Midwest Microlab. X-ray structural determinations were performed at the MIT diffraction facility using a Bruker X8 diffractometer with an APEX II CCD detector or a Bruker D8 Venture diffractometer with a Photon2 CPAD detector. Diffraction data was collected, integrated, and corrected for absorption using Bruker APEX3 software and its associated modules (SAINT, SADABS, TWINABS). Structural solutions and refinements (on F^2) were carried out using SHELXT and SHELXL-2018 in ShelXle.[5] Ellipsoid plots and figures were made using Mercury 2021.2.0.

$(IMes)_3Fe_4S_4Cl$,[6] Na[BAr^F_4],[7] and [Cp_2Fe][PF_6][8] were prepared according to literature procedures.

Statement on Compound Purity

The purity of all compounds was assessed by a variety of spectroscopic and analytical methods as detailed below. Compounds **1**, [**1**][PF_6] and [**1**][BAr^F_4] are air-sensitive but can be isolated as crystalline solids in high purity as determined by NMR, EPR, and Mössbauer spectroscopic analysis as well as H and N content from elemental analysis. Low C content was obtained by elemental analysis as has been observed for other members of this class of molecules[9–12] and in other contexts.[13] Elemental analysis results are as follows: [**1**][BAr^F_4]: Anal. Found: C, 54.02; H, 4.27; N, 4.04. Calcd. for $C_{95}H_{84}N_6Fe_3S_4BF_{24}\cdot(C_4H_{10}O)$: C, 55.40; H, 4.41; N, 3.92; **1**: Anal. Found: C, 57.07; H, 5.50; N, 6.41. Calcd. for $C_{63}H_{72}N_6Fe_3S_4\cdot(C_6H_4F_2)$: C, 62.63; H, 5.79; N, 6.35. Compound [**1**][PF_6] is typically contaminated with small amounts of [$(IMes)_3Fe_4S_4Cl$][PF_6] as measured by NMR

spectroscopy, but is reported here because it is a useful synthon for the synthesis of pure **1** and [**1**][BAr^F_4].

[$(IMes)_3Fe_4S_4Cl$][PF_6]

This compound was prepared using a modification of the procedure reported for [$(IMes)_3Fe_4S_4Cl$][BAr^F_4].[11] $(IMes)_3Fe_4S_4Cl$ (1.17 g, 0.900 mmol) was dissolved in DFB (40 mL). A suspension of [Cp_2Fe][PF_6] (298 mg, 0.900 mmol) in DFB (10 mL) was added dropwise. The mixture was stirred for 30 min, filtered through Celite, and concentrated to a volume of 20 mL. The product was precipitated by addition of hexanes (80 mL). The solids were collected on a frit and washed thoroughly with hexanes (3 x 10 mL) followed by benzene (3 x 5 mL) to remove Cp_2Fe and residual $(IMes)_3Fe_4S_4Cl$. Yield: 1.10 g (85%) ^{1}H NMR (400 MHz, DFB, 293 K) δ 6.37 (s, 6H, backbone C*H*), 2.16 (s, 18H, Mes *p*-C*H*$_3$), 2.00 (s, 36H, Mes *o*-C*H*$_3$). The mesityl C*H* resonances are obscured by the suppressed solvent.

[$(IMes)_3Fe_3S_4$][PF_6] ([**1**][PF_6])

[$(IMes)_3Fe_4S_4Cl$][PF_6] (500 mg, 0.346 mmol) was dissolved in DFB (20 mL). This solution was added rapidly to a stirring suspension of KTp (183 mg, 0.726 mmol, 2.1 equiv) in DFB (10 mL). The mixture was stirred for 1 h, then filtered through Celite and the solvent removed *in vacuo*. The black solids were extracted into benzene (50 mL), the solution was filtered through Celite to remove any remaining [$(IMes)_3Fe_4S_4Cl$][PF_6] and KTp, and the solvent removed *in vacuo.* The black solids were dissolved in DFB (20 mL) and a suspension of [Cp_2Fe][PF_6] (103 mg, 0.311 mmol, 0.9 equiv) in DFB (10 mL) was added. The solution was stirred for 5 min and filtered through Celite to remove the precipitate of KPF_6. The solution was concentrated to 20 mL and product was precipitated by addition of hexanes (80

mL). The solids were collected on a frit and washed with hexanes (3 x 10 mL), Et_2O (3 x 10 mL), and THF (3 x 5 mL) to remove Cp_2Fe and Tp_2Fe. Compound [**1**][PF_6] was typically contaminated with small amounts (≤ 10%) of [$(IMes)_3Fe_4S_4Cl$][PF_6] or, putatively, [$(IMes)_3Fe_4S_4Tp$][PF_6] but is a useful precursor for synthesis of [$(IMes)_3Fe_3S_4$][$BAr^F{}_4$] and $(IMes)_3Fe_3S_4$. Yield: 220 mg (total mass, corresponding to approximately 47% molar yield of [**1**][PF_6] accounting for ~10% [$(IMes)_3Fe_4S_4Cl$][PF_6]). ^{1}H NMR (400 MHz, DFB, 293 K) δ 6.82 (s, 6H, backbone C*H*), 6.77 (s, 12H, Mes *m*-C*H*) 2.32 (s, 18H, Mes *p*-C*H*$_3$), 2.04 (s, 36H, Mes *o*-C*H*$_3$). Representative NMR spectra of [$(IMes)_3Fe_3S_4$][PF_6] are shown in figure S9.2.

[$(IMes)_3Fe_3S_4$][$BAr^F{}_4$] ([**1**][$BAr^F{}_4$])

A solution of $NaBAr^F{}_4$ (29.5 mg, 0.0332 mmol, 0.9 equiv) in DFB was added to a solution of [**1**][PF_6] (50.0 mg, 0.0369 mmol) in DFB and the mixture was stirred for 5 min. The solvent was removed *in vacuo* and the product was extracted into Et_2O and filtered through Celite. The Et_2O solution was concentrated to 1 mL and *n*-pentane (9 mL) was added to precipitate the product. Yield: 49.7 mg (72%, based on limiting $NaBAr^F{}_4$). ^{1}H NMR (400 MHz, Et_2O, 293 K) δ 7.72 (s, 8H, [$BAr^F{}_4$]$^-$), 7.49 (s, 4H, [$BAr^F{}_4$]$^-$), 7.24 (s, 6H, backbone C*H*), 6.82 (s, 12H, Mes *m*-C*H*) 2.33 (s, 18H, Mes *p*-C*H*$_3$), 1.97 (s, 36H, Mes *o*-C*H*$_3$). EPR: $g_\parallel$ = 2.06, $g_\perp$ ~ 1.87 (5 K, 250 μW, 9.37 GHz). UV-vis (Et_2O) λ (nm) (ε (M^{-1} cm^{-1})) 344 (94200), 521 (23000). FT-IR (thin film, cm^{-1}) 3174 (w), 3142 (w), 3030 (w), 2978 (w), 2953 (w), 2922 (w), 2864 (w), 1610 (m), 1558 (w), 1486 (m) 1442 (w), 1406 (w), 1381 (w), 1354 (s), 1275 (s), 1233 (w), 1163 (m), 1125 (s), 1035 (w), 931 (w), 887 (m), 853 (m), 839 (m), 746 (m), 713 (m), 682 (m), 671 (m), 576 (w). Crystals suitable for X-ray diffraction were grown by layering *n*-pentane onto an Et_2O solution of [**1**][$BAr^F{}_4$] and storage at –35 °C overnight.

$(IMes)_3Fe_3S_4$ (**1**)

$[(IMes)_3Fe_3S_4][PF_6]$ (40.0 mg, 0.0295 mmol) was suspended in benzene (2 mL). A solution of Cp^*_2Co (8.8 mg, 0.027 mmol, 0.9 equiv) in benzene (1 mL) was added dropwise. The mixture was stirred for 20 min and filtered through Celite followed by removal of the solvent *in vacuo*. The solids were redissolved in DFB (0.2 mL) and *n*-pentane (10 mL) was added to precipitate the product. The product was washed with *n*-pentane (3 x 2 mL) and Et_2O (1 x 0.2 mL). Yield: 25.2 mg (78%, based on limiting Cp^*_2Co). ^1H NMR (400 MHz, C_6D_6, 293 K) δ 12.50 (s, 6H, backbone C*H*), 7.01 (s, 12H, Mes *m*-C*H*) 2.68 (s, 18H, Mes *p*-C*H*$_3$), 1.45 (s, 36H, Mes *o*-C*H*$_3$). Evan's method (C_6D_6, 295 K) μ_{eff} = 4.7 μ_B. UV-vis (Et_2O) λ (nm) (ε (M^{-1} cm^{-1})) 424 (26400), 535 (15100). FT-IR (thin film, cm^{-1}) 3130 (w), 3087 (w), 3075 (w), 3031 (m), 2967 (m), 2946 (m), 2914 (m), 2856 (m), 2734 (w), 1609 (m), 1555 (w), 1487 (s), 1440 (m), 1397 (m), 1377 (m), 1309 (m), 1269 (m), 1227 (m), 1162 (w), 1095 (w), 1076 (w), 1034 (m), 963 (w), 929 (m), 847 (s), 731 (m), 680 (s), 575 (m). Crystals suitable for X-ray diffraction were grown from the crude reaction mixture when $[(IMes)_3Fe_3S_4][PF_6]$ was reduced with 1.1 equiv Cp_2Co in DFB at room temperature. The reaction mixture was then filtered, layered with *n*-pentane, and stored at – 35 °C overnight.

B. NMR Spectra

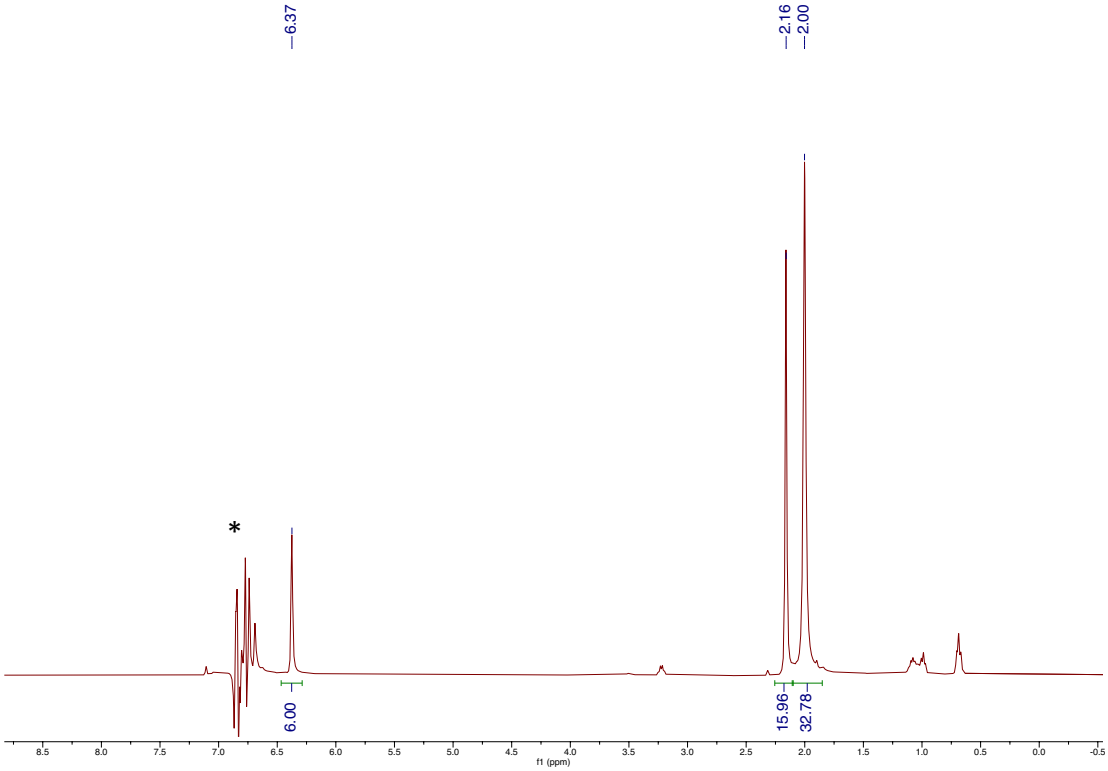

Figure S9.1: ^{1}H NMR spectrum of $[(IMes)_3Fe_4S_4Cl][PF_6]$ in DFB at 293 K. (*) Residual signal from suppressed ^{1}H resonances of the solvent

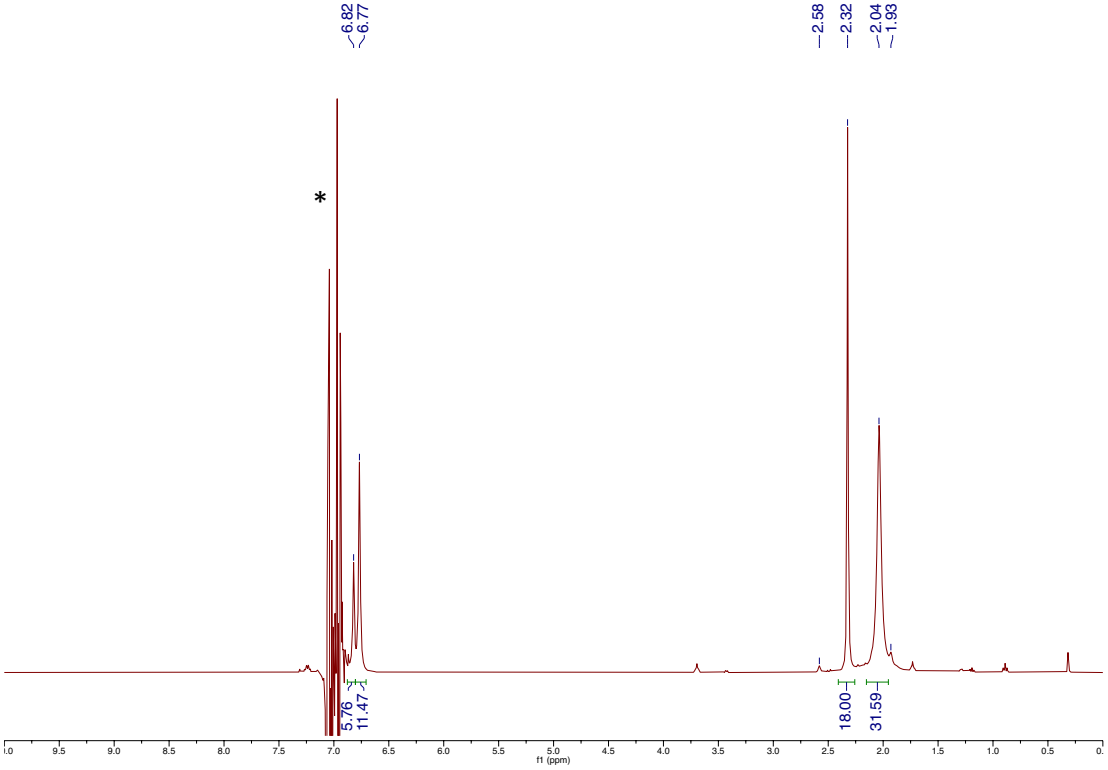

Figure S9.2: Representative ^{1}H NMR spectrum of as-prepared $[(IMes)_3Fe_3S_4][PF_6]$ ([**1**][PF_6]) in DFB at 293 K. Small amounts of putative $[(IMes)_3Fe_4S_4(Tp)][PF_6]$ are visible at 2.58 and 1.93 ppm. (*) Residual signal from suppressed ^{1}H resonances of the solvent

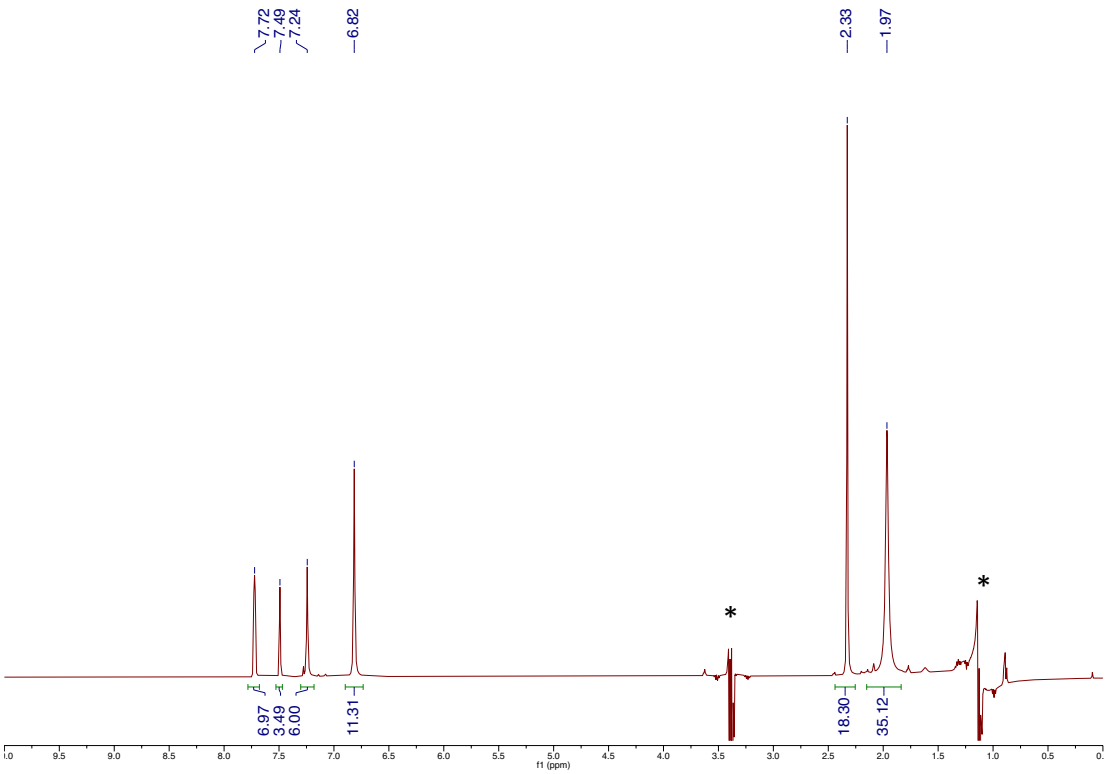

Figure S9.3: ^{1}H NMR spectrum of [(IMes)$_3$Fe$_3$S$_4$][BAr$^F_4$] ([**1**][BAr$^F_4$]) in DFB at 293 K. (*) Residual signal from suppressed ^{1}H resonances of the solvent

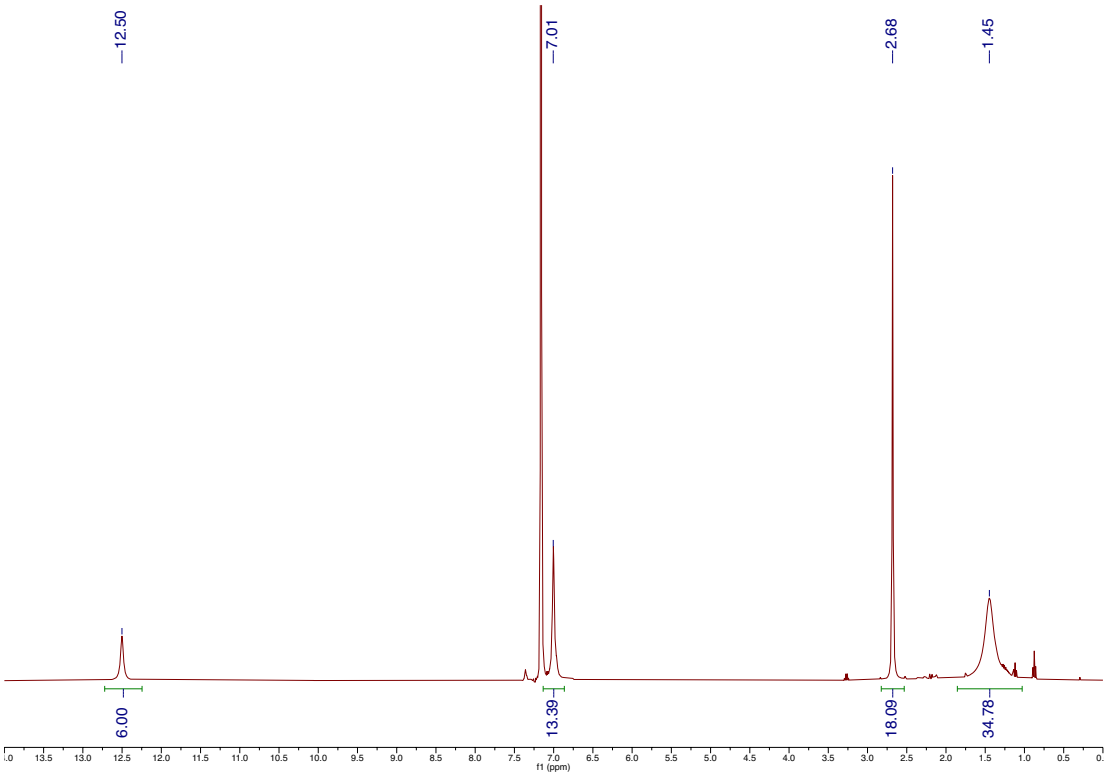

Figure S9.4: ^{1}H NMR spectrum of (IMes)$_3$Fe$_3$S$_4$ (**1**) in C_6D_6 at 293 K.

C. Abstraction of Fe^{2+} by KTp from $[(IMes)_3Fe_4S_4Cl][PF_6]$.

Addition of one equiv. KTp to $[(IMes)_3Fe_4S_4Cl][PF_6]$ in DFB immediately produced the NMR spectrum shown in blue (top) in figure S9.5. The spectrum contains resonances derived from the starting material, $[(IMes)_3Fe_4S_4Cl][PF_6]$, (dotted open circles) as well as small amounts of Tp_2Fe (black circles). Additionally, a new product (red circles) is apparent, which is tentatively assigned as $[(IMes)_3Fe_4S_4Tp][PF_6]$. Upon addition of a second equiv. KTp, the amounts of Tp_2Fe and **1**·KPF_6 increase and the amounts of $[(IMes)_3Fe_4S_4Cl][PF_6]$ and $[(IMes)_3Fe_4S_4Tp][PF_6]$ decrease. After 30 minutes, no $[(IMes)_3Fe_4S_4Cl][PF_6]$ and $[(IMes)_3Fe_4S_4Tp][PF_6]$ remain and the mixture has converted the products of the Fe abstraction reaction, Tp_2Fe and **1**·KPF_6. On the basis of the resonances marked with red circles appearing at early time points and with a subcess of KTp and disappearing upon addition of excess KTp, we assign this species tentatively as $[(IMes)_3Fe_4S_4Tp][PF_6]$, an expected intermediate in the abstraction of Fe^{2+}. This species is always formed as a mixture with $[(IMes)_3Fe_4S_4Cl][PF_6]$, Tp_2Fe and **1**·KPF_6, we have been unable to isolate and further characterize it.

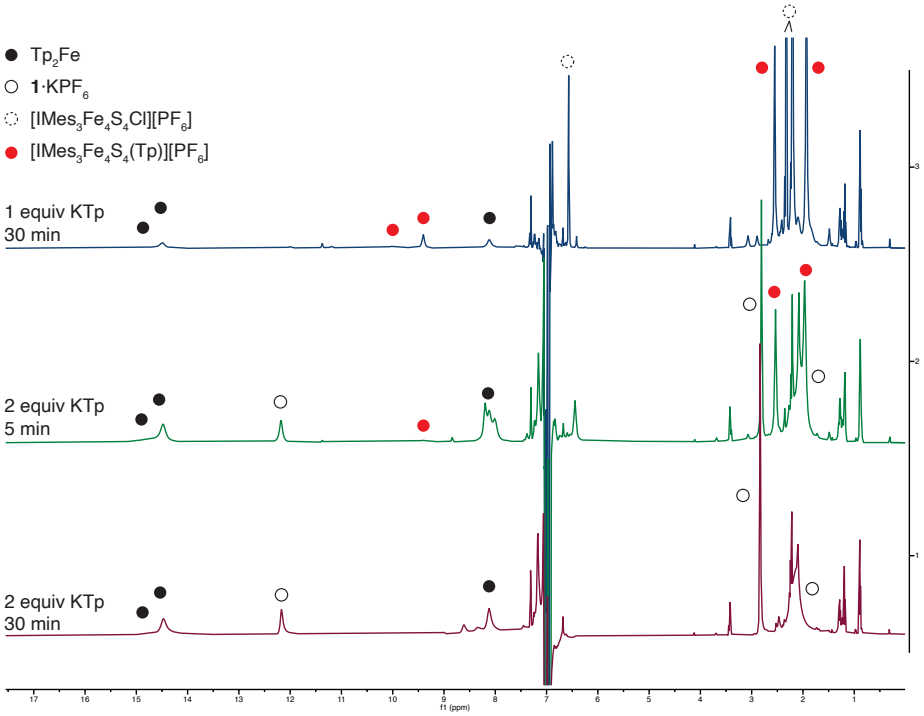

Figure S9.5: ^1H NMR spectra tracking the addition of KTp to $[(IMes)_3Fe_4S_4Cl][PF_6]$. (Top) 1 equiv. KTp, 30 min. (Middle) 2 equiv of KTp, 5 min. (Bottom) 2 equiv. of KTp, 30 min.

D. IR Spectra

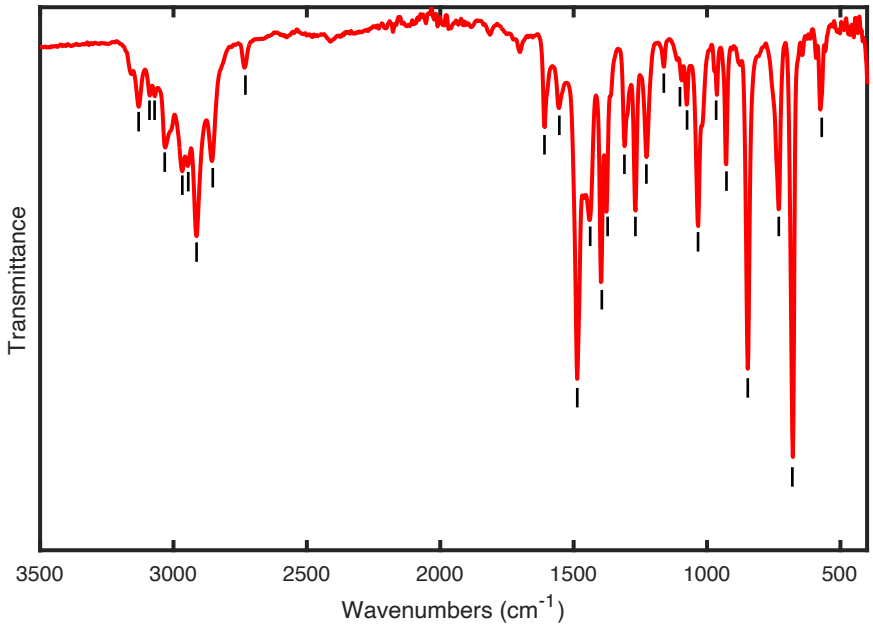

Figure S9.6: IR spectrum of $(IMes)_3Fe_3S_4$ (**1**) (thin film, cm^{-1}) 3130 (w), 3087 (w), 3075 (w), 3031 (m), 2967 (m), 2946 (m), 2914 (m), 2856 (m), 2734 (w), 1609 (m), 1555 (w), 1487 (s), 1440 (m), 1397 (m), 1377 (m), 1309 (m), 1269 (m), 1227 (m), 1162 (w), 1095 (w), 1076 (w), 1034 (m), 963 (w), 929 (m), 847 (s), 731 (m), 680 (s), 575 (m).

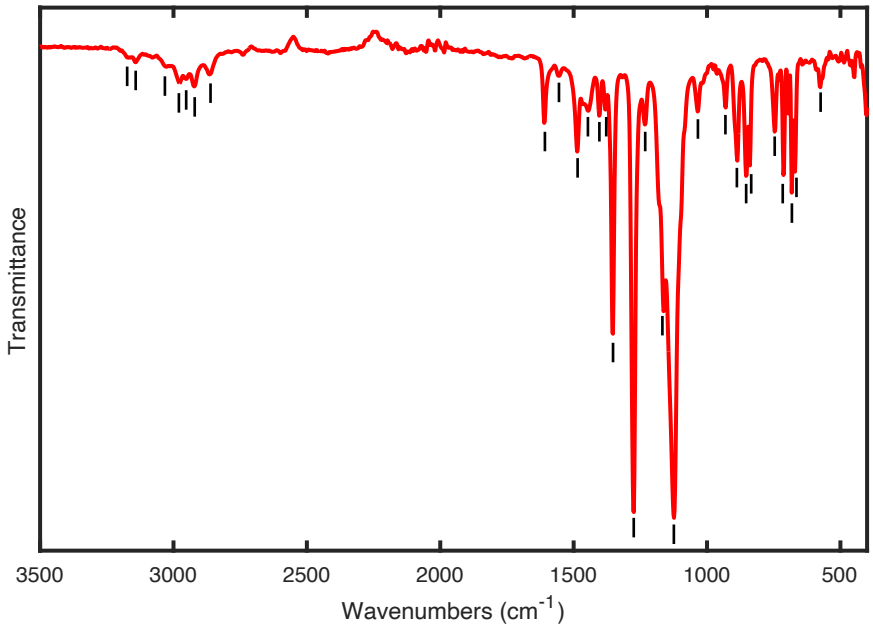

Figure S9.7: IR spectrum of $[(IMes)_3Fe_3S_4][BAr^F{}_4]$ ([**1**][$BAr^F{}_4$]) (thin film, cm^{-1}) 3174 (w), 3142 (w), 3030 (w), 2978 (w), 2953 (w), 2922 (w), 2864 (w), 1610 (m), 1558 (w), 1486 (m) 1442 (w), 1406 (w), 1381 (w), 1354 (s), 1275 (s), 1233 (w), 1163 (m), 1125 (s), 1035 (w), 931 (w), 887 (m), 853 (m), 839 (m), 746 (m), 713 (m), 682 (m), 671 (m), 576 (w)

E. UV-Vis Spectra

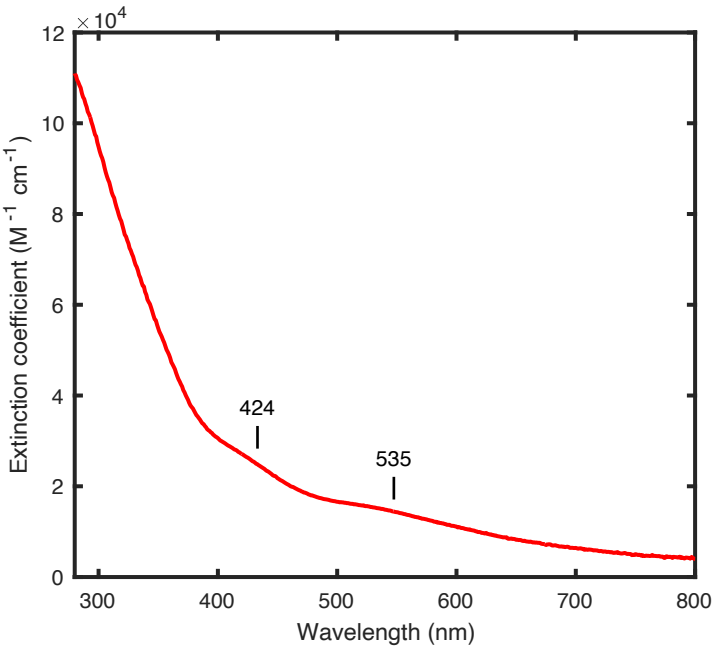

Figure S9.8: UV-Vis spectrum of $(IMes)_3Fe_3S_4$ (**1**) in Et_2O.

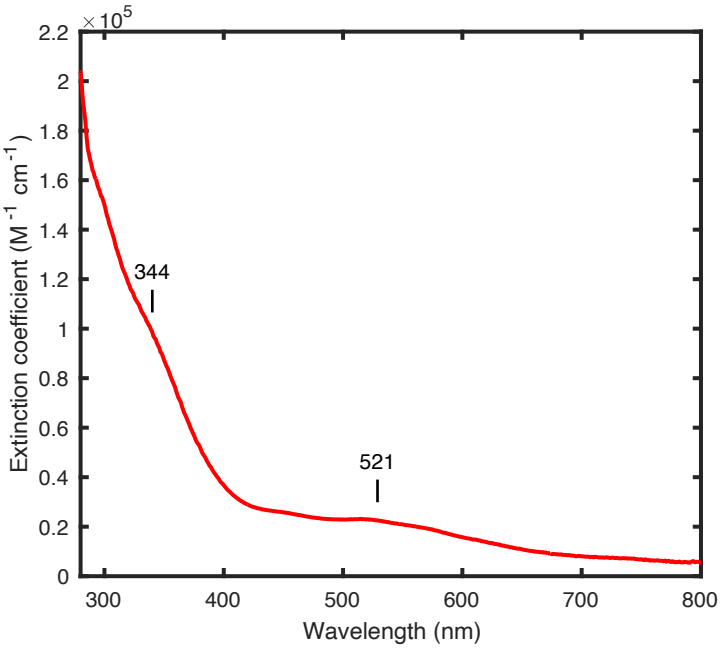

Figure S9.9: UV-Vis spectrum of $[(IMes)_3Fe_3S_4][BAr^F_4]$ ([**1**][BAr^F_4]) in Et_2O.

F. SQUID magnetometry

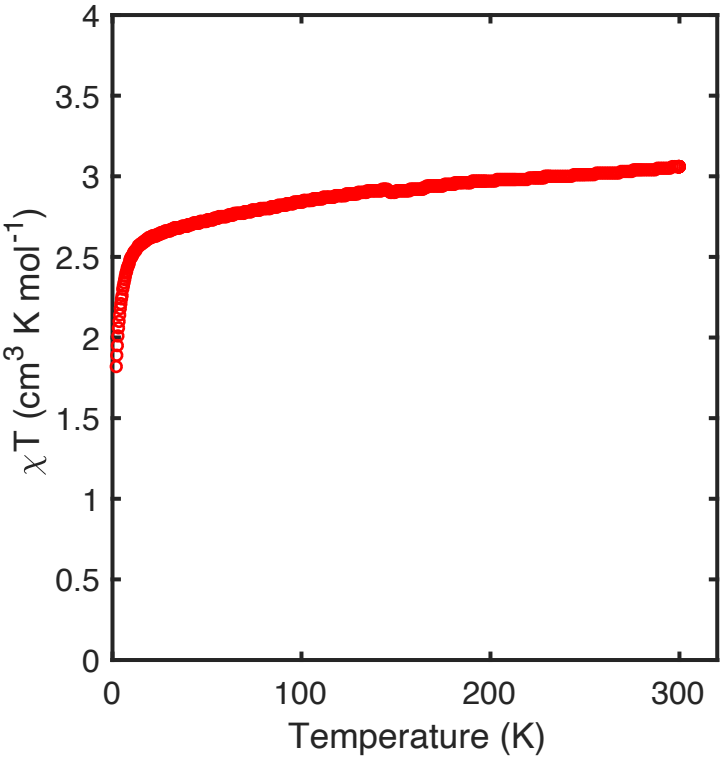

Figure S9.10: SQUID magnetometry data (χT vs. T) for **1** collected at a field of 0.5 T. Data are corrected for diamagnetic contributions using Pascal's constants. The value of χT (between 2.7 and 3.1 cm^3 K mol^{-1}) is close to the expectation value for an $S = 2$ system (3.0 cm^3 K mol^{-1}). The flat slope of χT vs T between 25 and 300 K is indicative of a well-isolated $S = 2$ ground spin state and consistent with the magnetic moment from Evan's method ($\mu_{eff} = 4.7\ \mu_B$)

G. Cyclic Voltammetry

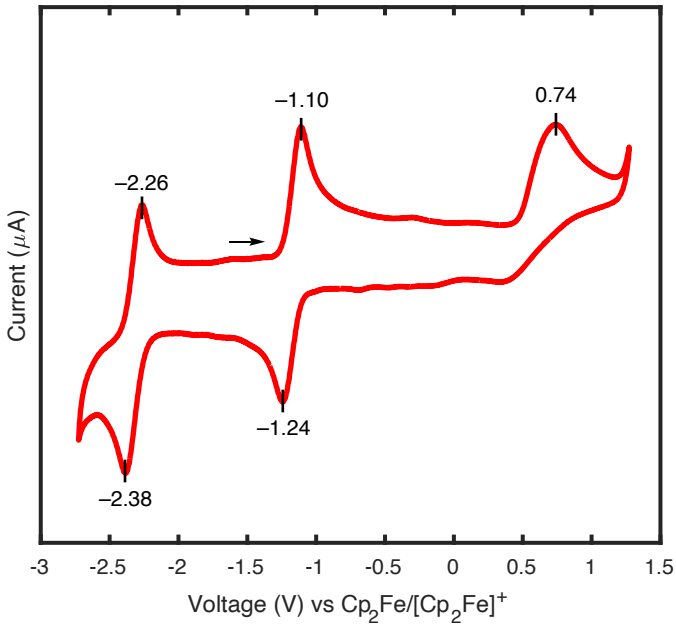

Figure S9.11: Cyclic voltammogram of **1** in DFB with 0.2 M TPABAr$^{F}_{4}$ using a glassy carbon working electrode, a silver wire counter electrode, and a silver wire reference electrode at a scan rate of 200 mv/s. Compound **1** undergoes a reduction at –2.32 V and an oxidation to [**1**]$^{+}$ at –1.17 V vs Fc/Fc^{+}.

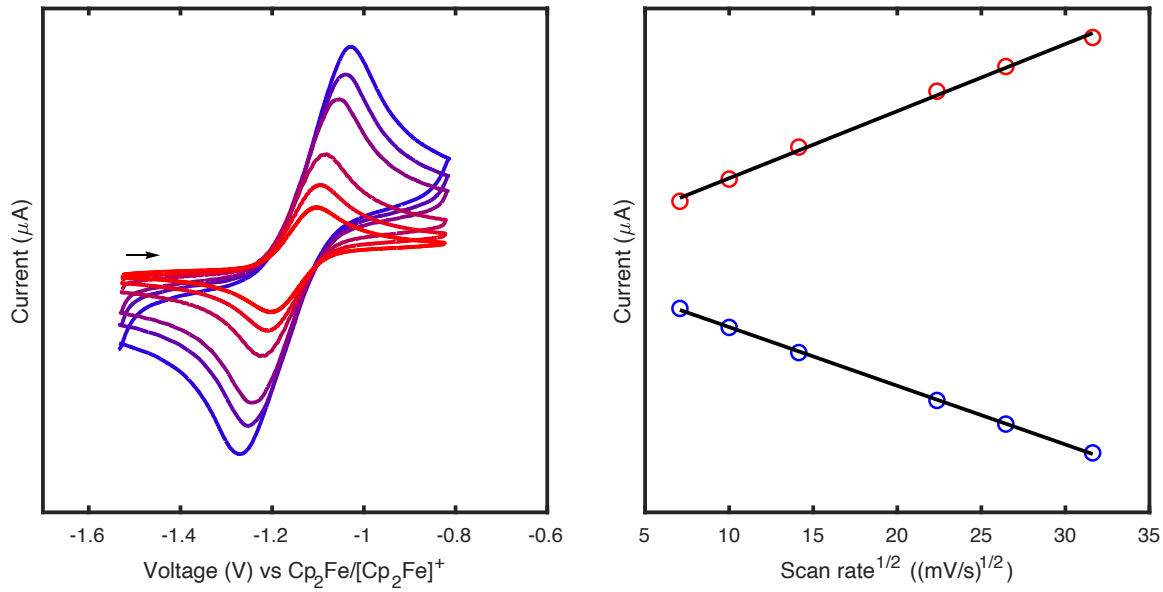

Figure S9.12: Cyclic voltammogram of **1** in DFB with 0.2 M TPABAr$^{F}_{4}$ showing the scan rate dependence of the oxidation of **1** to [**1**][BAr$^{F}_{4}$]. (Left) Cyclic voltammograms from 50 to 1000 mV/s. (Right) Plot showing current vs. square root of the scan rate for the oxidation event.

Mossbauer fitting parameters

Table S9.1: Tabulated parameters for fitting the Mössbauer spectrum of **1**

Site	δ (mm s^{-1})	$\lvert\Delta E_Q\rvert$ (mm s^{-1})	Γ (mm s^{-1})	Rel. area
1	0.279	0.682	0.293	1
2	0.420	1.520	0.262	1
3	0.397	1.243	0.413	1

Table S9.2: Tabulated parameters for fitting the Mössbauer spectrum of [**1**]$^+$

Site	δ (mm s^{-1})	$\lvert\Delta E_Q\rvert$ (mm s^{-1})	Γ (mm s^{-1})	Rel. area
1	0.222	0.720	0.263	1
2	0.225	1.041	0.327	2

H. Computational Details

General Considerations

All calculations were carried out using version 4.1.2 of the ORCA program package[14] using the broken-symmetry (BS) approach to approximate the multireference electronic states of Fe–S clusters. BS solutions were constructed using the FlipSpin feature of ORCA.

Coordinates for non-H atoms in $[\mathbf{1}]^+$ and **1** were taken from X-ray crystallographic coordinates. To improve the efficiency of the calculations, the mesityl substituents on the IMes ligands were simplified to H. The positions of all H atoms were optimized using the parameters described below and using the BP86 functional.

Single point calculations on $[\mathbf{1}]^+$ and **1** were performed using the TPSSh (10% Hartree-Fock) functional.[15,16] For Fe, S, C, and N atoms, the DKH-def2-TZVP basis set was used;[17] for H atoms, the DKH-def2-SVP basis set was used. For all calculations, the DKH2 relativistic correction[18] and the general-purpose Coulomb fitting basis set SARC/J were used;[19] all basis sets were fully decontracted. Solid-state effects were approximated using the CPCM solvation model with an infinite dielectric.[20] Wavefunctions were optimized along a low-spin BS surface generated from an initial high-spin calculation by flipping the spins on atoms i,j (for $[\mathbf{1}]^+$) or i (for **1)** BS determinants are named as BSij and BSi, respectively. Calculations were accelerated through the use of the RIJCOSX approximation with a fine auxiliary integration grid (GridX7).[21]

To analyze localized orbitals, we employed the intrinsic bond orbital (IBO) method developed by Knizia,[22] which applies Pipek-Mezey localization[23] in a basis of so-called intrinsic atomic orbitals (IAOs) and analyzed the resultant orbitals using a Löwdin population analysis.

Computational Analysis of [**1**]$^{+}$

There are two descriptions of the electronic coupling in $[Fe_3S_4]^{+}$ that produce an overall $S = 1/2$ ground spin state; they consist of a ferric site ($S = 5/2$) antiferromagnetically coupled to the other two ferric sites, with coupled spins of $S = 3$ or $S = 2$ for these two sites.[24] We computed all six BS determinants for [**1**]$^{+}$, flipping either one spin (corresponding to the solutions for which the spin-aligned Fe centers have $S = 3$) or two spins (corresponding to the solutions for which the spin aligned Fe centers have $S = 2$). A qualitative BS-DFT derived molecular orbital diagram for the lowest energy solution are shown in figure S9.13. Because BS-DFT aligns all electrons either parallel or antiparallel with one another, and therefore does not depict spin-canting, canted spins manifest as non-Hund electrons, as seen on Fe2 and Fe3 in BS1. All of the computed energies for solutions in which the isolated Fe^{3+} center is in the minority spin (BS 1,2,3) are within 4 kcal/mol (Table S9.3). Solutions in which the spins two Fe centers were flipped (i.e. BS12, BS13, BS23) either converged to the same state as BS1 or are significantly higher in energy than BS1 (+9.48 kcal/mol). The BS1, BS2, and BS3 solutions describe qualitatively similar electronic structure descriptions, differing in which Fe centers are involved in the $S = 3$ pair.

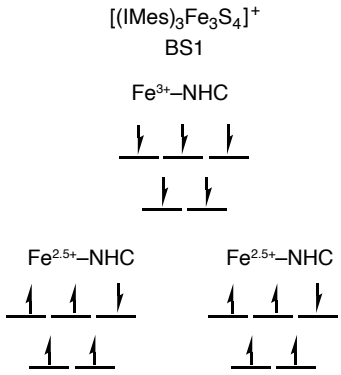

Figure S9.13: Qualitative MO diagram of the BS1 determinant of [**1**]$^{+}$

Table S9.3: Relative energies of computed BS determinants for [**1**]$^{+}$.

Determinant	S = 5/2 site	S = 3 or 2 sites	Rel. energy (kcal/mol)
BS1	Fe1	Fe2/Fe3 (S = 3)	0
BS2	Fe2	Fe1/Fe3 (S = 3)	+3.45
BS3	Fe3	Fe1/Fe2 (S = 3)	+3.02
BS12	Fe3	Fe1/Fe2 (S = 2)	–[a]
BS13	Fe2	Fe1/Fe3 (S = 2)	–[a]
BS23	Fe1	Fe2/Fe3 (S = 2)	+9.48

[a]Converged to the BS1 determinant

Computational Analysis of **1**

The proposed electronic structure for $[Fe_3S_4]^0$ clusters consist of a ferric site (S = 5/2) antiferromagnetically coupled to a spin-aligned mixed-valent pair (S = 9/2). We computed the electronic structure of **1** by constructing the three BS determinants, BS1, BS2, BS3 that could describe this electronic structure, corresponding to flipping the spins on one of the three Fe centers. In each case, the Fe center with minority spin was found to be a localized Fe^{3+} site (S = 5/2), which was antiferromagnetically coupled to a spin-aligned, mixed valent pair of $Fe^{2.5+}$ centers (S = 9/2, Figure S9.13). The determinant in which Fe1 was placed in the minority spin (BS1) was found to be the lowest in energy (Table S9.4), consistent with our assignment based on the contracted bond lengths at Fe1 in the crystal structure.

Table S9.4: Relative energies of computed BS determinants for **1**.

Determinant	Ferric site	Rel. energy (kcal/mol)
BS1	Fe1	0
BS2	Fe2	+4.18
BS3	Fe3	+3.87

I. Crystallographic Details

1·KPF_6: The structure contained solvent accessible voids in which the solvent could not be satisfactorily modeled; SQUEEZE[25] was used to account for the contributions of the disordered solvent to the diffraction data. The KPF_6 moiety and one mesityl group from an NHC ligand were disordered over two positions. The disorder was modeled using similarity restraints on 1-2 and 1-3 distances and displacement parameters and rigid bond restraints. One B-level alert arises in CheckCIF due to disorder of the minor component of the [PF_6] anion. A summary of the Fe–C/S bond lengths is provided in table S9.5 and the structure is shown in figure S9.14

[**1**][$BAr^F{}_4$]: Crystallized in a chiral space group with minor (ca. 2 %) inversion twinning which was refined using the inversion twin law and a BASF parameter. Several –CF_3 groups on the [$BAr^F{}_4$] anion and one mesityl group from an NHC ligand were disordered over two positions. The disorder was modeled using similarity restraints on 1-2 and 1-3 distances and displacement parameters and rigid bond restraints. Two B-level alerts arise in CheckCIF due to disorder of the [$BAr^F{}_4$] anion.

1·Cp_2CoPF_6: Lattice solvent was a mixture of disordered pentane and DFB. The disorder was modeled using similarity restraints on 1-2 and 1-3 distances and displacement parameters and rigid bond restraints.

1 in R–3c: The structure contained solvent accessible voids in which the solvent could not be satisfactorily modeled; SQUEEZE[25] was used to account for the contributions of the disordered solvent to the diffraction data. The molecule crystallizes in the rhombohedral space group R–3c with the [Fe_3S_4] cluster on the three-fold rotation axis with 1 Fe atom, 1.33 S atoms, and 1 IMes ligand in the asymmetric unit. The crystallographic symmetry leads to severe disorder of

the entire molecule. This disorder was modeled with similarity restraints on displacement parameters and rigid bond restraints on the entire molecule and by splitting the asymmetric unit into three parts, each consisting of one Fe, one IMes and one μ_2–S. Each component was restrained to 33% occupancy, reflecting the envisioned disorder of three inequivalent Fe centers over a C_3 axis. Even after modeling this disorder, the refinement was unsatisfactory based on large thermal displacement parameters (Figure S9.15) and unreasonable core Fe–S bond lengths (> 2.35 Å and < 2.10 Å). For this reason, although the connectivity in the structure of **1** is unambiguous, we do not discuss the structural parameters further.

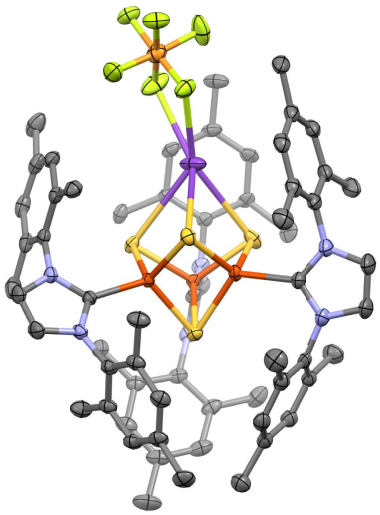

Figure S9.14: Crystallographic structure of **1**·KPF_6. Coloring scheme as in the main text. Ellipsoids at the 50% probability level.

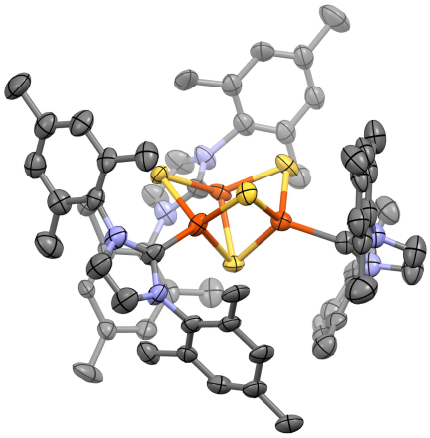

Figure S9.15: Crystallographic structure of **1** in space group R–3c. Coloring scheme as in the main text. Ellipsoids at the 50% probability level.

Table S9.5: Select bond lengths in **1**·KPF_6

Bond	Length (Å)
Fe1–S (avg.)	2.2509(7)
Fe2–S (avg.)	2.2367(7)
Fe3–S (avg.)	2.2788(7)
Fe1–C	2.089(1)
Fe2–C	2.080(1)
Fe3–C	2.081(2)
K–S (avg).	3.157(3)

Table S9.6: Comparison of synthetic [Fe_3S_4] cluster structure bond lengths

Bond	**1**	**1·KPF$_6$**	**[1]$^+$**	**[(LS3)Fe$_3$S$_4$]$^{3-}$**
Fe1–S (avg.)	2.2254(7)	2.2509(7)	2.218(1)	2.278(6)
Fe2–S (avg.)	2.2701(8)	2.2367(7)	2.203(1)	2.260(7)
Fe3–S (avg.)	2.2724(7)	2.2788(7)	2.202(1)	2.286(6)
Fe1–Fe2	2.6581(3)	2.6859(3)	2.6386(5)	2.712(2)
Fe1–Fe3	2.6795(3)	2.6616(3)	2.6422(5)	2.665(2)
Fe2–Fe3	2.6337(3)	2.6586(3)	2.6202(5)	2.731(2)

Table S9.7: Comparison of synthetic [Fe_3S_4] cluster structure bond angles

Bond	**1**	**1·KPF$_6$**	**[1]$^+$**	[(LS3)Fe_3S_4]$^{3-}$
μ_2S-Fe-μ_2S (avg).	113.88(2) °	112.83(7) °	109.1(1) °	112.6(2) °
μ_2S-Fe-μ_3S (avg).	104.16(2) °	103.85(9) °	104.0(2) °	104.0(2) °
Fe-μ_2S-Fe (avg).	72.99(2) °	73.72(2) °	74.26(3) °	73.5(1) °
Fe-μ_3S-Fe (avg).	70.61(2) °	71.18(2) °	71.33(3) °	71.8(1) °

J. References

(1) Smallcombe, S. H.; Patt, S. L.; Keifer, P. A. WET Solvent Suppression and Its Applications to LC NMR and High-Resolution NMR Spectroscopy. *J. Magn. Reson. Ser. A* **1995**, *117* (2), 295–303.

(2) Stoll, S.; Schweiger, A. EasySpin, a Comprehensive Software Package for Spectral Simulation and Analysis in EPR. *J. Magn. Reson.* **2006**, *178* (1), 42–55.

(3) Prisecaru, I. WMOSS4 Mössbauer Spectral Analysis Software, www.wmoss.org.

(4) Thomson, R. K.; Scott, B. L.; Morris, D. E.; Kiplinger, J. L. Synthesis, Structure, Spectroscopy and Redox Energetics of a Series of Uranium(IV) Mixed-Ligand Metallocene Complexes. *Comptes Rendus Chim.* **2010**, *13* (6–7), 790–802.

(5) Hübschle, C. B.; Sheldrick, G. M.; Dittrich, B. ShelXle: A Qt Graphical User Interface for SHELXL. *J. Appl. Crystallogr.* **2011**, *44* (6), 1281–1284.

(6) Brown, A. C.; Suess, D. L. M. Controlling Substrate Binding to Fe_4S_4 Clusters through Remote Steric Effects. *Inorg. Chem.* **2019**, *58* (8), 5273–5280.

(7) Yakelis, N. A.; Bergman, R. G. Safe Preparation and Purification of Sodium Tetrakis[(3,5-Trifluoromethyl) Phenyl]Borate ($NaBArF_{24}$): Reliable and Sensitive Analysis of Water in Solutions of Fluorinated Tetraarylborates. *Organometallics* **2005**, *24* (14), 3579–3581.

(8) Connelly, N. G.; Geiger, W. E. Chemical Redox Agents for Organometallic Chemistry. *Chem. Rev.* **1996**, *96* (2), 877–910.

(9) Sridharan, A.; Brown, A. C.; Suess, D. L. M. A Terminal Imido Complex of an Iron–Sulfur Cluster. *Angew. Chem. Int. Ed.* **2021**, *60* (23), 12802–12806.

(10) McSkimming, A.; Suess, D. L. M. Dinitrogen Binding and Activation at a Molybdenum–Iron–Sulfur Cluster. *Nat. Chem.* **2021**, *13* (7), 666–670.

(11) Brown, A. C.; Suess, D. L. M. Valence Localization in Alkyne and Alkene Adducts of Synthetic $[Fe_4S_4]^+$ Clusters. *Inorg. Chem.* **2022**. https://doi.org/10.1021/acs.inorgchem.2c01353.

(12) Kim, Y.; Sridharan, A.; Suess, D. L. M. The Elusive Mononitrosylated $[Fe_4S_4]$ Cluster in Three Redox States. *Angew. Chem. Int. Ed.* **2022**.

(13) Kuveke, R. E. H. H.; Barwise, L.; Ingen, Y. Van; Vashisth, K.; Roberts, N.; Chitnis, S. S.; Dutton, J. L.; Martin, C. D.; Melen, R. L. An International Study Evaluating Elemental Analysis. *ACS Cent. Sci.* **2022**, *8* (7), 855–863.

(14) Neese, F. The ORCA Program System. *Wiley Interdiscip. Rev. Comput. Mol. Sci.* **2012**, *2* (1), 73–78.

(15) Tao, J.; Perdew, J. P.; Staroverov, V. N.; Scuseria, G. E. Climbing the Density Functional Ladder: Nonempirical Meta–Generalized Gradient Approximation Designed for Molecules and Solids. *Phys. Rev. Lett.* **2003**, *91* (14), 3–6.

(16) Staroverov, V. N.; Scuseria, G. E.; Tao, J.; Perdew, J. P. Comparative Assessment of a New Nonempirical Density Functional: Molecules and Hydrogen-Bonded Complexes. *J. Chem. Phys.* **2003**, *119* (23), 12129–12137.

(17) Pantazis, D. A.; Chen, X. Y.; Landis, C. R.; Neese, F. All-Electron Scalar Relativistic Basis Sets for Third-Row Transition Metal Atoms. *J. Chem. Theory Comput.* **2008**, *4* (6), 908–919.

(18) Reiher, M. Relativistic Douglas-Kroll-Hess Theory. *Wiley Interdiscip. Rev. Comput. Mol. Sci.* **2012**, *2* (1), 139–149.

(19) Weigend, F. Accurate Coulomb-Fitting Basis Sets for H to Rn. *Phys. Chem. Chem. Phys.* **2006**, *8* (9), 1057–1065.

(20) Barone, V.; Cossi, M. Conductor Solvent Model. *J. Phys. Chem. A* **1998**, *102* (97), 1995–2001.
(21) Neese, F.; Wennmohs, F.; Hansen, A.; Becker, U. Efficient, Approximate and Parallel Hartree-Fock and Hybrid DFT Calculations. A "chain-of-Spheres" Algorithm for the Hartree-Fock Exchange. *Chem. Phys.* **2009**, *356* (1–3), 98–109.
(22) Knizia, G. Intrinsic Atomic Orbitals: An Unbiased Bridge between Quantum Theory and Chemical Concepts. *J. Chem. Theory Comput.* **2013**, *9* (11), 4834–4843.
(23) Pipek, J.; Mezey, P. G. A Fast Intrinsic Localization Procedure Applicable for Ab Initio and Semiempirical Linear Combination of Atomic Orbital Wave Functions. *J. Chem. Phys.* **1989**, *90* (9), 4916–4926.
(24) Kent, T. A.; Huynh, B. H.; Eckard, M. Iron-Sulfur Proteins: Spin-Coupling Model for Three-Iron Clusters. *Proc. Natl. Acad. Sci. U.S. A.* **1980**, *77* (11), 6574–6576.
(25) Spek, A. L. PLATON SQUEEZE: A Tool for the Calculation of the Disordered Solvent Contribution to the Calculated Structure Factors. *Acta Crystallogr. Sect. C Struct. Chem.* **2015**, *71*, 9–18.